



**HAL**  
open science

# **New pi-conjugated polymers for organic electronics : synthesis and study of materials designed for OFET and/or OLED applications**

Dizheng Liu

► **To cite this version:**

Dizheng Liu. New pi-conjugated polymers for organic electronics : synthesis and study of materials designed for OFET and/or OLED applications. Material chemistry. Sorbonne Université, 2020. English. NNT : 2020SORUS206 . tel-03891062

**HAL Id: tel-03891062**

**<https://theses.hal.science/tel-03891062>**

Submitted on 9 Dec 2022

**HAL** is a multi-disciplinary open access archive for the deposit and dissemination of scientific research documents, whether they are published or not. The documents may come from teaching and research institutions in France or abroad, or from public or private research centers.

L'archive ouverte pluridisciplinaire **HAL**, est destinée au dépôt et à la diffusion de documents scientifiques de niveau recherche, publiés ou non, émanant des établissements d'enseignement et de recherche français ou étrangers, des laboratoires publics ou privés.

# Sorbonne Université

Ecole doctorale Physique et Chimie des Matériaux (ED397)

*Institut Parisien de Chimie Moléculaire (CNRS-UMR8232)*

## **New $\pi$ -conjugated polymers for organic electronics: synthesis and study of materials designed for OFET and/or OLED applications**

Par Dizheng LIU

Thèse de doctorat de Chimie

Dirigée par Dr. David KREHER et Dr. Fabrice MATHEVET

Présentée et soutenue publiquement le 07/12/2020

Devant un jury composé de :

Pr AUBERT Pierre-Henri	Professeur LPPI, CY Cergy Paris Université	Rapporteur
Pr JOUINI Mohamed	Professeur ITODYS, Université Paris-Diderot	Rapporteur
Dr MERY Stéphane	Chercheur CNRS (HDR) IPCMS, Université de Strasbourg	Examineur
Dr LACAZE Emmanuelle	Directrice de Recherche CNRS INSP, Sorbonne Université	Examineur
Pr KREHER David	Professeur Université de Versailles Saint-Quentin	Directeur de thèse
Dr MATHEVET Fabrice	Chercheur CNRS IPCM, Sorbonne Université	Co-Encadrant



## Acknowledgements

This work was performed in the équipe Chimie des Polymère (ECP), at the Institut Parisien de Chimie Moléculaire (IPCM) directed by Dr. BOUTEILLER Laurent, whom I'd like to thank to welcome me in the group.

I would like to express my sincere gratitude to my supervisor Prof. KREHER David and my co-supervisor Dr. MATHEVET Fabrice for their continuous support and encouragement in my Ph.D. study as well as daily life, for their patience, which helped me a lot in the research and writing of this thesis. Besides, I would like to thank Dr. SOSA-VARGAS Lydia, who shared her immense experience in both research and daily life to help me to adapt to life and study in France.

I also want to thank my thesis committee: Prof. AUBERT Pierre-Henri, Dr. MERY Stéphane, Prof. JOUINI Mohamed, as well as Dr. LACAZE Emmanuelle, for their insightful comments and encouragement, but also for the hard question which incited me to widen my research from various perspectives.

I also want to thank Dr. Gaëlle Pembouong for SEC measurement and Claire Troufflard for NMR measurement. I also express my thanks to Dr. HEINRICH Benoît (IPCMS, Université de Strasbourg) for the XRD and SAXS tests and I thank Pohang Accelerator Laboratory (PAL) for allowing us to perform the GIWAXS measurements, MEST and POSTECH for supporting these experiments, Dr. Hyungju Ahn for adjustments and help, and other colleagues from the 9A USAXS beamline for assistance.

My sincere thanks also go to Dr. TENG Teng, Dr. HAN Shuaiyuan, Dr. LI Yan, Dr. AUFRAY Morgan, Dr. BRISSE Romain, Dr. BENCHORA Amina, and my colleagues: LIU Xiao, DU Weiwei, LI Haixia, and FERNEZ Quentin, for their assistance and care in the working and life. I also want to give my thanks to all the friendly members of ECP.

I am grateful for the financial support from CNRS (France) and China Scholarship Council (CSC). And I'd like to thank Prof. ADACHI Chihaya for allowing us to visit and work in the lab OPERA of Kyushu University (JAPAN) for around one month in 2019.

Last but not the least, I would like to thank my family: my parents, and my sister for supporting me spiritually throughout writing this thesis and my life in general.



## Summary

After the discovery of the conductivity property of polyacetylene by A. J. Heeger, A. G. MacDiarmid, and H. Shirakawa,<sup>1</sup> in 1977, organic  $\pi$ -conjugated systems and particularly polymers, have been intensively studied. Since then, many leading research groups have designed, synthesized, and investigated the charge transport properties of numerous different organic semiconductors (OSCs), to eventually incorporate them in specific electronic devices, and to replace the well-known inorganic semiconductors, such as silicon.

Indeed, these OSCs are attractive essentially because they can take advantage of organic material properties, such as lightweight, potentially low cost, and efficient thin-film and flexible device fabrication. Consequently, nowadays, OSC molecules and macromolecules are already introduced as active layers in electronic components such as organic light-emitting diodes (OLEDs), organic photovoltaic cells (OPVs), and organic field-effect transistors (OFETs).

To design these OSC materials for specific applications, it is important to understand how chemical modification alters electronic and photophysical properties and several strategies have emerged as highly effective means to accomplish this goal. Incorporating electron-withdrawing substituents onto the periphery of  $\pi$ -systems can improve the oxidative stability of these organic structures while increasing electron affinity. The replacement of elements (particularly bridging elements within the  $\pi$ -system) also serves as an effective means to alter the electronic structure and influence packing in the material. Finally, ring fusion to afford polycyclic aromatic systems can alter frontier orbital energies and tune the bandgap. These strategies have all been used in conjunction with cross-coupling to create a wide range of conjugated polymers.

This is why in this thesis, **chapter 1 provides a general introduction describing the design principles and controlled synthesis method for tuning electronic properties of conjugated organic semiconducting polymers**. Subsequently, **we present in chapter 2 (respectively chapter 3) the design, synthesis, and characterization of new polymers tested as alternatives for OFETs (respectively OLEDs)**.

More precisely, **chapter 2 deals with the design, synthesis, and characterization of new structured  $\pi$ -conjugated polymers for OFETs applications**. Indeed, in this context, charge-carrier transport properties depend not only on the intrinsic electronic properties of the materials, but also on the way the molecules are packed together in bulk. Therefore, one of the key parameters to improve the performance of such organic based components is the development of structured and/or more ordered

$\pi$ -conjugated systems. Representative technological examples are the area of organic microelectronics where patterning of p- and n-channel semiconductors is one of the major hurdles for the implantation of OSC in an organic complementary logic circuit. The first part is dedicated to the bibliography in this specific field, with an emphasis on a class of organic  $\pi$ -conjugated systems able to give spontaneously self-assembling, i.e. organic liquid crystals. In the second part we describe the synthesis and the characterization of two novel side-chain liquid crystal (SCLC) semiconducting polymers where: (i) the backbone is a  $\pi$ -conjugated polymer and (ii) the side groups are  $\pi$ -conjugated calamitic or discotic mesogens. Then we discuss the supramolecular architecture resulting from the phase separation, at the nanoscale level, of these two covalently linked  $\pi$ -conjugated systems that we expect to be able to self-organize in bulk. The charge transport properties of these two innovating polymers are also discussed.

Similarly built to the precedent one, **chapter 3 deals with the synthesis and the study of new TADF-based (Thermally Activated Delayed Fluorescence)  $\pi$ -conjugated polymers specifically designed for OLEDs applications.** Indeed, TADF emitters are the third generation of organic building blocks that are currently investigated for organic lightening. As a consequence, several macromolecular architectures have been investigated to try to obtain efficient TADF properties during the second part of the Ph.D. project. First, two series of new TADF polymers based on a donor (D) backbone and twisted acceptor (A) side-groups have been targeted. Second, interesting new types of TADF polymers based on through space D-A interactions have been designed. Thus, after describing the synthesis of all these D-A polymers, their photophysical properties such as photoluminescence quantum yield (PLQY) and fluorescence lifetime in both solution and solid-state have been carried out, to determine if they are TADF or not. The electroluminescence properties of these materials in OLED configuration have been measured as well, and preliminary EQE results are reported. The fabrication of optimized devices is also currently in progress and will be discussed.

## Content

Acknowledgements .....	3
Summary .....	5
Content .....	7
Chapter 1 General introduction to $\pi$ -conjugated polymers .....	9
1.1 General background on organic electronics.....	10
1.2 Fundamental concepts and mobility drawback.....	11
1.3 Molecular <i>versus</i> polymeric organic semiconductors.....	14
1.4 A brief history of conjugated polymers .....	15
1.5 Design principles .....	17
1.5.1 Polymer backbone.....	17
1.5.2 Side chain.....	21
1.6 Polymer synthesis .....	24
1.6.1 Backbone synthesis .....	25
1.6.2 Incorporation of side chains .....	33
1.7 Scope of this thesis .....	33
Chapter 2 $\pi$ -Conjugated polymers for organic field-effect transistors (OFETs) .....	35
2.1 Bibliography .....	37
2.1.1 Brief history of OFETs.....	37
2.1.2 OFETs construction and functionality .....	38
2.1.3 High-performance conjugated polymers for OFETs.....	41
2.1.4 Liquid crystals.....	47
2.1.5 Objectives: towards new liquid crystal side-chain polymers .....	58
2.2 Polythiophene-oxa .....	61
2.2.1 Synthesis and structural characterization .....	61
2.2.2 Thermal and self-organization behavior study of <b>Polythiophene-oxa</b> .....	66
2.2.3 Preliminary charge transport property studies in OFET configuration.....	67
2.2.4 Conclusion.....	67
2.3 PBTTT-Tri.....	69
2.3.1 Synthesis and structural characterization .....	69
2.3.2 Thermal behavior and self-organization study of <b>PBTTT-Tri</b> .....	74
2.3.3 Preliminary charge transport property study of <b>PBTTT-Tri</b> in OFET configuration ..	76
2.3.4 Conclusion.....	77
Chapter 3 TADF polymers for organic light-emitting diodes (OLEDs) .....	79
3.1 Bibliography .....	81
3.1.1 A brief introduction to organic light-emitting diodes (OLEDs).....	81

3.1.2 Thermally activated delayed fluorescence (TADF) .....	86
3.1.3 Linear polymeric TADF materials .....	96
3.1.4 Through-space conjugation (TSC) .....	112
3.1.5 Aim and outline of this chapter .....	116
3.2 Linear conjugated TADF polymers based on 26IPNDCz .....	118
3.2.1 Design, synthesis, and structural characterization.....	118
3.2.2 Photophysical properties .....	124
3.2.3 Conclusion.....	137
3.3 Linear conjugated TADF polymers based on Pm5.....	138
3.3.1 Design, synthesis, and structural characterization.....	138
3.3.2 Photophysical properties .....	142
3.3.3 Electroluminescent properties in device configuration .....	156
3.3.4 Conclusion.....	157
3.4 Through-space charge transfer (TSCT) TADF polymers based on 26IPNDCz .....	159
3.4.1 Design, synthesis, and structural characterization.....	159
3.4.2 Photophysical properties .....	162
3.4.3 Conclusion.....	170
3.5 Through-space charge transfer (TSCT) TADF polymers based on Pm5.....	171
3.5.1 Design, synthesis, and structural characterization.....	171
3.5.2 Photophysical properties .....	175
3.5.3 Conclusion.....	183
General conclusions and perspectives .....	185
Conclusions and perspectives .....	186
Appendices .....	189
Appendix 1. Experimental .....	190
Materials and methods .....	190
Synthetic procedures .....	192
Appendix 2. Calculations.....	210
Appendix 3. Figures.....	212
References .....	215
Abstract .....	233
Résumé en français.....	235

## **Chapter 1 General introduction to $\pi$ -conjugated polymers**

Organic semiconductors (OSCs), i.e.  $\pi$ -conjugated small molecules or polymers, have attracted researchers' attention due to their fascinating electronic and photophysical properties. These types of materials have been incorporated into a wide variety of electronic devices since they are lightweight, solution-processable, flexible, and they possess tunable properties.

To design conjugated materials for different applications, it is important to understand how chemical modifications alter electronic and photophysical properties, and several strategies have emerged as highly effective approaches to accomplish this goal. As an example, incorporating electron-withdrawing substituents onto the periphery of  $\pi$ -systems can improve the oxidative stability of these organic structures while increasing electron affinity. The replacement of elements (particularly bridging elements within the  $\pi$ -system) also serves as an effective means to alter the electronic structure and influence packing in the material. Finally, ring fusion to afford polycyclic aromatic systems can alter frontier orbital energies and tune the bandgap. These strategies have all been used in conjunction with new synthetic tools and methods, such as cross-coupling, to create a wide range of conjugated polymers. This is why in **chapter 1**, after a general introduction to the field, we will discuss some design principles for tuning electronic properties of  $\pi$ -conjugated organic semiconducting polymers, before to describe as well some specific controlled synthesis methods.

## 1.1 General background on organic electronics

The term "Organic Electronics" describes the general field of synthetically derived  $\pi$ -conjugated materials that exhibit the electronic attributes of conductors or semiconductors. These unique materials bring promise for a new generation of cost-effective, lightweight, flexible, and functional electronics. While there are a variety of new application spaces for these materials that continue to emerge, the core applications include organic light-emitting diodes (OLEDs)<sup>2</sup>, organic field-effect transistors (OFETs)<sup>3</sup>, organic photovoltaics (OPVs)<sup>4</sup>, electrochromic devices (ECDs)<sup>5</sup> and photodetectors<sup>6</sup>.

As a remark, these organic electronic devices typically trail behind their inorganic counterparts in terms of performance, but instead offer numerous advantages including mechanical flexibility<sup>7</sup>, adaptability to low-cost processing techniques<sup>8</sup>, synthetic tunability<sup>9</sup>, and biocompatibility<sup>10</sup>, providing a competitive edge in both commodity and niche markets.

On the commodity side, the ability to formulate liquid inks out of organic electronic materials opens up manufacturing possibilities through low-cost printing techniques such as screen-printing, blade coating, inkjet printing, rotogravure printing, aerosol spray coating, and slot-die coating. Many of these techniques are amenable to roll-to-roll (R2R) processing, in which reels of the substrate are continuously moved through the coating, drying, laminating, and cutting processes similar to what is done in the graphic printing industry. The high throughput nature of R2R processing reduces the costs

associated with manufacturing, allowing for simple electronic devices including sensors, logic circuits, photovoltaics, etc. to be produced more rapidly and at lower costs than electronic components composed of inorganic materials such as doped silicon.

On the niche side, the ability to print onto a variety of substrates opens up opportunities for the integration of electronics into plastic and paper-based products. Additionally, the ability to create flexible electronics can reduce the design limitations caused by rigid electronic components. Synthetic tunability of organic electronic materials allows for components to be made transparent or in a variety of colors. Finally, designing for biocompatibility can lead to new ways for electronics to interface with living systems.

For these reasons, research in organic electronics is not solely focused on increasing performance metrics to compete with traditional electronics, but is also focused on exploring the properties and processing methods that cannot be achieved through inorganic materials.

## 1.2 Fundamental concepts and mobility drawback

Organic electronic materials, whether molecular or polymeric, exhibit interesting optical and electronic properties, relying on the ability to move electrons through  $\pi$ -conjugated structures, which consist of alternating single bonds and double bonds that create a plane of  $sp^2$  hybridized orbitals with  $2p_z$  orbitals left perpendicular to that plane. These  $2p_z$  orbitals overlap to form a network of  $\pi$  bonds that can move electrons across the plane of conjugation.

For instance, as represented in Figure 1. 1, cis-/trans-polyacetylene is a linear polyene with a  $\pi$ -conjugated system, consisting of a long chain of carbon atoms with alternating single and double bonds between them, each with one hydrogen atom. And poly(para-phenylene) (PPP) and poly(para-phenylene vinylene) (PPV), containing a phenyl ring in their repeat units, are two kinds of typical light-emitting polymers.

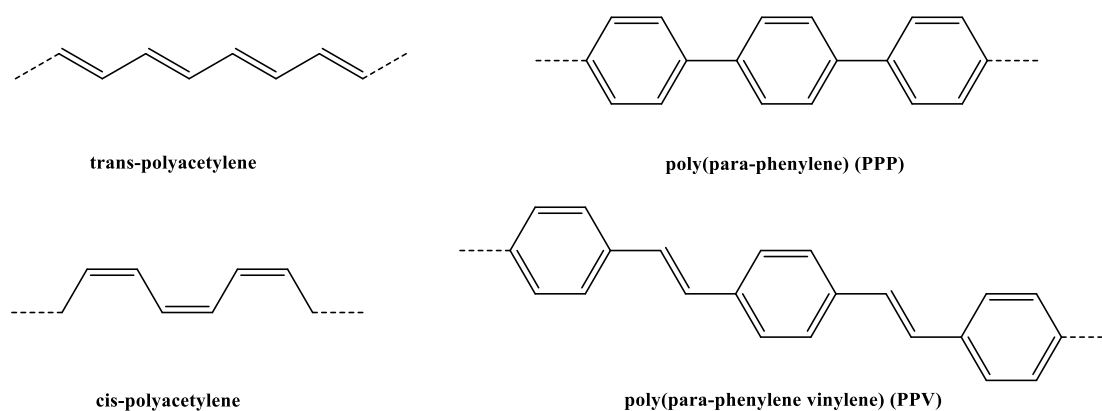


**Figure 1. 1** The chemical structures of cis-/trans-polyacetylene, PPP, and PPV.

The impact of increasing the extent of conjugation on electronic properties can be well understood by the progression from ethylene to butadiene, octatetraene and further to varying lengths polyenes. As shown in Figure 1. 2, with an increasing number of overlapping 2pz orbitals, there is a decrease in the energetic bandgap ( $E_g$ ) between the highest occupied molecular orbital (HOMO) and lowest-unoccupied molecular orbital (LUMO) of the system, transitioning these materials from insulators to materials that have similar bandgap between HOMO and LUMO as bandgap between valence bands (VB) and conduction bands (CB) in inorganic semiconductors.

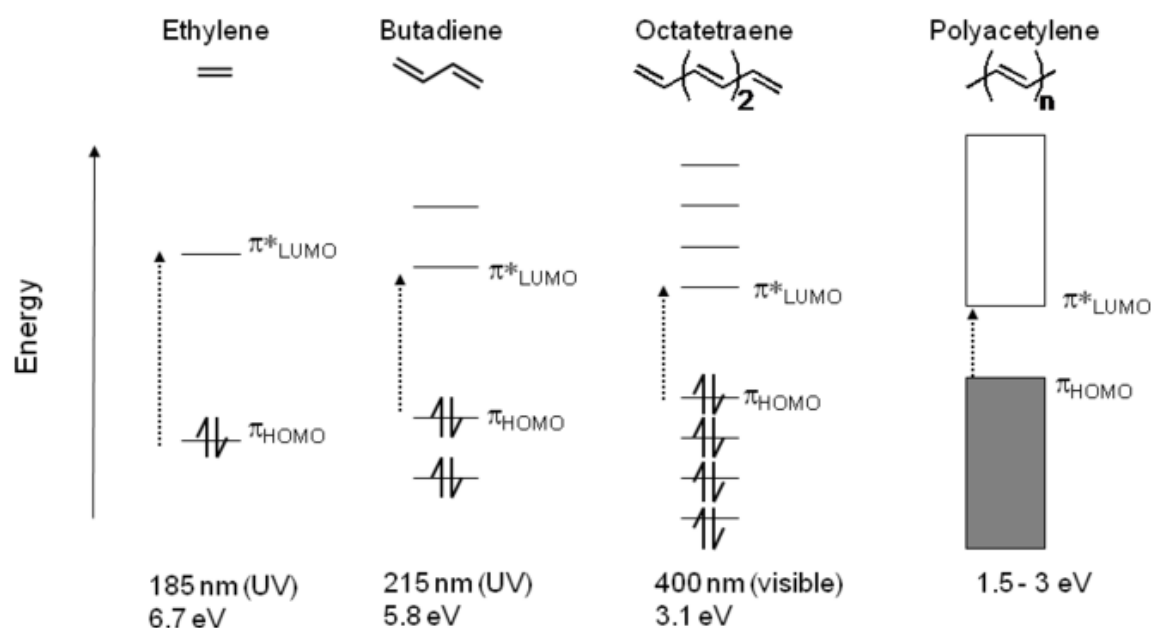


**Figure 1. 2** Diagram displaying the effect of decreasing bandgap between HOMO and LUMO as conjugation length increases, ultimately resembling the band-like structure observed within inorganic semiconductors.

If this trend were to continue, it could be assumed that eventually, an extent of conjugation would lead to a negligible bandgap between the HOMO and LUMO, as it is seen between the VB and CB in metal conductors. However, the instability of a quasi-one-dimensional structure of  $sp^2$  hybridized C-C bonds leads to a distortion of the chain to provide stabilization through a lower energy arrangement.<sup>11</sup> Known as Peierl's distortion, the physical effect of this stabilization is seen through bond-length alternation (BLA) of shorter bonds and longer bonds. This stabilization lowers the HOMO and raises the LUMO, preventing conjugated materials from achieving the zero-energy bandgap seen in conducting metals. Even though conductivity can be achieved in conjugated materials through doping mechanisms, as is the case in PEDOT:PSS,<sup>12</sup> most conjugated materials are used as semiconducting materials because of this limitation. As a consequence, one of the key drawbacks of organic materials is their relatively low charge carrier mobility compared to inorganics. Charge carrier mobility ( $\mu$ ), defined as the ratio between charge drift velocity ( $v$ ) and the amplitude of the applied electric field ( $E$ ), is effectively a

measure of the ability to transport charge across the materials and typically reported in  $\text{cm}^2 \cdot \text{V}^{-1} \cdot \text{s}^{-1}$ , and therefore plays an important role in semiconductors.

$$\mu = \frac{v}{E}$$

For crystalline inorganic materials, a highly ordered covalent network of atoms allows charges to delocalize into valence and conduction bands. Charges can be easily moved within these inorganic semiconductors, giving mobility values in the range of  $10^2$ - $10^3 \text{ cm}^2 \cdot \text{V}^{-1} \cdot \text{s}^{-1}$ .<sup>13</sup>

Since organic materials are packed by weak intermolecular interactions (Van der Waals forces, dipole-dipole), charges are localized onto single molecules and are transported through a slower “hopping” mechanism. In this mechanism, each molecule contributes discrete molecular orbitals, and charges can move between the frontier molecular orbitals of each individual molecule. In this sense, the array of HOMO and LUMO energy levels contributed from each molecule serve as an analogue to the valence and conduction bands observed in inorganic materials. Charge transport is therefore governed by a diffusion-related “hopping” between charged and neutral molecules, providing organic materials lower mobility values in the range of  $10^{-5}$ - $10 \text{ cm}^2 \cdot \text{V}^{-1} \cdot \text{s}^{-1}$ . This broad mobility range is attributed to the vast differences in molecular structure, intermolecular interactions, and morphology among organic materials. For example, highly pure rubrene single crystals have hole mobility values as high as  $40 \text{ cm}^2 \cdot \text{V}^{-1} \cdot \text{s}^{-1}$  due to their high degree of crystallinity and lack of grain boundaries,<sup>14</sup> while semicrystalline polymers such as P3HT show hole mobility values on the order of  $10^{-3}$ - $10^{-2} \text{ cm}^2 \cdot \text{V}^{-1} \cdot \text{s}^{-1}$ . Organic semiconductors can either transport holes (p-type), electrons (n-type), or both (ambipolar). Their charge carrier mobility is highly associated with the device performance, it is an important issue to explore high-mobility organic semiconductors.

**How to raise mobility in organic materials?** Since geometric fluctuations upon charging are related to intramolecular degrees of freedom, rigid molecules are traditionally pursued for high charge mobility systems.<sup>15</sup> Fused aromatic systems like polyacenes have low degrees of rotational freedom, thus require small energies for reorganization. For example, by restricting torsional rotation, naphthalene demands less reorganization energy ( $\sim 100 \text{ meV}$ ) than biphenyl. In addition, efficient packing increases the charge transfer integral and allows for the formation of an ordered network analogous to the covalent lattice seen within inorganic systems. Hence rigid molecules with a highly planar structure benefit from both small reorganization energy and the capability to closely pack in the solid-state. Using this design approach, organic molecules with hole mobility values on the order of  $10 \text{ cm}^2 \cdot \text{V}^{-1} \cdot \text{s}^{-1}$  have been successfully developed.<sup>14</sup> However, rigid and flat organic materials that can efficiently pack in the solid-state tend to suffer from insolubility and processability. For this reason, a delicate balance is required between solubility and the ability to pack efficiently in the solid-state.

### 1.3 Molecular *versus* polymeric organic semiconductors

Both molecular and polymeric conjugated materials have been investigated within organic electronics research, and each has its advantages and disadvantages, as summarized in Table 1.1. 1. Discrete molecular materials are monodispersed and can be purified *via* traditional workups, such as column chromatography, distillation, and sublimation. Though batch-to-batch variations in yield may exist, discrete molecules can be purified to the extent that the final materials will always be identical, facilitating their scale-up and industrial use. Moreover, discrete molecules have a great tendency towards order in the solid-state: creating efficiently packed, crystalline morphologies to gain higher charge mobility. But this high degree of order may cause discrete molecules to easily aggregate in solution, limiting their solution-processability. Owing to this limitation, many high-performance molecular systems are processed through vacuum deposition, a high energy process that is not amenable to R2R manufacturing. Besides, increased crystallinity in the solid-state morphology makes these materials brittle, inhibiting their use in flexible electronics applications, and may create grain boundaries to serve as charge traps.

**Table 1.1. 1** Summary of merits and demerits of different types of films

Films	discrete molecules	discrete molecules	polymer
	vacuum-processed	solution-processed	solution-processed
fabrication cost	high	low	low
material purity	high	high	low
thermal stability	high	low	high
large-area production	difficult	easy	easy
multicomponent layer	difficult	easy	easy
multilayer structure	easy	difficult	difficult
molecular orientation	high degree	small anisotropy	high degree

On the contrary, polymeric materials by nature always have a degree of dispersity and their purification is limited to the fractionation of disperse materials through precipitation, Soxhlet extraction, size exclusion chromatography, and continuous spin fractionation. The resulting variations in molecular weight and dispersity are not trivial and can have impacts on both optoelectronic and mechanical properties. In addition, the dispersity, chain entanglements, chain-ends, and existence of both amorphous and crystalline solid-state domains in polymeric systems inherently lead to a certain degree of disorder in solid-state morphology, which can be viewed as both an advantage and a flaw. For one thing, the disorder is beneficial for solubility, processability as well as mechanical malleability, facilitating their use in flexible electronics applications. For another, the disorder can disturb intermolecular interactions between conjugated backbones and create charge traps, leading to decreased charge mobility.

All that being said, many of these differences between molecular and polymeric materials are continuously becoming blurred. The solubility and mechanical flexibility of discrete molecules are improved by being made larger and incorporated with long aliphatic solubilizing chains, while conjugated polymeric systems with rigid backbones are achieving high charge mobility values that rival crystalline discrete molecules. Advancements in living polymerization of conjugated polymers through chain transfer coupling techniques are also leading to polymeric materials with low dispersity, decreasing the drawbacks from batch-to-batch variations.

While discrete molecular systems have obvious merit in the field of organic electronics, the objectives of this thesis project lend itself to focus on polymeric systems, which will be further discussed in this chapter.

#### 1.4 A brief history of conjugated polymers

**Discovery.** The earliest research into conjugated polymers dates back to the 1960s, with Donald Weiss and coworkers observing electronic properties in doped polypyrrole,<sup>16</sup> and the work of René Buvet and Marcel Jozefowicz on doped polyaniline.<sup>17</sup> Perhaps the most notable impulsion in this field came from the combined work of Alan MacDiarmid, Hideki Shirakawa, and Alan Heeger on metallic-like conductivity in iodine-doped polyacetylene.<sup>1</sup> Synthesized through Ziegler-Natta polymerization of acetylene, Shirakawa and coworkers observed the formation of a silvery film from the resulting polyacetylene. Though the neutral polymer displayed low conductivities, vapor-doping the films with iodine resulted in an increase in conductivity to  $\sim 10^2$  S/cm. This seminal work kicked off the field of conjugated polymers and earned these three scientists the Nobel Prize in chemistry in 2000.

In the following decades, research focused on extending the oxidative polymerization of other aromatic units to create conjugated heterocyclic polymers such as polythiophenes. Nevertheless, much of the early work concerning the synthesis of conjugated polyheterocycle was limited to oxidative polymerization along with electro-polymerization of monomers onto an electrode. The resulting conjugated polymers are typically insoluble in their neutral forms, even though their electronic properties could be well investigated, their molecular weights and dispersity were not clear. In the meanwhile, other conjugated polymers like PPP and PPV synthesized through polycondensation reactions, for instance, Wittig and Knoevenagel reactions, were also insoluble.

**Towards conjugated processable polymers.** For these reasons, the field has largely moved towards soluble conjugated polymers. Much of this progression in the 1990-2000s focused on the incorporation of side chains (R), typically aliphatic groups, onto the conjugated backbone. This modification not only afforded a final polymer good solubility in organic solvents, but provided a synthetic handle over molecular weight and dispersity. Side chains expanded the toolbox for conjugated polymer chemists and led to new families of soluble polymers based on new aromatic monomers that were previously inaccessible, including fluorene, carbazole, thiophene and its fused derivatives, benzothiadiazole and

its derivatives, rylene diimides, and diketopyrrolopyrrole (see structures in Figure 1. 3).

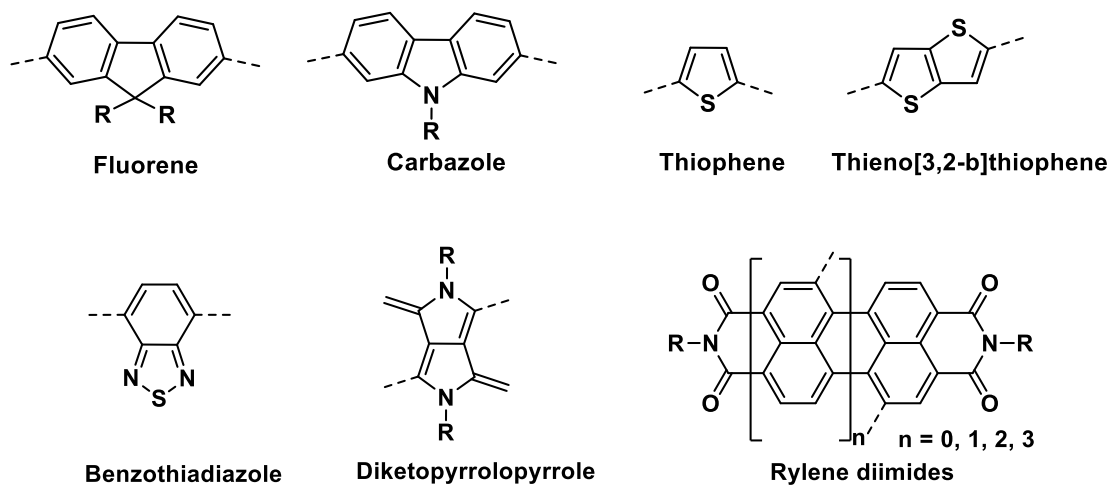


**Figure 1. 3** Typical building blocks for conjugated processable polymers: fluorene, carbazole, thiophene and its derivatives, benzothiadiazole, diketopyrrolopyrrole, and rylene diimides.

Good solubility makes it possible for the soluble conjugated polymers to be synthesized through solution-based polymerization methods, notably, Grignard metathesis (GRIM) method and palladium-catalyzed cross-coupling polymerizations, purified by removing catalyst and salts used/produced in the polymerization through traditional solution-based chemical techniques: it includes precipitation, filtration as well as chromatography, fractionation via Soxhlet extraction to reduce dispersity and obtain batches of varying molecular weight, and characterized in a solution using common techniques (NMR, SEC, UV-Vis, PL, etc.) to provide structural information that could not be obtained through solid-state analytical techniques. Moreover, good solubility is enabling solution-based processing methods, bringing conjugated polymers into the realm of printed electronics. It is worth mentioning that GRIM method enabled the room temperature synthesis of poly(3-hexylthiophene) (P3HT) with controlled degrees of polymerization and regioregularity, providing researchers with a controlled conjugated polymer “fruitfly” that has served as the basis for understanding structure-property relationships across the field.<sup>18</sup>

**Recent evolutions.** From the point view of monomer, GRIM method is limited primarily to electron-rich aromatic monomers. Thus, progression in palladium-catalyzed cross-coupling reactions (Stille coupling, Suzuki coupling, etc.) and their extension to polymerizations has largely expanded the scope of monomer breadth to include electron-deficient monomers and has also enabled a host of new conjugated homopolymers and random/block/alternating copolymers. These cross-coupling polymerizations have revolutionized the area of soluble conjugating polymers, providing the tools for organic chemists to design new monomers and polymers with nearly endless possibilities. Despite their efficiency and reliability, we have to keep in mind that these polymers, synthesized by such transition-metal catalyzed coupling reactions, suffer some environmental and performance issues such

as the use of hazardous monomers, toxic solvents, or transition-metal catalysts (e.g. Pd, Ni, Fe, etc.,) that end up as residual impurities in the final devices, thus acting as failure agents. Thus, many improvements have been currently developed, such as the use of less hazardous monomers (direct heteroarylation polymerization, DHAP) and less or no transition-metal catalyzed.<sup>19</sup>

**Future.** Today we have entered a new era where  $\pi$ -conjugated polymers could be made from bio-sourced monomers, the so-called biomass.<sup>20</sup> One typical example is the lignocellulose whose production cycle is rather short (1-50 years). Most importantly, the lignocellulose can be used for energy production without competing with food production. Furthermore, the lignocellulose is also a good candidate to provide a large palette of molecules. For example, cellulose, the most abundant biopolymer in nature, has a crystalline structure and consists of cellobiose repeating units. Cellulose can be applied in optoelectronic devices<sup>21</sup>. In addition to the lignocellulose, multiple biomasses with their characteristics exist in nature, demonstrating that biomass is a promising alternative to petroleum resources.

## 1.5 Design principles

To design conjugated polymers for optoelectrical applications, several general principles should be kept in mind, including (1) side chains to enhance the solubility and processability, (2) high molecular weights, (3) bandgap and absorption behavior, (4) HOMO and LUMO energy levels, and (5) suitable morphology with low barriers. These factors are dependent on each other and must be comprehensively considered for specific target properties.

For instance, side chains play a significant role in improving the solubility and the obtainable molecular weight of conjugated polymers, but also influence their intermolecular interactions through changes in morphology and thereby the charge carrier mobility. Tuning the energy bandgap for obtaining the desired absorptions will usually change the HOMO and LUMO energy levels, and thus change the emitting color in an organic light-emitting diode (OLED) or influence the open-circuit voltage ( $V_{oc}$ ) in a polymeric solar cell. Therefore, it is necessary to fully account for these designing principles and balance the guiding concepts in pursuit of ideal polymers for specific applications.

### 1.5.1 Polymer backbone

Most optoelectronic properties of conjugated polymers stem from the attributes of the conjugated backbone, making the polymer backbone design one of the most important aspects to consider when creating new materials tailored to a specific organic electronic application. The primary handles a synthetic chemist can control, in conjugated polymer backbones, include conjugation length, inter-ring torsion or dihedral angles, the electron density of the monomers, and the interplay between electron-rich and electron-poor comonomers in donor-acceptor architectures.

**Conjugation length.** We already introduced the concept that increasing the number of overlapping 2pz orbitals leads to a decrease in  $E_g$  until the effects of BLA limit any further reduction. However, for many conjugated polymeric systems, the bandgap and other electronic properties can be limited by the effective conjugation length of the backbone. The effective conjugation length can be thought of as the minimum number of monomer units necessary to saturate the optoelectronic properties of a conjugated polymer.

Bredas's team figured out a linear relationship for  $E_g$  and ionization potential (IP) to  $1/n$ , with  $n$  corresponding to the number of aromatic rings in a chain.<sup>22</sup> This means that increasing chain length will decrease the bandgap and increase the  $\lambda_{\max}$  of the polymer absorption. The change would diminish as the chain size increases, effectively reaching a plateau.

As an example, Miller and coworkers experimentally observed this trend using well-defined oligomers of 9,9-di- $n$ -hexylfluorenes ( $n = 3-10$ ). The absorption profile, shown in Figure 1. 4, continuously red-shifted with increasing chain length, but by 10 units the  $\lambda_{\max}$  already were close to the level of poly(9,9-din-hexylfluorene) with an average length of 54 fluorene units. Using the linear extrapolation of  $1/n$  to  $1/\lambda_{\max}$ , the authors determined the effective conjugation length of the polymer to be around 12 fluorene units or 24 aromatic rings.<sup>23</sup>

Using the same method, the effective conjugation length of polyacetylene and polythiophene can be estimated to be around 30 double bonds<sup>24</sup> and 20 rings<sup>25</sup>, respectively. The differences in effective conjugation length probably result from the presence of inter-ring torsion, of dihedral angles between aromatic monomer units, hindering the ability for a conjugated polymer to achieve periodicity in its conjugation.

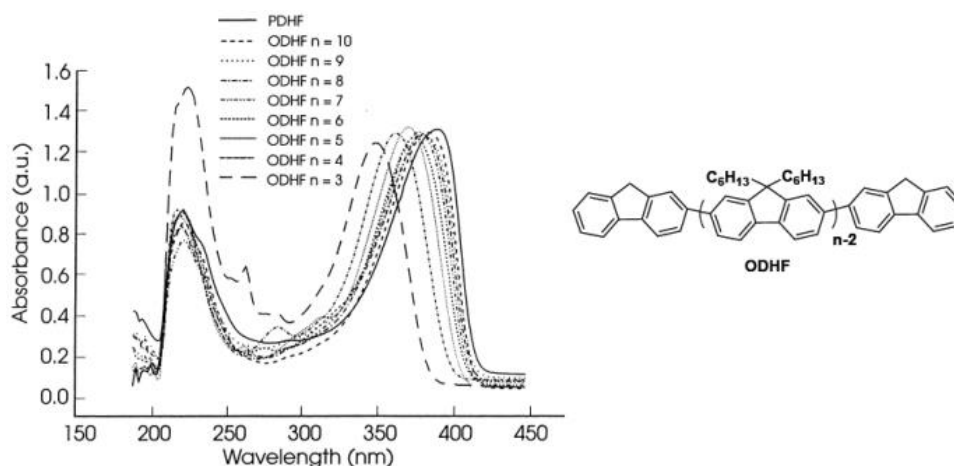


**Figure 1. 4** Absorption spectra of dihexylfluorene (ODHF) oligomers with increasing length compared to poly(dihexylfluorene) (PDHF) showing the red-shifting effect of increasing conjugation length.<sup>23</sup>

**Heteroatom exchange in conjugated scaffolds (atom engineering).** Salzner's group investigated the relationship between the geometries and electronic structures of various heterocyclic organic polymers using the fragment molecular orbital method (FMO), and concluded that the bandgap increase with

increasing  $\pi$ -donor strength of the heteroatom, as depicted in Figure 1. 5.<sup>11</sup> Consequently, heteroatom exchange can greatly affect the electronic structures, optical and electronic properties, and charge carrier mobility.<sup>26</sup> The most commonly used heteroatoms in conjugated molecules are sulfur (S), oxygen (O), and nitrogen (N) to bridge the carbon scaffold. Main-group elements, including silicon (Si), phosphorus (P), boron (B), selenium (Se), and tellurium (Te), are also replaced to achieve expected electronic properties. For example, Se and Te have been incorporated into S-containing donor-acceptor conjugated polymers to decrease the bandgap and improve hole mobility.<sup>26</sup>

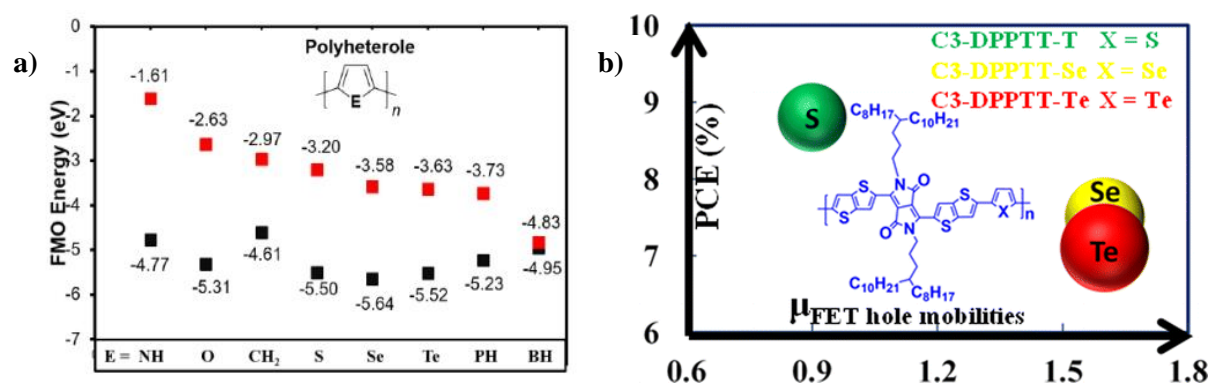


**Figure 1. 5** a) DFT calculations of HOMO-LUMO energy levels for polyheteroles;<sup>11</sup> b) PCE vs hole mobility of S, Se, Te-containing polymers.<sup>26</sup>

**Incorporation of polycyclic aromatics in conjugated materials.** The conjugated polymer backbone determines most of the electronic properties, e.g. the energy level, bandgap, and molecular packing. Conjugated molecules have two possible ground-state resonance structures: aromatic and quinoid form. Conjugated molecules in the aromatic form exhibit aromaticity and can convert to quinoid form through charge transfer, as shown in Figure 1. 6.

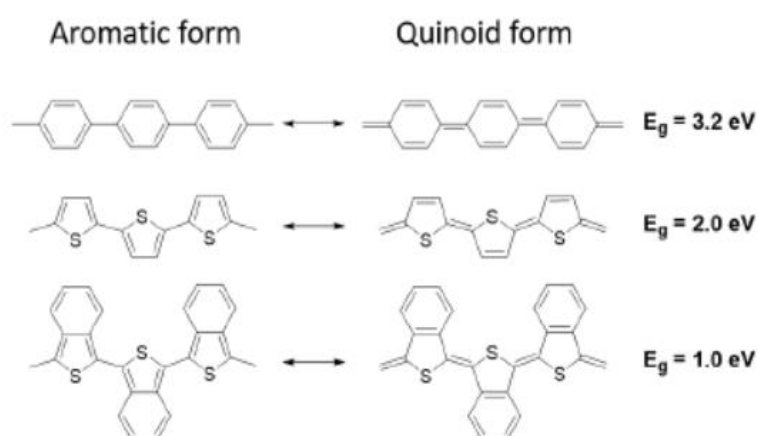


**Figure 1. 6** Aromatic and quinoid forms of polyphenylene, polythiophene, and polyisothianaphthene.

The resulting quinoid forms are less stable and thereby have a smaller bandgap, revealing that decreasing the aromaticity of the aromatic unit on the conjugated backbone is helpful to increase the population of quinoid form, and eventually produce materials with a lower bandgap. For instance,

polyisothianaphthene (PITN), with a benzene ring fused on 3,4-positions of thiophene unit of polythiophene, favors the quinoid form to retain the aromaticity of benzene, because benzene has higher aromatic resonance energy of benzene (1.56 eV), compared to that of thiophene (1.26 eV).<sup>27</sup> Hence, the fused-ring structure is a good choice for conjugated molecules to achieve a low bandgap.

**Torsion.** Torsion between aromatic rings has been proved to greatly affect the conformational and optoelectronic properties of conjugated polymers, by studying the influence of the regioregularity of alkyl substituents on the poly(3-alkylthiophene) properties and coming to the conclusion that the head-to-head sequences produce a steric hindrance, reduce the  $\pi$ -conjugation and further increase the bandgap).<sup>28</sup>

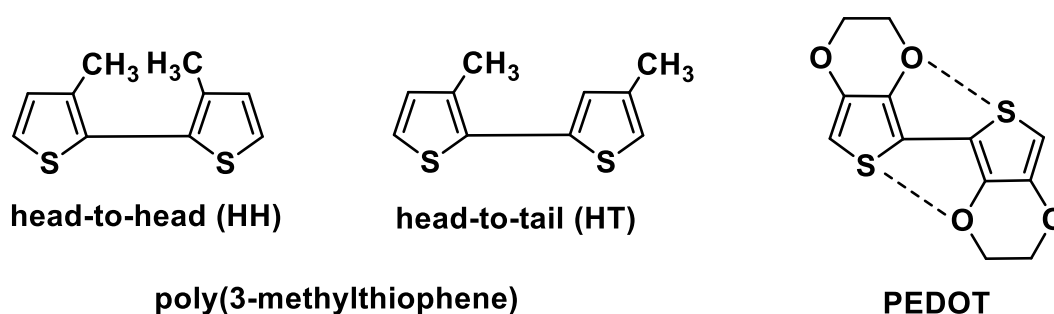


**Figure 1. 7** The two conjugations existing in poly(3-methylthiophene) and torsion in PEDOT.

Aside from regioregularity, torsion can also be manipulated by controlling the number and sorts of the substituted side chains, through the steric interactions between side chains in whether homopolymers or copolymers. Moreover, torsion can be created from electronic effects through heteroatom interactions. For example, in PEDOT, as shown in Figure 1. 8, the interactions between the sulfur atoms (S) in the thiophene backbone and the oxygen atoms (O) of the dioxethylene bridge effectively locks the backbone into coplanarity.<sup>29</sup> The high degree of coplanarity facilitates  $\pi$ - $\pi$  interactions, enable a higher degree of electron donation into the backbone from donating substituents, and increase the delocalization of charge across donor-acceptor copolymers.

**Electron density.** The extent to which monomers in the polymer backbone are electron-rich or electron-poor plays a pivotal role in the electronics of conjugated polymer systems. Electron-rich monomers are more easily oxidized, contributing to a lower oxidation potential  $E_{ox}$  of the resulting polymer. Lowering this  $E_{ox}$  can also be thought of as raising the HOMO level of the polymer, and therefore incorporation of electron-poor monomers serves to deepen the HOMO level. Since energy levels play an important role within organic electronic applications, allowing the polymer to inject or receive electrons from adjacent materials, the electron density of the monomers that make up a conjugated polymer is another approachable handle for organic chemists when designing new materials tailored for a specific application. Aside from the aromatic unit of the conjugated backbone, side-chain substituents can also be chosen for their ability to donate or withdraw electrons from the backbone as a handle over energy levels.

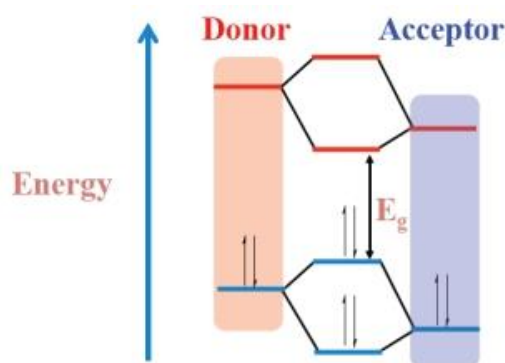


**Figure 1. 8** Orbital mixing diagram showing the effect of reduced bandgap ( $E_g$ ) achieved when bonding an electron-rich moiety (donor) with an electron-poor moiety (acceptor).

**Donor-acceptor copolymers.** Another significant approach to tuning bandgap within conjugated polymers is the use of a donor-acceptor or push-pull architecture along with the backbone. Proposed by Havinga et al. and visualized in Figure 1. 8, the donor-acceptor approach makes use of the orbital mixing between covalently connected electron-rich (donor) and electron-poor (acceptor) monomers to lower bandgap in the resulting conjugated copolymers and push absorption out to the near-IR.<sup>30</sup>

The built-in dipole created from the donor to the acceptor aids in the delocalization of electron density in the backbone, which has made these systems popular for bulk heterojunction (BHJ) OPV active layers in which the polymer is excited by ambient light and the resulting electron can be shuttled from the donor moiety to the acceptor moiety, and finally transferred to the LUMO of the acceptor (e.g. fullerene) in the blend.

### 1.5.2 Side chain

As previously introduced, the incorporation of side chains onto conjugated polymer backbones has vastly expanded the field by allowing for new structures to be synthesized through solution-based polymerizations, characterized through standardized methods, and processed *via* solution-based methods. However, solubility is just one of the many merits obtained through the incorporation of side chains. In the following section, we will explore how side chains can be used to modify solubility, solid-state morphology and microstructure, material functionality, and the interplay that exists between these properties.

**Solubility.** Good solubility is one of the most straightforward properties achieved through side chains. To gain good solubility in common organic solvents, both linear and branched aliphatic side chains are the most commonly used. For *n*-alkyl chains, the solubility of polymers increases along with longer chains, as more rotational degrees of freedom are added to the structure. Branched alkyl chains are also beneficial for enhancing solubility without the need to increase the chain length, as the branching disrupts side-chain interdigitation and also creates a chiral center, both leading to a more disordered, and more soluble, structure.

The aliphatic chains can further be modified by the replacement of heteroatoms, such as oxygen (O), to form oligoether, or terminated with ionic groups to form polyelectrolytes<sup>31</sup>, leading to better solubility in polar solvents. These side-chain motifs are shown below in Figure 1. 9.

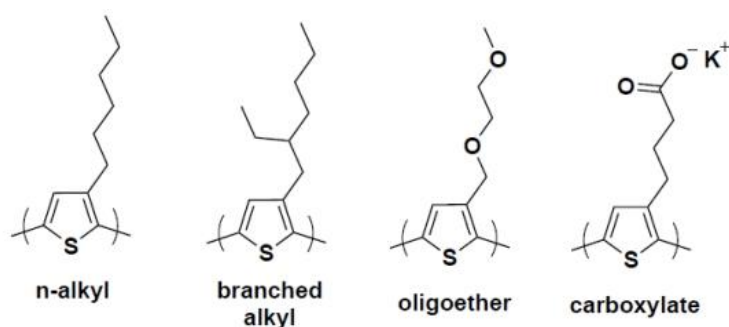


**Figure 1. 9** Examples of common side-chain motifs found in conjugated polymer systems.

In all of these examples, it must be noted that side chains are not simply supplemental pieces of the conjugated polymer that can not only be used for solubility purposes, but will have an impact on the polymer's structure and materials properties.

**Impact on morphology, structure, and optoelectronics.** Aside from solubility, side chains can also have a great influence on the solid-state morphology, structure as well as optoelectronic properties, with evidence of the addition of side chains on poly[*N*-9'-heptadecanyl-2,7-carbazole-*alt*-5,5-(4',7'-di-2-thienyl-2',1',3'-benzothiadiazole)] (PCDTBT) increasing the backbone torsion along with affecting electron delocalization,<sup>32</sup> as shown in Figure 1. 10.

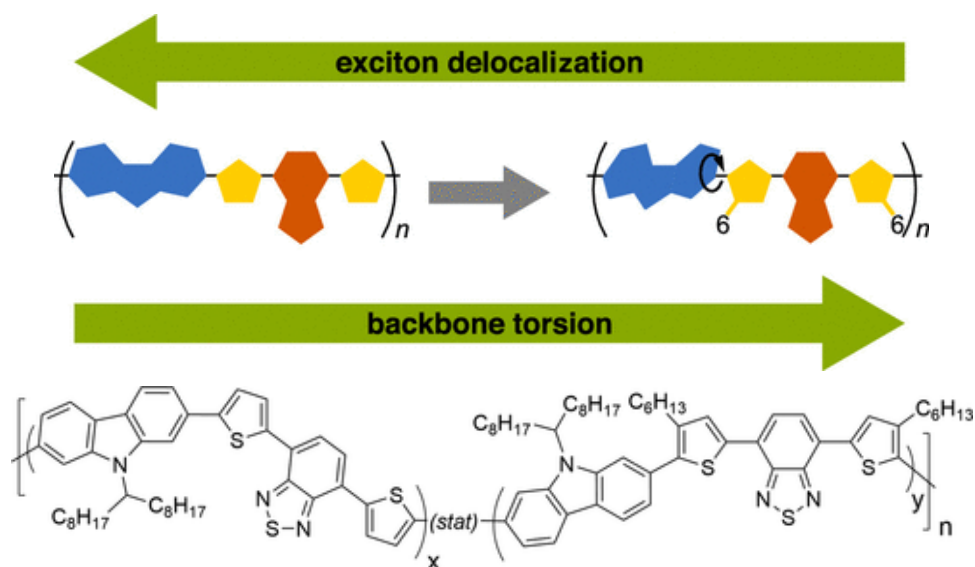


**Figure 1. 10** Schematic explanation for the impact of side chains on the morphology and the electronic structure.<sup>32</sup>

As the field moved towards branched aliphatic side chains in efforts to further increase solubility, it became apparent that there was a complex relationship between solubility and solid-state structure.

Replacing linear side chains with branched alternatives disrupts the ability to interdigitate, and while this greatly increases the solubility of the polymer, it also prevents the formation of ordered domains in the solid-state.

A recent example in the Reynolds group shows an isoindigo-terthiophene polymer that achieves ~5.1% in OPV devices when using linear hexyl chains, but drops to ~0.3% when using 2-ethylhexyl branched chains due to the total disruption of solid-state order.<sup>33</sup> Despite the tendency to disrupt order, branched side chains are still ubiquitous in modern conjugated polymer design due to their ability to solubilize flat, conjugated molecular units, and work from the OFET community has revealed that their effect on solid-state packing can be minimized by pushing the branching point further away from the conjugated backbone.<sup>34</sup>

The difficulty with side chains is that their effects, beyond solubility, can be difficult to predict and are often dependent on both repeat unit structure and intended application. Copolymers containing three or four side-chain sites per repeat unit are now commonplace, and each site adds another variable to contribute to the overall complexity. A notable example of the complex nature of side-chain effects is the hypothesis put forward by Graham et al. that in donor-acceptor copolymers for use in PCBM blend OPVs, having bulky side chains on the donor moiety and linear chains on the acceptor moiety yields the optimum device metrics.<sup>35</sup> The idea is that the bulky side chains direct PCBM molecules towards the less sterically hindered acceptor moiety, thereby improving electronic interactions and facilitating charge transfer. While this hypothesis is applicable for a handful of systems, there are certainly outliers, and there is probably no universal theory for predicting how side chains will impact a conjugated polymer backbone in the solid-state. Therefore, it is important for polymer chemists to perform side chain optimization studies on new conjugated backbones and observe the effects on the solid-state structure through X-ray scattering techniques like GIWAXS, GISAXS, and RSOXS. While many structure-property relationships can be hypothesized, new materials will emerge in direct conflict with those relations, and ultimately much of the field is still in a state of trial and error when it comes to side chains.

Aside from morphology, side chains can also affect the optoelectronic properties by donating or withdrawing electron density and altering inter-ring torsion angles. An interesting example from Guo et al. shows large changes in a series of naphthalene diimide (NDI) bithiophene copolymers by varying the side chains on the bithiophene.<sup>36</sup> Because the side chains are arranged in a head-to-head position, bulky branched chains create significant torsion between the thiophene units and render the polymer amorphous in the solid-state. When moving to linear chains, the torsion is decreased, leading to an increase in effective conjugation length observed by a red-shift (~38 nm) of the thin film's maximum absorption. Finally, using linear alkoxy chains leads to interactions between the oxygen on the side chain and sulfur on the thiophene backbone, causing an increase in planarity and also an increase in electron density due to the alkoxy donation. The combined effects red-shift thin film absorption max by ~278 nm relative to the branched side chain derivative. In this manner, side chains

have been widely used to modify planarity and electron density to control both the absorption profile and electronic bandgap.

**Functional and reactive side chains.** Side chains containing reactive and functional components have been used to append additional functionality into conjugated polymer designs. The first functionality is solubility modifiers: as mentioned above, according to the required solubility, different types of side chains, including linear/branched alkyl chain, ester alkyl chain, or polyelectrolytes can be designed and obtained. The second functionality is to form chemical or physical crosslinking. When the side chains are terminated with azide groups, chemical crosslinking can be reached by “click chemistry”. When the side chains are substituted by nitrogen (N), oxygen (O), fluorine (F), or ionic groups, physical crosslinking is formed by secondary reversible interactions such as hydrogen bonds and ion-ion interactions. The third functionality is side-chain cleavage, providing the ability to make use of side chains for the solubilizing properties, but then removing them in the solid-state to increase the density of conjugated backbone within thin films. For instance, silyl side chains that can be cleaved with strong acids, and *o*-nitrobenzyl units that can be cleaved *via* UV light and offer the ability to photopattern conjugated polymers.<sup>37,38</sup> These examples demonstrate the potential for side chains to impact more than just solubility, and over the last decade, researchers are just beginning to scratch the surface of the possibilities that exist within functional side chains.

## 1.6 Polymer synthesis

As  $\pi$ -conjugated polymers as semiconducting materials have attracted broad academic and industrial interest for a wide range of applications, this means such tailor-made conjugated materials have first to be designed and prepared. But as said before, the critical aspect of conjugated polymers lies in their preparation as their optical and electronic properties are intrinsically linked to their extended conjugation pathway. Robust, reproducible, and reliable polymerization methods are therefore of utmost importance. In particular, to obtain high molecular weight polymers with extended  $\pi$ -conjugation, multiple C-C bond couplings between two  $sp^2$  or  $sp$  hybridized carbon atoms are necessary.

Thus, in this part, we first review a few initial synthetic strategies but focus as well on more recent alternative routes to  $\pi$ -conjugated backbone: we will particularly put emphasis on Suzuki cross-coupling, Stille cross-coupling, and the GRIM polymerization technique, as we will eventually use these chemical tools to prepare our target materials. And new greener methods will also be discussed. Finally, we will briefly introduce the general approaches to the incorporation of side groups onto the polymeric backbones.

### 1.6.1 Backbone synthesis

**Traditional methods.** Initial synthetic methods for conjugated polymers included the Ziegler-Natta polymerization of acetylene<sup>39</sup> and oxidative polymerization of poly(phenylene)s, poly(thiophene)s, poly(pyrrrole)s, and poly(aniline)s.<sup>40–43</sup> Following these early methods, synthesis of poly(hetero-arene)s has increasingly relied on transition metal-catalyzed cross-couplings<sup>44</sup> such as Heck, Kumada, Negishi, Suzuki, Stille, and Sonogashira polycondensations (Figure 1. 11).

We should mention the importance of these Pd-catalyzed cross-coupling reactions for the formation of a C-C single bond allowing the polymerization of conjugated units. Professors R. F. Heck, E.i. Negishi, and A. Suzuki shared the 2010 Nobel Prize in Chemistry for the development of those synthetic tools.<sup>45–47</sup> Indeed, they helped a lot in the design of stable semiconducting polymers with tunable electronic and optical properties.

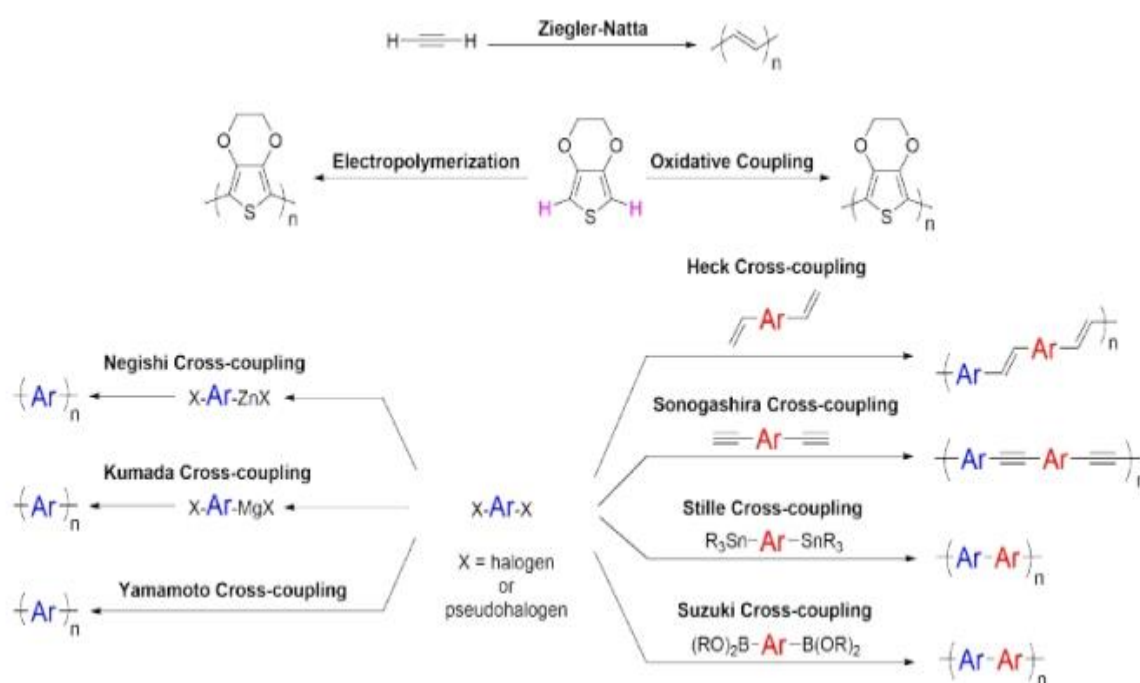
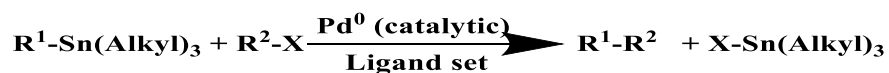


**Figure 1. 11** Traditional C-C coupling techniques for the preparation of  $\pi$ -conjugated backbones.<sup>44</sup>

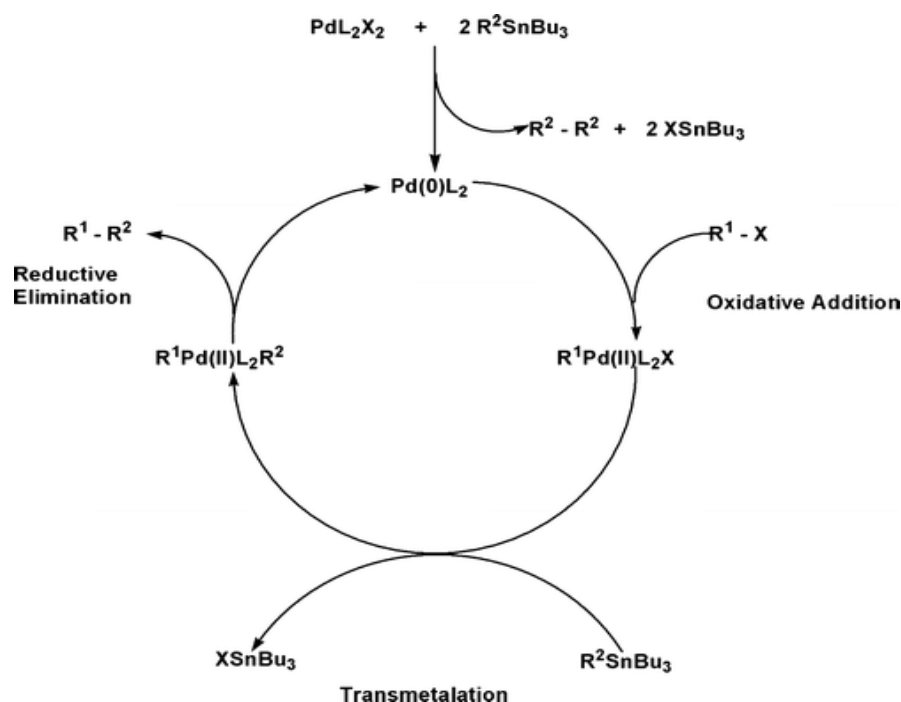
In the following, Stille coupling and Suzuki cross-coupling reactions will be introduced in detail, as we chose these methods to synthesize the polymers described in chapter 2 and 3, respectively.



**Scheme 1. 1** The synthetic route of Stille cross-coupling.

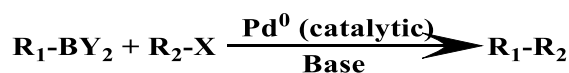
**Stille cross-coupling.** As depicted in Scheme 1. 2, Stille coupling is a versatile Pd-catalyzed C-C coupling reaction between organostannanes and halides or pseudohalides, with very few limitations on the  $\text{R}^2$ -groups. Well-elaborated methods allow the preparation of different products from all of the

combinations of halides and stannanes. The main drawback is the toxicity of the tin compounds used, and their low polarity, leading to poor solubility in water. The mechanism of the Stille reaction<sup>45</sup> has been extensively studied. As represented in Figure 1. 12, the catalytic cycle is composed of three steps: the first step is the oxidation addition of a halide or pseudohalide ( $R^1-X$ ) to a Pd(0) catalyst to form Pd(II); Next is the transmetalation of Pd(II) with an organostannanes **4**; the third step is the reductive elimination of **5** to yield the coupled product ( $R^1-R^2$ ) and the regenerated Pd(0) catalyst. The Stille coupling has been developed to achieve alternating conjugated polymers, which have potential applications in displaying technologies such as organic thin-film transistors (OTFTs), organic light-emitting diodes (OLEDs), and organic photovoltaics (OPVs).



**Scheme 1. 2** A general mechanism for Stille coupling.

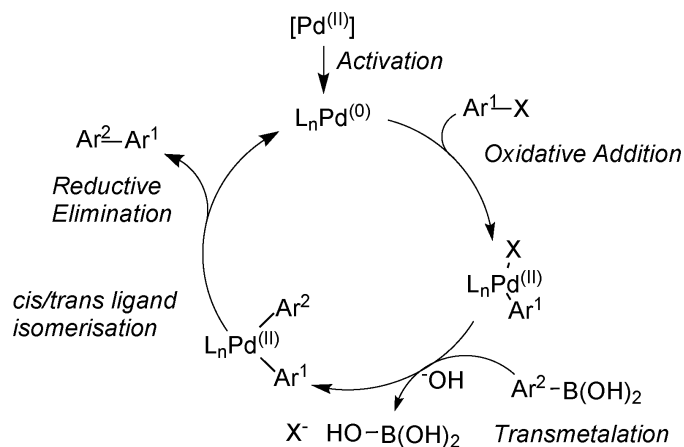
**Suzuki cross-coupling (Suzuki-Miyaura reaction).** As depicted in Scheme 1. 2, the Suzuki cross-coupling reaction is another Pd(0)-catalyzed coupling reaction between organic halides and organoborane compounds.



**Scheme 1. 3** The synthetic route of Suzuki coupling.

The reaction is suitable for aryl and alkenyl halides and aryl and alkenyl borane compounds. The advantages of Suzuki coupling over other similar reactions include the availability of common boronic acids, mild reaction conditions, and its less toxic nature. The mechanism of the Suzuki cross-coupling<sup>48,49</sup> is analogous to the catalytic cycle for the Stille reactions and has four distinct steps

(Scheme 1. 4). The initial step is the oxidative addition of an organic halide to the Pd(0)-species to form Pd(II). Next is the exchange of the anion attached to the palladium for the anion of the base (metathesis). The third step is the transmetallation between Pd(II) and the alkylborate complex. Although organoboron acids do not transmetallate to the Pd(II)-complexes, the corresponding ate-complexes readily undergo transmetallation. The quaternization of the boron atom with an anion increases the nucleophilicity of the alkyl group and it accelerates its transfer to the palladium in the transmetallation step. The final step is the reductive elimination to form the C-C sigma bond and generate Pd(0). Very bulky and electron-rich ligands (e.g., P(t-Bu)<sub>3</sub>) increase the reactivity of otherwise unreactive aryl chlorides by accelerating the rate of the oxidative addition step. Similar to Stille coupling, Suzuki coupling has also developed to Suzuki polycondensation as one of the most powerful tools for the synthesis of conjugated polymers.



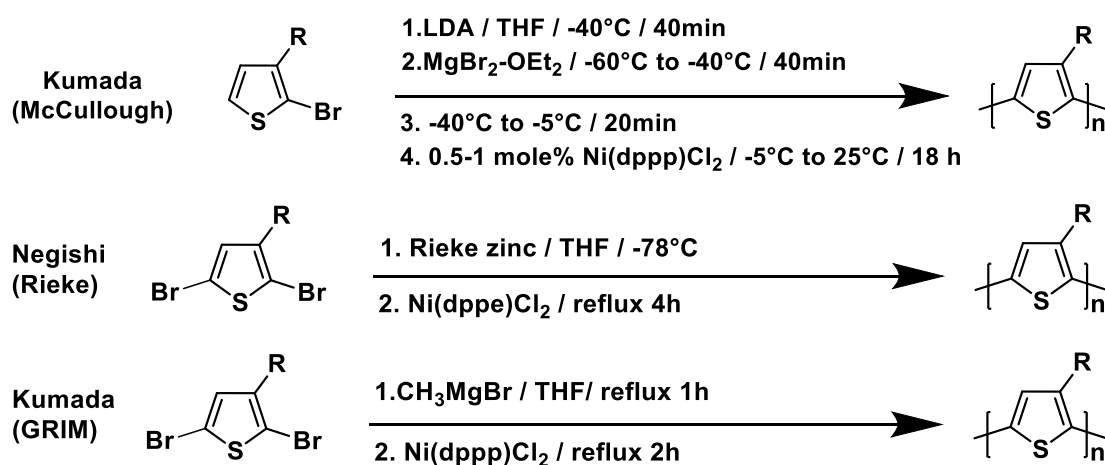
**Scheme 1. 4** A general mechanism for Suzuki coupling.

Potential side reactions of the Suzuki cross-coupling include oxygen-induced homocoupling of organoboron compounds, B-C bond cleavage, ipso-coupling, and participation of phosphine ligands. In some specific cases, dehalogenation<sup>50</sup>,  $\beta$ -hydride elimination<sup>51</sup>; and cleavage of some functional groups (e.g., amino group<sup>52</sup>) are also possible. In order to reveal the full scope of Suzuki polycondensation for the synthesis of high molar mass conjugated polymers, the reaction conditions must be optimized in terms of choice of monomers, catalyst, and solvent, based on careful consideration of the mechanism of the reaction. While much progress has been made, there still remains much scope to further improve these reactions.

The polymers prepared by Stille or Suzuki polycondensation often contain significant traces of the Pd catalysts. These have been proved to have adverse effects on the conjugated polymers' performance in transistors and in solar cells. The levels can be reduced by appropriate treatment, but total removal may be difficult without damaging the polymer. This is a problem with all metal-catalyzed polymerizations.

**Towards regioregular polymers.** In parallel, and following the first studies on poly(3-alkylthiophene)s, it became quite clear that the synthesis of well-defined head-to-tail coupled (which should yield the lowest steric hindrance from the side chains and possibly a more efficient three-dimensional packing) poly(3-alkylthiophene)s would lead to a significant improvement in the performance of these polymeric materials.<sup>53</sup> Therefore, in an attempt to bring more reliable synthetic procedures towards the field of electronic materials, a variety of synthetic strategies were utilized and allowed significant advances in this research field.

McCullough<sup>54</sup> and Rieke<sup>55</sup> independently reported the first preparations of well-defined regioregular poly(3-alkylthiophene)s by metal-catalyzed polymerization (Scheme 1. 5). These relatively complicated polymerization procedures have been optimized and simplified by McCullough's team, leading to the Grignard metathesis (GRIM) method.<sup>18</sup> As we would take advantage of GRIM polymerization method to obtain the polymers developed in chapter 2, below we detail a little more this polymerization method.



**Scheme 1. 5** Synthesis of processable regioregular poly(3-alkylthiophene)s.

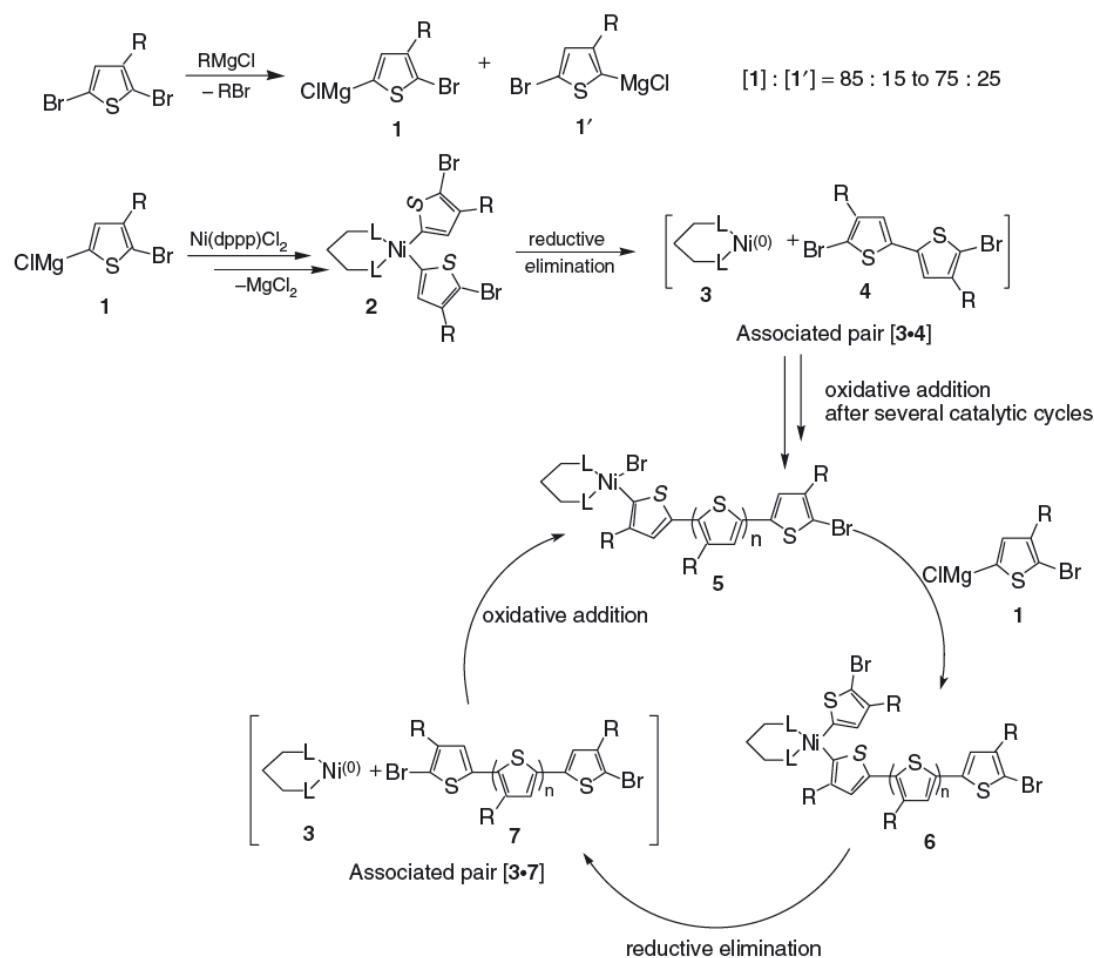
**Grignard metathesis (GRIM).** In contrast to the other described methods, GRIM method does not require low temperature conditions, making the process easier and faster. The mechanism (Scheme 1. 6) proposed by McCullough<sup>56</sup> consists of three consecutive steps: In the first step, 2,5-dibromo-3-alkylthiophene is treated with one Grignard reagent (RMgX) equivalent. Two species are formed: compounds **1** and **1'** in the proportions ~85% and ~15%, respectively. Due to the steric effect, only the monomer **1'** can react with the catalyst. Polymerization starts when the catalyst Ni(dppp)Cl<sub>2</sub> is added. The head-tail coupling rate is more than 99%, the yield is about 70% and with an I<sub>p</sub> around 1.2 and 1.4 is observed. The second step is the reaction of two equivalent 2-bromo-5-chloromagnesium-3-alkylthiophene monomers with Ni(dppp)Cl<sub>2</sub>, generating a bis(organo)-nickel compound, which undergoes reductive elimination resulting on the formation of an associated pair of the 5,5-dibromobithienyl (tail-tail coupling) and Ni(0). The associated pair is formed by coordination of 1,3-

bis(diphenylphosphino)-propane-nickel(0) to the thiophene ring in a  $\eta^2$ - or  $\eta^4$ -bonded fashion. The dimer undergoes a fast oxidative addition to the nickel(0) center, generating a new organo-nickel compound. Growth of the polymer chain occurs by insertion of one monomer at a time in which the Ni(dppp) moiety is incorporated into the polymer chain as an end group. Only one structural defect (one tail–tail coupling) for the polymer chain is generated during the proposed catalytic cycle between the first two thiophene units. With Grignard metathesis method, poly(3-alkylthiophene)s with relatively high molecular weights are produced early.

GRIM method is a controlled living polymerization, thus the degree of polymerization (DP) can be calculated with the following equation:

$$\frac{[M_0]}{[Ni(dppp)Cl_2]} = DP$$

where  $[M_0]$  and  $[Ni(dppp)Cl_2]$  are the initial concentrations of the monomer and the catalyst, respectively.



**Scheme 1. 6** Proposed mechanism of GRIM method for the synthesis of regioregular P3AT.

For instance, this existing polymerization method eliminates the need for highly reactive metals and can even lead to well-defined block copolymers. Moreover, among all poly(3-alkylthiophene)s investigated, regioregular poly(3-hexylthiophene) (rr-P3HT) has shown the best electronic properties

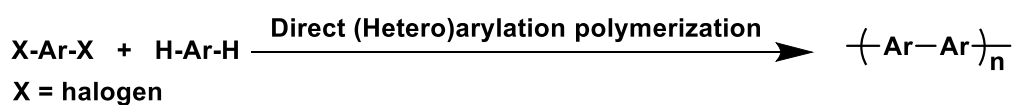
together with adequate processability. Both rr-P3HT and PEDOT are currently the most utilized conjugated polymers and are commercially available from various commercial sources.

However, all these state-of-the-art methods generally involve numerous synthetic steps and organometallic reagents that give rise to metal waste and various by-products. Low cost, environmentally friendly, and more efficient synthetic procedures would therefore be a great asset to the sustainable preparation of affordable and efficient conjugated polymers.

**Towards greener and cheaper polymerization methods.** As mentioned above, simple, reproducible, environmentally benign, and low-cost polymerization methods can be seen as the Holy-Grail for organic electronics. That's why the development of novel polymerization methods for producing conjugated materials is an ongoing topic.

Indeed, conventional (hetero)aryl-(hetero)aryl cross-coupling reactions for C-C bond formation after Suzuki, Stille, Negishi, or Kumada are of highest relevance in organic and macromolecular chemistry. One obvious disadvantage of these reactions is, however, the utilization of various organometallic reagents (or related anion equivalents) that produces stoichiometric amounts of by-products during coupling. These reagents and the resulting by-products are often toxic or environmentally risky, especially in the case of stannyl derivatives. In addition, synthesis of these organometallic monomers often requires multistep procedures as well as expensive purification steps. To overcome these shortcomings, much efforts has been made and direct hetero arylation polymerization (DHAP) appeared as one new technique involving less hazardous chemicals during the process.

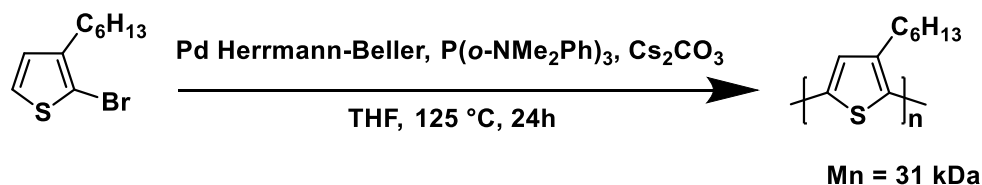
**Direct hetero arylation polymerization (DHAP).** DHAP is a metal-catalyzed coupling reaction between an arene and an aryl halide that enables the synthesis of  $\pi$ -conjugated polymers while generating fewer wastes and using 'simpler' and less hazardous monomers (Scheme 1. 7).



**Scheme 1. 7** Schematic representative of DHAP.

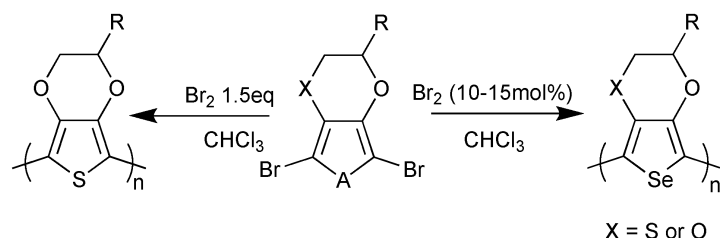
DHAP possesses multiple advantages, among which, the main one is that the monomers, arene and aryl halide, are easily accessible and can bear various substituents. Compared to Stille or Suzuki couplings, DHAP needs less synthetic steps and produces less harmful wastes. And DHAP is likely to synthesized polymers with similar or even better properties than those synthesized with Stille or Suzuki couplings.<sup>57</sup> However, limited by the mechanism, DHAP also suffers from the metal catalysts used. Moreover, DHAP are lack of regioselectivity, leading to branching reactions such as homo-coupling. These two problems can be avoided by choosing suitable experimental conditions (catalyst and solvent) and also blocking other positions. As an example, Ozawa's team successfully obtained

P3HT with high molecular weight ( $M_n = 31$  kDa,  $M_w/M_n = 1.60$ ) and high regioregularity (98%) comparable to those obtained using either McCullough, Rieke or GRIM methods (Scheme 1. 8).<sup>58</sup> To sum up, DHAP has imposed itself as an attractive method to procure well-defined and high molecular weight conjugated polymers.

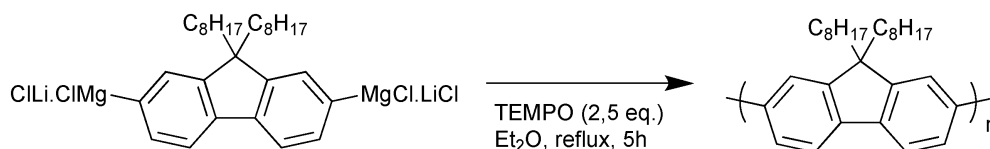


**Scheme 1. 8** Poly(3-hexylthiophene) obtained by DHAP.

**One step further: transition-metal free synthesis.** While organic electronics are ubiquitous in our daily lives, studies dealing with their environmental impact or their sustainability are scarce. As mentioned above, all transition-metal catalyzed cross-coupling reactions suffer from the catalytic system used. The hazardous impurities formed during the coupling reaction remains and acts as charge traps in the final polymers, affecting their properties. Therefore, new trials are made to prepare  $\pi$ -conjugated polymers *via* transition-metal free syntheses.<sup>20</sup> Up to now, it has been proved that  $\pi$ -conjugated polymers can be synthesized with halogen, such as bromine-catalyzed reaction<sup>59</sup> (Scheme 1. 9) and oxidative homocoupling of bis-Grignard reagents in nitroxide-mediated radical polymerization (NMRP) approach<sup>60</sup> (Scheme 1. 10).



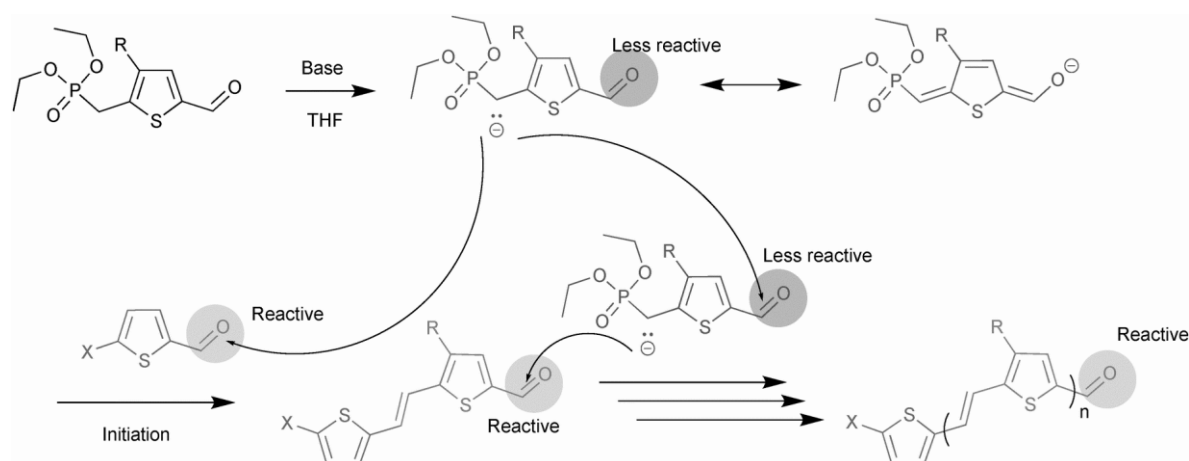
**Scheme 1. 9** Synthesis of PEDOT (left) and PEDOS (right) derivatives.<sup>59</sup>



**Scheme 1. 10** Synthesis of polyfluorene by oxidative homo-coupling of Grignard reagents.<sup>60</sup>

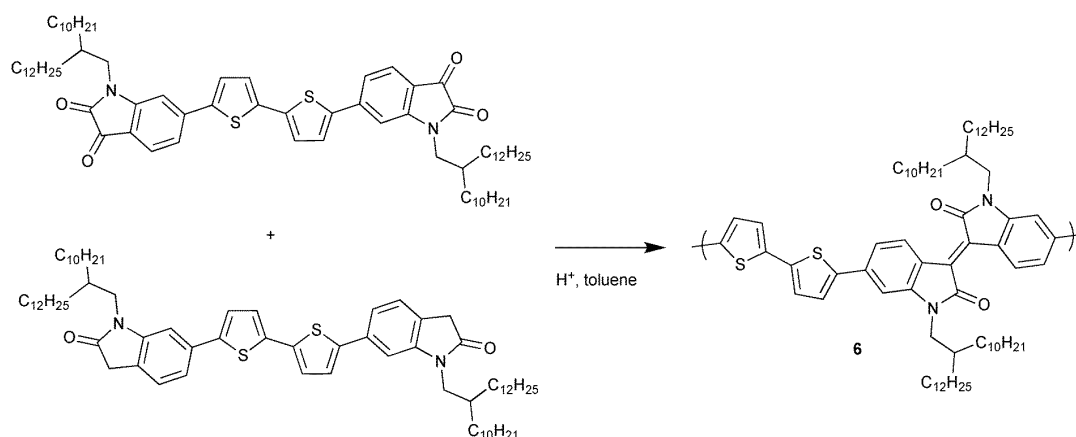
However, Kanbara's group investigated the role of terminal halogen atoms on the polymers' properties and concluded that the presence of terminal bromide had a bigger impact on the opto-electronic properties than residual palladium.<sup>61</sup> Therefore, it is crucial to limiting the use of not only transition metals but also halogens so that to avoid not only long and tedious purification but also additional

steps to remove the final halogen and improve the polymers' properties. Some condensation reactions with neither halogen atoms nor transition metals are exemplified as well, involving the synthesis of polyazomethines<sup>62</sup>, Knoevenagel reaction<sup>63</sup> and condensation of squaric acid<sup>64</sup> and Aldol condensation. Horner-Wadsworth-Emmons (HWE) reaction is also an efficient alternative to the Wittig reaction and enables well-controlled polymerization of various polymers. For example, Scheme 1. 11 illustrates the synthesis of a thiophene-based  $\pi$ -conjugated polymer *via* the HWE reaction.<sup>65</sup>



**Scheme 1. 11** Synthesis of a thiophene-based  $\pi$ -conjugated polymer *via* the HWE reaction.<sup>65</sup>

More interestingly, Zhang's team firstly investigated the synthesis of an isoindigo-based polymer using aldol condensation,<sup>66</sup> as presented in Scheme 1. 12.



**Scheme 1. 12** Aldol condensation of an isoindigo-based polymer.<sup>66</sup>

In addition to the above-mentioned alternative coupling reactions with or without halogen, it is also possible to perform polymerization *via* electro-polymerization or vapor phase deposition of appropriate monomers, in order to avoid the use of transition-metal catalysts. But the resulting polymers can't achieve well-defined  $\pi$ -conjugated structures.

Finally, we won't discuss it into details here but a new way of designing of  $\pi$ -conjugated polymers

using biomasses is currently explored. As examples, we can cite bio-based substrates having good potential in the field of organic electronics, i.e. cellulose and its derivatives. Indeed, cellulose was used recently as a promising monomer for the synthesis of various polymers and is also a promising building block for organic electronics.<sup>21</sup>

To sum up, while efforts have been made in parallel to design bio-based  $\pi$ -conjugated polymers or to develop alternative environment-friendly routes to semiconducting polymers, there is a great deal of room for development and progress in combining these two methodologies targeting more sustainable yet still efficient materials for organic electronics. It is obvious and promising that lignocellulosic biomass can be a source of a wide platform of substrates with various structures (aromatic, heterocyclic, linear, etc.) and functionalities (aldehyde, hydroxy, and methoxy for example).

### 1.6.2 Incorporation of side chains

As mentioned above, the incorporation of side chains onto conjugated backbones has afforded conjugated polymers better solubilities and processabilities. Commonly there are two approaches to grafting side chains: *post*-functionalization and *pre*-functionalization.

**Post-functionalization.** *Post*-functionalization involves two steps: the first step is that the polymer backbone terminated with functional groups and side chains terminated with other functional groups are synthesized, respectively. The second step is that the side chains are attached to the backbones through the chemical interaction between these functional groups. The commonly used reaction is the Williamson ether synthesis. The advantage of *post*-functionalization is that  $\pi$ -conjugated polymeric backbones can be synthesized by avoiding the influences of side chains. The disadvantage is that the substitution may be incomplete due to the steric hindrance and chemical equilibrium. No reaction or side reaction is also likely to occur in some reactive sites. That is to say, it is difficult to gain homopolymer using this strategy. When the backbones are terminated with halide atoms, the remaining halide atoms will have a large impact on the final polymer's optoelectronic properties.

**Pre-functionalization.** *Pre*-functionalization also involves two steps: the first step is that side chains are attached to the monomers *via* the substitution; the second step is the polymerization of the new monomers. Using *pre*-functionalization, even though it is sure that every repeating unit is well connected to a side chain, sometimes, the polymerization is not successful because the substitution of side chains may affect the distribution of electrons of the monomers. For example, when thiophene is substituted by a large side group, GRIM method might not be suitable to achieve controlled, high regioregular poly(3-alkylthiophene).

## 1.7 Scope of this thesis

This thesis focuses on the design, synthesis, and characterization of new  $\pi$ -conjugated polymers for

organic electronics. More particularly, **chapter 2** sets in the continuity of precedent studies of the team regarding the synthesis of a series of macromolecular liquid crystalline  $\pi$ -conjugated architectures specifically designed for OFETs at the Institut Parisien de Chimie Moléculaire (IPCM), in the Equipe de Chimie des Polymères (ECP). **Chapter 3** presents the first investigations performed in our lab on new light-emitting polymers developed for third-generation OLEDs, based on thermally activated delayed fluorescence (TADF) materials. Indeed, the group started an activity recently in this field, in the framework of a CNRS-JSPS project between OPERA (Kyushu University, Fukuoka, Japan) and IPCM.

**Chapter 2  $\pi$ -Conjugated polymers for organic field-effect transistors  
(OFETs)**

Electronic devices have witnessed a revolution in recent years, during which they've progressed from traditional Si-based devices to next-generation organic electronic devices.

On the one hand, compared with traditional silicon electronics, devices based on organic field-effect transistors (OFETs) offer unique advantages, including mechanical flexibility, solution processability, and tunable optoelectronic properties. This is why during the past several years impressive advances have been made in conjugated materials-based FETs. In particular, numerous FETs based on high-performance conjugated polymers have been developed thanks to the efforts of material design and device optimization, which provides a promising opportunity for applications in flexible displays, environmental monitoring, electronic skins and wearable devices.

On the other hand, liquid crystalline (LC) materials have large anisotropy of optical, electrical, magnetic, and physical properties because of their self-organized molecular structure and molecular alignment. Moreover, we explained already that charge-carrier transport properties depend not only on the intrinsic electronic properties of the materials, but also on the way the molecules are packed together in bulk. Therefore, one of the key parameters to improve the performance of OFET components is the development of structured and/or more ordered  $\pi$ -conjugated systems. In this context, LC conjugated polymers have recently attracted considerable attention from both fundamental and practical points of view, as various novel physical behaviors have been observed. In addition, these LC materials could be aligned under LC phase and improve consequently the efficiency of various applications such as polarized electroluminescence (EL) devices and organic thin film transistors.

As a consequence, this manuscript **chapter 2** starts with an introduction dedicated to bibliography (**section 2.1**): we will briefly detail the fundamental mechanisms governing OFETs, before to describe different families of liquid crystal materials. Then, we will present a class of organic materials able to give spontaneously self-assembling, i.e. organic liquid crystals, focusing on the  $\pi$ -conjugated systems and especially polymers.

The following two result sections (**section 2.2 and 2.3**) deal with the design, the synthesis and the characterization of new liquid crystal structured  $\pi$ -conjugated materials for future OFETs applications, looking for potential ambipolar properties. Indeed, only few nano-structure presenting two different electronic properties, such as electron donor and electron acceptor behaviors, have been investigated so far for OFET applications. Thus, after describing the multi-steps chemical strategy optimization, the thermal and self-organization behavior of our novel polymers are investigated. Preliminary charge transport properties are also evaluated in OFET configuration and discussed.

More precisely, in **section 2.2**, we describe the synthesis and the characterization of a supramolecular architecture resulting from the phase separation, at nanoscale level, of two covalently linked  $\pi$ -conjugated systems. We report the study of a so-called (**Polythiophene-oxa**), polymer composed of a

regioregular electron-donor poly(3-alkylthiophene) as the backbone and calamitic-type electron-acceptor oxadiazole entities as side groups.

In **section 2.3**, similarly are explored the properties of a so-called (**PBTTT-Tri**) which consists this time of an extended donor-type backbone, i.e. the poly(2,5-bis(3-alkylthiophen-2-yl)thieno[3,2-b]thiophene) (PBTTT), as well as discotic-type triphenylene side groups as acceptor counter-part.

## 2.1 Bibliography

### 2.1.1 Brief history of OFETs

Since discovered in 1986<sup>67</sup>, organic field-effect transistors (OFETs) have made exciting progress from a curiosity to a significant research area over the past two decades, and are currently widely applied in many electronic devices, including displays<sup>68</sup>, sensors<sup>69</sup>, radio frequency identification (RFID), and logic elements<sup>70</sup>.

**Why OFETs?** OFETs are attractive and widely explored, due to their semiconducting properties on the molecular level, the low thermal budget to construct the devices, the high degree of mechanical flexibility, as well as weak bonding (usually Van der Waals bonds) between organic molecules.<sup>71</sup> The weak bonding means that a small energetic input is required for organic semiconductors to self-assemble into favorable configurations on virtually any substrate to achieve some semiconducting properties.

**A very brief history of OFETs.** In 1986<sup>67</sup>, Tsumura, Koezuka, and Ando fabricated the first OFET device with a recognizable current gain by an *in-situ* polymerized polythiophene transistor, which is regarded as the most significant milestone for the development of OFETs. This is only in 1998 that a group at the Philips Research Laboratories in Eindhoven succeeded in producing an integrated circuit that consisted entirely of organic materials.<sup>72</sup> The field-effect charge-carrier mobilities of this first OFETs based solely on organic materials are less than  $10^{-2} \text{ cm}^2 \cdot \text{V}^{-1} \cdot \text{s}^{-1}$ , which was largely inferior to those of inorganic field-effect transistors based on amorphous silicon (a-Si) as a semiconductor ( $10^{-1} \text{ cm}^2 \cdot \text{V}^{-1} \cdot \text{s}^{-1}$ ). However, this success opened up completely new areas for application for organic field-effect transistors, particularly for developing cheap electronic components.

After much effort, the mobilities of solution-processed OFET components are now approaching those based on amorphous silicon,<sup>73</sup> owing to the advantage of ‘wet chemistry’. More specially, organic semiconductors can be manipulated and processed at much lower temperatures than that required for the processing of a-Si layers in the production of inorganic field-effect transistors. Besides, polymer films, *i.e.* polyethylene terephthalate (PET), that retain their shape only up to about 180°C are to be used as a substrate for cost-effective and flexible circuits in organic electronics, such as electronic paper.

Nowadays, the individual components in OFETs (electrodes, semiconductors, insulators, possibly

encapsulation) can be applied by different techniques: On the one hand, the layers can be deposited from the gas phase in analogy to the processing of most inorganic semiconductors (physical vapor deposition (PVD), chemical vapor deposition (CVD), sputtering), whereas on the other hand inexpensive solution techniques (e.g., spin coating, inkjet printing, and screen printing) are possible. Their use depends on the physical characteristics of the components, such as vapor pressure, stability, and solubility.

**In this context, more interested are the materials that can be applied from solution, *i.e.* solution-processable semiconductors**, as they should allow large-area processing in roll-to-roll methods, for example, for the electronic control of large active-matrix displays or in electronic labels. Moreover, it is expected that the avoidance of slow and cost-intensive vapor deposition methods in a high vacuum will bring cost advantages. As an example, for use in electronic labels (so-called RFID tags), a production cost of less than one cent per label will be required.<sup>74</sup>

This is the reason why for many complex chemical, physical, and technological questions that involve all OFET components (conductors, semiconductors, and insulators) and their interplay, **the organic semiconductor used is always a key component**. As a consequence, innovative approaches to the synthesis of organic semiconducting compounds that can be processed from solution and highlight their potential as semiconductors in OFETs. Both low molecular weight compounds (“small molecules” and oligomers) and polymeric semiconductors are suitable for this purpose, whatever they show liquid crystal properties or not.

**In this bibliographic section**, we focus on this important and rapidly developing field: we start with the basic knowledge on OFETs, before to present the state of the art in terms of high-performance polymers and end with the potential interest of liquid crystal polymers in particular.

### 2.1.2 OFETs construction and functionality

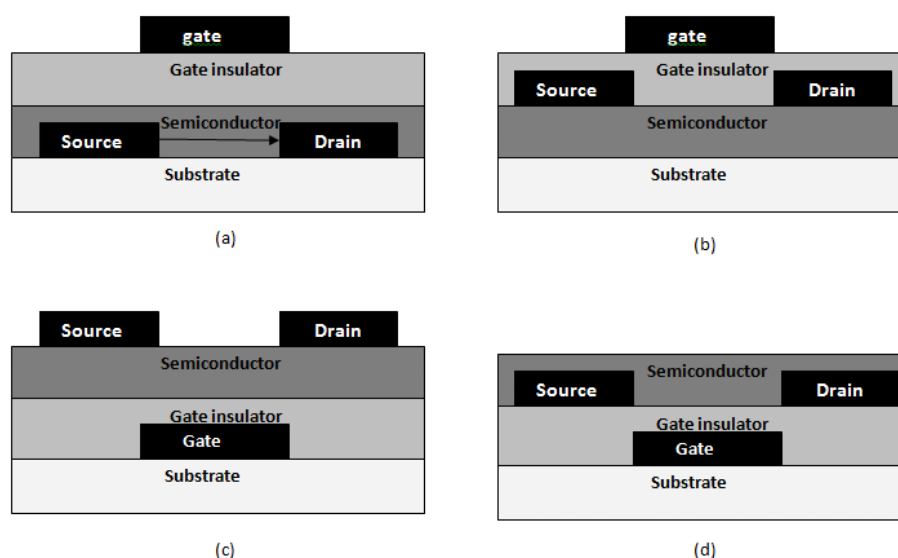


**Figure 2.1. 1** OFETs structures<sup>75</sup>: a) top-gate bottom-contact (TGBC); b) top-gate top-contact (TGTC); c) bottom-gate top-contact (BGTC); d) bottom-gate bottom-contact (BGBC).

OFET devices are voltage-controlled three-terminal switching devices, consisting of substrate, organic semiconductor layer, dielectric layer, gate electrode, and source-drain electrode.<sup>76</sup> As demonstrated in Figure 2.1. 1, there are four main types of OFET structures: bottom-gate top-contact (BGTC), bottom-gate bottom-contact (BGBC), top-gate top-contact (TGTC), and top-gate bottom-contact (TGBC). Generally speaking, p-type organic semiconductors prefer bottom-gate OFETs structures, while ambipolar or n-type organic semiconductors favor top-gate OFETs structure, since the gate electrode and the dielectric layer have a certain protective effect on the semiconductor active layer and can prevent air to a certain extent.

When a gate voltage ( $V_G$ ) is applied, free charges are induced at the interface between the semiconductor and dielectric layers. Furthermore, a small source/drain voltage ( $V_{SD}$ ) forms a current in the channel, because charges are produced due to the electrostatic effect. The induced charge density in the channel is controlled by the value of  $V_G$ , and the source/drain current ( $I_{SD}$ ) intensity is also changed during the process. So,  $V_G$  plays a part in adjusting the current “switches” of a FET.

The parameters of the device are mainly calculated through the output and transfer curves of FETs (scan  $V_{SD}$  at a constant  $V_G$  and scan  $V_G$  at a constant  $V_{SD}$ ). Figure 2.1. 2 shows the typical output and transfer characteristics for p-type and n-type transistors, where the effect of  $V_G$  and  $V_{SD}$  is clear.

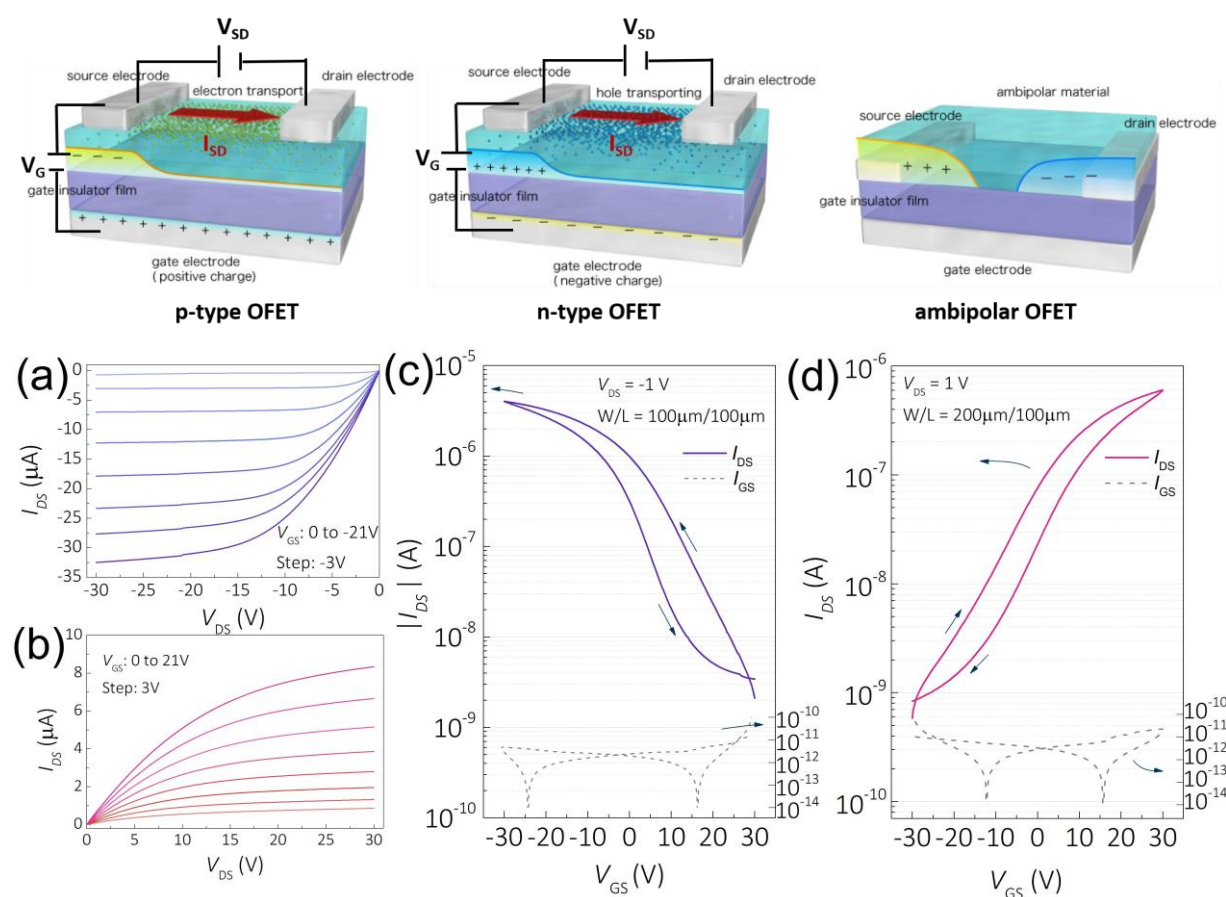


**Figure 2.1. 2** The structures of p-type, n-type, and ambipolar OFET devices. Output characteristics for p-type (a) and n-type (b) transistors; Transfer characteristics for p-type (c) and n-type (d) transistors.<sup>77</sup>

The following parameters are used to evaluate the performance of OFETs. Mobility ( $\mu$ ) reflects the carrier (electron or hole) transfer rate under a certain electric intensity. The physical meaning of threshold voltage ( $V_T$ ) is the minimum  $V_G$  required to induce the channel. When different  $V_G$  and  $V_{SD}$  are applied, the working modes are different. This value is obtained from a transfer ( $I_{SD}$  versus  $V_G$ ) measurement. The current ( $I$ )-voltage ( $V$ ) characteristics (Figure 2.1. 2) in the linear and saturated regimes are readily applicable to both inorganic and organic field-effect transistors:

$$\text{In the linear regime: } I_{SD} = \frac{W}{L} \mu C (V_G - V_T) V_{SD}$$

$$\text{In the saturated regime: } I_{SD} = \frac{W}{2L} \mu C (V_G - V_T)^2$$

Where  $I_{SD}$  and  $V_{SD}$  are the current and voltage bias between the source (S) and the drain (D) electrodes, respectively;  $V_G$  is the gate voltage applied between the gate (G) and the source (S) electrodes, producing charges in the channel because of the electrostatic effect;  $V_T$  is the threshold voltage at which the current starts to rise,  $C$  is the capacitance of the gate dielectric,  $W$  and  $L$  are the width and length of the conducting channel, respectively.

**Nevertheless, several challenges still exist.** Firstly, there is no unified theory for transport mechanism in semiconducting polymers, which needs to be thoroughly studied in the future for understanding the origin of the high performance. Secondly, a practical standard to measure  $\mu_{\text{effect}}$  without miscalculation has not been employed: indeed, the charge carrier mobility can be determined by various techniques, including time-of-flight (TOF) method, steady-state TF-SCLC method, DI-SCLC method, FET method, and pulse radiolysis time-resolved microwave conductivity (PR-TRMC) technique.<sup>78</sup>

Besides, the device performance is affected by many factors such as molecular packing, interface, and film morphology. More precisely, the charge carrier mobility of organic materials greatly relies on the intrinsic properties of charge carriers, namely, whether they are holes or electrons, molecular structures, and materials morphologies. Apart from that, the aggregation states of materials (such as amorphous and crystalline states) also have a big influence on the charge carrier mobility.

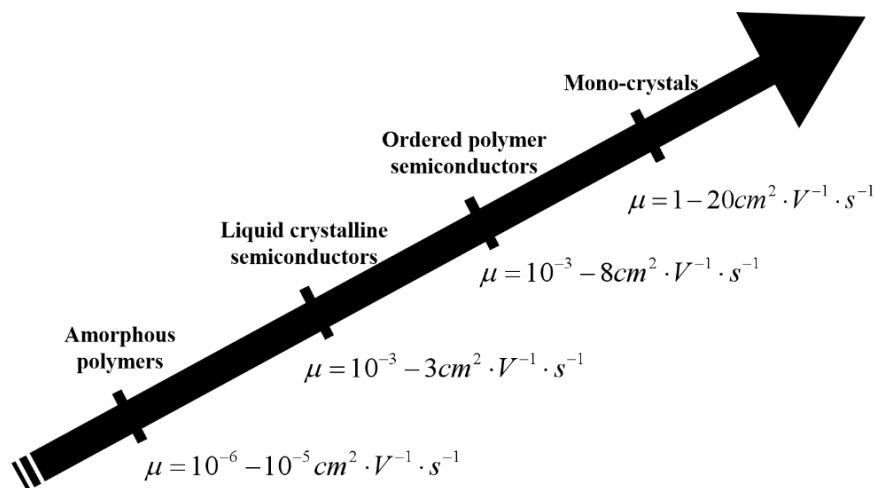


**Figure 2.1. 3** Influence of organization degree on charge transport properties.

As represented in Figure 2.1. 3, the mobility of charge-carrier increases along with increasing the aggregation degree of the organic materials.<sup>78</sup> Amorphous polymers exhibit the lowest mobility ( $10^{-6}$ - $10^{-5}$   $\text{cm}^2 \cdot \text{V}^{-1} \cdot \text{s}^{-1}$ ) as a consequence of a low degree of order. Single crystals possess the highest degree of order, corresponding to the highest mobility ( $1$ - $20$   $\text{cm}^2 \cdot \text{V}^{-1} \cdot \text{s}^{-1}$ ), but the processability and film quality have to be improved. Between them, liquid crystalline semiconductors and ordered polymer semiconductors both have efficient mobility ( $10^{-3}$ - $8$   $\text{cm}^2 \cdot \text{V}^{-1} \cdot \text{s}^{-1}$ ) and good processability for optoelectronic applications.

### 2.1.3 High-performance conjugated polymers for OFETs

After 30 years of development, much effort has been made to explore the effective material design strategy, the efficient fabrication technology, and the understanding of the relationship between materials and functional devices, to achieve high-performance conjugated polymers for OFET applications.<sup>79</sup> For example, the structures of conjugated polymers have evolved from donor-donor (D-D) to donor-acceptor (D-A) models, and the mobility has increased from the early  $10^{-5}$   $\text{cm}^2 \cdot \text{V}^{-1} \cdot \text{s}^{-1}$  to much higher values comparable with that of single crystals.<sup>67,80</sup>

Conjugated polymers can be classified as hole or electron (p- or n-type) transporting or ambipolar materials according to the type of orderly transferring charge carriers. Although significant progress has been made in the preparation of semiconducting polymers for OFET applications, currently, most high-performance OFETs based on D-A polymers are p-type devices, some of which even show high hole mobilities over  $50$   $\text{cm}^2 \cdot \text{V}^{-1} \cdot \text{s}^{-1}$  with good device stability.<sup>81</sup> In contrast, the development of ambipolar or n-type OFETs falls behind that of p-type devices.<sup>82</sup> Thus, studies on ambipolar or n-type polymers have gained increasing importance in the field of OFETs.<sup>79</sup>

**Below, we introduce the recent advances in high-performance D-A polymers, including p-type, ambipolar, and n-type counterparts,** trying to insist on the key factors explaining their efficiency.

#### 2.1.3.1 p-type polymers

As mentioned above, the most reported high-performance OFETs based on D-A polymers are p-type devices. Figure 2.1. 4 show the common donor (D) and acceptor (A) used, as well as the structures of some high-performance p-type polymers based on these D and A units.<sup>3</sup> The essential criteria for p-type high-performance D-A polymers include:

**Appropriate HOMO (-5.0 to -5.5 eV) and LUMO (>-3.5 eV) energy levels.** Most p-type D-A polymers hold the highest occupied molecular orbital (HOMO) energy levels in the range of  $-5.0$  to  $-5.5$  eV, which is generally close to the work function ( $\text{WF} = 5.1$  eV) of gold electrodes,<sup>83</sup> making it easy for the hole injection from the electrodes into the semiconducting layers.

**High molecular weight ( $M_n$ ).** Polymers with high  $M_n$  usually show improved crystallinity, better

domain connectivity, and reduced grain boundaries, thus enhancing the mobilities.<sup>84</sup> But it is worth noting that high  $M_n$  may also result in reduced solubility, further affecting the fabrication process. Thus, improving  $M_n$  is an effective way to increase mobility when good solubility is ensured.

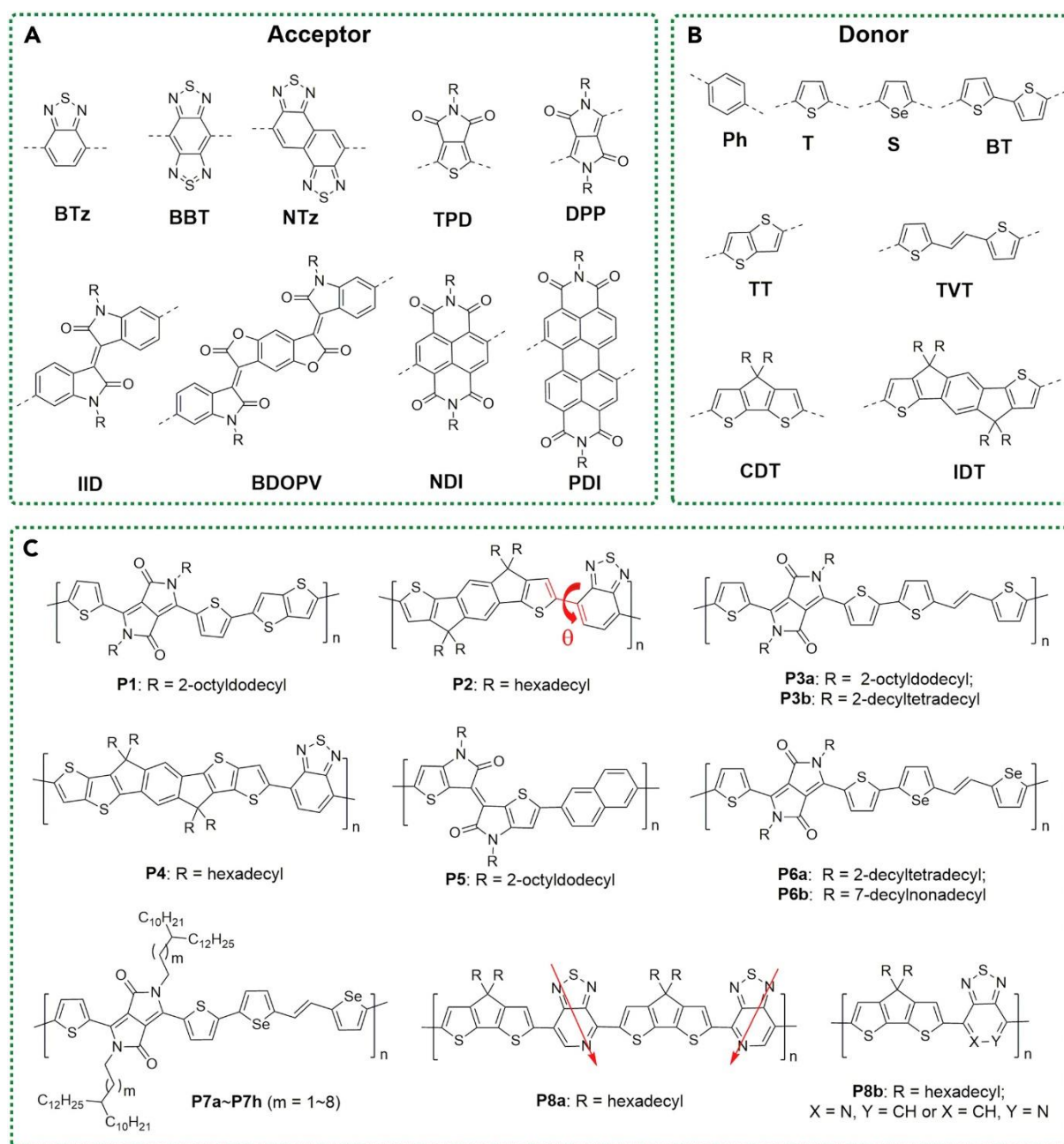


**Figure 2.1.** 4 D-A polymers for p-type OFETs<sup>3</sup>: (A) Common acceptors; (B) Common donors; (C) High-performance p-type polymers.

**Good backbone conjugation and coplanarity.** As charge transport occurs between  $\pi$  orbitals through backbone conjugation in polymeric semiconductors, an enhanced coplanarity will result in more effective backbone conjugation and closer  $\pi$ - $\pi$  stacking, thus improving the mobilities.<sup>3</sup>

**High crystallinity and uniform film morphology.** For OFET devices, the channel length (tens of micrometers) is usually larger than the polymer crystalline domain (tens of nanometers). This means

that many grain boundaries exist in the active layer between the source and drain electrodes. These grain boundaries hinder charge transport. Therefore, the polymer film with a high degree of crystallinity and well-connected morphology is favorable for achieving high mobility. Two methods, “side-chain engineering”<sup>85</sup> and “well-aligned film” (by unique device fabrication techniques)<sup>86</sup> are adopted to tune the crystallinity and morphology.

### 2.1.3.2 Ambipolar or n-type polymers

Compared with p-type polymers, so far, most reported ambipolar or n-type polymers are based on strong electron-withdrawing units.<sup>87</sup> The ideal ambipolar or n-type polymers are basically required to have<sup>88</sup>: **Suitable HOMO/LUMO levels** relative to the p-type emitter, thereby minimizing the barrier for the electron injection, reducing turn-on/operating voltage, and effectively blocking holes.

**High electron mobility ( $\mu_e$ )** to move the charge recombination zone away from near the cathode and improve the exciton generation rate.

However, low electron mobilities and inferior device stability impede the applications of ambipolar or n-type polymer FETs, because the LUMO energy level of most D-A polymers is between -3.3 and -4.0 eV, which is far from the work function of gold electrodes (WF = 5.1 eV). An effective approach to achieve ambipolar or n-type polymers is to lower their lowest unoccupied molecular orbital (LUMO) energy levels, thus facilitating the electron injection ability and enhance the device stability. Two strategies can be developed to lower the LUMO energy levels: introducing electron-withdrawing groups (EWGs)<sup>87</sup> (F, N, Cl, etc.) or acceptor dimers (“acceptor dimerization”)<sup>84</sup> into the polymer backbone. In addition to energy level modulation, “side-chain engineering”<sup>85</sup> can also improve the electron mobility of ambipolar or n-type polymers.

*\* Introducing EWGs (F, N, Cl, CN, and B) into the polymer backbone*

**Fluorine (F) substitution.**<sup>3</sup> So far, high electron mobilities of more than  $5 \text{ cm}^2 \cdot \text{V}^{-1} \cdot \text{s}^{-1}$  have been achieved in some F-containing polymers. Apart from lowering HOMO/LUMO energy levels, incorporating F atoms into a polymer leads to several unique advantages: (1) there is almost no steric hindrance, because F atom shows a small van der Waals radius of  $1.35 \text{ \AA}$ , which is slightly larger than that of H ( $r = 1.20 \text{ \AA}$ ); (2) it induces intramolecular or intermolecular F-H and F-S interactions, which may enhance the backbone coplanarity and promote better molecular crystallization; (3) it improves the device stability in the air, as the hydrophobicity of F-containing polymers can prevent the diffusion of moisture and oxygen into the films. Despite these advantages, F-containing polymers usually have poor solubility in common solvents, thus inferior solution-process ability. Moreover, the synthesis of F-substituted units, especially F-containing acceptors and polymers, is quite difficult.

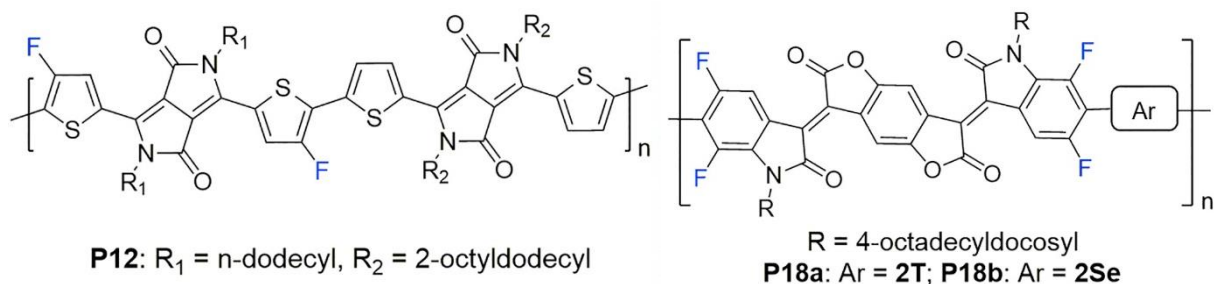


**Figure 2.1. 5** F-substituted polymers for ambipolar or n-type OFETs.<sup>89,90</sup>

**Nitrogen (N) substitution.**<sup>3</sup> N substitution usually refers to the replacement of C–H in an aromatic ring with  $sp^2\text{-N}$ . In addition to lowering the HOMO/LUMO energy levels, N-substituted polymers also have similar advantages with F-containing polymers including reduced steric hindrance and possible intramolecular or intermolecular N–H interactions. However, the replacement of C=C with C=N leads to worse  $\pi$ -conjugation, which is harmful to charge transport. Hence, the number and position of substituted N atoms in polymers should be carefully designed, which leads to additional challenges for material synthesis. As a remark, the introduction of N atoms into the acceptors rather than the donors may result as well in higher crystalline microstructure and better electron mobility.

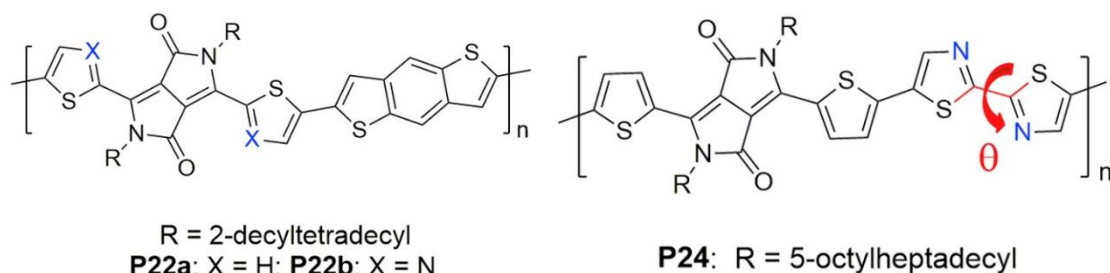


**Figure 2.1. 6** N-substituted polymers for ambipolar or n-type OFETs.<sup>91,92</sup>

**Chlorine (Cl) substitution.**<sup>3</sup> Similar to F substitution, Cl substitution can also lower both the HOMO and LUMO energy levels. As Cl atom has a larger van der Waals radius ( $1.80 \text{ \AA}$ ) than that of H ( $r = 1.20 \text{ \AA}$ ), Cl substitution may cause steric hindrance, thus distorting the backbone coplanarity, which is harmful for  $\pi$ -conjugation and intermolecular  $\pi$ - $\pi$  stacking. To date, only a few chlorinated polymers have been reported.<sup>93,94</sup>

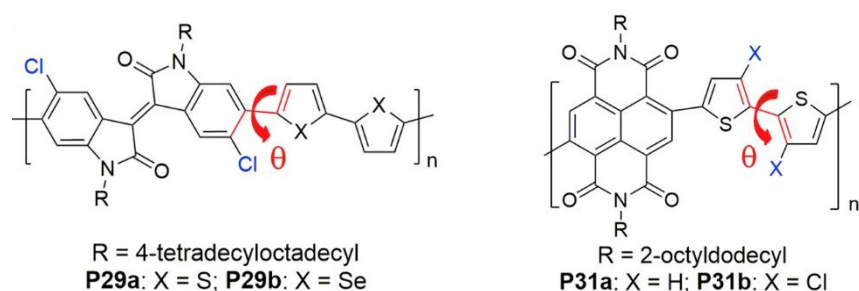


**Figure 2.1. 7** Cl-substituted polymers for ambipolar or n-type OFETs.<sup>93,94</sup>

**Cyano (CN) substitution.**<sup>3</sup> CN is a strong EWG, which can significantly lower the HOMO and LUMO energy levels. Owing to its bulky size, CN substitution can lead to steric hindrance and further to a twisted backbone, which is harmful for  $\pi$ -conjugation and intermolecular  $\pi$ - $\pi$  stacking.

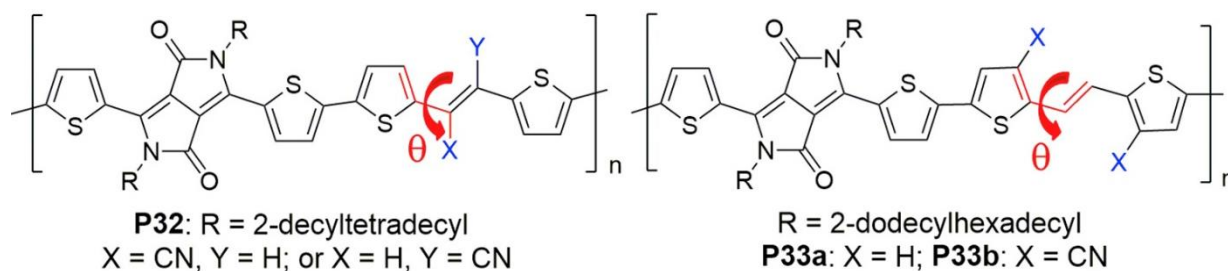


**Figure 2.1. 8** CN-substituted polymers for ambipolar or n-type OFETs.<sup>95,96</sup>

**Boron (B) substitution.**<sup>3</sup> So far, B-containing ambipolar or n-type polymers for OFETs are scarce, and most reported B-containing polymers have B-N units, which endows the acceptors with fixed planar configuration and low-lying HOMO/LUMO energy. The main challenge of B-containing polymers is also material synthesis. Furthermore, the relationship between material design and device performance is unclear, which needs further research.

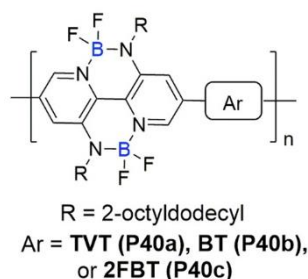


**Figure 2.1. 9** B-substituted polymers for ambipolar or n-type OFETs.<sup>97</sup>

*\* Acceptor dimerization*

The second strategy, namely “acceptor dimerization”, was recently developed by Liu et al.<sup>98</sup> This strategy introduces an acceptor dimer with stronger electron-withdrawing property into a polymer and provides a new access for ambipolar or n-type polymers (Figure 2.1. 10). Besides lowering HOMO/LUMO energy levels, this strategy does not cause steric hindrance, maintaining the backbone planarity and the acceptor dimers can be obtained by a general homocoupling reaction. Figure 2.1. 11 displays two reported polymers using the acceptor dimerization strategy, among them, **P42** exhibited excellent ambipolar performance with  $\mu_h$  and  $\mu_e$  values of 6.87 and 8.94 cm<sup>2</sup> V<sup>-1</sup> s<sup>-1</sup>, respectively.<sup>99</sup> **P44**-based TGBC OFETs with a CsF electrode-modifying layer showed unipolar n-type performance with a  $\mu_e$  of 0.82 cm<sup>2</sup> V<sup>-1</sup> s<sup>-1</sup>.<sup>100</sup>



**Figure 2.1. 10** Molecular structures of D-A and acceptor dimerization polymers.

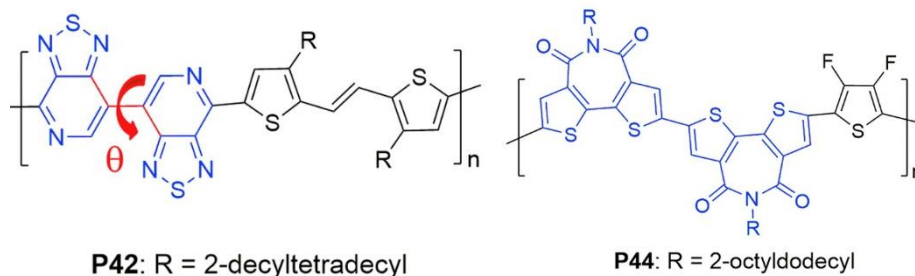


**Figure 2.1. 11** Reported ambipolar or n-type polymers by the acceptor dimerization strategy.<sup>99,100</sup>

\* *Side-chain engineering*

In addition to energy level modulation, “side-chain engineering” can also be used to improve the electron mobilities of n-type or ambipolar polymers. Indeed, incorporation of specific side chains into a polymer may result in closer  $\pi$ - $\pi$  stacking, larger crystalline correlation lengths, and better domain connectivity. Therefore, the modulated polymer can show better intermolecular charge transport and, thus, improved mobilities. Figure 2.1. 12 shows the molecular structures of reported polymers by side-chain engineering strategy for ambipolar or n-type OFETs. Such side chains include siloxane-solubilizing chains<sup>101</sup> and semifluoroalkyl chains<sup>102</sup>, among others. Note that this strategy can also be applied to other high-performance polymers to further improve their performance.

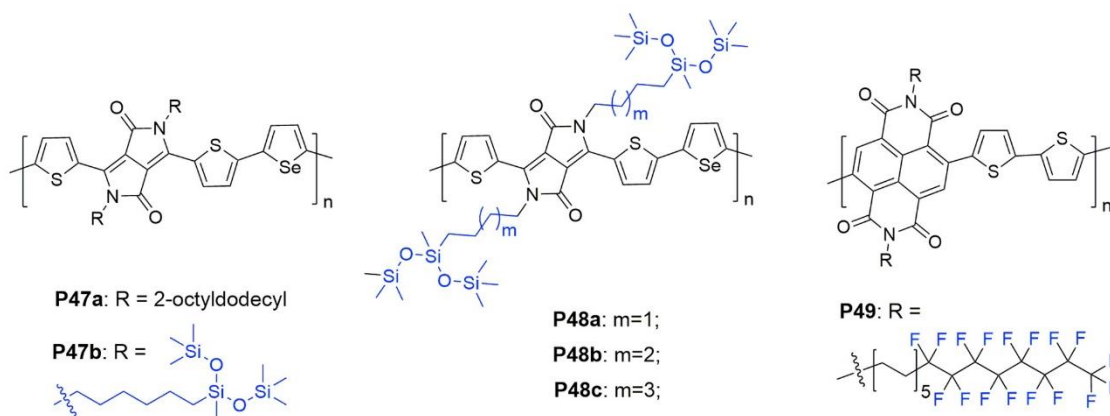


**Figure 2.1. 12** Ambipolar or n-type polymers by side-chain engineering.<sup>101–103</sup>

**We won't detail it in this manuscript but note that fabrication technology is as important as clever material design**, as for high-performance OFETs an effective solution-processable technique is the other key factor. Indeed, the solution processability of OFETs lays the foundation for low-cost and large-area flexible electronics. Usually, scientists control the crystallinity of molecules by improving

film-forming processes, such as by using high-boiling-point solvents, blends of good and poor solvent, or controlling the physical force effects (shear force, centrifugal force, or capillary force). Irrespective of small molecules or polymers, several solution-processable techniques are commonly used in the laboratory, such as spin-coating, drop-casting, bar coating, solution shearing, and printing.

**In this context, liquid crystal (LC) materials could be interesting,** as (LCs) are a state of matter exhibiting properties between those of conventional solid and those of isotropic liquid. More specifically, liquid crystals can present dynamic and order properties, leading to large and oriented self-organized domains. This way, the resulting ordered structures on large scale make it possible for liquid crystals to possess a good charge carrier mobility, thus making them potential good candidates in optoelectronic devices and especially for OFETs applications.<sup>2</sup>

#### 2.1.4 Liquid crystals

**Discovery.** Liquid crystalline materials were first discovered in cholesteryl ester by Friedrich Reinitzer in 1888.<sup>104</sup> The main discoveries of Reinitzer were high levels of optical activity and dual melting points in his samples. The samples were sent to Prof. Lehmann to perform systematic microscopy studies: he published two major findings on properties unique to liquid crystalline materials: anisotropy and fluidity. Consequently, Lehmann coined the word “liquid crystal”. Then, Pierre-Gilles de Gennes, a French physicist, advanced many theoretical studies on liquid crystalline materials and received a Physics Nobel Prize in 1991. In the present era, enthusiasm in liquid crystalline materials research stems from two sources: understanding novel liquid crystalline phases and the development of large-scale flexible electronics.

##### 2.1.4.1 LC phases and nanostructures

Today, liquid crystalline (LC) materials are omnipresent in all aspects of life. They are found almost everywhere: from self-assembling biological DNA to the working material of various display technologies. Liquid crystalline materials are a special phase of matter with the unique property of self-organization or self-assembly due to attractive van der Waals forces between individual molecules.<sup>105</sup> The liquid crystal phase exists between an isotropic liquid phase and a crystalline solid phase.<sup>106</sup> According to the formation condition of LC phase, liquid crystals are also divided into thermotropic and lyotropic phases, depending on the fact that phase transitions are observed due to temperature changes or under appropriate concentration and pressure, respectively.

Liquid crystalline molecules share many mechanical properties of liquids, such as high fluidity, as well as formation and coalescence of droplets. At the same time, liquid crystalline materials are similar to crystalline solid such that they exhibit electrical, mechanical, optical, and magnetic anisotropy. In short, liquid crystalline materials flow like liquids, while maintaining partial orientational and

positional ordering like solids (Figure 2.1. 13).

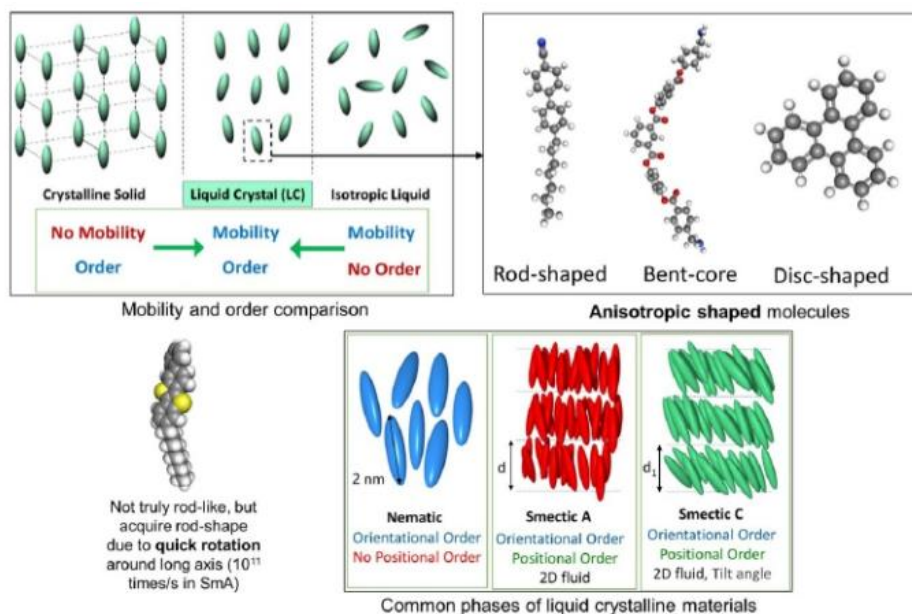


**Figure 2.1. 13** Mobility and order in liquid crystals and mesophases<sup>107</sup>.

One common property that all liquid crystalline materials have is the anisotropic shape of the molecules. The compound that displays liquid crystal properties is called a mesogen and it consists of both rigid and flexible parts. The rigid components make the mesogens align in one certain direction and show distinctive shapes like disk or rod. The flexible parts offer mobility to limit the degree of crystallization. The interplay of rigid and flexible segments induces a nanosegregation of these incompatible segments and provides the liquid crystal properties. Based on the shape of rigid mesogenic cores, mesogens can be divided into calamitic<sup>108</sup>, discotic<sup>109</sup>, sanidic<sup>110</sup> as well as bent-core<sup>111</sup> mesogens.

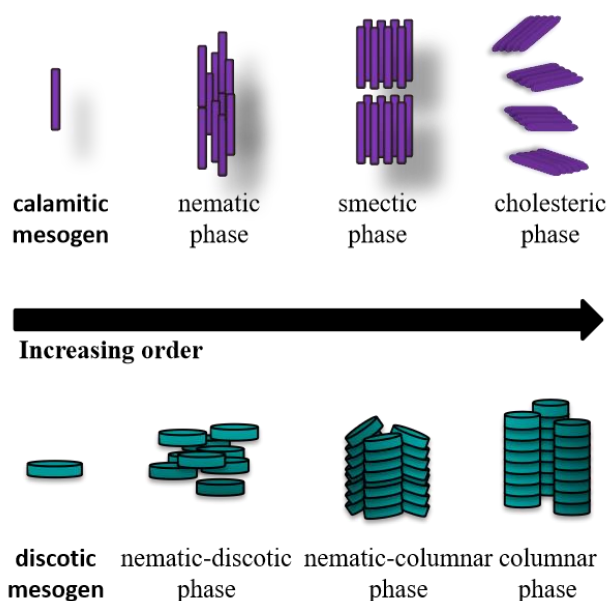


**Figure 2.1. 14** The formation of mesophases.

Calamitic and discotic mesogens are the most common ones observed. As shown in Figure 2.1. 14, nematic phase, smectic phase, and cholesteric phase can be formed by calamitic mesogens *via* self-organization in different degrees of order.

Among them, the nematic phases possess no positional order, but self-organize to have the long-range orientation order, demonstrating that the mesogens are parallel to each other along one defined direction. Considering liquid crystalline materials with an extended  $\pi$ -conjugated core, they can present charge transport properties. Smectic phases exhibit both positional and orientational order, meaning that the mesogens are ordered in layers to be a lamellar phase. Therefore, two-dimensional charge transport can be achieved in the layers.<sup>112</sup> For discotic mesogens, nematic-discotic, nematic-columnar, and columnar mesophases can be self-aligned and one-dimensional charge transport is favored along the column<sup>109</sup> (Figure 2.1. 15).

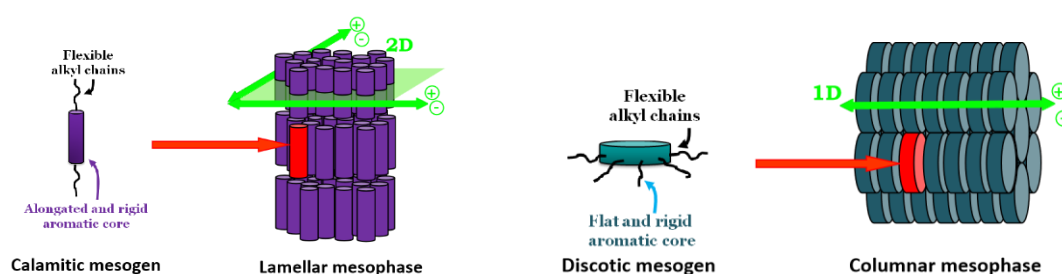


**Figure 2.1. 15** The electronic properties of lamellar and columnar mesophases.

**Similar to LC small molecules, LC polymers** are also composed of rigid and flexible segments. According to the position of the mesogenic core, LC polymers can mainly be divided into two types, as reported in Figure 2.1. 16: side-chain LC polymers and/or main-chain LC polymers. Note that the mesogens can be grafted onto the backbone *via* either a rigid or flexible spacer.

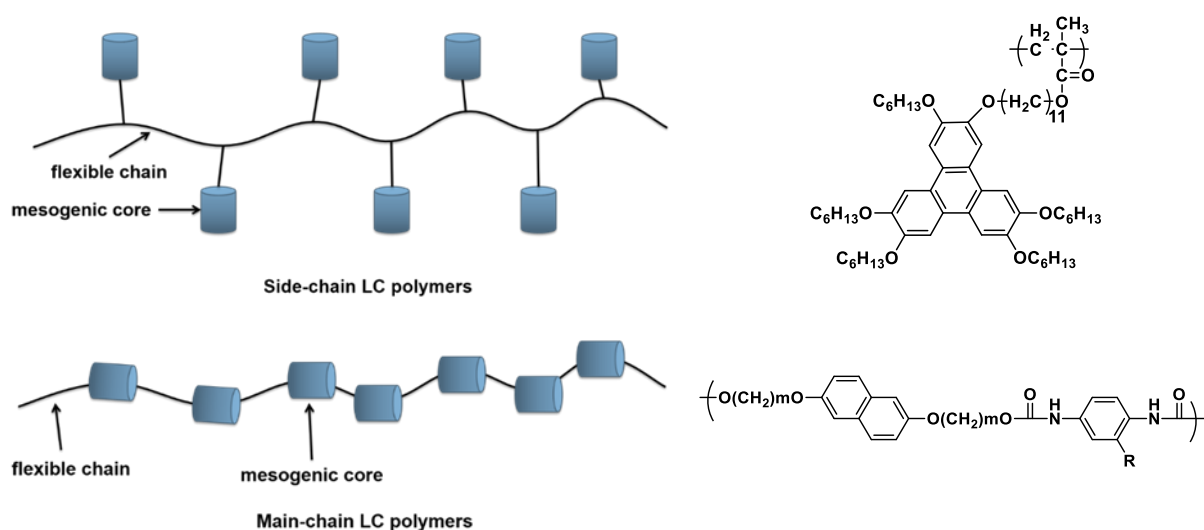


**Figure 2.1. 16** Side-chain and main-chain LC polymers (with 2 examples of chemical structures).

The liquid crystalline order can also be used as a criterion of classification of the materials, as in the case of low-molecular-weight compounds. A few examples of these structures are shown in Figure 2.1. 17.<sup>113</sup> Thermotropic polymorphism is influenced by the nature of the polymer backbone (flexible, rigid) and of the mesogens (calamitic, discotic, etc.), as well as by the type of architecture.

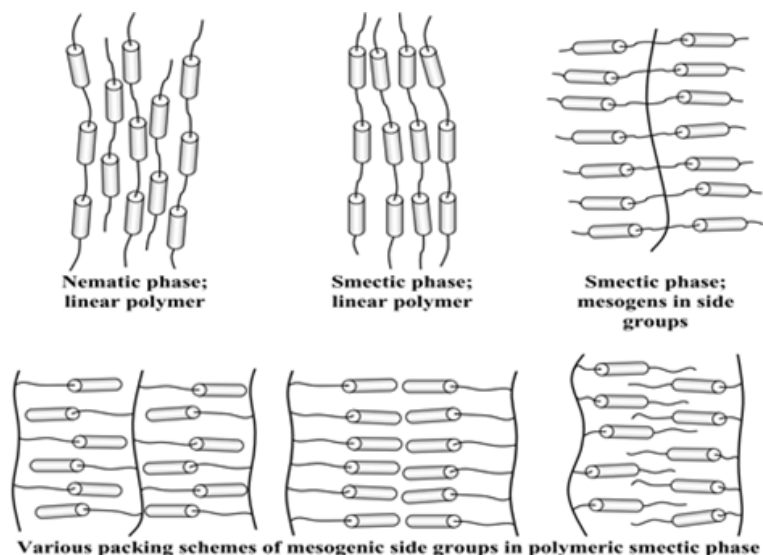


**Figure 2.1. 17** Basic types of ordering in LC polymers for main-chain and side-chain LC polymers.<sup>113</sup>

#### 2.1.4.2 LC properties characterization

To determine the LC properties and phase transitions, several techniques are often used, including polarized light microscope (POM), differential scanning calorimetry (DSC), and X-ray diffraction (XRD) measurements.

*Polarized light microscope (POM):* POM is an optical microscope containing polarized light and it is often used to study liquid crystals. As liquid crystals are optically “anisotropic” in LC phase and isotropic in liquid phase (high temperature), in theory, the birefringent textures can be observed under the polarized light in LC phase (Figure 2.1. 18) and only a black texture (no birefringence) is observed in liquid state due to the isotropic medium (high temperature). The texture type informs also about the nature of the LC phase obtained.

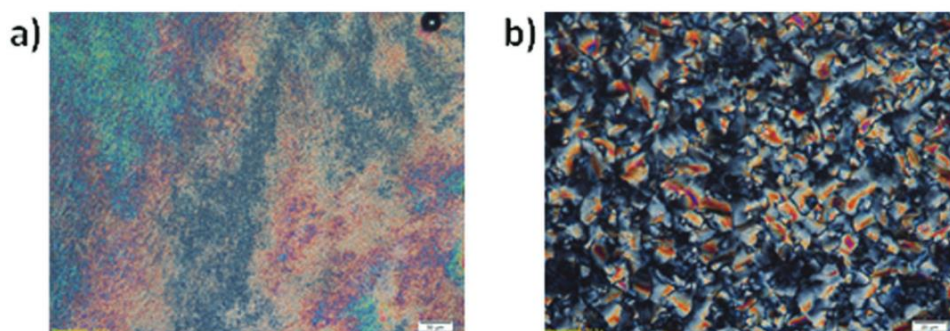


**Figure 2.1. 18** Birefringent texture observed under POM for one sample at room temperature and the mosaic texture observed upon cooling from the isotropic phase.<sup>114</sup>

*Differential Scanning Calorimetry (DSC):* DSC is a thermoanalytical technique to follow the thermal changes of the samples with the temperature changing. As we all know, the phase transitions take place along with the energy changes. Therefore, it is possible to use DSC to observe the small energy changes corresponding to the phase transitions from solid-state to LC state and from LC state to an isotropic liquid. For polymers, DSC can also observe the thermal change belonging to the glass transition. One example of DSC thermograms was shown in Figure 2.1. 19.<sup>114</sup>

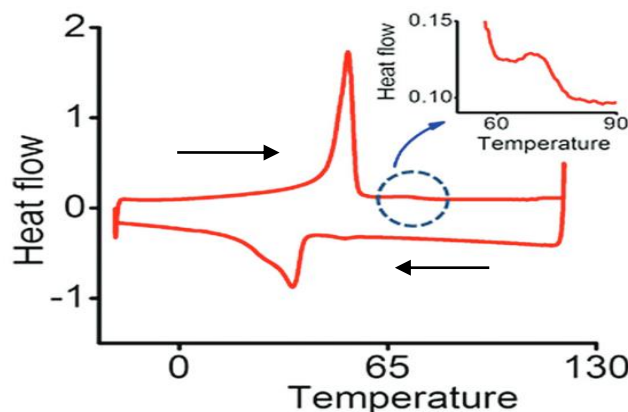


**Figure 2.1. 19** DSC thermograms obtained for one sample<sup>114</sup> showing phase transitions during heating and cooling cycles at a scan rate of  $5\text{ }^{\circ}\text{C}\cdot\text{min}^{-1}$ .

*X-ray diffraction (XRD):* XRD is an experimental technique to determine the diffraction pattern, revealing the information of phase and crystal structures. It can be further classified into single crystal XRD and powder XRD. In physics, Bragg's law gives the angles for coherent and incoherent scattering from a crystal lattice:

$$2d\sin\theta = n\lambda$$

where  $\theta$  is the scattering angle,  $n$  is a positive integer,  $\lambda$  is the wavelength of the incident wave. Thus, by this technique coupled to temperature changes, we can go back to key parameters both in the crystal lattice and corresponding to the ordering/packing in the LC phase (Figure 2.1. 20).

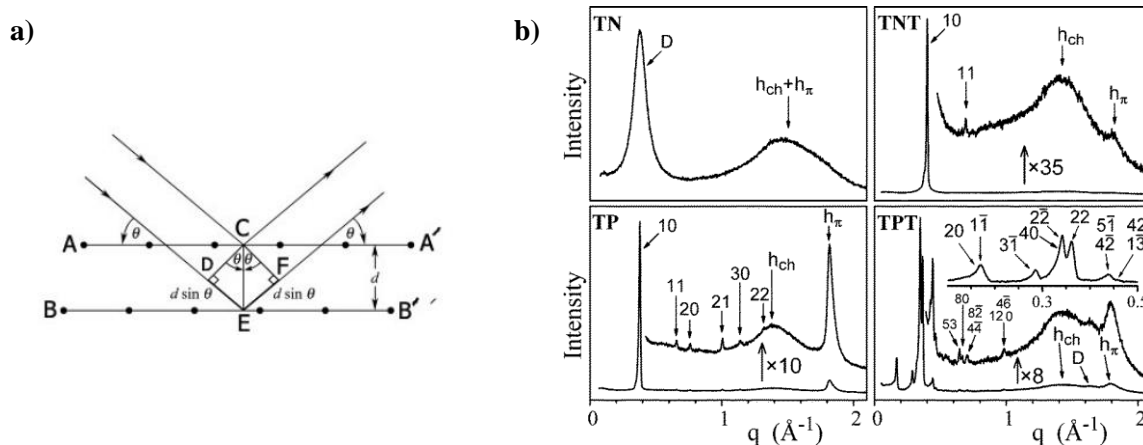


**Figure 2.1. 20** a) The principle of XRD; b) Typical XRD pattern of a columnar mesophase presenting Bragg's reflections of the columnar organization.<sup>115</sup>

### 2.1.4.3 Rapid state of the art regarding semiconducting LC small molecules

Recent research has shown that small-molecule organic semiconductors (OSCs) possessing liquid crystal (LC) properties are of great potential value in FET devices owing to their flexibility, tunability, proven efficacy in large-area thin-film devices, ability to operate over a wide temperature range, low cost, and solution-processability when compared to organic polymer and inorganic semiconductors.<sup>114</sup> Many liquid crystal small-molecule materials have been developed as good candidates for OFET applications, such as phenyl-terthiophene derivatives, di-thienyl-naphthalene, hexabenzocoronene, bis-(5'-hexylthiophen-2'-yl)-2,6-Anthracene, and dialkyl-BTBT derivatives. As an example, 2-decyl-7-phenyl-[1]benzothieno[3,2-b][1]benzothiophene (Ph-BTBT-10)<sup>116</sup> (Figure 2.1. 21), a smectic E (SmE) liquid crystalline material, was identified as a potentially good candidate for OFET materials in printed electronics, as it provides uniform and molecularly flat polycrystalline thin films reproducibly when SmE precursor thin films are crystallized, and also exhibits high durability of films up to 200 °C. Ph-BTBT-10 achieved a high mobility over  $10 \text{ cm}^2 \cdot \text{V}^{-1} \cdot \text{s}^{-1}$  after thermal annealing at 120 °C in bottom-gate-bottom-contact (BGBC) OFET configuration.

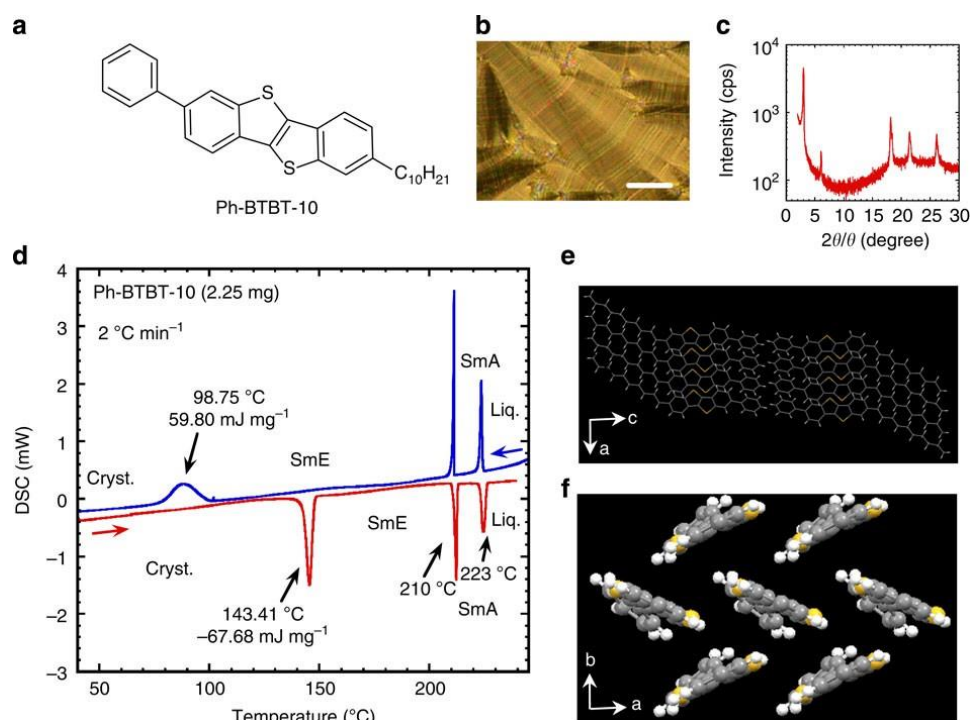


**Figure 2.1. 21 Ph-BTBT-10<sup>116</sup>:** (a) Chemical structure; (b) POM texture observed at 150 °C, the white bar indicates a scale of 50 μm; (c) XRD pattern of a liquid crystalline film exhibiting a polydomain texture acquired at 160 °C in an out-of-plane configuration; (d) DSC curves obtained on heating and cooling at 2 °C min<sup>-1</sup> and single-crystal structures of the (e) ac and (f) ab planes.

**We won't detail this research field as we focus our work on polymer materials.** But as introduced before already, it must be mentioned that in many cases the authors have not taken advantage of several valuable inherent properties of LC phases, specifically the well-known capability of many LCs

to be uniformly “aligned” to improve the device performance, particularly the OSC charge-carrier mobility in thin films. Moreover, the crystallization of liquid crystals at room temperature, generally observed for mesomorphic molecular semiconductors, induces several limitations in the semiconducting layers such as polycrystalline domains, providing a high density of grain boundaries and limited charge mobility. Because of this problem, recent research has focused as well on  $\pi$ -conjugated mesogenic polymers.

#### 2.1.3.4 Semiconducting LC polymers

As explained before, the electronic performance of conjugated polymers depends on the microstructure of the polymer films. We know in particular that, percolated network morphology with high crystallinity, ordered intermolecular packing and long-range order is beneficial for charge transport. In this context, the appearance of liquid crystalline ordering for some conjugated polymers provides a new solution to solve the difficulties in microstructure manipulation.

**Importance of the film morphology.** The importance of film morphology in electronic performance was already discussed a little claiming the role of the development of bottom-up approaches to regulate it.<sup>117</sup> It was then evidenced that some critical physical parameters, including the lattice constant,<sup>118</sup> crystallinity,<sup>119</sup> and orientational parameters,<sup>86</sup> determine the resulting charge mobility of semiconducting polymers in multiscale cases.<sup>120</sup>

In fact, during anisotropic charge transport in conjugated polymers, delocalized carriers are transported along and between backbones in ordered regions and hop to adjacent chains in disordered regions at different velocities.<sup>121</sup> The basic rules for tuning microstructures focus on how to reduce the probability of charge transport under unfavorable conditions and improve mobility in certain parts or regions of merit.<sup>122</sup> Improved mobility appears in films with improved crystallinity and sufficient intercrystallite connectivity, and the mobility can be further elevated *via* alignment techniques to achieve long-range anisotropic charge transport.<sup>123</sup>

In addition, driven by  $\pi$ - $\pi$  interactions, conjugated polymers can assemble into ordered structures in solutions or melts. However, the polymer microstructure is difficult to control because of the relatively weak interaction between conjugation groups and limited molecule mobility. Usually, a semicrystalline structure is attained from a polymer assembly. Thus, various efforts have been made to promote the molecular arrangement process by modulating the driving force for aggregation and improving chain mobility.<sup>124</sup> Unfavorable entropy loss also poses difficulties for polymer long-range alignment, and entanglement and polymer chain relaxation limit the film anisotropy. In other words, a balance between molecular interactions and molecular mobility should be realized to obtain a well-structured morphology.

This being said, with rigid backbones, highly anisotropic molecular structures, long flexible side chains, and strong  $\pi$ - $\pi$  interactions between polymers, the chemical structures for most solution-processed conjugated polymers exactly meet the chemical structure requirements for liquid crystals.

**LC Polymer designs.** The liquid crystalline state of semiconducting polymers was discovered in the 1990s, and the liquid crystallinity of conjugated polymers was applied to assist the construction of field-effect transistors and light-emitting diodes.<sup>125</sup> The liquid crystalline state was first studied for the second generation of conjugated polymers such as poly(phenylenevinylene) (PPV) derivatives, polyacetylene (PA) derivatives, polyfluorene (PF) derivatives, and polyalkylthiophene (PAT) derivatives. The discovery of liquid crystalline states has not been limited to traditional homopolymers. Some donor-acceptor (D-A) copolymers with rigid backbones and little crystallinity also exhibit liquid crystal properties.<sup>126</sup> In some reports from the past few years, the liquid crystalline systems were usually associated with a highly crystalline and anisotropic morphology, which appeared both for traditional homopolymers, such as P3HT, and many emerging D-A copolymers, thus stimulating studies on the influence of the liquid crystallinity of conjugated polymers on developing film microstructures.<sup>127</sup> Device performance results have also proved the benefits of liquid crystalline properties in terms of charge transport.<sup>125</sup>

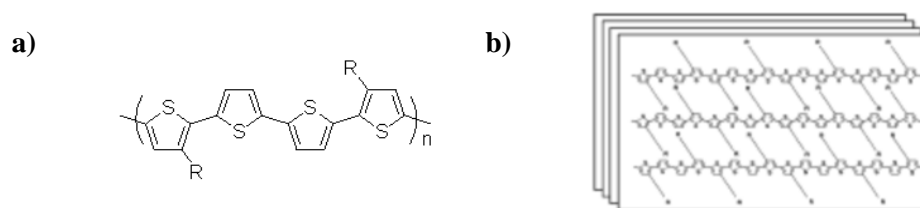


**Figure 2.1. 22** Schematic representation of (a) poly(3-alkylthiophene) and (b) its organization.<sup>128</sup>

As an illustration, in Figure 2.1. 22 is reported the main-chain LC poly(3,3''-dialkyl-quaterthiophene)<sup>128</sup> designed by Gardner et al. The position of the alkyl chains along the polymer and their orientation result in the formation of a three-dimensional lamellar system. Indeed, the interdigitation of alkyl chains between two neighboring polymers, and the planar conformation of the polymer leading to a stack of  $\pi$ -conjugated backbones by  $\pi$ -stacking, lead to this three-dimensional self-organization. Charge-carrier mobility in this compound is in the range of  $7 \times 10^{-2}$  to  $0.12 \text{ cm}^2 \text{ V}^{-1} \text{ s}^{-1}$

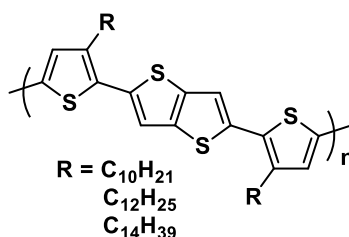


**Figure 2.1. 23** Structures of poly(2,5-bis(3-alkylthiophene-2-yl)thieno[3,2-b]thiophenes) (PBT TT).<sup>129</sup>

McCulloch et al. reported as well the well-known poly(2,5-bis(3-alkylthiophene-2-yl)thieno[3,2-b]thiophene) or (PBTtT) (Figure 2.1. 23) also showing LC properties.<sup>129</sup> This copolymer was synthesized *via* a Stille reaction between 2,5 -bis(trimethylstannyl)thieno[3,2-b]thiophene and 5,5'-dibromo-4,4'-dialkyl-[2,2']-bithiophene. Taking advantage of the lamellar pre-organization in the liquid crystalline state, the charge-carrier mobility of these polymers obtained after annealing in field-effect transistor configuration is ranging from 0.2 to 0.7 cm<sup>2</sup> V<sup>-1</sup> s<sup>-1</sup>.

For this PBTtT material, the delocalization of electrons from the fused aromatic unit into the backbone is less favorable than from a single thiophene ring, due to the larger resonance stabilization energy of the fused ring over the single thiophene ring. This reduced delocalization along the backbone results in a lowering of the polymer's highest occupied molecular orbital (HOMO) level. Furthermore, the rotational invariance of the linearly symmetrical thieno[3,2-b]thiophene in the backbone facilitates the adoption of the low-energy backbone conformation, promoting the formation of highly ordered crystalline domains. Therefore, PBTtT is more likely to achieve higher mobility than poly(3-alkylthiophene).

These two precedent examples were main-chain LC polymers but side-chain LC polymers exist, Indeed, the introduction of LC side groups grafted on  $\pi$ -conjugated backbone is an interesting approach as well,<sup>130</sup> as self-organization adopted by mesogenic side groups can induce an improvement of the polymer chain organization in the same time. As an example, Ben Zhong Tang's group described several  $\pi$ -conjugated side-chain LC polymers.<sup>131</sup> In Figure 2.1. 14 is shown a poly(phenylene) with cyanoterphenyl units (calamitic group) on each repeat unit: this polymer is self-organizing in the mesophase (smectic A type) with antiparallel interdigitation of the pendant groups.

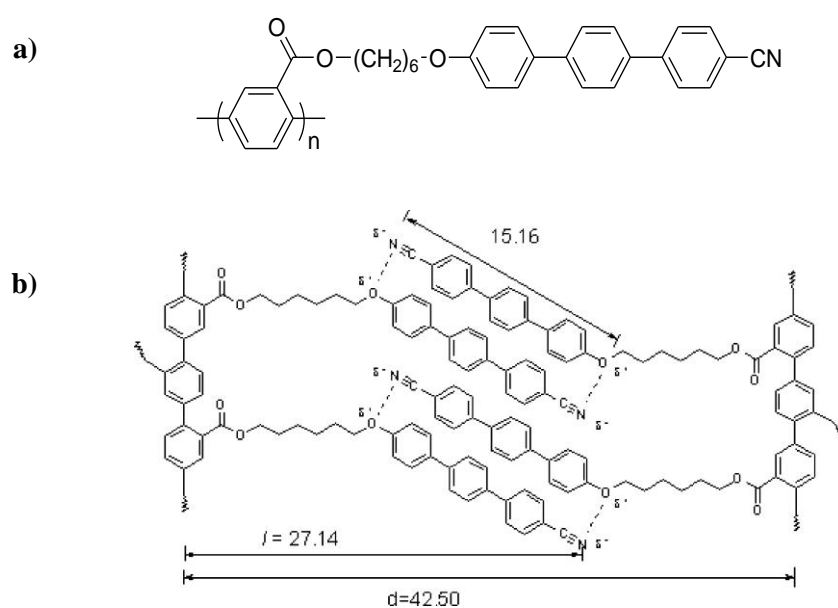


**Figure 2.1. 24** (a) Chemical structure of calamitic side-chain LC polymer, with poly(phenylene) as backbone and cyanoterphenyl as calamitic side chain part and (b) proposed SmA lamellar arrangement for the polymer.<sup>131</sup>

**Illustration of solid-state structure-property relationships with polythiophenes.** To better understand what's going on in a solid-state, the X-Ray analysis has been used extensively. Small substituents give little effect on regiochemistry while the orientation of larger substituents can dramatically affect the unit cell dimensions.<sup>132</sup> The prevalent packing model derives from a lamellar structure with rod-like main chains arranged in parallel and alkyl substituents between (Figure 2.1. 25a and b).

This form, designated type-I, packs  $\pi$ -systems face-to-face, 3.8–3.9 Å apart,<sup>133</sup> and staggered within the a-c molecular plane to allow nesting of side-chains. Viewed down the *b*-axis (Figure 2.1. 25b), a similar staggered offset makes the unit cell dimension equal to twice the  $\pi$ -stacking distance and minimizes eclipsing interactions in the stack. The head-to-tail architecture organizes alkyl substituents much like in a hexagonally close-packed solid alkane or polyethylene, promoting highly crystalline regions with *trans*-planar alkyl conformations.<sup>134</sup> Variations in alkyl length give corresponding expansion or contraction of the unit cell along the *a*-axis, with the other dimensions being minimally perturbed.<sup>135</sup> Electron diffraction patterns of crystalline microwires are consistent with the type-I motif, orienting the *b*-axis parallel with the long dimension of the “wire”.<sup>136</sup> Directionally crystallized rrP3HT, in contrast, has a fibrous morphology with the stacking axis rotated 90°, orienting the *c* axis parallel to the long axis of the fiber.<sup>137</sup>

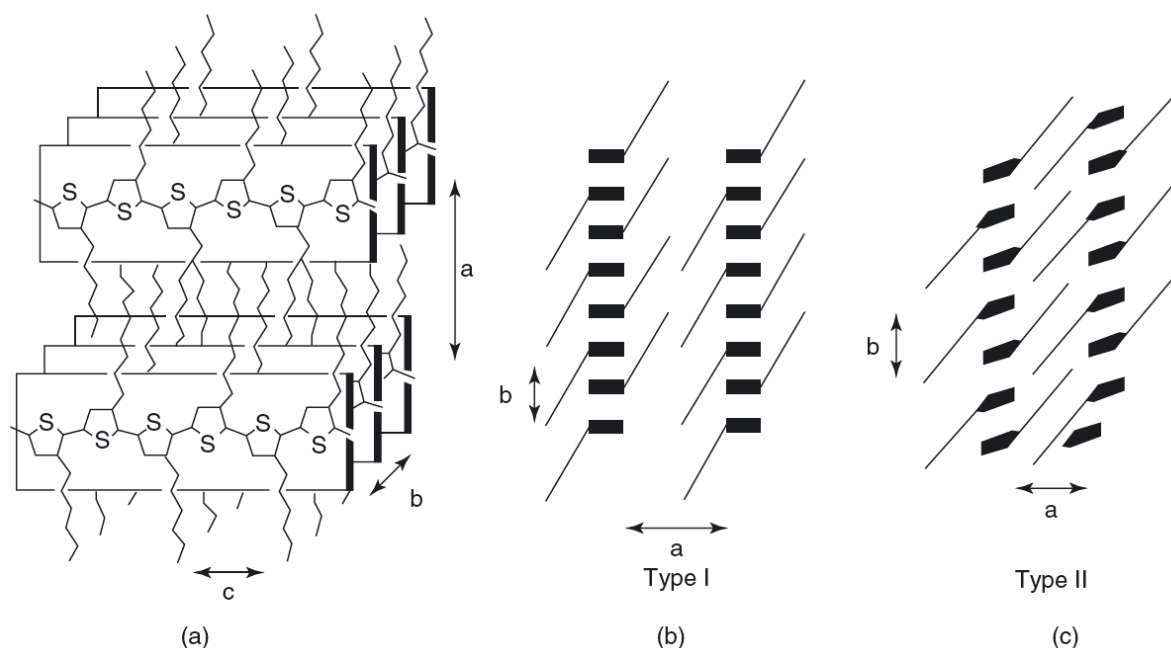


**Figure 2.1. 25** Structure of regioregular poly(3-hexylthiophene): (a) orientation of lamellae; (b) common (high temperature) form; (c) metastable interdigitated polymorph.

It is useful to note that the backbone and alkyl chains have competing organizational tendencies, leading sometimes to the observation of polymorphism.<sup>138</sup> As an example, a metastable modification, designated type-II, was characterized by Prosa et al. (Figure 2.1. 21c):<sup>139</sup> in this phase, alkyl chains are

more fully interdigitated, indicating that the side-chain crystallization drives the structure. Additionally, the phase concurrently forms with type-I (Figure 2.1. 21b) during solvent casting of films. Melting destroys this order while subsequent solidification in the absence of solvent precludes its formation. Moreover, Causin et al. determined that the type-II polymorph could be formed reproducibly by careful crystallization near the melting temperature. On the contrary, heating to the necessary temperatures to melt the side-chains causes reversion to the type-I structure upon cooling.<sup>139</sup> Besides, substituted polythiophenes are comb-like polymers, with both backbone and side-chains independently capable of crystallization. This allows complex behavior from competing processes and polymorphic behavior has been noted.<sup>134,138</sup> DSC data can then be combined with the temperature-dependent X-ray diffraction to study the different mesophases (mesophases transitions). For example, generally, the low-temperature transitions come from the alkyl substitutions (side chains) and high-temperature transitions are designated to “backbones”. Some additional transition (glass temperature) can be observed in rrP3AT, transforming a glassy crystal to a plastic crystal with different inter-ring torsion. This was dubbed a twist-glass transition.<sup>140</sup>

**To sum-up on liquid crystal polymers,** they are promising materials, with respect to the formation of uniform films by wet processes and good thermal durability. Moreover, the control of the supramolecular self-assemblies and the nanoscale morphologies of  $\pi$ -conjugated macromolecular architectures with long-range order, as well as the establishment of reliable structure-property relationships can be seen as major and fundamental issues.<sup>141</sup> In particular, better control of both the mesoscopic and nanoscale organization within thin organic semiconducting films is crucial to improve their charge carrier mobilities.

As we described, currently most efforts essentially focus on two different approaches, either based on the elaboration of conjugated block copolymers, (with different block functionalities),<sup>142</sup> or liquid-crystalline  $\pi$ -conjugated polymers, bearing conjugated mesogenic side-groups.<sup>143</sup>

The first class of materials takes advantage of the block copolymer ability for phase separation into well-ordered morphologies (spherical, cylindrical, or lamellar) to form separate conduction pathways for charge carriers, thanks to the antagonistic chemical nature of each block at the origin of nanosegregation.<sup>144</sup> However, optimal charge transport properties also require to form long-range correlated structures with an orientational control of the regular pathway alternation. This last objective is difficult to achieve by tuning the block structures and length.

On the contrary, it can be more easily envisaged with a liquid-crystalline polymeric architecture. Liquid crystalline materials are indeed outstanding examples of soft self-assemblies that combine order and fluidity, within components self-organizing into a wide diversity of long-range ordered, periodic structures.<sup>145</sup> In addition, liquid crystal assemblies can form thin films which are intrinsically self-healing since structural defects are automatically corrected during the process of self-assembly, and whose morphology can be controlled at the molecular level.

## 2.1.5 Objectives: towards new liquid crystal side-chain polymers

In this context, side-chain liquid-crystalline  $\pi$ -conjugated polymers consisting of  $\pi$ -conjugated backbones bearing side-on semiconducting mesogenic groups can be considered as a promising approach to control the phase separation into well-ordered morphologies of different functional components with periodicities ranging in the nanometer scale.

Up to now, only a few examples of such macromolecular architectures have been considered for charge transport properties.<sup>146</sup> Also, associated with electro-active components (donor and acceptor), such well-ordered morphologies could offer the possibility to form separate conduction pathways for charge carriers, by playing on their antagonistic chemical nature.

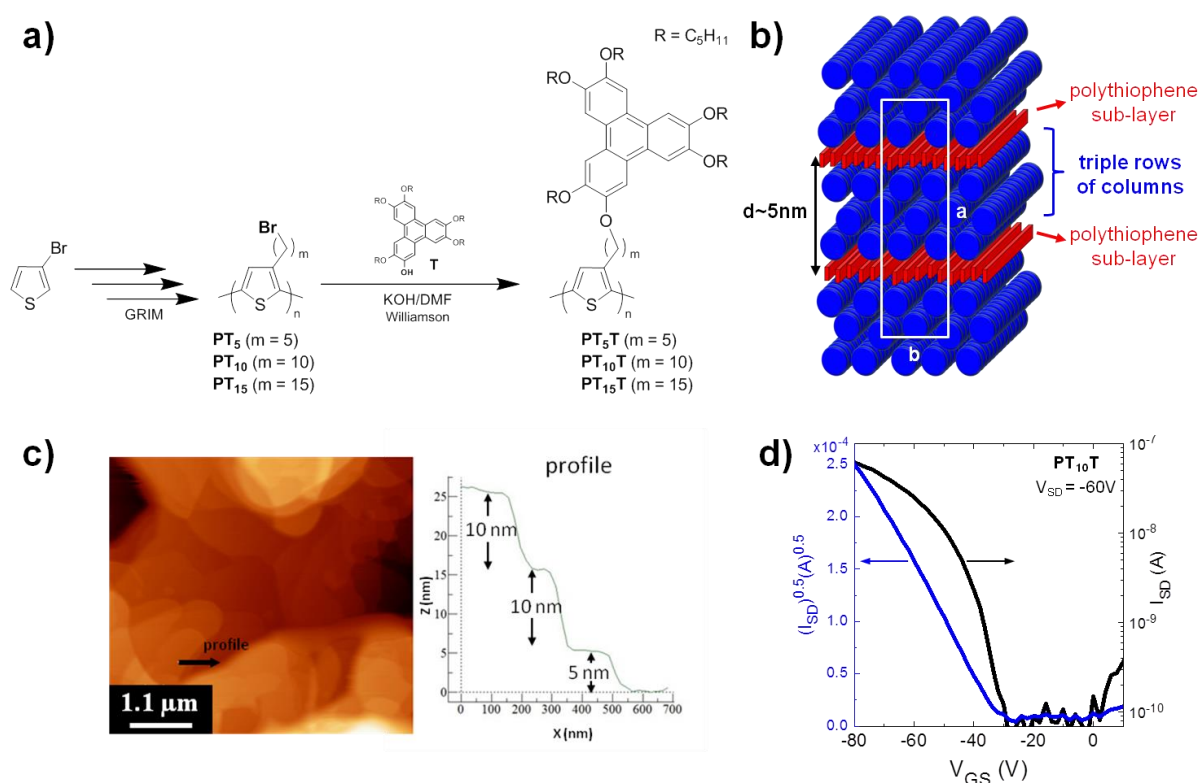


**Figure 2.1. 26** a) General synthetic route for the preparation of triphenylene side-chain homopolymers PT<sub>m</sub>T with different lengths of the aliphatic spacer. b) Schematic view of the lamello-columnar structure of PT<sub>10</sub>T consisting in the alternation of triple rows of triphenylene columns and the polythiophene sub-layers, arranged in a rectangular *p2gg* lattice involving twelve columns and two sub-layers (white frame). c) Topography AFM image of PT<sub>m</sub>T nanostructured thin film on a silanized silicon wafer and terrace step profile determined from topography. d) Typical transfer characteristic of a top-contact bottom-gate OFET based on PT<sub>m</sub>T polymers (PT<sub>10</sub>T).<sup>147,148</sup>

**Our research group contributed these last years to this type of polymer architecture.**<sup>115,147,149–152</sup>

More precisely, we designed and synthesized a new kind of side-chain liquid crystal  $\pi$ -conjugated polymers consisting of intricate polymeric systems associating regioregular poly(3-alkylthiophene) backbones with laterally pending  $\pi$ -conjugated mesogenic groups. Depending on the nature of the

mesogenic side-groups, this specific polymer design permits to obtain lamello-columnar or lamello-lamellar mesophases, resulting in an intertwined co-assembly either of lamellae and columns or of two different types of lamellae, as exemplified in Figure 2.1. 26, with one of our discotic-based triphenylene side-chain homopolymers.<sup>147,148</sup>

Associated as well with judicious side-groups, for example, n-type entities, we demonstrated that this simple and versatile strategy can produce distinct conductive channels for both types of charge carriers, and can lead to a new class of supramolecular ambipolar materials, easily processable, and potentially suitable for electronic and optoelectronic applications (see Figure 2.1. 27). Indeed, this homopolymer exhibited ambipolar conduction with an electron mobility of  $3.9 \times 10^{-6} \text{ cm}^2 \cdot \text{V}^{-1} \cdot \text{s}^{-1}$  and a hole mobility of  $3.3 \times 10^{-5} \text{ cm}^2 \cdot \text{V}^{-1} \cdot \text{s}^{-1}$ , after the annealing treatment at  $150^\circ\text{C}$  for 1 hour in glove-box.

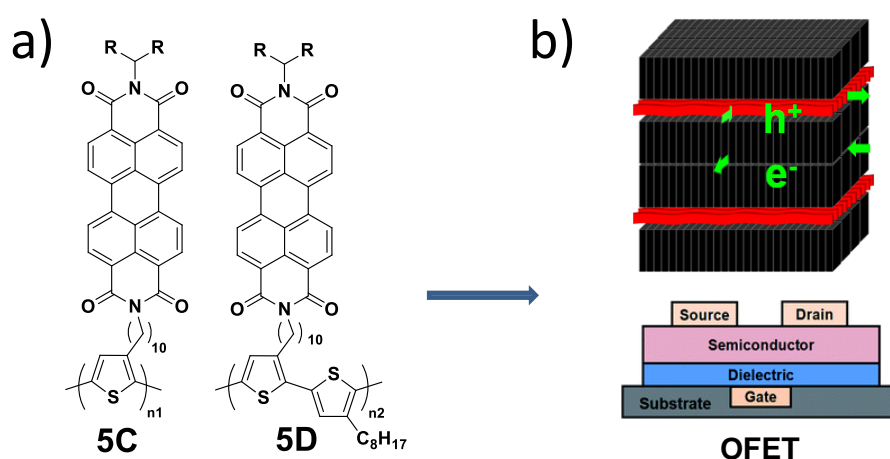
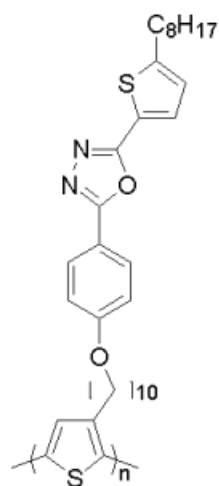


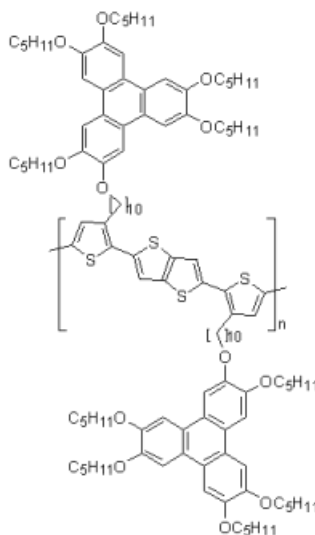
**Figure 2.1. 27** a) Chemical structures of the target donor-acceptor polymers; b) Schematic representation of the lamello-lamellar structure consisting in the alternation of double sub-layers of perylene moieties and of polythiophene sub-layers. (Yiming's thesis)<sup>150</sup>

As a consequence, we decided during the first part of my project to optimize and test new similar polymeric architectures as novel potential self-organized complex semiconducting materials. More specifically, we targeted two chemical structures (Figure 2.1. 28), the so-called **Polythiophene-oxa** type and/or **PBTtT-Tri** type, which differ both by their backbone (polythiophene or PBTtT, respectively) and mesogen pendent group (calamitic oxadiazole-based or discotic triphenylene), respectively.

More precisely, in **section 2.2** is reported the study of (**Polythiophene-oxa**), a polymer composed of a regioregular poly(3-alkylthiophene) as the backbone and calamitic-type electron-acceptor oxadiazole entities as side groups. Similarly, in **section 2.3** are explored the properties of **PBTtT-Tri** which consists of a poly(2,5-bis(3-alkylthiophen-2-yl)thieno[3,2-b]thiophene) (PBTtT) backbone and discotic-type triphenylene side groups.



**Polythiophene-oxa**



**PBTTT-Tri**

**Figure 2.1. 28** Target polymer chemical structures designed for OFET applications (**chapter 2**)

For both types of macromolecular architectures, first of all, the multi-steps chemical strategy optimization is described, before to present the chemical structure evidencing by NMR and SEC essentially. Second, the thermal and self-organization behavior of the polymers are further investigated by POM, DSC, and XRD. Third, preliminary charge transport properties of the materials, evaluated in OFET configuration, are discussed. Finally, we will conclude this part with some perspectives based on the new design guidelines providing by this study.

## 2.2 Polythiophene-oxa

In this section, we focus on designing a supramolecular architecture resulting from the phase separation, at the nanoscale level, of two covalently linked  $\pi$ -conjugated systems that enable to self-assemble in a lamella-lamellar nanostructure. To realize our objective, we adopted the strategy that combines a well-defined  $\pi$ -conjugated polymer backbone and  $\pi$ -conjugated mesogenic groups as side-chains to produce a unique semi-conducting liquid crystal macromolecular architecture. More specifically, the target polymer, namely, **Polythiophene-oxa**, is composed of a regioregular poly(3-decylthiophene) as the backbone and calamitic-type electron-acceptor oxadiazole entities, *i.e.* 2-(4-decyloxy-phenyl)-5-(5-octyl-thiophene-2-yl)-[1,3,4]oxadiazole, as side groups (Figure 2.2. 1).

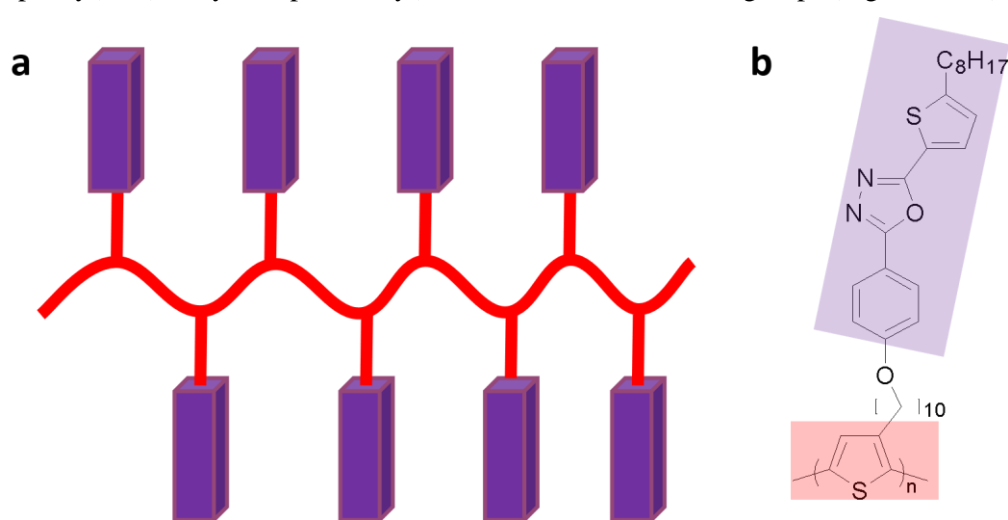
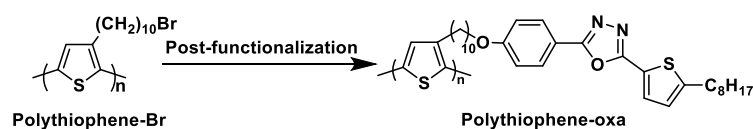


**Figure 2.2. 1** (a) Schematic representation and (b) chemical structure of the target polymer **Polythiophene-oxa**.

### 2.2.1 Synthesis and structural characterization

According to the previous work in our group, the target **Polythiophene-oxa** was prepared *via* the *post*-functionalization method, as described in Scheme 2.2. 1: this means that before this last step, both the precursory regioregular poly(3-decylthiophene) end-terminated with bromide (**Polythiophene-Br**) and the side group 2-(4-decyloxy-phenol)-5-(5-octyl-thiophene-2-yl)-[1,3,4]oxadiazole (**OF**) have to be prepared, individually.



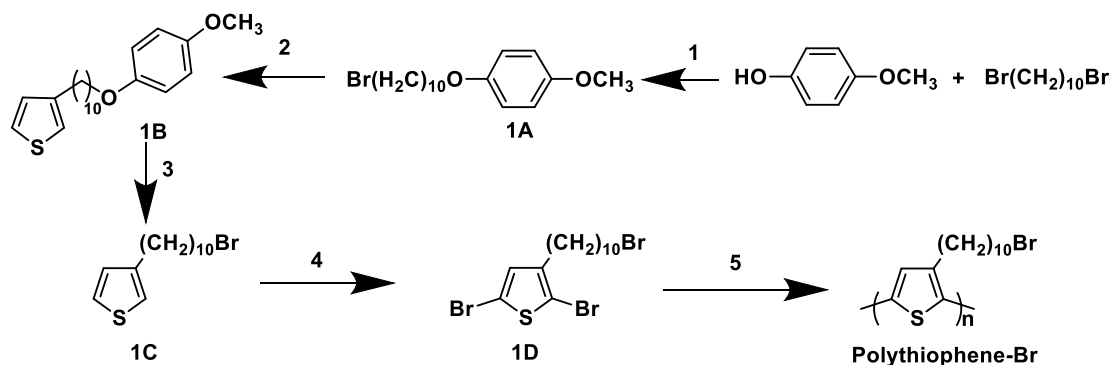
**Scheme 2.2. 1** *Post*-functionalization synthetic route towards **Polythiophene-oxa**.

Therefore, first, we will describe the synthesis and structural properties of **Polythiophene-Br**. Second,

we will detail the multi-step synthesis of the functionalized calamitic oxadiazole-type side-group **0F**. Finally, we will present the synthesis and structural properties of target **Polythiophene-oxa**.

#### *Synthesis of the regioregular precursory **Polythiophene-Br***

According to the previous work in our team, 3-( $\omega$ -bromodecyl)thiophene (**1C**) can be obtained by lithiation with *n*-butyllithium of commercially available 3-bromothiophene, followed by quenching with an excess of dibromodecane. Unfortunately, during the lithiation, 2-( $\omega$ -bromodecyl)thiophene is also produced as a by-product and consequently, the isomers can only be separated through very complex column chromatography (with hexane or PE as the eluent) as the polarities of the two isomers are very close to each other. Moreover, before this separation is needed a distillation to remove the starting material (3-bromothiophene). Thus, final yields in pure 3-( $\omega$ -bromodecyl)thiophene (**1C**) *via* this methodology were poor and not reproducible, which let us develop another synthetic pathway. More precisely, to avoid isomers formation and as shown in scheme 2.2. 2, we chose another synthetic route including three steps.



**Scheme 2.2. 2** Synthetic route towards **Polythiophene-Br**: 1)KOH, 59%; 2)Mg, Ni(dppp)Cl<sub>2</sub>, 3-bromothiophene, 58% ; 3)HBr, acetic anhydride, 45%; 4)NBS, dry THF, acetic acid, 76%; 5) iMgCl<sub>2</sub>, Ni(dppp)Cl<sub>2</sub>, 50%.

The objective of the first step was to protect only one Br of 1,10-dibromodecane and we managed indeed to obtain the intermediate molecule **1A** with a yield of 59%. The second step is a Grignard reaction between the molecule **1A** and 3-bromothiophene, which was successful with a relatively good yield as well (58%). Then, the third step is a deprotection reaction to obtain the desired molecule **1C**, which was then converted to the monomer **1D** through a “classical” bromination experimental procedure, using more specifically NBS.

Then, the precursory regioregular polymer **Polythiophen-Br** was obtained *via* GRIM method with Ni(dppp)Cl<sub>2</sub> as the catalyst, in a yield of 50%.

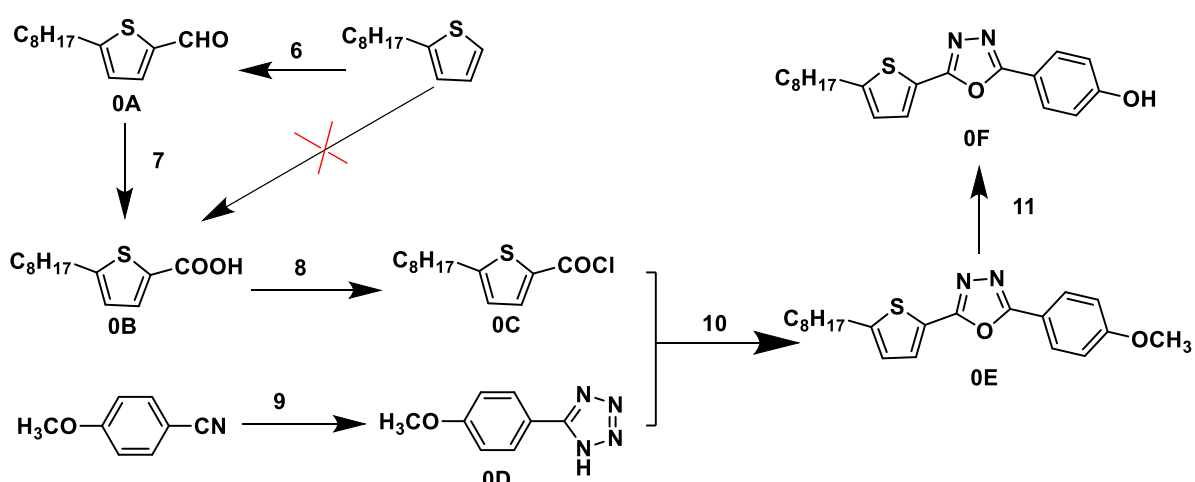
#### *Synthesis of 2-(4-decyloxy-phenol)-5-(5-octyl-thiophene-2-yl)-[1,3,4]oxadiazole (**0F**)*

As depicted in Scheme 2.2. 3, in order to obtain the side group 2-(4-decyloxy-phenol)-5-(5-octyl-

thiophene-2-yl)-[1,3,4]oxadiazole (**0F**), we first synthesized two building blocks: 5-octyl-thiophene-2-carbonylchloride (**0C**) and 5-(4-methoxy-phenyl)-2-*H*-tetrazole (**0D**).

On the one hand, 5-octyl-thiophene-2-carbonylchloride (**0C**) was obtained from 5-octyl-thiophene-2-carboxylic acid (**0B**) by using thionyl chloride and the conversion was complete. In previous works in our group, the acid group of **0B** could be formed starting from *n*-octyl thiophene, through the intermediate 2-lithio-thiophene generated *in-situ* and the subsequent addition of carbon dioxide (CO<sub>2</sub>). However, in my case, this procedure didn't work. Thus, as illustrated in Scheme 2.2. 3, I decided to first obtain the corresponding aldehyde from the reaction of *n*-octyl thiophene and POCl<sub>3</sub> under 90°C for 2h. Then the aldehyde group (-CHO) of the intermediate **0A** was converted into a carboxylic acid (-COOH) group using Jones reagents.

On the other hand, 5-(4-methoxy-phenyl)-2-*H*-tetrazole 2-3 was obtained from the reaction between 4-methoxybenzonitrile and sodium azide in the presence of ammonium chloride. The product was purified by precipitation and the yield was about 73%.



**Scheme 2.2. 3** The synthetic route towards the side group 2-(4-decyloxy-phenol)-5-(5-octyl-thiophene-2-yl)-[1,3,4]oxadiazole (**0F**): 6) DMF, POCl<sub>3</sub>, 90 °C, 2h, 90%; 7) Jones reagent, RT, overnight, 84%; 8) thionyl chloride, Ar, toluene, reflux, 5 h, 100%; 9) NaN<sub>3</sub>, NH<sub>4</sub>Cl, DMF, 100 °C, 24 h, 73%; 10) pyridine, reflux, Ar, 12 h, 74%; 11) BBr<sub>3</sub>, dry DCM, 50%.

The intermediated product **0E** was then obtained through the reaction between **0C** and **0D** via N-acylation of the tetrazole moiety, in a 74% yield. Finally, the subsequent ether cleavage with BBr<sub>3</sub> released the hydroxyl group, and the final side group 2-(4-decyloxy-phenol)-5-(5-octyl-thiophene-2-yl)-[1,3,4]oxadiazole (**0F**) was obtained with a yield of 50%.

#### *Synthesis and structural characterization of target polymer Polythiophene-oxa*

As explained in the precedent Scheme 2.2.1 and depicted in Scheme 2.2.4, the target polymer **Polythiophene-oxa** was eventually gained via a *post*-functionalization strategy which performs a



After the functionalization, the signal at 3.39 ppm belonging to  $\alpha$ -CH<sub>2</sub>Br of **Polythiophene-Br** vanished completely and the new signal at 3.94 ppm attributed to the  $\alpha$ -CH<sub>2</sub>O appeared, demonstrating that the substitution is almost 100%. In the meanwhile, the protons of benzene rings exhibited the peaks at 7.96 and 6.94 ppm, the latter peak is overlapped with the signal of polythiophene backbone. The signals at 7.55 and 6.80 ppm are attributed to the protons of the thiophene rings in the side groups. Moreover, the signal around 2.82 ppm is ascribed to the  $\alpha$ -CH<sub>2</sub> peaks of the HT thiophene rings in the backbone and the side groups, and the  $\alpha$ -CH<sub>2</sub> peak of the TT terminal is around 2.58 ppm. The absolute number of repeating units can also be estimated:  $X_{n,NMR} = 3.95 / 0.24 + 2 = 18$ . The broad, overlapping peaks in the range of 0.91-1.75 ppm belong to other alkyl protons.

Size exclusion chromatography (SEC) was also performed to confirm the relative number-average molecular weight ( $M_{n,SEC}$ ) and the dispersity ( $M_w/M_n$ ) of the polymers, using THF as the eluent at 40 °C and polystyrene (PS) as the calibration standard. As the polythiophene have a quite different hydrodynamic volume in THF with that of PS, the relative number-average molecular weight ( $M_{n,SEC}$ ) of regioregular poly(3-alkylthiophene) obtained from SEC measurements is usually 1.5-2 folds of the absolute number-average molecular weight ( $M_{n,NMR}$ ) calculated from the NMR spectra.<sup>153</sup> **Polythiophene-Br** exhibit the relative number-average molecular weight ( $M_{n,SEC} = 1.03 \times 10^4$ ) with narrow dispersity ( $M_w/M_n = 1.22$ ), giving the number of repeating units ( $X_{n,SEC}$ ) of 34, which is in close agreement with the absolute value calculated from the NMR spectra ( $X_{n,NMR} = 20$ ,  $X_{n,SEC}/X_{n,NMR} = 1.7$ ). The narrow dispersity indicates that **Polythiophene-Br** may achieve well-defined polymeric architecture. After the substitution, the SEC curve shifted to the region of higher molecular weight (Figure 3.2. 3). The target **Polythiophene-oxa** have the relative number-average molecular weight ( $M_{n,SEC} = 1.8 \times 10^4$ ) with narrow dispersity ( $M_w/M_n = 1.47$ ), giving the number of repeating units ( $X_{n,SEC}$ ) of 31, also in agreement with the NMR results ( $X_{n,NMR} = 18$ ,  $X_{n,SEC}/X_{n,NMR} = 1.7$ ). The summary of the polymer characteristics is given in Table 2.2. 1.

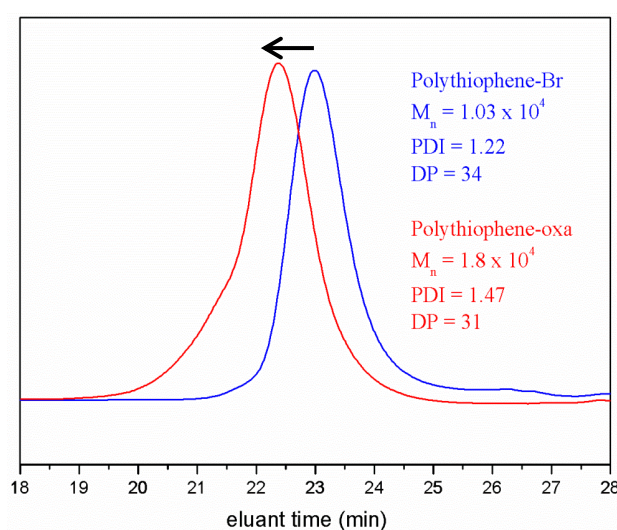


**Figure 2.2. 3** SEC curves of **Polythiophene-Br** and **Polythiophene-oxa** in THF (Polystyrene as calibration standard).

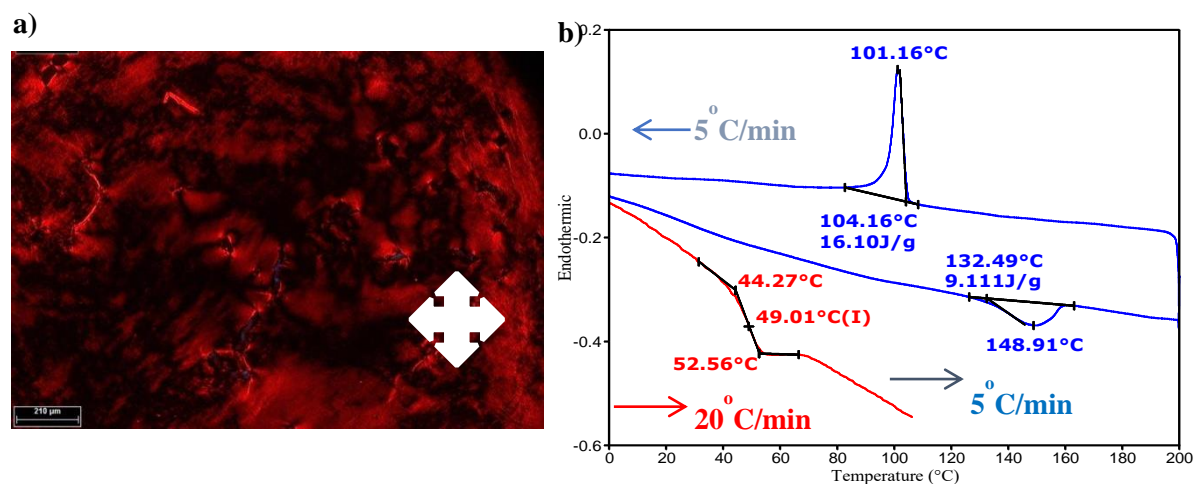
**Table 2.2. 1** The structural information of **Polythiophene-Br** and **Polythiophene-oxa**

Polymers	$M_{n,SEC}$	$M_w/M_n$	$X_{n,SEC}$	$X_{n,NMR}$	$X_{n,SEC}/X_{n,NMR}$
<b>Polythiophene-Br</b>	$1.03 \times 10^4$	1.22	34	20	1.7
<b>Polythiophene-oxa</b>	$1.8 \times 10^4$	1.47	31	18	1.7

### 2.2.2 Thermal and self-organization behavior study of **Polythiophene-oxa**

The thermal behavior of **Polythiophene-oxa** was examined by POM and DSC (Figure 2.2.4). Because of the high viscosity of the obtained thin film, **Polythiophene-oxa** doesn't develop any characteristic optical mesophase texture under POM. However, on heating, a birefringent and homogeneous texture can be observed from room temperature to around 140 °C indicating an anisotropic medium. On further heating, the viscous bright phase started to transform slowly to a non-birefringent isotropic phase.

In DSC thermograms, an endothermic peak at 132 °C ( $\Delta H = 9.1$  J/g) was observed on the DSC trace recorded upon heating, corresponding to the transition from the mesophase to the isotropic phase, which is consistent with the POM observations. On cooling, an exothermic peak was detected at 104 °C ( $\Delta H = 16.1$  J/g), attributed to the transition from the isotropic phase to the mesophase. This transition is observed on cooling with a large hysteresis ( $\sim 30$  °C), which is classical for macromolecular systems. In addition, the glass transition was observed at around 50 °C.

**Figure 2.2.4** (a) POM image and (b) DSC thermogram of **Polythiophene-oxa**.

Next, the self-organization property of **Polythiophene-oxa** was investigated by XRD and the XRD pattern at 100 °C is shown in Figure 2.2. 5a. The set of sharp and intense equidistant reflections in the small-angle region is assigned to Miller indices 001, 002, 003 and 004, and is attributed to a lamellar phase. The sharpness of the small-angle reflections indicates the long-range correlation of the lamellar organization with an interlamellar distance of 5.5 nm. Besides, the diffuse halo in the wide-angle region corresponds to the molten state of the aliphatic chains ( $h_{ch}$ ) and the average distance of the

oxadiazole cores, reflecting the liquid nature of the mesophase. Therefore, the self-organization model of **Polythiophene-oxa** is probably composed of the alternation of bilayer of calamitic mesogens and of polythiophene backbone monolayers as represented in Figure 2.2. 5b.

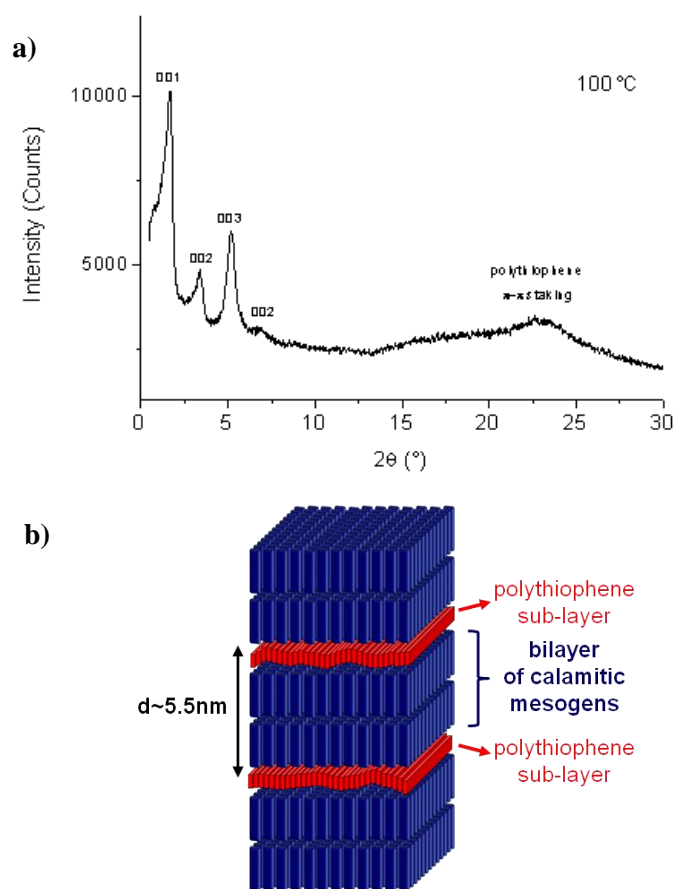


**Figure 2.2.5** (a) The XRD pattern and (b) schematic representation of the **Polythiophene-oxa** self-organization and illustration of preferential orientation on substrate.

### 2.2.3 Preliminary charge transport property studies in OFET configuration

Preliminary charge transport properties of **Polythiophene-oxa** thin films were examined in OFETs with a top-contact bottom-gate configuration. The output and charge transfer characteristics of the transistor after annealing at 120  $^\circ\text{C}$  for 2 h are displayed in Figure 2.2. 6.

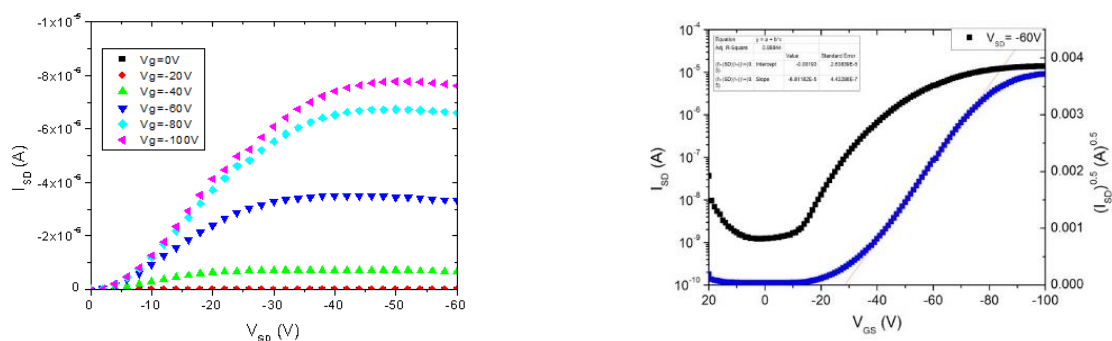


**Figure 2.2. 6** The output (left) and transfer (right) characteristics of a top-contact bottom-gate OFET based on **Polythiophene-oxa** after annealed at 120  $^\circ\text{C}$  for 2h.

The result indicated that the as-prepared **Polythiophene-oxa** transistor exhibits p-type conduction and a hole mobility in the saturated regime was found to be  $\sim 1.2 \times 10^{-3} \text{ cm}^2 \text{ V}^{-1} \text{ s}^{-1}$ . The  $I_{\text{on}}/I_{\text{off}}$  ratio was  $10^4$  and the threshold voltage ( $V_{\text{th}}$ ) was 30V.

#### 2.2.4 Conclusion

In this section, a new side-chain liquid crystal polymer (**Polythiophene-oxa**) was synthesized and its structure was characterized by NMR and SEC measurements.

First, we developed an innovative chemical route, even though with more steps, to reach purer bromo-alkyl-substituted thiophen monomer leading to an improved method for the preparation of precursor regioregular bromo-alkyl-substituted polythiophene backbone. Then, the final polymer **Polythiophene-oxa** obtained by *post*-functionalization of the precursor polymer presents a small dispersity and a complete grafting of the side groups.

This material was evidenced to self-organize with an alternation of bilayer of calamitic mesogens side groups and of polythiophene backbone monolayers. A first attempt in device configuration was tested to evaluate its charge transport property, in OFET configuration, and hole conduction with a mobility was about  $1.2 \times 10^{-3} \text{ cm}^2 \text{ V}^{-1} \text{ s}^{-1}$  was measured.

If replacing the side group with the mesogens with stronger electron affinity, it is likely to obtain a material with ambipolar charge transport properties.

## 2.3 PBTTT-Tri

In the last decade, regioregular poly(3-alkylthiophene) has been proved to be a good semiconducting polymer exhibiting high charge carrier mobility for organic electronic applications. In this context, our research team has prepared for ten years a series of liquid crystalline side-chain semiconducting polymers, comprising a regioregular poly(3-alkylthiophene) backbone bearing triphenylene discotic mesogen pendants.

To study the influence of the type of polymeric backbone on the supramolecular self-assembling behavior, and on charge transport properties, in this section, we designed two new side-chain  $\pi$ -conjugated polymers, which are expected to exhibit liquid-crystalline properties. More precisely, the new two polymers were designed to comprise poly(2,5-bis(3-alkylthiophene-2-yl)thieno[3,2-b]thiophene) (PBTTT) as the backbone and either the discotic-type monohydroxy triphenylene derivative or the calamitic-type 2-(4-decyloxy-phenyl)-5-(5-octyl-thiophene-2-yl)-[1,3,4]oxadiazole (**OF**) as the side groups (Figure 2.3. 1).

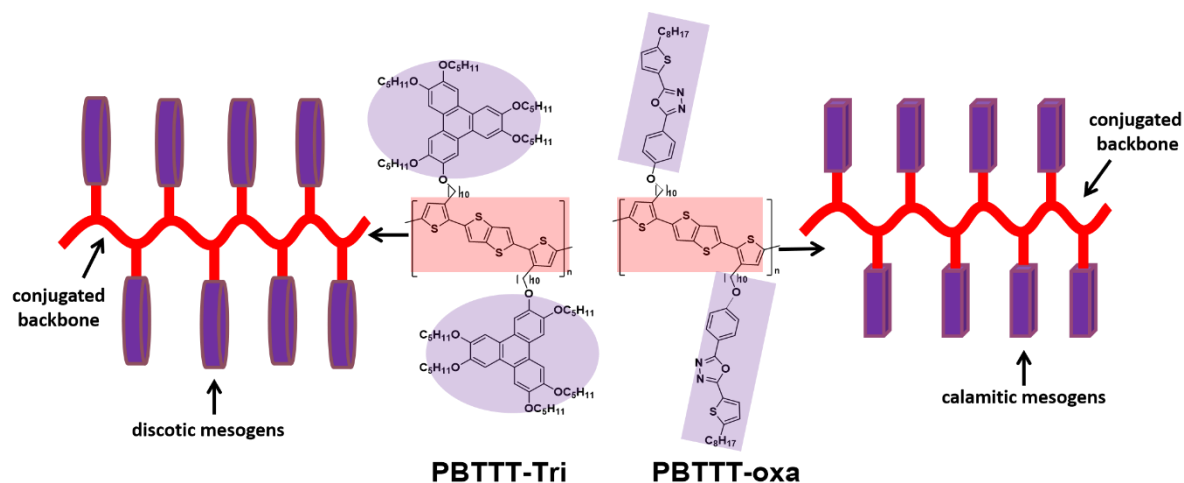
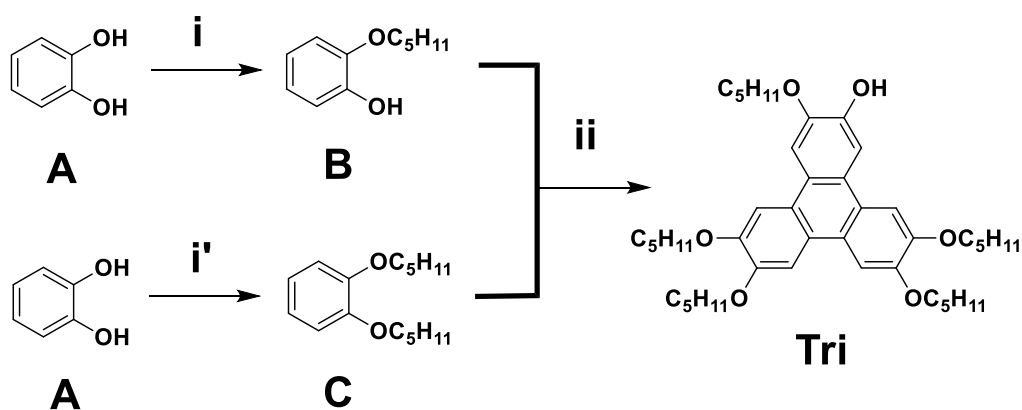


**Figure 2.3. 1** Chemical structures of desired new side-chain  $\pi$ -conjugated polymers **PBTTT-Tri** and **PBTTT-oxa**.

### 2.3.1 Synthesis and structural characterization

In this part, we also decided to use the *post*-functionalization method to prepare the target polymers **PBTTT-Tri** and **PBTTT-oxa**.

Then, first, we reproduced the synthesis of the monohydroxy triphenylene derivative (**Tri**), according to an optimized procedure developed precedently in our group. More specifically, we chose the “statistic cyclization” method described by Kong et al<sup>144</sup> as the main synthetic route to prepare this intermediate (Scheme 2.3. 1).

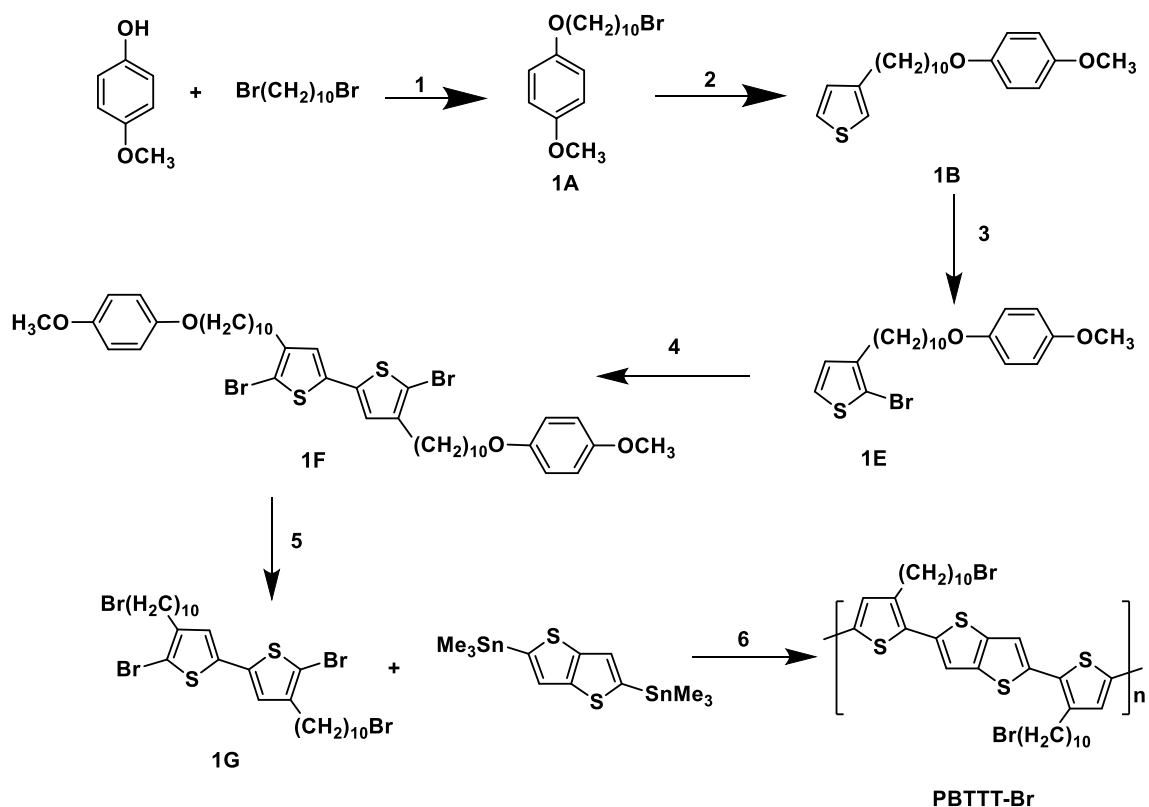


**Scheme 2.3. 1** Synthesis of monohydroxyalkoxy triphenylene **Tri**. Conditions: i) 1-bromopentane (1 equivalent),  $K_2CO_3$ , KI, TBAB, ethanol, reflux, 24h, 79%; i') 1-bromopentane (2.2 equivalent),  $K_2CO_3$ , KI, TBAB, ethanol, reflux, 24h, 83%; ii)  $FeCl_3$ , DCM/MeCN,  $0^\circ C$ , 2h, 22%.

This synthetic route for the preparation of the discotic entity (**Tri**) includes three steps. The two first ones concern the preparation of building blocks **B** and **C** obtained by classical Williamson etherification of catechol through adjusting the ratio of bromoalkane. The last step is a ferric chloride oxidatively catalyzed statistic cyclization. The key point in this “statistic” method is to precisely maintain the ratio between **B** and **C** as 1:2 to reduce the byproducts (symmetric, dihydroxy, trihydroxy, etc.). The yield of the last step is quite low and the purification of compound (**Tri**) is tricky due to the presence of the multiple byproducts formed by the statistic cyclization (mainly the symmetric one). On parallel, we synthesized again 2-(4-decyloxy-phenyl)-5-(5-octyl-thiophene-2-yl)-[1,3,4]oxadiazole (**OF**) whom chemical route has already been described in **section 2.2**. This is the reason why we present below only the synthesis and structural characterization of the precursory polymer (**PBTTT-Br**) as well as the target polymers (**PBTTT-Tri** and **PBTTT-oxa**).

#### *Synthesis of precursor **PBTTT-Br***

Following the literature, the precursor **PBTTT-Br** was prepared in 6 steps, as shown in scheme 2.3.2: the first two steps, Williamson ether synthesis and Grignard reaction, aim to obtain 3-decylthiophene with protection group, with a yield of 59% and 58%, respectively. The molecule **1E** was obtained from the bromination of molecule **1B** using 1.1 equivalent of NBS, in a yield of 81%. The homo-coupled dimer bis(3-alkylthiophene) derivate (**1F**) was gained from molecule **1E** in the presence of  $PdCl_2(PhCN)_2$ , KF, and  $AgNO_3$  in dry DMSO, with a good yield of 62%. The 5<sup>th</sup> step is the deprotection reaction under the action of  $BBr_3$  to achieve the monomer **1G** in relatively good yield.

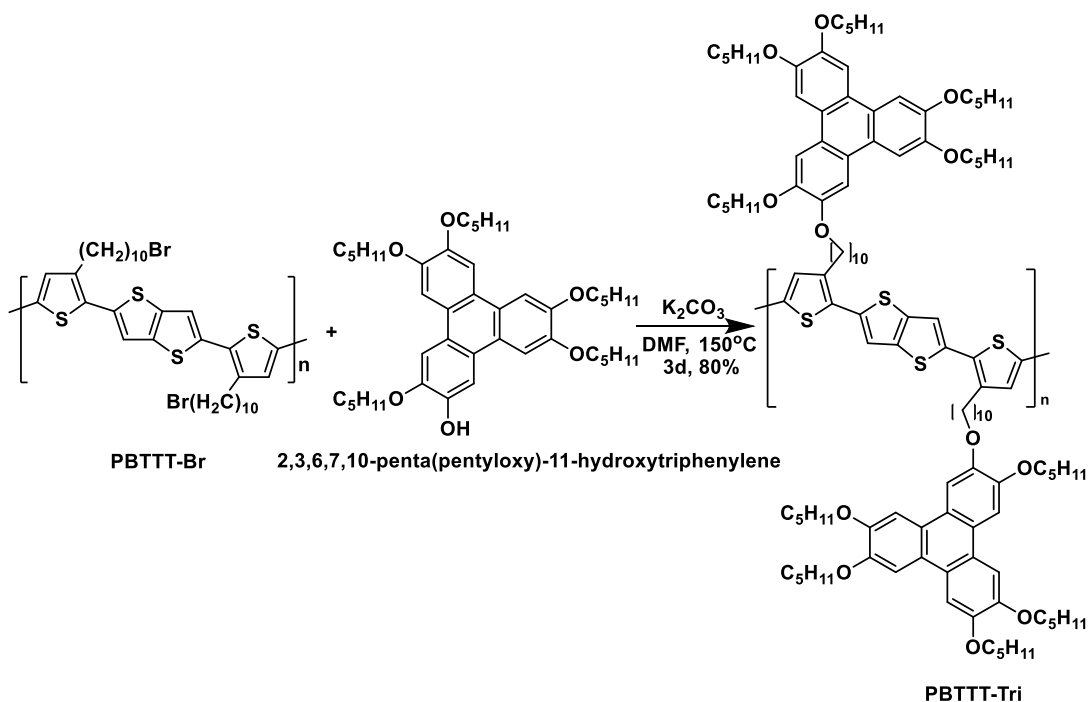


**Scheme 2.3. 2** Synthesis of precursor **PBTTT-Br**. Condition: 1) KOH, 59%; 2) Mg, Ni(dppp)Cl<sub>2</sub>, 3-bromothiophene, 58%; 3) NBS, dry DMF, 81%; 4) PdCl<sub>2</sub>(PhCN)<sub>2</sub>, KF, AgNO<sub>3</sub>, DMSO, 60°C, 62%; 5) BBr<sub>3</sub>, CH<sub>2</sub>Cl<sub>2</sub>, 68%; 6) Pd<sub>2</sub>(dba)<sub>3</sub>, P(*o*-tolyl)<sub>3</sub>, chlorobenzene,  $\mu$ W, 80%.

Then, the precursor **PBTTT-Br** was obtained *via* microwave-assisted Stille polycondensation of the monomers **1G** and 2,5-bis(trimethylstannyl)thieno[3,2,b]thiophene. Compared to conventional heating, the use of microwave irradiation has been reported to improve the molecular weight and dispersity, mainly because of the direct transfer of energy of reactants, which significantly reduces reaction time.<sup>45</sup> In my case, after adding all the reactants and degassed, the microwave tube was sealed and heated in the microwave with stirring subsequently at 140 °C for 2 min, at 160 °C for 2 min, and at 180 °C for 25 min. After the precipitation, filtration, and purification with Soxhlet, the precursor **PBTTT-Br** was obtained with a quite high yield of 90%.

#### Synthesis of target polymers **PBTTT-Tri** and **PBTTT-oxa**

The target polymer **PBTTT-Tri** was finally prepared *via* Williamson ether reaction between the precursor **PBTTT-Br** and 2,3,6,7,10-penta(pentyloxy)-11-hydroxytriphenylene, as depicted in scheme 2.3.3. After precipitation, filtration, and purification by Soxhlet to remove any trace of residual **Tri** and non-grafted polymer, pure target polymer **PBTTT-Tri** was gained with a yield of 80%.



**Scheme 2.3. 3** Synthetic route towards liquid-crystalline semiconducting polymer **PBT TT-Tri**.

The complete substitution was confirmed by NMR ( $\text{CDCl}_3$ , 50 °C) and SEC measurements. More precisely, as shown in Figure 2.3. 2, **PBT TT-Br** exhibits a single peak at 7.26 ppm belonging to the proton of thieno[3,2,b]thiophene and another single peak at 7.04 ppm attributed to the proton of thiophene in the backbone. The triplet signals at 3.40 ppm are ascribed to the proton of the methylene groups in the  $\alpha$ -position to the terminal bromine atom ( $-\text{CH}_2\text{Br}$ ) and the signal at 2.79 ppm are attributed to the  $\alpha$ - $\text{CH}_2$  peaks of the thiophene rings. Moreover, the broad, overlapping signals in the range of 1.32-1.86 ppm are ascribed to other protons of alkyl side chains.

After the substitution, a new signal belonging to the triphenylene rings of **PBT TT-Tri** appeared at 7.80 ppm, the signals attributed to the protons of thiophene and thieno[3,2,b]thiophene shifted to 7.21 and 7.00 ppm. In the meanwhile, the signal corresponding to  $\text{CH}_2\text{Br}$  group at 3.40 ppm in precursor polymer disappeared completely, while a new signal ascribed to the protons in  $\alpha$  to the oxygen atom appeared at 4.20 ppm, indicative of the complete substitution. Besides, the signals attributed to the  $\alpha$ - $\text{CH}_2$  peaks of the thiophene rings shifted from 2.79 to 2.74 ppm. The signals corresponding to the alkyl protons changes to the range of 0.96-1.93 ppm. Moreover, the integrals of the characteristic peaks are consistent with the chemical structures of the polymers.

As **PBT TT-Br** and **PBT TT-Tri** have several possible end groups, we can't obtain the absolute number of the repeating units ( $X_n$ ) using the same method in the cases of **Polythiophene-Br** and **Polythiophene-oxa**. Apart from NMR measurements, SEC was conducted to characterize the relative number-average molecular weight ( $M_n$ ) and the dispersity ( $M_w/M_n$ ). After the substitution, the SEC curve shifted to a higher-molecular-weight region (Figure 2.3. 3). For **PBT TT-Br**, the  $M_n$  is  $1.5 \times 10^4$  and  $M_w/M_n$  is 1.6, giving the value of  $X_{n,\text{SEC}}$  of 20. For **PBT TT-Tri**, the  $M_n$  is  $2.0 \times 10^4$  and  $M_w/M_n$  is

1.5, giving the value of  $X_{n,SEC}$  of 10, much smaller than that of **PBTTT-Br**. Similar to poly(3-alkylthiophene), no matter **PBTTT-Br** or **PBTTT-Tri** has a rigid conjugated backbone, quite different from the calibration standard polystyrene (PS). Therefore, the values of  $X_{n,SEC}$  obtained from SEC measurements have a big difference from the realistic values.

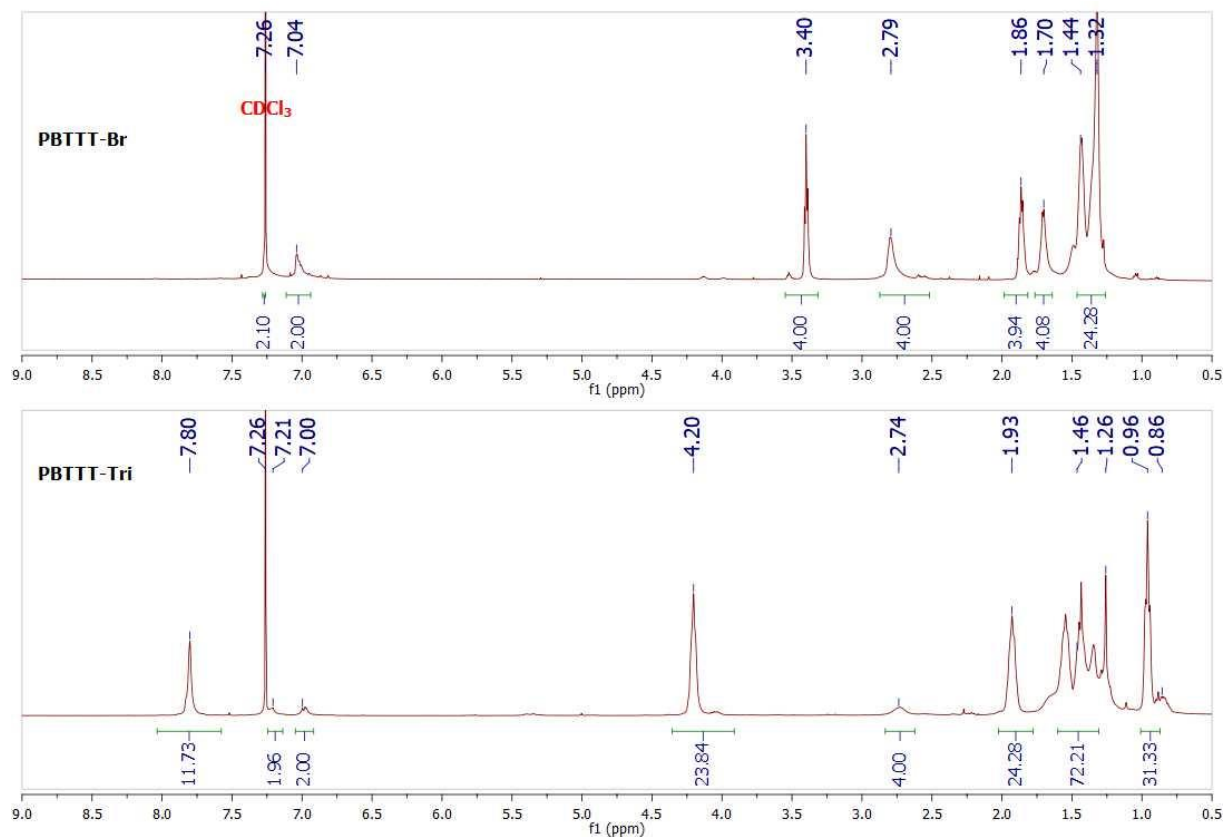


**Figure 2.3. 2**  $^1\text{H}$  NMR spectra of **PBTTT-Br** (top) and **PBTTT-Tri** (bottom) in  $\text{CDCl}_3$  at  $50\text{ }^\circ\text{C}$ .

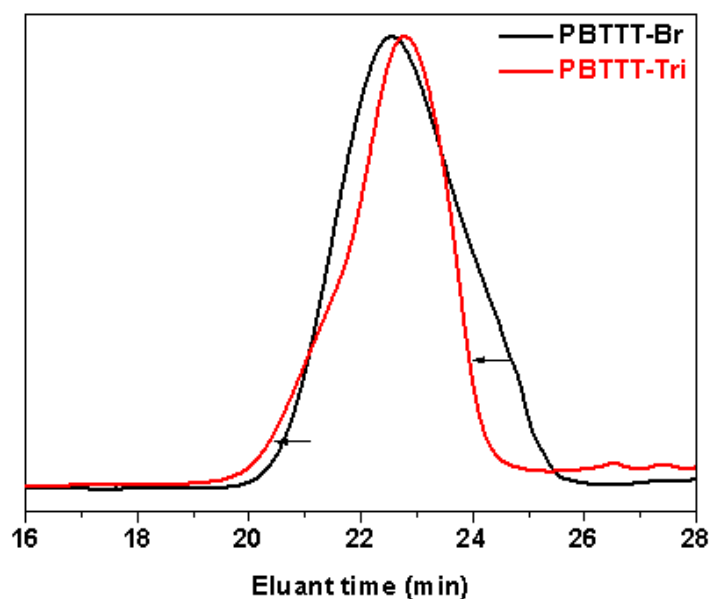


**Figure 2.3. 3** SEC curves of **PBTTT-Br** and **PBTTT-Tri**.

**Table 2.3. 1** The structural information of **PBTTT-Br** and **PBTTT-Tri**

Polymers	$M_{n,SEC}$	$M_w/M_n$	$X_{n,SEC}$
<b>PBTTT-Br</b>	$1.5 \times 10^4$	1.6	20
<b>PBTTT-Tri</b>	$2.0 \times 10^4$	1.5	10

Unfortunately, when substituted with 2-(4-decyloxy-phenyl)-5-(5-octyl-thiophene-2-yl)-[1,3,4]oxadiazole (**0F**) in dry DMF under 150°C, precipitation appeared almost immediately after starting the reaction. After removing the solvent DMF, the remained mixture could not readily dissolve in solvents including boiling DMF, DMA, and chlorobenzene. Limited by the solubility, **PBTTT-oxa** could not be purified and then we didn't characterize it.

### 2.3.2 Thermal behavior and self-organization study of **PBTTT-Tri**

The thermal behavior and self-organization of **PBTTT-Tri** were investigated using polarized-light optical microscopy (POM), differential scanning calorimetry (DSC), small-angle X-ray scattering (SAXS), and grazing-incidence wide-angle scattering (GIXS).

Observed under POM, **PBTTT-Tri** doesn't develop any characteristic optical textures due to the high viscosity of the obtained thin film, and consequently, it is not possible to identify a typical mesophase texture. Nevertheless, a birefringent viscous phase was observed by POM at room temperature, revealing the existence of an anisotropic medium (Figure 2.3. 4 a). On heating to 100 °C, the viscous phase transformed progressively into a non-birefringent isotropic phase. Then on cooling from the previous isotropic state to room temperature, no birefringence was observed, indicating its amorphous character.

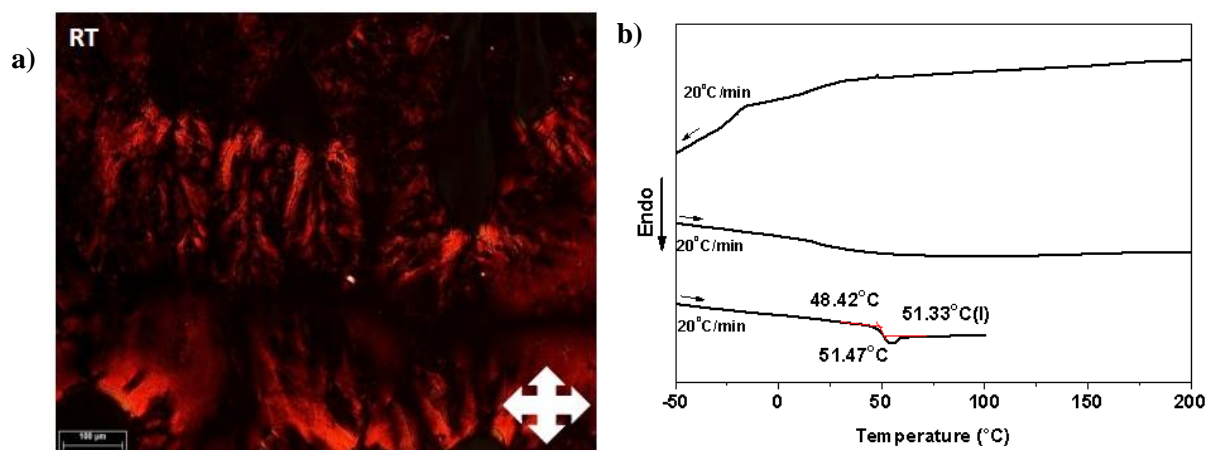


**Figure 2.3. 4** (a) POM image of **PBTTT-Tri** at room temperature; (b) DSC thermograms of **PBTTT-Tri** on heating and cooling at a rate of 20 °C/min.

DSC experiments confirmed POM observations. More precisely, DSC traces were recorded on heating and cooling at a rate a 20 °C min<sup>-1</sup> and the thermograms are displayed in Figure 2.3. 4 a. The DSC

trace upon the first cycle of heating contains a signal characteristic of glass transition around 48 °C, which is typical behavior of macromolecular systems. In the meanwhile, **PBTTT-Tri** didn't show a clear endothermic peak until 300 °C. On cooling, there is neither an exothermic peak nor an obvious glass transition. On further cycles of heating and cooling at rates of 10 °C min<sup>-1</sup>, 2 °C min<sup>-1</sup>, and 1 °C min<sup>-1</sup>, no obvious thermal transition was observed (Figure S1).

Subsequently, the SAXS pattern of **PBTTT-Tri** in the pristine bulk state (Figure 2.3. 5 a) and GIXS pattern of the as-prepared film deposited on a silicon wafer substrate were performed (Figure 2.3. 6 a). Concerning the SAXS measurements, in the small-angle region (high- $q$ ), the pattern displayed the broadened reflection (10) of a lamellar periodicity  $d = 48.7 \text{ \AA}$  and a scattering signal from the average distance between piled triphenylene rings  $D_{\text{Tri}} = 16.5 \text{ \AA}$ , overlapping with the (30) reflection of the lamellar arrangement. In the wide-angle region (low- $q$ ),  $\pi$ - $\pi$  stacking into columns is lowly regular, as shown by the broad  $h_{\pi}$  scattering signal, otherwise unresolved from backbone contribution and hardly separable from molten chain scattering  $h_{\text{ch}}$ . Concerning the GIXS study, anisotropic scattering is observed with two clear diffraction peaks apparent along the near out-of-plane direction  $q_z$  (where  $q_x \approx 0$ ), revealing the presence of preferential orientation in the film with the polymer layers parallel to the substrate.

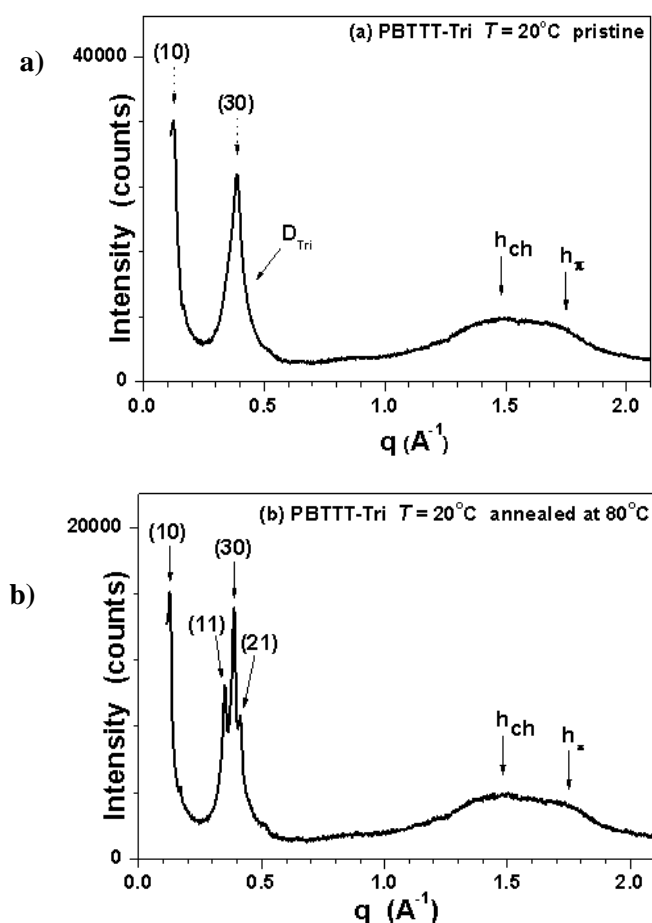


**Figure 2.3. 5** SAXS patterns of **PBTTT-Tri** in pristine state (a) and after annealed at 80 °C (b).

The annealing of **PBTTT-Tri** leads to a change of the polymer arrangement and the film morphology. SAXS pattern of **PBTTT-Tri** after annealing at 80 °C (Figure 2.3. 5 b) and GIXS pattern of annealed thin film deposited on a silicon wafer substrate (Figure 2.3. 6 b) were also performed. In the SAXS measurements, two additional sharp peaks were observed in the small-angle region (high- $q$ ), indicative of the development at the long-range of the lamellar periodicity and the appearance of a long-range correlated rectangular sublattice ( $a = d = 48.7 \text{ \AA}$ ;  $b = 19.4 \text{ \AA}$ ). In the low- $q$  region, the broad  $h_\pi$  scattering signal and the molten chain scattering  $h_{ch}$  were still overlapped. In the GIXS study, more peaks were observed along the near out-of-plane direction  $q_z$  (where  $q_x \approx 0$ ) and the relative positions of these peaks, indicative of a long-range correlated rectangular sublattice forming in parallel with the substrate in the film. This lamello-columnar mesophase has the same structure as that of  $(PT_{10}T)_n$  and  $(PBTT)_n$  already reported<sup>24</sup>, which consists in the alternation of triple rows of triphenylene columns and of backbone monolayers with the edge-on polymer orientation as illustrated in Figure 2.3. 7.

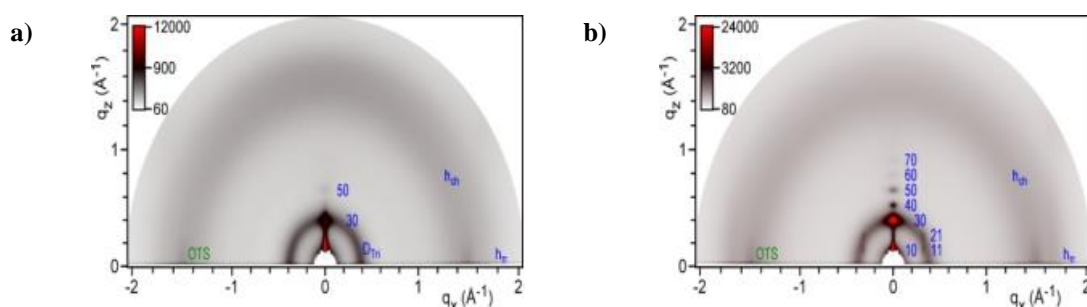


**Figure 2.3. 6** GIXS patterns of **PBTTT-Tri** transistor thin films spun-cast on silicon wafer recorded in pristine state (a) and after annealed at 50 °C (b). (GIXS measurements were performed at PAL synchrotron, Pohang, Korea).

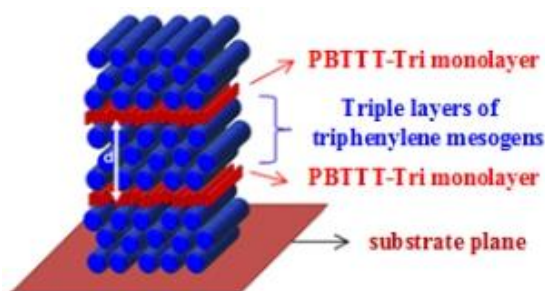


**Figure 2.3. 7** Schematic representation of the **PBTTT-Tri** self-organization and illustration of preferential orientation on substrate.

### 2.3.3 Preliminary charge transport property study of **PBTTT-Tri** in OFET configuration

Preliminary charge transport properties of **PBTTT-Tri** thin films were examined in OFETs with a top-contact bottom-gate configuration. The **PBTTT-Tri** thin film was spun-casting on a silicon wafer substrate, and the gold source (S) and drain (D) electrodes were vapor-deposited on top of the **PBTTT-Tri** layer through a shadow mask.

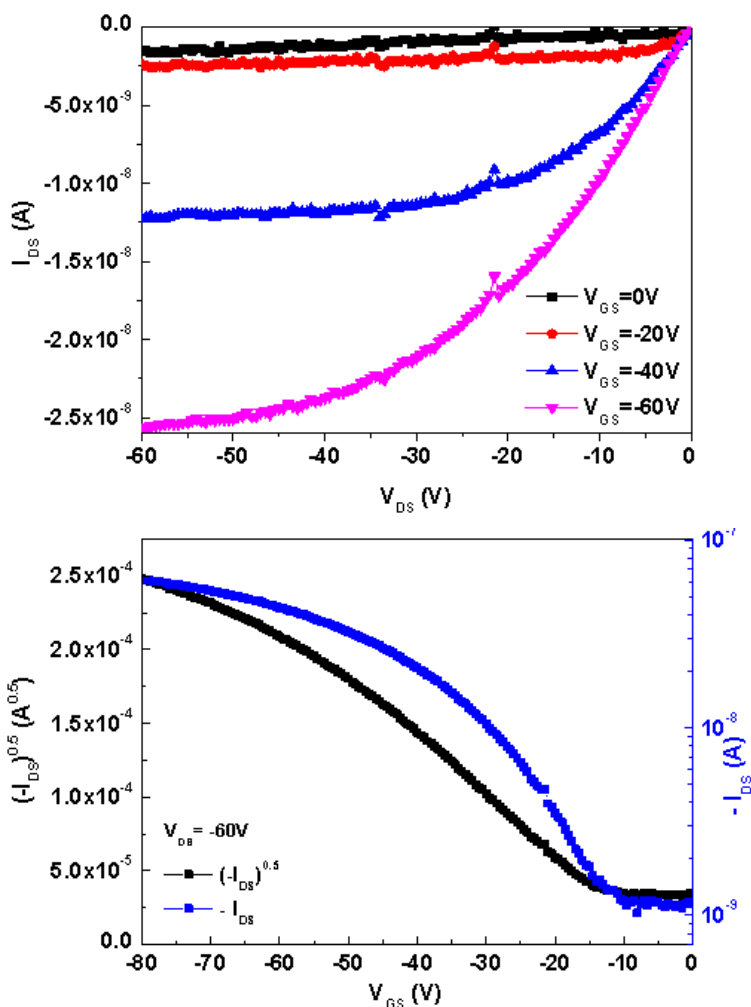


**Figure 2.3. 8** Output and transfer characteristics of a top-contact bottom gate OFET based on **PBTTT-Tri** after annealed at 50 °C for 15 min and 60 °C for another 15 min.

The output and charge transfer characteristics of the as-prepared **PBTTT-Tri** transistor were displayed in Figure S2. The result demonstrated that the as-prepared **PBTTT-Tri** transistor exhibits p-type conduction and its hole mobility in the saturated regime was found to be  $\sim 9.8 \times 10^{-6} \text{ cm}^2 \text{ V}^{-1} \text{ s}^{-1}$ . After annealing at 50 °C for 15 min and 60 °C for another 15min (Figure 2.3. 8), its hole mobility increases to  $1.2 \times 10^{-5} \text{ cm}^2 \text{ V}^{-1} \text{ s}^{-1}$ , which is close to the mobility value for PT<sub>10</sub>T ( $\sim 1.4 \times 10^{-5} \text{ cm}^2 \text{ V}^{-1} \text{ s}^{-1}$ )<sup>24</sup>, a side-chain polymer presenting also triphenylene mesogens as side groups and regioregular polythiophene as the backbone.

### 2.3.4 Conclusion

To sum up, in this section, we designed two new side-chain liquid crystal polymers (**PBTTT-Tri** and **PBTTT-oxa**), presenting poly(2,5-bis(3-alkylthiophene-2-yl)thieno[3,2-b]thiophene) as backbone. However, due to the solubility, only **PBTTT-Tri** was successfully synthesized and its structure was well characterized by NMR and SEC measurements.

First, we reproduced the monohydroxy triphenylene derivative (**Tri**) and 2-(4-decyloxy-phenyl)-5-(5-octyl-thiophene-2-yl)-[1,3,4]oxadiazole (**OF**) as side groups, according to the optimized procedures. Second, we successfully synthesized the desired BTTT monomer in five steps, followed the microwave-assisted Stille polycondensation to prepare the precursor **PBTTT-Br**, with a quite high yield of 90%. Finally, two polymers (**PBTTT-Tri** and **PBTTT-oxa**) were prepared *via* Williamson ether reaction, but only pure **PBTTT-Tri** was obtained, in a yield of 80%.

Subsequently, we investigated the thermal behavior and self-organization property of **PBTTT-Tri**. The polymer presents liquid crystalline properties and self-organizes in a supramolecular arrangement with the alternation of triple rows of triphenylene columns and the backbone monolayer parallel to the substrate plane. A first attempt to evaluate its preliminary charge transport properties was performed in OFET configuration. **PBTTT-Tri** exhibits p-type conduction and its hole mobility in the saturated regime is around  $1.2 \times 10^{-5} \text{ cm}^2 \cdot \text{V}^{-1} \cdot \text{s}^{-1}$ . The mobility value could probably be improved by optimizing the conditions for constructing the OFET device, for example, adding an OTS layer to promote the orientation of the film, or adopting other OFET architecture.

## **Chapter 3 TADF polymers for organic light-emitting diodes (OLEDs)**

Organic light-emitting diodes (OLEDs) have achieved a great breakthrough and reached the stage of commercialization since the pioneering work of demonstrating the first practical organic electroluminescent diode utilizing a fluorescent organic material as the emitter by C.W.Tang and VanSlyke in the 1980s.<sup>154</sup> OLEDs are a promising alternative to LCDs for display fabrication, as OLEDs feature high efficiency, good image quality, large viewing angle, and multicolor emission. In addition to these merits, the OLEDs have no demand for backlighting and can be deposited on either rigid or flexible substrates (glass, silicon as well as plastics), so they're likely to be thinner, lighter, and flexible, consequently, regarded as one of the most important potential candidates for displays and lightening sources. To date, the OLEDs have already developed into three generations: conventional fluorescent OLEDs, phosphorescent OLEDs, and delayed fluorescent OLEDs. Among the 3<sup>rd</sup> generation, thermally activated delayed fluorescence (TADF) is the most important branch.

As a result, this manuscript **chapter 3** starts with an introduction dedicated to the bibliography (**section 3.1**): we will briefly introduce the fundamental mechanisms relating to OLEDs, before to detail the fundamental mechanisms of TADF, structure-property relationship in TADF molecules, as well as the photophysics of TADF molecules. Then we will present some examples of the reported TADF materials, including small molecules, dendrimers, and especially linear polymers. Finally, we will give a brief introduction to through-space conjugation.

The following four result sections (**section 3.2-3.5**) deal with the design, synthesis, and characterization of new  $\pi$ -conjugated polymers, expected to exhibit TADF behaviors. After describing the multi-steps chemical strategy, the photophysical properties of the obtained polymers were investigated. Besides, preliminary electroluminescent properties of **S2** polymers were also studied. More specifically, **in section 3.2 and section 3.3**, two classes of potential linear TADF polymers (**S1** and **S2** series) are investigated respectively, based on a donor part fixed in the backbone and acceptor parts endowed in the side chains. In parallel, **in section 3.4 and section 3.5** we apply the through-space conjugation (TSC) system on the TADF platform, by designing two other types of polymers (**S3** and **S4** series).

### 3.1 Bibliography

#### 3.1.1 A brief introduction to organic light-emitting diodes (OLEDs)

Organic light-emitting diodes (OLEDs) are now at the stage of commercialization since the pioneering work of the first organic electroluminescent diode based on a fluorescent material in the 1980s.<sup>154</sup> OLEDs are a promising alternative to LCDs and are one of the most important potential candidates for displays and lightening sources.

#### \* *Work principle and structural architecture of OLED devices*

As depicted in Figure 3.1. 1, every OLED device has an anode and a cathode for the charge injection, at least one electrode being transparent. Normally, transparent conducting oxide films such as ITO are used as anodes due to their high work function for hole injection, whereas metals with low work function, particularly aluminum (Al), are good candidates for cathodes. During the last several decades, the OLED devices have developed from monolayer to multilayer structures across three generations of organic light-emitting materials as dopants.

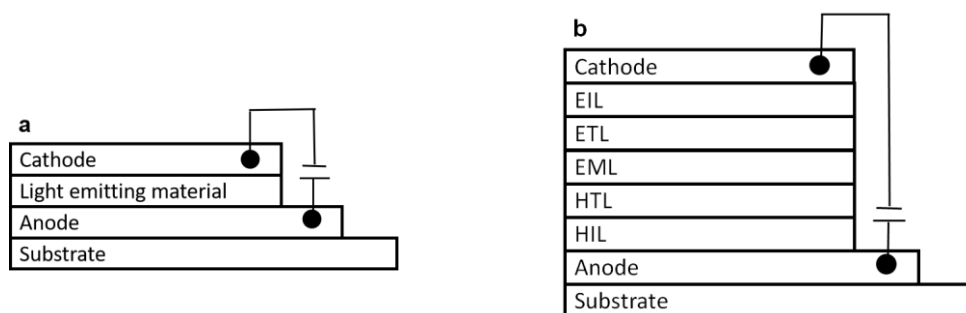


**Figure 3.1. 1** (a) monolayer OLED device; (b) multilayer OLED device.

In the monolayer OLED device architecture, the simplest one (Figure 3.1. 1a), the organic emissive layer acts as both emitter and charge transport material simultaneously. Once the device is electrically excited, electrons from the cathode and holes from the anode are injected into the organic emissive layer. Then both positive and negative charges migrate through the organic emissive layer under the influence of the electric field between the two electrodes. After encountering and recombination, the oppositely charged species can form either singlet or triplet excitons in a singlet:triplet ratio of 1:3 as a result of spin-statistics (Figure 3.1. 2).<sup>155</sup> The carrier injection efficiency, the ratio of excitons formed by recombination to the injected charged species, has an important effect on the device performance. In order to improve the device performance, multilayer OLED structural architecture was proposed (Figure 3.1. 1b).

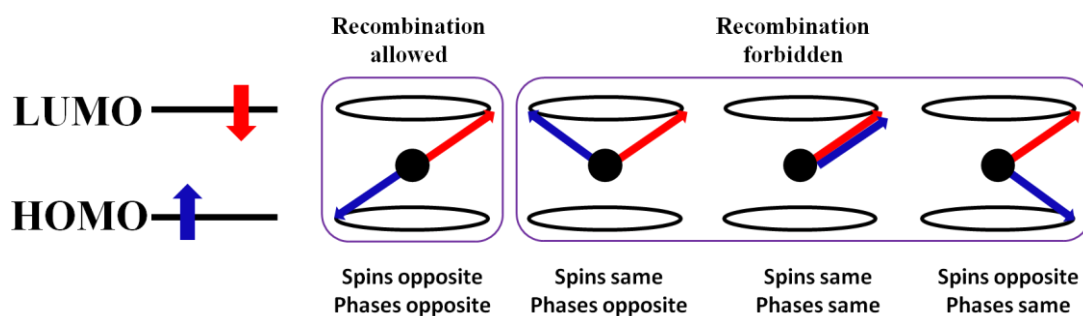


**Figure 3.1. 2** Spin statistics<sup>156</sup>: the recombination with spins and phases in two potential directions, producing four excitons, including one singlet exciton and three triplet excitons.<sup>157</sup>

Multilayer OLED architecture may consist of several layers between an anode and a cathode. Among them, the electron-injection layer (EIL) and the electron-transporting layer (ETL) help to reduce the electron-injection barriers and facilitate the electrons transport from the cathode to the emissive layer (EML). Similarly, the role of the hole-injection layer (HIL) and the hole-transporting layer (HTL) is to reduce the hole-injection barrier and assist the transport of holes from the anode to the emissive layer (EML). The emissive layer (EML) serves as the emitter. Besides, the electron-blocking layer (EBL) and hole-blocking layer (HBL) can prevent the electrons or holes from moving through the layer, respectively. It's worth pointing out that one functional layer may serve two functions. For instance, some doped emissive layers act as both the emitter and charge-transporting material. To obtain high device efficiency, it is necessary to choose suitable materials which have a good overlap of the corresponding HOMO and LUMO levels. Furthermore, the devices require that electrons and holes exhibit similar charge transport mobilities to ensure that the combination of charge species can occur in the emissive layer.

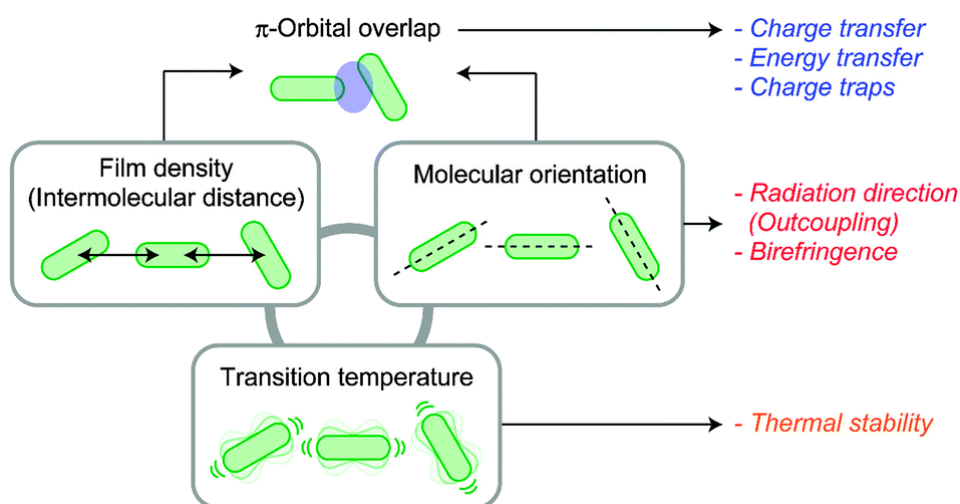


**Figure 3.1. 3** Schematic diagram outlining the importance of the film density, molecular orientation, and transition temperature of amorphous organic semiconductor films in OLEDs.

The methods of preparation of the functional layers have a great influence on the film density, transition temperature, and molecular orientation, which is tightly associated with device performances.<sup>158</sup> As described in Figure 3.1. 3, film density mainly affects the charge and energy transfer properties, transition temperature determines the thermal ability of films and devices, and molecular orientation concerning the birefringence and radiation direction strongly affects the electrical and optical characteristics of devices. To date, OLED functional layers can be fabricated by either vacuum deposition or solution process. Considering the realistic demands, it is necessary to facilitate the development of high-performance solution-processed OLEDs.

### \* *OLED performances*

Generally speaking, OLED device performance can be judged by optical and electronic properties, including efficiency, operating lifetime, and emission color quality. Efficiency includes external quantum efficiency (EQE), current efficiency (CE), power efficiency (PE). Among them, EQE of an OLED device, defined as the number of photons that escape the device surface per number of electrons injected, is the parameter people care most and can be described in equation 3.1.1<sup>159,160</sup> :

$$\eta_{\text{ext}} = \frac{n^{\circ} \text{ of photons}}{n^{\circ} \text{ of electrons}} = \gamma \chi \phi_{\text{PL}} \eta_{\text{out}} = \eta_{\text{int}} \eta_{\text{out}} \quad (3.1.1)$$

Where  $\gamma$  is a charge balance factor representing the fraction of charge carriers that pass that from excitons in the device,  $\chi$  is the fraction of excitons that decay on the emissive dopants (radiative decay),  $\phi_{\text{PL}}$  is the intrinsic photoluminescence quantum efficiency (PLQY) of the emissive molecules,  $\eta_{\text{ext}}$  is the light out-coupling efficiency, and  $\eta_{\text{int}}$  is the internal quantum efficiency (IQE), concerning the conversion from excitons to photons.

According to Snell's law,  $\eta_{\text{ext}}$  of planar OLEDs is only about 20% due to various factors, such as the total internal reflection, surface plasmon coupling and metal absorption. Therefore, theoretically, assuming  $\gamma$  and  $\chi$  to be 1, the IQE is limited to be 25% for conventional fluorescence-based devices and 100% for phosphorescent and TADF devices, and the corresponding EQE is 5% and 20%, respectively. People have focused on efficiency enhancement over the last few decades via cavity engineering, low-index transport layers, and horizontal dipole orientation.<sup>161</sup> The EQE value of OLEDs can be experimentally confirmed by an integrating sphere, in the meanwhile, the current efficiency (CE) and power efficiency (PE) can be calculated from equation (3.1.3) and (3.1.4) as follows:

$$\text{Current density (j): } j \text{ (A/m}^2\text{)} = \frac{i \text{ (A)}}{\text{device area (m}^2\text{)}} \quad (3.1.2)$$

$$\text{Current efficiency (cd/A): CE (cd/A)} = \frac{L \text{ (cd/m}^2\text{)}}{j \text{ (A/m}^2\text{)}} \quad (3.1.3)$$

$$\text{Power efficiency (lm/W): PE (lm/W)} = \frac{L \text{ (cd/m}^2\text{)} \cdot \text{device area (m}^2\text{)} \cdot \pi}{i \text{ (A)} \cdot V} \quad (3.1.4)$$

Where  $i$ ,  $V$ , and  $L$  refer to current, voltage, and luminance, respectively, and can be determined by electroluminescence experimental. Equation (3.1.4) is reliable on the assumption that the emission of the OLED device is isotropic.

Efficiency “roll-off” effect, expressed as efficiency dropping quickly with increasing luminance, is the most common phenomenon in OLED devices. It is attributed to the interplay of a range of different non-linear processes, including triplet-triplet annihilation (TTA), singlet-singlet annihilation (SSA), singlet-triplet annihilation (STA), exciton-polaron interaction, field-induced quenching, changes in charge carrier balance and outcoupling efficiency, Joule heating and degradation. To maintain high emission brightness, a higher working voltage is required accompanied by larger power consumption and shorter device lifetime. Therefore, the efficiency “roll-off” effect is a serious problem for practical applications. The possible approaches to suppressing this effect have been put forward: 1) decreasing the exciton lifetime, 2) reducing molecular aggregation, 3) broadening the recombination zone, 4) reducing the Förster radius, and 5) introducing triplet managers.<sup>162</sup>

The device lifetime, defined as the time the luminance drops to one-half of its initial device brightness at a constant current density, is dominated by the degradation of OLEDs. So far, there are essentially three degradation mechanisms: catastrophic failure, “dark spot” growth, and intrinsic degradation.<sup>163</sup> During the last two decades, to slow down the degradation and achieve a long device lifetime, much efforts have been made consisting of choosing organic functional materials with good thermal, electrochemical stabilities, choosing metallic cathodes with a good anti-oxidation ability such as Al, minimizing contamination by strict control of the functional layer growth condition, adopting proper encapsulation for protecting the devices from moisture, oxygen and so on.<sup>164</sup>

Emission color quality of OLED devices is tightly associated with the applications in the display and lightening field. Emission color quality is determined by emission wavelength, brightness, luminance, and CIE xy color coordinate. Both of emission wavelength and brightness are subjective attributes of light. The former can be determined by an emission spectrum, whereas the latter can only be perceived rather than be measured objectively. Luminance, the amount of light that emitted from the OLEDs and fell within the given area and direction, is measured as the luminous intensity per unit area in the given area and direction with a SI unit of candela per square meter ( $\text{cd}/\text{m}^2$ ). C.I.E xy color coordinates, a scientific description of the color regard of luminance, is usually used to determine the content of three primary colors. For example, the CIE coordinate of the pure white emission is (0.33, 0.33). The devices with C.I.E coordinates close to (0.33, 0.33) are probably good candidates for lightening application.

### ***\*The development of emissive materials for OLED applications***

To date, OLED devices can be classified into three generations with different emission mechanisms: Conventional purely fluorescent organic light-emitting diodes (FOLEDs), phosphorescent organic

light-emitting diodes (PhOLEDs), and delayed fluorescent organic light-emitting diodes.

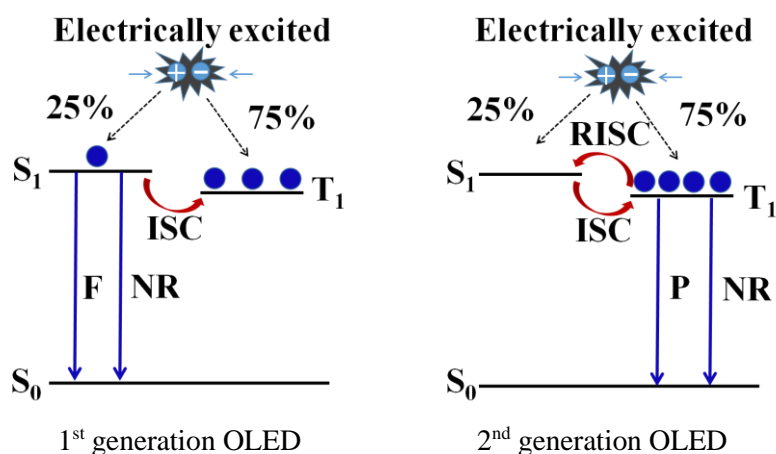


**Figure 3.1. 4** Schematic illustration for the emission mechanism of FOLEDs and PhOLEDs.

Conventional purely fluorescent organic light-emitting diodes (FOLED, Figure 3.1. 4) (1<sup>st</sup> generation OLED emitters) can harvest only the singlet excitons with the maximum internal/external quantum efficiency (IQE/EQE) of 25%/5% as a result of spin-statistics. In the 1980s, C.W.Tang and Van Slyke fabricated the first reported OLED device with the structure of 8-hydroxyquinoline aluminum ( $\text{Alq}_3$ ) emitting layer located between an anode and a cathode by vacuum deposition method and observed fluorescence at a low bias (below 10 V).<sup>154</sup> Since then, numerous researchers have explored many other organic electroluminescent materials. For example, Friend *et al.* built a similar OLED device using PPV as the organic emitting material.<sup>2</sup>

To improve the utilization of excitons, phosphorescent organic light-emitting diodes (PhOLEDs, Figure 3.1. 4) were proposed as the 2<sup>nd</sup> generation OLED emitters. The idea is to incorporate rare noble metals (for example, Ir<sup>165,166</sup>, Au<sup>167</sup>, and Pt<sup>168</sup>) to form organometallic complex emissive centers, which enable to induce strong spin-orbit coupling (SOC) effect and mix the wave functions of singlet and triplet excitons, consequently making the radiative decay of triplet excitons possible and obtaining theoretically 100% internal quantum efficiency (IQE). Suzuki *et al.* created the first PhOLED device with a benzophenone dispersed PMMA film as an emitting layer.<sup>169</sup> Later on, many PhOLEDs with excellent device performance have been explored. However, PhOLEDs have significant drawbacks: 1) the limited supply and high cost of noble metals; 2) short device lifetime in the blue emission region; 3) lower stability than FOLED, especially in the blue emission region; 4) uncertain toxicity. These shortcomings limit their development in the display and lighting industries. To overcome these problems, people try to use other metals such as Copper (Cu)<sup>170</sup> instead of precise noble metals, or optimize the device performance with the assistance of degradation mechanism<sup>171</sup>, or harvest triplet excitons through ‘hot exciton’ materials,<sup>172</sup> triplet-triplet annihilation (TTA)<sup>173</sup> or thermally activated delayed fluorescence (TADF) process<sup>174</sup>.

### 3.1.2 Thermally activated delayed fluorescence (TADF)

Thermally activated delayed fluorescence (TADF) (also named as *E*-type delayed fluorescence) was first observed in eosin by Parker *et al.* in 1961<sup>175</sup> and applied for the first time in OLED devices by Adachi *et al.* in 2009<sup>176</sup>. In this case, delayed fluorescence is produced by thermal activation from the triplet state of molecules. By controlling chemical structure and conformation, many TADF materials based on either organic small molecules or polymers have been explored over the last ten years. These materials can give rise to different emission colors and exhibit good device performance. Therefore, TADF-based OLEDs are considered as the 3<sup>rd</sup> generation OLED emitters.

**TADF mechanism**<sup>177</sup>. For electroluminescent molecules, once being electrically excited, singlet and triplet excitons in the high-energy states ( $S_n$  or  $T_m$ ) are formed by electron-hole recombination through electrostatic binding in a singlet:triplet ratio of 1:3. According to Kasha's rule, these excitons normally convert to the excitons with the corresponding low-energy states ( $S_1$  or  $T_1$ ) *via* the fast internal-conversion (IC) process. For ideal TADF molecules, the 25%  $S_1$  excitons dissipate through fluorescence radiative decay and non-radiative (NR) decay immediately, or transform to triplet excitons *via* intersystem crossing (ISC) process, whereas the other 75%  $T_1$  excitons up-convert to  $S_1$  state *via* endothermic reverse intersystem crossing (RISC) process, then decay to the ground state ( $S_0$ ).

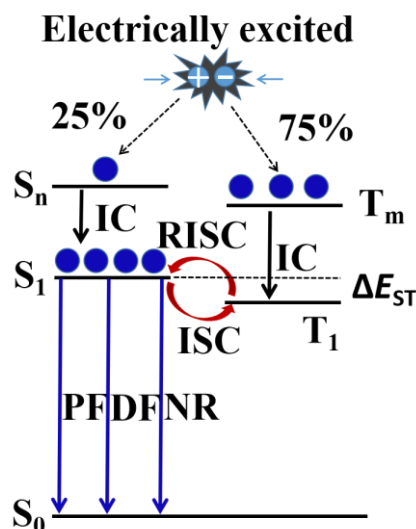


**Figure 3.1. 5** Schematic illustrations for the emission mechanism of TADF molecules.

Consequently, two sorts of fluorescence with distinct lifetimes are generated during the electroluminescence of TADF emitters: prompt fluorescence (PF) radiated from singlet excitons directly with lifetimes in nanosecond regime and delayed fluorescence (DF) radiated from the transformation of triplet excitons with lifetimes in the range of hundreds of nanoseconds to dozens of milliseconds. The overall fluorescence yield of TADF emitters is the sum of prompt and delayed fluorescence yield. Taking the recycling of singlet and triplet states, the total emission of a TADF molecule ( $\phi_F$ ) is the sum of  $\phi_{PF}$  and  $\phi_{DF}$ , which refer to the photoluminescence quantum yield

(PLQY) of the prompt and delayed components, respectively.<sup>178</sup>

Theoretically, a nearly 100% internal quantum efficiency (IQE) can be achieved by maximum harvesting both singlet and triplet excitons and suppressing vibrational decay. Thus, an efficient RISC process from  $T_1$  to  $S_1$  is crucial to achieving high photoluminescent efficiency. As the RISC process is endothermic and sensitive to temperature, the dependence of the RISC rate constant ( $k_{RISC}$ ) on temperature can be expressed by the Boltzmann distribution in the Arrhenius equation (3.1.5)<sup>179</sup>.

$$k_{RISC} = A \exp\left(\frac{-\Delta E_{ST}}{k_B T}\right) \quad (3.1.5)$$

Where  $k_B$  is the Boltzmann constant,  $T$  is temperature, and  $\Delta E_{ST}$  is the singlet-triplet splitting energy. From this equation (3.1.5), it is clear that a small  $\Delta E_{ST}$  is very important to overcome the energy barrier and promote the RISC process, achieving high fluorescent efficiency.

From a molecular standpoint,  $\Delta E_{ST}$  is the energy difference between the lowest singlet ( $E_{S1}$ ) and triplet ( $E_{T1}$ ) states. Small  $\Delta E_{ST}$  can be gained by decreasing the HOMO/LUMO overlap integral ( $J$ ) through the spatial separation of HOMO/LUMO on donor-acceptor or conjugation-breaking molecular structures. For TADF molecules, both  $\Delta E_{ST}$  and  $k_{RISC}$  of the charge transfer (CT) singlet excited states are in direct proportion to the HOMO/LUMO overlap integral  $J$  simultaneously, making it challengeable to figure out the most suitable  $J$  to realize efficient delayed fluorescence.

#### \* Structure-property relationship in TADF molecules

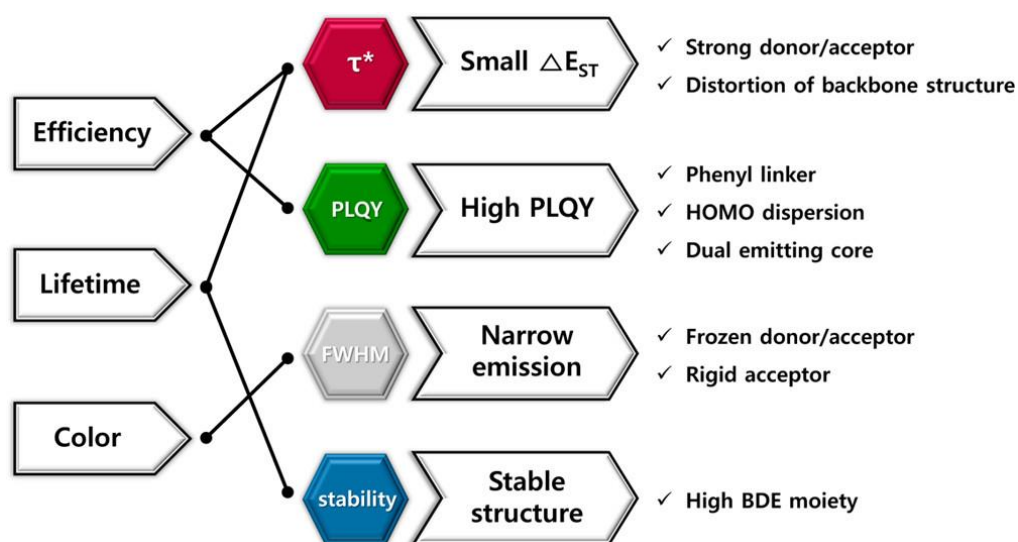


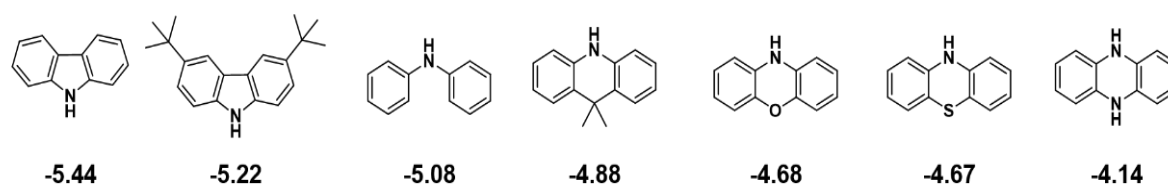
**Figure 3.1. 6** Schematic diagram relating to the material parameters, device performances, and molecular design strategy.<sup>180</sup>

As discussed above, the molecular structure decides the HOMO/LUMO distribution and the CT character, which can directly affect the TADF intrinsic parameters including photoluminescence quantum yield (PLQY), fluorescence lifetime, molecular stability as well as FWHM (short for “full width at half-maximum of the emission spectrum”). Further speaking, these parameters are directly

associated with device characteristics, including device efficiency, the “roll-off” effect, as well as the device lifetime, and emission color quality.<sup>180</sup> Therefore, the understanding of the structure-property relationship is beneficial for designing and optimizing the targeted parameters of TADF molecules along with a little sacrifice of other properties. A schematic diagram, shown in Figure 3.1. 6, is relating to the material parameters, device performances, and molecular design strategy.

The most widely used chemical structure architecture for TADF molecules is donor-acceptor (D-A) types where HOMO is located on the donors and LUMO is situated on the acceptors. Such architectures can be applied in either single D-A molecules or in organic exciplexes<sup>181</sup> formed with two individual donor and acceptor molecules. In this context, the molecular calculation is a useful method to effectively estimate the energy levels and the distribution of HOMO and LUMO.<sup>180</sup> The estimated results are helpful to judge the electron-donating/accepting abilities and assist the selection of donor and acceptor moieties. The most common donors and acceptors tested in this field are summarized in Figure 3.1. 7.

#### Donor (HOMO, eV)



#### Acceptor (LUMO, eV)

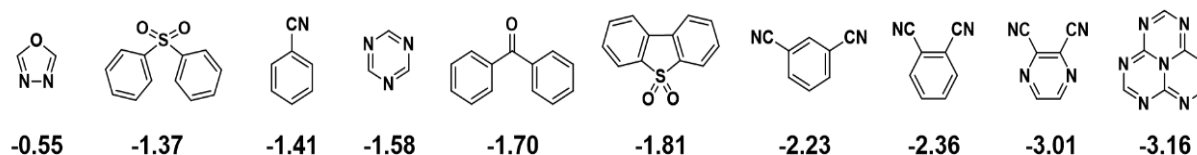


**Figure 3.1. 7** Chemical structures of representative donors and acceptors.<sup>177</sup>

**Photoluminescence quantum yield (PLQY).** For TADF molecules, the enhancement of PLQY remains important in developing high-efficiency TADF-based OLEDs. Due to the fact that i) TADF combines prompt and delayed components and ii) the predominant contribution to PLQY of TADF molecules is from triplet excitons, PLQY is tightly related to  $\Delta E_{ST}$ . From a molecular structure standpoint, a small  $\Delta E_{ST}$ , implying high PLQY, can be realized by the introduction of phenyl linker, HOMO dispersing, or ‘multiple emitting core’ structures.<sup>180</sup>

*Phenyl linker strategy.* Phenyl linker is introduced to avoid the extensive separation of HOMO and LUMO and increase the oscillator strength by inducing the HOMO and LUMO of the molecules to extend to the aromatic phenyl linker. However, this molecular design usually leads to large  $\Delta E_{ST}$  ( $E_S - E_T$ ), where the increased  $E_S$  arises from the weakened CT character by the increased HOMO/LUMO overlap, and the decreased  $E_T$  is attributed to the increased conjugation of the phenyl linker. As large

$\Delta E_{ST}$  is not desirable for other photophysical parameters, intensifying the CT character is suggested to decrease the  $E_S$  by adopting strong donor/acceptor moieties<sup>182</sup> or distorted backbone structure<sup>183</sup> or both<sup>184</sup>. The distorted backbone structures increase CT character by the steric hindrance owing to the increased dihedral angle from the *ortho*-phenyl linkage.

*HOMO dispersing strategy.* HOMO dispersing structure is also useful to increase the HOMO/LUMO overlap between the donors and acceptors in the backbone structure, resulting in high oscillator strength and high PLQY. For example, 4CzIPN (Figure 3.1. 8) with four HOMO managing carbazole moieties achieved much higher PLQY than DCzIPN with two carbazole units.<sup>185</sup>

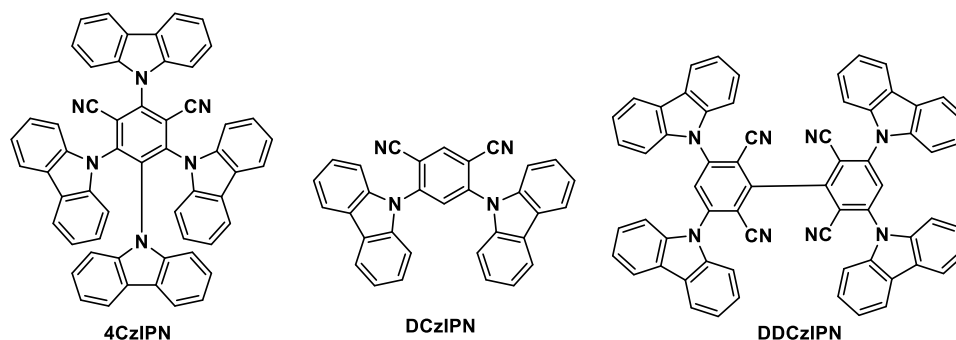


**Figure 3.1. 8** The chemical structures of 4CzIPN, DCzIPN, and DDCzIPN.

*Multiple emitting core strategy.* Multiple emitting core design is also effective for high PLQY. The idea is to insert several TADF emitters into one TADF molecule to enhance light absorption and emission. As an example, DDCzIPN, prepared by direct coupling of two DCzIPN, has higher PLQY (0.91) than that of DCzIPN (0.67) (Figure 3.1. 8).<sup>186</sup> The drawback of this strategy is the emission red-shift as a result of the reduced molecular energy owing to the increased extent of conjugation. To overcome this drawback, one molecular structure coupling two TADF emitters *via* a donor moiety was proposed and proved to be useful.<sup>187</sup>

**Delayed fluorescence lifetime ( $\tau_{DF}$ ).** For TADF emitters, a short delayed fluorescence lifetime is required with the aim of low efficiency “roll-off” ratio of devices, because triplet excitons may be deactivated *via* non-radiative decay when staying in  $T_1$  state for too long time to up-convert to singlet excitons by RISC process. Therefore, an efficient RISC process is a guarantee for a small  $\tau_{DF}$ , that is to say, a large  $k_{RISC}$  and a small  $\Delta E_{ST}$  are necessary for a short DF lifetime. As discussed above, strengthening CT character between the donor and acceptor units is a good way to reducing  $\Delta E_{ST}$  and can be realized by adopting strong donor/acceptor moieties, multiple emitting cores, or distorted backbone structures.<sup>182–184</sup>

**Material stability.** TADF material stability is another important factor for the degradation of OLEDs. The basic demand is that the materials remain stable when exposed to positive or negative polarons and excitons during the device operation. From a chemical structure standpoint, the donor and acceptor moieties, as well as their linkage, should also be stable under charge states. Hence, donor and acceptor moieties featuring large bond dissociation energy (BDE) are favorable for long-term stable

TADF emitters.<sup>180</sup> Among multiple candidates, carbazole derived donors and triazine or benzonitrile derived acceptors with high BDE are good choices for stable TADF molecules. For example, TCzIPN (4-(9*H*-carbazol-9-yl)-6-(9,9''-diphenyl-9*H*,9''*H*-[3,3':6',3''-tercarbazol]-9'-yl) isophthalonitrile, Figure 3.1. 9) exhibited three times longer lifetime than the current TADF emitters, as the weak C-N bond was stabilized by a small dihedral angle between donor and an aromatic linker.<sup>188</sup> Besides, TADF materials should also have good thermal stability, as OLED devices give rise to heat during the operation.

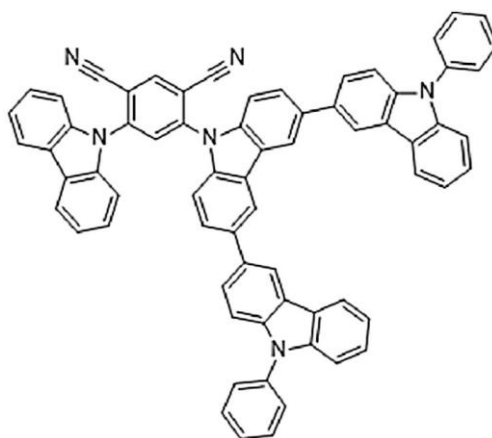


**Figure 3.1. 9** The chemical structure of TCzIPN

**Fluorescence emission.** Considering realistic demands, narrow emission is desirable for TADF-based displays. However, TADF emitters show a broader emission spectrum than conventional fluorescent emitters, as the delayed fluorescence of TADF emitters is originated from various CT singlet excited states generated in several forms with various energy levels. In order to realize narrow emission, one possible method is to restrict the rotation between donor and acceptor moieties *via* introducing a large steric hindrance<sup>189</sup> or adopting a fused structure.<sup>190</sup> For instance, DABNA-1 and DABNA-2 (Figure 3.1. 10) adopting a polycyclic aromatic backbone structure show a small FWHM less than 30 nm.<sup>190</sup> In addition, introducing rigid acceptor moieties can also locally rigidify the molecule to achieve narrow emission.<sup>191</sup>

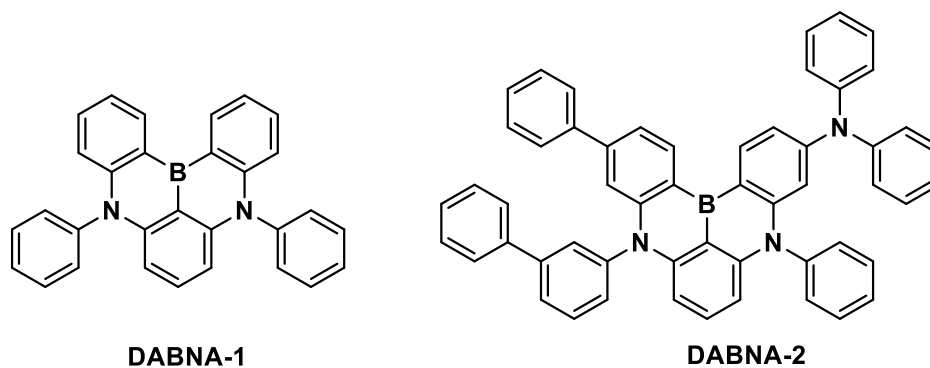


**Figure 3.1. 10** The chemical structures of DABNA-1 and DABNA-2.

### \* Photophysics of TADF molecules

As we all know, many TADF materials have been exploited, hence, for the reason of practical application, the investigation of the photophysical properties of TADF molecules has been a crucial issue for the exploit of TADF materials.

**Solvatochromism.** The solvatochromism effect is the phenomenon that the emission from TADF molecules shows the remarkable bathochromic shift along with increasing the media polarity, due to the stronger stabilization effect of higher polar media on their charge transfer (CT) excited states in contrast to ground states.<sup>192</sup> Usually, TADF molecules show narrow and well-resolved emission in non-polar solvents such as hexane and benzene. With increasing the solvent polarity, the luminescence spectra tend to redshift and become broad and featureless, which is the typical strong charge transfer (CT) character of the excited state (Figure 3.1. 11). When the CT excited states are strong enough, it is even possible that the CT emission is completely quenched in some polar solvents and shows broad and structureless in some nonpolar solvents. It is worth noting that the solvatochromism phenomenon works not only in the solution but also in the condensed state.<sup>193</sup> Take doped EMLs as an example, the TADF materials are dispersed in host matrices which serve as the solid solvent of TADF emitters. CT emission can also be observed in the doped solid films and the molecular polarities of the host materials should have a great effect on the emission colors of TADF devices, so the emission color is tunable by changing the content of host materials in the EMLs for the devices.<sup>178,194</sup>

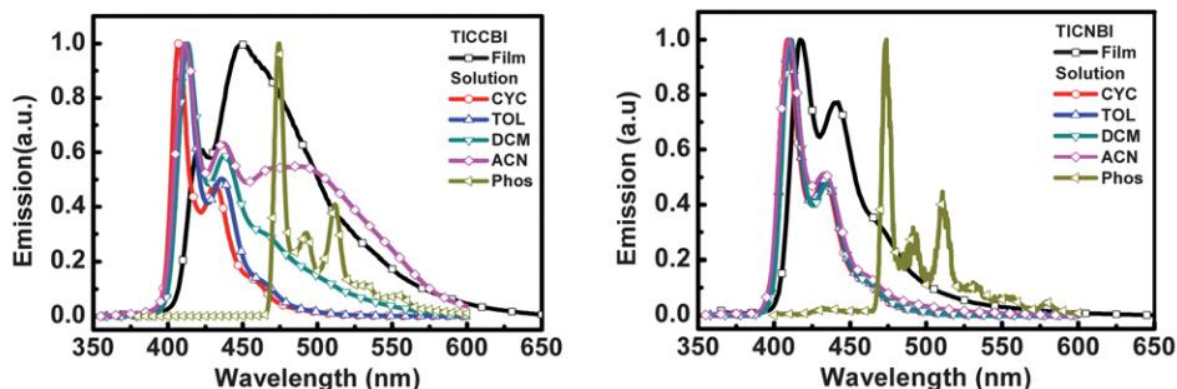


Figure 3.1. 11 UV-vis and PL spectra of TICNBI in various solutions and neat films.<sup>166</sup>

**Oxygen quenching effect on PLQY.** According to the TADF mechanism, the delayed fluorescence (DF), in the case of TADF materials, is transformed from a triplet excited state. As triplet oxygen ( $^3\text{O}_2$ ) from the air can quench triplet excitons by interacting with them, it is theoretically assumed that DF is completely quenched exposed in air-equilibrated condition, so the simplest method of preliminary checking for the existence of DF is the oxygen-free measurements.<sup>178</sup> Moreover, all measurements concerning DF require oxygen-free environments, which can be realized by two methods: 1) vacuum environment by degassing completely, suitable for solid samples; 2) inert environment by bubbling with inert gases like  $\text{N}_2$  or Ar, suitable for liquid samples. The integrals of the steady-state

fluorescence spectrum obtained in the presence and absence of oxygen are proportional to the PLQY of PF ( $\phi_{PF}$ ) and total TADF emission ( $\phi_F = \phi_{PF} + \phi_{DF}$ ), respectively

**Fluorescence decay of TADF molecules.** In order to strictly confirm the presence of DF in TADF materials, the fluorescence decay, defined as the temporal response of fluorescence intensity during the emission, should be measured in the oxygen-free condition,<sup>178</sup> being demonstrated as a fast decay followed by an emissive tail. The fast decay is attributed to PF, occurring in a few nanoseconds, whereas the long emissive tail confirms the existence of DF, whose lifetime usually ranges between 1 $\mu$ s to 10ms. The fluorescence decay is well fitted by the sum of two exponentials as expressed in equations<sup>194</sup>:

$$I(t) = A_{PF} \exp\left(-\frac{t}{\tau_{PF}}\right) + A_{DF} \exp\left(-\frac{t}{\tau_{DF}}\right) \quad (3.1.6)$$

$$\frac{\phi_{DF}}{\phi_{PF}} = \frac{A_{DF}\tau_{DF}}{A_{PF}\tau_{PF}} \quad (3.1.7)$$

Where  $I(t)$  is the overall fluorescence intensity of TADF materials,  $\tau_{PF}$  and  $\tau_{DF}$  correspond to the PF and DF lifetime,  $A_{PF}$  and  $A_{DF}$  are the integrals of related PF and DF components collected, respectively. From the above equations, the  $\phi_{DF}/\phi_{PF}$  ratio can be easily determined.

**Temperature dependence of TADF.** As the non-radiative (NR) decay is limited at low temperature, the prompt fluorescence (PF) exhibits a slightly longer lifetime and higher intensity. In contrast, delayed fluorescence (DF) strongly depends on temperature, as it arises from the RISC process through thermal activation. Both the intensity and lifetime of DF obey the Arrhenius kinetics and change significantly with temperature. Typically, strong DF can be observed at room temperature, accompanied without phosphorescence, whereas the integral of DF decreases and the phosphorescence appears along with the decreasing temperature. Finally, the DF will be completely inhibited and only phosphorescence exists, when the temperature is low enough. At this point, the thermal energy can't overcome the energy barrier and can't support the triplet-singlet up-conversion of excitons, resulting in the suppression of DF. For most TADF molecules, 77 K (liquid nitrogen) is low enough to the total suppression of DF. However, when the  $\Delta E_{ST}$  is very small, delayed fluorescence (DF) still exists around 77K, because the thermal energy at 77 K is still sufficient to allow the DF process. Therefore, the temperature dependence of DF is a fundamental proof of the source of the delayed components in the TADF mechanism.<sup>178,194</sup>

**Time-resolved emission spectrum (TRES).** As PF and DF arise from the same singlet excited state ( $E_{S1}$ ), in principle, their emission spectra are identical. However, in some cases, changes happen in the photoluminescence spectra. For example, due to several conformers with slightly different energy levels, the emission shift of the time-resolved emission spectra (TRES) may be observed. TRES is a good alternative to fluorescence steady-state spectroscopy and records the 3D emission spectrum as a function of time. Apart from PF and DF, phosphorescence can also be observed at low temperature. As phosphorescence comes from the triplet excited state ( $E_{T1}$ ), the emission spectra of

phosphorescence and PF are different. Based on this principle, TRES is considered as another technique to determine the source of the delayed components.

**Determination of  $\Delta E_{ST}$  and  $\Delta E_a^{TADF}$ .** As stated above,  $\Delta E_{ST}$ , the difference of the energy of the lowest singlet ( $E_{S1}$ ) and triplet ( $E_{T1}$ ) states, is the most important parameter in determining the lifetime of DF ( $\tau_{DF}$ ) as well as DF/PF ratio ( $\phi_{DF}/\phi_{PF}$ ). The general requirement for  $\Delta E_{ST}$  in designing TADF materials is less than 0.2 eV. From an experimental point of view, according to the photo energy formula (3.1.8), the value of  $E_{S1}$  and  $E_{T1}$  can be determined directly from *onset* or *maximum* of the prompt fluorescence and phosphorescence spectra, respectively. It is worth noting that it is necessary to observe phosphorescence at a very low temperature (< 20 K) when the  $\Delta E_{ST}$  is lower than 0.01 eV, to ensure no delayed fluorescence occurs.

$$E = h\nu = \frac{hc}{\lambda} \approx \frac{1240 \text{ (eV}\cdot\text{nm)}}{\lambda} \quad (3.1.8)$$

Where  $E$  is the energy level,  $h$  is the Planck constant,  $c$  is the speed of light in vacuum,  $\lambda$  is the wavelength. As  $h$  and  $c$  are both constants,  $E$  changes in reverse relation to  $\lambda$ .

$\Delta E_a^{TADF}$  refers to the activation energy of TADF and can be estimated from Arrhenius plot where DF intensity or  $k_{RISC}$  is plotted against temperature  $T$ . Generally speaking,  $\Delta E_a^{TADF}$  is close to  $\Delta E_{ST}$  and the values often stay in relation  $\Delta E_{ST} \gg \Delta E_a^{TADF}$ .<sup>194</sup>

**Power dependence of TADF with exciton dose.** As both TADF and TTA are thermally activated processes, it's necessary to find out the origin of delayed fluorescence. Power dependence measurement is a convenient approach to distinguish TADF from TTA. In principle, TADF is an intramolecular process and the emission intensity is linearly with exciton dose, whereas TTA is a bimolecular process whose emission intensity shows a quadratic dependence on the exciton dose.<sup>194</sup> However, in some cases, TADF and TTA coexist and can be revealed by power dependence of emission integral that shows slopes between 1 and 2.<sup>178</sup>

### \* *Examples of TADF materials*

Over the years, many TADF materials have been explored and widely applied in optoelectronic fields including fluorescence imaging<sup>195</sup>, mechanoluminescence<sup>196</sup>, and OLED devices<sup>197</sup>. On the basis of molecular structures, TADF materials can be classified into three groups: TADF small molecules, TADF dendrimers, and TADF linear polymers.

#### A. TADF small molecules

TADF small molecules are the most extensively studied and well-developed materials for OLEDs, due to their high purity, high PLQY, and tremendous possibility with chemical modification. However, their inferior film-forming ability and superior crystallization ability may strongly affect the film

morphology and lead to low efficiency and device stability. Various donors and acceptors have been used to manage the TADF characteristics and the full-color emission has been realized. Some TADF small molecules are shown in Figure 3.1. 12.

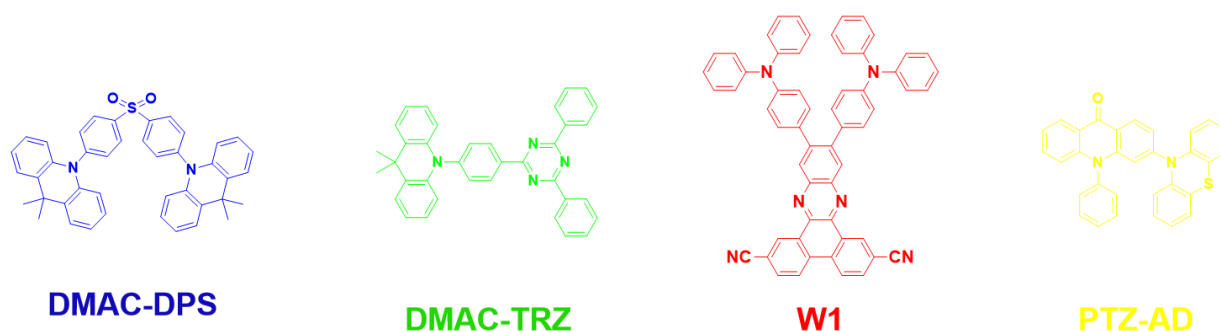


**Figure 3.1. 12** Some examples of TADF small molecules with different emission colors.<sup>198–201</sup>

DMAC-DPS<sup>200</sup> is a typical blue TADF molecule exhibiting blue emission ( $\lambda_{\text{max}} = 460 \text{ nm}$ ) with a high PLQY of 80% in oxygen-free toluene or doped mCP film and 90% in doped DPEOP film. The OLED based on DMAC-DPS dopant showed blue emission with a high EQE<sub>max</sub> of 19.5% and an EQE of 16.0% at a luminance of 1000 cd/m<sup>2</sup>. DMAC-TRZ<sup>198</sup>, with 9,9-dimethyl-9,10-dihydroacridine (DMAC) as the donor and 2,4,6-triphenyl-1,3,5-triazine (TRZ) as the acceptor, shows high thermal stability and a distinct glass transition around 90 °C, ensuring the successful formation of stable amorphous neat film by vacuum deposition. DMAC-TRZ not only exhibits high PLQY (~90%) in doped films but also possesses low concentration quenching and high PLQY (~83%) in neat films. The OLED devices achieved green emission with a high EQE of 20% at 100 cd/m<sup>2</sup> using DMAC-TRZ as a non-doped emitting layer and blue-green emission with a higher EQE of 26.5% at 100 cd/m<sup>2</sup> using DMAC-TRZ as the emitting dopant. PTZ-AD<sup>201</sup> is a high-efficiency yellow TADF emitter with dual conformations, whereas the quasi-axial conformer shows classical fluorescence emission, and the quasi-equatorials conformer exhibiting TADF characteristics is the main configuration of PTZ-AD. The yellow non-doped TADF devices based on PTZ-AD achieved EQE<sub>max</sub> of 17.08%, CE<sub>max</sub> of 50.48 cd/A, and PE<sub>max</sub> of 60.04 lm/W, which are close to EQE<sub>max</sub> of 20.23%, CE<sub>max</sub> of 61.04 cd/A, and PE<sub>max</sub> of 68.45 lm/W of PTZ-AD-based doped devices. Liao *et al.* reported a high-efficiency red TADF material, namely W1<sup>199</sup>, with a high PLQY of 57.1% and 93.7% in neat and doped films, respectively. The OLED device using W1 as the emitting dopant displayed superior device performance with an EQE<sub>max</sub> of 24.97% at a  $\lambda_{\text{EL}}$  of 608 nm (doping ratio: 10%). However, the efficiency ‘roll-off’ effect is very severe and EQE decreased to 8.73% at 100 cd/m<sup>2</sup> and 3.88% at 1000 cd/m<sup>2</sup>.

## B. TADF dendrimers

Dendrimers, typically composed of a central core and peripheral branches of dendrons, are a specific category of macromolecules. Due to their distinct structures, dendrimers usually exhibit the

advantages of both small molecules and polymers.<sup>202</sup> Dendrimers have a precise molecular structure allowing for reproductivity and their property can be finely tuned through chemical modification. As another advantage, dendrimers have high molecular weight and solution processability.<sup>203</sup> In addition, dendritic architecture prevents it from aggregation and eliminate concentration quenching.<sup>204</sup> Carbazole (Cz) is the most widely used dendron in constructing dendrimers, due to its good hole-transporting properties, high thermal stability, and excellent crosslinking abilities.<sup>205</sup> The high steric hindrance from branched Cz is beneficial to reducing the non-radiative decay, avoiding concentration quenching, thus leading to high PLQY. Generally, TADF dendrimers can be divided into conjugated and non-conjugated TADF dendrimers, on the basis of the connection method between the dendrons and the core (Figure 3.1. 13).

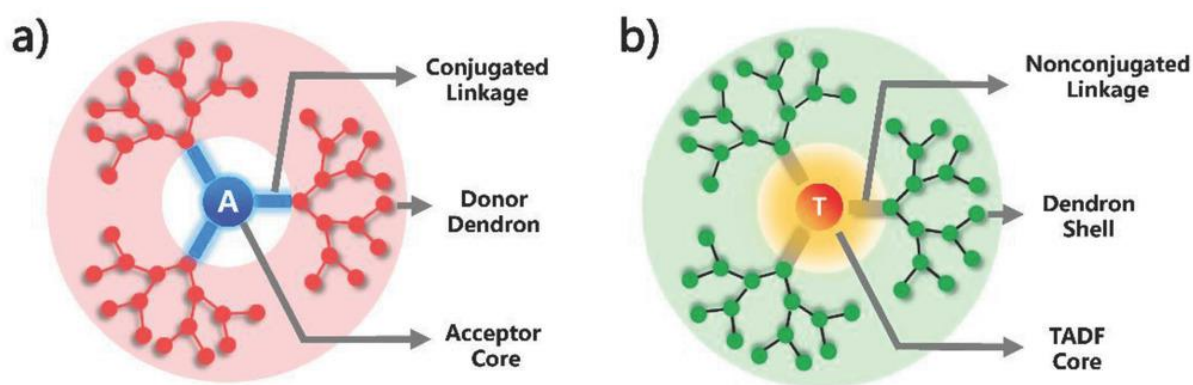


**Figure 3.1. 13** TADF dendrimers with conjugated (a) and non-conjugated (b) linkages.

*TADF dendrimers with conjugated linkages.* In most conjugated TADF dendrimers, the electron-accepting units are located at the central core while the electron-donating dendrons are connected to the core *via* conjugated linkages. The photophysical properties of these TADF dendrimers are more complicated than the individual TADF counterparts. As the HOMO migrates from the internal donor moieties to the peripheral dendrons with increasing dendrimer generation, while the LUMO remains located on the acceptor core, the distance between HOMO and LUMO levels increases and the absorption coefficient of the CT band decreases.<sup>177</sup> Therein the branched dendrons feature a gradient HOMO level with an electron-rich periphery, demonstrating the possibility of realizing an ideal HOMO/LUMO overlap between the core and dendrons by managing the HOMO distribution through tuning the dendron generation. Nevertheless, the photoluminescence spectrum shows little change with increasing dendron generation, because the emission from a CT state only depends on the neighboring donor moieties of the TADF core as a result of a highly twisted spatial structure.<sup>206</sup> And emission red-shift happens when HOMO delocalizes over the donor moieties and peripheral dendrons as a result of a relatively planar conjugated structure. CzDMAC-DPS and DCzDMAC-DPS (Figure 3.1. 14a) exhibit excellent photophysical properties and good thermal stability. The non-doped solution-processed OLED device with CzDMAC-DPS as EML was fabricated to realize a greenish-

blue emission with a high  $\text{EQE}_{\text{max}}$  of 12.2%.<sup>207</sup>

*TADF dendrimers with non-conjugated linkages.* In non-conjugated TADF dendrimers, the TADF unit is located at the core and the dendrons connect to the TADF core *via* non-conjugated aliphatic chains. The insulating aliphatic linkage guarantees that the TADF character is well retained, and the branched dendrons compensate for the loss of charge injection and transport abilities owing to the non-conjugated linkages. One severe problem of this strategy is that the incorporation of oxygen atoms for the ease of synthesis may change the emission characteristics of TADF units.<sup>204</sup> In POCz-DPS<sup>208</sup> (Figure 3.1. 14b), DMOC-DPS core and bipolar phosphine oxide carbazole (POCz) dendrons are connected by hexyl chains. The bipolar dendrons not only improve the morphological stability but also restrain the concentration quenching effect of the TADF core. The spin-coated OLEDs featuring POCz-DPS as the host-free emitter achieved a high  $\text{EQE}_{\text{max}}$  of 7.3% and higher color purity relative to those of devices based on DMOC-DPS.

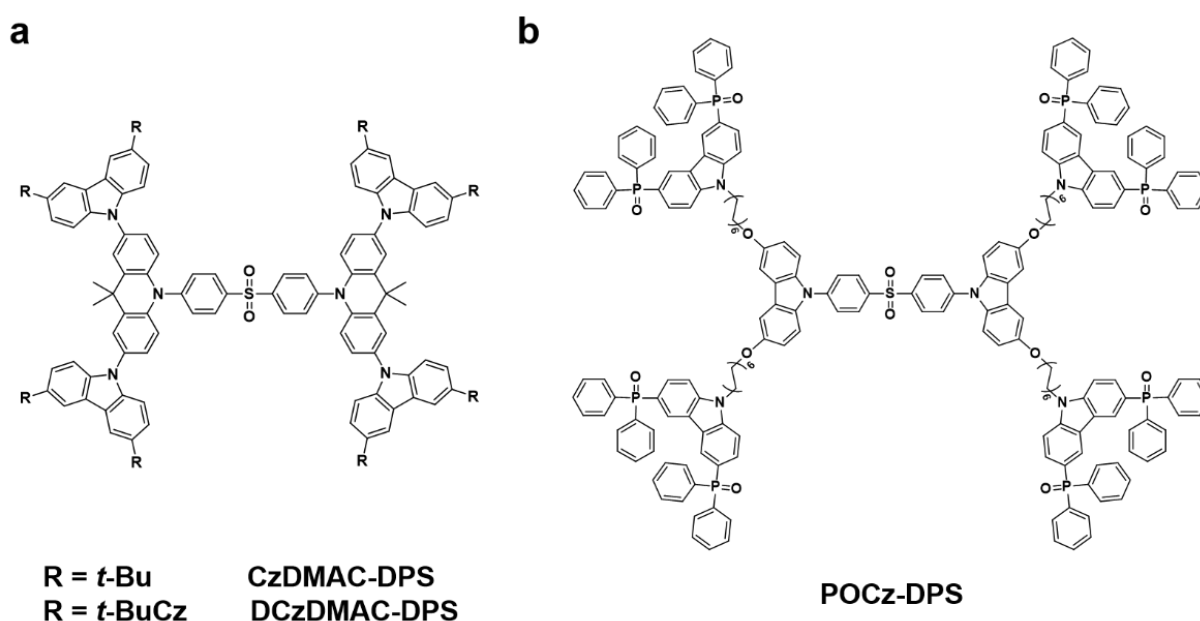


**Figure 3.1. 14** TADF dendrimers with (a) conjugated<sup>207</sup> and (b) non-conjugated<sup>208</sup> linkages.

### 3.1.3 Linear polymeric TADF materials

In addition to small molecules and dendrimers, the TADF character can also be realized in linear polymers. However, linear polymeric TADF-based OLEDs always suffer from low efficiency, short lifetime as well as poor film morphology. To optimize device performance, on one hand, many suitable functional materials are explored by controlling the molecular structures and conformations. On the other hand, the fabrication condition requires to be well managed. For example, to avoid concentration quenching, most polymeric OLEDs take advantage of the host matrix. However, the introduction of the host may lead to wider luminescence spectra, bathochromic shift (red-shift), and extra luminescence ascribed to host units.<sup>209</sup> Therefore, it remains a challenge to develop polymeric

OLEDs with excellent device performance.

To overcome the limitation, TADF materials need to satisfy the realistic demands as follows.<sup>203</sup> From a point view of production, TADF polymers are fabricated *via* solution-process, so good solubility and good film-forming ability are necessary in order to produce uniform film morphology without defects or aggregation. For commercial applications, the OLEDs require a long device lifetime and high efficiency. For a long device lifetime, TADF polymers need to possess good thermal, photochemical, and electrochemical stabilities. To achieve high efficiency, similar to TADF small molecules, TADF polymers are required to realize a small singlet-triplet energy splitting ( $\Delta E_{ST}$ ) and high photoluminescence quantum efficiency (PLQY) at the same time. As polymers contain a large number of atoms, it is difficult to manage the HOMO and LUMO distribution and eliminate concentration quenching originated from inter- and intra-molecular triplet-triplet annihilation (TTA).

Despite many efforts made to overcome these limitations, TADF was not observed in polymeric architecture until the first linear TADF polymer was reported by Nikolaenko *et al.* in 2015<sup>210</sup> (Figure 3.1. 15, Table 3.1.2). In this case, suitable donor and acceptor moieties are chosen as distinct monomers to generate the charge transfer emitter (TADF unit) during the polymerization. A third high triplet level component served as a host to isolate the TADF units to inhibit the aggregation and provide the desired solubility and film-forming ability. This promising strategy was successfully applied to a fully solution-processable TADF polymer platform. Followed this pioneering work, many different structural architectures for linear polymeric TADF have been explored.

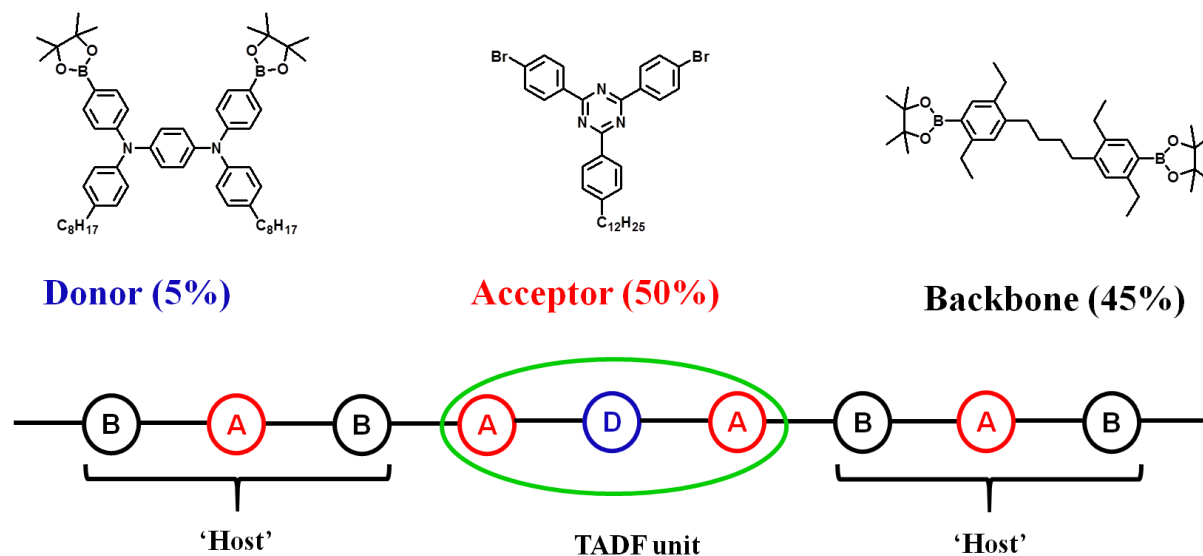


**Figure 3.1. 15** The chemical structure of the first reported linear TADF polymer.<sup>210</sup>

So far, the dominant strategy in the designing of TADF polymers is to take advantage of known TADF small molecules by inserting known TADF-active building blocks into polymeric structures either as pendant groups, as main chain constituents, or as dendrimer cores and dendrons.<sup>211</sup> TADF characters can be realized in either through-bond charge transfer (TBCT) or through-space charge transfer (TSCT). In TBCT systems, donor and acceptor moieties are connected directly by either  $\sigma$ -bond or

twisted spacer. In TSCT systems, donor and acceptor units are physically separated. No matter which system is adopted, the HOMO and LUMO are spatially separated. TADF polymers show similar photophysical properties to their small-molecule motifs, such as solvatochromism and oxygen quenching.<sup>177</sup> Based on this strategy, several chemical architectures have been proposed, and they can be classified as linear conjugated TADF polymers and linear non-conjugated TADF polymers, according to the backbone.

\* *Linear conjugated TADF polymers*

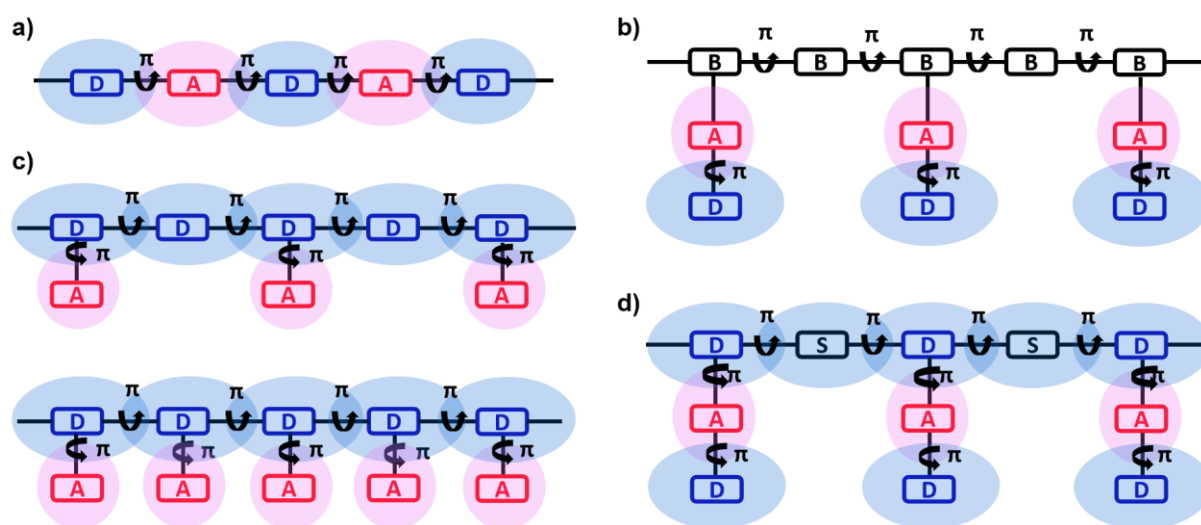


**Figure 3.1. 16** Schematic representatives of linear conjugated TADF polymers (D: donor, A: acceptor, B: conjugated backbone, S: conjugated spacer).

According to the position of donor and acceptor units, the linear conjugated TADF polymers can further be classified into four categories as shown in Figure 3.1. 16: a) alternating donor and acceptor in the main chain; b) TADF emitters pendant in side chain; c) donors located in the backbone while acceptors grafted in the side chain; d) polymers based on D1-A-D2 type small-molecule TADF emitter. The photoluminescent and electroluminescent characteristics of typical TADF conjugated polymers are summarized in Table 3.1.1.

*Linear conjugated TADF polymers with twisted alternating donor/acceptor units in the main chain.*

This strategy (Figure 3.1. 16a) is derived from TADF small molecules. The separated frontier orbital distribution, with HOMO locating on the donor part and LUMO on the acceptor part, would lead to a small  $\Delta E_{ST}$  to facilitate the RISC process.

As an example, in 2016, Adachi *et al.* developed a class of butterfly-shaped conjugated TADF polymers,<sup>212</sup> namely pCzBP and pAcBP (Figure 3.1. 17), with electron-accepting benzophenone unit linked with electron-donating carbazole or acridine groups, respectively. These TADF polymers showed relatively small  $\Delta E_{ST}$  values (<0.2 eV), which enabled efficient triplet exciton harvesting *via*

up-conversion from  $T_1$  states to  $S_1$ . As a result, pCzBP and pAcBP achieved PLQYs of 23% and 46% in doped films, respectively. The solution-processed doped OLEDs using pCzBP and pAcBP as emitting dopants produced green ( $\lambda_{EL} = 500 \text{ nm}$ ) and yellow ( $\lambda_{EL} = 548 \text{ nm}$ ) emission with a maximum external quantum efficiency ( $\text{EQE}_{\text{max}}$ ) of  $8.1\% \pm 0.7\%$  and  $9.3\% \pm 0.9\%$ , respectively. Besides, the OLEDs based on pAcBP showed a small efficiency roll-off, as the EQE remained 8.0% at a luminance of 1000 cd/A.

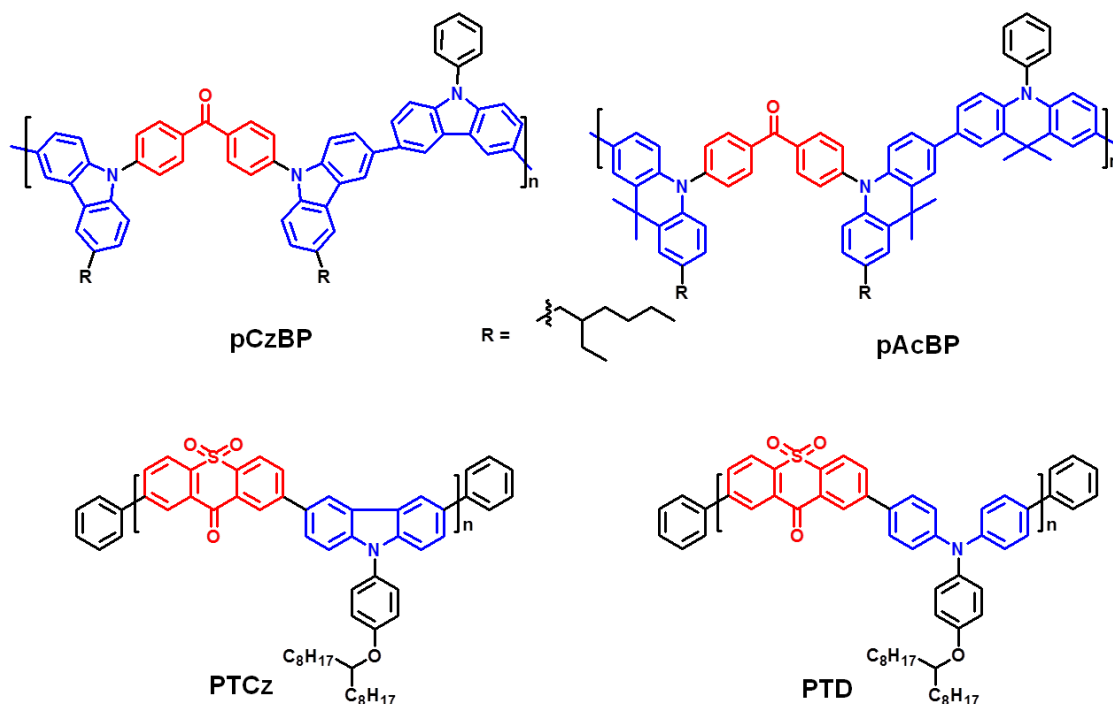


**Figure 3.1. 17** TADF conjugated polymers with alternating donor and acceptor in the backbone (pCzBP and pAcBP,<sup>212</sup> PTCz and PTD<sup>213</sup>).

*Linear conjugated TADF polymers with TADF units in the side chain.* In this strategy (Figure 3.1. 16b), the TADF units are completely out of the backbone and are introduced as pendants in the side chain, so the TADF effect is not influenced by the backbone. And the conjugated backbone can serve as host materials.

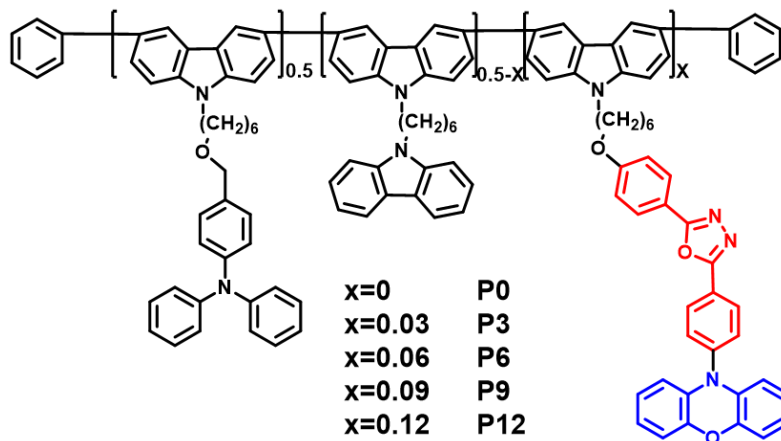


**Figure 3.1. 18** Chemical structures of linear conjugated polymers with pendant TADF units.<sup>214</sup>

For example, Yang *et al.* reported a series of polycarbazole featuring TADF character, by grafting TADF emitter 10-(4-(5-phenyl[1,3,4]oxadiazol-2-yl)phenyl)-10*H*-phenoxazine (PXZ-OXD<sup>215</sup>, Figure 3.1. 18).<sup>214</sup> Herein, polycarbazole acts as a charge transport channel and the host, while the grafted triphenylamine (TPA) or carbazole (Cz) units are designed to promote the hole injection. P3-P12 all exhibited TADF character and their PLQYs range from 27.5% (P3) to 33.7% (P12) in degassed neat films. The solution-processed OLEDs based on P9 and P12 produced bluish-green emission ( $\lambda_{\text{EL}} = 498 \text{ nm}$  for P9,  $\lambda_{\text{EL}} = 506 \text{ nm}$  for P12) with maximum EQEs of 4.0% and 4.3%, corresponding to the exciton utilization efficiency (EUE) of 59.5% and 63.7%. However, the solution-processed OLEDs based on P3 and P6 produced blue and sky-blue emission ( $\lambda_{\text{EL}} = 478 \text{ nm}$  for P3,  $\lambda_{\text{EL}} = 492 \text{ nm}$  for P6) with low maximum EQEs of 1.2% and 1.1%, corresponding the EUEs of 21.8% and 20.2%, respectively.

*Linear conjugated TADF polymers with donors located in the backbone and acceptors grafted in the side chain.* In this strategy (Figure 3.1. 16c), only donors are fixed in the backbone, and acceptors are grafted in the side chains, so that the HOMO spreads over the entire backbone while the LUMO is only localized on the pendant acceptors. The efficient spatially separation of HOMO and LUMO offers a small  $\Delta E_{\text{ST}}$ . For the moment, most researchers favor this chemical architecture to achieve TADF nature in conjugated polymers, among them, most cases are copolymers, where the extra donor groups serve as both emitting and host materials and help to manipulate TADF content and the distribution of molecular orbitals.

Several series of TADF polymers were developed using electron-donating acridine and carbazole groups as the conjugated backbones (Figure 3.1. 19). The acceptors with different electron-accepting abilities were grafted onto the backbone through the nitrogen atom of 9,10-dihydroacridine group with a large dihedral angle to form a pre-twisted intramolecular charge transfer structure (TICT).<sup>216</sup> PAPCC and PAPTc are two alternating TADF copolymers with phenyl cyanogen and dibutyltriazine groups as acceptors, respectively.<sup>216</sup> PAPTc exhibited a small  $\Delta E_{\text{ST}}$  of 0.13 eV and high PLQY of 28% in neat films in air, while the  $\Delta E_{\text{ST}}$  and PLQY of PAPCC are 0.37 eV and 8%, indicating that strong acceptor is favorable for small  $\Delta E_{\text{ST}}$  and high PLQY. Consistent with PLQY, the solution-processed OLEDs based on PAPTc and PAPCC displayed green EL emission ( $\lambda_{\text{EL}} = 521 \text{ nm}$  for PAPTc,  $\lambda_{\text{EL}} = 508 \text{ nm}$  for PAPCC) with a maximum EQE of 12.63% and 1.34%, respectively. To optimize the device performance, TAPC was introduced to generate an interfacial exciplex host of TAPC/TmPyPB to restrain triplet quenching of PAPTc emitter.<sup>217</sup> The resulting solution-processed doped OLEDs using PAPTc as the emitting dopant exhibited a superior EQE<sub>max</sub> of 14.9% and an extremely low efficiency roll-off.

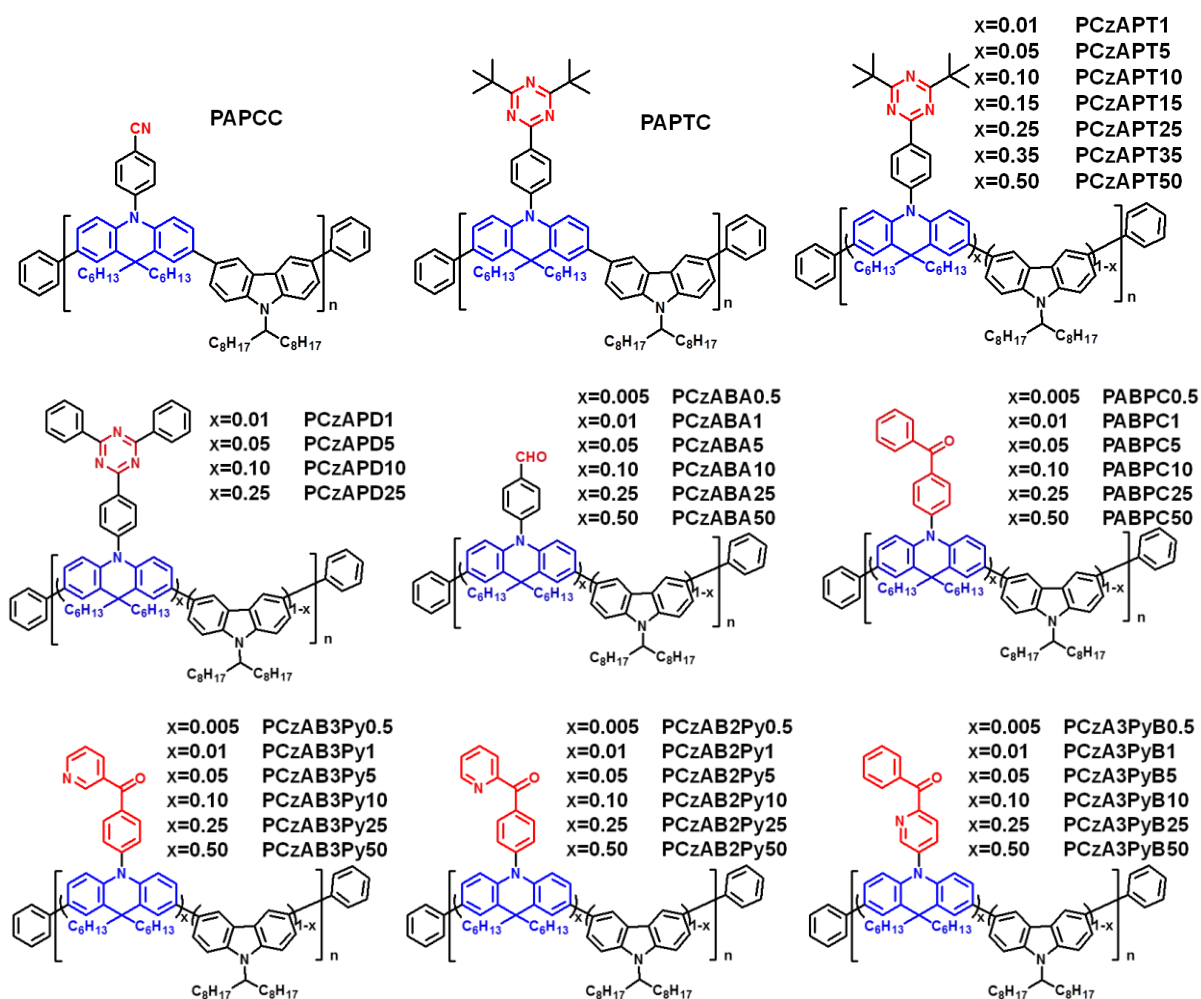


**Figure 3.1. 19** TADF polymers with acridine and carbazole as the electron-donating backbone.

To further understand the relationship of luminescent performances and polymer structure, a series of random copolymers PCzAPT<sub>x</sub> (Figure 3.1. 19)<sup>218</sup> was prepared using the same acceptor and donor moieties as PAPT<sub>C</sub>. Except for PCzAPT<sub>1</sub>, all other polymers exhibited obvious TADF nature. The polymers with low TADF content exhibited enhanced PLQY in neat films. And PCzAPT<sub>35</sub> and PCzAPT<sub>50</sub> showed higher PLQY in blend films with decreasing doping ratio from 25% to 5%. Even though PCzAPT<sub>5</sub> exhibited the highest PLQY of 92.1% in neat film, the non-doped solution-processed OLED based on PCzAPT<sub>10</sub> displayed the highest EQE<sub>max</sub> of 16.9%, as the oligomeric carbazole segments act as blocking segments, suppressing the intra- and interchain quenching process. To further improve the electroluminescent performances, a more rigid acceptor was chosen to replace the tert-butyl groups with phenyl rings on the triazine parent, creating a classic TADF unit DMAC-TRZ<sup>198</sup>. The resulting conjugated TADF polymers PCzATD<sub>x</sub><sup>219</sup> with various TADF content exhibited small ΔE<sub>ST</sub> (0.08-0.14 eV) and enhanced PLQYs of 65-90% in degassed neat films. The non-doped solution-processed OLEDs based on PCzATD<sub>x</sub> displayed yellow emission with an EQE<sub>max</sub> of 15.5% (PCzATD<sub>5</sub>) and possessed a low turn-on and driving voltages at 2.53 V and 4.05 V (1000 cd/m<sup>2</sup>) with extremely small efficiency roll-off of 0.5%.

Instead of triazine acceptors with formyl groups, PCzABAx (Figure 3.1. 19)<sup>220</sup> exhibited PLQYs between 35% and 51% in neat films under a nitrogen atmosphere. The non-doped solution-processed OLEDs using PCzABAx as emitters produced green emission and the OLED based on PCzABA10 showed the best device performance with an EQE<sub>max</sub> of 10.6% and an extremely small efficiency roll-off with EQE<sub>1000</sub> of 10.3%. With benzophenone as acceptor, PABPCx<sup>221</sup> showed small  $\Delta E_{ST}$  (0.09-0.18 eV) and PLQYs from 58% to 77% in neat films under nitrogen atmosphere. The PABPC5-based solution-processed OLED showed the best EL performance with an EQE<sub>max</sub> up to 18.1% and also a very slow roll-off with an EQE of 17.8% at a luminance of 1000 cd/m<sup>2</sup>.

Besides, three isomeric benzolpyridine derivatives were selected as pendant acceptors to create three categories of conjugated TADF polymers with varying TADF content<sup>222</sup>, named PCzA3PyBx, PCzAB2Pyx, PCzAB3Pyx, respectively (Figure 3.1. 19). All these polymers exhibited a small  $\Delta E_{ST}$  of less than 0.2 eV. The PLQYs range of PCzA3PyBx, PCzAB2Pyx, and PCzAB3Pyx in neat films under nitrogen atmosphere are 15 ~ 47%, 23 ~ 68%, and 31 ~ 68%, respectively. PCzA3PyB50, PCzAB2Py50, and PCzAB3Py50 with 50 mol% TADF content produced yellow to orange emission with the longest EL wavelength in each group ( $\lambda_{EL} = 588 \text{ nm}$  for PCzA3PyB50,  $\lambda_{EL} = 600 \text{ nm}$  for PCzAB2Py50, and  $\lambda_{EL} = 585 \text{ nm}$  for PCzAB3Py50). With decreasing TADF content in these polymers, the electroluminescent emission blueshift from green to yellow region ( $\lambda_{EL} = 568 \text{ nm}$  for PCzA3PyB5,  $\lambda_{EL} = 573 \text{ nm}$  for PCzAB2Py5, and  $\lambda_{EL} = 557 \text{ nm}$  for PCzAB3Py5). PCzA3PyB5, PCzAB2Py5, and PCzAB3Py5 possessed the best electroluminescent performance in each group, with external EQEs of 5.2%, 11.9%, and 12.2%, respectively.

Besides TADF conjugated polymers with acridine/carbazole backbone, several TADF conjugated polymers (Figure 3.1. 20) were derived from yellow-emitting PTZ-DBTO2<sup>223</sup>. COPO2<sup>223</sup> is an alternating TADF conjugated copolymer exhibiting large efficiency roll-off with an EQE<sub>max</sub> of 11.05% at 5.5 V. To improve its EL performance, alkyl chains were introduced into the polymers to provide solubility, and carbazole (Cz) or triphenylamine (TPAs) units serve as host units to tune TADF characteristics. Homo, Cop-50, and Cop-10 are homopolymer, alternating copolymer, and random copolymer, respectively. All these polymers had a  $\Delta E_{ST}$  smaller than 0.1 eV, but their PLQYs are only 10%, 18%, and 21% in doped films in the air, as a result of the aggregation effect. The non-doped Cop-10-based solution-processed OLED device could reach an EQE<sub>max</sub> of 15.7% with a low turn-on voltage of 3.2 V.<sup>224</sup> In PTDP-x, TPA is also a blue emitter. PTDP-5 and PTDP-10 exhibited a quite high PLQY close to 100% in doped films under nitrogen condition, and their  $\Delta E_{ST}$  are 30 meV and 23 meV, respectively. As only the yellow emission from TADF units is affected by oxygen, the emission color is different in the presence and absence of oxygen. The PTDP-10-based doped solution-processed OLED achieved a 4.8% EQE<sub>max</sub> with the CIE coordinates of (0.44, 0.43), while PTDP-5-based OLED produced warm white emission with 7.1% EQE<sub>max</sub>.<sup>225</sup>

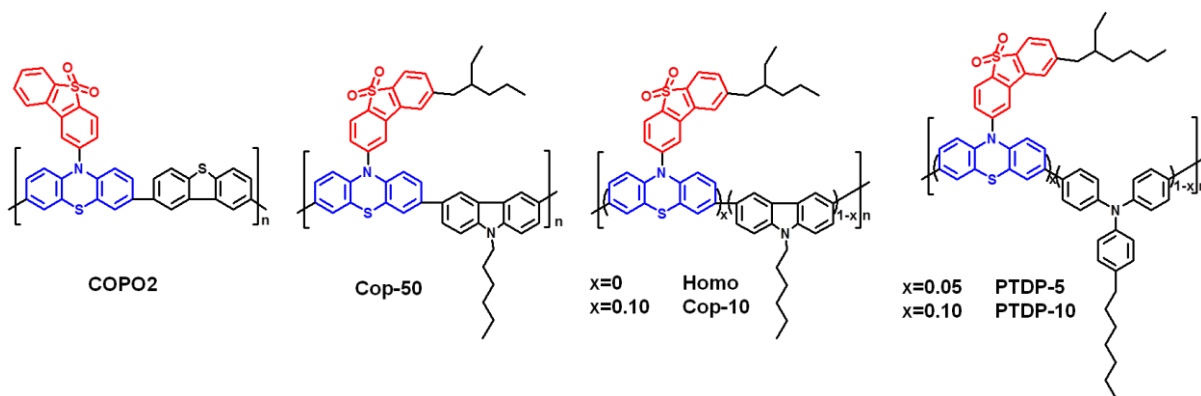


**Figure 3.1. 20** Chemical structures of TADF polymers designed based on PTZ-DBTO2.

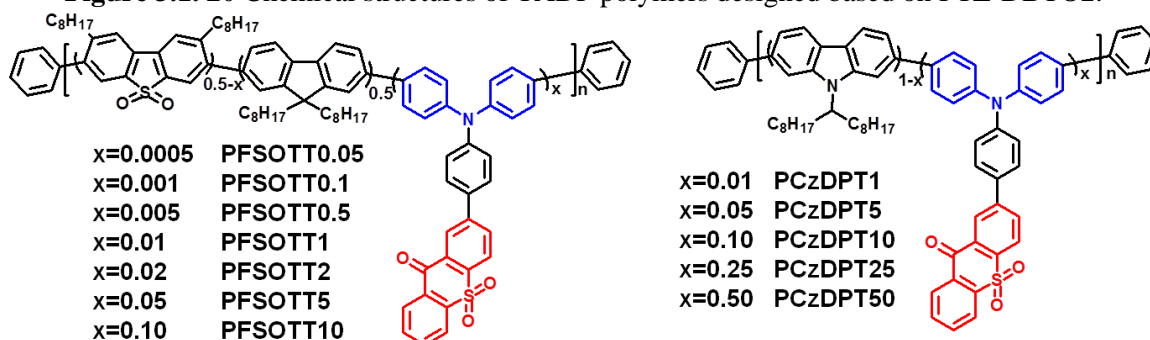


**Figure 3.1. 21** Chemical structures of TADF polymers PFSOTT<sub>x</sub>.

Cheng *et al.* prepared two groups of conjugated TADF polymers, namely PFSOTT<sub>x</sub><sup>226</sup> and PCzDPT<sub>x</sub><sup>213</sup> (Figure 3.1. 21) based on TADF unit TXO-TPA<sup>227</sup>. PFSOTT<sub>x</sub><sup>226</sup> exhibited high PLQY in doped films free of oxygen. By tuning the TADF content, PFSOTT0.05 and PFSOTT0.1 exhibited cold white electroluminescent emission with low EQE<sub>max</sub> (<1%), as a result of the simultaneous blue emission from the backbone and orange emission from the TADF unit. Other polymers displayed orange to red emission. The different emission colors indicated that a single polymer containing the TADF unit can also achieve white electroluminescence when the orange TADF unit content is well managed. PCzDPT<sub>x</sub><sup>213</sup> is also red-emitting TADF polymers and deep-red and NIR OLEDs have been fabricated employing PFSOTT2:PCzDPT<sub>x</sub>:mCP as an emitting layer, where PFSOTT2 acts as a sensitizer of the other TADF polymer with lower PLQY and longer emissive wavelength. It provides a promising approach to design deep-red and NIR OLEDs.

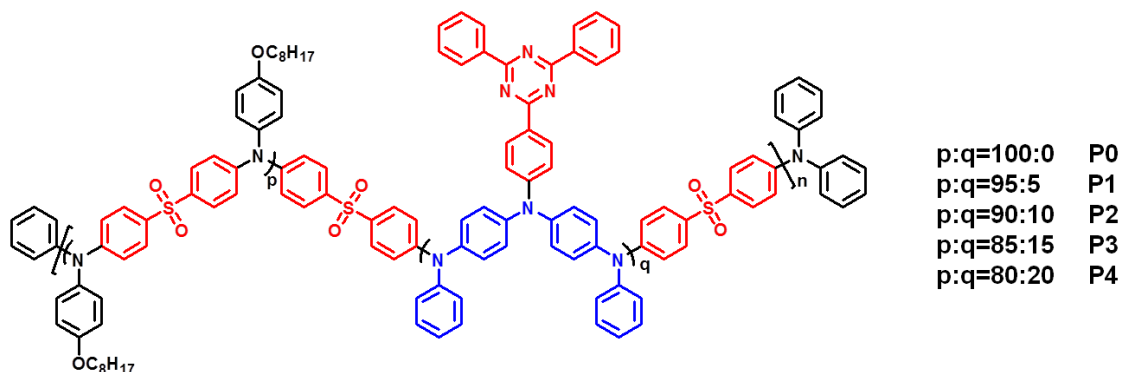


**Figure 3.1. 22** Polymers with twisted D/A backbone and pendant triazine derivate acceptor.

Huang et al. proposed a strategy of incorporating a D-A type TADF unit (di-triphenylamine-functionalized triazine) into the polymer backbone consisting of alternating donor and acceptor units (Figure 3.1. 22)<sup>228</sup>. By tuning the  $\pi$ -conjugation length and the redox potential of the donor and acceptor moieties, the obtained polymer can show a small  $\Delta E_{ST}$  ( $\leq 0.2$  eV) and the PLQYs of the blend films range from 64 to 81%. By employing P0, P1, and P3 blend film as emitters, the EQE<sub>max</sub> of 5.3%, 6.1%, and 8.7% of the corresponding OLEDs were achieved for pure blue, sky-blue, and bluish-green emission, respectively.

Besides copolymers, it is also possible to realize TADF in a conjugated homopolymer with polymerization-induced extended  $\pi$ -conjugation, resulting from the reduced energy splitting between the respective singlet and triplet charge-transfer states (<sup>1</sup>CT and <sup>3</sup>CT) of the building blocks ( $\Delta E_{ST}$ ) through a polymerization-induced extension of the  $\pi$ -conjugated electron-donating system. For example, despite the repeating unit without featuring TADF nature, polycarbazoles, having a planar triazine<sup>229</sup> or benzophenone<sup>230,231</sup> at carbazole N-position, showed significant delayed fluorescence (Figure 3.1. 23).

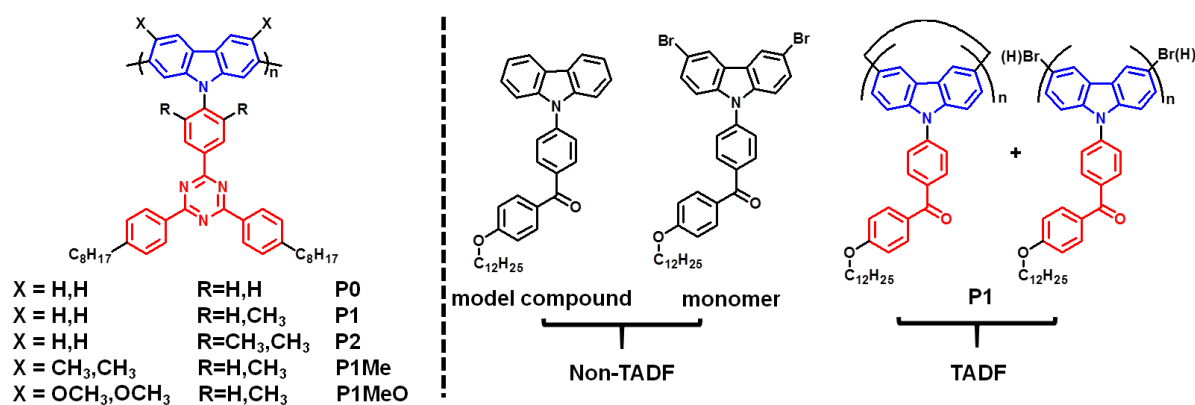


**Figure 3.1. 23** Chemical structures of linear conjugated TADF homopolymers.

*Linear conjugated TADF polymers based on D1-A-D2 type small-molecule TADF emitter.* In this strategy, one donor is located in the backbone, and in the meanwhile, the other donor and the acceptor are pendants in the side chain. Dual donors are used to enhance the TADF effect.<sup>232</sup>

For example, Yang *et al.* designed and synthesized a series of linear conjugated polymer PCzDP-x by using 10-(4-((4-(9H-carbazol-9-yl)phenyl)-sulfonyl)phenyl)-10H-phenoxazine (PXZ-DP-Cz) as the TADF unit (Figure 3.1. 24)<sup>214</sup>. All polymers showed obvious TADF features and bluish-green OLEDs based on PCzDP-10 achieved an EQE<sub>max</sub> of 16.1%. By comparing all the device performances, it can be concluded that nearly 100% exciton utilization efficiency (EUE) could be achieved by introducing a TADF small molecule as an assistant dopant to sensitize the TADF polymer.

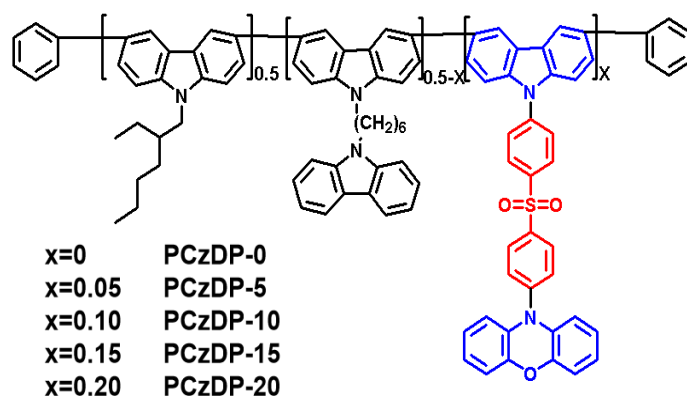


**Figure 3.1. 24** Chemical structure of PCzDP- $x$ .<sup>214</sup>

**Table 3.1.1** Photoluminescence and electroluminescence of linear conjugated TADF polymers

Polymers	$\lambda_{\text{PL}}$ (nm)	$\Delta E_{\text{ST}}$ (eV)	$\phi_{\text{PL}}/\phi_{\text{DF}}$ (%)	$\tau_{\text{PF}}$ (ns)/ $\tau_{\text{DF}}$ ( $\mu$ s)	$\lambda_{\text{EL}}$ (nm)	$V_{\text{on}}$ (V)	$I_{\text{max}}$ (cd/m <sup>2</sup> )	CE/PE/ EQE	C.I.E	EL
pCzBP <sup>212</sup>	508 <sup>b</sup>	0.18 <sup>b</sup>	23/16 <sup>b</sup>	13/74 <sup>b</sup>	500	6.0	5100	24.9/9.0/8.1	0.28,0.43	G
pAcBP <sup>212</sup>	540 <sup>b</sup>	0.10 <sup>b</sup>	46/27 <sup>b</sup>	24/10 <sup>b</sup>	548	4.3	30800	31.8/20.3/9.3	0.38,0.57	Y
PTCz <sup>213</sup>	573	0.19 <sup>a</sup>	17/16.3	29.9/2.35	590	-	2733	6.5/13.7/8.6	0.51, 0.48	R
PTD <sup>213</sup>	629	0.05 <sup>a</sup>	8/7.9	22.9/2.53	670	-	514	0.91/0.46/0.24	0.64, 0.36	R
PCzDPT5 <sup>213</sup>	591 <sup>c</sup>	-	50/14	38.4/5.24	432, 602	-	2553	3.2/5.2/4.1	0.55, 0.41	R
P12 <sup>214</sup>	494	-	33.7/4.5	8.82/2.36	506	3.1 <sup>c</sup>	-	10.7/11.2/4.3	0.24,0.43	G
PAPCC <sup>216</sup>	487	0.37	8/0.5	5.8/0.50	508	3.0	554	3.6/3.67/1.34	0.25,0.47	G
PAPTC <sup>216</sup>	507	0.13	28/3.9	13.8/0.68	521	2.6	10251	41.8/37.1/12.63	0.30,0.59	G
PCzAPT10 <sup>218</sup>	507	-	90/57.3	11.1/2.52	-	2.57	33262	-/48.5/16.9	0.35,0.54	G
PCzATD5 <sup>219</sup>	531	0.09	89/45	27.9/1.1	555	2.57	15456	48.7/50.5/15.5	0.41,0.55	Y
PCzABA10 <sup>220</sup>	521	0.22	51/34.8	21/1.272	-	2.7	-	35.3/30.1/10.6	0.39,0.57	-
PABPC5 <sup>221</sup>	525	0.12	77/41.9	22/1.286	-	2.6	-	60.5/61.2/18.1	0.40,0.56	-
PCzAB2Py5 <sup>222</sup>	555	0.10	62/28.3	32/0.951	573	3.0	-	34.2/26.3/11.9	0.48,0.51	Y
PCzA3PyB5 <sup>222</sup>	555	0.16	35/13.3	19/1.134	568	2.6	-	15/14.4/5.2	0.47,0.51	GY
PCzAB3Py5 <sup>222</sup>	544	0.10	65/27.3	32/0.876	557	2.9	-	39.2/33.1/12.2	0.44,0.54	G
Cop-10 <sup>224</sup>	540	0.0428	21/9.9	82/2650	578	3.2	3000	42.9/45/15.7	0.46,0.49	Y
PTDP-5 <sup>225</sup>	427, 537 <sup>b</sup>	0.06	100%/-	14.7/283	428, 600	3.7	1247	4.8/11.6/7.1	0.38,0.35	W
PFSOTT2 <sup>226</sup>	416, 567	0.26	76 (99 <sup>b</sup> ) /7.8	25.4/6.2	616	9	3771	8.1/1.8/4.8	0.55,0.43	R
P3 <sup>228</sup>	508	0.18	81/72	4.4/124.5	507	3.9	-	26.0/18.5/8.7	0.23,0.40	G
PCzDP-10 <sup>214</sup>	500	-	74/53	19.5/2.0	496	-	-	38.6/14.3/16.1	0.22,0.40	BG
Poly(AcBPCz-TMP) <sup>232</sup>	498	0.12	68	27.2/4.44	507	3.2	13500	68.8/60.0/23.5	0.25,0.52	G

$\lambda_{\text{PL}}$  is the maximum wavelength of luminescent emission in neat films;  $\Delta E_{\text{ST}}$  is calculated from the equation  $\Delta E_{\text{ST}}=E_{\text{S}}-E_{\text{T}}$ , where  $E_{\text{S}}$  is obtained from the photoluminescent spectrum at room temperature,  $E_{\text{T}}$  is from phosphorescent spectrum;  $\phi_{\text{PL}}$  is the total photoluminescent quantum efficiency (PLQY),  $\phi_{\text{DF}}$  is the quantum efficiency contributed by delayed fluorescence,  $\tau_{\text{PF}}$  is the lifetime of prompt fluorescence,  $\tau_{\text{DF}}$  is the lifetime of delayed fluorescence,  $\phi_{\text{PL}}$ ,  $\phi_{\text{DF}}$ ,  $\tau_{\text{PF}}$ ,  $\tau_{\text{DF}}$  were measured in neat films free-oxygen;  $\lambda_{\text{EL}}$  is the electroluminescent peak;  $V_{\text{on}}$  is the turn-on voltage at 1 cd/m<sup>2</sup>;  $I_{\text{max}}$  is the maximum luminance; CE/PE/ EQE refer to maximum current efficiency, maximum power efficiency, and maximum external quantum efficiency, respectively; C.I.E is short of The Commission Internationale de L'Eclairage coordinates; C B, G, R, Y, and W are short for blue, green, red, yellow and white, respectively; GY is greenish-yellow and BG is bluish-green. <sup>a</sup> Measured in toluene, <sup>b</sup> measured in blend film; c: measured at 10 cd/m<sup>2</sup>.

**\* Linear non-conjugated TADF polymers**

As illustrated in Figure 3.1. 25, it's possible to realize TADF in a linear non-conjugated polymer with: a) TADF units in the main chain; b) TADF units in side chain; c) TADF achieved *via* through-space conjugation (TSC) of donor and acceptor moieties pendant in the side chain. The photoluminescent and electroluminescent characteristics of typical TADF conjugated polymers are summarized in Table 3.1.2.

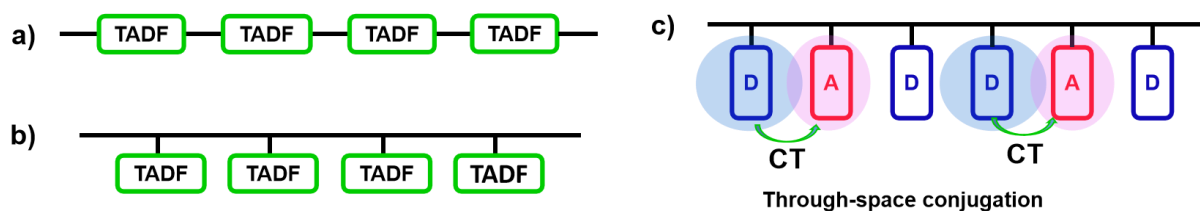


**Figure 3.1. 25** Structural architectures of linear non-conjugated TADF polymers.

*Linear non-conjugated TADF polymers with TADF units in the main chain.* In this first strategy, the TADF emitters are inserted in the backbone and isolated by non-conjugated spacers. The TADF emitters give the polymers TADF character and the non-conjugated spacer provides good solubility and reduces the aggregation-caused quenching.

So far, only two TADF polymers with this structured strategy have been proposed. One is polymer LEP, the first reported TADF linear polymer<sup>210</sup> (Figure 3.1. 15). The other TADF polymer named P(DMTRZ-Cp) (Figure 3.1. 26) is an alternating copolymer, in which 1,1-diphenylcyclohexane (Cp) moiety was introduced not only to serve as a linker breaking conjugation of backbone, but also to help enhance the solubility.<sup>233</sup> P(DMTRZ-Cp) displays strong TADF features with a small  $\Delta E_{ST}$  (0.023 eV) and a high PLQY over 90% in the blend film with mCP. A series of green-emitting OLED devices employing P(DMTRZ-Cp):mCP blend film as the emissive layer were fabricated and the best device performance was achieved with a low turn-on voltage of 4 V, a maximum current efficiency of 50.5%, and an  $EQE_{max}$  of 15.4% with CIE coordinates of (0.35, 0.57) when the doping ratio of P(DMTRZ-Cp) in mCP reached 25 wt%.

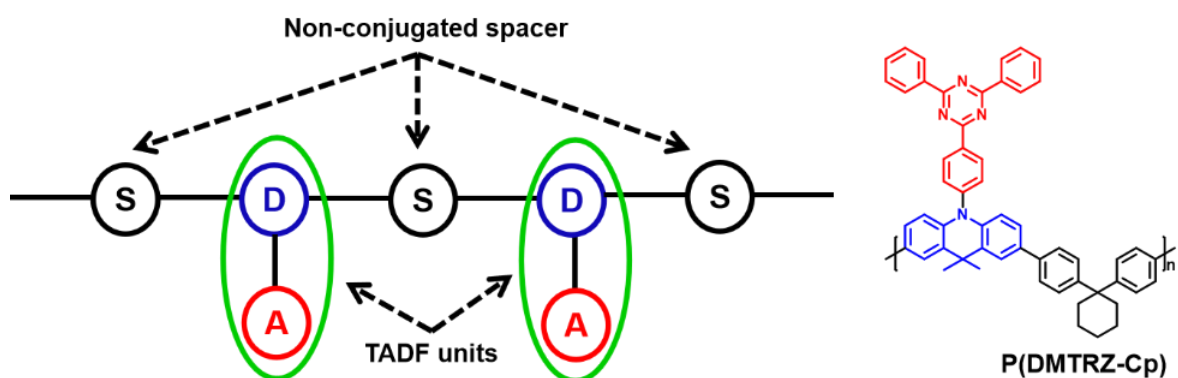


**Figure 3.1. 26** Chemical structure of P(DMTRZ-Cp) with non-conjugated cyclohexane units.

*Linear non-conjugated TADF polymers with TADF units in the side chain.* In this second strategy, the TADF units are hanging in the side chains and exhibit TADF nature. The non-conjugated backbone, especially the vinyl backbone, provides good solubility and reduces the intra- and intermolecular triplet-triplet annihilation of adjacent TADF units.

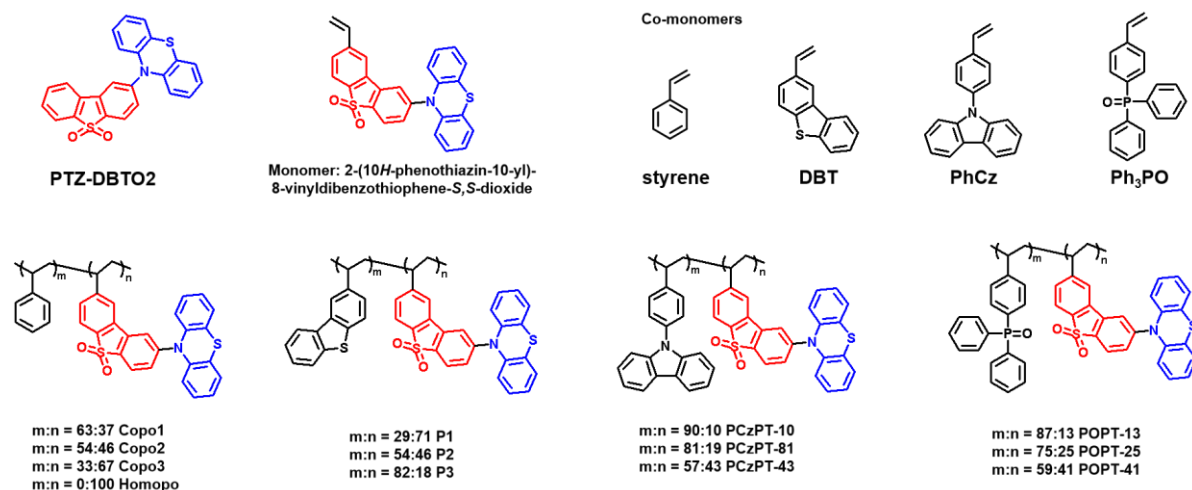


**Figure 3.1. 27** The chemical structures of PTZ-DBTO2, the relating monomer, polymers, and co-monomers

Based on TADF small molecule PTZ-DBTO2<sup>223</sup>, several series of TADF polymers (the chemical structures are shown in Figure 3.1. 27) have been designed and reported, with varying comonomers and ratios of TADF units. The doped spin-coated OLEDs, based on Homopo and Copox, gave out green emission with a longer emission wavelength in the sequence Copo1 (533 nm) < Copo2 (536 nm) < Copo3 (539 nm) < Homopo (556 nm), indicating the styrene units prevented the aggregation and improved the color purity. Among them, the best EL performance was achieved for Copo1-based device with 20.1% EQE<sub>max</sub>, but only remained 5.3% at 100 cd/m<sup>2</sup>.<sup>234</sup> PCzPT-x and POPT-x were prepared to further explore the effect of a hole- and electron-transporting spacers on TADF features.<sup>235</sup> PCzPT-x and POPT-x had small  $\Delta E_{ST}$  of 0.05-0.07 eV and 0.09-0.13 eV. The PLQYs of PCzPT-x were smaller than 25% while POPT-25 can reach 51% in toluene in nitrogen. Consistent with the photoluminescent properties, POPT-x displayed better TADF performance than PCzPT-x. POPT-25 also achieved the best EL performance in a solution-processed device with an EQE<sub>max</sub> of 5.2%, a CE of 16.8 cd/A, and a PE of 7.8 lm/W with the CIE coordinates of (0.36, 0.50). P1-P3 had small  $\Delta E_{ST}$  (0.04-0.09 eV) and exhibited obvious TADF and aggregation-enhanced emission (AEE) characteristics.<sup>236</sup> P3-based OLED showed warm-white emission with an EQE<sub>max</sub> of 10.4%, which is the first reported white-emissive non-conjugated TADF polymers.

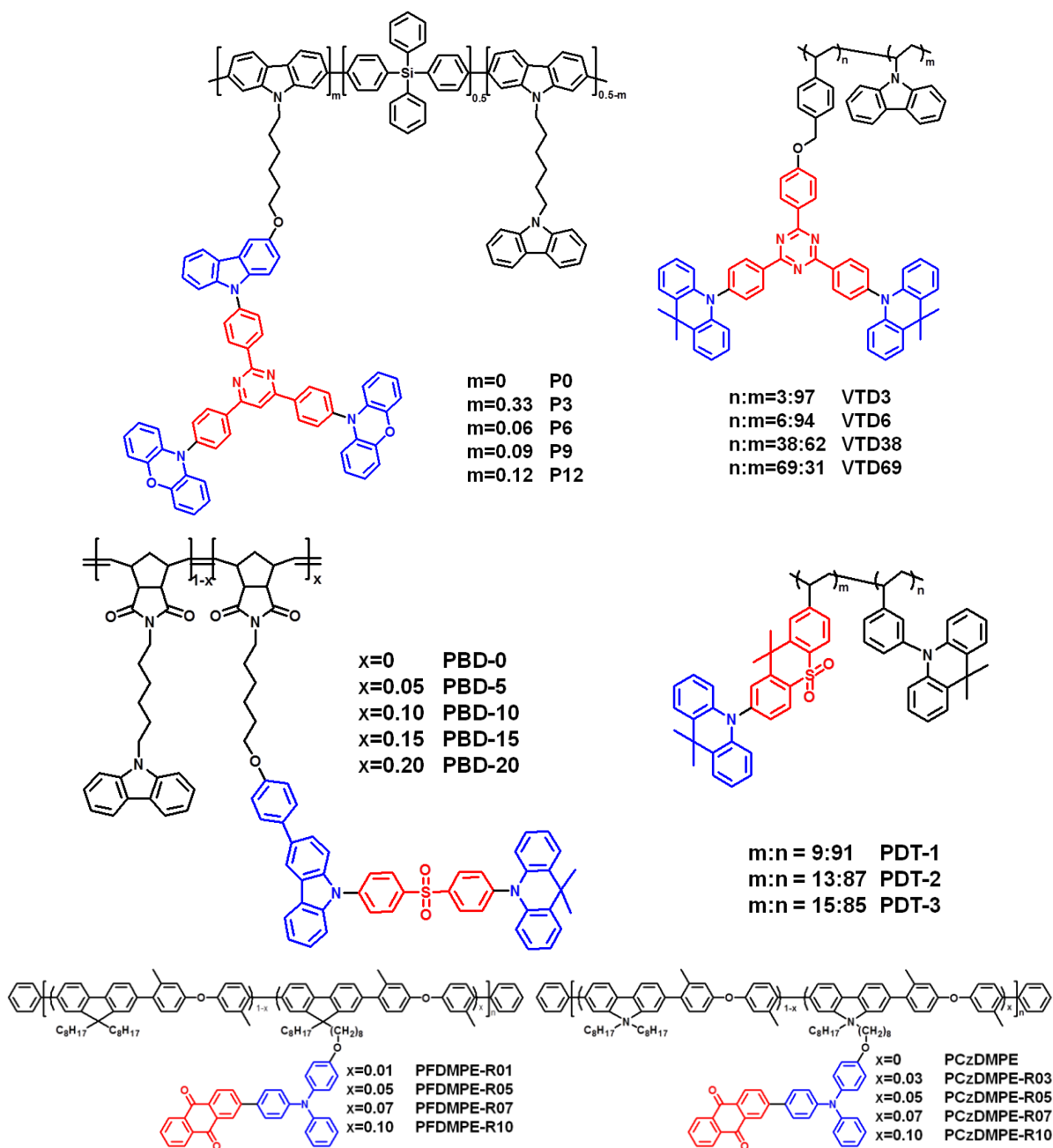


**Figure 3.1. 28** Chemical structures of non-conjugated TADF polymers: green ( $Px^{237}$ ,  $VTDx^{238}$ ) blue ( $PBD-x^{239}$  and  $PDT-x^{240}$ , red ( $PFDMPPE-Rx$  and  $PCzDMPE-Rx^{241,242}$ ).

In addition to the vinyl backbone, Zhou *et al.* prepared a series of green TADF polymers (Figure 3.1. 28) with the backbones comprising both a non-conjugated tetraphenyl-silane moiety and a conjugated carbazole unit, where the non-conjugated silane moiety provides the high  $E_T$  and improves the charge transport properties.<sup>237</sup> Obvious TADF character was observed in the polymers with the high PLQY ranging from 64% to 71% in the neat films. The non-doped solution-processed OLEDs based on these polymers exhibited green light ( $\lambda_{EL} = 540\sim 552$  nm) with an  $EQE_{max}$  of 7.0%. The polymers  $VTDx$  are also green-emitting ( $\lambda_{EL} = 498\sim 525$  nm) TADF materials with a small  $\Delta E_{ST}$  of 0.06-0.14 eV and a high PLQY of 51-74% in neat films under nitrogen.<sup>238</sup> Besides, other non-conjugated TADF

polymers with blue emission (PBD- $x^{239}$  and PDT- $x^{240}$ ) and red emission (PFDMPPE-R $x$  and PCzDMPE-R $x^{241,242}$ ) have been reported.

TADF is achieved via through-space conjugation of donor and acceptor moieties pendant in the side chain. In this third approach, the electron donors and acceptors are physically separated resulting in a small overlap of HOMO and LUMO, leading to small  $\Delta E_{ST}$ . Thus, TADF properties could be achieved via the through-space charge transfer (TSCT) effect. These polymers are favorable for blue emission, as a consequence of avoiding emission red-shift originated from extension conjugation.

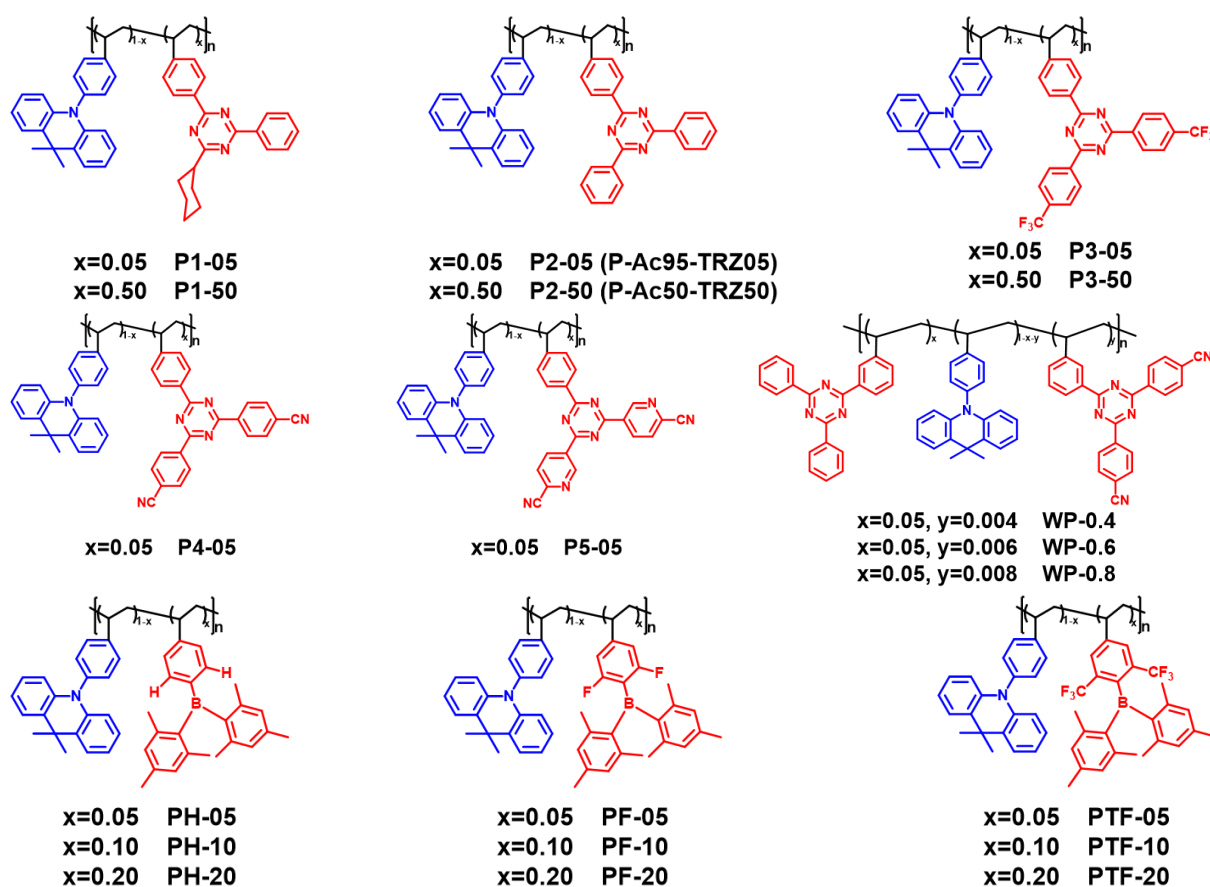


**Figure 3.1. 29** Chemical structures of through-space charge transfer TADF polymers.

Wang's group successfully prepared several series of TSCT polymers exhibiting a TADF nature.<sup>243–245</sup> In these TSCT polymers (Figure 3.1. 29), 9,9-dimethyl-10-phenyl-acridine are chosen as the pendant donor unit, and triazine or triacrylboron derivatives are selected as the pendant acceptors. Using triazine acceptors, P2-05 (also named P-Ac95-TRZ05<sup>243</sup>) achieved a small  $\Delta E_{ST}$  (0.021 eV) and a high neat film state PLQY of 51% under  $N_2$  at room temperature, and it exhibited sky-blue electroluminescent emission in a non-doped solution-processed device with a high  $EQE_{max}$  of 12.1% and low efficiency roll-off of 4.9% (at 1000  $cd\ m^{-2}$ ), together with CIE coordinates of (0.176, 0.269). Based on P2-05, acceptors with different electron-accepting capabilities were selected to tune the TSCT strength

between donor and acceptor. All these polymers featured aggregation-induced emission. The PLQYs of the polymer neat films are 29%, 51%, 74%, 34%, and 6%, respectively, for the polymers from P1-05 to P5-05, while those for P1-50, P2-50, and P3-50 ARE 32%, 60%, and 64%. The emission colors range from deep blue (P1-05,  $\lambda_{EL} = 455 \text{ nm}$ ), sky-blue (P2-05,  $\lambda_{EL} = 472 \text{ nm}$ ), green (P3-05,  $\lambda_{EL} = 525 \text{ nm}$ ), yellow (P4-05,  $\lambda_{EL} = 568 \text{ nm}$ ) to red (P5-05,  $\lambda_{EL} = 616 \text{ nm}$ ), realizing full-color emission. Moreover, white emission was also realized by incorporating two donor/acceptor pairs in one polymer (WP-y) with simultaneous sky-blue and yellow emission.<sup>244</sup>

By adopting triarylboron acceptors, the resulting three groups of TSCT polymers (PH-x, PF-x, and PTF-x)<sup>245</sup> exhibited small  $\Delta E_{ST}$  smaller than 0.2 eV. With the substituents changing from H to F and  $\text{CF}_3$ , the polymers displayed deep-blue (429 nm) to sky-blue (483 nm) emission accompanied with the improved PLQY from 26 to 53% in the solid-state, due to the increment of the electron-accepting ability of triarylboron units. PTF-20 showed promising electroluminescent performance with an  $\text{EQE}_{\text{max}}$  of 7.0%, suggesting that they are prospective candidates for luminescent polymers.

Besides, Hudson *et al.* described a miktoarm copolymer  $\text{ACR}_{75\text{-}CO}\text{-TRZ}_{75\text{-}BB}$ , which can aggregate into bottlebrush nanofibers with homopolymer side chains and the through-space charge transfer (TSCT) arising from the resulting interfaces formed between donor and acceptor can give rise to thermally activated delayed fluorescence (TADF) along with the properties of original donor and acceptor components.<sup>246</sup> The stimuli-responsive TADF character strongly relies on the aggregation of the nanofibers (Figure 3.1. 30). The bottlebrush nanostructure may prove to be an effective method for preparing blended, multi-components films for organic semiconductors, where maximizing D-A interactions or preserving the individual properties of each component of a blend may be necessary, for example, in organic photovoltaics or ambipolar films for charge transport.

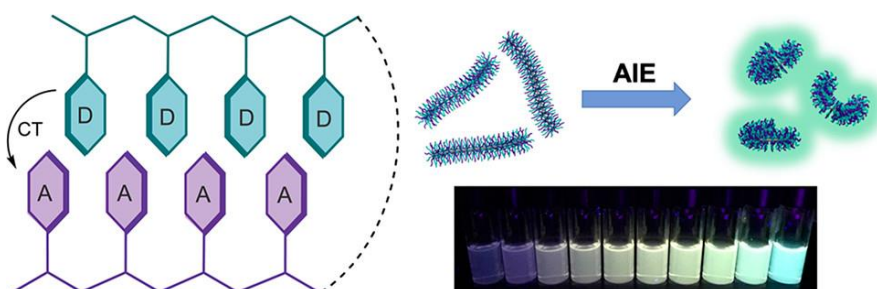


**Figure 3.1. 30** TSCT polymers achieving TADF from interface-dependent aggregation.

**Table 3.1.2** Photoluminescence and electroluminescence of non-conjugated TADF polymers

Polymers	$\lambda_{\text{PL}}$ (nm)	$\Delta E_{\text{ST}}$ (eV)	$\phi_{\text{PL}}/\phi_{\text{DF}}$ (%)	$\tau_{\text{PF}}(\text{ns})/\tau_{\text{DF}}(\mu\text{s})$	$\lambda_{\text{EL}}$ (nm)	$V_{\text{on}}$ (V)	$L_{\text{max}}$ ( $\text{cd}/\text{m}^2$ )	CE/PE/ EQE	C.I.E	EL
LEP <sup>210</sup>	535	0.22	43.6	-	-	-	-	-/-/10	0.32,0.58	G
P(DMTRZ-Cp) <sup>233b</sup>	513	0.023	97/48	12.2/1.8	528	4.0	-	50.5/31.8/15.4	0.35,0.57	G
Cop1 <sup>234</sup>	535	0.35	-	-	533	5.8	-	40.1/61.3/20.1	0.36,0.55	G
PCzPT-19 <sup>235b</sup>	538	0.06 <sup>a</sup>	21/10.3	35.1/10.2	552	5.2	4388	4.1/1.8/1.2	0.40,0.55	G
POPT-25 <sup>235b</sup>	541	0.11 <sup>a</sup>	36/21.2	36.7/3.0	540	6.4	3386	16.8/7.8/5.2	0.36,0.50	G
P2 <sup>236</sup>	542	0.06	23.5 <sup>d</sup> /-	-	-	2.9	1764	11/12.3/4.5	0.45,0.40	Y
P3 <sup>236</sup>	535	0.04	19.5 <sup>d</sup> /-	-	-	2.9	1753	23/32.8/10.4	0.37,0.38	W
PDTPT-1 <sup>247</sup>	445 521	0.03 <sup>f</sup> .02 <sup>g</sup>	69/21 <sup>e</sup> ,61 <sup>f</sup>	- /6.9 <sup>e</sup> ,15.5 <sup>f</sup>	-	3.5	2900	38.8/20.3/14.2	0.33,0.42	W
P12 <sup>237</sup>	533	-	64/22	24.1/1.9	552	4.4	14490	20.6/7.3/6.9	0.40,0.54	G
VTD38 <sup>238</sup>	501	0.07	70.9/35	22.0/3.3	517	4.0	1953	76.3/53.2/22	0.30,0.53	G
PBD-10 <sup>239</sup>	457	-	42/20	26.4/5.9	478	3.8	-	13.5/-/7.3	0.20,0.29	B
PDT-2 <sup>240</sup>	444	0.03	54/40.8	-/5.87	436	5.0	993	8.7/3.9/5.3	0.15,0.09	B
PFDMPPE-R05 <sup>242</sup>	592	-	32/-	4.2/126	606	9.8	1677	10.3/3.2/5.62	0.57,0.42	R
PCzDMPE-R07 <sup>241</sup>	393 582	-	27/	5.4/145	611	5.2	1124	3.35/1.88/2.03	0.58,0.41	R
PTF-20 <sup>244</sup>	483	0.08	53	24/0.98	-	-	-	20.1/-/7.0	0.29,0.47	B
P1-05 <sup>245</sup>	453	0.04	29/15.4	66/0.36	455	3.2	1902	10.6/-/7.1	0.17,0.17	DB
P2-05 <sup>245</sup>	474	0.02	51/43.9	40/1.91	472	3.2	6150	21.8/-/12.1	0.18,0.27	B
P3-05 <sup>245</sup>	518	0.04	74/68.8	44/1.98	525	3.0	10273	50.3/-/16.2	0.34,0.55	G
P4-05 <sup>245</sup>	554	0.05	34/29.6	53/0.82	568	3.2	5339	21.1/-/7.8	0.46,0.50	Y
P5-05 <sup>245</sup>	616	0.05	6/0.36	44/0.94	616	4.6	1283	1.7/-/1.0	0.57,0.41	R
WP-0.4 <sup>245</sup>	-	-	-	-	-	3.2	5173	37.9/34.8/14.1	0.31,0.42	W
P1 <sup>248</sup>	423	-	2.9,15.1/ -	-	-	-	-	-	-	-
P2 <sup>248</sup>	447	-	7.4,33.8/6270	-	-	-	-	-	-	-
P3 <sup>248</sup>	481	-	19.0/14.1	-	-	-	-	-	-	-
P4 <sup>248</sup>	541	-	20.9/1.4,9.4	-	-	-	-	-	-	-
P5 <sup>248</sup>	519	-	24.0/1.7,10.4	-	-	-	-	-	-	-
P6 <sup>248</sup>	536	-	22.0/2.7	-	-	-	-	-	-	-
P7 <sup>248</sup>	525	-	5.7,36.7/2.5	-	-	-	-	-	-	-

$\lambda_{\text{PL}}$  is the maximum wavelength of luminescent emission in neat films;  $\Delta E_{\text{ST}}$  is calculated from the equation  $\Delta E_{\text{ST}} = E_{\text{S}} - E_{\text{T}}$ , where  $E_{\text{S}}$  is obtained from the photoluminescent spectrum at room temperature,  $E_{\text{T}}$  is from phosphorescent spectrum;  $\phi_{\text{PL}}$  is the total photoluminescent quantum efficiency (PLQY),  $\phi_{\text{DF}}$  is the quantum efficiency contributed by delayed fluorescence,  $\tau_{\text{PF}}$  is the lifetime of prompt fluorescence,  $\tau_{\text{DF}}$  is the lifetime of delayed fluorescence,  $\phi_{\text{PL}}$ ,  $\phi_{\text{DF}}$ ,  $\tau_{\text{PF}}$ ,  $\tau_{\text{DF}}$  were measured in neat films free-oxygen;  $\lambda_{\text{EL}}$  is the electroluminescent peak;  $V_{\text{on}}$  is the turn-on voltage at 1  $\text{cd}/\text{m}^2$ ;  $L_{\text{max}}$  is the maximum luminance; CE/PE/ EQE refer to maximum current efficiency, maximum power efficiency, and maximum external quantum efficiency, respectively; C.I.E is short of The Commission Internationale de L'Eclairage coordinates, B, G, R, Y, W is short for blue, green, red, yellow, white, respectively; GY is greenish-yellow and BG is bluish-green.

<sup>a</sup> Measured in toluene, <sup>b</sup> measured in blend film; <sup>c</sup> measured at 10  $\text{cd}/\text{m}^2$ ; <sup>d</sup> measured in the air; <sup>e</sup> measured in pristine film at RT in vacuum at 440 nm; <sup>f</sup> measured in pristine film at RT in vacuum at 520nm

### 3.1.4 Through-space conjugation (TSC)

The concept of through-space conjugation (TSC) dates back to the study of [2.2]paracyclophane (PCP) in 1949.<sup>249</sup> In PCP, two benzene rings are confined in a coplanar with unusual boat conformation retaining aromaticity. The resulting short distance between the two aromatic rings enables a strong transannular electronic communication, realizing the charge and energy transport. The efficient intramolecular charge transfer (ICT) in the TSC system plays an important role in constructing functional  $\pi$  systems of organic optoelectronic materials. In comparison with the through-bond conjugation (TBC) system, the TSC system with more efficient dispersing charges can effectively slow down the non-radiative charge recombination process and thus stabilize the ICT states, having a positive influence on the fluorescence of molecules with ICT effect.<sup>250</sup> Moreover, TSC systems possess more flexibility and possibilities in designing optoelectronic materials with stable ICT states, because of its non-covalent structure and spatial delocalization of  $\pi$  electrons. To date, several other TSC systems have been exploited, derived from cyclophane<sup>251</sup>, hexaarylbenzene<sup>252</sup>, naphthalene<sup>253</sup>, xanthene<sup>254</sup>, and so on (Figure 3.1. 31).

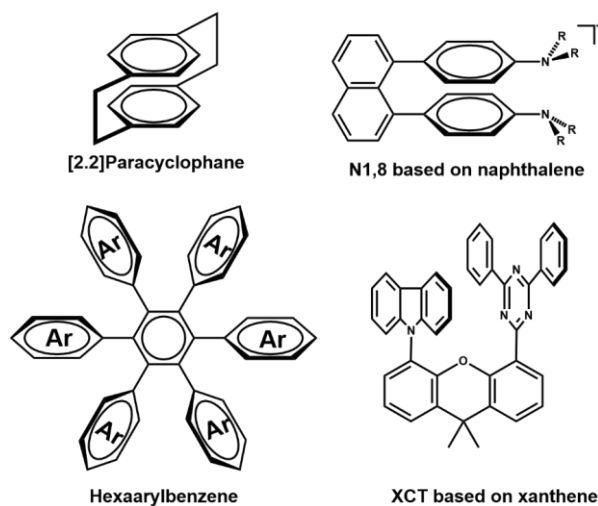


**Figure 3.1. 31** TSC systems based on cyclophane, hexaarylbenzene, xanthene, and naphthalene.

#### *Through-space conjugation (TSC) in construction of TADF emitters*

For TADF emitters, one of the vital issues is the pathway to the immoderate overlap of HOMO and LUMO to achieve simultaneously a small singlet-triplet energy splitting ( $\Delta E_{ST}$ ) to facilitate the up-conversion from  $T_1$  to  $S_1$  by efficient reverse intersystem crossing (RISC) and a large transition dipole moment to guarantee a high photoluminescence quantum yield (PLQY). TSC system is a good candidate for establishing TADF emitters, especially in the blue regime. As the emission red-shift can be suppressed by avoiding the conjugation extension originated from the through-bond charge transfer (TBCT). The reported TADF emitters with the TSC system, also called through-space charge transfer (TSCT) TADF emitters, can be simply divided into three groups: small molecules, dendrimers, and

linear polymers.

#### A. TSCT small-molecule TADF emitters

In 2015, Swager's group designed and synthesized triptycene-based through-space charge transfer (TSCT) TADF materials TPA-QNX(CN)<sub>2</sub> and TPA-PRZ(CN)<sub>2</sub> where the donor and acceptor units are endowed in different arms of the triptycene scaffold and physically separated in 120° orientation (Figure 3.1. 32).<sup>255</sup> Through-space conjugation (TSC) enables the intramolecular HOMO/LUMO overlap, leading to TADF effect. Inspired by this finding, they developed U-shaped through-space TADF molecules (XPT, XCT, and XtBuCT, Figure 3.1. 33) where a donor and an acceptor bridged by 9,9-dimethylxanthene are in close proximity to realize the efficient spatial charge transfer.<sup>254</sup> These materials displayed obvious TADF nature as well as AIE behavior. The OLED device using XPT dispersing in DPEPO film as the emitter gave rise to electroluminescence with a 10% EQE<sub>max</sub>. The comparison between U-shaped and L-shaped D-A molecular structures (Figure 3.1. 33) evidenced that the connection style between donor and acceptor moieties plays a crucial role in the CT character and  $\Delta E_{ST}$ .<sup>256</sup> However, it is noteworthy controlling the bridge flexibility and avoiding intramolecular dimerization quenching, because the flexible bridge probably causes strong dipole-dipole attraction between donor and acceptor units, further resulting in large reorganization to form intramolecular dimer species, whose local triplet excited states are high enough to quench the RISC process and thus reduce delayed fluorescence.<sup>257</sup>

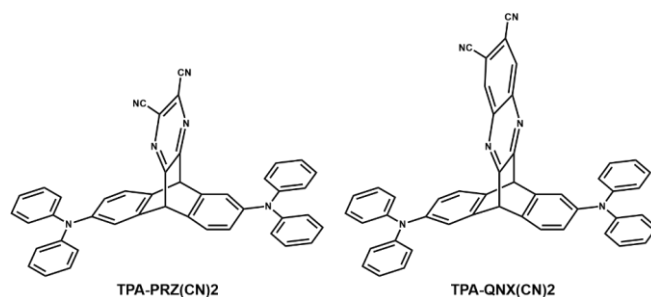


**Figure 3.1. 32** Chemical structures of triptycene-based TADF materials.

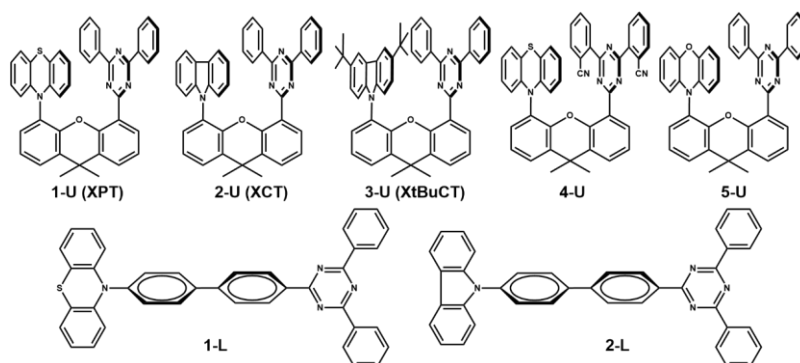


**Figure 3.1. 33** Chemical structures of conventional through-bond conjugated D-A (L-shaped) and through-space conjugated (U-shaped) architectures.

TADF character can also be achieved in TSC systems based on cyclophane (Figure 3.1. 34). *Cis*- and *trans*-Bz-PCP-TPA are the first examples of through-space conjugated TADF emitters with a [2.2]paracyclophane (PCP) core and stacked donor-acceptor in coplanar units.<sup>258</sup> Both of the isomers displayed blue TADF emission, short delayed fluorescence lifetime, but low PLQY in films. Cp-ecl and Cp-sta are two isomers consisting of a dithia[3.3]paracyclophane core with a donor ditolylphenylamine unit grafted at the upper deck of cyclophane in an eclipsed and staggered configuration concerning the two acceptor nitrile groups at the lower deck.<sup>259</sup> The isomers showed efficient TADF emission and short reversible intersystem crossing (RISC) lifetimes. Besides, *S<sub>p</sub>*-CzpPhTrz and *R<sub>p</sub>*-CzpPhTrz are sky-blue TADF molecules comprising a triazine acceptor and an indolo[2.2]paracyclophane donor.<sup>260</sup> The indolo[2.2]paracyclophane donor, also named as carbazolophane (Czp), is established by the incorporation of a [2.2]paracyclophane moiety within the carbazole, offering TSCT between the donor and acceptor units. The enhanced donor strength and increased torsion between the donor and phenyl linker make the TADF emission more effective, achieving good device performance with a 17% EQE<sub>max</sub>.

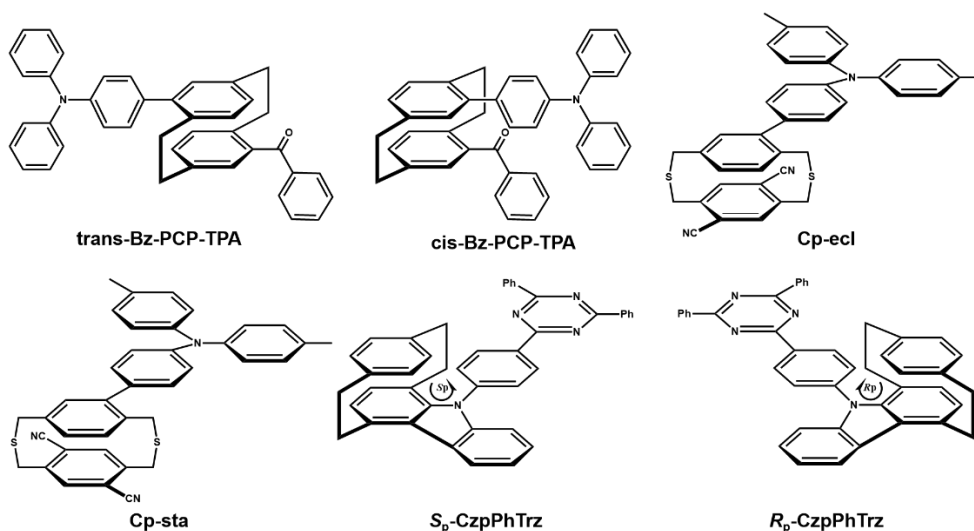


**Figure 3.1. 34** Chemical structures of TSCT TADF materials based on cyclophane.

As mentioned above, TSC systems are favorable for blue emission, due to the limitation of conjugation extension. In addition to *S<sub>p</sub>*-CzpPhTrz and *R<sub>p</sub>*-CzpPhTrz, 4ArDPDPO2A (Figure 3.1. 35) is also one series of high-efficiency blue TADF molecules with D-A-D structure where a homo-conjugated acceptor 5,10-diphenyl-5,10-dihydrophosphanthrene oxide (DPDPO2A) is incorporated to bridge four (3,6-di-*t*-butyl)-carbazolyl groups.<sup>261</sup> Obvious TADF character was attributed to the TSC effect of homo-conjugated acceptors. Among all the molecules, 4tBCzDPDPO2A exhibited the optimized TADF transitions with PLQY of 81% and EQE<sub>max</sub> of 23.7%. QAFCN (Figure 3.1. 35) is another blue through-space TADF molecule with an sp<sup>3</sup>-hybrid carbon-centered D-σ-A structure where 5,5-dimethyl-5,9-dihydroquinolino[3,2,1-de]acridine (QA) is functionalized as the donor.<sup>262</sup> In relation to the corresponding classic spiro TADF emitter ACRFLCN, QAFCN showed emission blue-

shift as a result of the deeper HOMO energy level and higher  $E_{S1}$  owing to the rigidity and twisted geometry. Moreover, the shorted D/A distance ascribed to the deformed geometry enhanced the rigidity and facilitated the TSCT in QAFCN, leading to high PLQY and an  $EQE_{max}$  of 17.9%. The emission blue-shift and good device performance indicated that QA is a promising candidate for donors in constructing efficient blue TADF emitters with the unconjugated connection.

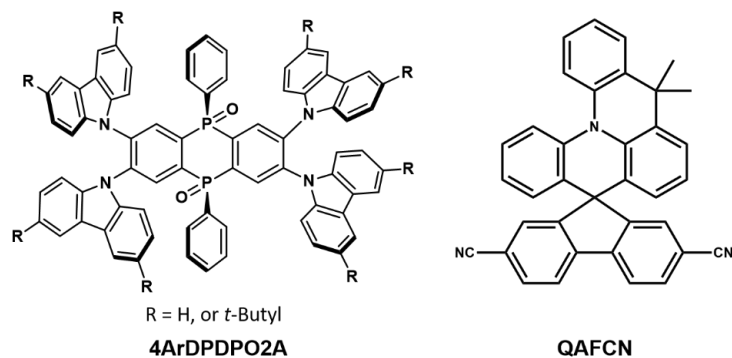


**Figure 3.1. 35** Chemical structures of two blue through-space conjugated TADF materials.

#### B. TSCT dendritic TADF emitters

As we all know, most TADF materials suffer from ‘concentration quenching’ and exhibit weaker emission in the aggregated state than in dilute solution. However, dendritic structures can effectively suppress molecular aggregations. The star-shaped hexaarylbenzene (HAB) has a remarkable nonplanar structure due to easily rotatable peripheral aromatic units with respect to the central ring, mimicking the shape of a propeller. The intriguing nonplanar, propeller-shaped geometry makes it possible that HAB derivatives rarely undergo molecular aggregations in any state and show high emission properties in solid-state with high thermal stability and glass-transition temperature.<sup>263</sup> Therefore, HABs are favorable for establishing TSCT dendritic TADF emitters.

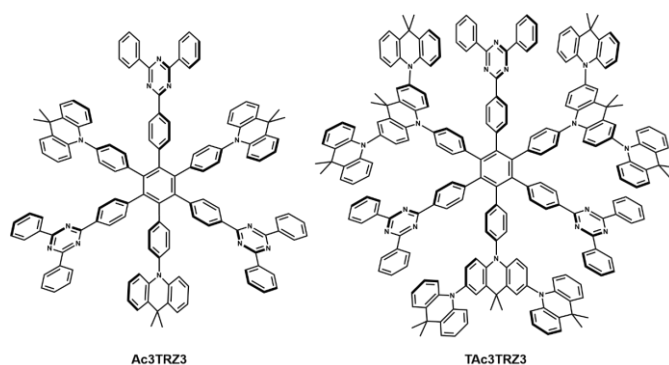


**Figure 3.1. 36** Chemical structures of the TSCT-HABs

Wang *et al.* reported two TSCT-HABs (Figure 3.1. 36) with alternating circularly-arrayed donors (acridan or dendritic acridan) and acceptors (triazine) around the hexaphenylbenzene (HPB) core, exhibiting obvious TADF nature and AIE phenomenon in high-efficiency solution-processed

OLEDs.<sup>264</sup> The TSCT-HABs have a small  $\Delta E_{ST}$  of 0.04-0.08 eV and show distinct delayed fluorescence with lifetimes of 3.16-3.54  $\mu$ s in the solid-states. Among them, TAc<sub>3</sub>TRZ3 with strong dendritic teracridan donor exhibits the highest PLQYs of 36% and 63% in neat and doped films, and the associated solution-processed doped OLED displays the best device performance with an EQE<sub>max</sub> up to 14.2%.

### C. TSCT linear polymeric TADF emitters

TSCT linear polymeric TADF emitters have already been described in detail in **chapter 3.1.3** and here we make a simple summary. Wang's group developed several TSCT linear polymeric TADF emitters with physical-separated pendant donor and acceptor units, and proved it a promising approach to realize full-color and white emission.<sup>243-245</sup> As summarized in Table 3.1.2, the  $\Delta E_{ST}$  of boron-containing TADF molecules is smaller than 0.1 eV, and the  $\Delta E_{ST}$  of other molecules is even no more than 0.05 eV. The PLQY of boron-containing TADF molecule PTF-20 can reach to 53% in the neat film under N<sub>2</sub>, and the PLQY of P3-05 is as high as 74% in the same condition. TSCT linear polymeric TADF emitters favor blue emission as a result of avoiding emission red-shift induced by electron delocalization. By managing the electron-withdrawing abilities through changing the substituents, the emission color ranges from deep blue to red. Moreover, white emission is realized by duplex TSCT channels with blue and yellow emission simultaneously. Besides, these TSCT linear TADF polymers exhibit significant AIE phenomena. Besides, Hudson *et al.* discovered the interface-dependent aggregation-induced TADF character in bottlebrush nanofibers constructed by miktoarm copolymer ACR<sub>75-CO</sub>-TRZ<sub>75</sub>-BB, due to the formed donor and acceptor interfaces with the nanofibers.<sup>246</sup>

#### 3.1.5 Aim and outline of this chapter

In this context, we will present the first investigations carried out in our lab on new light-emitting polymers developed for third-generation OLEDs, based on thermally activated delayed fluorescence (TADF) materials. Indeed, our group recently started the activity in this field, in the framework of a CNRS-JSPS project between OPERA (Kyushu University, Fukuoka, Japan) and IPCM.

Moreover, as explained in a long **bibliography section 3.1**, the TADF phenomenon is capable of achieving 100% of IQE through up-conversion from the triplet excited state to the singlet excited state. Besides, the common strategy in designing TADF emitters is playing with electron-donating D and electron-accepting A groups, as well as a separating central core, many macromolecular designs being currently investigated. **The aim of our research here is thus to design and develop different families of D-A polymers** which are reported in Figure 3.1. 37.

More precisely, two families of polymers will be studied: **in section 3.2 and section 3.3**, we will

investigate the first family consisting of two new series of potential linear TADF polymers (**S1** and **S2** series) based on a carbazole-based donor backbone and acceptor moieties such as dicyano-benzene or cyano-pyrimidine, grafted as side groups. **In section 3.4 and section 3.5**, we will investigate the second family consisting of two novel series of potential TADF polymers based on through-space conjugation (TSC) between the same donor and acceptor units as those utilized in the first family (**S3** and **S4** series).

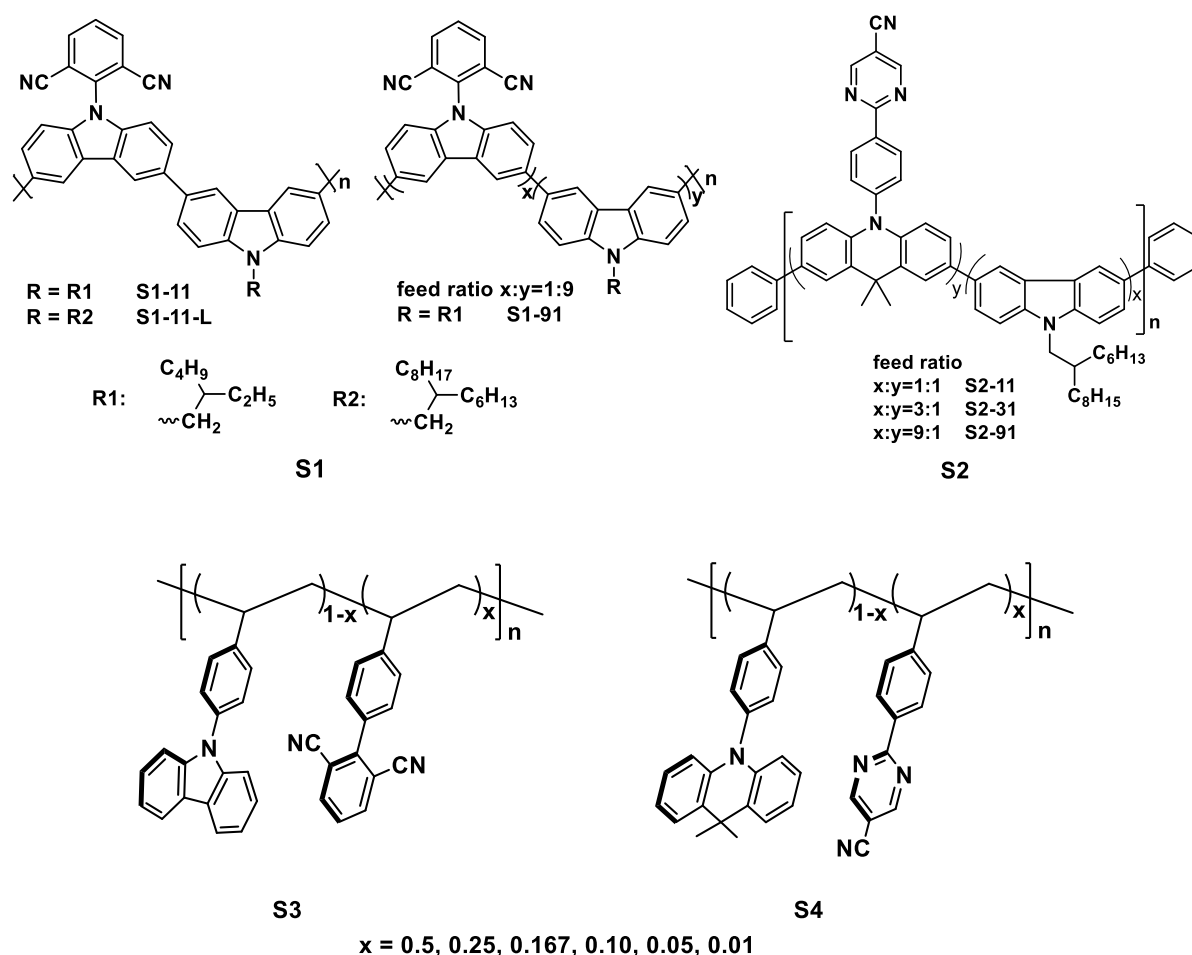


**Figure 3.1. 37** The chemical structures of the four series of **S1**, **S2**, **S3**, and **S4** polymers

Concerning these four series of novel polymers designed as potential TADF materials, in all cases, we first describe their synthesis, before to fully characterize them. In particular, their photophysical properties will be checked in solution, in solid-state but also in device configurations, to try to find rules and structure/properties relationships that could be later on generalized. Preliminary solution-processed OLED devices are eventually tested, in collaboration with OPERA laboratory (Japan).

### 3.2 Linear conjugated TADF polymers based on 26IPNDCz

**26IPNDCz**, comprising a dimeric phenylcarbazole and four cyano substituents on the phenyl rings, is an “acceptor-donor-acceptor” (A-D-A) type TADF monomer. As reported by Adachi’s group<sup>265</sup>, **26IPNDCz** possesses the twisting angle between the carbazole and isophthalonitrile planes of 69°, leading to the adequate HOMO-LUMO separation. **26IPNDCz** exhibits blue-green emission with a small  $\Delta E_{ST}$  of 0.06 eV and PLQY of 72% in doped DPEPO film (10 wt%). The lifetime of prompt and delayed fluorescence are 28 ns and 9.2  $\mu$ s, respectively, in oxygen-free toluene at room temperature. The OLED device based on **26IPNDCz** doped DPEPO film (10 wt%) possesses an  $EQE_{max}$  of 4.3% at 100 mA/cm<sup>2</sup>.

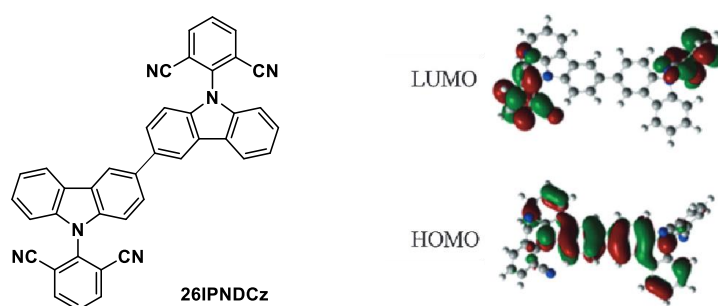


**Figure 3.2.1** The molecular structure of **26IPNDCz** with the calculated spatial distributions of HOMO and LUMO energy levels.

#### 3.2.1 Design, synthesis, and structural characterization

##### Initial design

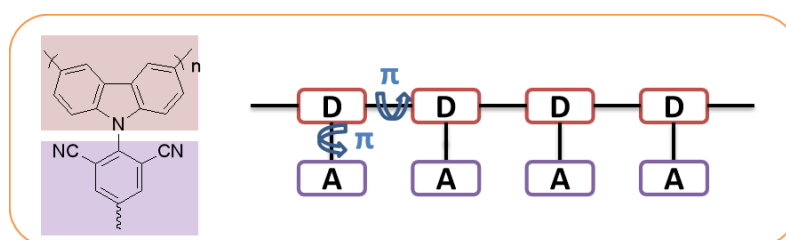
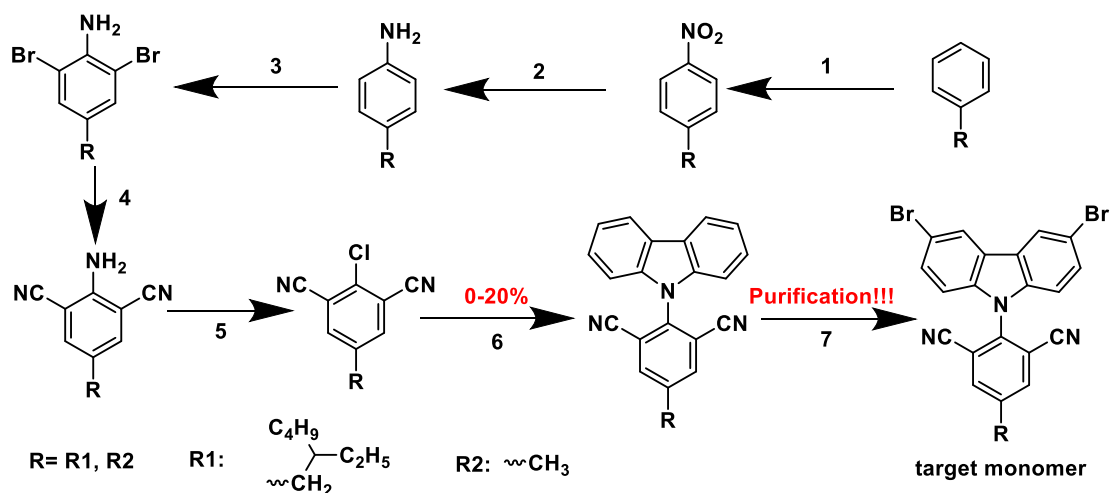


**Figure 3.2.2** The initial design of homopolymer based on **26IPNDCz**.

Derived from **26IPNDCz**, as shown in Figure 3.2.2, one homopolymer was initially designed with poly(3,6-carbazole) (electron-donating unit) as backbone and isophthalonitrile (electron-withdrawing unit) as side groups. Besides, one branched alkyl chain (Ethylhexyl: -C<sub>8</sub>H<sub>15</sub>) was also planned on the benzene ring to provide sufficient solubility.



**Scheme 3.2.1** The synthetic route towards target monomer (for homopolymerization).

To achieve the target homopolymer, a benzene ring bearing a substituent ethylhexyl R1 ( $-C_8H_{15}$ ) was used and 7 steps were proposed to get the desired monomer, as shown in Scheme 3.2.1. However, the 6<sup>th</sup> step was not successful and we then modified the synthetic route to start from a benzene ring bearing only a methyl group R2 ( $-CH_3$ ). When using  $-CH_3$ , the 6<sup>th</sup> step was successful but with low yield (<20%). However, after the bromination (7<sup>th</sup> step), due to the low solubility of the starting material and the target monomer in common solvents, it was difficult to get pure the target monomer. Most importantly, the low solubility of this monomer would also lead to poor solubility of the homopolymer, which means that the target homopolymer ( $R=-CH_3$ ) is not a good choice as TADF polymer, considering the fabrication of thin film. Therefore, we decided to modify our polymer design, and an additional comonomer with a long alkyl chain was introduced to improve the final solubility of the polymers (see the final design in Figure 3.2. 3). Besides, this new strategy can limit the possible aggregation-caused quenching and improve the TADF properties.

### Final design

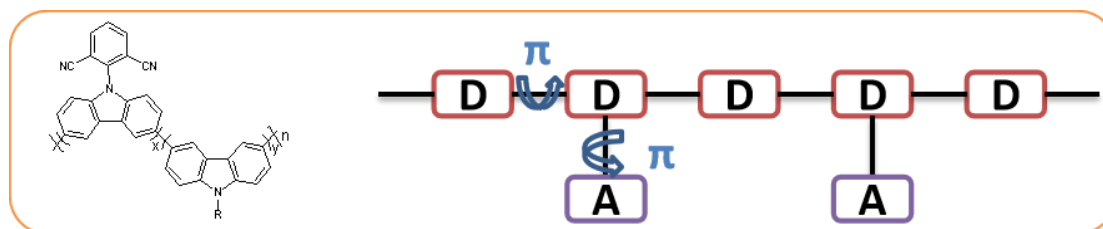
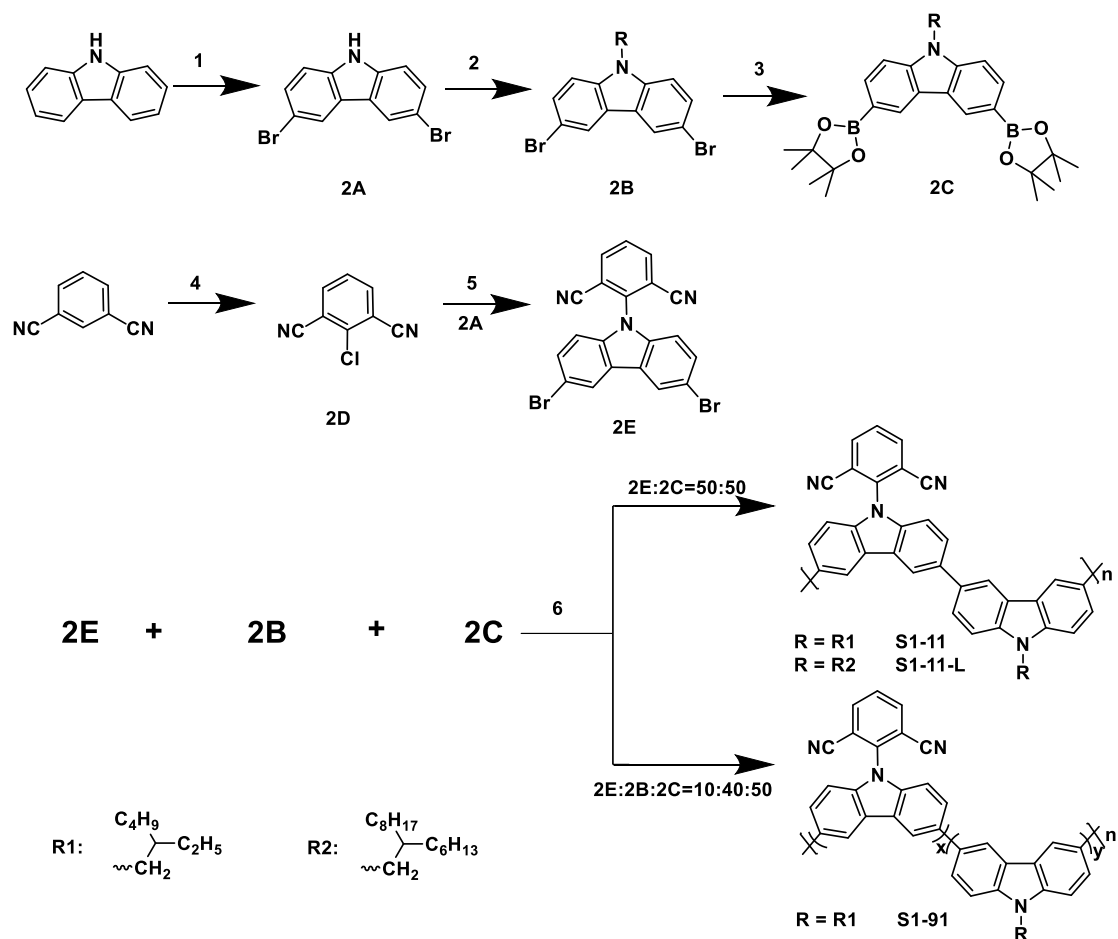


**Figure 3.2. 3** The final design of copolymer based on **26IPNDCz**.

In this strategy, we first prepared the monomer **2E**, expected to be TADF chromophore in the polymer, in three steps: the two building blocks, 3,6-dibromocarbazole (**2A**) and 2-chloroisophthalonitrile (**2D**) were successfully synthesized in one step, respectively. On the one hand, **2A** was obtained through the bromination reaction of the commercial carbazole with NBS as the source of the bromine radical ( $Br\cdot$ )

and the yield was as high as 74%. On the other hand, **2D** was synthesized by lithiation with freshly prepared LDA, followed by the addition of an excess of  $C_2Cl_6$ . The total yield for this reaction reaches 51%. **2E** was obtained through the reaction between **2A** and **2D** in the presence of NaH. As shown in the  $^1H$  NMR spectrum in THF (Figure 3.2. 4), the signals at 8.45, 7.59, and 7.12 ppm are attributed to the protons of 4-, 1- and 2-position of carbazole unit, respectively, while the doublet signal at 8.36 ppm and triplet signal at 7.95 ppm belong to the protons of isophthalonitrile units. The chemical shifts and the integrals of all signals are in agreement with the molecular structure of **2E**, confirming the success of the reaction. However, the yield of this reaction is low (10%). This low yield may originate from the elimination reaction which plays a dominant role under the used conditions (*NaH, dry DMF, Ar, RT, 24 h*), compared to the substitution reaction. To improve the yield, other reaction conditions were attempted, including the use of  $K_2CO_3$  instead of NaH, the increasing of temperature until 80-120°C, and the change of the reaction time. However, all these efforts failed. As our objective was mainly to prepare the target monomer, we didn't go further to improve the reaction conditions.



**Scheme 3.2.3** The synthetic pathway towards **S1** polymers. *Condition: 1) NBS, dry DMF, RT, 24 h, 76%; 2) NaH, dry DMF, RT, argon, 4 days, 53%; 3) bis(pinacolato)diboron, Pd(dppf) $_2$ Cl $_2$ , KOAc, 1,4-dioxane, argon, 85 °C, 24 h, 29%; 4) LDA,  $C_2Cl_6$ , dry THF, Ar, 51%; 5) NaH, dry DMF, Ar, RT, 24 h, 10%; 6) Pd(PPh $_3$ ) $_4$ ,  $K_2CO_3$ , THF/H $_2$ O, 85 °C, 3 d, 15-30%.*

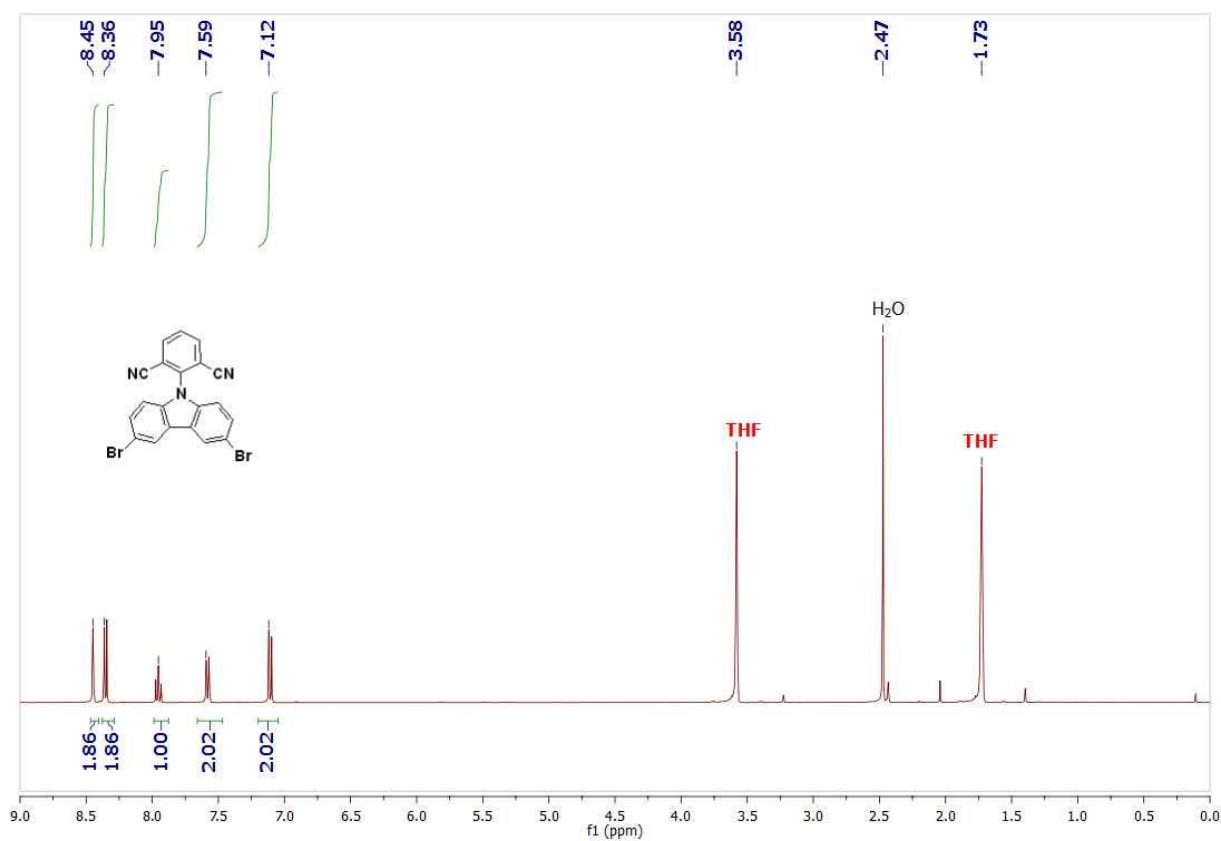


Figure 3.2. 4  $^1\text{H}$  NMR spectrum of **2E** in THF.

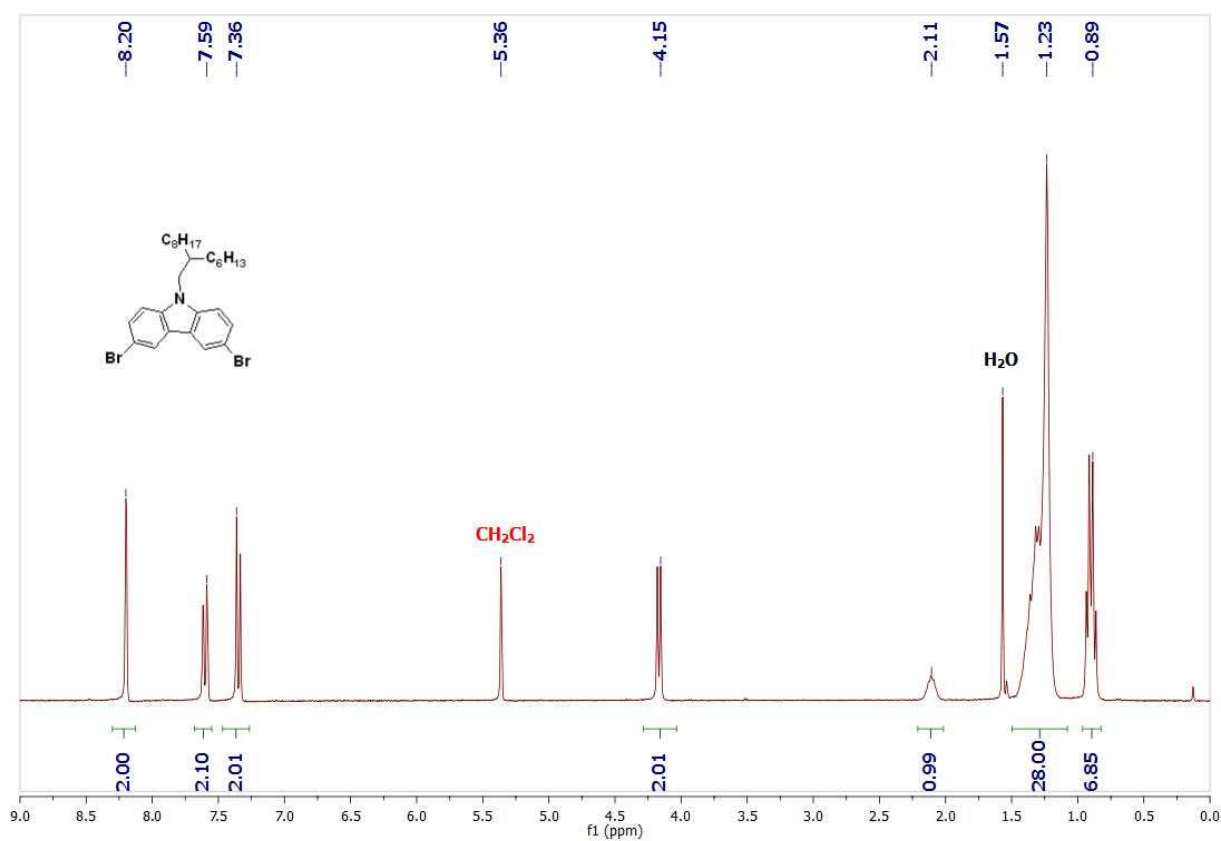
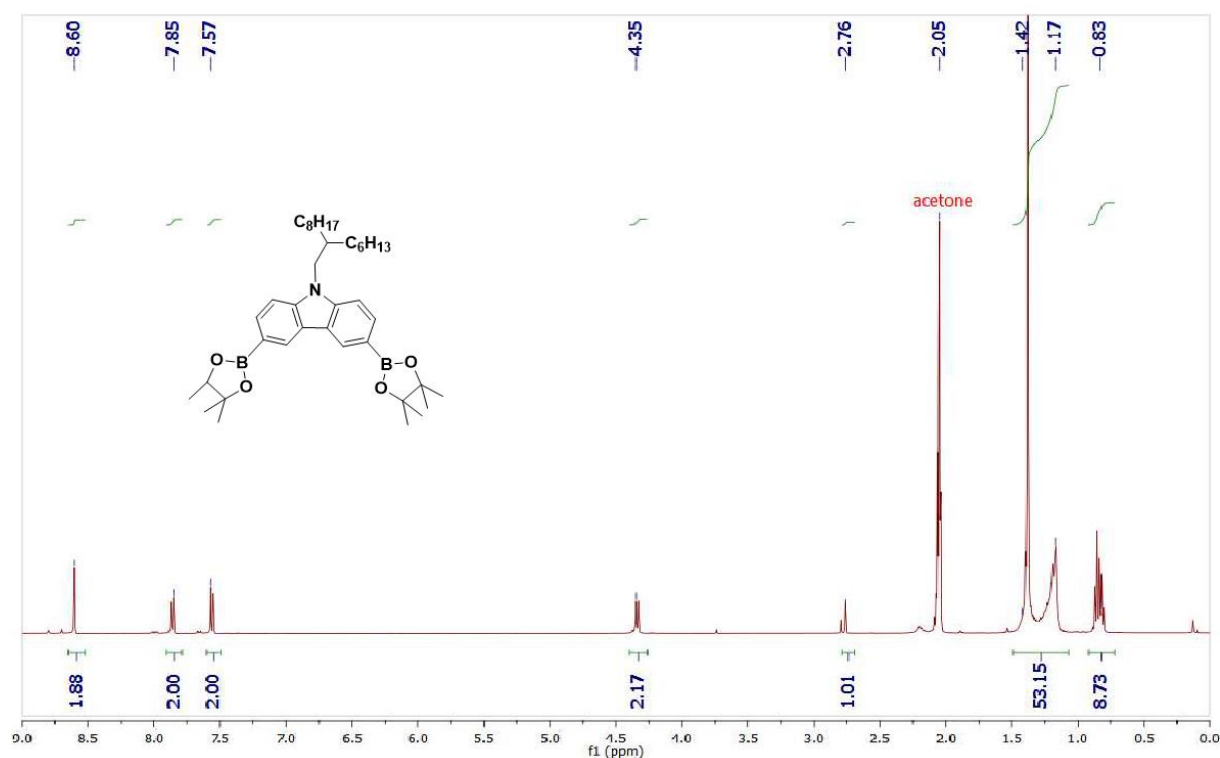


Figure 3.2. 5  $^1\text{H}$  NMR spectrum of **2B(-R2)** in  $\text{CD}_2\text{Cl}_2$ .

Apart from **2E**, two different branched alkyl chains were incorporated onto the carbazole and the corresponding two alkylated carbazoles **2B** and **2C** were prepared. The comonomer **2B** was obtained from 3,6-dibromocarbazole (**2A**), by introducing a long alkyl chain onto the N-position of carbazole. Subsequently, the second comonomer **2C** was further prepared from **2B** via the esterification, using bis(pinacolato)diboron. Their chemical structures were also determined by <sup>1</sup>H NMR spectra, as depicted in Figure 3.2. 5 and Figure 3.2. 6. For **2B** in CD<sub>2</sub>Cl<sub>2</sub>, the signals at 8.20, 7.59, and 7.36 ppm are ascribed to protons of the carbazole unit. The signal at 4.15 ppm is attributed to the α-CH<sub>2</sub> group to the N atom of carbazole and the broad signal at 2.11 ppm belongs to the -CH- groups of the alkyl chain. In addition, the broad signals in the range of 0.89-1.23 ppm are ascribed to other alkyl protons. Similarly, **2C** in acetone-d<sub>6</sub> exhibited well-resolved signals of the protons of the carbazole unit at 8.60, 7.85, and 7.57 ppm. The signals at 4.35 ppm and 2.76 ppm belong to protons of the α-CH<sub>2</sub> and -CH- groups, respectively.



**Figure 3.2. 6** <sup>1</sup>H NMR spectrum of **2C(-R2)** in acetone.

Three linear conjugated polymers with different molar ratios of TADF unit, namely **S1** polymers, were designed with the electron-donating carbazole units fixed on the backbone and the electron-accepting isophthalonitrile unit grafted onto the carbazole rings through the N position. The synthetic route towards the monomers and polymers is shown in Scheme 3.2.3.

**S1** polymers were synthesized by Suzuki coupling copolymerization of the monomer **2E**, **2B**, and **2C** with the molar feed ratio of 50:0:50, 50:0:50, and 10:40:50 and the conversion is 15-30%. Based on the **R** group and molar feed ratio, the polymers were named as **S1-11**, **S1-11-L**, and **S1-91**,

respectively. Among them, **S1-11** and **S1-11-L** are alternating copolymers with short and long alkyl chains, respectively, whereas **S1-91** is a random copolymer with short alkyl chains. The three polymers are readily soluble in common organic solvents, such as THF, DCM, and  $\text{CHCl}_3$ , thus they are suitable for thin-film formation through spin-coating.

As depicted in Figure 3.2.7, the signals of the polymers in NMR spectra are broad and overlapped, which is 'typical' for macromolecules. The signals around 4.2 ppm belong to the protons of  $-\text{CH}_2$  groups connected to the N atom of carbazole units, while the overlapped signals in the range of 0.8-2.5 ppm belong to the alkyl protons in the branched alkyl chain attached to the poly(3,6-carbazole) backbone. Besides, the signals from 7.0 to 9.0 ppm are ascribed to the protons of aromatic rings.

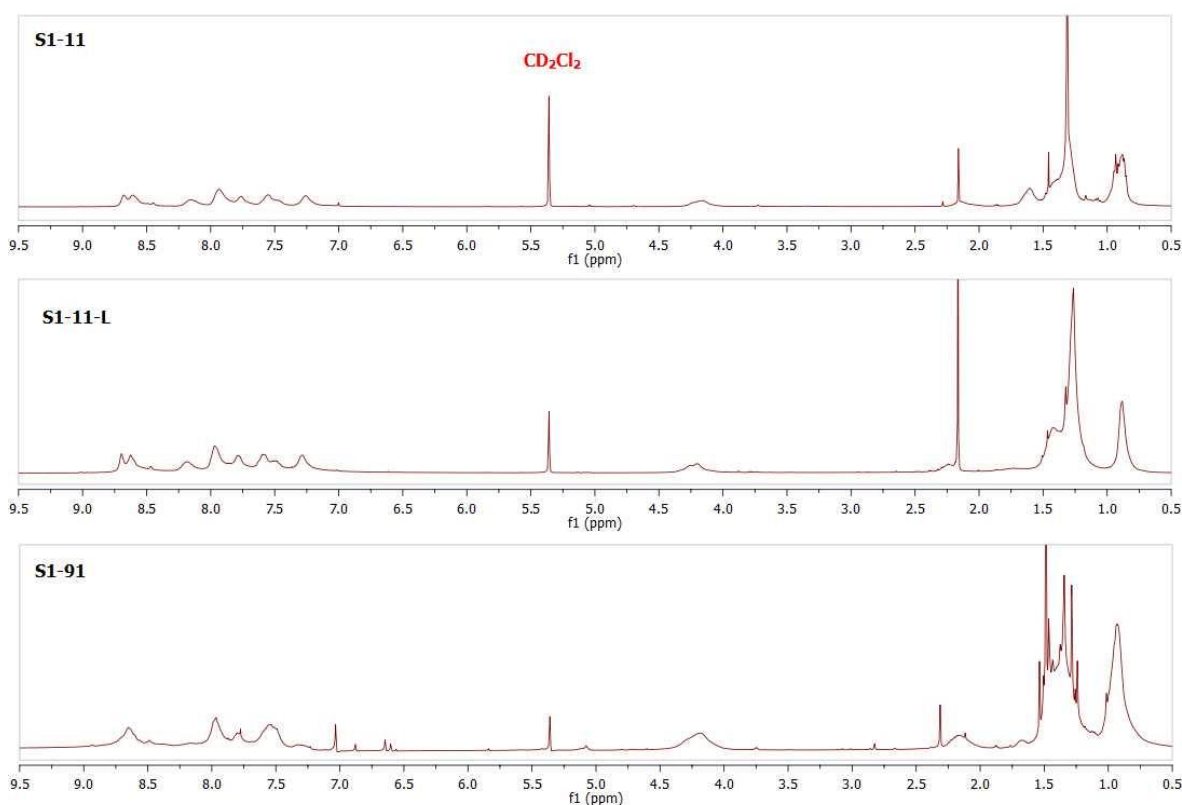


**Figure 3.2.7** The  $^1\text{H}$  NMR spectra of **S1** polymers in  $\text{CD}_2\text{Cl}_2$ .

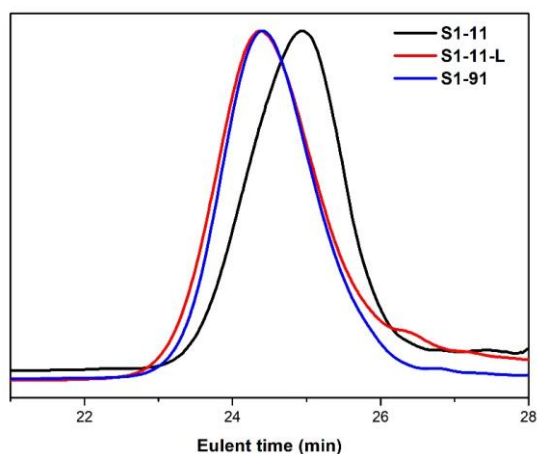


**Figure 3.2.8** The SEC curves of **S1** polymers.

The dispersity and molecular weight of **S1** polymers were determined by Size exclusion chromatography (SEC) in THF with polystyrene as standard (Figure 3.2.8). Their relative number-average molecular weights ( $M_{n,SEC}$ ) are 4.5-5.7 kDa, with the dispersity ( $M_w/M_n$ ) of 1.20-1.41, indicating a degree of polymerization ( $X_{n,SEC}$ ) of 7-10 (see Scheme 3.2.3).

The elemental analysis (EA) was also used to determine the composition of the polymers. From Table 3.2.1, we can see that there is a large difference between the results from EA and the theoretical values. The possible reasons are: 1) for each polymer, the sum of the ratios of C, H, and N atoms is not 100%, revealing that Br exists in the polymers as end group, while the theoretical values are calculated without considering the end groups; 2) In polymerization, the real ratio of the components in the polymers is not equal to the feeding ratio: even for alternating polymers (**S1-11** and **S1-11-L**), the real composition presents three possibilities.

**Table 3.2.1** The structural characterization of **S1** polymers

Polymers	$M_{n,SEC}$ (kDa)	$X_{n,SEC}$	$M_w/M_n$	C:H:N <sup>a</sup>	C:H:N <sup>b</sup>
<b>S1-11</b>	5.7	10	1.22	76.43 : 6.39 : 7.61	84.48 : 5.67 : 9.85
<b>S1-11-L</b>	4.8	7	1.41	62.22 : 4.82 : 9.51	84.48 : 5.67 : 9.85
<b>S1-91</b>	4.5	8	1.20	64.41 : 5.64 : 4.35	86.21 : 7.76 : 6.03

<sup>a</sup> result from elemental analysis; <sup>b</sup> theoretical values from feeding ratio without considering end groups

### 3.2.2 Photophysical properties

After the structural characterization, the steady-state and the time-resolved fluorescence measurements of **S1** polymers were recorded in both solution and solid-state, in collaboration with the OPERA laboratory of Prof. Chihaya Adachi at Kyushu University. Indeed, in the scope of the JSPS core-to-core program between OPERA and IPCM, I had the opportunity to spend one month at OPERA lab in 2019.

#### 3.2.2.1 In dilute solution

##### *Steady-state measurements*

The steady-state UV-vis absorption and photoluminescence (PL) spectra of **S1** polymer series in dilute toluene and chloroform solutions are depicted in Figure 3.2.9 and Figure 3.2.10, respectively, and their photophysical properties in solvents are summarized in Table 3.2.2. The photoluminescence quantum yields (PLQYs) of the polymers were measured in the air atmosphere and after nitrogen-bubbling for 15 min. The **S1** polymers achieve much higher PLQY in toluene than that in  $CHCl_3$ , and **S1-11-L** possesses the highest PLQY of 29% in toluene in the  $N_2$  atmosphere. The **S1** polymers exhibit similar UV-vis absorption spectra and their main characteristic peaks are located at 306-309 nm in toluene and

308-311 nm in  $\text{CHCl}_3$ , corresponding to the  $\pi$ - $\pi$  transition of the backbones. The small red-shift of the main peak for each polymer in  $\text{CHCl}_3$  compared to that in toluene results from the small solvatochromism effect in their ground state. Besides, all **S1** polymers exhibit weak absorption around 400 nm, ascribed to the intramolecular charge transfer (CT), characteristic of D-A systems.

The PL spectra of **S1** polymers in toluene are quite different from that in  $\text{CHCl}_3$ . In toluene, all PL spectra are broad, and **S1-11** and **S1-11-L** exhibit a single emission peaked at 534 nm and 528 nm, respectively, attributed to the intramolecular charge transfer (CT) transition from the D-A TADF chromophore. However, **S1-91** shows a dual emission: one weak emission peaked around 425 nm assigned to the  $\pi$ - $\pi$  transition from carbazole fragments, and another broad and intense band peaked at 525 nm results from the CT emission of TADF units. Note that the dual emission also indicates the incomplete inter/intra-chain energy transfer from the carbazole fragment to the TADF unit.

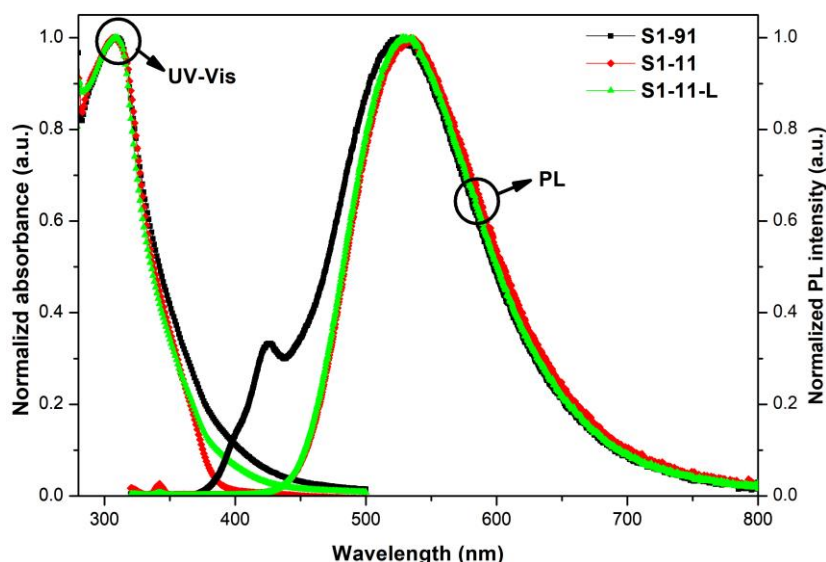


**Figure 3.2.9** The normalized UV-Vis absorption and PL spectra of **S1** polymers in toluene.

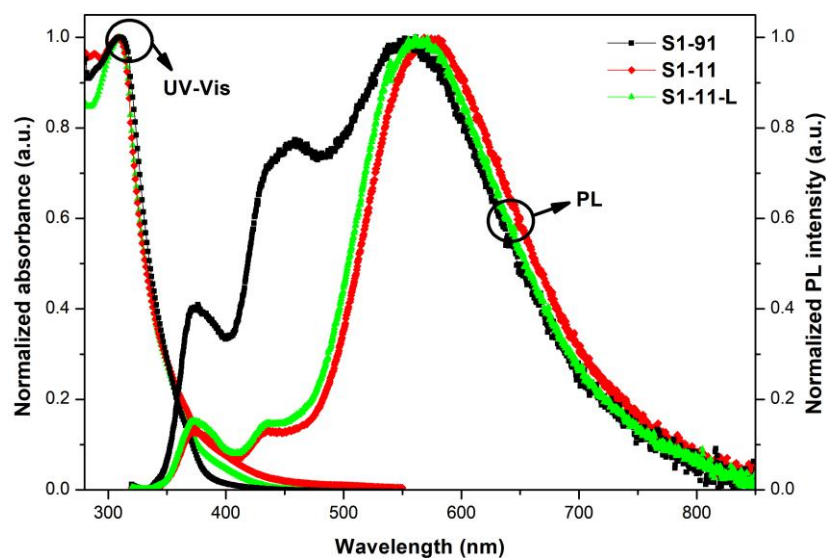


**Figure 3.2.10** The normalized UV-Vis absorption and PL spectra of **S1** polymers in  $\text{CHCl}_3$ .

In CHCl<sub>3</sub>, the PL spectra show multiple featureless emissions. This is due to the decrease of the intensity of the CT band in a polar solvent that accentuates the contribution of other emissions. The main peaks are located at 568, 561, and 562 nm for **S1-11**, **S1-11-L**, and **S1-91**, respectively, corresponding to CT emission of the TADF chromophore. The obvious redshift of these peaks in CHCl<sub>3</sub> in comparison with toluene is consistent with the D-A character of the materials. The emissions (374 nm) are assigned to the  $\pi$ - $\pi$  transition from carbazole fragments.

According to the absorption and emission spectra, the Stokes shift can be calculated for **S1-11**, **S1-11-L** and **S1-91** as 228 nm (13953 cm<sup>-1</sup>), 220 nm (13528 cm<sup>-1</sup>) and 216 nm (13315 cm<sup>-1</sup>) in toluene and 260 nm (14862 cm<sup>-1</sup>), 252 nm (14537 cm<sup>-1</sup>) and 251 nm (14361 cm<sup>-1</sup>) in CHCl<sub>3</sub>, respectively.

The photoluminescence quantum yields (PLQYs) of the polymers were measured in the air atmosphere and after nitrogen-bubbling for 15 min. As generally observed for D-A systems, the **S1** polymers achieve much higher PLQY in toluene than that in CHCl<sub>3</sub>, and **S1-11-L** possesses the highest PLQY of 29% in oxygen-free solution.

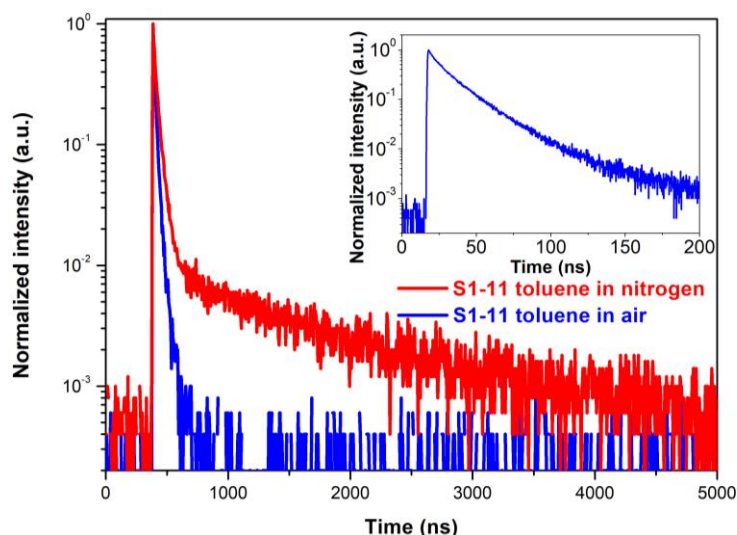
**Table 3.2.2** Photophysical parameters of **S1** polymers in solvents.

	$\lambda_{\text{abs}}^{\text{a}}$ (nm)	$\lambda_{\text{abs}}^{\text{b}}$ (nm)	$\lambda_{\text{PL}}^{\text{a}}$ (nm)	$\lambda_{\text{PL}}^{\text{b}}$ (nm)	PLQY <sub>toluene</sub> <sup>c/d</sup> (%)	PLQY <sub>CHCl<sub>3</sub></sub> <sup>c/d</sup> (%)	Stokes shift (cm <sup>-1</sup> ) <sup>a/b</sup>
<b>S1-11</b>	306	308	534	374,438,568	12 / 19	2.0 / 2.4	13953 / 14862
<b>S1-11-L</b>	308	309	528	374,438,561	14 / 29	2.4 / 2.9	13528 / 14537
<b>S1-91</b>	309	311	425,525	374,460,562	8.3 / 28	1.1 / 2.0	13315 / 14361

<sup>a</sup> Measured in toluene; <sup>b</sup> Measured in CHCl<sub>3</sub>; <sup>c</sup> Measured in air atmosphere; <sup>d</sup> Measured after nitrogen-bubbling for 15 min.

#### Time-resolved measurements

The fluorescence decays of **S1** polymer series in toluene at room temperature were measured as well, by time-resolved fluorescence spectroscopy with time-correlated single-photon counting (TCSPC) in both air and nitrogen atmosphere (Figure 3.2.11).



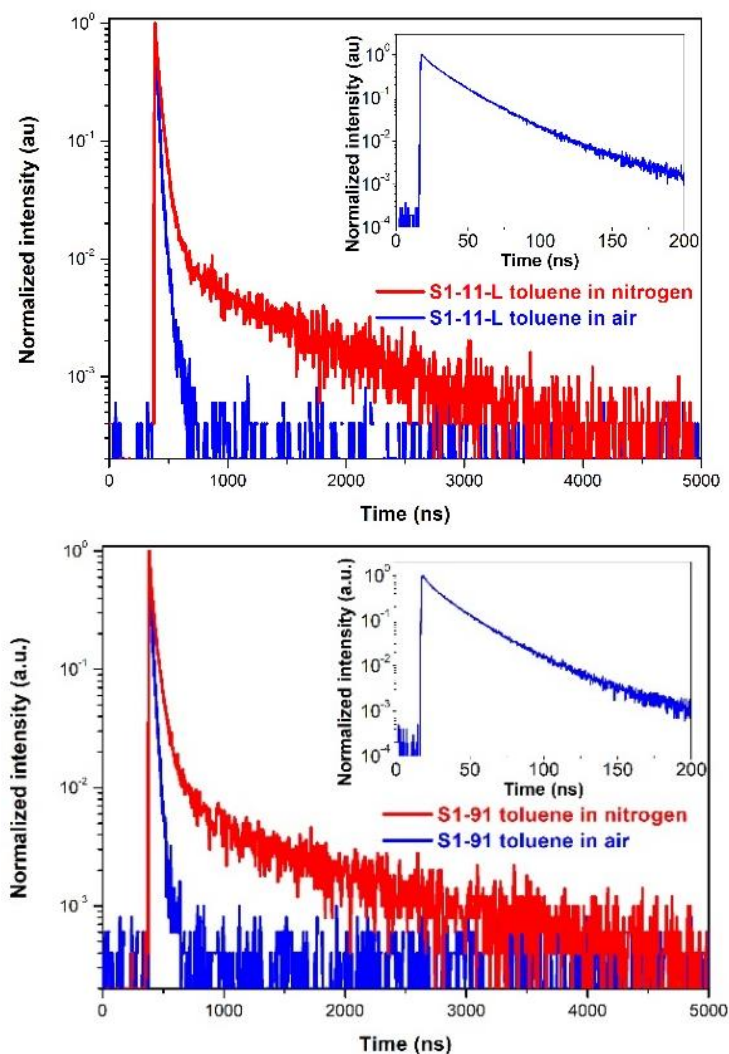


**Figure 3.2.11** The transient PL decay curves of **S1** polymers in toluene.

Both PF and DF components are clearly observed in decay curves. As shown in Table 3.2.3, the PF and DF lifetimes can both be calculated using the mono-exponential function and the data are summarized in Table 3.2.3. Among the polymers, **S1-11** exhibits the emission with the shortest PF and the longest DF lifetimes, while **S1-91** holds the longest PF and the shortest DF lifetimes. The values of PF lifetimes for **S1-11**, **S1-11-L**, and **S1-91** are 33.4, 39.6, and 42.8 ns, respectively, and the DF lifetimes of the polymers are around 0.7-1.0  $\mu\text{s}$ , which is rather short, indicative of a quick reverse intersystem crossing process.

**Table 3.2.3** PF and DF lifetimes of **S1** polymers in toluene

	$A_{\text{PF}}$	$\tau_{\text{PF}}$	$A_{\text{DF}}$	$\tau_{\text{DF}}(\mu\text{s})$	$\phi_{\text{DF}}/\phi_{\text{PF}}$
<b>S1-11</b>	3844.64	33.4	47.8644	1.01	27.4 / 72.6
<b>S1-11-L</b>	4170.43	39.6	57.11	0.75	20.5 / 79.5
<b>S1-91</b>	3542.61	42.8	59.8249	0.70	21.5 / 78.5

### 3.2.2.2 In solid-state

#### Steady-state measurements

The steady-state UV-Vis absorption and PL spectra of **S1** polymers in the neat film are shown in Figure 3.2.12 and the photophysical parameters are reported in Table 3.2.4. The absorption spectra show the main characteristic peaks (312, 307, and 315 nm for **S1-11**, **S1-11-L**, and **S1-91**, respectively), corresponding to the  $\pi$ - $\pi$  transition. The optical energy gap of 2.60, 2.67, and 2.34 eV for **S1-11**, **S1-11-L**, and **S1-91**, respectively, were obtained from the onset of absorption.

The PL spectra display broad CT emissions peaked at 529, 513, and 530 nm for **S1-11**, **S1-11-L**, and **S1-91**, respectively. The Stokes shift can be calculated in the neat film for **S1-11**, **S1-11-L**, and **S1-91**: 217 nm ( $13148\text{ cm}^{-1}$ ), 206 nm ( $13080\text{ cm}^{-1}$ ), and 215 nm ( $12878\text{ cm}^{-1}$ ).

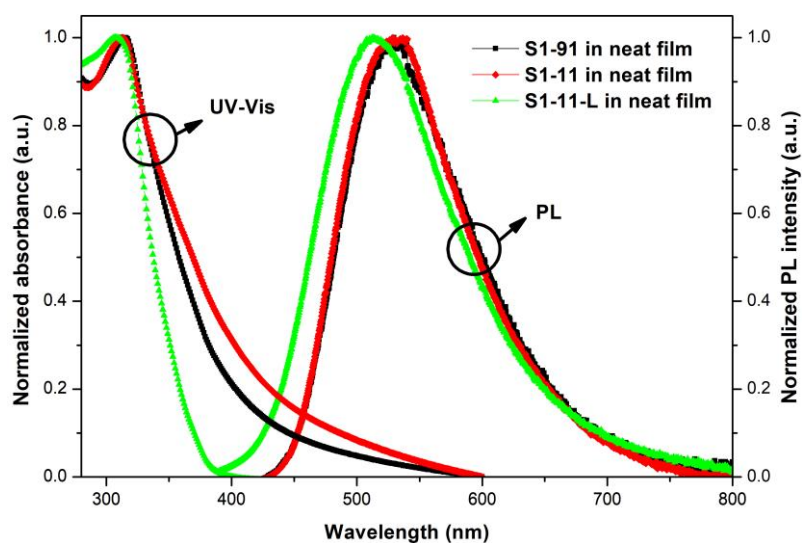


**Figure 3.2.12** The normalized UV-Vis absorption and PL spectra of **S1** polymers in the neat film.

**Table 3.2.4** The photophysical parameters of **S1** polymers in the neat film

	$\lambda_{\text{abs, neat}}$ (nm)	$\lambda_{\text{PL, neat}}$ (nm)	PLQY <sub>neatfilm</sub> <sup>a/b</sup> (%)	HOMO <sup>c</sup> (eV)	Eg <sup>d</sup> (eV)	LUMO <sup>e</sup> (eV)	$\Delta E_{\text{ST}}$ <sup>f</sup> (eV)	Stokes shift ( $\text{cm}^{-1}$ )
<b>S1-11</b>	312	529	3.3 / 3.4	-5.66	2.60	-3.06	0.01	13148
<b>S1-11-L</b>	307	513	1.8 / 1.7	-5.61	2.67	-2.94	0.02	13080
<b>S1-91</b>	315	530	4.4 / 4.5	-5.67	2.34	-3.33	0.02	12878

<sup>a</sup> Measured in air atmosphere; <sup>b</sup> Measured in argon atmosphere; <sup>c</sup> Measured by photoelectron spectroscopy; <sup>d</sup> the optical energy gap calculated from absorption spectra; <sup>e</sup> deduced from the HOMO and Eg values; <sup>f</sup> calculated from streak camera experiments.

To estimate the energy levels of excited states of **S1** polymers in neat film, their singlet and triplet energies ( $E_{\text{S}}$  and  $E_{\text{T}}$ ) were determined according to the fluorescent and phosphorescent spectra, respectively (Figure 3.2.13). The  $E_{\text{S}}$  values of **S1-11**, **S1-11-L**, and **S1-91** are 2.86, 3.00, and 2.33 eV, and the  $E_{\text{T}}$  values of **S1-11**, **S1-11-L**, and **S1-91** are 2.85, 2.98, and 2.31 eV. Based on these later

values, the  $\Delta E_{ST}$  values of **S1-11**, **S1-11-L**, and **S1-91** were calculated to be 0.01, 0.02, and 0.02 eV, respectively.

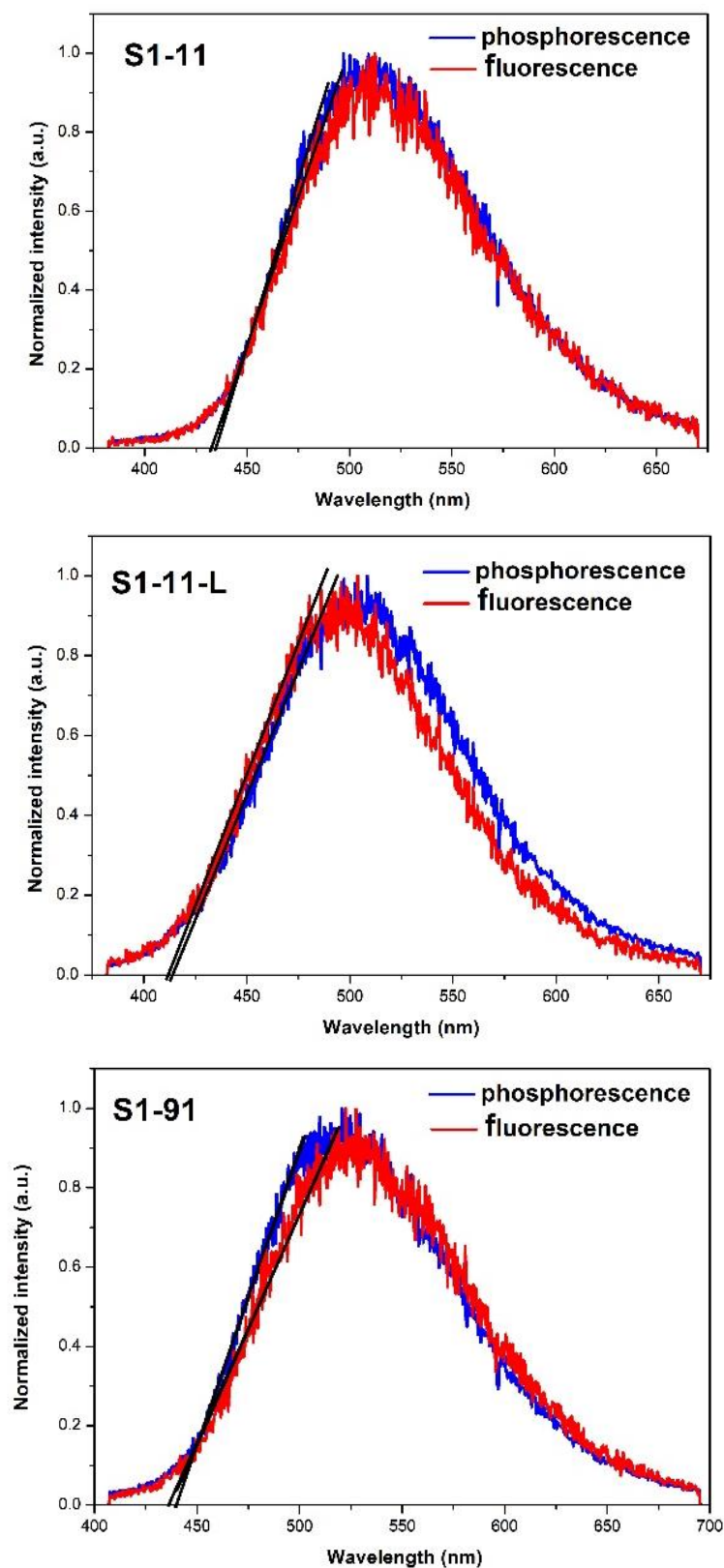


**Figure 3.2.13** Fluorescence (300K) and phosphorescence (17K) spectra of **S1** polymers in neat film measured by a streak camera.

As represented in Figure 3.2.14, the HOMO energy level of **S1** polymers was determined in neat films by photoelectron spectroscopy and the values are equal to -5.66, -5.61, and -5.67 eV for **S1-11**, **S1-11-L**, and **S1-91**, respectively. The LUMO energy level for each polymer was estimated as the sum of the HOMO level and the optical energy gap.

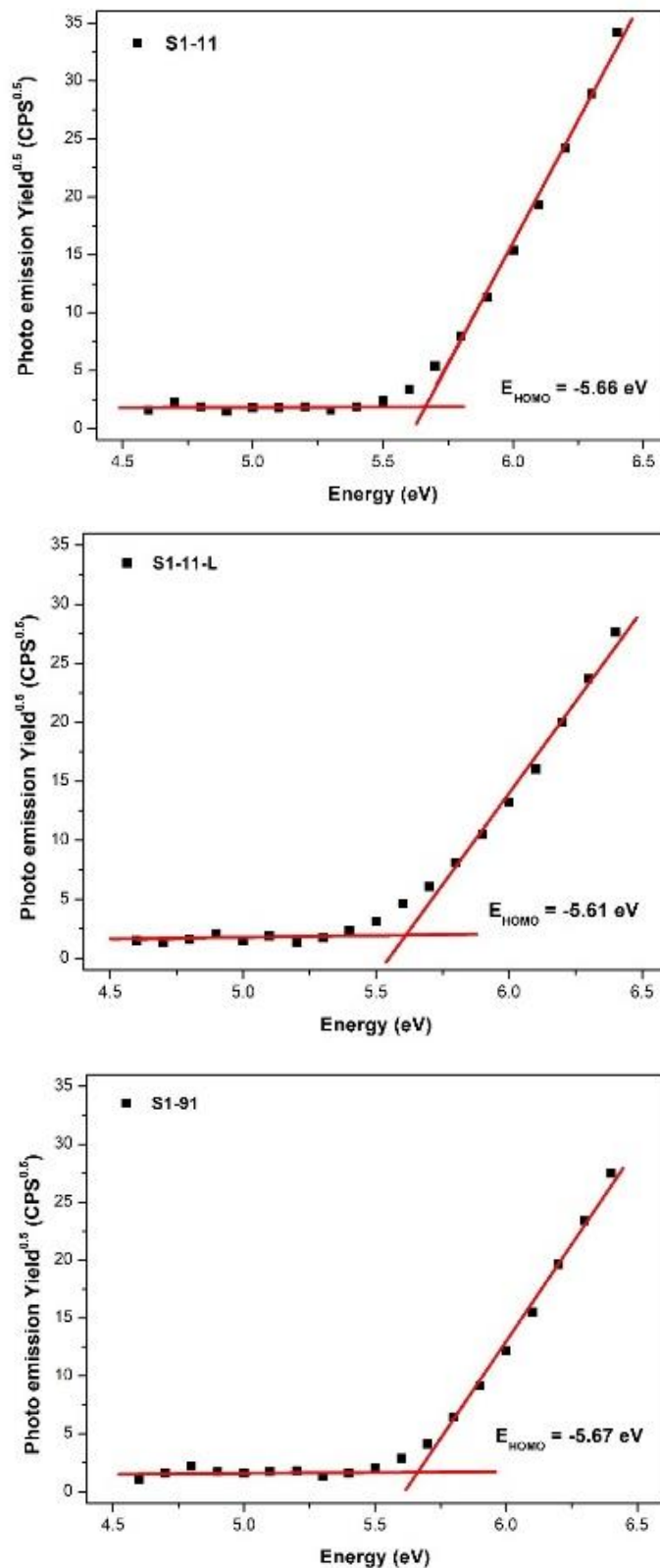


Figure 3.2.14 Photoelectron spectra of **S1** polymers in neat film.

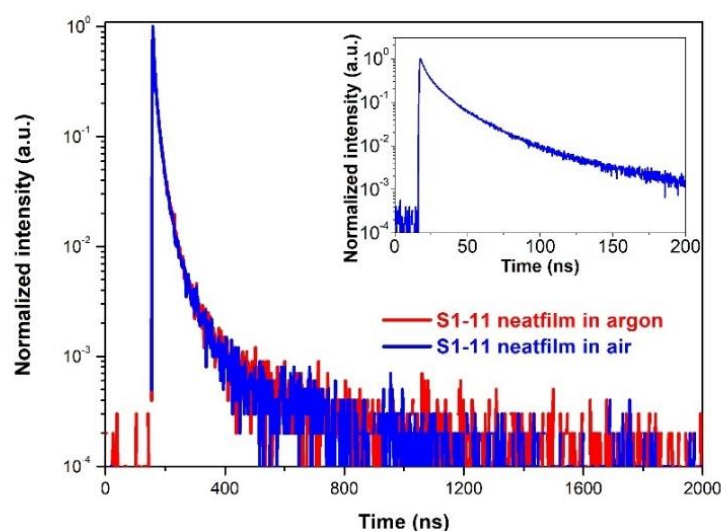
PLQYs of **S1** polymers (Table 3.2.4) in the neat film was much lower than that measured in toluene, probably due to the aggregation-caused quenching. Taking HOMO, LUMO, and triplet energy level into account, mCP (1,3-Bis(N-carbazolyl)benzene) was chosen as the host material to fabricate blend films. Therefore, the PLQYs of the obtained blend films were measured. As shown in Table 3.2.5, PLQYs in mCP doped films with different ratios of **S1** polymers increase with the decrease content of the polymer concentration, indicating the reduction of the concentration quenching. For **S1-91**, PLQY doesn't increase too much with the decreasing content of the polymer, probably since TADF chromophores are already dispersed well along the polymer backbone.

**Table 3.2.5** PLQYs of **S1** polymers in mCP doped films with different content (Argon atmosphere)

	100%	50%	40%	30%	20%	10%	5%
<b>S1-11</b>	3.4	8.8	11.9	14.1	17.5	24.6	25.8
<b>S1-11-L</b>	1.7	11.1	12.5	14.2	17.0	21.0	24.1
<b>S1-91</b>	4.5	3.4	5.1	5.5	9.2	8.0	16.3

#### *Time-resolved measurements*

The fluorescence decays of **S1** polymers in neat films at room temperature were also measured by time-resolved fluorescence spectroscopy with time-correlated single-photon counting (TCSPC) in both air and argon atmosphere (Figure 3.2.15). All the decay curves are composed of one PF and one DF components, indicating the TADF character of the polymers in neat film. Unfortunately, no real difference in decays is observed between the air and argon environment. This indicates that the simple flow of argon around the **S1** polymer films is probably not enough to remove all the oxygen quenchers. The PF lifetimes of the polymers can be calculated from the mono-exponential function and the values of **S1-11**, **S1-11-L**, and **S1-91** are 8.7, 7.3, and 13.6 ns, respectively. Besides, the delayed fluorescence can be fitted with a bi-exponential function. These very short DF lifetimes (Table 3.2.6) are consistent with the very low PLQY and TADF activity of the **S1** polymer series in neat films.



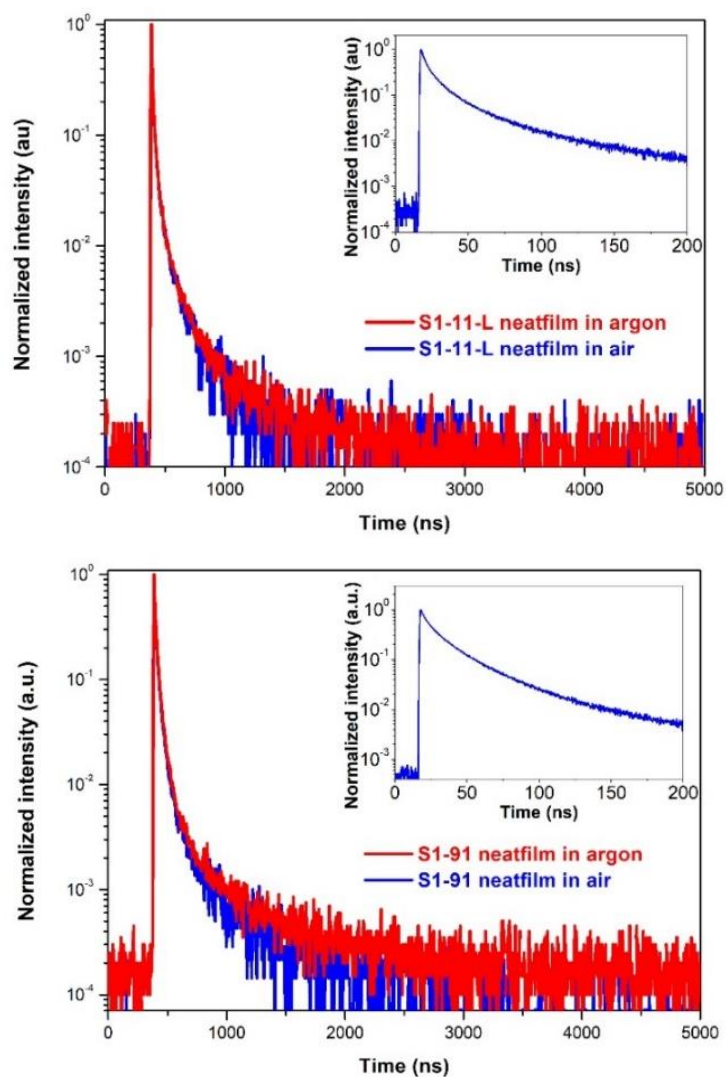


**Figure 3.2.15** Fluorescence decays of **S1** polymers in neat films at room temperature.

**Table 3.2.6** PF and DF lifetimes of **S1** polymers in neat films (argon atmosphere)

	$A_{PF}$	$\tau_{PF}$ (ns)	$A_{DF1}$	$\tau_{DF1}$ (ns)	$A_{DF2}$	$\tau_{DF2}$ (ns)	$\phi_{DF1}/\phi_{DF2}/\phi_{PF}$
<b>S1-11</b>	0.1517	8.7	0.00306	30.0	0.00244	128	5.3 / 18.1 / 76.5
<b>S1-11-L</b>	0.33248	7.3	0.02667	80.7	0.00304	342	38.3 / 18.5 / 43.2
<b>S1-91</b>	0.09785	13.6	0.00567	83.2	0.00183	451	17.9 / 31.4 / 50.6

The temperature dependence of the transient PL decay spectra of **S1** polymers in neat films was further investigated by a streak camera from 100 to 300 K in vacuum. As shown in Figure 3.2.16, obvious prompt and delayed fluorescence components can be observed. We can note that under vacuum, The DF components of the different neat films are much longer than those studied previously by TCSPC equipment under a simple argon flow. This also indicates that the previous PLQYs in neat film determined under Ar flow are probably underestimated.

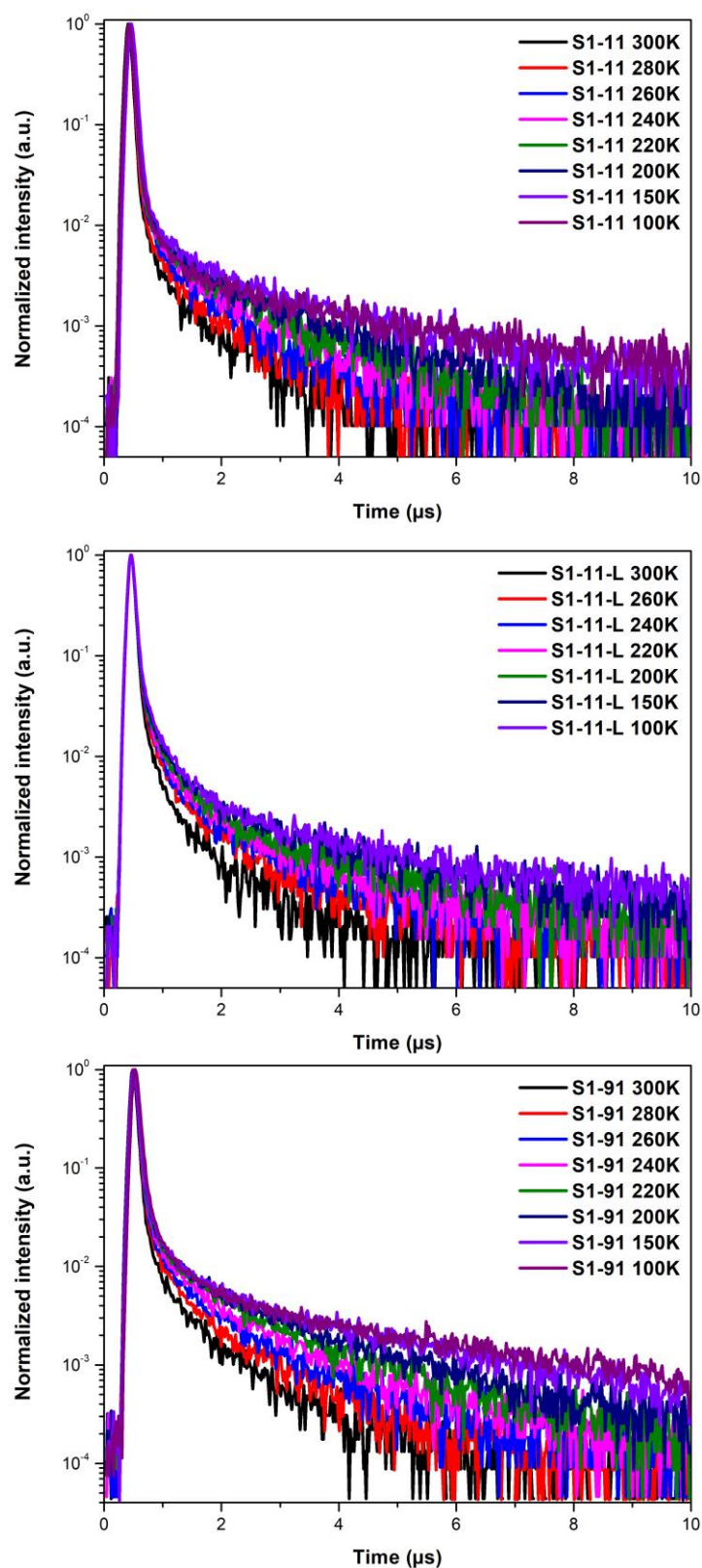


**Figure 3.2.16** Temperature-dependent transient PL decay curves of **S1** polymers in neat film ranging from 100 to 300 K measured by a streak camera.

In contrast to the PF decays which show almost no variation with temperature, delayed fluorescence decay spectra show clear temperature dependence for the three **S1** polymers and they can be fitted

with a bi-exponential function (details in Table 3.2.7, Table 3.2.8, and Table 3.2.9). For **S1-11** and **S1-91**, the DF lifetime increases with decreasing temperature from 300 K to 100 K. That is consistent with a longer triplet lifetime at low temperature, resulting from a slower reverse intersystem crossing rate according to the TADF mechanism.

**Table 3.2.7** The DF lifetimes of **S1-11** in neat films measured by a streak camera (100-300K)

T (K)	$A_{DF1}$	$\tau_{DF1}(\mu s)$	$A_{DF2}$	$\tau_{DF2}(\mu s)$	$R^2$
100	0.00257	0.290	0.00279	2.87	0.95358
150	0.00435	0.259	0.00483	2.02	0.96951
200	0.00312	0.258	0.0043	1.74	0.98119
220	0.00108	0.207	0.00427	1.37	0.98151
240	0.03547	0.166	0.00625	1.24	0.98419
260	0.00981	0.159	0.00486	1.07	0.98541
280	0.01175	0.107	0.00554	0.79	0.98664
300	0.02242	0.092	0.00530	0.66	0.99023

**Table 3.2.8** The DF lifetimes of **S1-11-L** in neat films measured by a streak camera (100-300K)

T (K)	$A_{DF1}$	$\tau_{DF1}(\mu s)$	$A_{DF2}$	$\tau_{DF2}(\mu s)$	$R^2$
100	0.00981	0.299	0.00403	2.04	0.98595
150	0.01355	0.268	0.00509	1.78	0.98155
200	0.01349	0.281	0.00395	1.63	0.98237
220	0.00779	0.348	0.00338	1.75	0.97106
240	0.00207	0.210	0.00333	1.28	0.9733
260	0.00635	0.231	0.00339	1.23	0.98225
300	0.00255	0.192	0.0022	0.96	0.98162

**Table 3.2.9** The DF lifetimes of **S1-91** in neat films measured by a streak camera (100-300K)

T (K)	$A_{DF1}$	$\tau_{DF1}(\mu s)$	$A_{DF2}$	$\tau_{DF2}(\mu s)$	$R^2$
100	0.01052	1.17	0.00947	6.84	0.99484
150	0.01122	1.27	0.00978	5.06	0.99645
200	0.01952	0.91	0.01179	3.48	0.99689
220	0.01442	0.88	0.00906	3.23	0.99608
240	0.01046	0.72	0.00746	2.91	0.99603
260	0.01344	0.71	0.00605	2.71	0.99628
280	0.00556	0.38	0.00299	1.52	0.98709
300	0.00462	0.31	0.00326	1.12	0.97942

The fluorescence decays of **S1** polymer doped films (10% in mCP) at room temperature were also investigated by time-resolved fluorescence spectroscopy with TCSPC in both air and argon

atmosphere, as shown in Figure 3.2.17.

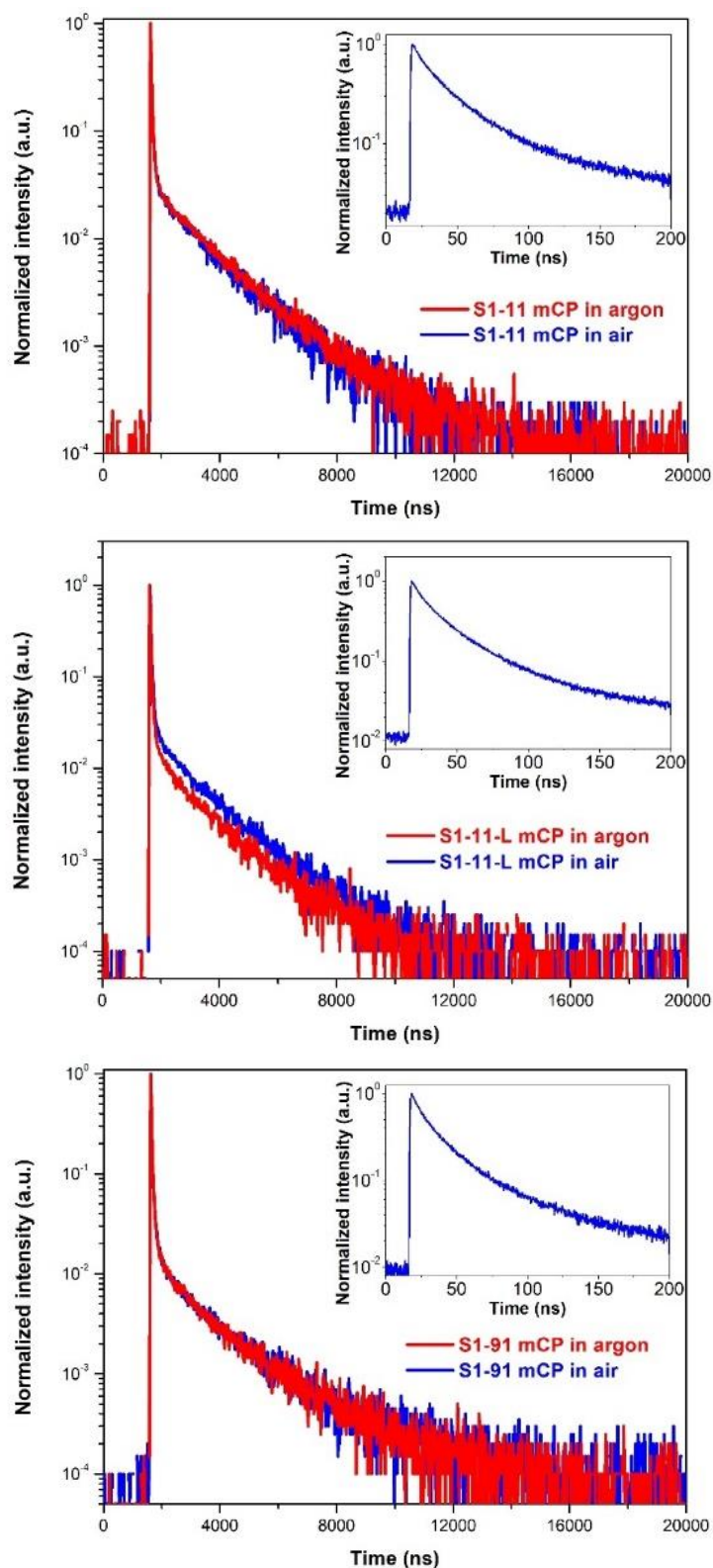


**Figure 3.2.17** The fluorescence decays of S1 polymers mCP doped films (10 wt%) studied by TCSPC

Prompt and delayed fluorescence can be clearly observed and their components can also be fitted with a bi-exponential function, as shown in Table 3.2.10. That indicates a clear TADF behavior for all the

**S1** polymers in mCP with typical PF and DF lifetime values of about 35-40.1 ns and 1.2-1.6  $\mu$ s, respectively. Note that such small DF values are interesting because they indicate a rapid RISC that could limit the roll-off in the device configuration.

**Table 3.2.10** The PF and DF lifetimes of **S1** polymers in mCP doped films (argon atmosphere)

	$A_{PF}$	$\tau_{PF}$ (ns)	$A_{DF}$	$\tau_{DF}$ ( $\mu$ s)	$\phi_{DF}/\phi_{PF}$
<b>S1-11</b>	8682.21	40.1	303.814	1.55	57.5 / 42.5
<b>S1-11-L</b>	34187.8	34.5	349.267	1.22	26.6 / 73.4
<b>S1-91</b>	32409	35.1	297.162	1.55	28.9 / 71.1

The temperature dependence of the transient PL decay spectra of **S1-91** in mCP doped film (10 wt%) was also investigated by a streak camera from 50 to 300 K in vacuum (Figure 3.2.18). We can clearly observe two components in all PL decay curves, among them, the PF components are overlapped with each other. While the delayed components show clear temperature dependence and each component can be fitted with a bi-exponential function (Table 3.2.11). For each component, the DF lifetime increases with decreasing temperature. That is consistent with the TADF mechanism in which a longer triplet lifetime at lower temperature results from a slower reverse intersystem crossing rate. Note that, as also observed for neat films, the DFs in mCP doped film under vacuum are much longer than those under argon, for example, **S1-91** shows a DF lifetime at 300K about 11.8  $\mu$ s in vacuum vs 1.6  $\mu$ s under Ar flow (Table 3.2.10 vs Table 3.2.11). Here also, the previous PLQYs in mCP doped film determined under argon flow (Table 3.2.5) are probably underestimated.

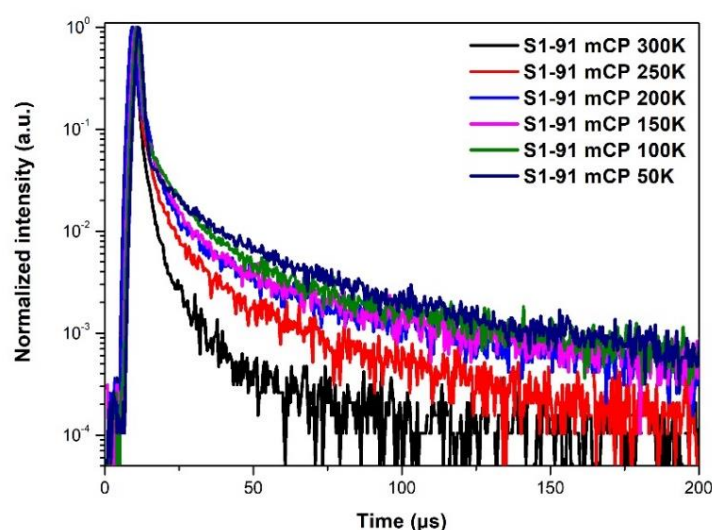


**Figure 3.2.18** Temperature dependence of **S1-91** in mCP doped film (10 wt%) in vacuum.

**Table 3.2.11** DF lifetimes of **S1-91** in mCP doped film (10 wt%) measured by a streak camera

T (K)	A <sub>1</sub>	$\tau_{DF1}(\mu s)$	A <sub>2</sub>	$\tau_{DF2}(\mu s)$	R <sup>2</sup>
50	0.01779	31.4	0.02602	6.84	0.99339
100	0.01443	25.3	0.02727	5.59	0.99722
150	0.0165	22.7	0.11138	4.13	0.99704
250	0.01085	16.4	0.01606	2.78	0.99495
300	0.00509	11.8	0.02496	2.20	0.99596

### 3.2.3 Conclusion

To summarize, we designed and synthesized a new series of green-emitting polymers with poly(3,6-carbazole) as backbone and isophthalonitrile as side groups. The polymers were successfully prepared *via* Suzuki polycondensation. The structures of monomers and **S1** polymer series were characterized by NMR, SEC, and elemental analysis.

The photophysical properties of **S1** polymers were investigated in detail by both steady and time-resolved measurements. More specifically, the absorption, emission, and phosphorescence (17K) spectra were recorded in solution and solid-states. From these spectra, we determined the singlet and triplet energy levels, the optical bandgap, and Stokes shifts of these polymers. Small  $\Delta E_{ST}$  values (0.01-0.02 eV) were also estimated suggesting possible TADF properties. Moreover, photoelectron spectroscopy in neat films, combined with optical measurements, was used to determine the HOMO/LUMO energy levels of polymers.

From the time-resolved measurements, we can confirm that **S1-11**, **S1-11-L**, and **S1-91** exhibit TADF activity both in solution and solid-state. Due to aggregation-caused quenching, PLQYs of **S1** polymers in neat films are much lower than those in diluted degassed toluene solutions. mCP was chosen as the host material for blend films to improve PLQYs in solid-state up to 14 times. Among the polymers, **S1-11-L** holds the highest PLQY of 29% in oxygen-free toluene. In a neat film, a low PLQY of 1.7% in argon can be obtained and this value increases to 24% by preparing 5 wt% mCP doped film. Compared to the reported TADF polymers, the PLQYs of the **S1** polymer series are quite modest, but the electroluminescent properties (device performance) of this series should be investigated in the near future.

### 3.3 Linear conjugated TADF polymers based on Pm5

**Pm5** is a ‘donor-acceptor’ type TADF molecule<sup>266</sup>, with 9,9-dimethylacridine (DMAC) as the donor part bridged *via* a phenylene ring to a cyano-pyrimidine acceptor unit. As shown in Figure 3.3.1, **Pm5** possesses a highly twisted configuration (with a large dihedral angle around 88°) between the DMAC ring and the phenylene bridge, presumably owing to strong ortho-ortho interaction between acridine and central phenylene ring. In the meanwhile, we observe a planar conformation (with a dihedral angle close to 0°) between the CN-substituted pyrimidine and the phenylene ring.

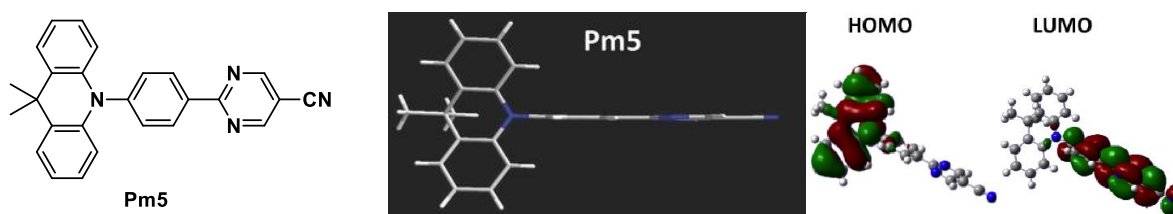


**Figure 3.3.1** The molecular structure and conformation of **Pm5** with the calculated spatial distributions of HOMO and LUMO energy levels<sup>266</sup>

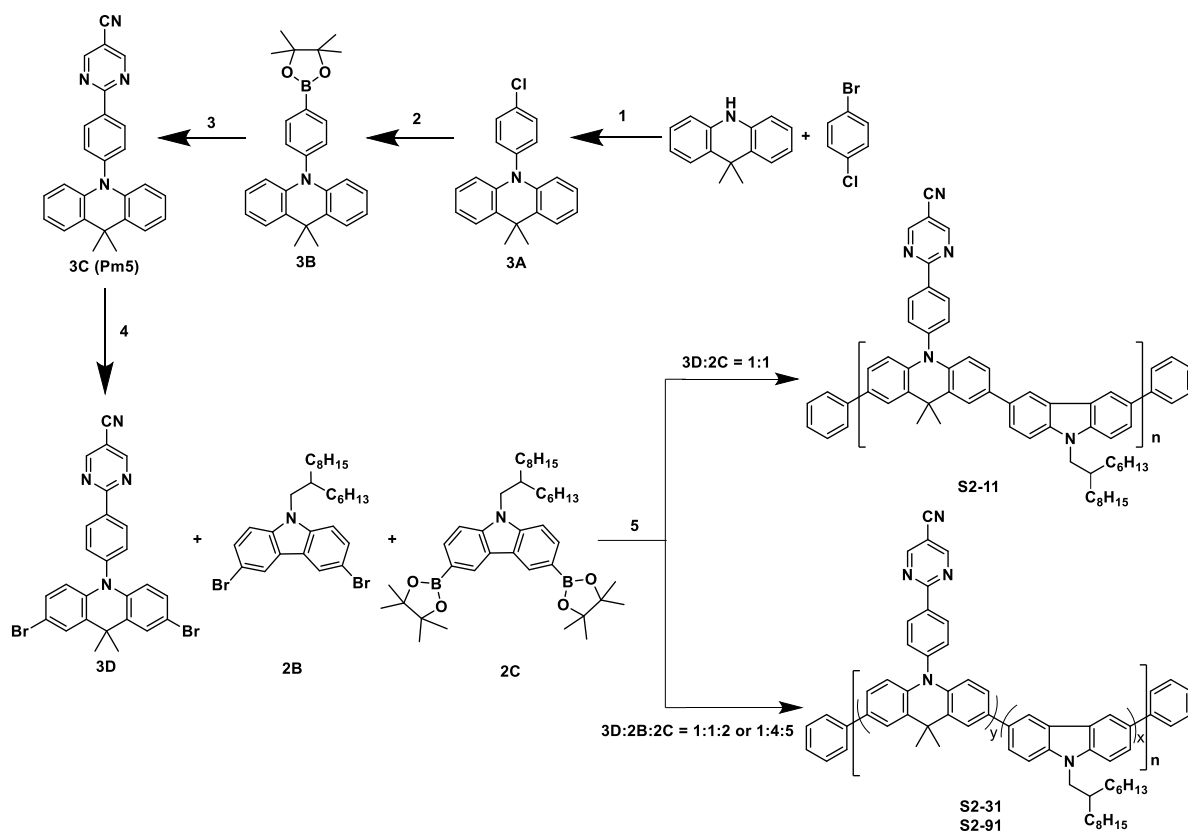
**Pm5** exhibits green emission with a small  $\Delta E_{ST}$  of 0.04 eV and a high PLQY up to 95% (55.7% from prompt fluorescence and 39.3% from delayed fluorescence) in doped mCPCN films (8 wt%). The lifetimes of prompt and delayed fluorescence are 23.7 ns and 5.2  $\mu$ s, respectively. The OLED device based on **Pm5** doped mCPCN film (8 wt%) has a high  $EQE_{max}$  of 30.6%, a current efficiency of 103.7 cd/A, and a power efficiency of 116.3 lm/W together with CIE coordinates of (0.34, 0.57).

#### 3.3.1 Design, synthesis, and structural characterization

As **Pm5** exhibits excellent TADF properties, we proposed to utilize this TADF chromophore into copolymers, in following the same strategy as in section 3.2. Hence, **Pm5** needs to be brominated on the 3,6-positions to obtain the monomer **3D** (Scheme 3.3.1). Considering the solubility, the comonomers **2B** and **2C** were also chosen, as carbazole provides the excellent hole-transporting ability, while branched long alkyl chains offer good solubility. Before polymerization, we prepared again **2B** and **2C** following the same synthetic procedures as described in section 3.2.

As shown in scheme 3.3.1, the monomer **3D** was synthesized in 4 steps: we started from the coupling reaction between 9,9-dimethyl-9,10-dihydroacridine and 1-bromo-4-chlorobenzene in toluene, using  $Pd_2(dba)_3$ ,  $P(t-Bu)_3/HBF_4$  and  $t-BuONa$  as the catalytic system and obtained the molecule **3A** with a yield of 65%. Then, the -Cl group of the molecule **3A** was converted to pinacolborane group of the molecule **3B** in a yield of 52%, catalyzed by  $Pd(OAc)_2$ , Sphos, and KOAc. The third step is a “typical” Suzuki coupling reaction under the function of  $Pd(dppf)_2Cl_2$  and  $Cs_2CO_3$ , to gain the TADF

chromophore **3C** (**Pm5** in the literature<sup>266</sup>) with a yield of 52%. The last step is the “traditional” bromination reaction using NBS, and then, after purification, the monomer **3D** was obtained with a yield of 77%.



**Scheme 3.3.1** The synthetic route of **S2** polymers. Conditions: 1)  $Pd_2(dba)_3$ ,  $P(t-Bu)_3/HBF_4$ ,  $t-BuONa$ , toluene,  $110\text{ }^\circ\text{C}$ , Ar, 18 h, 65% ; 2) bis(pinacolato)diboron,  $Pd(OAc)_2$ , Sphos, 1,4-dioxane, KOAc,  $101\text{ }^\circ\text{C}$ , 3 h, 52%; 3) 2-chloropyrimidine-5-carbonitrile,  $Pd(dppf)_2Cl_2$ ,  $Cs_2CO_3$ , 1,4-dioxane/ $H_2O$ , 52%; 4) NBS, DCM/DMF, dark, 77%; 5)  $Pd(PPh_3)_4$ ,  $K_2CO_3$ , THF/ $H_2O$ ,  $85\text{ }^\circ\text{C}$ , 3 d, 28-40%.

The chemical structure of **3D** was determined by  $^1H$  NMR spectrum. As shown in Figure 3.3. 2, the single peak at 1.66 ppm is attributed to the methyl groups ( $-CH_3$ ). The singlet peak at 9.11 ppm belongs to the proton of the pyrimidine ring, and the doublet peak at 8.78 ppm corresponds to the protons of the benzene ring, which are close to the pyrimidine ring. The doublet peak at 7.49 ppm is ascribed to the protons of the benzene ring, which are close to the acridine ring. The peaks at 7.56, 7.09, and 6.24 ppm belong to the protons of the acridine ring. Besides the chemical shifts, the integrals of each shift are consistent with the chemical structure of **3D**.

**S2** polymer series was synthesized *via* Suzuki coupling copolymerization of the monomer **3D**, **2B** and **2C** with the molar feed ratio of 50:0:50, 25:25:50 and 10:40:50, respectively, using  $Pd(PPh_3)_4$  and  $K_2CO_3$  as the catalytic system and THF/ $H_2O$  as the solvent and then stirring at  $85\text{ }^\circ\text{C}$  for 3 days under argon atmosphere. After purification, pale yellow solids were obtained and their conversion is 28-40%. In terms of the molar feed ratio of acridine and carbazole units in the backbone, these polymers were

denoted as **S2-11**, **S2-31** and **S2-91**. Among them, **S2-11** is alternating copolymers.

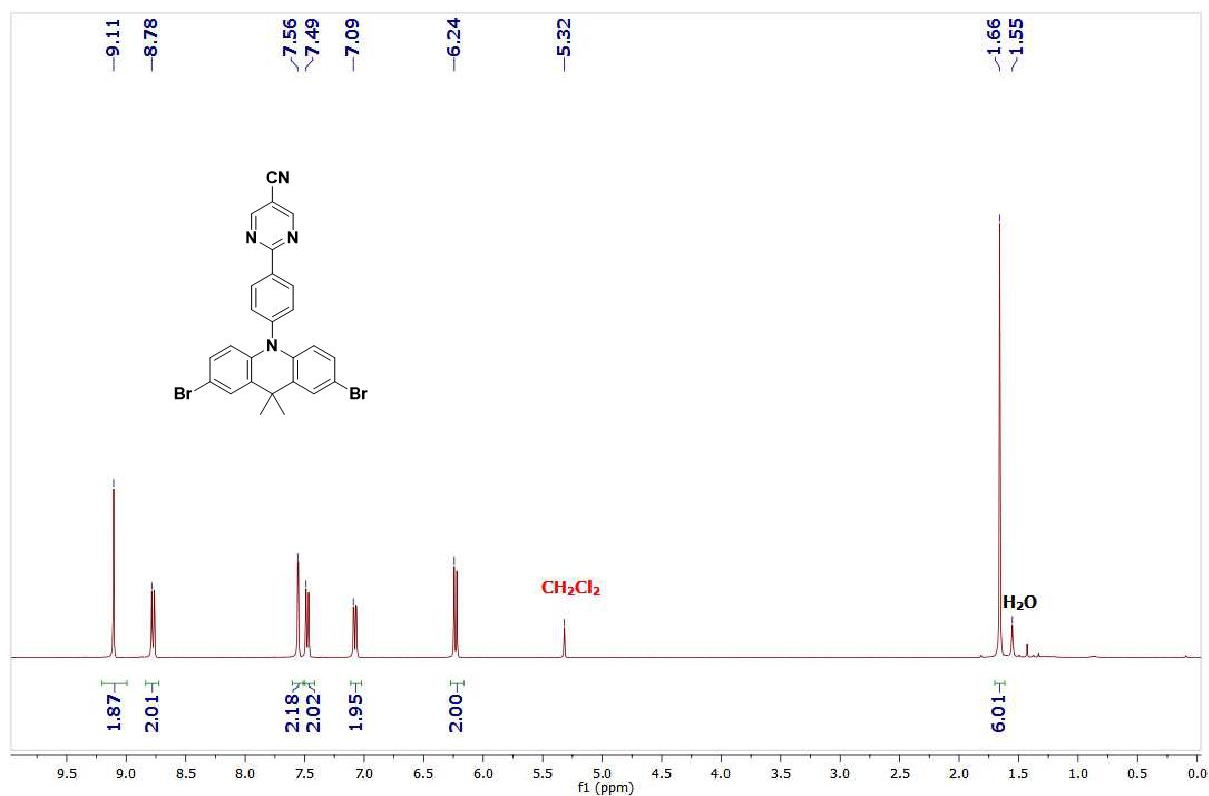


Figure 3.3.2  $^1\text{H}$  NMR spectrum of the monomer **3D** in  $\text{CD}_2\text{Cl}_2$ .

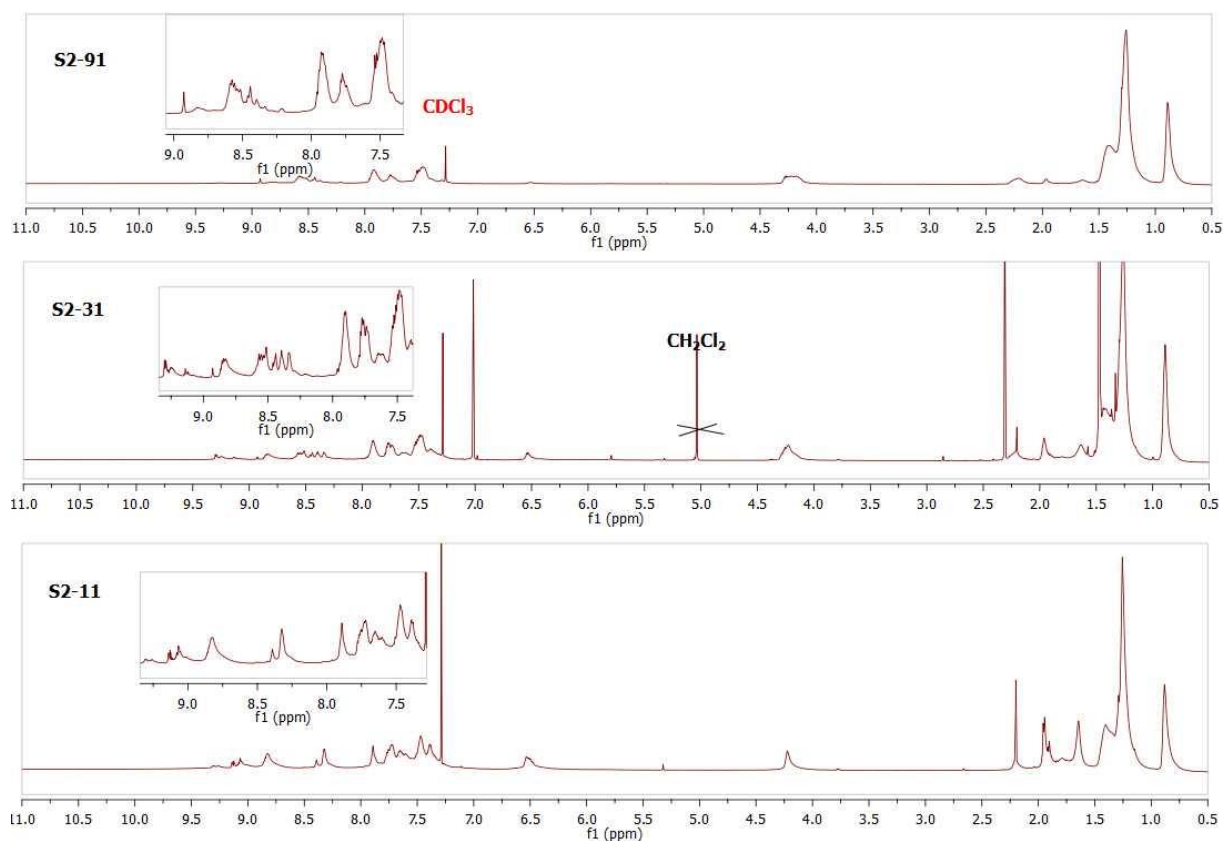
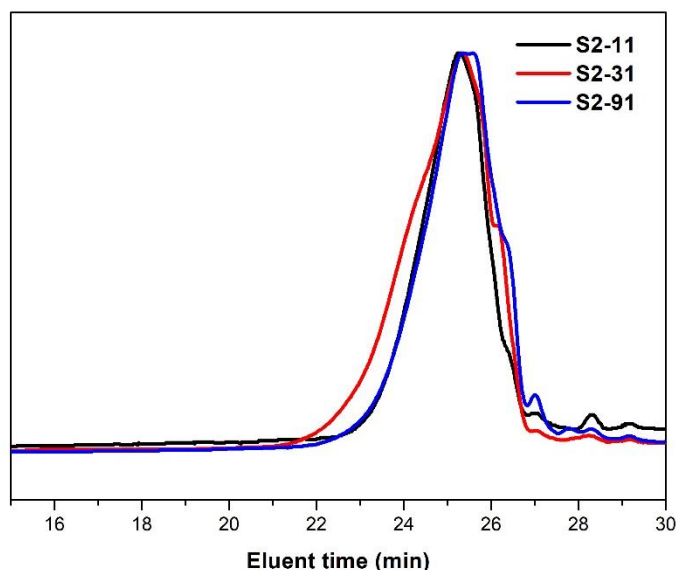


Figure 3.3.3  $^1\text{H}$  NMR spectra of **S2** polymers in  $\text{CDCl}_3$  (600MHz).

The obtained polymers can be readily dissolved in common polar organic solvents, including THF, DCM, and CHCl<sub>3</sub>. The structures of monomers and polymers were confirmed by NMR measurements (Figure 3.3.3) and elemental analysis (Table 3.3.1). Compared to the NMR spectra of monomers, the signals of the polymers in NMR spectra are broad and overlapped. The signals around 4.25 ppm are attributed to the protons of -CH<sub>2</sub> groups connected to the N atom of carbazole units, while the overlapped signals in the range of 0.8-2.5 ppm belong to the alkyl protons in the side groups attached to the carbazole groups as well as the methyl groups in the acridine units. Besides, the signals from 9.0 to 9.5 ppm are ascribed to the acridine rings.

The dispersity and molecular weight of **S2** polymers were also determined by SEC in THF at 40 °C with polystyrene as standard (Figure 3.3.4). Their relative number-average molecular weights ( $M_{n,SEC}$ ) are 3.4-4.2 kDa, with the dispersity ( $M_w/M_n$ ) of 1.28-1.56. The molecular weights are not so large and the number of repeating units ( $X_{n,SEC}$ , see the structures in scheme 3.3.1) are calculated to be 4.3-5.1, thus these polymers can also be regarded as oligomers.

The elemental analysis (EA) was also used to determine the composition of the polymers. As shown in Table 3.3.1, similar to the results of the **S2** polymer series, there is also a difference between the real and the theoretical values. This phenomenon results from the remained Br or pinacol ester in the polymers, as well as the theoretical values calculated from the feeding ratio of monomers.



**Figure 3.3.4** SEC curves of **S2** polymers.

**Table 3.3.1** The physical properties of **S2** polymers

Polymers	$M_{n,SEC}$ (kDa)	$X_{n,SEC}$	$M_w/M_n$	Conversion (%)	C:H:N <sup>a</sup>	C:H:N <sup>b</sup>
<b>S2-11</b>	3.9	5.1	1.28	40	80.08 : 6.89 : 8.52	83.79 : 7.16 : 9.05
<b>S2-31</b>	4.2	5.4	1.56	28	83.25 : 9.18 : 4.69	85.82 : 8.14 : 6.04
<b>S2-91</b>	3.4	4.3	1.45	29	83.70 : 9.48 : 4.38	86.76 : 8.79 : 4.44

<sup>a</sup> result from elemental analysis; <sup>b</sup> theoretical values from feeding ratio without considering end groups

### 3.3.2 Photophysical properties

The steady-state and the time-resolved fluorescence of **S2** polymers were investigated in solution and solid-state. These investigations were performed in collaboration with the OPERA laboratory at Kyushu University in the scope of the JSPS core-to-core program between OPERA and IPCM (one month stay at OPERA in 2019).

#### 3.3.2.1 In dilute solution

##### *Steady-state measurements*

The steady-state UV-vis absorption and photoluminescence (PL) spectra of **S2** polymers in dilute toluene and chloroform are depicted in Figure 3.3.5 and Figure 3.3.6, respectively, and their photophysical properties in two different solvents are summarized in Table 3.3.2.

The absorption spectra of these polymers are almost identical in toluene and CHCl<sub>3</sub>. The main absorption locates at 288-308 nm, assigned to the  $\pi$ - $\pi$  transition of the backbones. The shoulder around 336 nm gradually intensifies with the increasing content of the **Pm5** unit, attributed to the extended conjugation of acridine rings with respect to 3,6-carbazole rings. The very weak absorption at long wavelength ( $\geq 400$  nm) is ascribed to the intramolecular charge transfer (CT) typical of D-A systems. In contrast, the PL spectra of **S2** polymers in toluene are quite different from that in CHCl<sub>3</sub>. In toluene, all PL spectra of these polymers are broad, and among them, **S2-31** and **S2-91** show a dual emission: one weak emission around 420 nm assigned to the  $\pi$ - $\pi$  transition from carbazole fragment, and another intense and broad band peaked at 579 nm for **S2-31** and 548 nm for **S2-91**), attributed to the CT emission of the TADF chromophores. The dual emissions could arise from the incomplete inter/intra-chain energy transfer from the carbazole fragment to the **Pm5** unit.

**S2-11** displays only a broad emission with a maximum at 601 nm, which is ascribed to the CT band from the TADF chromophore, implying that the energy transfer from the polymer backbone to the **Pm5** unit is complete. In CHCl<sub>3</sub>, **S2-11** and **S2-31** exhibit ambiguous and featureless emission spectra with emission bands slightly red-shifted from 601 nm to 604 nm for **S2-11** and from 579 nm to 584 nm for **S2-31**, due to their CT character. Another interesting point is that **S2-91** exhibits a well-resolved dual emission peaked at 385 nm and 516 nm in CHCl<sub>3</sub>, which is remarkably blue-shifted compared to toluene. The possible reason for the redshift in toluene is that these polymers form aggregates with each other, due to poor solubility, whereas no aggregation forms in CHCl<sub>3</sub>. The elimination of aggregation results in a blue shift in emission, as a result of the increase of the S<sub>0</sub>-S<sub>1</sub> energy gap. In the meanwhile, the higher polarity of CHCl<sub>3</sub> than toluene decreases this energy gap, resulting in the red-shift of the emission. Both aggregation and solvatochromism affect the emission spectra of **S2** polymers simultaneously and compete with each other. For **S2-91**, which is the polymer with the more important separation between the **Pm5** units, the elimination of aggregation plays a

predominant role, consequently, a significant blue shift occurs. While for **S2-11** and **S2-31**, the interplay of aggregation and solvatochromism leads to little change in the conjugation of the polymers, resulting in a small red shift in emission.

Based on the previous reports, it can be deduced that the TADF chromophore in **S2** polymers consists of the **Pm5** unit and the two directly connected carbazole rings. Therefore, these polymers would display a similar main emission band, which is attributed to intramolecular CT from the same TADF chromophore. However, the main emission maxima of these polymers in toluene are gradually red-shifted with increasing **Pm5** content ratio in the polymers, which is another indication of the existence of aggregation in toluene.

According to the absorption and emission spectra, the Stokes shift was calculated as well for **S2-11**, **S2-31**, and **S2-91**, being comprised between 13000 and 19000  $\text{cm}^{-1}$  in toluene or  $\text{CHCl}_3$  (see table 3.3.2).

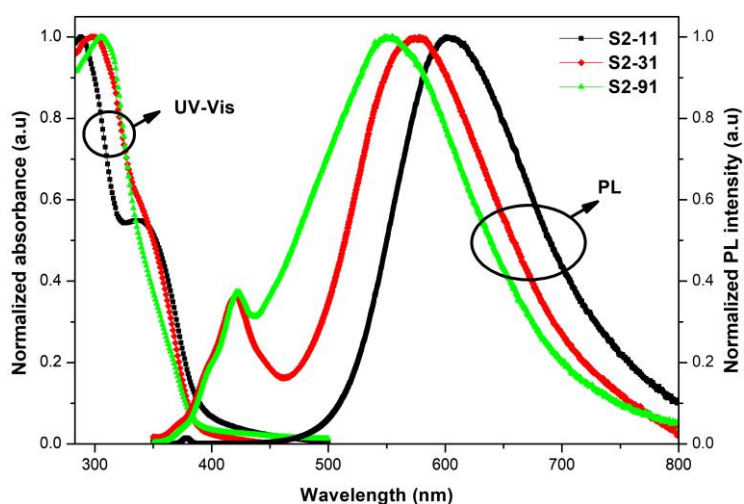


**Figure 3.3.5** The normalized UV-vis absorption and PL spectra of **S2** polymers in toluene.

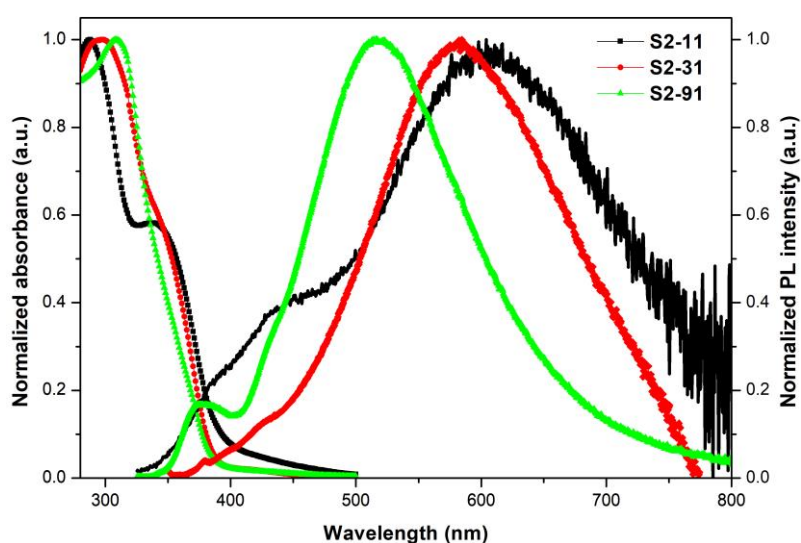


**Figure 3.3.6** The normalized UV-vis absorption and PL spectra of **S2** polymers in  $\text{CHCl}_3$ .

**Table 3.3.2** Photophysical parameters of **S2** polymers in solvents

	$\lambda_{\text{abs}}^{\text{a}}$ (nm)	$\lambda_{\text{abs}}^{\text{b}}$ (nm)	$\lambda_{\text{PL}}^{\text{a}}$ (nm)	$\lambda_{\text{PL}}^{\text{a}}$ (nm)	PLQY <sub>toluene</sub> <sup>c/d</sup> (%)	PLQY <sub>CHCl<sub>3</sub></sub> <sup>c/d</sup> (%)	Stokes shift (cm <sup>-1</sup> ) <sup>a/b</sup>
<b>S2-11</b>	288,336	288,335	601	604	10 / 27	0.7 / 0.8	18100 / 18200
<b>S2-31</b>	298,341	298,343	420,597	584	16 / 44	1.3 / 0.6	16300 / 16400
<b>S2-91</b>	305	308	421,548	380,516	9 / 23	1.5 / 2.8	14500 / 13100

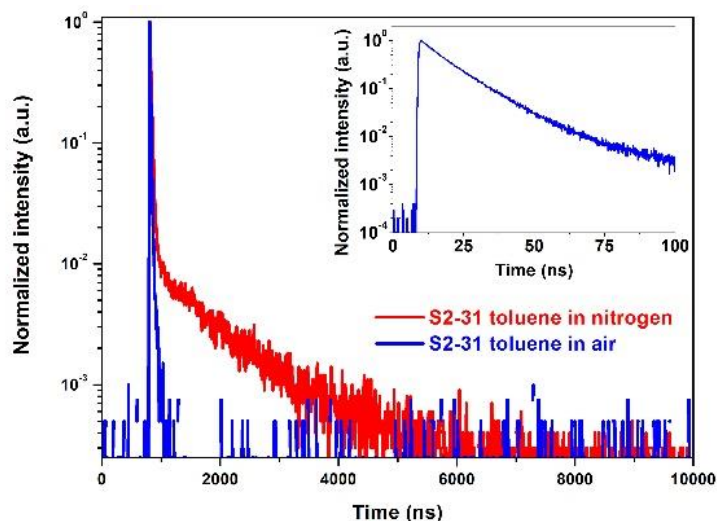
<sup>a</sup> Measured in toluene; <sup>b</sup> Measured in CHCl<sub>3</sub>; <sup>c</sup> Measured in air atmosphere; <sup>d</sup> Measured after nitrogen-bubbling for 15 min.

The photoluminescence quantum yields (PLQYs) of the polymers were measured in the presence and absence of oxygen, as oxygen would normally quench the emission from the triplet excited state. As summarized in Table 3.3.2, all **S2** polymers achieve much higher PLQY in toluene than that in CHCl<sub>3</sub>, and **S2-31** achieves the highest PLQY of 16% and 44% in toluene in air and N<sub>2</sub> atmosphere, respectively. Such behavior indicates that these polymers could present TADF properties.

#### *Time-resolved measurements*

The TADF characteristics of the polymers in toluene were further confirmed by time-resolved fluorescence spectroscopy with time-correlated single-photon counting (TCSPC). As demonstrated in Figure 3.3.7, the transient PL decay spectra in air and nitrogen atmosphere are given in Figure 3.3.7 and the PF and DF lifetimes were examined in detail.

In each PL decay curve, PF and DF components can be easily observed and be fitted with a mono-exponential function, respectively. The data are recorded in Table 3.3.3. The DF ratio of each polymer is not so high (< 25%). Moreover, short delayed components (< 1 $\mu$ s) were clearly observed after nitrogen-bubbling for 15 min, indicating that the delayed components are originated from the triplet states of the polymers. The obvious existence of DF components is consistent with the large PLQY difference (2-3 folds) in the air and nitrogen atmosphere.



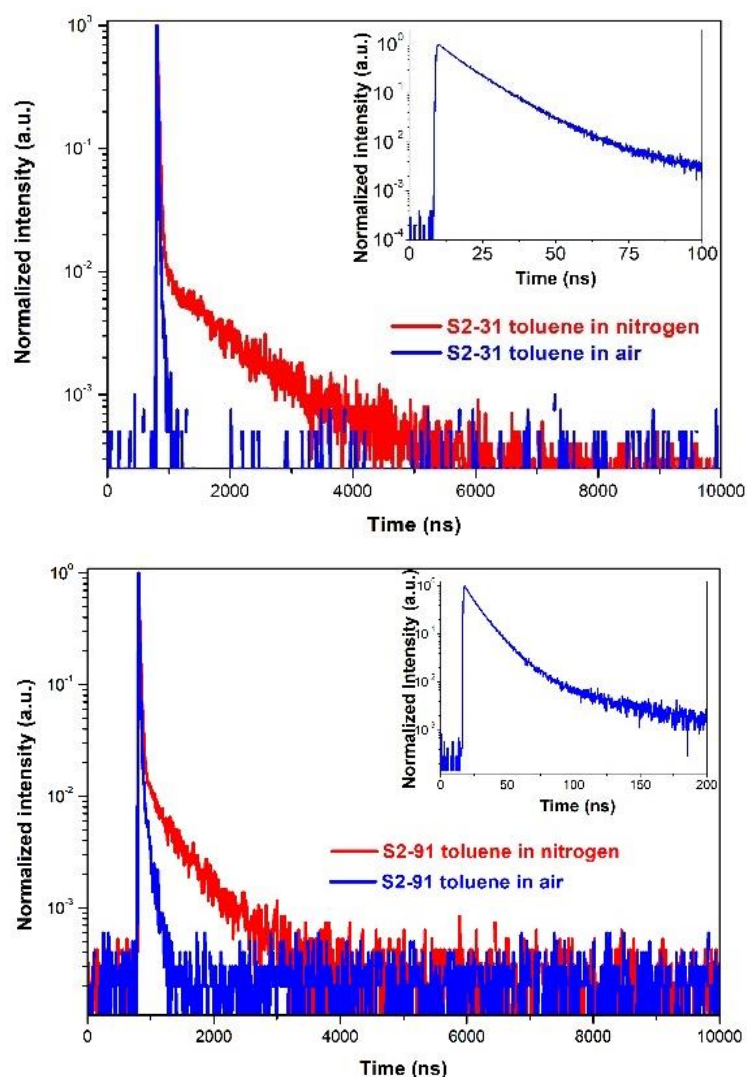


**Figure 3.3.7** The transient PL decay spectra of **S2** polymers in toluene.

**Table 3.3. 3** PF and DF lifetimes of **S2** polymer in toluene measured by TCSPC

	$A_{PF}$	$\tau_{PF}$	$A_{DF}$	$\tau_{DF}(ns)$	$\phi_{DF}/\phi_{PF}$
<b>S2-11</b>	12696.5	17.4	93.0805	532	18.3 / 81.7
<b>S2-31</b>	15009.2	20.8	105.877	896	23.3 / 76.7
<b>S2-91</b>	14627	19.4	154.543	458	20.0 / 80.0

### 3.3.2.2 In solid-state

#### Steady-state measurements

The steady-state UV-Vis absorption and PL spectra of **S2** polymers in neat films were shown in Figure 3.3.8. The photophysical properties are summarized in Table 3.3.4. The absorption spectra of **S2** polymers in neat films are similar to that in dilute solution, with maxima corresponding to the  $\pi$ - $\pi$  transition maxima at 293, 296, and 306 nm for **S2-11**, **S2-31**, and **S2-91**, respectively. **S2-11** also

displays a shoulder around 342 nm, resulting from the extended conjugation of acridine rings concerning the 3,6-carbazole ring. However, in these spectra, the long-wavelength absorption of **S2-11** and **S2-31** corresponding to the CT band of TADF chromophores ( $\geq 400$  nm) almost disappears, which is in adequation with the low PLQYs of **S2-11** and **S2-31** in neat films (Table 3.3.4). Furthermore, the optical energy gap of 2.43, 2.32, and 2.30 eV for **S2-11**, **S2-31**, and **S2-91**, respectively, were obtained from the onset of absorption.

The PL spectra of **S2** polymers only exhibit single broad emissions, with maxima around 605, 581, and 545 nm for **S2-11**, **S2-31**, and **S2-91**, respectively. The absence of dual emissions observed in solution indicates that the energy transfer from the carbazole fragment to the TADF chromophore is more efficient in neat films than that in dilute solution, similarly to previous conclusions in some publications<sup>217</sup>.

In addition, the gradual redshift of the emission band with the increasing **Pm5** unit content in the polymers is also due to the gradual change of the polarity of the medium (more and more polar). From the absorption and emission spectra, the Stokes shift can be calculated for **S2-11**, **S2-31**, and **S2-91** as well and the values are quite similar to the ones determined in solution (Table 3.3.4).

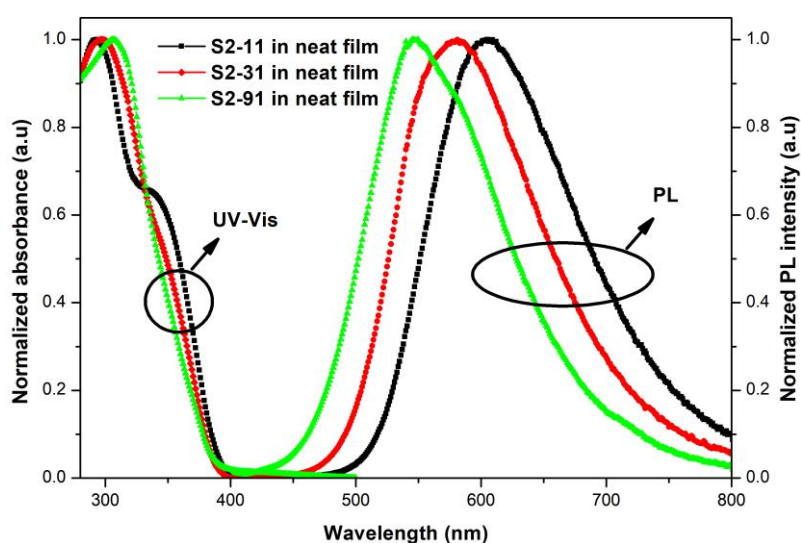


**Figure 3.3.8** The UV-vis absorption and PL spectra of **S2** polymers in neat films.

**Table 3.3.4** The photophysical parameters of **S2** polymers in the neat film

	$\lambda_{\text{abs}}$ (nm)	$\lambda_{\text{PL}}$ (nm)	PLQY <sup>a,b</sup> (%)	HOMO <sup>c</sup> (eV)	Eg <sup>d</sup> (eV)	LUMO <sup>e</sup> (eV)	$\Delta E_{\text{ST}}$ <sup>f</sup> (eV)	Stokes shift (cm <sup>-1</sup> )
<b>S2-11</b>	293,342	605	6 / 6	-5.53	2.43	-3.10	0.06	17601
<b>S2-31</b>	296	581	12 / 12	-5.52	2.32	-3.20	0.07	16572
<b>S2-91</b>	306	545	13 / 23	-5.53	2.30	-3.23	0.10	14331

<sup>a</sup> Measured in air atmosphere; <sup>b</sup> Measured in argon atmosphere; <sup>c</sup> Measured by photoelectron spectroscopy; <sup>d</sup> the optical energy gap calculated from absorption spectra; <sup>e</sup> deduced from HOMO and Eg difference; <sup>f</sup> calculated from streak camera experiments

To estimate the energy levels of the excited states of **S2** polymers in neat film, the singlet and triplet energy values ( $E_S$  and  $E_T$ ) were determined from the fluorescence and phosphorescence spectra, respectively (Figure 3.3.9). The  $E_S$  values of **S2-11**, **S2-31**, and **S2-91** are 2.50, 2.63, and 2.81 eV, and the  $E_T$  values of **S2-11**, **S2-31**, and **S2-91** are 2.44, 2.56, and 2.71 eV, respectively. The  $\Delta E_{ST}$  values of **S2-11**, **S2-31**, and **S2-91** were calculated to be 0.06, 0.07, and 0.10 eV, respectively.

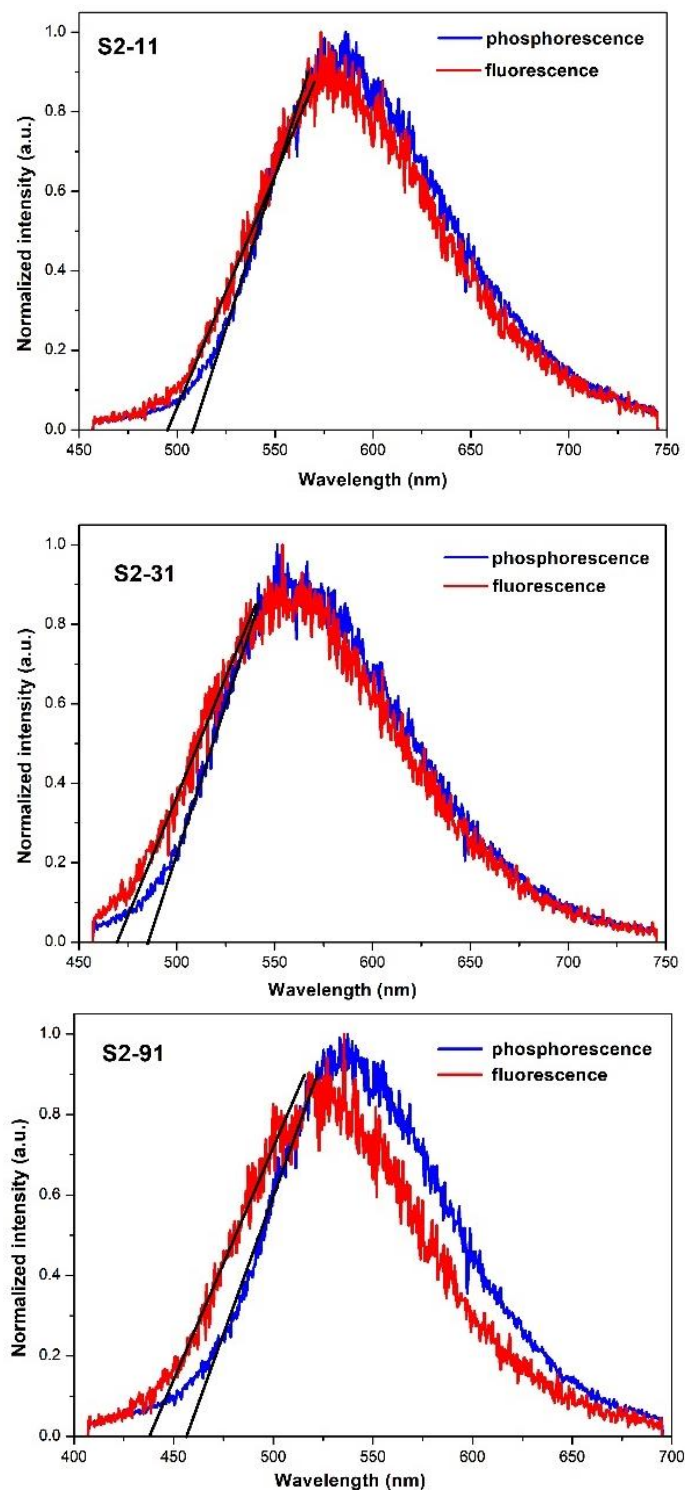


**Figure 3.3.9** Fluorescence (300K) and phosphorescence (17K) spectra of **S2** polymers in neat film measured by a streak camera.

As shown in Figure 3.3. 10, the HOMO energy level of **S2** polymers was determined in neat films by photoelectron spectroscopy, and the values of **S2-11**, **S2-31**, and **S2-91** neat films are -5.53, -5.52, and -5.53 eV, respectively. The LUMO energy level for each polymer was estimated by the sum of the HOMO energy level and the optical energy gap (Table 3.3.4).

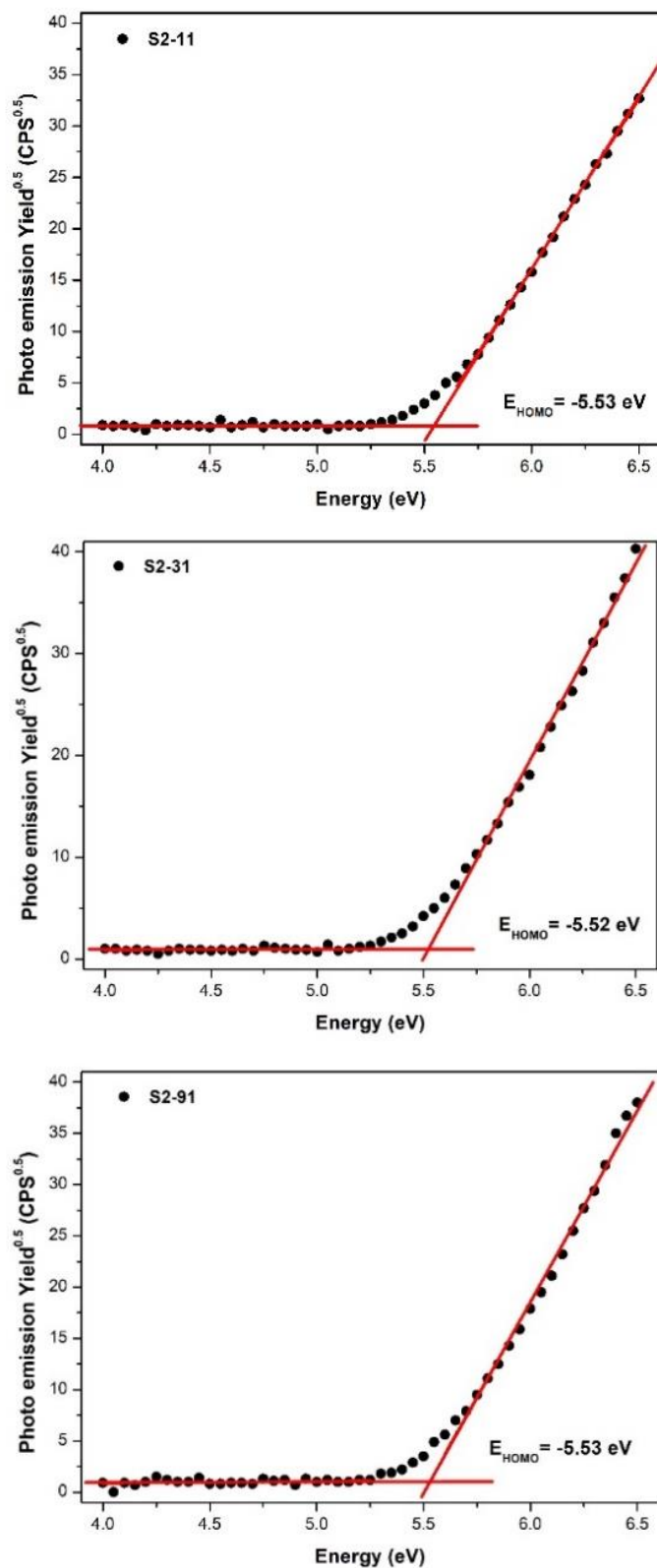


Figure 3.3. 10 Photoelectron spectra of S2 polymers in neat film.

The PLQYs of **S2-11** and **S2-31** neat films measured in argon atmosphere are 6 % and 12 %, respectively, much lower than that in toluene. These low values are probably due to important concentration quenching phenomena. Thus, CBP was selected as the matrix to fabricate blend films. The PLQYs of the blend films with different concentrations of **S2** polymers were examined and the results are summarized in Table 3.3.5.

PLQYs of **S2-11** and **S2-31** neat films clearly increase by decreasing the ratio of **S2-11** or **S2-31** in blend films, confirming the aggregation-caused quenching in neat film. Note that **S2-91** exhibits the same PLQY in the neat film as that in toluene, demonstrating that this polymer, in which the TADF units are already dispersed along the polymer backbone, is less sensitive to aggregation quenching.

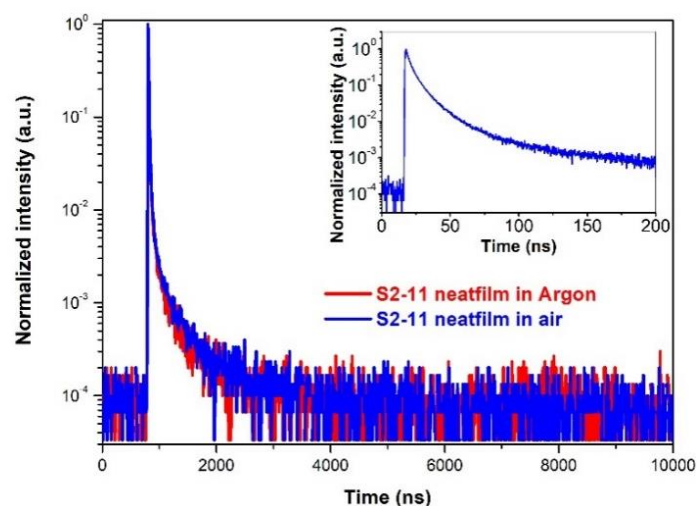
**Table 3.3.5** PLQYs of **S2** polymers in CBP doped films with different content

	100%	50%	40%	30%	20%	10%	5%
<b>S2-11</b>	5.8	10.3	12.9	16.8	24.3	26.0	39.9
<b>S2-31</b>	12.3	15.4	17.8	23.4	26.6	34.4	35.3
<b>S2-91</b>	22.9	18.5	24.5	21.4	26.6	27.6	29.6

#### *Time-resolved measurements*

TADF feature of **S2** polymers was further confirmed by analysis of the neat and doped films transient PL characteristics using time-resolved fluorescence spectroscopy with time-correlated single-photon counting (TCSPC) and a streak camera.

The transient PL decay spectra of **S2** polymers in neat films were preliminarily recorded by the TCSPC technique (Figure 3.3. 11). For **S2-11** and **S2-31**, the PL decay curves are almost overlapped in either argon or air atmosphere, while **S2-91** displays a clear difference. Similar to the phenomena in toluene, both PF and DF components can be clearly observed in the transient PL decay curves in argon: the PF component can be fitted with a mono-exponential, while the DF component can be fitted with a bi-exponential function. The data are summarized in Table 3.3. 6. And the polymers possess shorter PF and DF lifetimes, with an increasing ratio of the acceptor units in the polymer.



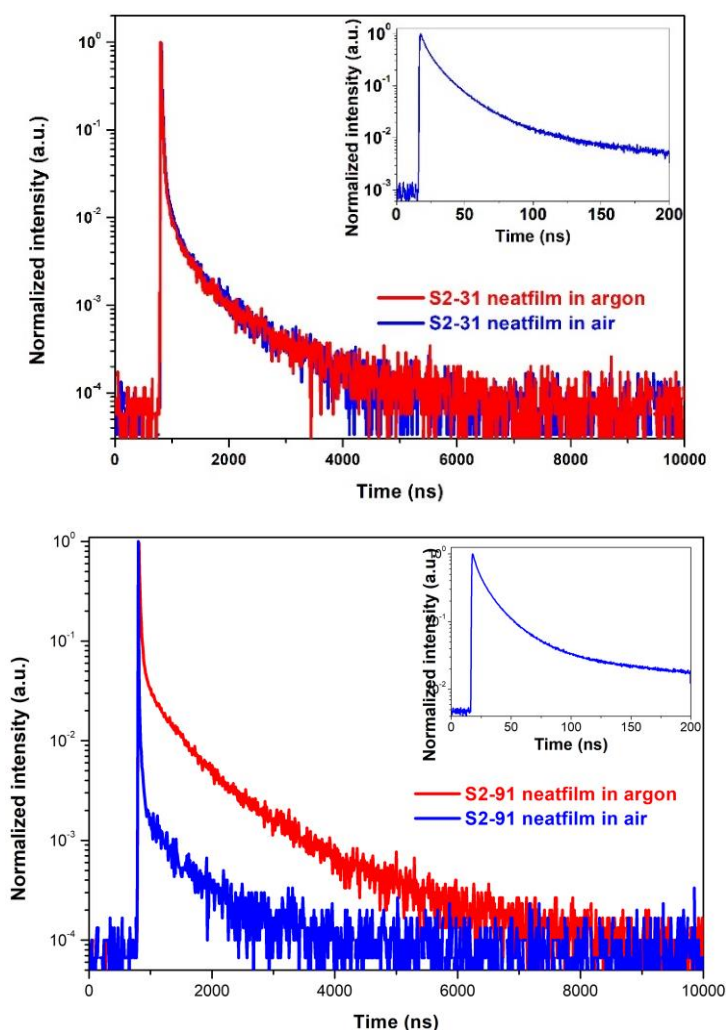


**Figure 3.3. 11** Transient PL decay spectra of **S2** polymers in neat films recorded by TCSPC.

**Table 3.3. 6** The photophysical parameters of **S2** polymers in neat films measured by TCSPC

	$A_{PF}$	$\tau_{PF}$ (ns)	$A_{DF1}$	$\tau_{DF1}$ ( $\mu$ s)	$A_{DF2}$	$\tau_{DF2}$ ( $\mu$ s)	$\phi_{DF1}/\phi_{DF2}/\phi_{PF}$
<b>S2-11</b>	3.75745	4.5	0.00379	0.06	0.0014	0.41	1.3 / 3.3 / 95.4
<b>S2-31</b>	0.14959	9.8	0.00882	0.12	0.00463	0.68	18.0 / 56.0 / 26.0
<b>S2-91</b>	0.61875	11.1	0.00181	0.26	0.00073	1.06	5.9 / 9.5 / 84.6

The temperature dependence of **S2** polymers in neat films was also measured by streak camera from 50 to 300 K and their PL decay curves were shown in Figure 3.3. 12. The fluorescence decay spectra of **S2** polymers consist of a similar nanosecond-scale component and a varying microsecond-scale component, which are ascribed to the prompt and delayed fluorescence, respectively. As already observed in section 3.2.2.2, the DF components of the different neat films in vacuum are longer than those observed by TCSPC under simple argon flow. This indicates that the Ar flow is not enough to remove all the O<sub>2</sub> in the films and that the PLQYs in neat film determined previously are probably a little underestimated. The DF lifetimes of **S1** polymers at room temperature in vacuum are

summarized in Table 3.3.7. The PF components exhibit almost no variation with temperature, but the DFs change significantly with temperature as shown in Figure 3.3.12.

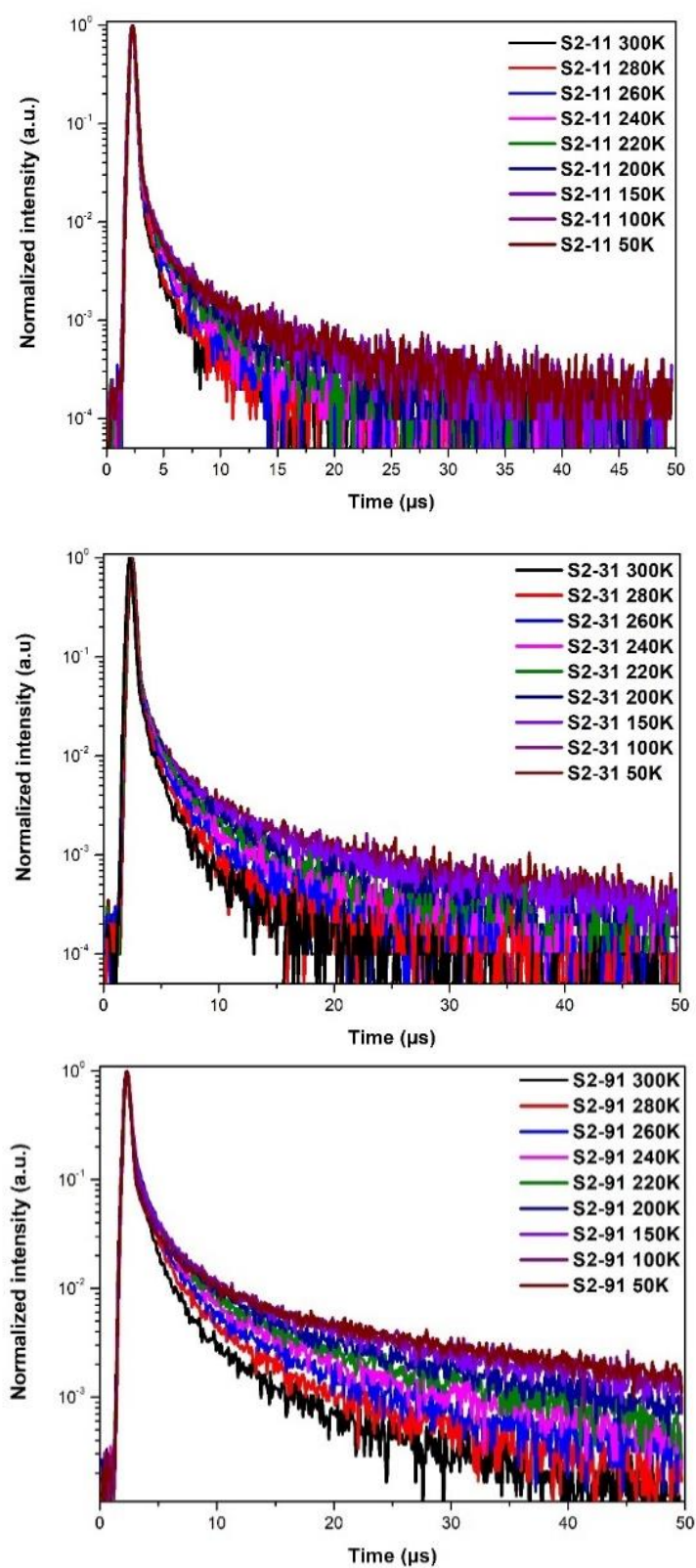


**Figure 3.3. 12** The temperature-dependent PL decay spectra of S2 polymers in neat films measured by a streak camera from 50 to 300 K.

The delayed fluorescence component can be fitted with a bi-exponential function. As shown in Table 3.3.7, 3.3.8, and 3.3.9, with the temperature decrease, the DF lifetimes increase, which is consistent with the TADF mechanism.

**Table 3.3. 7** DF lifetimes of **S2-11** in the neat films (50-300K)

T (K)	$A_{DF1}$	$\tau_{DF1}(\mu s)$	$A_{DF2}$	$\tau_{DF2}(\mu s)$	$R^2$
50	0.00993	0.855	0.00419	5.49	0.98781
100	0.01423	0.717	0.00516	5.15	0.98927
150	0.02187	0.678	0.00771	3.92	0.9915
200	0.0222	0.663	0.00732	3.55	0.99342
220	0.01503	0.599	0.0069	3.16	0.99325
240	0.01267	0.540	0.00779	2.49	0.99042
260	0.01375	0.517	0.00766	2.28	0.99190
280	0.01151	0.375	0.00758	1.83	0.99614
300	0.22728	0.303	0.01199	1.73	0.99426

**Table 3.3. 8** DF lifetimes of **S2-31** in the neat films (50-300K)

T (K)	$A_{DF1}$	$\tau_{DF1}(\mu s)$	$A_{DF2}$	$\tau_{DF2}(\mu s)$	$R^2$
50	0.01046	0.939	0.00812	5.60	0.99182
100	0.01177	1.037	0.00715	6.16	0.99451
150	0.04293	0.924	0.01014	5.18	0.99456
200	0.0271	0.799	0.01076	4.19	0.99437
220	0.01675	0.882	0.00826	4.01	0.99666
240	0.01651	0.781	0.00802	3.81	0.99674
260	0.0268	0.676	0.01144	2.87	0.99577
280	0.0289	0.555	0.01336	2.24	0.99623
300	0.22597	0.389	0.03118	1.64	0.99508

**Table 3.3. 9** DF lifetimes of **S2-91** in the neat films (50-300K)

T (K)	$A_{DF1}$	$\tau_{DF1}(\mu s)$	$A_{DF2}$	$\tau_{DF2}(\mu s)$	$R^2$
50	0.01598	1.34	0.01495	8.76	0.99602
100	0.0616	1.17	0.02545	6.73	0.99623
150	0.04202	1.17	0.0231	6.65	0.99724
200	0.07957	1.08	0.02571	6.05	0.99756
220	0.07159	1.08	0.02295	5.89	0.9980
240	0.02879	0.94	0.0208	5.04	0.99778
260	0.04818	0.90	0.02188	4.51	0.99798
280	0.0497	0.78	0.02262	3.77	0.99745
300	0.12344	0.68	0.02806	2.99	0.99805

The transient PL decay curves of **S2** polymers were further investigated in CBP doped films (10 wt%), as represented in Figure 3.3. 13. Similar to the curves in neat films, even though there is no distinct difference between the PL decay curves in argon and air atmosphere, all the PL decay curves are composed of two obvious components: prompt and delayed components.

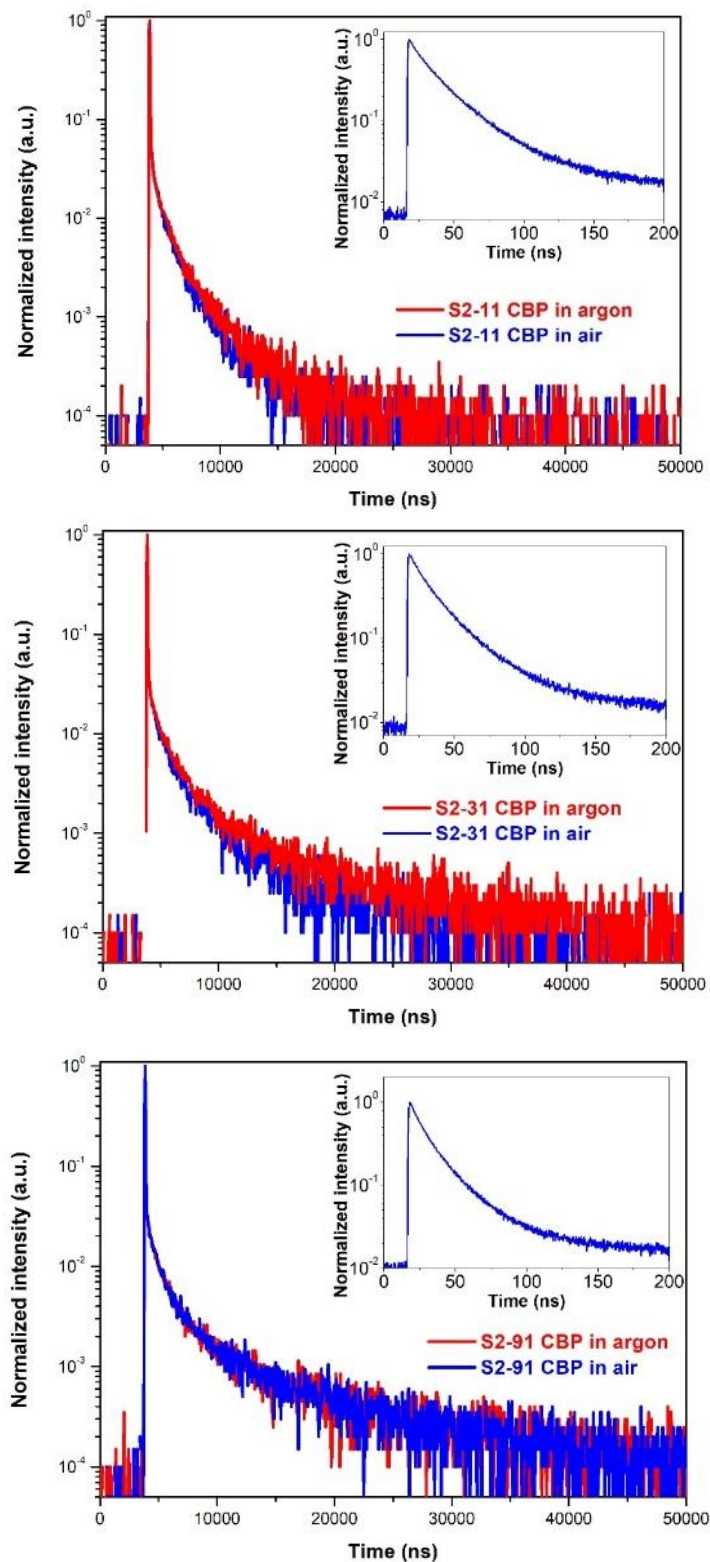


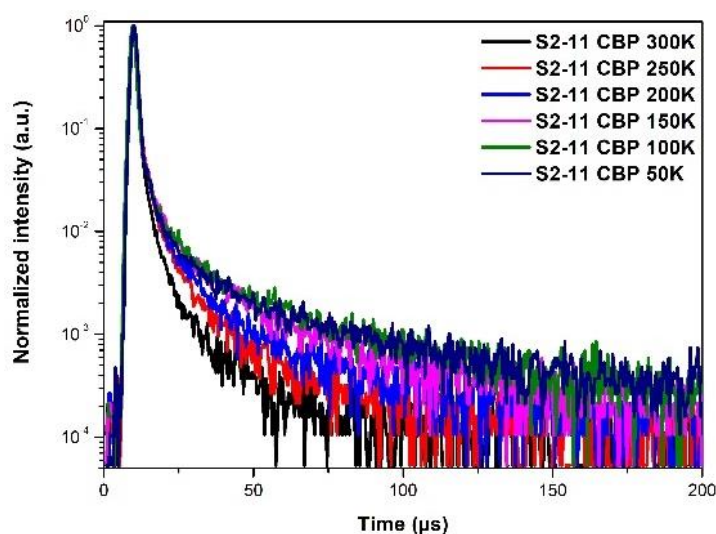
**Figure 3.3. 13** The fluorescence decay curves of **S2** polymers in CBP doped films at room temperature.

The PF and DF lifetimes of the polymers in CBP doped films were calculated and the detailed information is shown in **Table 3.3. 10**. In CBP doped film (10 wt%), all the polymers exhibit relatively short DF lifetime with values of 0.64-0.89  $\mu\text{s}$  and 2.4-5.3  $\mu\text{s}$ , indicative of a rapid reverse intersystem crossing (RISC) potentially interesting in device configuration (low the roll-off).

**Table 3.3. 10** The photophysical parameters of **S2** polymers in CBP doped films (10 wt%)

	$A_{\text{PF}}$	$\tau_{\text{PF}}(\text{ns})$	$A_{\text{DF1}}$	$\tau_{\text{DF1}}(\mu\text{s})$	$A_{\text{DF2}}$	$\tau_{\text{DF2}}(\mu\text{s})$	$\phi_{\text{DF1}}/\phi_{\text{DF2}}/\phi_{\text{PF}}$
<b>S2-11</b>	1.01824	20.2	0.0114	0.64	0.0014	2.43	23.3 / 10.9 / 65.8
<b>S2-31</b>	1.5673	16.2	0.01794	0.85	0.00599	4.21	23.2 / 38.3 / 38.5
<b>S2-91</b>	0.4106	14.4	0.02375	0.89	0.00434	5.32	42.1 / 46.1 / 11.8

The temperature dependence of the transient PL decay spectra of **S2** polymers in CBP doped film (10 wt%) was also investigated by a streak camera from 50 to 300 K in vacuum (Figure 3.3.14). We can clearly observe two components in all PL decay curves, among them, the PF components are overlapped with each other. While the delayed components show clear temperature dependence and can be fitted with a bi-exponential function (Table 3.3.11, Table 3.3.12, and Table 3.3.13). For each component, the DF lifetime increases with decreasing temperature. That is consistent with the TADF mechanism in which a longer triplet lifetime at lower temperature results from a slower RISC rate. Note that, as also observed for neat films, the DFs in CBP doped films under vacuum are much longer than those under argon with values at room temperature about 3.3-18.7  $\mu\text{s}$ , in vacuum vs 2.4-5.3  $\mu\text{s}$  under Ar flow (Table 3.3.11, Table 3.3.12 and Table 3.3.13 vs Table 3.3.12). However, these DF components are still small and, as mentioned previously, indicate a rapid RISC potentially interesting in device configuration (low the roll-off). Note also that, here again, the previous PLQYs in CBP doped film determined under argon flow (Table 3.3.13) are probably underestimated.



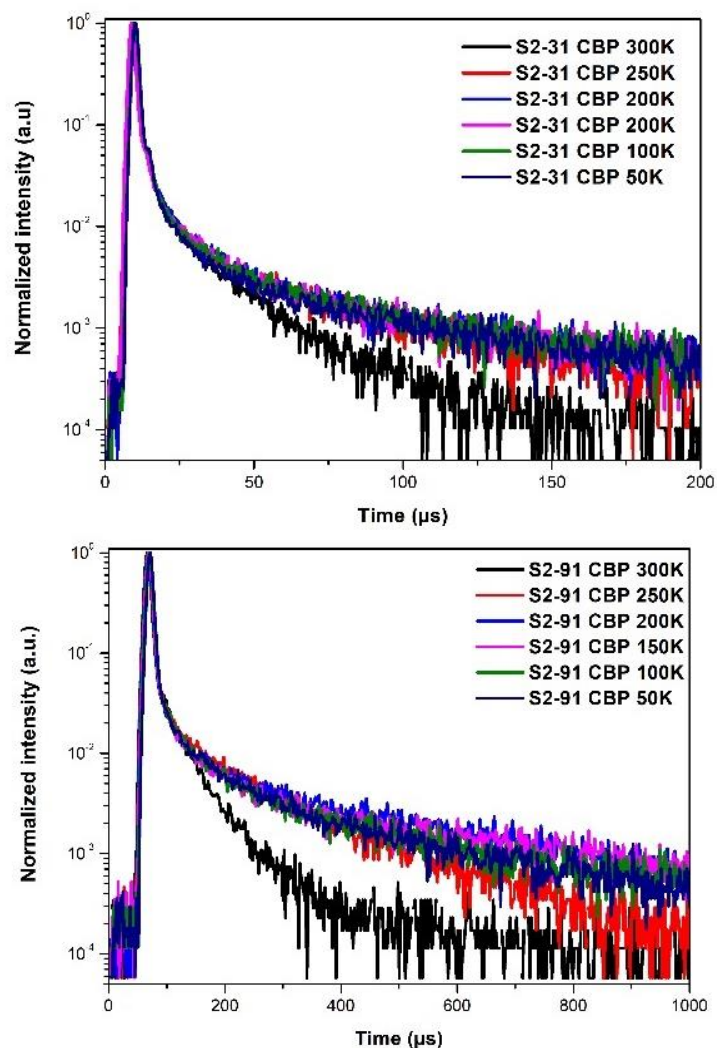


**Figure 3.3. 14** Temperature-dependent PL decay spectra of S2 polymers CBP doped films (10 w%t) measured in vacuum by a streak camera from 50 to 300 K.

**Table 3.3. 11** DF lifetimes of S2-11 in CBP doped films (10 wt%) (50-300K)

T (K)	$A_{DF1}$	$\tau_{DF1}(\mu s)$	$A_{DF2}$	$\tau_{DF2}(\mu s)$	$R^2$
50	0.04781	2.99	0.00819	23.6	0.98932
100	0.03827	2.58	0.01221	18.9	0.99428
150	0.01393	2.80	0.00973	18.5	0.99487
200	0.02346	2.49	0.0093	14.3	0.99565
250	0.01426	2.16	0.00918	11.1	0.99772
300	0.03866	2.04	0.00748	9.5	0.99719

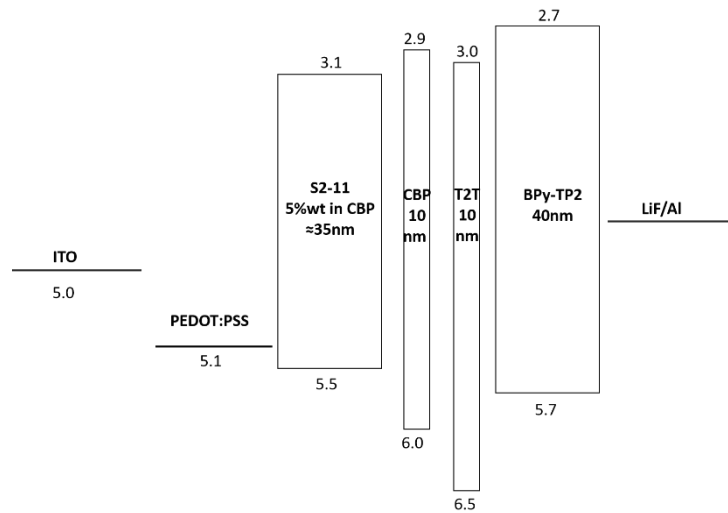
**Table 3.3. 12** DF lifetimes of **S2-31** in CBP doped films (10 wt%) (50-300K)

T (K)	$A_{DF1}$	$\tau_{DF1}(\mu s)$	$A_{DF2}$	$\tau_{DF2}(\mu s)$	$R^2$
50	0.00646	11.3	0.00549	76.3	0.98686
100	0.00994	13.4	0.00561	89.0	0.98732
150	0.00904	9.04	0.00755	62.3	0.98968
200	0.01734	7.41	0.0092	57.7	0.99292
250	0.12638	5.82	0.01556	42.9	0.99282
300	0.04433	3.46	0.02736	18.8	0.99726

**Table 3.3. 13** DF lifetimes of **S2-91** in CBP doped films (10 wt%) (50-300K)

T (K)	$A_{DF1}$	$\tau_{DF1}(\mu s)$	$A_{DF2}$	$\tau_{DF2}(\mu s)$	$R^2$
50	0.00607	10.7	0.00866	82.8	0.98783
100	0.00906	9.52	0.01086	72.1	0.99054
150	0.01045	7.81	0.01094	63.7	0.99118
200	0.02272	6.93	0.01371	63.4	0.98686
250	0.03154	5.72	0.01874	62.2	0.99002
300	0.07876	3.34	0.03695	32.2	0.99534

### 3.3.3 Electroluminescent properties in device configuration

**Figure 3.3. 15** Energy level diagram for the OLED device based on **S2-11**.

We investigated the electroluminescence properties of **S2-11** in OLED configuration. A first solution-processed OLED device was fabricated with the following architecture: ITO/PEDOT:PSS/5% **S2-11** and 95% CBP (35 nm)/CBP (10 nm)/T2T (10 nm)/BPy-TP2 (40 nm)/LiF/Al (see Figure 3.3.15), where PEDOT: PSS and LiF act as the hole- and electron-injecting layer, CBP acts as both the host and hole-transporting layer (HTL), T2T/BPy-TP2 serves as the electron-transporting layer (ETL), and 5% **S2-11** and 95% CBP is used as the emitting layer (EML).

The current density-voltage-luminance ( $J$ - $V$ - $L$ ) characteristics, the EQE *versus* the current density and luminance curves, and the EL spectra for the device are displayed in Figure 3.3. 16. The yellow-emitting OLED device revealed a maximum luminance ( $L_{\max}$ ) of around 5600 cd/m<sup>2</sup>, a peak current efficiency of 4.9 cd/A, an EQE<sub>max</sub> of 1.9% at a low current density, and an EQE<sub>500</sub> of 1.3% at a high luminance of 500 cd/m<sup>2</sup>. Besides, the turn-on voltage at 1 cd/m<sup>2</sup> is around 10 V, and the intensity of electroluminescence increases along with the increment of voltage until 17 V. Even though the preliminary electroluminescent properties of **S2-11** didn't meet the requirements for the applications, further optimizations can be realized through changing the parameters of fabrication methods, as well as doped emitting films and other layers.

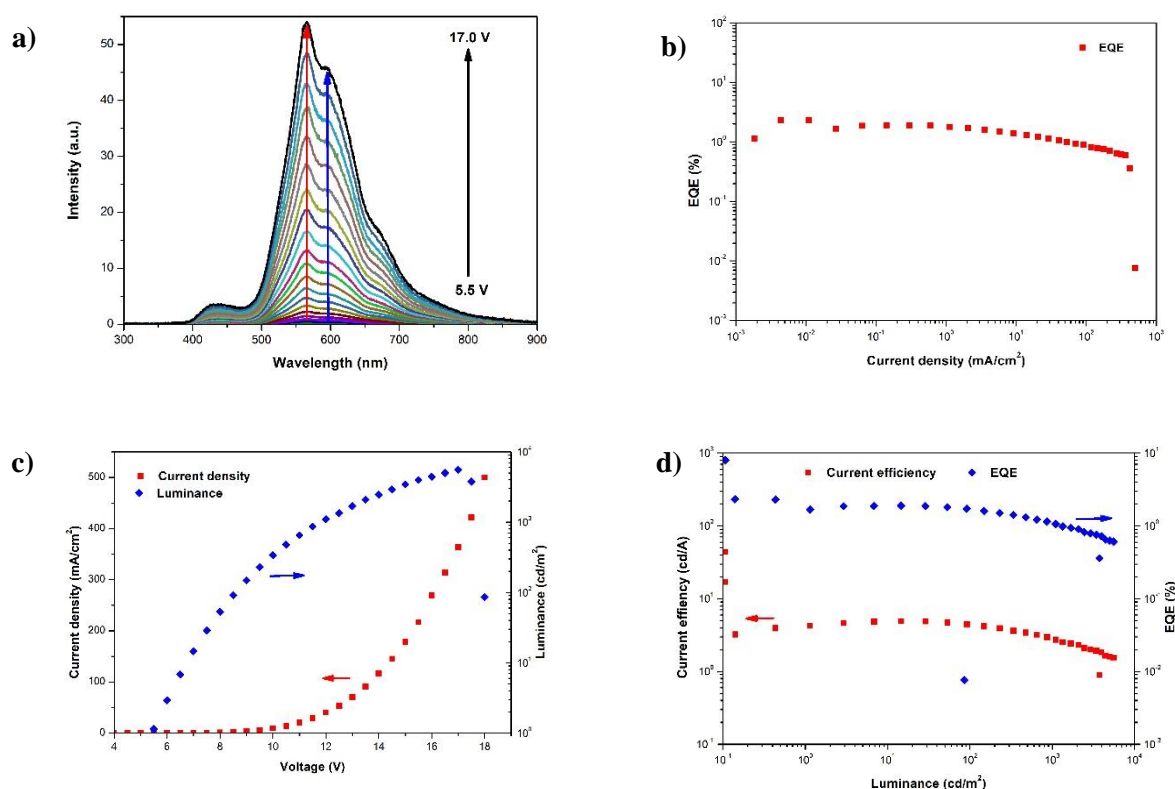


**Figure 3.3. 16** OLED performance of **S2-11**: a) EL spectra at various voltage; b) EQE vs current density c) Current density-voltage-luminance curves; d) Current efficiency and EQE vs luminance.

### 3.3.4 Conclusion

To conclude, we designed and synthesized a new series of yellow-emitting TADF polymers with acridan/carbazole as the backbone and cyano-pyrimidine units as side-groups. The polymers were successfully prepared *via* Suzuki polycondensation. The structures of monomers and **S2** polymers were characterized by NMR, SEC, and elemental analysis.

Their photophysical properties were investigated in solution (toluene and CHCl<sub>3</sub>) and solid-state with steady and time-resolved measurements. The UV-Vis absorption, PL, and phosphorescence (17K)

spectra were recorded. From these spectra, we determined the singlet and triplet energy levels, the optical bandgap, and Stokes shifts of these polymers. Small  $\Delta E_{ST}$  values (0.06-0.1 eV) was also estimated suggesting possible TADF properties., Also, the HOMO/LUMO energy levels of **S2** polymers were determined in neat films by photoelectron spectroscopy, combined with optical measurements.

From the time-resolved measurements, we can confirm that all **S2** polymers exhibit TADF activity. Among the polymers, **S2-31** holds the highest PLQY of 44% in oxygen-free toluene. In the neat film, low PLQYs from 6% to 23% in argon can be obtained and a value as high as 44% can be observed by preparing 5 wt% CBP doped film (**S2-11**).

One solution-processed OLED device using **S2-11** CBP blend film as the EML was prepared and achieved a maximum luminance ( $L_{max}$ ) of around 5600 cd/m<sup>2</sup>, with an EQE of 1.9%. The electroluminescent properties could be further optimized by changing the parameters of the device fabrication, as well as doped emitting films and other layers.

### 3.4 Through-space charge transfer (TSCT) TADF polymers based on 26IPNDCz

As mentioned in **section 3.1.5**, compared to the through-bond conjugation (TBC) system, the through-space conjugation (TSC) systems possess more flexibility and possibilities in designing optoelectronic materials with stable ICT states, owing to its non-covalent structure and spatial delocalization of  $\pi$  electrons.

As described in **section 3.2**, **S1** polymers with TBC system, derived from **26IPNDCz**<sup>265</sup>, have been proved to be TADF polymers, while their PLQYs in solid-state are only modest.

Therefore, in this section, to achieve higher PLQY, we tried to apply the TSC system on the donor (carbazole) and acceptor (isophthalonitrile) units utilized in **S1** polymers. Thus, we designed and synthesized a new series of vinyl polymers **S3** (Figure 3.4.1) which are expected to exhibit TADF character *via* through-space charge transfer (TSCT). In this context, we will present the design, synthesis, structural characterization, and photophysical properties of such polymers.

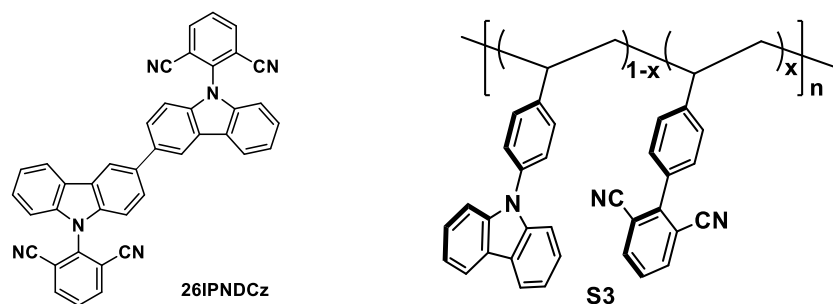
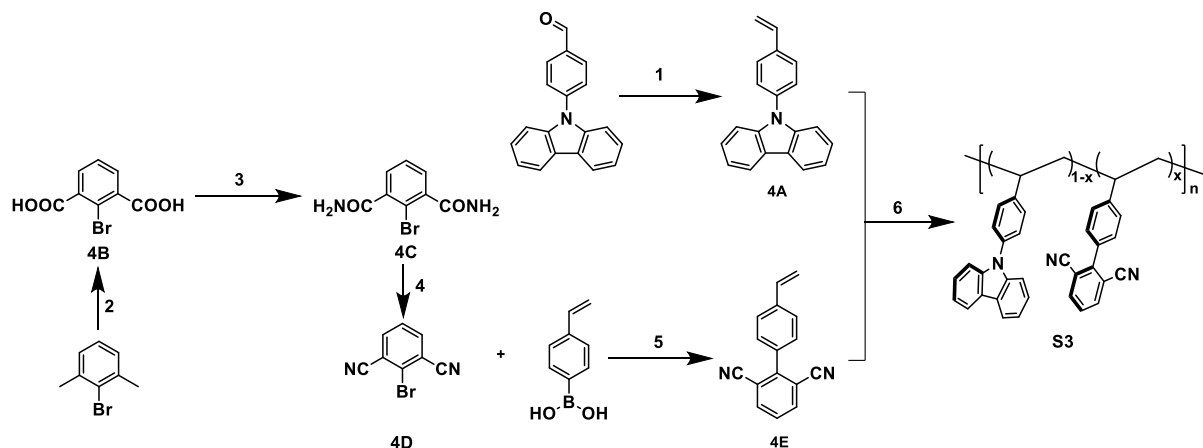


**Figure 3.4.1** Chemical structures of TADF model **26IPNDCz** and **S3** polymer series.

#### 3.4.1 Design, synthesis, and structural characterization

As depicted in Scheme 3.4.1, in order to obtain **S3** polymers with varying ratios of donor and acceptor components, the two monomers **4A** and **4E** were successfully synthesized following the literatures<sup>267–269</sup>, before the polymerization. The electron-donating monomer **4A** was obtained from the commercially available molecule N-(4-formylphenyl)carbazole with a yield of 90%. The electron-withdrawing monomer **4E** was obtained in 4 steps: firstly, the methyl groups of the starting material 2,6-dimethyl-bromobenzene were oxidized by  $\text{KMnO}_4$  to be an acid group ( $-\text{COOH}$ ); secondly, the acid groups of the molecule **4B** was converted to carbonyl chloride groups ( $-\text{COCl}$ ) using thionyl chloride at  $85\text{ }^\circ\text{C}$  in a quantitative yield and then treated by  $\text{NH}_3 \cdot \text{H}_2\text{O}$  at  $0\text{ }^\circ\text{C}$  to give the molecules **4C** with a yield of 52%; thirdly, the  $-\text{CONH}_2$  groups of the molecule **4C** was converted to cyano groups ( $-\text{CN}$ ) to lead to the molecule 2-bromoisophthalonitrile (**4D**) with a high yield of 96%; finally, the monomer **4E** was obtained *via* Suzuki reaction between the molecule **4D** and the commercially available 4-vinylphenylboronic acid, using  $\text{Pd}_2(\text{dba})_3$  as the catalyst, Sphos as the ligand, and  $\text{K}_3\text{PO}_4$  as the base, with a yield of 70%. The detailed synthetic procedures of the two molecules (**4A** and **4E**)

and the intermediates are described in the appendix and their chemical structures were confirmed by both proton and carbon NMR spectra.



**Scheme 3.4.1** Synthetic pathway of **S3** polymers. Condition: 1) triphenylmethylphosphonium iodide, *t*-BuOK, dry THF, argon, 0 °C, 90%; 2) KMnO<sub>4</sub>, H<sub>2</sub>O/*t*-BuOH, 110 °C, overnight, 50%; 3) SOCl<sub>2</sub>, 85 °C, 4 h; NH<sub>3</sub>·H<sub>2</sub>O, 0 °C, 30 min, 52%; 4) POCl<sub>3</sub>, NaCl, reflux, 4 h, 96%; 5) Pd<sub>2</sub>(dba)<sub>3</sub>, Sphos, K<sub>3</sub>PO<sub>4</sub>, 1,4-dioxane/H<sub>2</sub>O, argon, 100 °C, 30 min, 70%; 6) AIBN, dry toluene, 60 °C, 48 h, 23-40%.

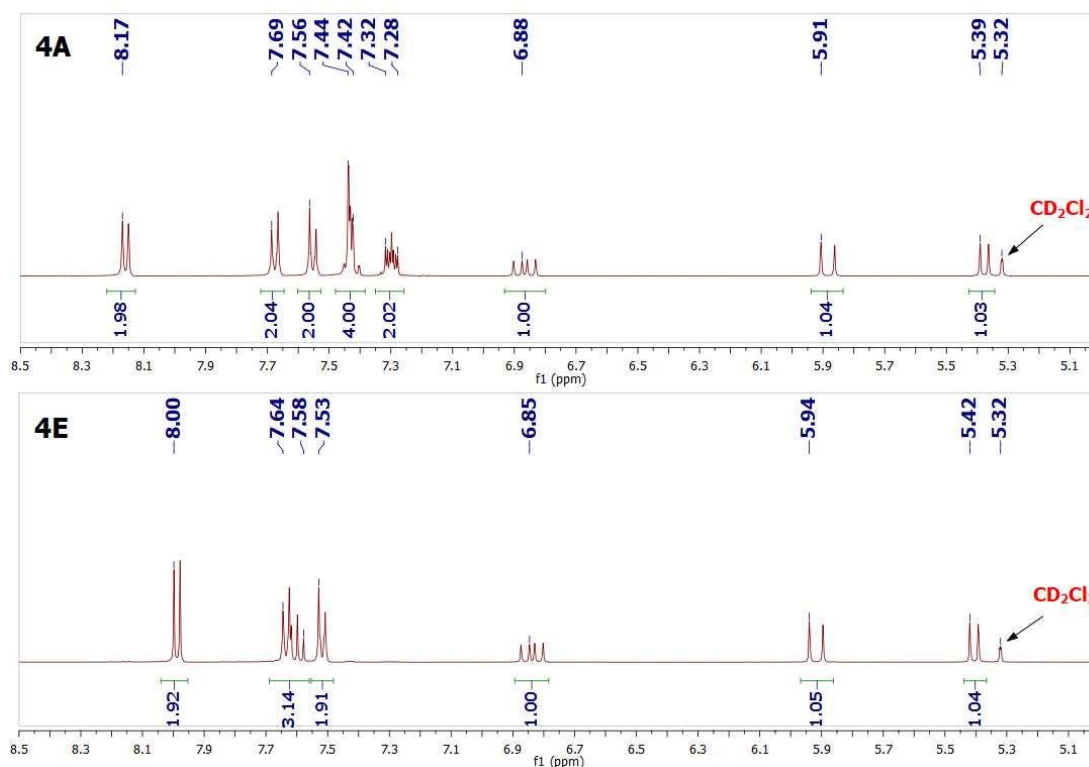


**Figure 3.4.2** <sup>1</sup>H NMR spectra of monomers **4A** and **4E**.

**S3** polymers were prepared by radical polymerization in dry toluene at 60 °C for 48 h, using **4A** and **4E** as monomers together with 5% AIBN as initiator. The **S3** polymer series include six polymers, namely **S3-11**, **S3-31**, **S3-51**, **S3-91**, **S3-955**, **S3-991**, corresponding to the different feed ratios of **4A** : **4E** = 1:1, 3:1, 5:1, 9:1, 95:5, 99:1, respectively.

$^1\text{H}$  NMR spectra of **S3** polymers are represented in Figure 3.4.3. After polymerization, the signals attributed to the vinyl groups ( $-\text{CH}=\text{CH}_2$ ) of the two monomers **4A** and **4E** vanished completely, indicating that no monomers remain in the final polymers. In the meanwhile, new signals, ascribed to the protons of the polymer backbones ( $-\text{CH}-\text{CH}_2-$ ), appear from 2.75 to 1.60 ppm, and the sharp peaks from 8.17 to 7.28 ppm, corresponding to signals of protons of the aromatic rings, became broad. These observations demonstrated that the polymerization is successful. The broad peak around 7.7 ppm is attributed to the proton of the electron-accepting unit (**4E**) and it becomes smaller and smaller, along with the increment of feed ratio of **4A**.

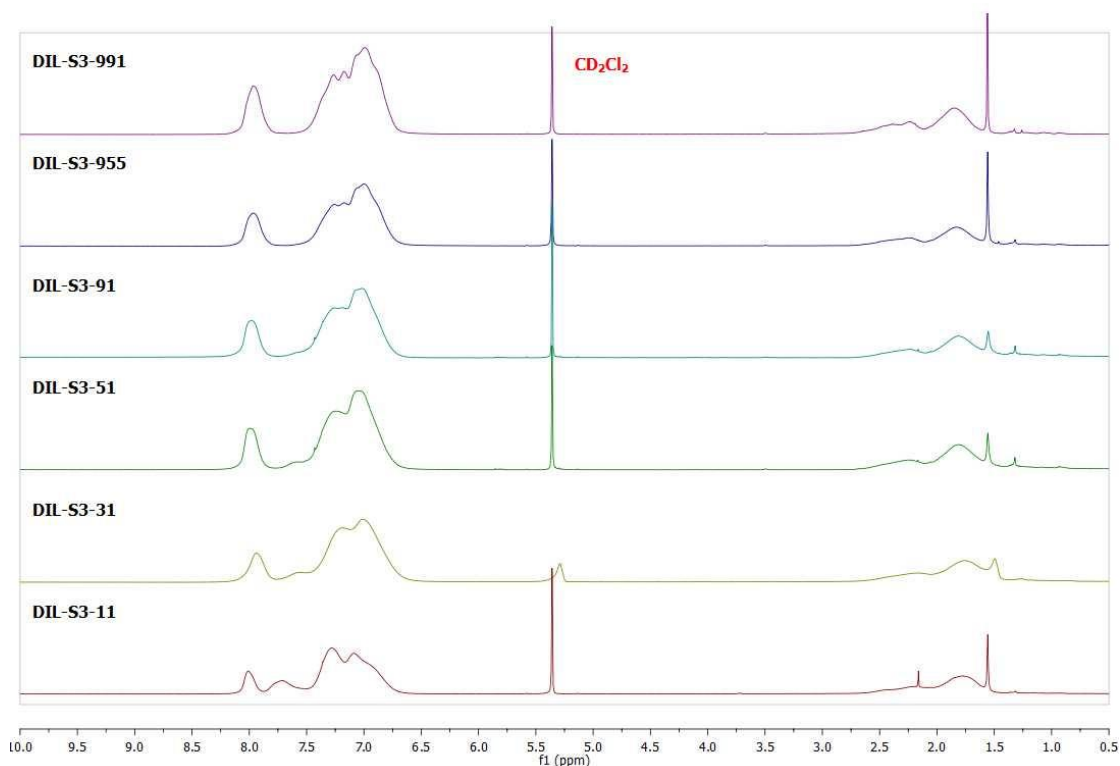


**Figure 3.4.3**  $^1\text{H}$  NMR spectra of **S3** polymer series in  $\text{CD}_2\text{Cl}_2$ .

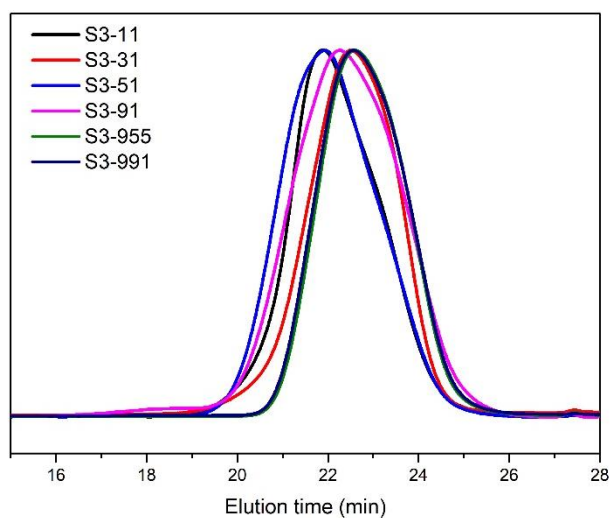


**Figure 3.4.4** SEC curves of **S3** polymers.

Size exclusion chromatography (SEC) was used to study the dispersity and molecular weight of **S3** polymers (Figure 3.4.4). The relative number-average molecular weights ( $M_{n,SEC}$ ) of these polymers are in the range of 18-27 kDa, with the dispersity ( $M_w/M_n$ ) of 1.40-1.76. The real ratios of **4A** and **4E** in copolymers were calculated as well from elemental analysis results (Table 3.4.1) and the resulting degree of polymerization ( $X_{n,SEC}$ ) is between 67 and 103. Besides, the sole SEC peaks confirmed that no small molecules (oligomers or monomers) remain in the polymers.

**Table 3.4.1** Physical properties of **S3** polymers

Polymers	$x_t$	$x_{EA}$	$M_{n,SEC}$ (kDa)	$X_{n,SEC}$	$M_w/M_n$	Conversion (%)	C:H:N
<b>S3-11</b>	0.500	0.549	25	101	1.58	34	84.53 : 4.78 : 8.52
<b>S3-31</b>	0.250	0.312	21	82	1.51	26	85.58 : 5.12 : 6.99
<b>S3-51</b>	0.167	0.208	27	103	1.60	40	86.68 : 5.23 : 6.35
<b>S3-91</b>	0.100	0.123	20	76	1.76	38	86.86 : 5.33 : 5.83
<b>S3-955</b>	0.050	0.049	18	67	1.40	23	87.41 : 5.47 : 5.42
<b>S3-991</b>	0.010	-	18	67 <sup>a</sup>	1.42	26	87.92 : 5.53 : 4.91

$x_t$  value is the theoretical content of **4E** unit in the polymers, calculated from the feed ratio;  $x_{EA}$  value is the real content of **4E** unit in the polymers, calculated from the EA results;  $M_{n, SEC}$  is the relative number-average molecular weight obtained from SEC measurements in THF eluent, calibrated by polystyrene;  $M_w/M_n$  is dispersity; C:H:N is the ratio of C, H and N elements in the polymers, obtained from elemental analysis. Here, the  $x_{EA}$  value of **S3-991** can't be calculated correctly, because the content of **4E** ( $C_{16}H_{10}N$ ) is too low concerning 2-cyanoprop-2-yl unit ( $C_4H_6N$ ), which comes from the decomposition of AIBN and initiates the polymerization.  
<sup>a</sup> calculated according to the feed ratio of **4A** and **4E**.

### 3.4.2 Photophysical properties

After the chemical structure characterization, the photophysical properties of **S3** polymers in both solution and solid-states were measured at the OPERA laboratory of Prof. Chihaya Adachi at Kyushu University in the scope of the JSPS core-to-core program. Unfortunately, I couldn't go to OPERA myself in 2020 due to the COVID19 pandemic.

#### 3.4.2.1 In dilute solution

##### *Steady-state measurements*

The steady-state UV-vis absorption, photoluminescence (PL), and phosphorescence spectra of **S3** polymers (**S3-11**, **S3-31**, and **S3-91**) in dilute toluene solutions are depicted in Figure 3.4.5. The polymers show absorption at around 294 nm which are mainly ascribed to the  $\pi$ - $\pi$  transition of carbazole and isophthalonitrile units in diluted toluene. In the meanwhile, these polymers display well-resolved emission spectra whose maximum are located at 424, 425, and 427 nm for **S3-11**, **S3-31**, and **S3-91**, respectively.

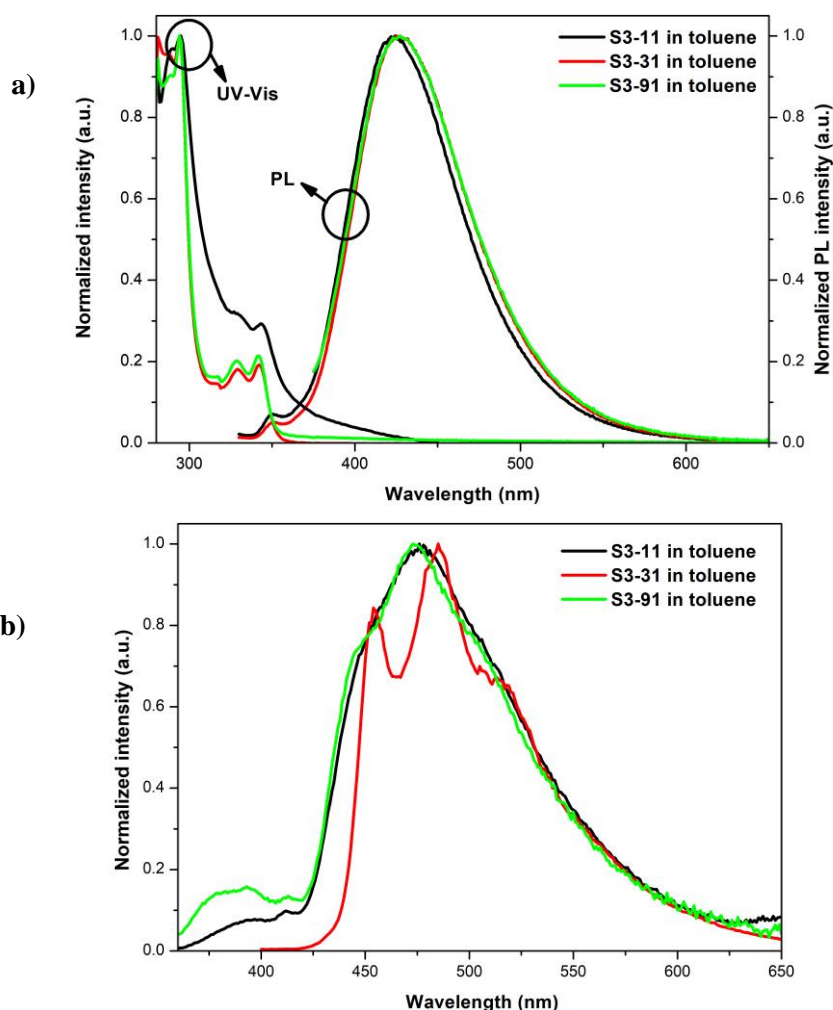


**Figure 3.4. 5** The normalized (a) UV-Vis absorption and PL (RT) and (b) phosphorescence (77K) spectra of **S3** polymers in toluene.

**Table 3.4. 2** The photophysical parameters of **S3** polymers in toluene

	$\lambda_{\text{abs}}$ (nm)	$\lambda_{\text{PL}}$ (nm)	$\lambda_{\text{Phos}}$ (nm)	PLQY <sub>toluene</sub> <sup>a/b/c</sup>	Stokes shift (cm <sup>-1</sup> )
<b>S3-11</b>	295,331,345	424	476	18 / 59 / 3	10313
<b>S3-31</b>	294,334,340	425	485,455	11 / 46 / 2	10484
<b>S3-91</b>	294,331,340	427	473	11 / 65 / -	10594

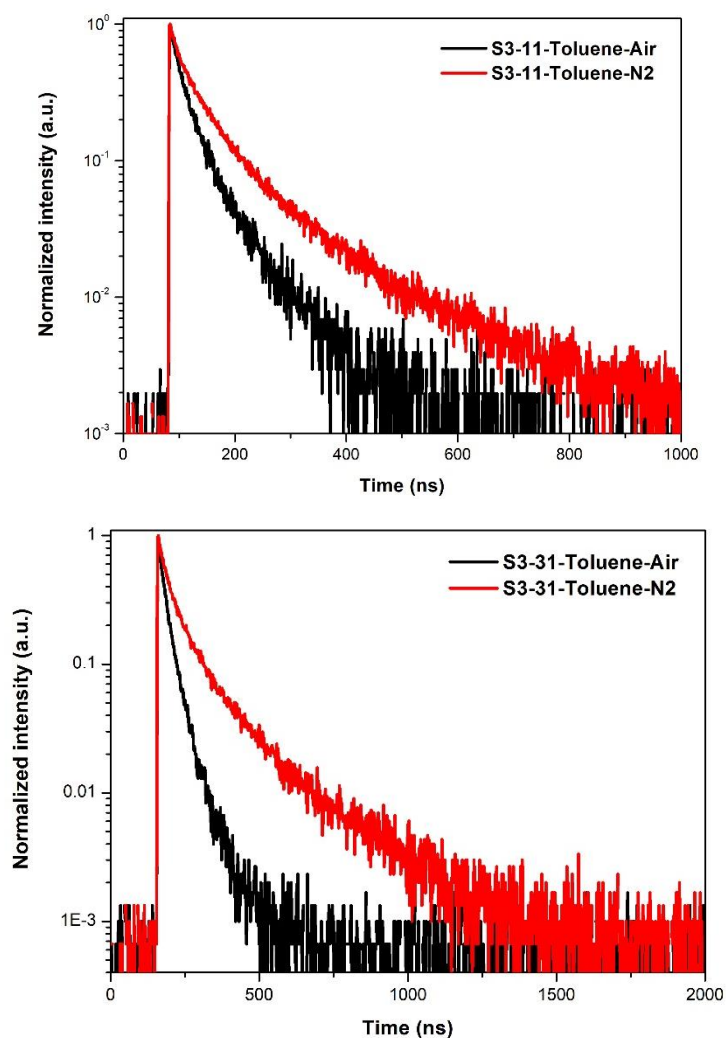
<sup>a</sup> Measured in air atmosphere; <sup>b</sup> Measured after nitrogen-bubbling for 15 min; <sup>c</sup> Measured after oxygen-bubbling for 15 min

From the main absorption and emission spectra, the Stokes shift of **S3-11**, **S3-31**, and **S3-91** can be calculated and the values are: 129 nm (10313 cm<sup>-1</sup>), 131 nm (10484 cm<sup>-1</sup>), and 133 nm (10594 cm<sup>-1</sup>), respectively.

The PLQYs of **S3-11**, **S3-31**, and **S3-91** in toluene were measured under air, nitrogen, and oxygen atmosphere (Table 3.4.2). The PLQYs of each polymer in nitrogen are almost 4-6 folds of those in air. Moreover, in oxygen, their PLQYs are very small, indicating that triplets are involved in photoluminescence properties.

### Time-resolved measurements

The transient PL decay spectra in toluene were measured by time-resolved fluorescence spectroscopy with TCSPC. As shown in Figure 3.4. 6, all transient PL decay curves of **S3-11**, **S3-31**, and **S3-91** display two different behaviors in air and nitrogen, suggesting that oxygen affects the decay process of fluorescence and the delayed component is originated from triplets. For each polymer, the decays of fluorescence in nitrogen can be fitted with a bi-exponential function  $y = y_0 + A_1 * \exp(-\frac{x}{\tau_1}) + A_2 * \exp(-\frac{x}{\tau_2})$  and the data are summarized in Table 3.4. 3. With increasing the content of accepting units in the polymers, both the prompt and DF lifetimes decrease. We can note that in solution, the DF lifetimes are relatively rapid for these polymers, as an example, **S3-91** presenting a DF lifetime of about 0.23  $\mu$ s.



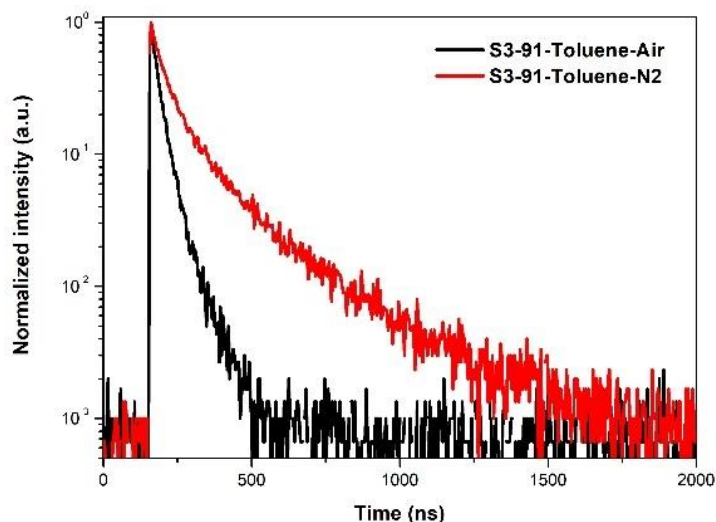


**Figure 3.4. 6** The transient PL decay curves of **S3-11**, **S3-31**, and **S3-91** in toluene under air and nitrogen atmosphere.

**Table 3.4. 3** PF and DF lifetimes of **S3** polymers in toluene

	$A_{PF}$	$\tau_{PF}(ns)$	$A_{DF}$	$\tau_{DF}(ns)$	$\phi_{DF}/\phi_{PF}$
<b>S3-11</b>	675.246	30.4	269.246	117	60.4 / 39.5
<b>S3-31</b>	2100.84	42.1	511.699	182	51.3 / 48.7
<b>S3-91</b>	1942.26	52.1	480.601	229	52.1 / 47.9

The prompt and delayed lifetimes were calculated from the PL decay curves in nitrogen, with a bi-exponential function.

### 3.4.2.2 In solid-state

#### *Steady-state measurements*

The steady-state UV-Vis absorption, PL, and phosphorescence spectra of **S3** polymers in the neat film are shown in Figure 3.4. 7. The absorption spectra show main peaks at 285, 291, and 296 nm for **S3-11**, **S3-31**, and **S3-91**, respectively, which are mainly attributed to the  $\pi$ - $\pi$  transition of carbazole and isophthalonitrile in the thin film. The optical energy gap of 2.86, 2.87, and 2.89 eV for **S3-11**, **S3-31**, and **S3-91**, respectively, were obtained from the onset of absorption spectra (Table 3.4.4).

The PL spectra display broad emission bands at 435, 431, and 426 nm for **S3-11**, **S3-31**, and **S3-91**, respectively, corresponding to the CT character of the excited state. As the content of the acceptor increases from 10 to 50%, the emission wavelength is slightly red-shifted by 4-9 nm, consistent with the increase of the media polarity surrendering the TSCT polymers.<sup>270</sup> Moreover, the Stokes shift can be determined by the main characteristics of absorption and emission spectra: 150 nm ( $12099\text{ cm}^{-1}$ ), 140 nm ( $11162\text{ cm}^{-1}$ ), 130 nm ( $10310\text{ cm}^{-1}$ ), corresponding to **S3-11**, **S3-31**, and **S3-91** in neat film, respectively (Table 3.3.4). The PLQYs of **S3-11**, **S3-31**, and **S3-91** in neat films under argon are consequently in the range of 13-15%, much lower than those in dilute toluene solution.

To estimate the TADF activity of **S3** polymers, their singlet and triplet energies were determined according to the fluorescence and phosphorescence spectra, respectively. The  $E_S$  values of **S3-11**, **S3-31**, and **S3-91** are 2.71, 2.73, and 2.75 eV and the  $E_T$  values of **S3-11**, **S3-31**, and **S3-91** are 2.43, 2.46, and 2.48 eV, respectively. The  $\Delta E_{ST}$  values of **S3-11**, **S3-31**, and **S3-91** were calculated to be 0.28, 0.27, and 0.27 eV, which is quite large compared to those reported TADF polymers, indicating that these polymers might exhibit no or very weak TADF activity in solid-state (Table 3.3.4).

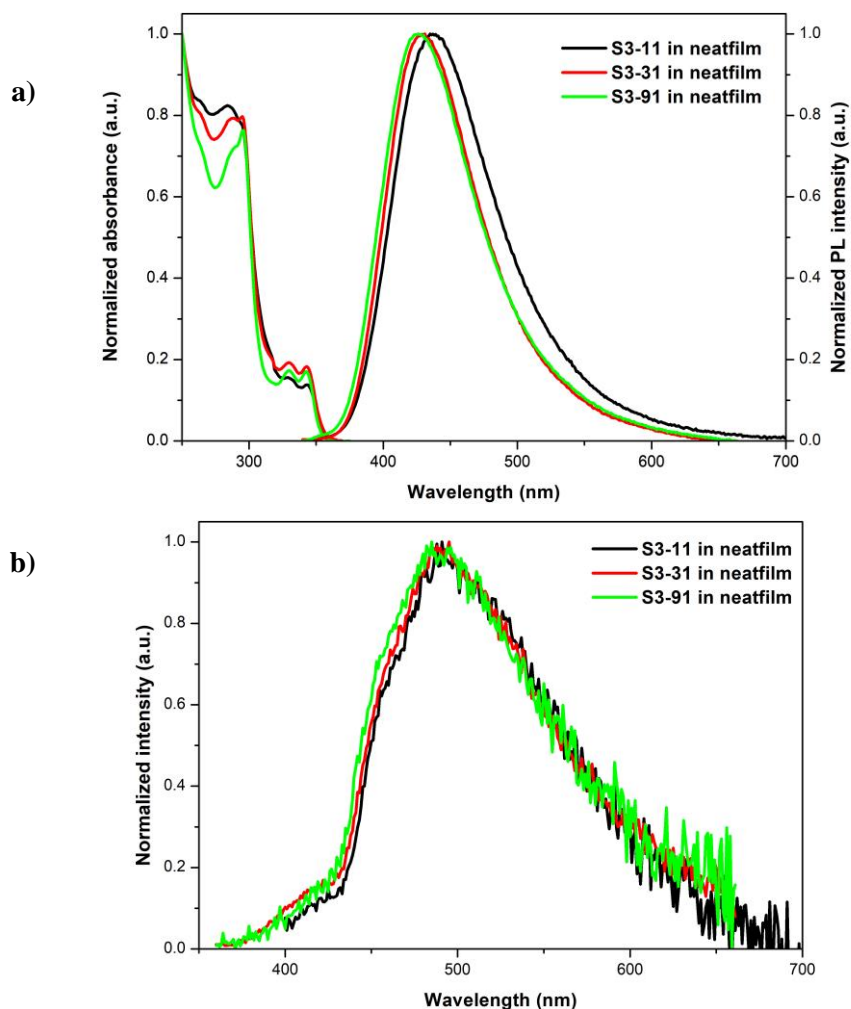


**Figure 3.4. 7** The normalized UV-Vis absorption, PL (a), and phosphorescence (b) spectra of **S3** polymers in neat films at room temperature.

**Table 3.4. 4** The photophysical parameters of **S3** polymers in the neat film

	$\lambda_{\text{abs}}$ (nm)	$\lambda_{\text{PL}}$ (nm)	$\lambda_{\text{Phos}}$ (nm)	PLQY <sup>a</sup> (%)	HOMO <sup>b</sup> (eV)	Eg <sup>c</sup> (eV)	LUMO <sup>d</sup> (eV)	$\Delta E_{ST}$ <sup>e</sup> (eV)	Stokes shift (cm <sup>-1</sup> )
<b>S3-11</b>	285,330,343	435	491	13	-6.19	2.86	-3.33	0.28	12099
<b>S3-31</b>	291,330,343	431	495	15	-6.20	2.87	-3.33	0.27	11162
<b>S3-91</b>	296,331,343	426	485	13	-6.22	2.89	-3.33	0.27	10310

<sup>a</sup> Measured in the neat film under argon atmosphere; <sup>b</sup> Measured by photoelectron spectroscopy; <sup>c</sup> the optical energy gap calculated from absorption spectra; <sup>d</sup> deduced from the HOMO and Eg values; <sup>e</sup> calculated from the fluorescence (RT) and phosphorescence (77K) spectra.

As represented in Figure 3.4.8, the HOMO energy level of **S3** polymers was determined in neat films by photoelectron spectroscopy and the values are equal to -6.19, -6.20, and -6.22 eV for **S3-11**, **S3-31**, and **S3-91**, respectively. LUMO energy level can be deduced as the sum of the HOMO and the optical energy gap.

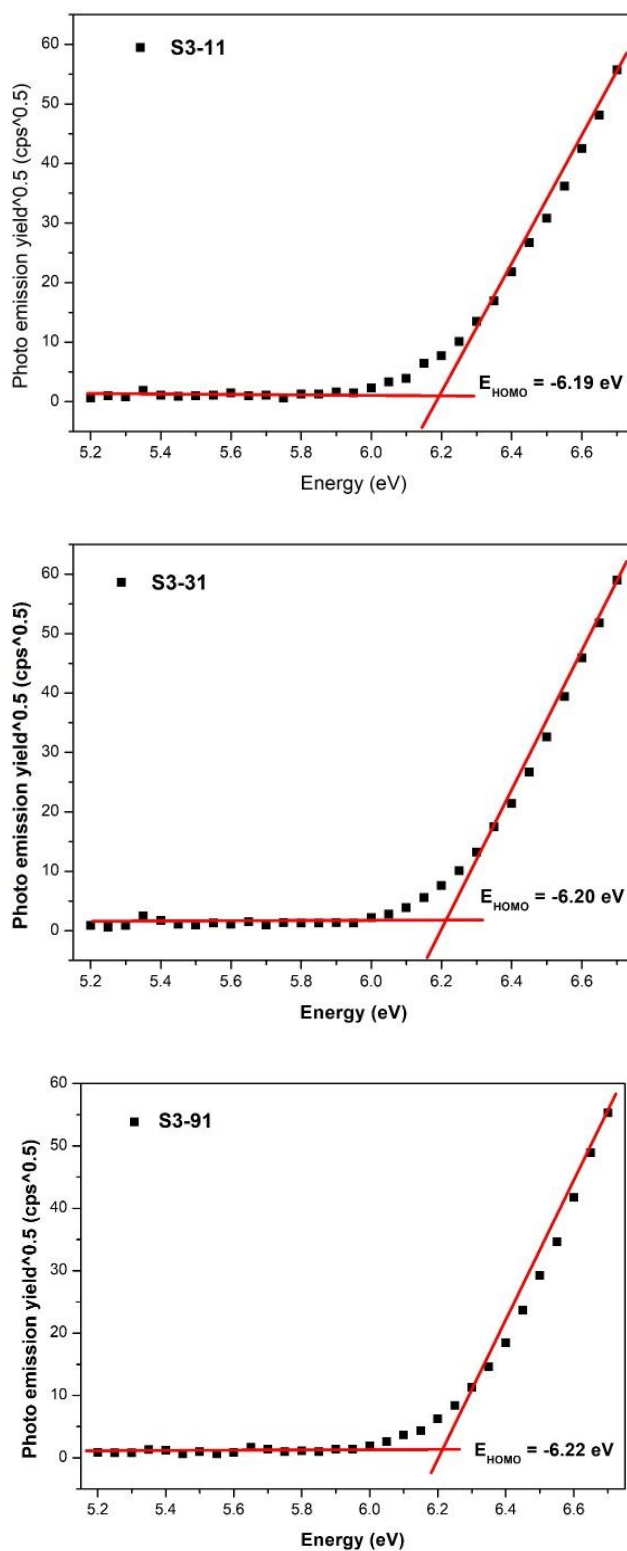


**Figure 3.4. 8** The photoelectron spectra of **S3** polymers in neat film.

### Time-resolved measurements

Here, we investigated transient PL decay characteristics of **S3** polymers by a streak camera in vacuum, as shown in Figure 3.4.9. These PL decay curves of **S3-11**, **S3-31**, and **S3-91** can be divided into two parts: delayed emissions with lifetimes in the microsecond scale, together with prompt emissions with lifetimes in the nanosecond scale. The prompt components of each polymer can be fitted with a mono-exponential function and the delayed components can be fitted with a bi-exponential: the data are recorded in Table 3.4. 5.

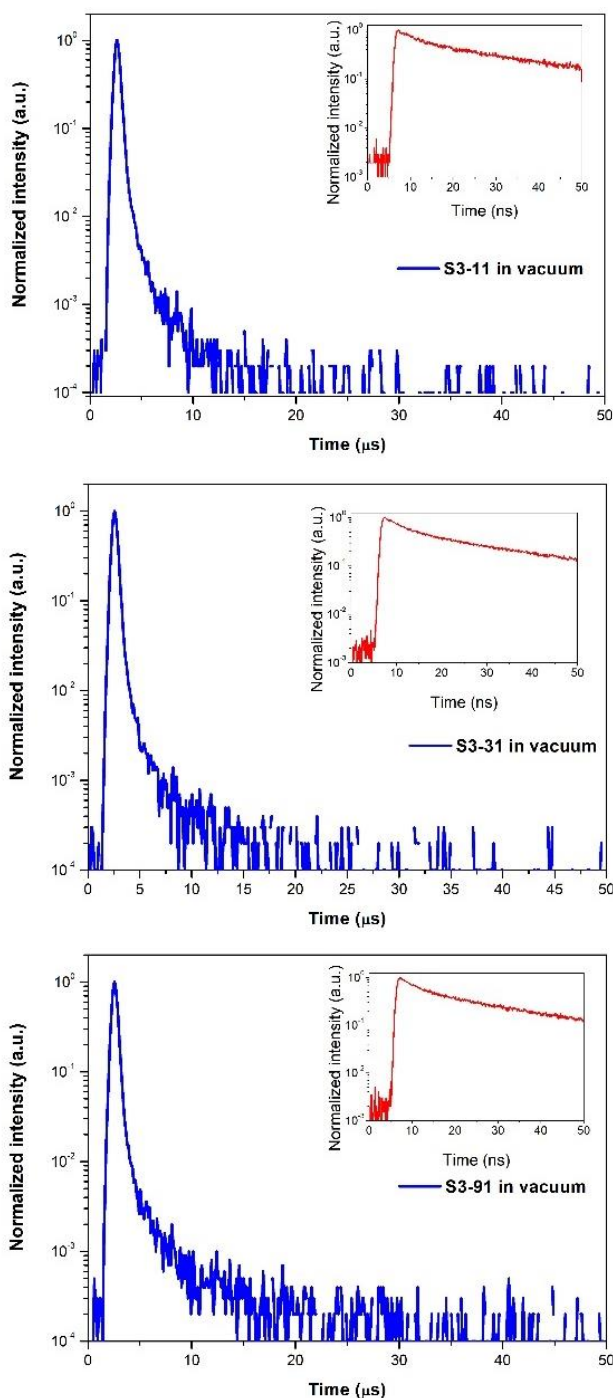


**Figure 3.4. 9** The PL decay curves of **S3** polymers in neat films tested by a streak camera in vacuum at room temperature (inset: 50ns scale).

The prompt lifetimes of these polymers in neat films are calculated to be 11.1, 8.5, and 9.8 ns, for **S3-11**, **S3-31**, and **S3-91**, respectively. In contrast to prompt fluorescence, **S3-31** exhibit the delayed fluorescence with the longest lifetimes and **S3-11** with the shortest lifetimes.

**Table 3.4. 5** PF and DF lifetimes of **S3** polymers in the neat films

	$A_{PF}$	$\tau_{PF}(ns)$	$A_{DF1}$	$\tau_{DF1}(\mu s)$	$A_{DF2}$	$\tau_{DF2}(\mu s)$	$\phi_{DF1}/\phi_{DF2}/\phi_{PF}$
<b>S3-11</b>	0.77202	11.1	0.10542	0.20	0.02197	1.01	40.7 / 42.8 / 16.5
<b>S3-31</b>	0.77454	8.5	0.0098	0.37	0.00475	1.81	19.3 / 45.7 / 35.0
<b>S3-91</b>	0.88303	9.8	0.02963	0.22	0.01300	1.35	19.9 / 53.6 / 26.5

The prompt and delayed lifetimes were calculated from the PL decay curves (50 ns and 50  $\mu s$  scale, respectively) in vacuum measured by a streak camera.

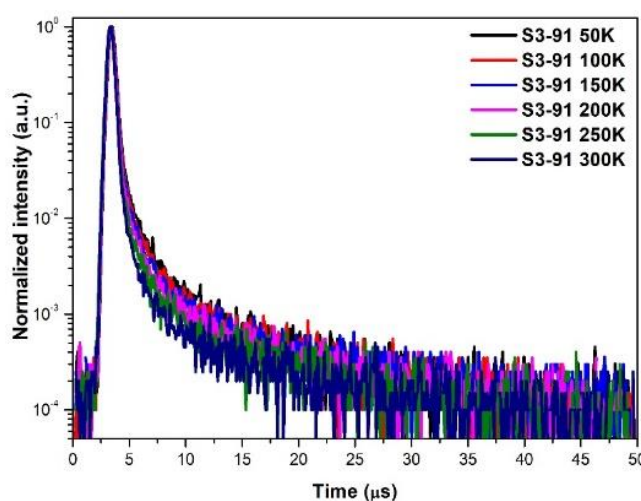


**Figure 3.4. 10** Temperature-dependent transient PL decay curves over the 50 to 300 K temperature range for **S3-91** neat film.

**Table 3.4. 6** DF lifetimes of **S3-91** in neat films measured by a streak camera (50-300K)

T (K)	$A_{DF1}$	$\tau_{DF1}(\mu s)$	$A_{DF2}$	$\tau_{DF2}(\mu s)$	$\tau_{DF,av}(\mu s)$	$R^2$
50	0.00553	0.56228	0.00664	3.1166	2.78	0.99098
100	0.02142	0.63832	0.00602	3.54987	2.41	0.99357
150	0.0216	0.66920	0.00452	3.87327	2.42	0.99144
200	0.02733	0.63928	0.00378	4.25053	2.37	0.98755
250	0.0152	0.49809	0.00392	3.26435	2.24	0.97945
300	0.01523	0.60157	0.00206	4.31297	2.42	0.9797

The average lifetime is calculated using  $\tau_{DF,av} = \sum A_i \tau_i^2 / \sum A_i \tau_i$

Besides, the temperature-dependent PL decay spectra of **S3-91** were recorded by a streak camera from 50 to 300K, as represented in Figure 3.4 10. The PL decay curved could be divided into two parts: prompt and delayed components. The prompt components of all curves are overlapped with each other, illustrating that the prompt fluorescence shows almost no variation with temperature, which is

consistent with the negligible internal conversion. The delayed fluorescence changes *vs* temperature can be fitted with a bi-exponential function. However, the lifetimes of the delayed component, summarized in Table 3.4. 6, didn't increase along with the decreasing temperature, suggesting that **S3-91** presents in the neat film no or weak TADF properties.

### 3.4.3 Conclusion

In this section, we designed and synthesized a new series of vinyl polymers namely, **S3** polymers, with TSB interactions between the donor (carbazole) and the acceptor (isophthalonitrile) units. Before polymerization, the donor and acceptor monomers were successfully synthesized in a 6-step procedure. The **S3** polymer series were prepared *via* radical polymerization at 60°C for 48h with 5% AIBN as the initiator and dry toluene as the solvent. The chemical structures of the monomers and polymers were confirmed by the proton and carbon NMR spectra. SEC measurements demonstrated that **S3** polymers hold the relative number-average molecular weights ( $M_{n,SEC}$ ) of 18-27 kDa, with the dispersity ( $M_w/M_n$ ) of 1.40-1.76, and the degree of polymerization (DP) of 67-103. Besides, the real components in these polymers were further calculated from the result of elemental analysis.

Subsequently, we investigated the photophysical properties of these materials in both solution and neat film by steady-state and time-resolved measurements. The UV-vis absorption, photoluminescence, and phosphorescence spectra of **S3-11**, **S3-31**, and **S3-91** in dilute toluene and neat films were measured. The optical energy level ( $E_g$ ), singlet and triplet energy levels ( $E_S$  and  $E_T$ ) of polymers were determined from the onsets of UV-Vis absorption, photoluminescence, and phosphorescence spectra in neat film.

For each polymer in toluene solution, their transient PL decay curves under air and nitrogen atmosphere show distinct changes with the varying oxygen content, suggesting that triplet states are involved in photoluminescent properties. This observation is also in agreement with the PLQYs changes in different atmospheres. In toluene, the PLQYs are 46-65% and decrease a lot in presence of oxygen. And in neat films, the PLQYs are only 13-15%, revealing the presence of aggregation-caused quenching in solid-state.

To further study the PL decay behavior of these polymers, a streak camera was utilized to record the time-resolved transient PL spectra. And the temperature dependence of PL decay of **S3-91** was further studied from 50 to 300K in vacuum. Although the DF lifetimes of **S3-91** at each temperature was fitted with a bi-exponential function, the resulting DF lifetimes don't show a clear temperature dependence, demonstrating that **S3-91** presents no or very weak TADF properties in solid-state. This could be consistent with the relatively large  $\Delta E_{ST}$  ( $>0.27$  eV) observed for this polymer series in neat film. Additional studies such as in host/guest systems should be performed to investigate more deeply the potential TADF activity of these materials.

### 3.5 Through-space charge transfer (TSCT) TADF polymers based on Pm5

In this section, using the same strategy as in section 3.4, we designed another series of TSCT polymers (**S4**) but incorporating this time in the side chain and separately the donor and acceptor entities used in the TADF chromophore **Pm5**<sup>266</sup> (see Figure 3.5.1).

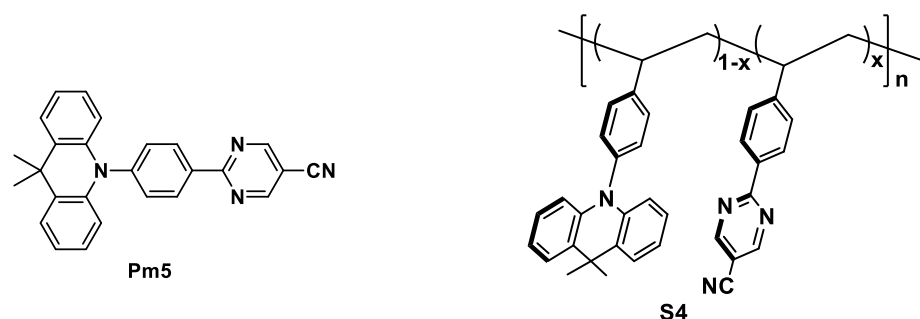
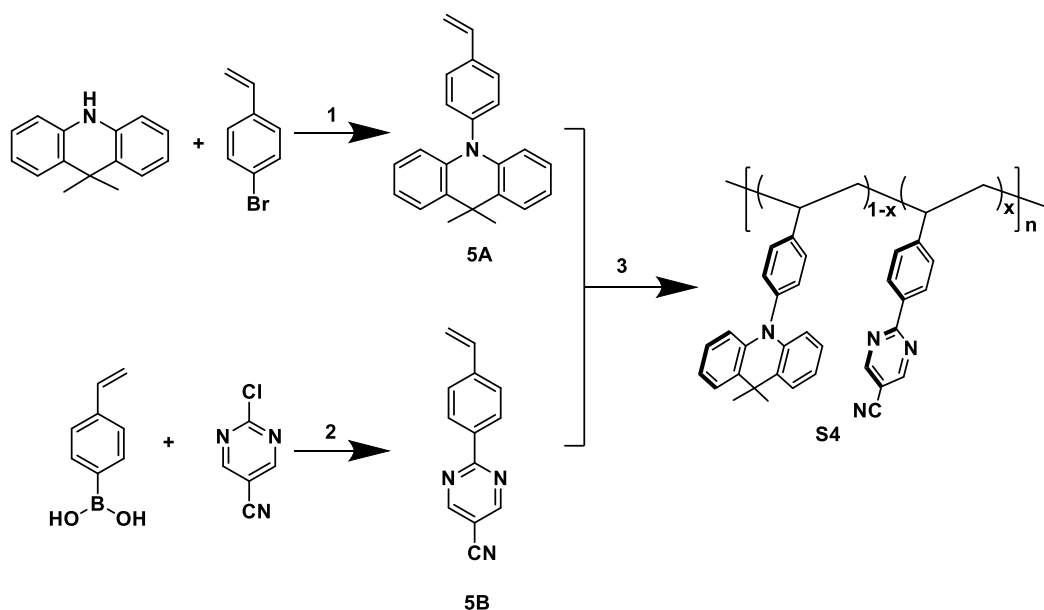


**Figure 3.5. 1** The chemical structures of the TADF model (**Pm5**) and **S4** polymers.

After the description of the synthetic aspects, we will characterize their photophysical properties and determine if these new materials exhibit TADF activity with high PLQY.

#### 3.5.1 Design, synthesis, and structural characterization



**Scheme 3.5.1** Synthetic routes towards **S4** polymers. Condition: 1)  $Pd_2(dba)_3$ ,  $P(t-Bu)_3/HBF_4$ ,  $t-BuONa$ , toluene, 110 °C, 18 h, 65%; 2)  $Pd_2(dba)_3$ ,  $Sphos$ ,  $K_3PO_4$ , 1,4-dioxane/ $H_2O$ , 100 °C, 4 h, 20%; 3) AIBN, toluene, 60 °C, 48 h, 33-45%.

For the synthesis of this polymer series **S4**, two monomers were prepared in one step from the commercially available starting materials, respectively. As shown in Scheme 3.5.1, on the one hand, the electron-donating monomer **5A** was obtained from the reaction between the -NH group of 9,9-

dimethyl-9,10-dihydroacridine and the -Br group of 1-bromo-4-vinylbenzene, using Pd<sub>2</sub>(dba)<sub>3</sub> as the catalyst, P(*t*-Bu)<sub>3</sub>/HBF<sub>4</sub> as the ligand, and *t*-BuONa as the base, with a yield of 65%.

On the other hand, the electron-accepting monomer **5B** was successfully synthesized *via* a Suzuki coupling between the commercially available 2-chloropyrimidine-5-carbonitrile and 4-vinylphenylboronic acid molecules, using Pd<sub>2</sub>(dba)<sub>3</sub> as the catalyst, Sphos as the ligand, and K<sub>3</sub>PO<sub>4</sub> as the base, with a yield of 20%. The possible reason for the relatively low yield is that the used catalyst-ligand-base system is probably not suitable for this reaction.

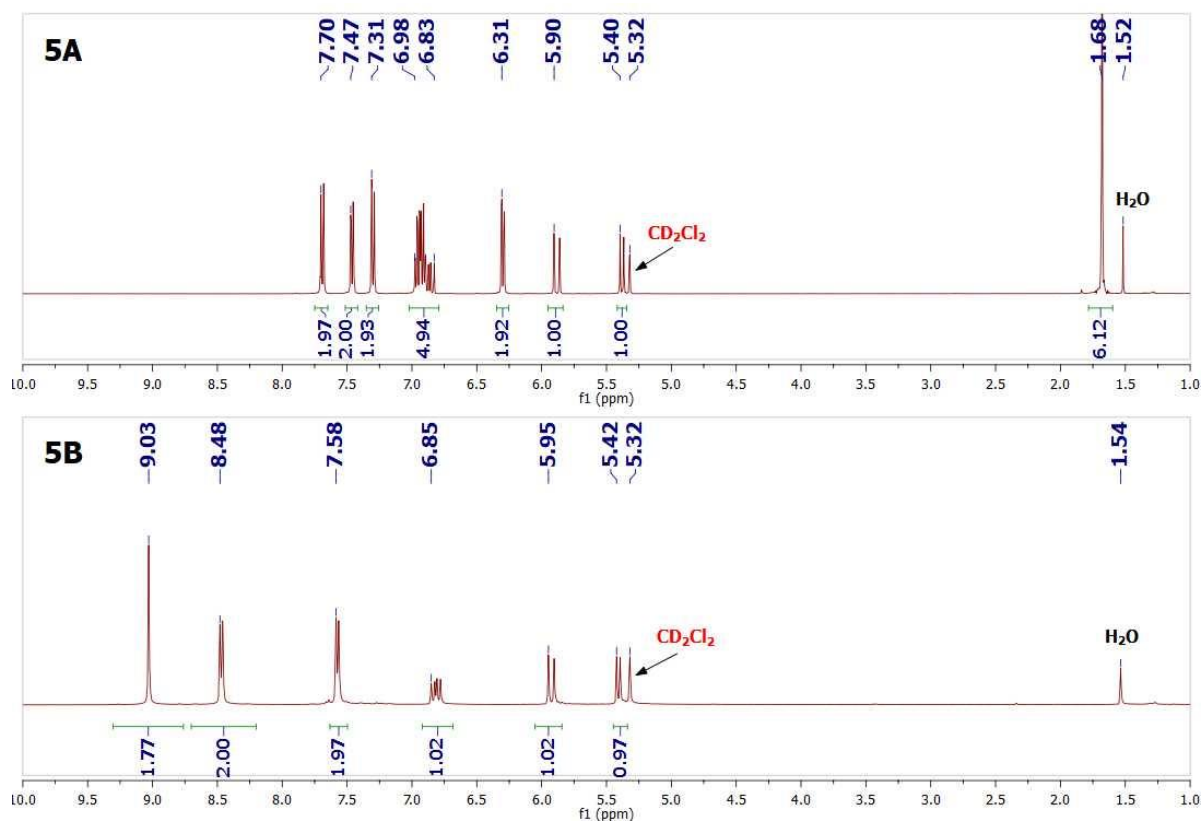


**Figure 3.5. 2** <sup>1</sup>H NMR spectra of **5A** and **5B** in dichloromethane.

The detailed synthetic procedures are recorded in the appendix and the chemical structures of **5A** and **5B** were confirmed by both proton and carbon NMR spectra. As shown in Figure 3.5. 2, for **5A**, the signals at 6.31, 5.90, and 5.40 ppm belong to the protons of vinyl groups (-CH=CH<sub>2</sub>), the signal at 1.68 ppm is attributed to the protons of methyl groups, while the signals between 7.70 to 6.83 ppm are ascribed to protons of aromatic rings.

For **5B**, the protons of vinyl groups (-CH=CH<sub>2</sub>) are located at 6.85, 5.95, and 5.42 ppm, and the protons of aromatic rings are ranging from 9.03 ppm to 7.58 ppm. In each spectrum, the integrals of all peaks are consistent with the molecular structure.

Based on the chemical structure evidence from NMR spectra, we used these monomers without further purification. **S4** polymers with various ratios of the electron-donating and electron-withdrawing units were prepared from the radical polymerization in dry toluene at 60 °C for 48 h, using **5A** and **5B** as

monomers together with 5% AIBN as initiator. More precisely, we isolated six **S4** polymers, namely **S4-11**, **S4-31**, **S4-51**, **S4-91**, **S4-955**, **S4-991**, corresponding to the different feed ratios of **5A** : **5B** = 1:1, 3:1, 5:1, 9:1, 95:5, 99:1, respectively. We can observe that these polymers are pale yellow solids and their color is darker with the increasing feed ratio of the acceptor (**5B**). After polymerization, as observed in figure 3.5.3, the signals belonging to the vinyl groups of **5A** and **5B** disappeared completely, demonstrating that no monomers (or oligomers) remain in the polymers. Besides, new signals, ascribed to the protons of the polymer backbones, appear from 2.50 to 1.60 ppm, and the sharp peaks corresponding to signals of protons of the aromatic rings became broad, indicative of the successful polymerization.

The broad peaks in the range of 7.90-9.0 ppm are attributed to electron-accepting units (**5B**) in the polymers. The broad peaks, in the range of 5.7-6.3, 6.67-7.09 ppm, correspond to the signals of protons of the electron-donating unit (**5A**). The peak around 7.3 ppm is probably attributed to both aromatic side groups.

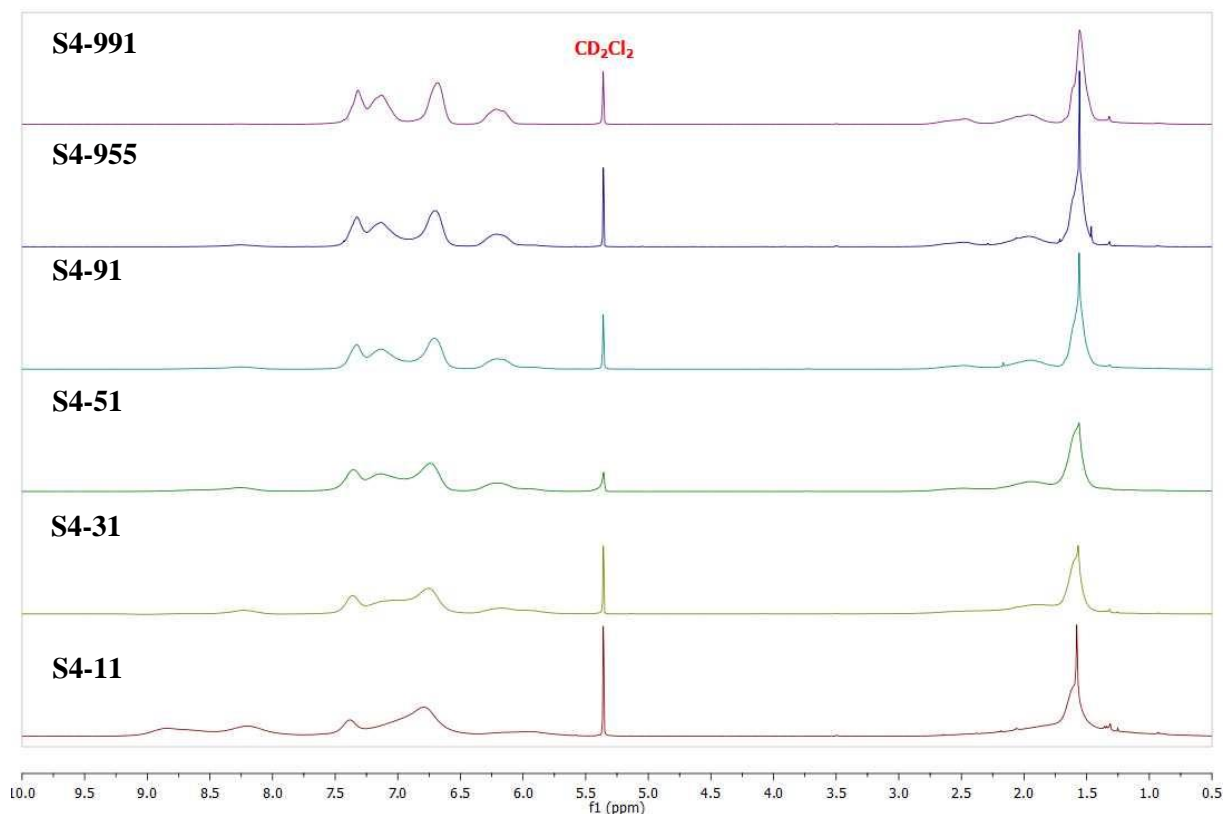


**Figure 3.5. 3**  $^1\text{H}$  NMR spectra of **S4** polymers.

We can also observe from the zoom of the proton NMR spectra (Figure 3.5. 4) that the peaks from 7.9 to 9.0 ppm gradually vanish, and the peaks in the range from 5.70-7.09 ppm become larger and larger, with increasing the feed ratio of the electron-donating unit (**5A**), also revealing that the real ratios of the electron-donating unit (**5A**) are increasing with the increasing feed ratios of **5A**.

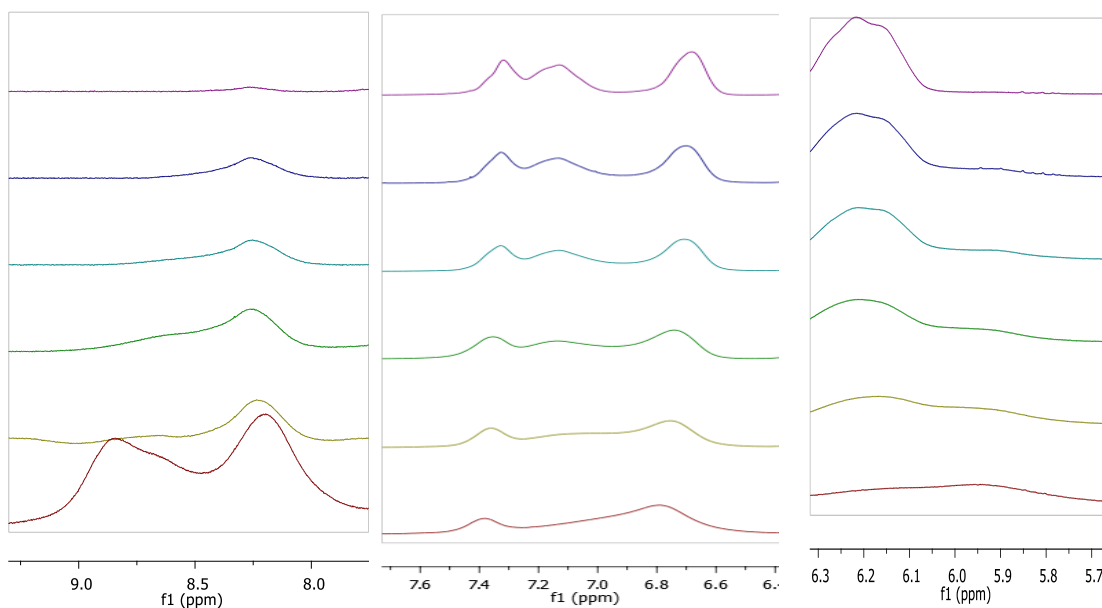


**Figure 3.5. 4** The zoom of  $^1\text{H}$  NMR spectra of **S4** polymer.

Also, the dispersity and molecular weight of **S4** polymers (Figure 3.5. 5) were investigated by Size exclusion chromatography (SEC). **S4** polymers hold the relative number-average molecular weights ( $M_{n,SEC}$ ) of 19-39 kDa, with the dispersity ( $M_w/M_n$ ) of 1.44-1.98.

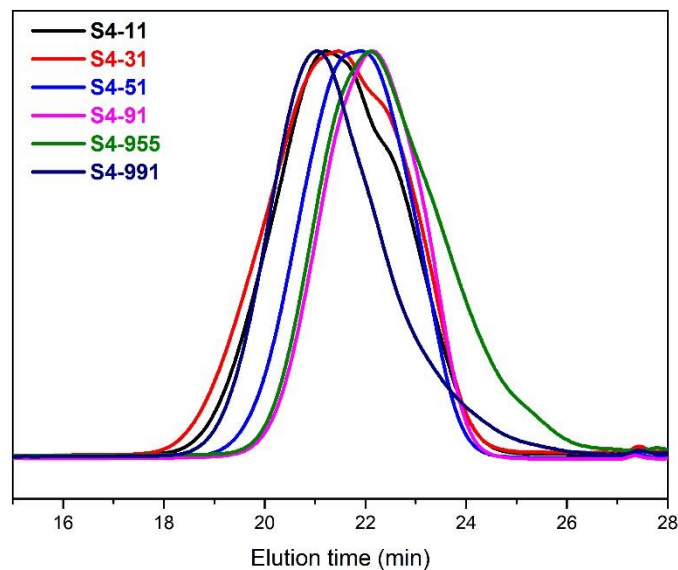


**Figure 3.5. 5** SEC curves of **S4** polymers.

The real ratio of **5A** and **5B** in our **S4** copolymers were calculated from elemental analysis and the main results are reported in Table 3.5. 1. From all these data, we can essentially say that the degree of polymerization ( $X_{n,SEC}$ ) is between 70 and 174. Furthermore, the sole SEC peaks are confirming the NMR conclusions, i.e. no residual monomers or oligomers are remaining.

**Table 3.5. 1** The structural information of **S4** polymers

Polymers	$x_t$	$x_{EA}$	$M_{n,SEC}$ (kDa)	$X_{n,SEC}$	$M_w/M_n$	Conversion (%)	C:H:N
<b>S4-11</b>	0.500	0.410	39	145	1.85	33	84.53 : 4.78 : 8.52
<b>S4-31</b>	0.250	0.278	39	174	1.98	45	85.58 : 5.12 : 6.99
<b>S4-51</b>	0.167	0.220	33	136	1.52	38	86.68 : 5.23 : 6.35
<b>S4-91</b>	0.100	0.172	28	109	1.44	38	86.86 : 5.33 : 5.83
<b>S4-955</b>	0.050	0.129	19	70	1.90	39	87.41 : 5.47 : 5.42
<b>S4-991</b>	0.010	0.080	38	133	1.94	36	87.92 : 5.53 : 4.91

$x_t$  value is the theoretical content of **5B** unit in the polymers, determined by the feed ratio;  $x_{EA}$  value is the real content **5B** unit in the polymers, calculated from the elemental analysis results;  $M_{n,SEC}$  is the relative number-average molecular weight obtained from SEC measurements in THF eluent, calibrated by polystyrene;  $M_w/M_n$  is dispersity; C:H:N is the ratio of C, H and N elements in the polymers, obtained from elemental analysis.

### 3.5.2 Photophysical properties

After the structural characterization, the photophysical properties of **S4** polymers (**S4-11**, **S4-31**, and **S4-91**) in both solution and solid-states were measured at the OPERA laboratory in the scope of the JSPS core-to-core program. Unfortunately, I couldn't go to OPERA myself in 2020 due to the COVID19 pandemic.

#### 3.5.2.1 In dilute solution

##### *Steady-state measurements*

The steady-state UV-vis absorption, photoluminescence (PL), and phosphorescence spectra of **S4-11**, **S4-31**, and **S4-91** in dilute toluene solution are depicted in Figure 3.5. 6, and data are summarized in Table 3.5. 2. The main absorption bands of **S4-11**, **S4-31**, and **S4-91** are located at 299, 292, and 290 nm, respectively, and are mainly attributed to the  $\pi$ - $\pi$  transition of unsaturated aromatic side groups. Moreover, the absorption spectrum of **S4-11** shows a weak and broad CT band in the range of 350-400 nm, originating from the intramolecular charge transfer (CT) between the donor and acceptor units.

Concerning fluorescence properties, **S4-91** demonstrated a dual emission: the main emission, attributed to the intramolecular charge transfer (CT) transition, shows a maximum at 565 nm and its intensity decreases a lot when changing from  $N_2$  to  $O_2$  atmosphere (see Figure 3.5. 6b). This indicates that this emission is originated from the triplets, which are effectively quenched by oxygen; the other emission maximum is situated at 374 nm, ascribed to the residual emission of acridine fragments.

Note as well that the PL spectra of **S4-11** and **S4-31** are almost identical to that of **S4-91** in the range of 400-800 nm, displaying a unique emission band located at 564 and 566 nm, respectively. According to the absorption and emission spectra, the Stokes shift in toluene can be calculated for **S4-11**, **S4-31**, and **S4-91** as 265 nm ( $15714\text{ cm}^{-1}$ ), 274 nm ( $16579\text{ cm}^{-1}$ ), and 275 nm ( $16784\text{ cm}^{-1}$ ), respectively.

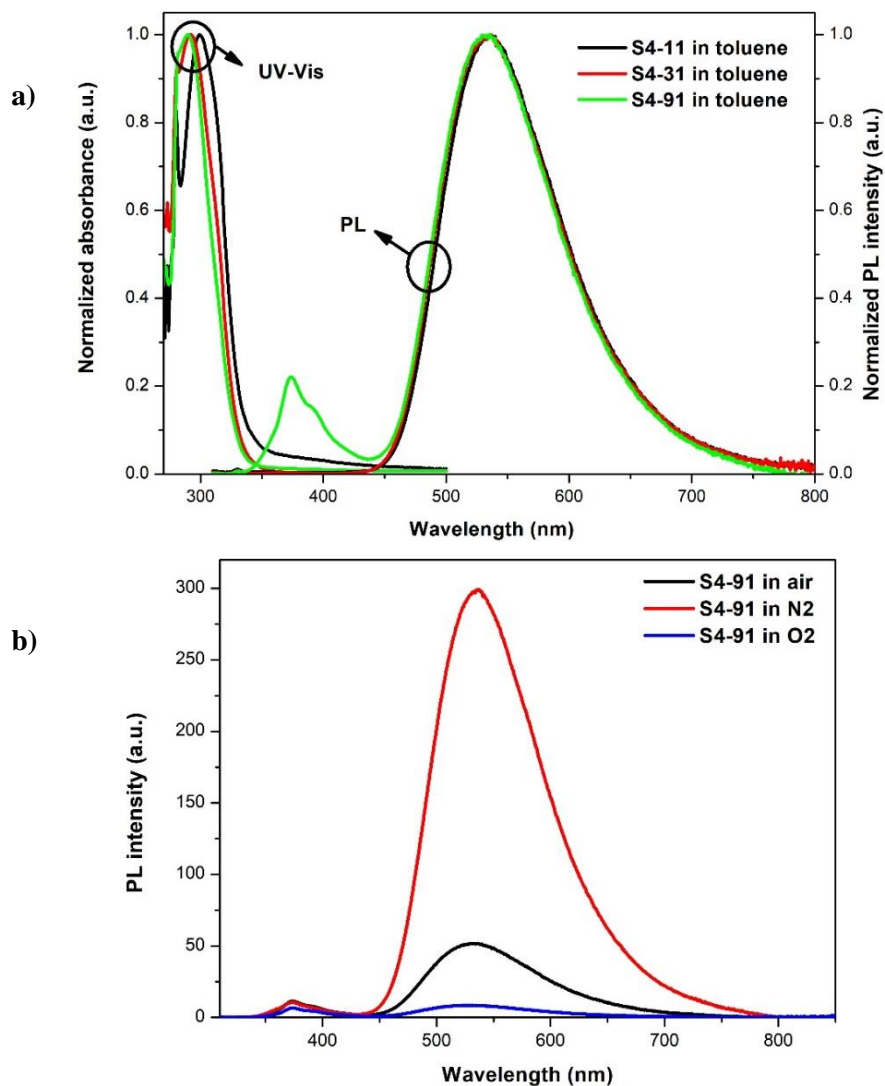


**Figure 3.5. 6** a) The normalized UV-Vis absorption and PL spectra of **S4-11**, **S4-31**, and **S4-91** in toluene; b) The PL spectra of **S4-91** in toluene at the air, N<sub>2</sub>, and O<sub>2</sub> atmosphere.

**Table 3.5. 2** The photophysical parameters of **S3** polymers in toluene

	$\lambda_{\text{abs}}$ (nm)	$\lambda_{\text{PL}}$ (nm)	$\lambda_{\text{Phos}}$ (nm)	PLQY <sup>a/b/c</sup> (%)	Stokes shift (cm <sup>-1</sup> )
<b>S3-11</b>	299	564	530	13 / 57 / 1.6	15714
<b>S3-31</b>	292	566	499	11 / 57 / 3.0	16579
<b>S3-91</b>	290	374,565	490	11 / 63 / 2.5	16784

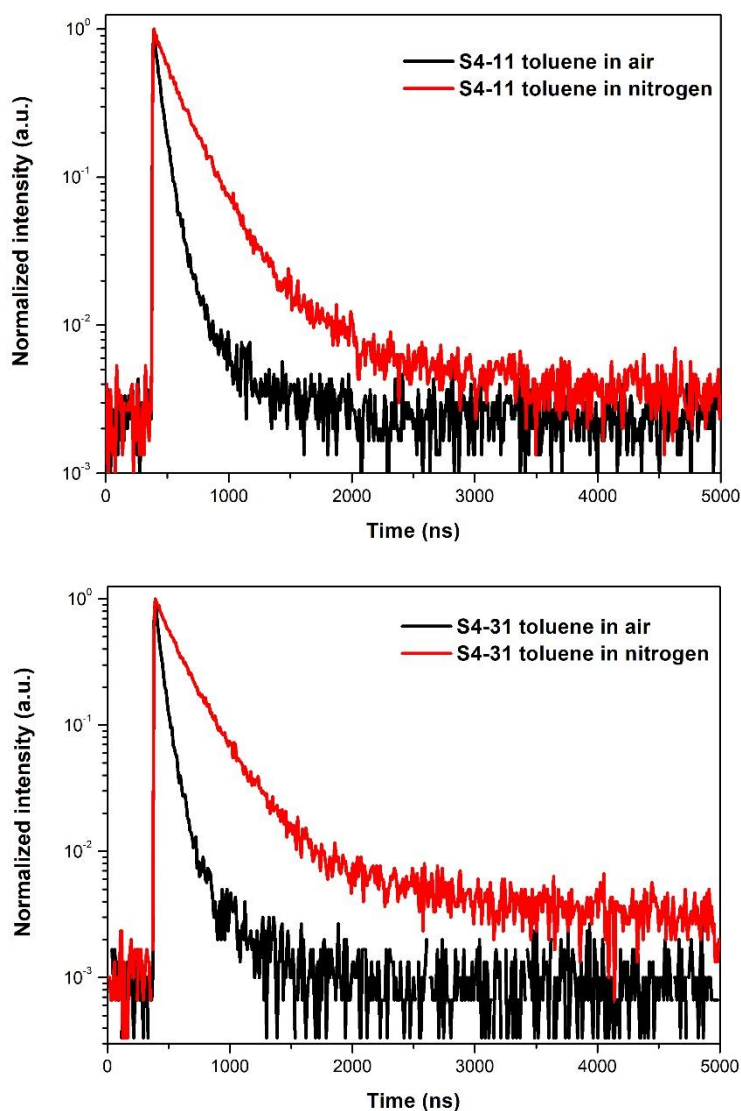
<sup>a</sup> Measured in air atmosphere; <sup>b</sup> Measured after nitrogen-bubbling for 15 min; <sup>c</sup> Measured after oxygen-bubbling for 15 min

The photoluminescence quantum yields (PLQYs) of **S4-11**, **S4-31**, and **S4-91** were measured both in the air atmosphere and after nitrogen-bubbling for 15 min. As shown in Table 3.5.2, the PLQYs of these polymers in N<sub>2</sub> are in the range of 57-63%, almost 5 folds of that measured in air (11-13%) and 25-35 folds of that measured under oxygen flux (1.6-3.0%), indicating that the PLQYs arise from the

triplets. This is in agreement with the change of emission intensity of fluorescence spectra in different atmosphere observed in Figure 3.5.6b.

#### *Time-resolved measurements*

Theoretically, **S4** polymers were designed to exhibit TADF activity *via* through-space conjugation, thus these polymers might only display TADF behavior in solid-state rather than in dilute solution. However, **S4** polymers are not readily soluble in toluene. As a consequence, the polymers might aggregate in toluene to some extent, thus leading to through-space conjugation in this specific solvent. We conducted the measurements of transient fluorescence decay under air and N<sub>2</sub> atmosphere for the series of **S4** polymers in toluene. As shown in Figure 3.5.7, when exposing the solutions to air, the delayed component disappeared, revealing that the delayed emission is originated from the triplet states.



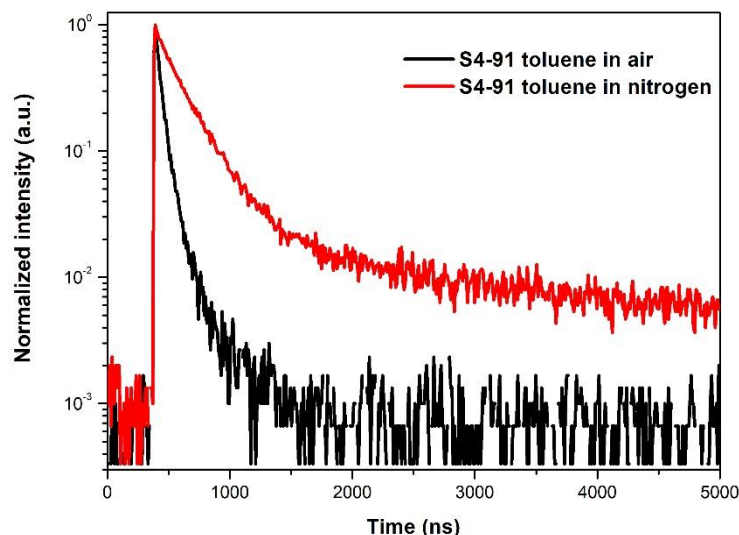


**Figure 3.5. 7** The transient PL decay curves of **S4-11**, **S4-31**, and **S4-91** in toluene under air and N<sub>2</sub> atmosphere

All these polymers exhibit obvious prompt and delayed components, corresponding to the TADF nature, and the PL decay curves in nitrogen can be fitted with a bi-exponential function  $y = y_0 + A_1 * \exp(-\frac{x}{\tau_1}) + A_2 * \exp(-\frac{x}{\tau_2})$ . Thus, as reported in Table 3.5.3, each polymer is composed of one prompt component and one delayed component. The lifetimes of both components increase with the decreasing of acceptor units in the polymer. More specifically, **S4-11** exhibited the fluorescence decay with the shortest DF lifetimes, while **S4-91** with the longest DF lifetimes. These polymers, and more particularly **S4-91**, show clear TADF activity in oxygen-free toluene.

**Table 3.5. 3** PF and DF lifetimes of **S4** polymers in toluene

	A <sub>PF</sub>	$\tau_{PF}$ (ns)	A <sub>DF</sub>	$\tau_{DF}$ ( $\mu$ s)	$\phi_{DF}/\phi_{PF}$
<b>S4-11</b>	2756.98	203	213.433	0.58	18.2 / 81.8
<b>S4-31</b>	2757.15	217	46.1219	1.40	9.8 / 90.2
<b>S4-91</b>	2748.85	214	66.5285	2.17	19.7 / 80.3

The prompt and delayed lifetimes were calculated from the PL decay curves (time scale: 5000ns) in nitrogen, respectively, with a bi-exponential function.

### 3.5.2.2 In solid-state

#### Steady-state measurements

The steady-state UV-Vis absorption, photoluminescence, and phosphorescence spectra of **S4** polymers in the neat film are shown in Figure 3.5. 8 and the data are summarized in Table 3.5. 4. The absorption spectra of **S4** polymers demonstrate the main band at 297, 293, and 290 nm for **S4-11**, **S4-31**, and **S4-91**), corresponding to the  $\pi$ - $\pi$  transition of the aromatic groups. The optical energy gap of 2.95, 2.97,

and 3.05 eV for **S4-11**, **S4-31**, and **S4-91**, respectively, were obtained from the onset of absorption peaks. The PL spectra display similar sole and broad CT emission with maxima at 541, 532, and 505 nm for **S4-11**, **S4-31**, and **S4-91**, respectively. Note that the slight blue-shift of the emission spectra when the quantity of acceptor units decreases along the polymer backbones is consistent with the decrease of the medium polarity.

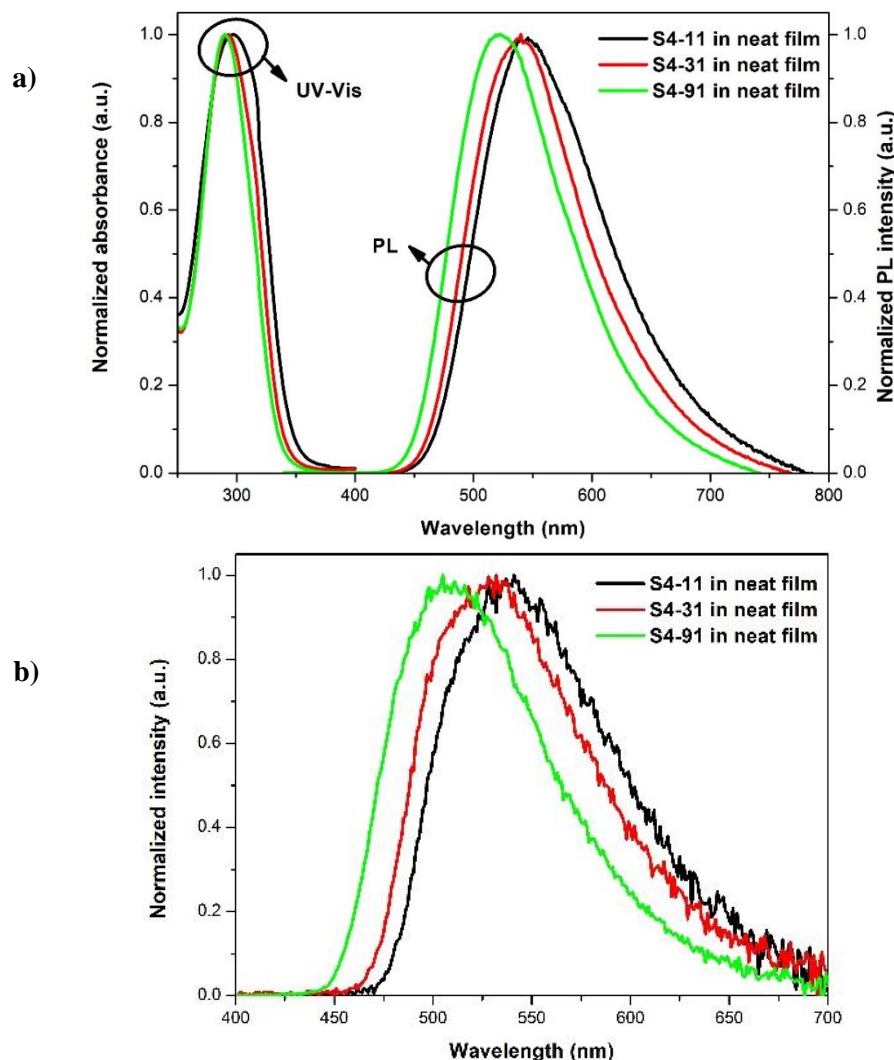


**Figure 3.5. 8** The normalized UV-vis absorption, photoluminescence (a), and phosphorescence spectra (b, at 77K) of **S4-11**, **S4-31**, and **S4-91** in neat film.

**Table 3.5. 4** The photophysical parameters of **S4** polymers in the neat film

	$\lambda_{\text{abs}}$	$\lambda_{\text{PL}}$	$\lambda_{\text{Phos}}$	PLQY <sup>a</sup>	HOMO <sup>b</sup>	Eg <sup>c</sup>	LUMO <sup>d</sup>	$\Delta E_{\text{ST}}$ <sup>e</sup>	Stokes shift
	(nm)	(nm)	(nm)	(%)	(eV)	(eV)	(eV)	(eV)	(cm <sup>-1</sup> )
<b>S4-11</b>	297	540	541	23	-5.99	2.95	-3.04	0.05	15152
<b>S4-31</b>	293	540	532	33	-5.95	2.97	-2.98	0.04	15611
<b>S4-91</b>	290	522	505	52	-5.95	3.05	-2.90	0.03	15326

<sup>a</sup> Measured in argon atmosphere; <sup>b</sup> Measured by photoelectron spectroscopy; <sup>c</sup> the optical energy gap calculated from the onset of absorption spectra of polymers in the neat film; <sup>d</sup> deduced from the HOMO and Eg values; <sup>e</sup> calculated from the onsets of fluorescence (RT) and phosphorescence spectra (77K).

The Stokes shift can be calculated and equal for **S4-11** (**S4-31** and **S4-91** respectively) in neat film, 243 nm ( $15152\text{ cm}^{-1}$ ) (247 nm ( $15611\text{ cm}^{-1}$ ) and 232 nm ( $15326\text{ cm}^{-1}$ ), respectively).

As represented in Figure 3.5. 9, the HOMO energy level of **S4** polymers was also determined in neat films by photoelectron spectroscopy and the values are -5.99, -5.95, and -5.95 eV for **S4-11**, **S4-31**, and **S4-91**, respectively. Thus, LUMO energy levels were deduced from the HOMO and the optical energy gap measured by UV-Visible measurements (see Figure 3.5.4).

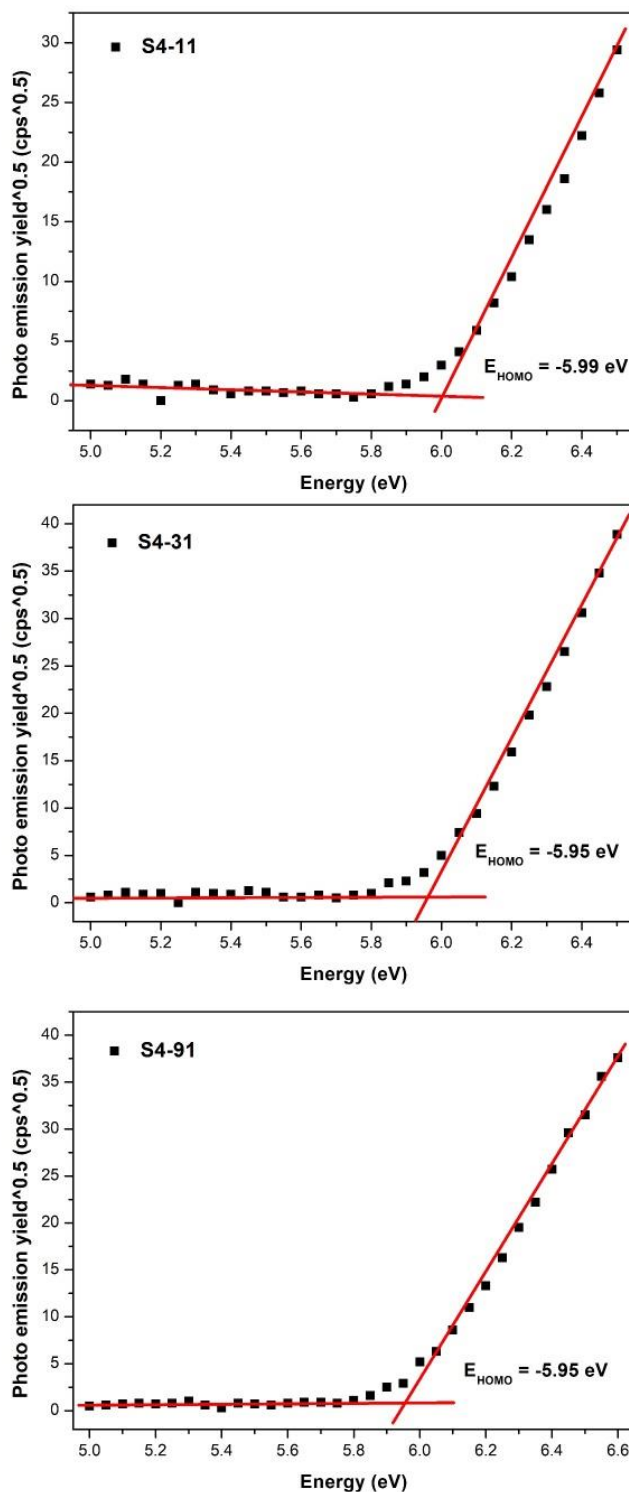


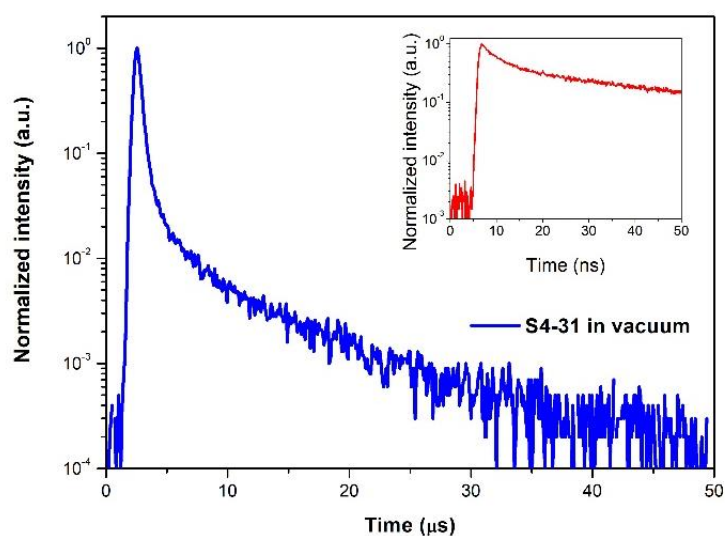
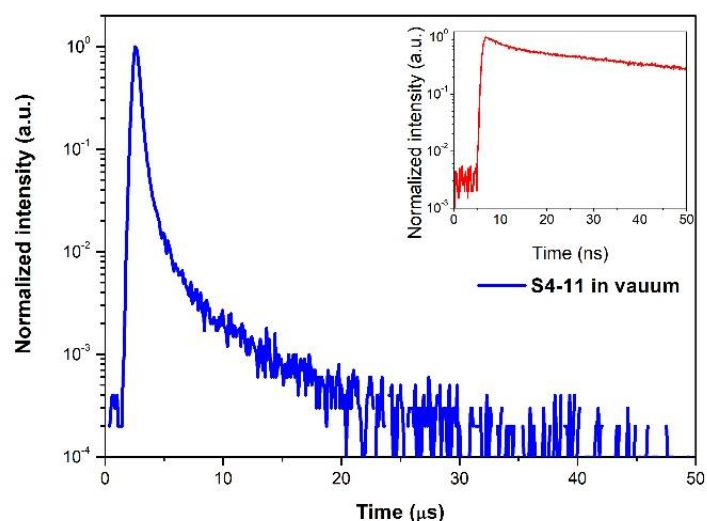
**Figure 3.5. 9** The photoelectron spectra of **S4** polymers in neat film.

Finally, the PLQYs of **S4-11**, **S4-31**, and **S4-91** in neat films under nitrogen atmosphere were measured to be 23, 33, and 53%, respectively, which are lower than those in dilute toluene (57-63%). This indicates that aggregation-caused quenching must exist in these neat films, especially in the case of **S4-11** and **S4-31**.

#### *Time-resolved measurements*

To further confirm the TADF behavior of **S4** polymers in neat film, streak camera measurements were utilized to investigate time-resolved transient PL spectra in vacuum at room temperature.

As shown in Figure 3.5. 10, the transient PL spectra were recorded with two time-scales: 50 ns and 50  $\mu$ s. All these polymers exhibit distinct prompt and delayed components, corresponding to the TADF nature, and the prompt component can be fitted with a mono-exponential function, while the delayed component is fitted with a bi-exponential function (calculation details in Table 3.5. 4).



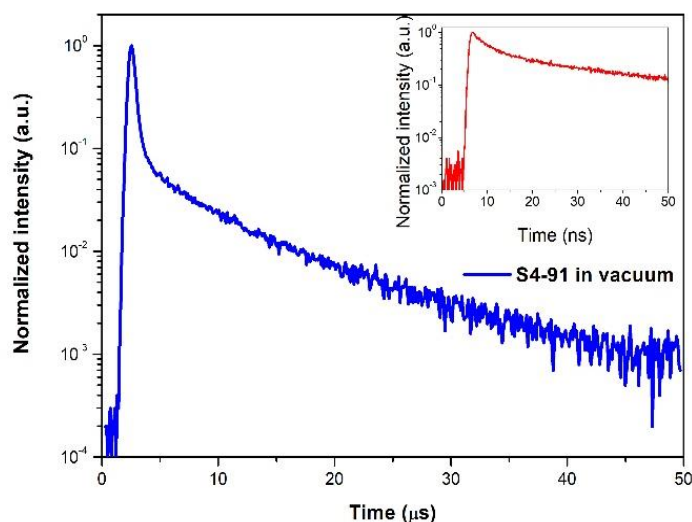


**Figure 3.5. 10** The PL decay curves of **S4-11**, **S4-31**, and **S4-91** in neat film measured by a streak camera at RT in vacuum.

The polymers exhibit longer emission lifetimes when the acceptor content in backbones decreases (Table 3.5.5). This behavior is consistent with the higher PLQYs also observed and could be explained by the reduction of the concentration quenching from **S4-11** to **S4-91**.

**Table 3.5. 5** PF and DF lifetimes of **S4** polymers in neat films

	$A_{PF}$	$\tau_{PF}(ns)$	$A_{DF1}$	$\tau_{DF1}(\mu s)$	$A_{DF2}$	$\tau_{DF2}(\mu s)$	$\phi_{DF1}/\phi_{DF2}/\phi_{PF}$
<b>S4-11</b>	0.61802	11.7	0.01404	0.63	0.00874	3.6	18.6 / 66.2 / 15.2
<b>S4-31</b>	0.75455	6.7	0.03148	0.78	0.01522	5.8	20.8 / 74.9 / 4.3
<b>S4-91</b>	0.52133	6.4	0.04456	0.91	0.05574	7.2	9.1 / 90.1 / 0.8

The prompt and delayed lifetimes were calculated from the PL decay curves (50 ns and 50  $\mu s$  scale, respectively) in vacuum measured by a streak camera.

As **S4-91** presents the highest PLQY and largest DF component, the temperature-dependent time-resolved measurements of this polymer were performed as shown in Figure 3.5. 11, and the data are summarized in Table 3.5. 6.

**Table 3.5. 6** DF lifetimes of **S4-91** in the neat film measured by a streak camera

T (K)	$A_{DF1}$	$\tau_{DF1}(\mu s)$	$A_{DF2}$	$\tau_{DF2}(\mu s)$	$\tau_{DF,av}(\mu s)$	$R^2$
100	0.01251	0.840	0.01711	11.6	11.0	0.99199
150	0.01805	0.793	0.02361	10.9	10.3	0.99391
200	1.318E-4	0.753	0.02171	9.70	9.7	0.9948
250	0.06689	0.694	0.04602	8.28	7.5	0.99542
300	0.01702	0.894	0.04619	7.40	7.1	0.99704

The average lifetime is calculated using  $\tau_{DF,av} = \sum A_i \tau_i^2 / \sum A_i \tau_i$

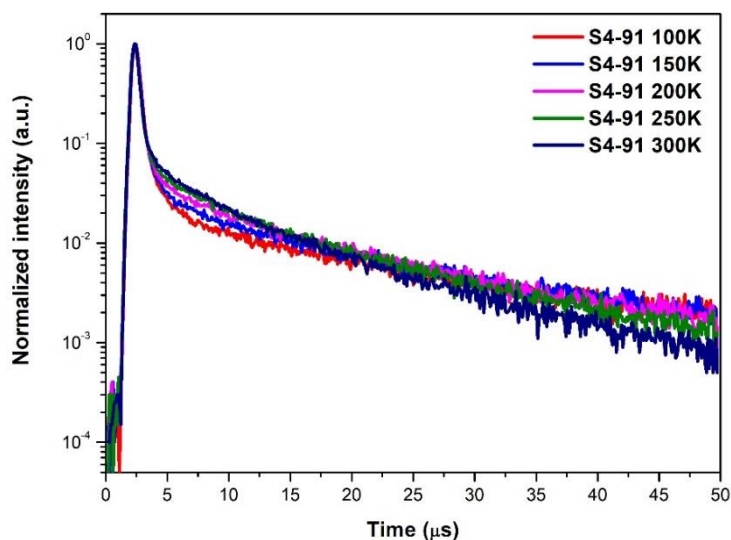


**Figure 3.5. 11** The temperature-dependent time-resolved PL spectra of **S4-91** measured by a streak camera (100-300K) in vacuum.

All the curves exhibit two clear components, prompt fluorescence (PF) in the nanosecond scale and DF in the microsecond scale. The positive temperature dependence of the decays in the DF region from 100 to 300K reveals the monomolecular process, confirming their TADF mechanism. And 50 K is too low for the polymers to realize the up-conversion from the triplet to singlet state.

### 3.5.3 Conclusion

In this section, we designed and synthesized a new series of vinyl polymers namely, **S4** polymers, with TSB interactions between the donor (acridan) and the acceptor (cyano-pyrimidin) units. The two donor and acceptor monomers were successfully synthesized from commercially available starting materials, respectively, using  $\text{Pd}_2(\text{dba})_3$  as the catalyst. The **S4** polymer series were prepared *via* radical polymerization at 60°C for 48h with 5% AIBN as the initiator and dry toluene as the solvent. The chemical structures of the monomers and polymers were confirmed by NMR and the real ratio of the electron-donating and electron-withdrawing units were further calculated from elemental analysis. Moreover, SEC measurements demonstrated that the relative number-average molecular weights ( $M_{n,\text{SEC}}$ ) of these polymers range from 19 to 39 kDa, with a relatively low dispersity (1.44-1.98).

Small  $\Delta E_{\text{ST}}$  values of 0.03-0.05 eV indicate a possible easy up-conversion from triplet to singlet states (RISC). The investigation of the photophysical properties of these polymers in solution and neat film was carried out. In toluene, the PLQYs are about 57-63% in oxygen-free toluene and the photoluminescence time-resolved measurements showed proper TADF properties with  $\mu\text{s}$  scale fluorescence lifetimes. In solid-state (neat film), the PLQYs of polymers reached relatively high values such as 52% for **S4-91** which also presents proper prompt and delayed components, confirming the TADF properties of these through-space conjugated macromolecular systems.

Note that the potential of these materials in solution-processed OLEDs should be investigated very soon and we expect relatively good device efficiencies with low roll-off properties, considering the good PLQYs and the short delayed fluorescence lifetimes of these materials.

## **General conclusions and perspectives**

## Conclusions and perspectives

Organic semiconductors (OSCs), i.e.  $\pi$ -conjugated small molecules or polymers, have attracted researchers' attention due to their fascinating electronic and photophysical properties. These OSCs have been widely applied in organic electronics, such as organic electroluminescent diodes (OLEDs), organic photovoltaic cells (OPVs), and organic field-effect transistors (OFETs), since they are light-weight, solution-processable, flexible, and they possess tunable properties. This Ph.D. thesis aims to design and synthesize new  $\pi$ -conjugated polymers for OFET and/or OLED applications.

The first objective of this Ph.D. thesis (**chapter 2**) was the design, synthesis, and characterization of new side-chain liquid-crystalline  $\pi$ -conjugated polymers consisting of  $\pi$ -conjugated backbones bearing side-on semiconducting mesogenic groups, which can self-organize into an ordered nanostructure. Two target polymers, i.e. **Polythiophene-oxa** and **PBTTT-Tri**, were successfully synthesized through optimized procedures and their chemical structures were determined by NMR, SEC, and elemental analysis. More precisely, **Polythiophene-oxa** is composed of regioregular poly(3-alkylthiophene) as the backbone and calamitic-type electron-acceptor oxadiazole entities as side groups. Similarly, **PBTTT-Tri** consists of a poly(2,5-bis(3-alkylthiophen-2-yl)thieno[3,2-b]thiophene) (PBTTT) backbone and discotic-type triphenylene side groups.

The thermal behavior and self-organization of the polymers were further investigated by POM, DSC, XRD, SAXS, and GIWAX. The preliminary charge transport properties were also evaluated in OFET configuration. More specifically, **Polythiophene-oxa** was able to self-organize with an alternation of bilayer of calamitic mesogens side groups and of polythiophene backbone monolayers, and it exhibits p-type conduction with a hole mobility of around  $1.2 \times 10^{-3} \text{ cm}^2 \text{ V}^{-1} \text{ s}^{-1}$  in the saturated regime. **PBTTT-Tri** can self-organize in a supramolecular arrangement with the alternation of triple rows of triphenylene columns and the backbone monolayer parallel to the substrate plane. **PBTTT-Tri** exhibits p-type conduction and its hole mobility in the saturated regime is around  $1.2 \times 10^{-5} \text{ cm}^2 \cdot \text{V}^{-1} \cdot \text{s}^{-1}$ . These results are promising and further investigation to promote charge transport properties of the polymers will be performed.

The second objective of this thesis (**chapter 3**) was to design and explore 2 new families of donor-acceptor (D-A) polymers as potential TADF materials. These polymers were successfully synthesized by multi-step chemical strategy and their chemical structures were also determined by NMR, SEC, and elemental analysis. As part of this project, I had the great opportunity to work for around one month in the laboratory of Prof. Chihaya Adachi (OPERA Laboratory) at Kyushu University in Fukuoka (Japan). In OPERA, I carried out the photophysical experiments by myself.

More particularly, two groups of polymers, **S1** and **S2**, were linear conjugated polymers with the architecture of donor units fixed in the backbone and acceptor units endowed in the side chains. These

polymers all exhibit typical TADF nature. Besides, one solution-processed OLED device, using **S2-11** CBP blend film as the EML, was prepared and achieved a maximum luminance ( $L_{\max}$ ) of around 5600 cd/m<sup>2</sup>, with an EQE of 1.9%. The electroluminescent properties could be further optimized by changing the parameters of the device fabrication, as well as doped emitting films and other layers.

**S3** and **S4** polymers were designed to achieve TADF character by through-space conjugation (TSC). Unfortunately, only **S4** polymers show TADF nature, while the fluorescence decay curves of **S3** polymers don't show temperature dependence. Anyway, the preliminary results of **S4** polymers are very promising and their photophysical properties in blend films and electroluminescent properties will be investigated soon.

To conclude the work undertaken during my Ph.D., I'd like to point out that this work was focused on the design and organic synthesis. Several synthetic procedures were optimized, in the meanwhile, some synthetic routes were given up. Through numerous attempts, I learned a lot about organic chemistry, experiment skills, and scientific research.



## **Appendices**

## Appendix 1. Experimental

### Materials and methods

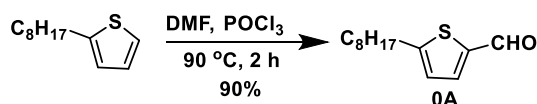
*Materials.* All chemicals were purchased from commercial suppliers including Sigma Aldrich, Alfa, Acros, TCI, or Chemflow, and they were used without further purification. The solvents used came from VWR Chemicals or Acros, and were dried over an MBraun solvent purification system (MB SPS-800). The purifications by chromatography were either carried out by gravity column chromatography using silica gel (Si 60, 40-63  $\mu\text{m}$ , Merck) or by flash chromatography (Combiflash Companion).

*Structural characterization.* The nuclear magnetic resonance (NMR) experiments were performed on Bruker spectrometers.  $^1\text{H}$  NMR spectra were recorded at 300, 400, or 600 MHz, relatively,  $^{13}\text{C}$  NMR spectra were recorded at 75, 101, or 150 MHz. The proton and carbon chemical shifts are reported in ppm using the residual deuterated solvent signal as internal standard<sup>271</sup>:  $\text{CDCl}_3$  (7.26, 77.16),  $\text{CDCl}_2$  (5.32, 53.84), acetone (2.05, 29.84 / 206.26), and DMSO (2.50, 39.52). The abbreviations for describing the multiplicity of NMR peaks are: s = singlet, d = doublet, t = triplet, q = quartet, and m = multiplet. The size exclusion chromatography (SEC) was performed using an Agilent 1100 Series SEC equipped with a 300 mm x 7.5 PLgel Mixed-D 5  $\mu\text{m}$  10-4  $\text{\AA}$ , a refractive-index (RI) detector, and diode-array UV-vis detector (DAD) (calibration: polystyrene standards). The column temperature and the flow rate were fixed to 40°C and 1mL/min in THF (HPLC-Grade). The THF solution used was filtered using a cellulose filter (pore size: 0.20  $\mu\text{m}$ ) before sample injection.

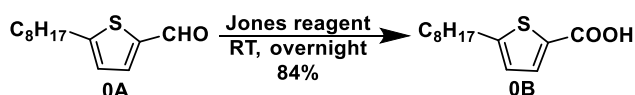
The optical textures of the mesophases were studied with a Leitz polarizing microscope equipped with a Mettler FP82 hot-stage and an FP80 central processor. The transition temperatures and enthalpies were measured by differential scanning calorimetry with a TA Instruments DSCQ1000 instrument operated at a scanning rate of 20°C min<sup>-1</sup> on heating and cooling. The SAXS patterns were obtained with a transmission Guinier-like geometry. A linear focalized monochromatic Cu K $\alpha$ 1 beam ( $\lambda = 1.5405 \text{ \AA}$ ) was obtained using a sealed-tube generator (600 W) equipped with a bent quartz monochromator. In all cases, the crude powder was filled in Lindemann capillaries of 1 mm diameter and 10  $\mu\text{m}$  wall-thickness. The diffraction patterns were recorded with a curved Inel CPS120 counter gas-filled detector linked to a data acquisition computer (periodicities up to 90  $\text{\AA}$ ) and on image plates scanned by Amersham Typhoon IP with 25  $\mu\text{m}$  resolution (periodicities up to 120  $\text{\AA}$ ). GIWAXS measurements were conducted at PLS-II 9A U-SAXS beamline of Pohang Accelerator Laboratory (PAL) in Korea. Samples consisted in layers on a silicon wafer of thirty to sixty nanometers thickness. The X-rays coming from the vacuum undulator (IVU) were monochromated using Si(111) double crystals and focused on the detector using K-B type mirrors. Patterns were recorded with a Rayonix 2D SX 165 CCD detector. The sample-to-detector distance was about 225 mm for an energy of 11.015 keV (1.1256  $\text{\AA}$ ).

*Photoluminescence and electroluminescence characteristics.* UV/Vis spectra were recorded on a Shimadzu UV- 2501 recording spectrophotometer and the fluorescence spectra were recorded on a Hitachi F-4600 fluorescence spectrophotometer. The PLQY measurements were performed on a Quantaaurus-QY measurement system (C11347-11, Hamamatsu Photonics). The steady-state fluorescence decay and lifetime were measured by a single photon counting spectrometer from Edinburgh Instruments (FLS920) with a Picosecond Pulsed UV-LASTER (LASTER377) as the excitation source. Prompt fluorescence (PF), delayed fluorescence (DF), and phosphorescence spectra in solid states were measured under vacuum using a streak camera system (C4334, Hamamatsu Co.). A nitrogen gas laser (MNL200, LASERTECHNIK BERLIN) with an excitation wavelength of 337nm was used. Excitation light was absolutely cut off by putting a 370 nm long band-pass filter (SCF-50S-37L, SIGMA KOKI CO., LTD.) in front of the photo-detector. The current density-voltage-luminance (J-V-L) characteristics of the OLED were measured using a semiconductor parameter analyzer (Agilent Co., HP4155C) with an optical power meter (Newport, Model 1835-C).

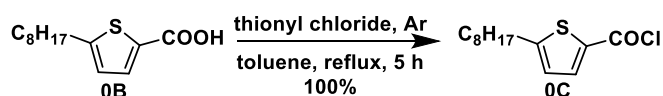
## Synthetic procedures



**5-*n*-Octylthiophene-2-carbaldehyde (0A).** To a solution of 2-*n*-octylthiophene (3.94 g, 20 mmol) in DMF (4.7 mL, 60 mmol), POCl<sub>3</sub> (5.6 mL, 60 mmol) was added dropwise at 0 °C, stirring being continued for 20 min at this temperature. The mixture was warmed to 90 °C and refluxed for 2 h. Then the mixture was poured slowly into ice water and neutralized by NaOH to pH = 7. After extraction with CHCl<sub>3</sub>, the organic phase was dried by anhydrous MgSO<sub>4</sub>. The crude product was purified by column chromatography on silica gel using ethyl acetate/petrum ether (v/v = 1/4) as the eluent to obtain a yellow oil (Yield: 4 g, 90%). <sup>1</sup>H NMR (300 MHz, CDCl<sub>3</sub>): δ<sub>H</sub> = 9.80 (1H, s, -CHO), 7.60 (1H, d, *J* = 3.6 Hz, 2-H<sub>arom</sub>), 6.89 (1H, d, *J* = 3.6 Hz, 1-H<sub>arom</sub>), 2.86 (2H, t, *J* = 7.6 Hz, -CH<sub>2</sub>-Ar), 1.70 (2H, m, H<sub>aliph</sub>), 1.38-1.25 (10H, m, H<sub>aliph</sub>), 0.87 (3H, t, *J* = 6.6 Hz, -CH<sub>3</sub>). <sup>13</sup>C NMR (75 MHz, CDCl<sub>3</sub>): δ<sub>C</sub> = 182.72, 157.89, 141.72, 137.10, 125.94, 31.93, 31.40, 30.96, 29.35, 29.27, 29.14, 22.75, 14.19.

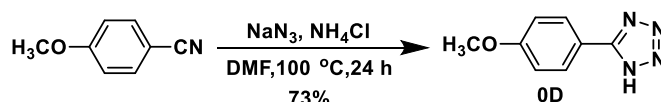


**5-*n*-Octylthiophene-2-carboxylic acid (0B).** The preparation of Jones reagent: H<sub>2</sub>SO<sub>4</sub> (98%, 30 mL) was slowly added into water (120 mL). After cooling down to room temperature, CrO<sub>3</sub> (39 g, 0.39 mmol) was dissolved into the above solution. Jones reagent (12 mL) was added to a stirred solution of 5-*n*-octylthiophene-2-carbaldehyde (2.89 g, 12.9 mmol) in acetone (40 mL) in the ice water bath (<20 °C). The mixture was stirred at room temperature overnight. The solution was decanted from the green precipitation of Cr<sub>2</sub>O<sub>3</sub> and concentrated to about 10% of volume. The precipitation was washed with ether. Combining the ether solution and concentrated acetone solution, the resulting solution was washed with water to remove sulfuric acid (3 x 30 mL). The organic phase was extracted with a saturated NaHCO<sub>3</sub> solution (3 x 30 mL). HCl (37%) was added into NaHCO<sub>3</sub> solution until a white precipitate appeared. After filtrating, a white solid was dried in vacuum (2.6 g, 84%). <sup>1</sup>H NMR (300 MHz, CDCl<sub>3</sub>): δ<sub>H</sub> = 10.90 (1H, s, -COOH), 7.73 (1H, d, *J* = 3.8, 2-H<sub>arom</sub>), 6.82 (1H, d, *J* = 3.8, 1-H<sub>arom</sub>), 2.85 (2H, t, *J* = 7.6 Hz, -CH<sub>2</sub>-Ar), 1.73 (2H, m, H<sub>aliph</sub>), 1.33-1.28 (10H, m, H<sub>aliph</sub>), 0.88 (3H, t, *J* = 6.6 Hz, -CH<sub>3</sub>). <sup>13</sup>C NMR (75 MHz, CDCl<sub>3</sub>): δ<sub>C</sub> = 168.06, 156.29, 135.49, 129.90, 125.69, 31.97, 31.53, 30.73, 29.39, 29.31, 29.17, 22.79, 14.23.

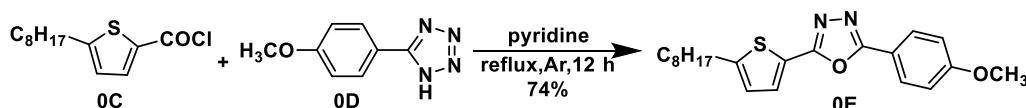


**5-*n*-Octylthiophene-2-carbonyl chloride (0C).** 5-*n*-octylthiophene-2-carboxylic acid (2.6 g, 10.8 mmol) was dissolved in 15 mL of toluene under an atmosphere of Ar. Thionyl chloride (3.9 mL, 54

mmol) was added dropwise *via* a syringe at 60 °C and then the solution was heated to reflux for 5 h. The reaction mixture was cooled to room temperature. Toluene and excess thionyl chloride were removed in vacuum to give a yellow oil (2.7 g, >95%). <sup>1</sup>H NMR (300 MHz, CDCl<sub>3</sub>): δ<sub>H</sub> = 7.82 (1H, d, *J* = 4.0 Hz, 1-H<sub>arom</sub>), 6.89 (1H, d, *J* = 4.0 Hz, 2-H<sub>arom</sub>), 2.86 (2H, t, *J* = 7.6 Hz, -CH<sub>2</sub>-Ar), 1.71 (2H, m, Haliph), 1.33-1.27 (10H, m, Haliph), 0.88 (3H, t, *J* = 6.8 Hz, -CH<sub>3</sub>). <sup>13</sup>C NMR (75 MHz, CDCl<sub>3</sub>): δ<sub>C</sub> = 160.77, 159.41, 138.78, 134.13, 126.47, 31.92, 31.32, 31.01, 29.32, 29.26, 29.11, 22.76, 14.20.



**5-(4-Methoxy-phenyl)-2-h-tetrazole (0D).** 5-(4-methoxy-phenyl)-2-h-tetrazole was synthesized according to the thesis of Andrea Castiglione (Pierre and Marie Curie University). 4-methoxybenzonitrile (6.66 g, 50 mmol), sodium azide (4.88 g, 75 mmol), and ammonium chloride (4.01 g, 75 mmol) were dissolved in 80 mL of DMF under an atmosphere of Ar. The resulting solution was heated at 100°C for 24 hours. The reaction was allowed to cool down to room temperature and HCl was added until precipitation of a white powder occurred and was filtered as well as dried (Yield: 6.4 g, 73%). <sup>1</sup>H NMR (300 MHz, DMSO-*d*<sub>6</sub>): δ<sub>H</sub> = 16.60 (1H, s, NH), 7.98 (2H, d, *J* = 9.0 Hz, 1-H<sub>arom</sub>), 7.6 (2H, d, *J* = 9.0 Hz, 1-H<sub>arom</sub>), 3.84 (3H, s, -CH<sub>3</sub>). <sup>13</sup>C NMR (75 MHz, DMSO-*d*<sub>6</sub>): δ<sub>C</sub> = 161.47, 154.78, 128.64, 116.32, 114.83, 55.44.

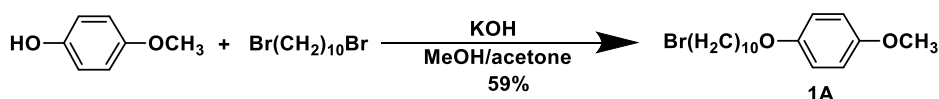


**2-(4-Methoxy-phenyl)-5-(5-octyl-thiophene-2-yl)-[1,3,4]oxadiazole (0E).** 5-n-octylthiophene-2-carbonyl chloride (**0C**) (2.7 g, 10.5 mmol) and 5-(4-methoxy-phenyl)-2-h-tetrazole (**0D**) (1.54 g, 8.7 mmol) were dissolved in 10 mL of pyridine under an atmosphere of Ar. The resulting solution was heated under reflux for 12 hours. The reaction was cooled down to room temperature and successively quenched by pouring 50 mL of water, causing the precipitation of a yellow solid (Yield: 2.4 g, 74%). <sup>1</sup>H NMR (300 MHz, CDCl<sub>3</sub>): δ<sub>H</sub> = 8.04 (2H, m, 3-H<sub>arom</sub>), 7.62 (1H, d, *J* = 3.7, 2-H<sub>arom</sub>), 7.02 (2H, m, 4-H<sub>arom</sub>), 6.85 (1H, m, 1-H<sub>arom</sub>), 3.89 (3H, s, -OCH<sub>3</sub>), 2.87 (2H, t, *J* = 7.5 Hz, -CH<sub>2</sub>-Ar), 1.73 (2H, m, H<sub>aliph</sub>), 1.41-1.28 (10H, m, H<sub>aliph</sub>), 0.88 (3H, t, *J* = 6.7 Hz, -CH<sub>3</sub>). <sup>13</sup>C NMR (75 MHz, CDCl<sub>3</sub>): δ<sub>C</sub> = 162.36, 151.69, 129.60, 128.74, 125.43, 122.67, 116.49, 114.58, 55.58, 31.95, 31.58, 30.36, 29.39, 29.31, 29.15, 22.77, 14.22.

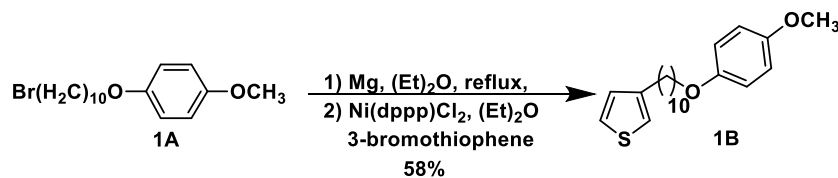


**2-(4-Phenol)-5-(5-octyl-thiophene-2-yl)-[1,3,4]oxadiazole (0F).** 2-(4-methoxy-phenyl)-5-(5-octyl-

thiophene-2-yl)-[1,3,4]oxadiazole (**0E**) (2.7 g, 7.3 mmol) was dissolved in 10 mL of freshly distilled CH<sub>2</sub>Cl<sub>2</sub> under an atmosphere of Ar. The resulting solution was cooled down at 0°C and subsequently stirred for 10 minutes. BBr<sub>3</sub> (11 mL, 11.0 mmol) was added dropwise *via* a syringe at this temperature, the resulting suspension being then kept and stirred for 3 hours at room temperature. This “mixture” was diluted with 100 mL of CH<sub>2</sub>Cl<sub>2</sub>. The organic phase was washed with water (3 x 100 mL), dried over anhydrous MgSO<sub>4</sub>, and concentrated under reduced pressure. The crude product was submitted to column chromatography over silica gel, using the mixture of ethyl acetate and CH<sub>2</sub>Cl<sub>2</sub> (v/v=40:1) as eluant, and subsequently concentrated under reduced pressure to yield a white powder (Yield: 1.3 g, 50 %). <sup>1</sup>H NMR (300 MHz, DMSO-*d*<sub>6</sub>): δ<sup>H</sup> = 10.32 (1H, s, OH), 7.90 (2H, m, 3-H<sub>arom</sub>), 7.67 (1H, d, *J* = 3.7 Hz, 2-H<sub>arom</sub>), 6.98 (2H, m, 1-H<sub>arom</sub>), 6.94 (1H, m, 4-H<sub>arom</sub>), 2.83 (3H, t, *J* = 7.5 Hz, -CH<sub>2</sub>Ar), 1.62 (2H, m, H<sub>aliph</sub>), 1.28-1.21 (10H, m, H<sub>aliph</sub>), 0.82 (3H, t, *J* = 6.7 Hz, CH<sub>3</sub>). <sup>13</sup>C NMR (75 MHz, DMSO-*d*<sub>6</sub>): δ<sup>C</sup> = 163.38, 160.85, 159.52, 150.88, 129.93, 128.51, 126.05, 121.75, 116.16, 113.86, 31.24, 30.92, 29.32, 28.65, 28.62, 28.40, 22.07, 13.89.

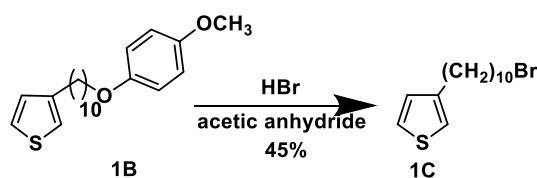


**1-(10-Bromodecyloxy)-4-methoxybenzene (1A).** 1,10-Dibromodecane (82.60 g, 0.2752 mol) was dissolved in acetone (170 mL) and the solution was heated to reflux under a normal atmosphere. Then a solution of KOH (9.26 g, 0.1651 mol) and 4-methoxyphenol (17.08 g, 0.1376 mol) in methanol (170 mL) was added during about 1 h. The resulting suspension was heated to reflux for 24 h, concentrated, diluted with water, and extracted with diethyl ether. The organic phase was washed with diluted NaOH solution and water, dried over anhydrous MgSO<sub>4</sub>. The solvent was removed by rotary evaporation and white solid was obtained by recrystallization from petroleum ether (Yield: 28.3 g, 59%). <sup>1</sup>H NMR (400 MHz, CDCl<sub>3</sub>): δ<sub>H</sub> = 6.83 (4H, s), 3.90 (2H, t, *J* = 6.6 Hz), 3.77 (3H, s), 3.41 (2H, t, *J* = 6.9 Hz), 1.86 (2H, m), 1.73 (2H, m), 1.48-1.41 (4H, m), 1.38-1.28 (8H, m). <sup>13</sup>C NMR (100 MHz, CDCl<sub>3</sub>): δ<sub>C</sub> = 153.79, 153.42, 115.55, 114.74, 68.76, 55.86, 34.15, 32.96, 29.57, 29.51, 29.48, 28.87, 28.29, 26.17.

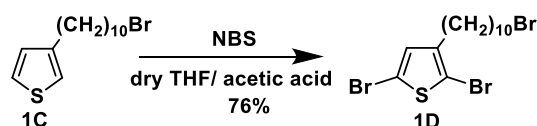


**3-(10-(4-Methoxyphenoxy)decyl)thiophene (1B).** All glassware and solvents are dried carefully before use. Freshly washed magnesium turnings (0.51 g; 21 mmol) and dry diethyl ether (5 mL) were placed in a three necked-flask and the mixture was heated to reflux gently under argon. After adding one grain of iodine, a solution of 1-(10-bromodecyloxy)-4-methoxybenzene (B1) (2.43 g; 7.1 mmol)

in dry diethyl ether (100 mL) was added dropwise in the above mixture over 1 h and the resulting Grignard mixture was stirred under reflux overnight. 3-Bromothiophene (1.21 g; 7.455 mmol), Ni(dppp)Cl<sub>2</sub> (0.038 g; 0.07 mmol), and dry diethyl ether (40 mL) were placed in a second flask and the mixture was cooled down to 0 °C. The resulting Grignard mixture was then slowly transferred via cannula to the second flask under argon. The mixture was heated to reflux for 24 h before quenched by a cold 0.2 M HCl and extracted with CH<sub>2</sub>Cl<sub>2</sub>. The organic phase was washed with water until pH = 7 and then dried over MgSO<sub>4</sub>. White solid was obtained after removing the solvent by vacuum evaporation and further purified by column chromatography (petroleum ether: diethyl ether = 15:1, silica gel) (Yield: 1.8 g, 58%). <sup>1</sup>H NMR (400 MHz, CDCl<sub>3</sub>): δ<sub>H</sub> = 7.24 (1H, dd, *J* = 4.9 Hz, *J* = 3.0 Hz), 6.96-6.92 (2H, m), 6.84 (4H, s), 3.91 (2H, t, *J* = 6.6 Hz), 3.77 (3H, s), 2.63 (2H, t, *J* = 7.8 Hz), 1.76 (2H, m), 1.63-1.59 (2H, m), 1.49-1.39 (2H, m), 1.39-1.26 (10H, m). <sup>13</sup>C NMR (100 MHz, CDCl<sub>3</sub>): δ<sub>C</sub> = 153.81, 153.46, 143.37, 128.41, 125.15, 119.89, 115.59, 114.76, 68.81, 55.88, 30.69, 30.42, 29.69, 29.64, 29.58, 29.54, 29.46, 26.20.

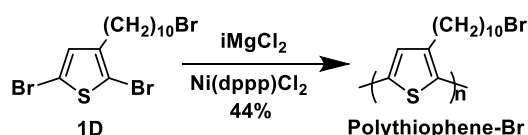


**3-(10-Bromodecyl)thiophene (1C).** A mixture of HBr (4 mL, 48 wt%, 36 mmol) and acetic anhydride (5.6 mL, 60 mmol) was added under argon to 3-(10-(4-Methoxyphenoxy)decyl)thiophene (1.82 g, 6 mmol), and the reaction mixture was heated to 100 °C for 24 h. After dilution with water, the mixture was extracted three times with diethyl ether. The combined organic phases were washed with saturated NaHCO<sub>3</sub> solution until pH neutrality. After adding petroleum ether, the solution was settled overnight for hydroquinone precipitating completely. The solution was then filtered and submitted to a short silica gel column with petroleum ether as the eluant. Colorless oil was obtained after removing the solvent (Yield: 0.82 g, 45%). <sup>1</sup>H NMR (400 MHz, CDCl<sub>3</sub>): δ<sub>H</sub> = 7.24 (1 H<sub>arom</sub>, dd, *J* = 4.9 Hz, *J* = 2.9 Hz), 6.95-6.22 (2H<sub>arom</sub>, m), 3.41 (2H, t, *J* = 6.9 Hz, -CH<sub>2</sub>-Br), 2.63 (2H, t, *J* = 7.7 Hz, -CH<sub>2</sub>-Ar), 1.86 (2H<sub>aliph</sub>, m), 1.63 (2H<sub>aliph</sub>, m), 1.40-1.25 (12H<sub>aliph</sub>, m). <sup>13</sup>C NMR (100 MHz, CDCl<sub>3</sub>): δ<sub>C</sub> = 143.32, 128.39, 125.15, 119.89, 34.15, 32.97, 30.67, 30.40, 29.58, 29.54, 29.42, 28.88, 28.30.

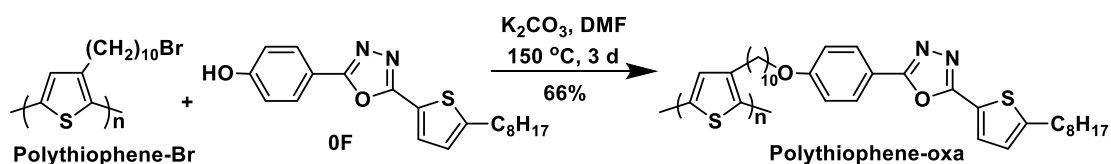


**2,5-Dibromo-3-(10-bromodecyl)thiophene (1D).** 3-(10-Bromodecyl)thiophene (**1C**) (1.14 g, 2.7 x 10<sup>-3</sup> mol) and N-Bromosuccinimide (1.06 g, 5.9 x 10<sup>-3</sup> mol) were dissolved in the mixture of 5 mL dry THF and 5 mL acetic acid. After stirring the reaction mixture at room temperature for 24 h, the reaction mixture was poured into cold water (15 mL) and extracted with diethyl ether (3 x 15 mL). The

organic phase was washed with water (3 x 15 mL), dried over anhydrous MgSO<sub>4</sub> and concentrated under reduced pressure. The crude product was deposited upon a column chromatography with silica gel, using petroleum ether as eluant, to give a colorless oil (Yield: 0.94 g, 76 %); <sup>1</sup>H NMR (400 MHz, CDCl<sub>3</sub>): δ<sub>H</sub> = 6.77 (1 H<sub>arom</sub>, s), 3.41 (2H, t, *J* = 6.8 Hz, -CH<sub>2</sub>-Br), 2.50 (2H, t, *J* = 7.6 Hz, -CH<sub>2</sub>-Ar), 1.85 (2H<sub>aliph</sub>, m), 1.55-1.29 (14H<sub>aliph</sub>, m); <sup>13</sup>C NMR (100 MHz, CDCl<sub>3</sub>): δ<sub>C</sub> = 143.08, 131.08, 110.45, 108.08, 34.17, 32.97, 29.68, 29.59, 29.52, 29.43, 29.18, 28.88, 28.30.

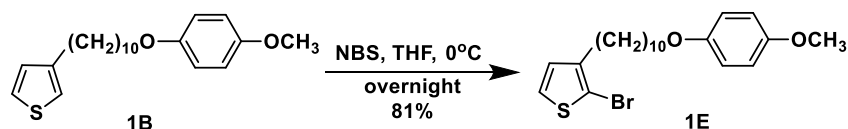


**Poly[3-(10-bromodecyl)thiophene (polythiophene-Br).** All glassware and solvents were carefully dried before use. 2,5-dibromo-3-(10-bromodecyl)thiophene (**1D**) (1.1 g, 2.4 x 10<sup>-3</sup> mol) was poured into 100 ml of dry THF at 0°C under argon atmosphere. A solution of isopropyl magnesium chloride (2.4 ml, 2.4 x 10<sup>-3</sup> mol, 2.0 M in THF) was added drop by drop through a syringe and the resulting pale yellow solution was stirred for 1h at 0°C. A suspension of Ni(dppp)Cl<sub>2</sub> (20 mg, 3.68 x 10<sup>-4</sup> mol, 1.5 mol %) in THF (5 ml) was quickly injected into the flask. The resulting red solution was gently warmed to room temperature and left overnight under constant stirring. The polymerization was quenched by pouring a 6 M solution of HCl (30 ml) followed by extraction with chloroform (30 ml). The organic layer was successively washed by water (3 x 30 ml), dried over MgSO<sub>4</sub>, and concentrated under reduced pressure. The crude product was then precipitated using methanol and the resulting purple solid was filtered through a Soxhlet thimble. The title compound was obtained (Yield: 320 mg, 44%) after successive extraction with methanol; M<sub>n</sub> = 1.03 x 10<sup>4</sup>, M<sub>w</sub>/M<sub>n</sub> = 1.2, DP = 34 (SEC-THF, PS Standard); <sup>1</sup>H NMR (600 MHz, CDCl<sub>3</sub>): δ<sub>H</sub> = 6.98 (1H, s, H<sub>arom</sub>), 3.39 (2H, t, *J* = 6.8 Hz, -CH<sub>2</sub>-Br), 2.80 (2H, m, -CH<sub>2</sub>-Ar), 1.90-1.60 (4H, m, H<sub>aliph</sub>), 1.50-1.31 (12H, m, H<sub>aliph</sub>); <sup>13</sup>C NMR (50 MHz, CDCl<sub>3</sub>): δ<sub>C</sub> = 139.98, 133.80, 130.59, 128.73, 34.16, 34.14, 32.95, 30.64, 29.64, 29.59, 29.56, 28.91, 28.31.

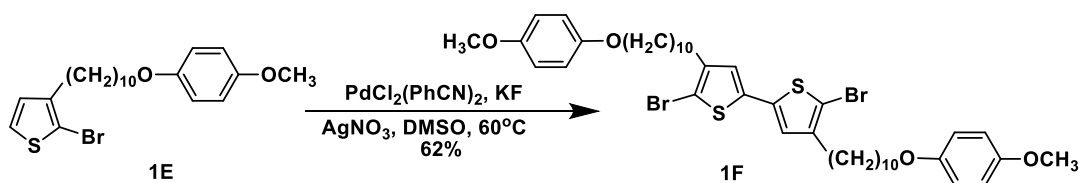


**Poly[2-(5-(octylthiophen-2-yl)-5-[4-(10-thiophen-3-decyloxy)-phenyl]-[1,3,4]oxadiazole (polythiophene-oxa).** 2-(4-phenol)-5-(5-octylthiophen-2-yl)-[1,3,4]oxadiazole (**A6**) (356 mg, 1 mmol), K<sub>2</sub>CO<sub>3</sub> (280 mg, 2 mmol) were dissolved in 100 mL DMF under argon. After 30 minutes, a solution of poly[3-(10-bromodecyl)thiophene] (**B5**) (151 mg, 0.5 mmol) in THF (3 mL) was added to the mixture. The resulting purple solution was stirred at 110 °C for 3 days, before being extracted at room temperature with chloroform (3 x 100 mL). The organic layer was successively washed with

water (3 x 100 mL), dried over anhydrous MgSO<sub>4</sub>, and concentrated under reduced pressure. The crude product was precipitated using methanol (50 mL) and the resulting solid was washed through a Soxhlet thimble. The crude product was submitted to semipreparative SEC, using chloroform as the eluant, the solution was collected in thirty bottles. A purple powder was obtained (Yield: 191 mg, 66 %). SEC: M<sub>n</sub> = 1.8 x 10<sup>4</sup>, M<sub>w</sub>/M<sub>n</sub> = 1.47, DP = 31 (SEC-THF, PS Standard); <sup>1</sup>H NMR (600 MHz, CDCl<sub>3</sub>): δ<sub>H</sub> = 7.96 (2H, s, H<sub>arom</sub>), 7.55 (1H, s, H<sub>arom</sub>), 6.96 (3H, m, H<sub>arom</sub>), 6.80 (1H, s, H<sub>arom</sub>), 3.94 (2H, s, -CH<sub>2</sub>-O), 2.82 (4H, m, -CH<sub>2</sub>-Ar), 1.75-1.69 (8H, m, H<sub>aliph</sub>), 1.42-1.31 (22H, m, H<sub>aliph</sub>), 0.86 (3H, s).

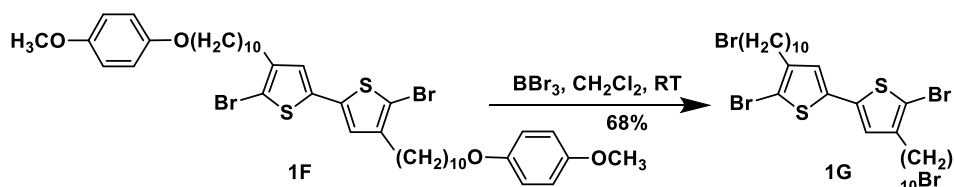


**2-Bromo-3-(10-(4-methoxyphenoxy)decyl)thiophene (1E).** 3-(10-(4-Methoxyphenoxy)-decyl)thiophene (**1B**, 2.2 g, 6.35 mmol) and N-bromosuccinimide (1.246 g, 7 mmol) were dissolved in 10 mL of dry DMF. After stirring at room temperature in dark overnight, the mixture was poured into cold water (100 mL) and extracted with diethyl ether (3 x 100 mL). The organic phase was washed with water (3 x 100 mL), dried over anhydrous MgSO<sub>4</sub> and the solvent was removed in vacuum. The crude product was further purified by column chromatography (petroleum ether, silica gel) as a yellow liquid (Yield: 2.2 g, 81%). <sup>1</sup>H NMR (400 MHz, CDCl<sub>3</sub>) δ<sub>H</sub> = 7.19 (d, *J* = 5.6 Hz, 2H), 6.83(s, 4H), 6.78(d, *J* = 5.6 Hz, 2H), 3.90(t, *J* = 6.6 Hz, 2H), 3.77(s, 3H), 2.56(t, *J* = 7.5 Hz, 2H), 1.75(m, 2H), 1.56(m, 2H), 1.44(m, 2H), 1.30(m, 10H). <sup>13</sup>C NMR (101 MHz, CDCl<sub>3</sub>) δ<sub>C</sub> = 153.81, 153.46, 142.09, 128.37, 125.27, 115.58, 114.76, 108.93, 77.16, 68.82, 55.89, 30.43, 29.85, 29.68, 29.61, 29.54, 29.33, 26.20.

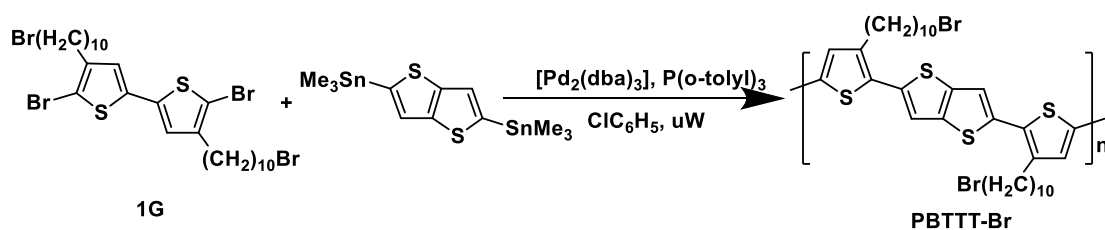


**5,5'-Dibromo-4,4'-bis[10-(4-methoxyphenoxy)decyl]-2,2'-bithiophene (1F).** All glasswares were dried in an oven (60 °C) before manipulation. 2-bromo-3-(10-(4-methoxyphenoxy)decyl)thiophene (1.7 g, 4 mmol), PdCl<sub>2</sub>(PhCN)<sub>2</sub> (46 mg, 0.12 mmol), potassium fluoride (KF) (0.465 g, 8 mmol) were added to 18 mL dry DMSO under argon. After stirring for 5 min, AgNO<sub>3</sub> (1.36 g, 8 mmol) was added in one portion. After stirring at 60 °C for 3 h, the same amount of PdCl<sub>2</sub>(PhCN)<sub>2</sub>, KF and AgNO<sub>3</sub> were added and the mixture was stirred at 60 °C for another 18 h. After cooling down to room temperature, the mixture was filtered over a silica gel plug and the residue was washed with 250 mL of CH<sub>2</sub>Cl<sub>2</sub>. The filtrate was washed with saturated NH<sub>4</sub>Cl solution (250 mL), water (3 x 150 mL) and then dried over anhydrous MgSO<sub>4</sub>. The solvent was removed by evaporator and the reddish crude product was further purified by column chromatography (PE:DCM =1:1, silica gel) as white solid (Yield: 1.05 g,

62%).  $^1\text{H}$  NMR (400 MHz,  $\text{CDCl}_3$ ):  $\delta_{\text{H}}$  = 6.83 (s, 8H), 6.77 (s, 2H), 3.90 (t,  $J$  = 6.6 Hz, 4H), 3.76 (s, 6H), 2.52 (t,  $J$  = 7.8 Hz, 4H), 1.77 (m, 4H), 1.57 (m, 4H), 1.44-1.31(m, 24H).  $^{13}\text{C}$  NMR (101 MHz,  $\text{CDCl}_3$ )  $\delta_{\text{C}}$  = 153.80, 153.45, 143.09, 136.31, 124.59, 115.57, 114.75, 108.01, 68.80, 55.87, 29.74, 29.67, 29.62, 29.60, 29.53, 29.48, 29.31, 26.19.

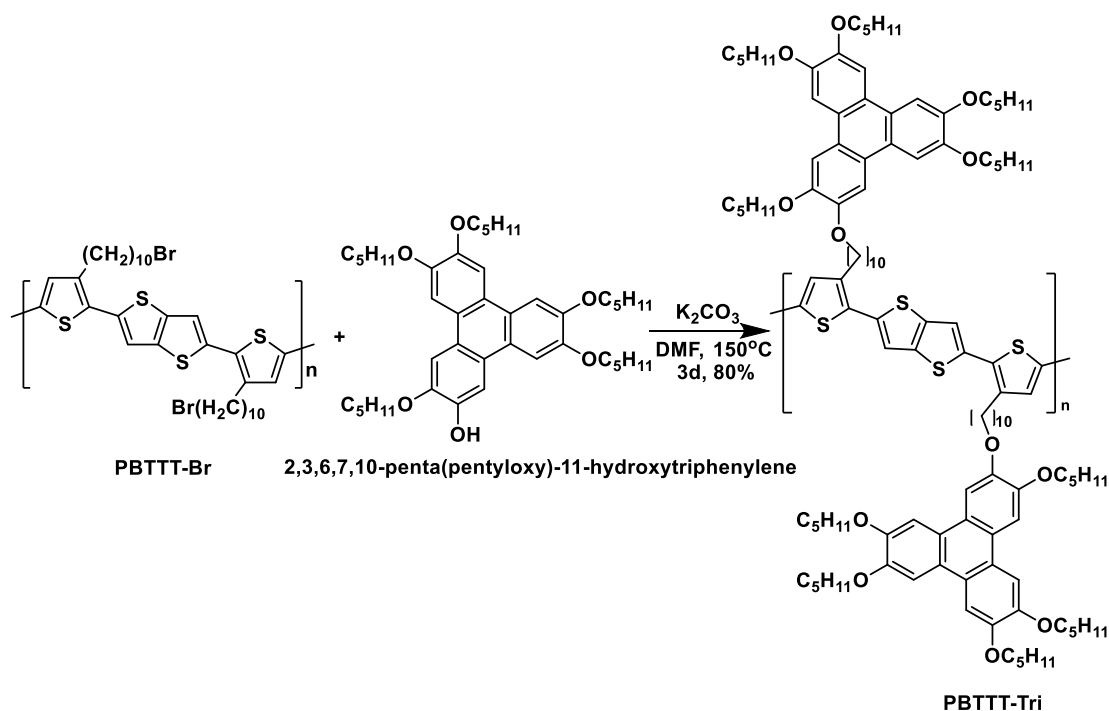


**5,5'-Dibromo-4,4'-bis[10-bromodecyl]-2,2'-bithiophene (1G).** 5,5'-Dibromo-4,4'-bis[10-(4-methoxyphenoxy)decyl]-2,2'-bithiophene (**1F**) (509.2 mg, 0.6 mmol) was dissolved in dry  $\text{CH}_2\text{Cl}_2$  (10 mL) under argon and the solution was heated to reflux. Then boron tribromide (1M solution in  $\text{CH}_2\text{Cl}_2$ ; 1.2 mL, 1.2 mmol) was added in three portions. Each time 0.4 mL of  $\text{BBr}_3$  was added and stirred about 45 min before the next portion was added. Then the reaction mixture was poured into a saturated  $\text{NH}_4\text{Cl}$  solution and extracted with  $\text{CH}_2\text{Cl}_2$ . The organic phase was washed with saturated  $\text{NaHCO}_3$  solution twice and water twice, then dried over anhydrous  $\text{MgSO}_4$ . The solvent was removed by evaporation and the crude product was purified by column chromatography (PE, silica gel), giving a white solid (Yield: 310 mg, 68 %).  $^1\text{H}$  NMR (400 MHz,  $\text{CDCl}_3$ ):  $\delta_{\text{H}}$  = 6.77 (2H, s), 3.40 (4H, t,  $J$  = 6.86 Hz), 2.52 (4H, t,  $J$  = 7.64 Hz), 1.85 (4H, m), 1.58(4H, m), 1.42-1.30 (24H, m).  $^{13}\text{C}$  NMR (100 MHz,  $\text{CDCl}_3$ ):  $\delta_{\text{C}}$  = 143.08, 136.32, 124.61, 108.05, 34.15, 32.99, 29.73, 29.68, 29.54, 29.46, 29.29, 28.89, 28.32.

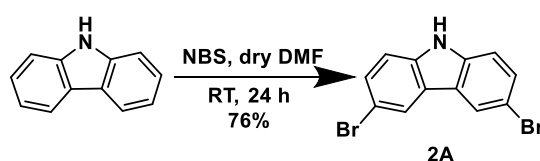


**Poly(2,5-bis(3-(10-bromo)decyl)thiophen-2-yl)thieno[3,2,b]thiophene (PBTTT-Br).** 5,5'-Dibromo-4,4'-bis(10-bromodecyl)-2,2'-bithiophene (93 mg, 0.12 mmol) and 2,5-bis(trimethylstannyl)thieno[3,2,b]thiophene (57 mg, 0.12 mmol) were added into a microwave tube, dissolved in dry chlorobenzene (1.3 mL), and the solution was degassed with argon for 20 min.  $\text{P}(\text{o-tolyl})_3$  (3 mg, 9.9  $\mu\text{mol}$ ) and  $\text{Pd}_2(\text{dba})_3$  (2.2 mg, 2.4  $\mu\text{mol}$ ) were added and the mixture was degassed again for 5 min. The microwave tube was sealed and heated in the microwave with stirring subsequently at 140  $^\circ\text{C}$  for 2 min, at 160  $^\circ\text{C}$  for 2 min, and at 180  $^\circ\text{C}$  for 25 min. The reaction time was calculated after the representative temperature had been reached. After cooling down to 50  $^\circ\text{C}$ , the reaction solution was diluted by adding chlorobenzene (3 mL) and was precipitated in the mixture of methanol (40 mL) and conc. hydrochloric acid (2mL). The resulting suspension was stirred overnight.

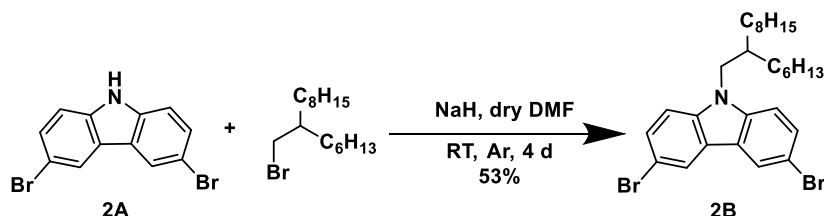
The dark-red precipitate was filtered, purified by Soxhlet extraction with acetone, pentane, and methanol (each 24 h). The polymer was then dissolved in chlorobenzene and precipitated from a warm solution of methanol to lead to a dark-red solid (Yield: 81mg, 90%). SEC:  $M_{n,SEC} = 1.5 \times 10^4$ ,  $M_w/M_n = 1.6$ .  $^1\text{H NMR}$  (600 MHz,  $\text{CDCl}_3$ ,  $T = 50^\circ\text{C}$ ):  $\delta_{\text{H}} = 7.26$  (s, 2H), 7.04 (s, 2H), 3.40 (br t, 4H), 2.79 (br t, 4H), 1.86 (m, 4H), 1.70 (m, 4H), 1.44-1.32 (m, 24H).



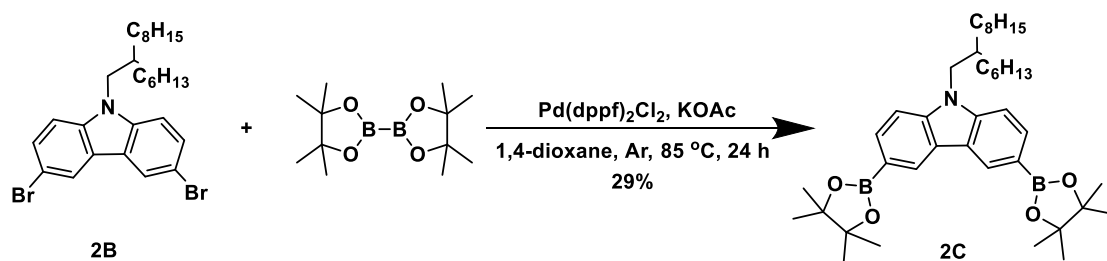
**PBTTT-Tri.** 2,3,6,7,10-Penta(pentyloxy)-11-hydroxytriphenylene (81 mg, 0.12 mmol),  $\text{K}_2\text{CO}_3$  (33 mg, 0.24 mmol) were dissolved in 30 mL DMF under argon. After 30 minutes, a solution of PBTTT-Br (22.3 mg, 0.03 mmol) in THF (3 mL) was added to the mixture. The resulting purple solution was stirred at  $150^\circ\text{C}$  for 3 days, before being extracted at room temperature with chloroform (3 x 50 mL). The organic layer was successively washed with water (3 x 50 mL), dried over anhydrous  $\text{MgSO}_4$ , and concentrated under reduced pressure. The crude product was precipitated using methanol (60 mL) and the resulting solid was washed through a Soxhlet thimble. The crude product was submitted to semipreparative SEC, using chloroform as the eluant, the solution was collected in thirty bottles. A purple powder was obtained (Yield: 45 mg, 80%). SEC:  $M_n = 2.0 \times 10^4$ ,  $M_w/M_n = 1.5$ .  $^1\text{H NMR}$  (600 MHz,  $\text{CDCl}_3$ )  $\delta_{\text{H}} = 7.80$  (s, 12H), 7.21 (s, 2H), 7.00 (s, 2H), 4.21(s, 24H), 2.74 (s, 24H), 1.93(s, 24H), 1.55 -1.26 (m, 72H), 1.34-0.96 (m, 30H).  $^{13}\text{C NMR}$  (151 MHz,  $\text{CDCl}_3$ )  $\delta_{\text{C}} = 149.41$ , 124.01, 108.06, 70.11, 30.92, 29.82, 29.42, 28.60, 22.72, 14.19. Calculate for elemental analysis C: 74.72; H: 8.67; O: 9.95; S: 6.65; found: C: 70.96; H: 8.49; O: 8.43; S: 6.37.



**3,6-Dibromo-9H-carbazole (2A).** A solution of N-bromosuccinimide (NBS, 22.35 g, 0.125 mol) in 50 mL of DMF was slowly with stirring added into a solution of carbazole (10 g, 0.167 mol) in 20 mL of DMF with an ice bath. After reacting for 4 hours, the reaction mixture was poured into 600 mL of ice water. After filtration, the collected mixture was purified from recrystallization in a mixture of EtOH and H<sub>2</sub>O (Yield: 76%). <sup>1</sup>H NMR (400 MHz, CDCl<sub>3</sub>) δ 8.08, 8.04, 7.48, 7.46, 7.24, 7.21. <sup>13</sup>C NMR (101 MHz, CDCl<sub>3</sub>) δ 138.36, 129.32, 124.11, 123.27, 112.65, 112.22.

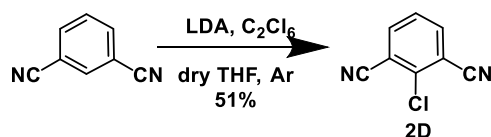


**3,6-Dibromo-9-(2-hexyldecyl)-9H-carbazole (2B).** 3,6-Dibromocarbazole (**2A**) (3.25 g, 10 mmol) was dissolved in 50 mL of dry DMF. After bubbling for 15 min, NaH (260 mg, 12 mmol) was added into the above solution under an argon atmosphere. After stirring for 1 h, 9-(bromomethyl)pentadecane (4.58 g, 15 mmol) was added under argon. After stirring at room temperature for 4 days, 2 mL of water was added to quench the reaction and DMF was removed *via* distillation. The resulting mixture was further dissolved in DCM and the organic phases were washed with water and dried over anhydrous MgSO<sub>4</sub>. After filtration and evaporation, the obtained crude was purified by column chromatography (eluent: PE:EA=5:1) and a transparent viscous liquid was eventually collected (Yield: 2.9 g, 53%). <sup>1</sup>H NMR (300 MHz, CD<sub>2</sub>Cl<sub>2</sub>) δ 8.20, 7.59, 7.36, 5.36, 4.15, 2.11, 1.57, 1.23, 0.89.

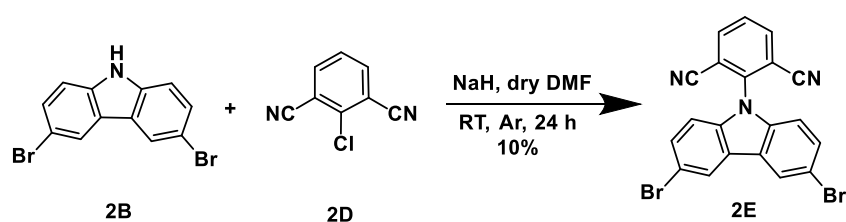


**3,6-bis(4,4,5,5-tetramethyl-1,3,2-dioxaborolan-2-yl)-9-(2-hexyldecyl)-9H-carbazole (2C).** A mixture of 3,6-dibromo-9-(2-hexyldecyl)-9H-carbazole (**2B**) (1.65 g, 3 mmol), KOAc (1.77 g, 18 mmol), bis(pinacolato)diboron (2.29 g, 9 mmol) was dissolved in dry 1,4-dioxane (75 mL). Pd(dppf)<sub>2</sub>Cl<sub>2</sub> (439 mg, 0.6 mmol) was added into above solution under argon atmosphere. After freeze-pump-thaw for three times, the mixture was sealed and heated under Ar at 85 °C for 24 h. After cooling down, ethyl acetate was added and the resulting solution was washed with water and dried over anhydrous MgSO<sub>4</sub>. After filtration and evaporation, the crude product was further purified using silica gel chromatography (eluent: PE: EA =10:1) to give a yellow solid (yield: 559 mg, 29%). R = R<sub>2</sub>: <sup>1</sup>H NMR (400 MHz, Acetone) δ = 8.60 (s, 2H), 7.87 (dd, 2H, *J* = 8.22, 1.04 Hz), 7.55 (d, 2H, *J* = 8.20

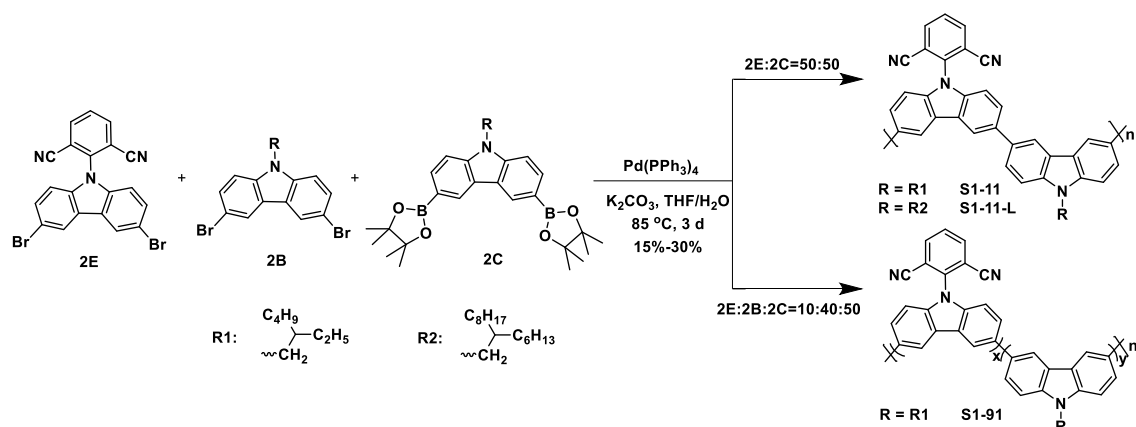
Hz), 4.33 (d,  $J = 7.75$  Hz), 2.76 (m, 1H), 1.38 (s, 28H), 1.17 (m, 16H), 0.86 (m, 8H).  $^{13}\text{C}$  NMR (101 MHz, Acetone)  $\delta = 144.02, 132.92, 128.13, 123.27, 109.77, 84.24, 32.57, 32.43, 29.84, 27.22, 27.15, 25.31, 23.29, 23.23, 14.33$ .



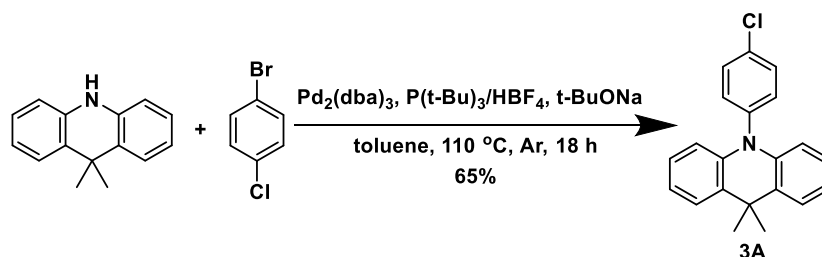
**2-Chloroisophthalonitrile (2D).** 2-Chloroisophthalonitrile (**2D**) was prepared referring to the literature<sup>272</sup>. Preparation of LDA: Anhydrous diisopropylamine (6.6 mL, 46.82 mmol) was dissolved in 100 mL of anhydrous THF under argon and the solution was cooled down to  $-78$  °C. *n*-BuLi (2.5M in hexane) (19 mL, 46.82 mmol) was added dropwise and the solution was stirred for 30 min at this temperature. A solution of isophthalonitrile (5 g, 39.02 mmol) in anhydrous THF (100 mL) was added dropwise at  $-95$  °C into the above LDA solution and the resulting solution was stirred for 1 h. Hexachloroethane (14.8 g, 62.44 mmol) dissolved in anhydrous THF (150 mL) was added to the reaction mixture at this temperature and the mixture was allowed to be stirred for 1 h. Then the mixture was warmed to room temperature and stirred for another 24 h. the reaction was quenched by adding a saturated ammonium chloride solution. The product was extracted by diethyl ether, washed with water and brine sequentially, dried over anhydrous  $\text{MgSO}_4$ , and solvent removed under vacuum. The product was purified by flash column chromatography (petroleum: diethyl ether = 4:1) and isolated as a pale yellow solid (Yield: 6.35 g, 51%).  $^1\text{H}$  NMR (300 MHz,  $\text{CDCl}_3$ ): 7.85 (2H, d,  $J = 7.9$  Hz), 7.48 (1H, t,  $J = 7.9$  Hz)



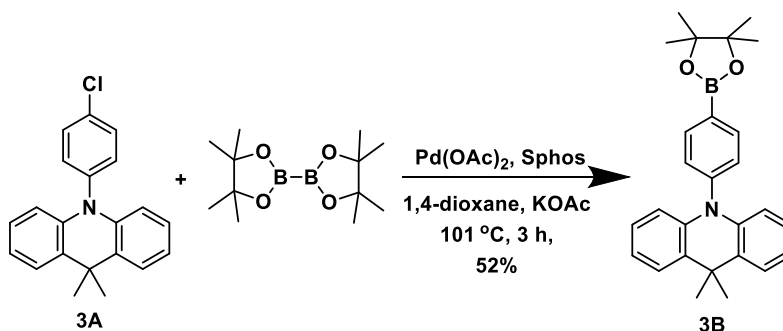
**2-(3,6-Dibromo-9H-carbazol-9-yl)isophthalonitrile (2E).** 3,6-Dibromocarbazole (**2B**) (10 mmol) was dissolved in dry DMF and NaH was added slowly into the solution under argon atmosphere. After stirring for 1 h, 2-chloroisophthalonitrile (**2D**) (10 mol) was added slowly and the mixture was stirred at room temperature for 24 h. The reaction was quenched by adding 2 mL of water and DMF was removed under vacuum. The obtained mixture was dissolved in DCM and washed by water, brine, and dried over anhydrous  $\text{MgSO}_4$ . After filtration and evaporation, the crude product was further purified by column chromatography to give, among other fractions, a yellow solid (Yield: 450 mg, 15%).  $^1\text{H}$  NMR (400 MHz, THF)  $\delta$  10.81, 8.44, 8.36, 7.95, 7.59, 7.11.



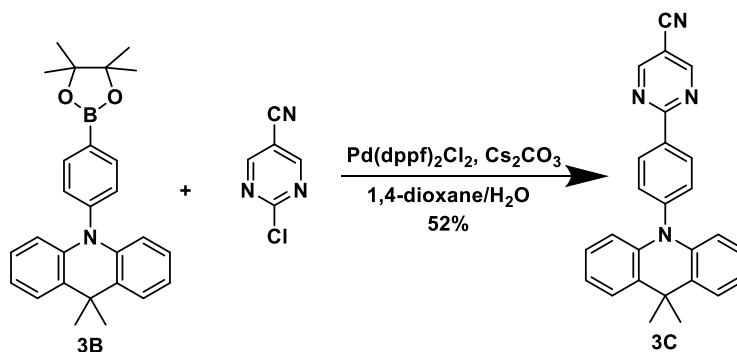
**General procedure for the polymerization of S1 polymers.** S1 polymers were prepared *via* Suzuki coupling polycondensation of monomers **2B**, **2C**, and **2E**. The general procedure is as follows: monomers (**2B**, **2C**, and **2E**) were dissolved in THF and  $\text{K}_2\text{CO}_3$  aqueous solution (2M) was added. Under an argon atmosphere,  $\text{Pd}(\text{PPh}_3)_4$  (5%) was added into the above mixture and the oxygen was removed by freeze-pump-thaw cycling (3 times). After sealing it, the mixture was heated at 85 °C for 3 days. After cooling down, the mixture was precipitated in cold acetone for three times, and a yellow solid was collected after filtration (Yield: 15-30%).



**10-(4-Chlorophenyl)-9,9-dimethyl-9,10-dihydroacridine (3A).** A mixture of 9,9-dimethyl-9,10-dihydroacridine (2.09 g, 10 mmol), 1-bromo-4-chlorobenzene (2.3 g, 12 mmol), and *t*-BuONa (1.92 g, 20 mmol) was dissolved in 100 mL of toluene. After freeze-pump-thaw cycling for three times,  $\text{Pd}_2(\text{dba})_3$  (183 mg, 0.2 mmol) and  $\text{P}(\text{t-Bu})_3/\text{HBF}_4$  (0.8 mmol) were added to the initial mixture, always under argon flow. The resultant mixture was refluxed at 110 °C for 18 h. After cooling down to RT, the precipitate was removed by filtration, and the mixture was washed by brine, then dried over anhydrous  $\text{MgSO}_4$ . After filtration and evaporation, the crude product was further purified by column chromatography (eluent: DCM:PE=1:10) and (**3A**) was isolated as a white powder (Yield: 2.1g, 65%).  $^1\text{H}$  NMR (400 MHz,  $\text{DMSO-d}_6$ )  $\delta$  = 7.73 (d, 2H,  $J$  = 6.82 Hz), 7.50 (m, 2H), 6.98 (m, 4H), 6.14 (d, 2H,  $J$  = 6.84 Hz), 1.61 (s, 6H).  $^{13}\text{C}$  NMR (101 MHz,  $\text{DMSO}$ )  $\delta$  = 140.49, 139.93, 133.44, 131.68, 130.11, 126.91, 125.85, 121.12, 113.95, 35.95, 31.63.

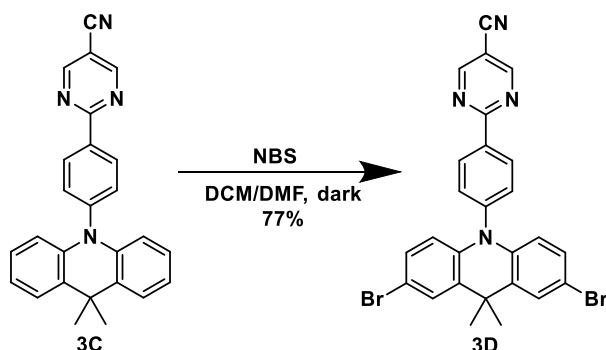


**9,9-Dimethyl-10-(4-(4,4,5,5-tetramethyl-1,3,2-dioxaborolan-2-yl)phenyl)-9,10-dihydroacridine (3B).** A mixture of 10-(4-chlorophenyl)-9,9-dimethyl-9,10-dihydroacridine (**3A**) (3.2 g, 10 mmol), bis(pinacolato)diboron (3.05 g, 10 mmol) and KOAc (2.9 g, 30 mmol) in 100 mL of 1,4-dioxane was degassed via freeze-pump-thaw cycling for three times, then  $\text{Pd}(\text{OAc})_2$  (110 mg, 0.5 mmol) and Sphos (200 mg, 0.5 mmol) were added to the above mixture under argon atmosphere. The mixture was refluxed for 3 h. After cooling down to RT,  $\text{CH}_2\text{Cl}_2$  was added and the resulting mixture was washed by water. After separation, the organic part was dried over anhydrous  $\text{MgSO}_4$ . After removing the solvents, the crude product was purified by column chromatography (first with eluent: PE:toluene=10:1, and after the first spot with the eluent PE:EA=10:1). The target expected white solid was obtained after recrystallization in PE (Yield: 4.3 g, 52%).  $^1\text{H}$  NMR (400 MHz,  $\text{CH}_2\text{Cl}_2$ )  $\delta$  = 8.08 (, 2H), 7.50 (, 2H), 7.39 (, 2H), 6.96 (, 4H), 6.29 (, 2H), 1.71 (s, 6H), 1.43 (s, 12H).  $^{13}\text{C}$  NMR (101 MHz,  $\text{CH}_2\text{Cl}_2$ )  $\delta$  = 144.42, 141.21, 137.60, 130.96, 130.54, 126.69, 125.59, 120.95, 114.48, 84.53, 36.35, 31.41, 25.15.

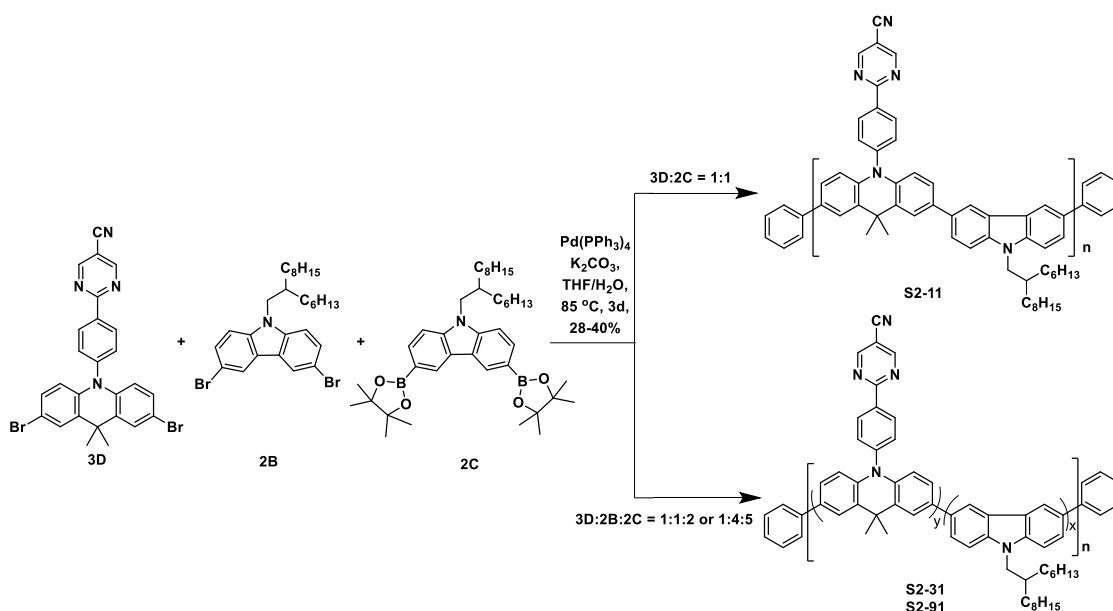


**2-[4-(9,9-Dimethyl-9H-acridin-10-yl)-phenyl]-pyrimidine-5-carbonitrile (3C).** A mixture of 2-chloropyrimidine-5-carbonitrile (10 mmol), 9,9-Dimethyl-10-(4-(4,4,5,5-tetramethyl-1,3,2-dioxaborolan-2-yl)phenyl)-9,10-dihydroacridine (**3B**) (9.22 mmol), and  $\text{Cs}_2\text{CO}_3$  (30 mmol) were dissolved in mL of 1,4-dioxane, and after freeze-pump-thaw cycling for three times,  $\text{Pd}(\text{dppf})_2\text{Cl}_2$  (0.8 mmol) was added to the mixture under argon atmosphere. After reflux for 24h, the mixture was poured into water. After separation, the organic phase was dried over anhydrous  $\text{MgSO}_4$ , followed by filtration and evaporation. The crude product was further purified by column chromatography (eluent: DCM:PE = 2:1) to give finally a yellow solid (Yield: 2.0g, 52%).  $^1\text{H}$  NMR (400 MHz,  $\text{CD}_2\text{Cl}_2$ )  $\delta$  =

9.09 (s, 2H), 8.75 (d, 2H,  $J = 8.4$  Hz), 7.51 (m, 4H), 6.93 (quint, 4H,  $J = 3.2$  Hz), 6.34 (d,  $J = 8.0$  Hz, 2H), 1.67 (s, 6H).  $^{13}\text{C}$  NMR (101 MHz,  $\text{CD}_2\text{Cl}_2$ )  $\delta = 166.04, 160.64, 146.07, 141.17, 136.10, 132.27, 131.99, 131.24, 126.93, 125.88, 121.54, 115.54, 114.90, 107.80, 36.60, 31.46$ .

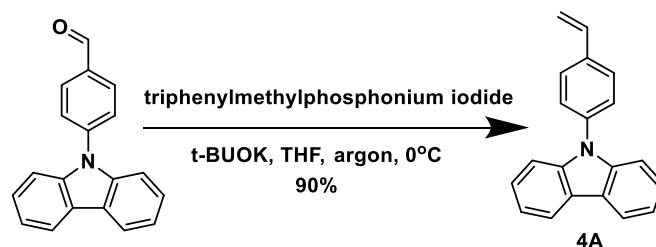


**2-(4-(2,7-Dibromo-9,9-dimethylacridin-10(9H)-yl)phenyl)pyrimidine-5-carbonitrile (4D).** On the one hand, 2-[4-(9,9-Dimethyl-9H-acridin-10-yl)-phenyl]-pyrimidine-5-carbonitrile (**3C**) (2.16 g, 5.5 mmol) was dissolved in 20 mL of dry DMF. On the other hand, NBS (2.06 g, 11.55 mmol) was dissolved in dry DCM (200 mL). then, this last solution was added dropwise to the first solution during 4 h and the dark. The mixture was then stirred at RT overnight, before being poured into water. The organic phase was further washed with brine and dried over anhydrous  $\text{MgSO}_4$ . After filtration and removing solvents, the crude product was purified *via* column chromatography (eluent: PE:DCM=2:1). Yellow solid was gained after recrystallization in ethanol (Yield: 2.3 g, 77%).  $^1\text{H}$  NMR (400 MHz,  $\text{CD}_2\text{Cl}_2$ )  $\delta = 9.11$  (s, 2H), 8.78 (d, 2H,  $J = 8.66$  Hz), 7.56 (d, 2H,  $J = 2.30$  Hz), 7.49 (d, 2H,  $J = 8.50$  Hz), 7.09 (dd, 2H,  $J = 8.84, 2.28$  Hz), 6.24 (d, 2H,  $J = 8.84$  Hz), 1.66 (s, 6H).

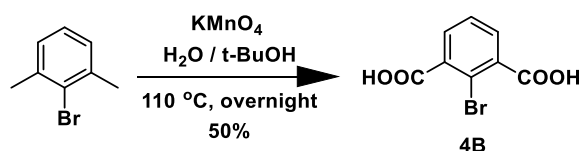


**The general process of polymerization of S2.** S2 polymers were prepared *via* Suzuki coupling polycondensation of monomers **3D**, **2B**, and **2C** with molar feed ratios of 50:0:50, 25:25:50, and 10:40:50. The three polymers were named as **S2-11**, **S2-31**, and **S2-91**, based on the molar feed ratio

of acridine rings and carbazole units in the backbone. The procedure of the polymerization is as follows: monomers dissolved in THF, and  $K_2CO_3$  aqueous solution (2M) were mixed. Then,  $Pd(PPh_3)_4$  was added with keeping the argon flowing. After freeze-pump-thaw cycling for three times, the mixture was sealed and heated at 85 °C for 3 days. Later, bromobenzene (2 mol equiv.) was added and the mixture was heated again at 85 °C for 24 h. After that, phenyl boron (2 mol equiv.) was added and the mixture was heated at 85 °C for another 24 h. After cooling down, the mixture was precipitated in acetone at 0 °C for three times. A final pure yellow solid was collected with a yield of 28-40%.

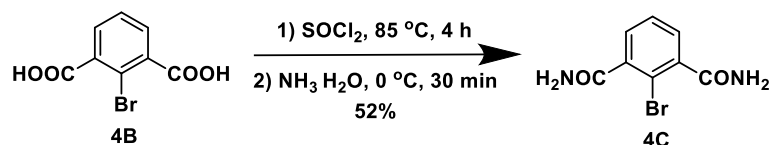


**9-(4-Vinylphenyl)-9H-carbazole (4A).** 9-(4-Vinylphenyl)-9H-carbazole was synthesized according to the literature<sup>269</sup>. To a solution of triphenylmethylphosphonium iodide (3.27 g, 8.1 mmol) in 6mL of THF, t-BuOK (1 g, 8.7 mmol) was added under argon at 0 °C and the solution turns yellow. After stirring for 30min, N-(4-formylphenyl)carbazole (1.465g, 5.4 mmol) was added at 0 °C under argon. The reaction was stirred for 24h at room temperature. The yellow solution was then extracted with methylene chloride ( $CH_2Cl_2$ ). The organic phase was washed with water and dried over anhydrous  $MgSO_4$ . The crude product was obtained *via* removing solvent and subsequently purified by silica gel column chromatography (eluent: toluene) to give a white powder (Yield: 1.3 g, 90%).  $^1H$  NMR (400 MHz,  $CDCl_3$ )  $\delta$  = 8.17 (d,  $J$  = 7.8 Hz, 2H), 7.66 (d,  $J$  = 8.4 Hz, 2H), 7.56 (d,  $J$  = 8.4 Hz, 2H), 7.43 (m, 4H), 7.30 (m, 2H), 6.84 (dd,  $J$  = 17.6, 10.9 Hz, 1H), 5.89 (d,  $J$  = 17.6 Hz, 1H), 5.39 (d,  $J$  = 10.9 Hz, 1H).  $^{13}C$  NMR (101 MHz,  $CDCl_3$ )  $\delta$  = 140.97, 137.26, 136.89, 136.15, 127.74, 127.26, 126.09, 123.56, 120.45, 120.11, 114.87, 109.95.  $^1H$  NMR (400 MHz,  $CD_2Cl_2$ )  $\delta$  = 8.17 (d,  $J$  = 7.81 Hz, 2H), 7.69(d,  $J$  = 8.38 Hz, 2H), 7.56(d,  $J$  = 8.38 Hz, 2H), 7.44-7.42 (m, 4H), 7.32-7.28 (m, 2H), 6.88 (dd,  $J$  = 10.87, 17.69 Hz, 1H), 5.91 (d,  $J$  = 17.65 Hz, 1H), 5.39 (d,  $J$  = 10.93 Hz, 1H).  $^{13}C$  NMR (101 MHz,  $CD_2Cl_2$ )  $\delta$  = 141.23, 137.48, 137.20, 136.40, 127.99, 127.43, 126.38, 123.76, 120.61, 120.36, 114.92, 110.20, 53.84.

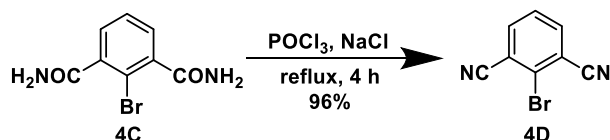


**2-Bromobenzene-1,3-dicarboxylic acid (4B).** Following the reference<sup>268</sup>, 2,6-dimethyl-bromobenzene (10 g, 54 mmol) was dissolved in the mixture of t-BuOH (77mL) and water (150 mL), and the mixture was heated to 110 °C. Then,  $KMnO_4$  (51.2 g, 324 mmol, 6 equiv.) was added portionwise into the hot mixture during 1 hour. The reaction mixture was heated at 110 °C for

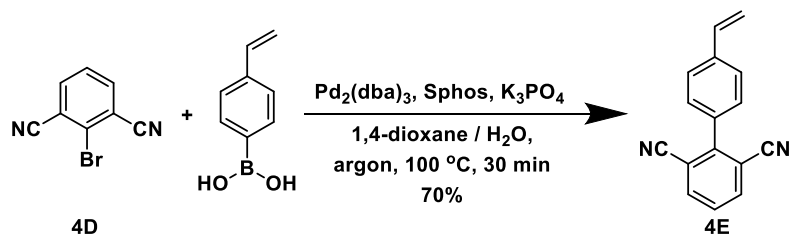
overnight. After cooling down to room temperature, 5 mL of ethanol was added to quench the reaction. The hot mixture was filtered through a 5 cm plug of Celite and the plug was washed with ethanol (10 mL). After removing the solvents from the filtrate under pressure, the remaining solution was acidified with 20% HCl (80 mL). The white precipitate observed was filtered, washed with water (20 mL), and collected (Yield: 6.7 g, 50%).  $^1\text{H}$  NMR (400 MHz, DMSO)  $\delta$  = 13.57 (br, s, 2H, COOH), 7.71 (d,  $J$  = 7.6 Hz, 2H, Ar), 7.52 (t,  $J$  = 7.6 Hz, 1H, Ar).  $^{13}\text{C}$  NMR (75 MHz, DMSO)  $\delta$  = 168.21, 137.17, 131.20, 128.26, 116.67.



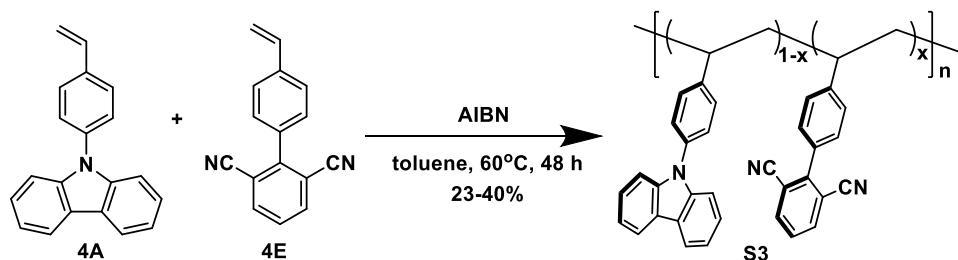
**2-Bromobenzene-1,3-dicarboxamide (4C).** 2-Bromobenzene-1,3-dicarboxamide was synthesized according to the literature<sup>267</sup>. Well dried 2-bromobenzene-1,3-dicarboxylic acid (6.6 g, 2.7 mmol) was suspended in  $\text{SOCl}_2$  (30 mL) and the mixture was heated to 85 °C for 4 h. After cooling down to room temperature, the excess of  $\text{SOCl}_2$  was removed under pressure to get 2-bromoisophthaloyl dichloride. The latter was then dissolved in dry DCM (30 mL). The resulting solution was added to 80 mL of an aqueous solution of  $\text{NH}_3$  dropwise at 0 °C and a white precipitate appeared during the adding. The mixture was stirred at 0 °C for 30 min to make sure all products have precipitated. After filtration, the collected white solid was washed with water and n-hexane before being dried at 50 °C under pressure (Yield: 3.4 g, 52%).  $^1\text{H}$  NMR (400 MHz, DMSO)  $\delta$  = 7.88 (s, 2H,  $\text{NH}_2$ ), 7.57 (s, 2H,  $\text{NH}_2$ ), 7.45-7.41 (m, 1H), 7.38-7.36 (m, 2H).  $^{13}\text{C}$  NMR (101 MHz, DMSO)  $\delta$  = 169.32, 140.51, 128.42, 127.53, 115.36.



**2-Bromobenzene-1,3-dicarbonitrile (4D).** According to the literature<sup>267</sup>, 2-bromobenzene-1,3-dicarboxamide (3.3 g, 13.6 mmol), and NaCl (1.85 g, 30 mmol) were suspended in  $\text{POCl}_3$  (17 mL, 17.7 mmol) and the mixture was refluxed for 4 h. After cooling down to room temperature, the excess  $\text{POCl}_3$  was removed in vacuum. Then the residue was poured into ice water and stir for 10 min. The brown precipitate was formed, filtered, and washed with water. After drying, the crude product was further recrystallized in hexane to give light brown solids (Yield: 2.7g, 96%).  $^1\text{H}$  NMR (400 MHz,  $\text{CDCl}_3$ )  $\delta$  = 7.89 (d,  $J$  = 8.06 Hz, 2H), 7.59 (t,  $J$  = 8.0 Hz, 1H).  $^{13}\text{C}$  NMR (101 MHz,  $\text{CDCl}_3$ )  $\delta$  = 137.74, 128.92, 128.55, 118.33, 115.77.



**4'-Vinyl-biphenyl-2,6-dicarbonitrile (4E).** 4'-Vinyl-biphenyl-2,6-dicarbonitrile was prepared *via* Suzuki reaction. 4-Vinylphenylboronic acid (0.74 g, 5 mmol) and 2-bromobenzene-1,3-dicarbonitrile (1.35 g, 6.5 mmol) were dissolved in 125 mL of 1,4-dioxane. Then,  $\text{K}_3\text{PO}_4$  aqueous (2M, 25 mL) was added to the above solution, before  $\text{Pd}_2(\text{dba})_3$  (458 mg, 0.5 mmol), and Sphos (205 mg, 0.5 mmol) were added as well. After three freeze-thawing cycles, the mixture was heated at 100 °C for 0.5 h. The hot reaction mixture was filtered through a 5 cm plug of Celite, before the mixture was washed with water, brine, and finally dried over anhydrous  $\text{MgSO}_4$ . After removing the solvent, the crude product was further purified by silica gel column chromatography (eluent: PE:DCM = 1:1) to give a white powder (Yield: 0.8 g, 70%).  $^1\text{H NMR}$  (400 MHz,  $\text{CDCl}_3$ )  $\delta$  = 7.96 (d,  $J$  = 7.90 Hz, 2H), 7.60 (m, 3H), 7.51 (d,  $J$  = 8.32 Hz, 2H), 6.80 (dd,  $J$  = 10.95 Hz,  $J$  = 17.60 Hz, 1H), 5.89 (d,  $J$  = 17.64 Hz, 1H), 5.40 (d,  $J$  = 10.94 Hz, 1H).  $^{13}\text{C NMR}$  (101 MHz,  $\text{CDCl}_3$ )  $\delta$  = 148.69, 139.61, 137.25, 136.02, 133.43, 129.59, 128.46, 126.87, 116.76, 116.06, 114.44.  $^1\text{H NMR}$  (400 MHz,  $\text{CD}_2\text{Cl}_2$ )  $\delta$  = 8.00 (d,  $J$  = 7.90 Hz, 2H), 7.64-7.58 (m, 3H), 7.53 (d,  $J$  = 8.32 Hz, 2H), 6.85 (dd,  $J$  = 10.95 Hz,  $J$  = 17.60 Hz, 1H), 5.94 (d,  $J$  = 17.64 Hz, 1H), 5.42 (d,  $J$  = 10.94 Hz, 1H).  $^{13}\text{C NMR}$  (101 MHz,  $\text{CD}_2\text{Cl}_2$ )  $\delta$  = 148.74, 139.81, 137.54, 136.28, 134.22, 129.94, 128.93, 126.97, 117.05, 116.14, 114.67.



**The general process of polymerization of S3.** Monomers (4A and 4E) and AIBN (5%) were dissolved in dry toluene. After three freeze-thawing cycles, the mixture was placed in a temperature-controlled oil bath at 60 °C. The mixture was stirred for 48 h before exposure to the atmosphere. The resulting polymer was precipitated in acetone for three times, collected by centrifugation, and dried under a high vacuum to obtain a white solid (Conversion: 23-40%).

S3-11:  $^1\text{H NMR}$  (400 MHz,  $\text{CD}_2\text{Cl}_2$ )  $\delta$  = 7.97, 7.67, 7.24, 7.05, 2.41, 2.14, 1.74, 1.52.

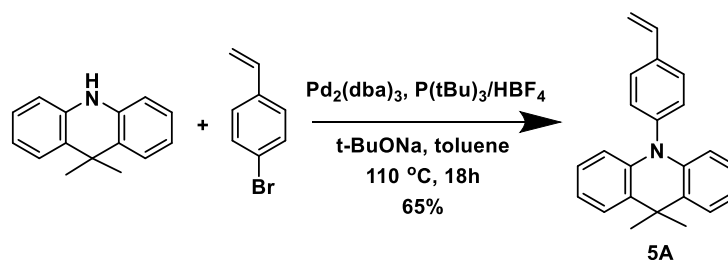
S3-31:  $^1\text{H NMR}$  (400 MHz,  $\text{CH}_2\text{Cl}_2$ )  $\delta$  = 7.97, 7.59, 7.22, 7.04, 2.21, 1.78, 1.53.

S3-51:  $^1\text{H NMR}$  (400 MHz,  $\text{CD}_2\text{Cl}_2$ )  $\delta$  = 7.96, 7.20, 7.00, 2.20, 1.78, 1.52.

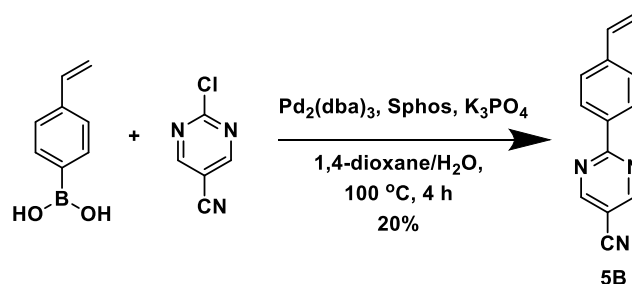
S3-91:  $^1\text{H NMR}$  (400 MHz,  $\text{CD}_2\text{Cl}_2$ )  $\delta$  = 7.94, 7.21, 7.16, 6.97, 2.20, 1.77, 1.51.

S3-955:  $^1\text{H NMR}$  (400 MHz,  $\text{CD}_2\text{Cl}_2$ )  $\delta$  = 7.93, 7.22, 7.13, 6.96, 2.20, 1.79, 1.52.

S3-991:  $^1\text{H}$  NMR (400 MHz,  $\text{CD}_2\text{Cl}_2$ )  $\delta$  = 7.93, 7.22, 7.13, 6.95, 2.35, 2.20, 1.81, 1.52.

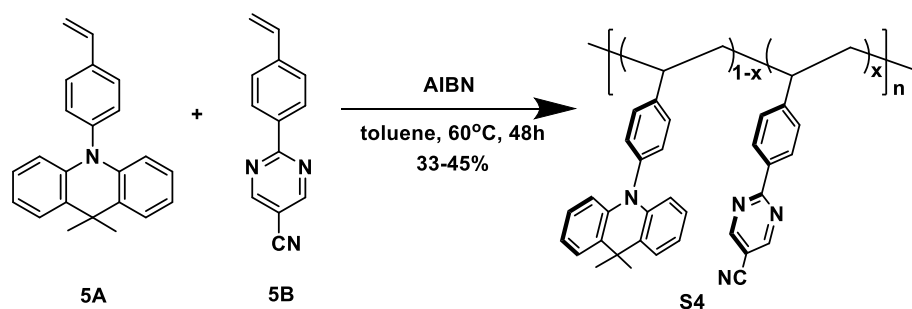


**10-(4-ethenylphenyl)-9,9-dimethyl-9,10-dihydroacridine (5A).** The mixture of 9,9-dimethyl-9,10-dihydroacridine (2.09 g, 10 mmol), 1-bromo-4-vinylbenzene (2.20 g, 12 mmol), sodium *tert*-butoxide (1.92 g, 20 mmol),  $\text{Pd}_2(\text{dba})_3$  (183 mg, 0.2 mmol), and  $\text{P}(\text{t-Bu})_3/\text{HBF}_4$  (232 mg, 0.8 mmol) was stirred in 100 mL of dry toluene. After three freeze-thawing cycles, the mixture was heated at  $110\text{ }^\circ\text{C}$  for 18 h. After cooling down to room temperature, the crude was extracted with  $\text{CHCl}_3$  and the organic phases washed with brine, before drying them by adding anhydrous  $\text{MgSO}_4$ . After removing the solvents, a final silica gel column chromatography (eluent: PE/DCM = 4/1) allowed to isolate the product as a white powder (Yield: 2 g, 65%).  $^1\text{H}$  NMR (400 MHz,  $\text{CDCl}_3$ )  $\delta$  = 7.68 (d,  $J$  = 8.26 Hz, 2H), 7.47 (d,  $J$  = 7.56Hz, 2H), 7.31 (d,  $J$  = 8.30 Hz, 2H), 6.95 (m, 4H), 6.83 (dd, 1H), 6.32 (d, 2H), 5.89 (d, 1H), 5.39 (d, 1H), 1.70 (s, 6H).  $^{13}\text{C}$  NMR (101 MHz,  $\text{CDCl}_3$ )  $\delta$  = 141.01, 140.81, 137.62, 136.22, 131.55, 130.14, 128.72, 126.49, 125.36, 120.68, 115.11, 114.17, 36.11, 31.41.  $^1\text{H}$  NMR (400 MHz,  $\text{CD}_2\text{Cl}_2$ )  $\delta$  = 7.70 (d,  $J$  = 8.26 Hz, 2H), 7.47(dd,  $J$  = 1.75Hz,  $J$  = 7.56Hz, 2H), 7.31(d,  $J$  = 8.30 Hz, 2H), 6.98-6.83 (m, 5H), 6.31(dd,  $J$  = 1.55 Hz,  $J$  = 7.94Hz, 2H), 5.90 (d,  $J$  = 17.59 Hz, 1H), 5.40 (d,  $J$  = 10.89 Hz, 1H), 1.68(s, 6H).  $^{13}\text{C}$  NMR (101 MHz,  $\text{CD}_2\text{Cl}_2$ )  $\delta$  = 141.32, 141.12, 137.97, 136.47, 131.77, 130.51, 128.97, 126.70, 125.60, 120.93, 115.18, 114.42, 36.33, 31.44.



**2-(4-Vinylphenyl)pyrimidine-5-carbonitrile (5B).** 2-(4-Vinylphenyl)pyrimidine-5-carbonitrile was prepared *via* Suzuki reaction. 4-Vinylphenylboronic acid (1.8 g, 10 mmol) and 2-chloropyrimidine-5-carbonitrile (1.4 g, 10 mmol) were dissolved in 200 mL of 1,4-dioxane. Then, aqueous  $\text{K}_3\text{PO}_4$  (2M, 25 mL) was added to the above solution, as well as  $\text{Pd}_2(\text{dba})_3$  (458 mg, 0.5 mmol) and Sphos (205 mg, 0.5 mmol) subsequently. After three freeze-thawing cycles, the mixture was heated at  $100\text{ }^\circ\text{C}$  for 4 h. The reaction mixture was filtered hot through a 5 cm plug of Celite, before to be washed with water, brine. After drying over anhydrous  $\text{MgSO}_4$ , filtration and removing of the solvent, the crude product was further purified by silica gel column chromatography (eluent: toluene) to give a yellow powder

(Yield: 0.4 g, 20%).  $^1\text{H}$  NMR (400 MHz,  $\text{CDCl}_3$ )  $\delta$  = 9.03 (s, 2H), 8.52 (d,  $J$  = 8.39 Hz, 2H), 7.59 (d,  $J$  = 8.31 Hz, 2H), 6.75 (dd,  $J$  = 10.88 Hz,  $J$  = 17.56 Hz, 1H), 5.92 (d,  $J$  = 17.79 Hz, 1H), 5.42 (d,  $J$  = 10.92 Hz, 1H).  $^{13}\text{C}$  NMR (101 MHz,  $\text{CDCl}_3$ )  $\delta$  = 166.09, 159.84, 141.86, 136.27, 135.14, 129.66, 126.86, 116.57, 115.18, 106.80.  $^1\text{H}$  NMR (400 MHz,  $\text{CD}_2\text{Cl}_2$ )  $\delta$  = 9.03 (s, 2H), 8.48 (d,  $J$  = 8.39 Hz, 2H), 7.58 (d,  $J$  = 8.31 Hz, 2H), 6.85 (dd,  $J$  = 10.88 Hz,  $J$  = 17.56 Hz, 1H), 5.95 (d,  $J$  = 17.79 Hz, 1H), 5.42 (d,  $J$  = 10.92 Hz, 1H).  $^{13}\text{C}$  NMR (101 MHz,  $\text{CD}_2\text{Cl}_2$ )  $\delta$  = 166.14, 160.28, 142.01, 136.50, 135.63, 129.79, 127.06, 116.56, 115.49, 107.19, 62.53.



**General process of polymerization of S4.** The polymerization of **S4** is also a radical polymerization with 5% AIBN as initiator. Thus, the experimental conditions are the same ones as for **S3** polymers. Using **5A** and **5B** as monomers, the resulting **S4** polymers are yellowish solids with conversions ranging from 33% to 45%.

S4-11:  $^1\text{H}$  NMR (400 MHz,  $\text{CD}_2\text{Cl}_2$ )  $\delta$  = 8.80, 8.16, 7.34, 6.75, 1.54.

S4-31:  $^1\text{H}$  NMR (400 MHz,  $\text{CD}_2\text{Cl}_2$ )  $\delta$  = 8.19, 7.32, 6.71, 6.12, 1.85, 1.53.

S4-51:  $^1\text{H}$  NMR (400 MHz,  $\text{CH}_2\text{Cl}_2$ )  $\delta$  = 8.22, 7.32, 7.10, 6.71, 6.18, 2.45, 1.91, 1.53.

S4-91:  $^1\text{H}$  NMR (400 MHz,  $\text{CD}_2\text{Cl}_2$ )  $\delta$  = 8.21, 7.29, 7.09, 6.67, 6.17, 2.44, 1.91, 1.52.

S4-955:  $^1\text{H}$  NMR (400 MHz,  $\text{CD}_2\text{Cl}_2$ )  $\delta$  = 8.22, 7.29, 7.09, 6.66, 6.17, 2.44, 1.93, 1.52.

S4-991:  $^1\text{H}$  NMR (400 MHz,  $\text{CD}_2\text{Cl}_2$ )  $\delta$  = 8.22, 7.28, 7.09, 6.64, 6.18, 2.43, 1.92, 1.52.

## Appendix 2. Calculations

### Section 3.4: S3 polymers

As the formula of **4A** and **4E** are  $C_{20}H_{15}N$  and  $C_{16}H_{10}N_2$ , respectively, so the real compositions of **S3** polymers can be calculated according the following equations and the results are recorded in Table S1.

$$\frac{C\%}{H\%} = \frac{12[(20(1-x) + 16x)]}{15(1-x) + 10x} = \frac{48(5-x)}{5(3-x)}$$

$$\frac{C\%}{N\%} = \frac{12[(20(1-x)+16x)]}{14[(1-x)+2x]} = \frac{48(5-x)}{14(1+x)}$$

$$\frac{H\%}{N\%} = \frac{15(1-x)+10x}{14[(1-x)+2x]} = \frac{5(3-x)}{14(1+x)}$$

**Table S1** The physical properties of **S3** polymers calculated from EA results

polymers	$x_t$	$x^a$ (C:H)	$x^b$ (C:N)	$x^c$ (H:N)	$x_{EA}^d$
<b>S3-11</b>	0.500	0.625	0.541	0.556	0.549
<b>S3-31</b>	0.250	0.301	0.313	0.311	0.312
<b>S3-51</b>	0.167	0.247	0.205	0.210	0.208
<b>S3-91</b>	0.100	0.133	0.122	0.124	0.123
<b>S3-955</b>	0.050	-	0.052	0.046	0.049
<b>S3-991</b>	0.010	-	-	-	-

$x_t$  value is calculated from the feed ratio; <sup>a</sup>  $x$  value calculated according to the C:H ratio of EA results; <sup>b</sup>  $x$  value calculated according to the C:N ratio of EA results; <sup>c</sup>  $x$  value calculated according to the H:N ratio of EA results; <sup>d</sup>  $x_{EA}$  value is the average of  $x^b$  and  $x^c$ . These data were calculated on the condition of only considering repeating units.

As we all know, in radical polymerization, AIBN serves as an initiator to decompose, eliminating a molecule of nitrogen gas to form two 2-cyanoprop-2-yl radicals, which initiate the polymerization. Therefore, every polymer chain involves one 2-cyanoprop-2-yl end group with the formula of  $C_4H_6N$ , regardless of the length of polymers chains. For **S3-991**, the  $x$  values can't be calculated correctly, mainly because the existence of 2-cyanoprop-2-yl unit affects strongly the composition of polymers. Corresponding to the number-average molecular weight ( $M_{n,SEC} = 1.8 \times 10^4$ ), the average degree of polymerization ( $X_{n,SEC}$ ) of **S3-991** is around 67, therefore, theoretically, **4A:4E:2-cyanoprop-2-yl unit** = 99:1:1.5. The content of 4E and 2-cyanoprop-2-yl unit is so close to each other, so 2-cyanoprop-2-yl unit can't be ignored when doing the calculation. Strictly speaking, the DP value is attributed to absolute number-average molecular weight ( $M_n$ ), which is different from the relative number-average molecular weight ( $M_{n,SEC}$ ) obtained in SEC measurements. That's why here we can't give the  $x$  values.

Section 3.5: **S4** polymers

The formula of **5A** and **5B** are C<sub>23</sub>H<sub>21</sub>N and C<sub>13</sub>H<sub>9</sub>N<sub>3</sub>, so the real composition can be calculated by the following equations.

$$\frac{\text{C}\%}{\text{H}\%} = \frac{12[(23(1-x)+13x)]}{21(1-x)+9x} = \frac{4(23-10x)}{7-4x},$$

$$\frac{\text{C}\%}{\text{N}\%} = \frac{12[(23(1-x)+13x)]}{14[(1-x)+3x]} = \frac{6(23-10x)}{7(1+2x)},$$

$$\frac{\text{H}\%}{\text{N}\%} = \frac{21(1-x)+9x}{14[(1-x)+3x]} = \frac{3(7-4x)}{14(1+2x)}$$

**Table S2** The physical properties of **S3** polymers calculated from EA results

polymers	$x_t$	$x^a$ (C:H)	$x^b$ (C:N)	$x^c$ (H:N)	$x_{EA}^d$
<b>S4-11</b>	0.500	1.034	0.345	0.474	0.410
<b>S4-31</b>	0.250	0.931	0.226	0.331	0.278
<b>S4-51</b>	0.167	0.913	0.169	0.270	0.220
<b>S4-91</b>	0.100	0.876	0.126	0.218	0.172
<b>S4-955</b>	0.050	0.830	0.088	0.171	0.129
<b>S4-991</b>	0.010	0.818	0.041	0.120	0.080

$x_t$  value is calculated from the feed ratio; <sup>a</sup>  $x$  value calculated according to the C:H ratio of EA results; <sup>b</sup>  $x$  value calculated according to the C:N ratio of EA results; <sup>c</sup>  $x$  value calculated according to the H:N ratio of EA results; <sup>d</sup>  $x_{EA}$  value is the average of  $x^b$  and  $x^c$ . These data were calculated on the condition of only considering repeating units.

### Appendix 3. Figures

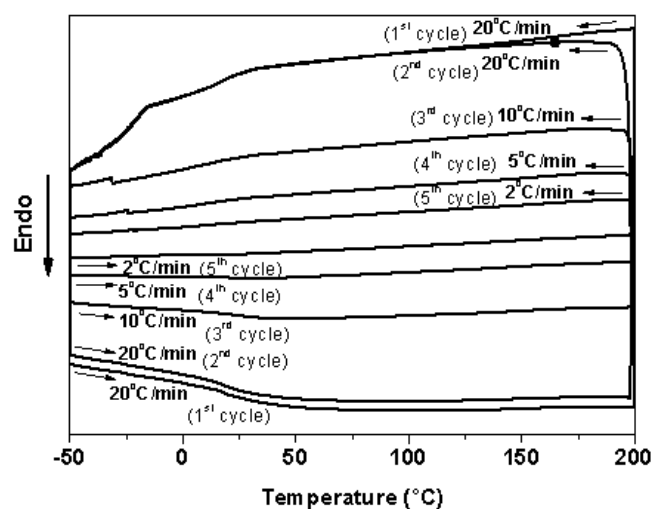


**Figure S1** DSC telegrams of PBTTT-Tri on heating and cooling at a rate of 20 °C/min, 10 °C/min, 5 °C/min, and 2 °C/min.

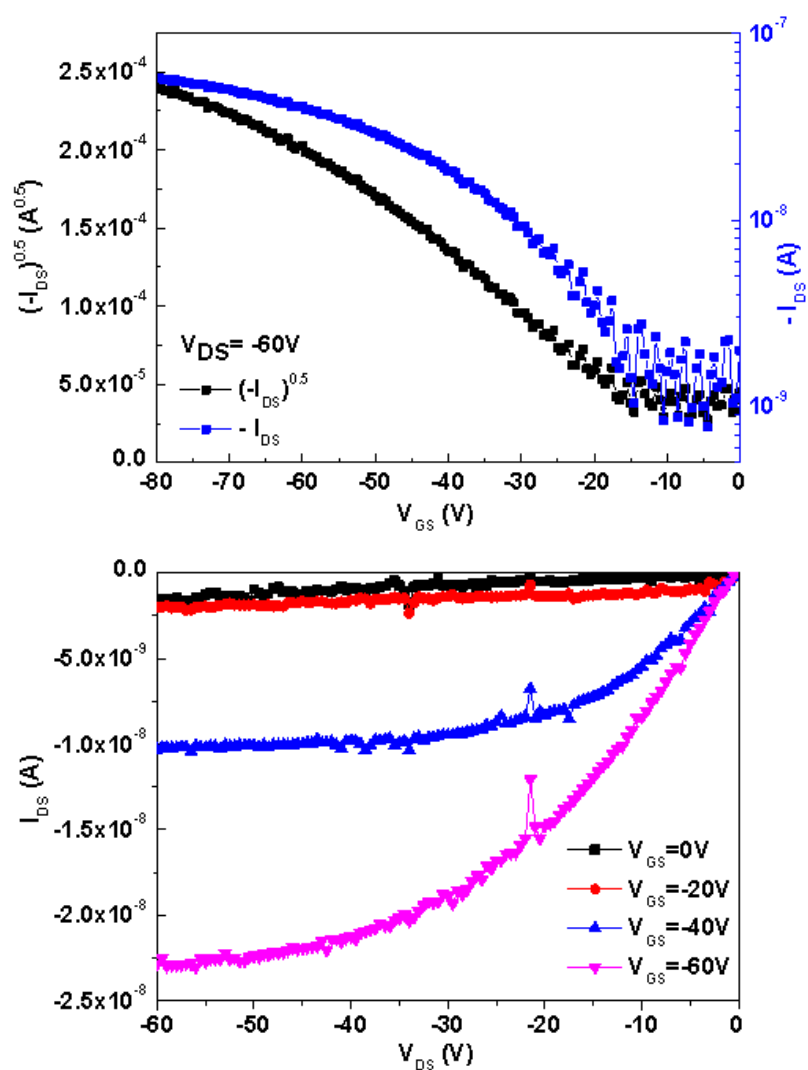


**Figure S2** The output and transfer characteristics of the as-prepared PBTTT-Tri transistor.

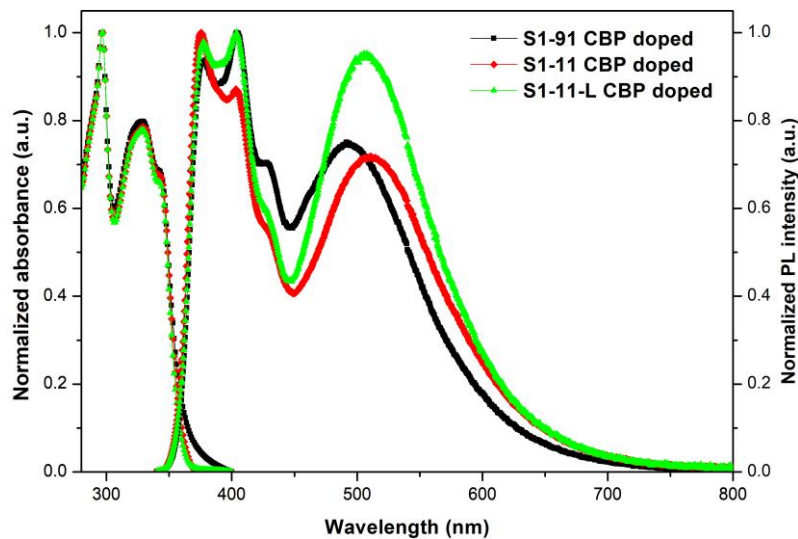


**Figure S3** Absorption and emission spectra of **S1** polymers in CBP doped film (10 wt%).

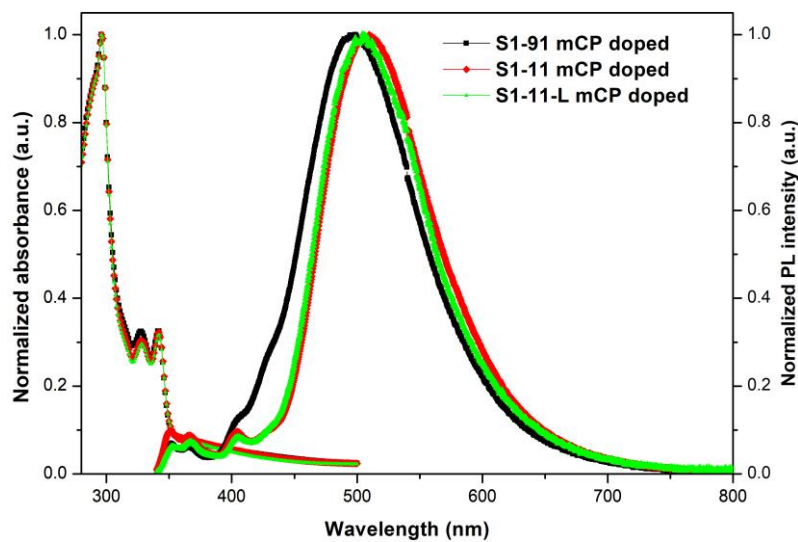


**Figure S4** Absorption and emission spectra of **S1** polymers in mCP doped film (10 wt%).

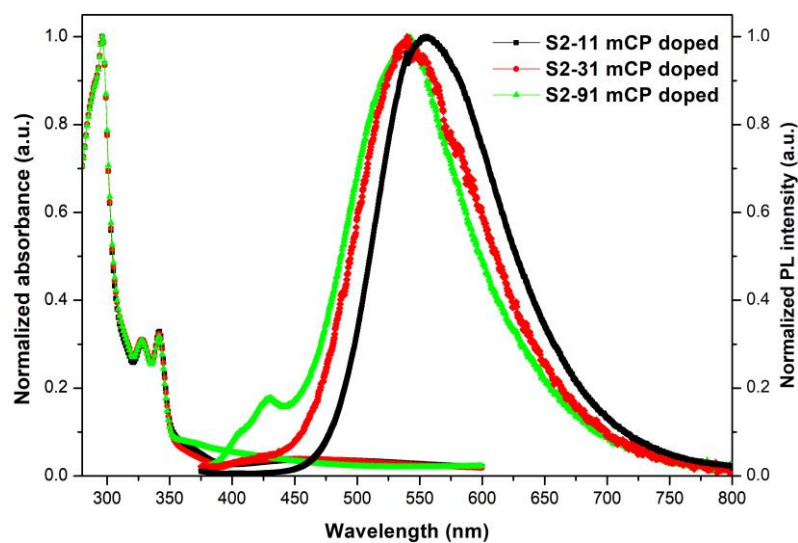


**Figure S5** Absorption and emission spectra of **S2** polymers in blend films (10 wt% in mCP).

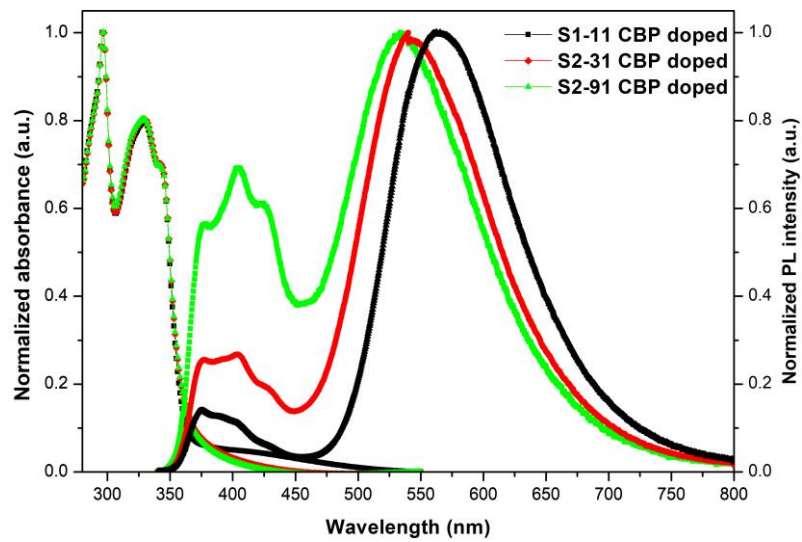


**Figure S6** Absorption and emission spectra of **S2** polymers in blend films (CBP).

## References

- (1) Shirakawa, H.; Louis, E. J.; MacDiarmid, A. G.; Chiang, C. K.; Heeger, A. J. Synthesis of Electrically Conducting Organic Polymers: Halogen Derivatives of Polyacetylene, (CH). *J. Chem. Soc. Chem. Commun.* **1977**, No. 16, 578–580. <https://doi.org/10.1039/C39770000578>.
- (2) Burroughes, J. H.; Bradley, D. D. C.; Brown, A. R.; Marks, R. N.; Mackay, K.; Friend, R. H.; Burns, P. L.; Holmes, A. B. Light-Emitting Diodes Based on Conjugated Polymers. *Nature* **1990**, *347* (6293), 539–541. <https://doi.org/10.1038/347539a0>.
- (3) Yang, J.; Zhao, Z.; Wang, S.; Guo, Y.; Liu, Y. Insight into High-Performance Conjugated Polymers for Organic Field-Effect Transistors. *Chem* **2018**, *4* (12), 2748–2785. <https://doi.org/10.1016/j.chempr.2018.08.005>.
- (4) Wang, C.; Dong, H.; Jiang, L.; Hu, W. Organic Semiconductor Crystals. *Chem. Soc. Rev.* **2018**, *47* (2), 422–500. <https://doi.org/10.1039/c7cs00490g>.
- (5) Argun, A. A.; Cirpan, A.; Reynolds, J. R. The First Truly All-Polymer Electrochromic Devices. *Adv. Mater.* **2003**, *15* (16), 1338–1341. <https://doi.org/10.1002/adma.200305038>.
- (6) Chen, S.; Teng, C.; Zhang, M.; Li, Y.; Xie, D.; Shi, G. A Flexible UV–Vis–NIR Photodetector Based on a Perovskite/Conjugated-Polymer Composite. *Adv. Mater.* **2016**, *28* (28), 5969–5974. <https://doi.org/10.1002/adma.201600468>.
- (7) Yi, H. T.; Payne, M. M.; Anthony, J. E.; Podzorov, V. Ultra-Flexible Solution-Processed Organic Field-Effect Transistors. *Nat. Commun.* **2012**, *3* (May), 1–7. <https://doi.org/10.1038/ncomms2263>.
- (8) Søndergaard, R. R.; Hösel, M.; Krebs, F. C. Roll-to-Roll Fabrication of Large Area Functional Organic Materials. *J. Polym. Sci. Part B Polym. Phys.* **2013**, *51* (1), 16–34. <https://doi.org/10.1002/polb.23192>.
- (9) Liang, Y.; Feng, D.; Wu, Y.; Tsai, S.-T.; Li, G.; Ray, C.; Yu, L. Highly Efficient Solar Cell Polymers Developed via Fine-Tuning of Structural and Electronic Properties. *J. Am. Chem. Soc.* **2009**, *131* (22), 7792–7799. <https://doi.org/10.1021/ja901545q>.
- (10) Rivnay, J.; Owens, R. M.; Malliaras, G. G. The Rise of Organic Bioelectronics. *Chem. Mater.* **2014**, *26* (1), 679–685. <https://doi.org/10.1021/cm4022003>.
- (11) Salzner, U.; Lagowski, J.; Pickup, P.; Poirier, R. Comparison of Geometries and Electronic Structures of Polyacetylene, Polyborole, Polycyclopentadiene, Polypyrrole, Polyfuran, Polysilole, Polyphosphole, Polythiophene, Polyselenophene and Polytellurophene. *Synth. Met.* **1998**, *96* (1998), 177–189.
- (12) Lövenich, W. PEDOT-Properties and Applications. *Polym. Sci. Ser. C* **2014**, *56* (1), 135–143. <https://doi.org/10.1134/S1811238214010068>.
- (13) Wang, L.; Nan, G.; Yang, X.; Peng, Q.; Li, Q.; Shuai, Z. Computational Methods for Design of Organic Materials with High Charge Mobility. *Chem. Soc. Rev.* **2010**, *39* (2), 423–434. <https://doi.org/10.1039/b816406c>.
- (14) Takeya, J.; Yamagishi, M.; Tominari, Y.; Hirahara, R.; Nakazawa, Y.; Nishikawa, T.; Kawase, T.; Shimoda, T.; Ogawa, S. Very High-Mobility Organic Single-Crystal Transistors with in-Crystal Conduction Channels. *Appl. Phys. Lett.* **2007**, *90* (10), 102120. <https://doi.org/10.1063/1.2711393>.
- (15) Malagoli, M.; Brédas, J. L. Density Functional Theory Study of the Geometric Structure and Energetics of Triphenylamine-Based Hole-Transporting Molecules. *Chem. Phys. Lett.* **2000**, *327* (1), 13–17. [https://doi.org/https://doi.org/10.1016/S0009-2614\(00\)00757-0](https://doi.org/https://doi.org/10.1016/S0009-2614(00)00757-0).
- (16) McNeill, R.; Siudak, R.; Wardlaw, J. H.; Weiss, D. E. Electronic Conduction in Polymers. I. The Chemical Structure of Polypyrrole. *Aust. J. Chem.* **1963**, *16* (6), 1056–1075.
- (17) De Surville, R.; Jozefowicz, M.; Yu, L. T.; Pepichon, J.; Buvet, R. Electrochemical Chains Using Protolytic Organic Semiconductors. *Electrochim. Acta* **1968**, *13* (6), 1451–1458. [https://doi.org/https://doi.org/10.1016/0013-4686\(68\)80071-4](https://doi.org/https://doi.org/10.1016/0013-4686(68)80071-4).
- (18) Loewe, R. S.; Khersonsky, S. M.; McCullough, R. D. A Simple Method to Prepare Head-to-Tail Coupled, Regioregular Poly(3-Alkylthiophenes) Using Grignard Metathesis. *Adv. Mater.* **1999**, *11* (3), 250–253. [https://doi.org/10.1002/\(SICI\)1521-4095\(199903\)11:3<250::AID-ADMA250>3.0.CO;2-J](https://doi.org/10.1002/(SICI)1521-4095(199903)11:3<250::AID-ADMA250>3.0.CO;2-J).

- (19) Morin, P. O.; Bura, T.; Leclerc, M. Realizing the Full Potential of Conjugated Polymers: Innovation in Polymer Synthesis. *Mater. Horizons* **2016**, *3* (1), 11–20. <https://doi.org/10.1039/c5mh00164a>.
- (20) Gomez, I. J.; Arnaiz, B.; Cacioppo, M.; Arcudi, F.; Prato, M. Upgrading the Chemistry of  $\pi$ -Conjugated Polymers toward More Sustainable Materials. *J. Mater. Chem. B* **2018**, *6* (35). <https://doi.org/10.1039/x0xx00000x>.
- (21) Karakawa, M.; Chikamatsu, M.; Nakamoto, C.; Maeda, Y.; Kubota, S.; Yase, K. Organic Light-Emitting Diode Application of Fluorescent Cellulose as a Natural Polymer. *Macromol. Chem. Phys.* **2007**, *208* (18), 2000–2006. <https://doi.org/10.1002/macp.200700154>.
- (22) Bredas, J. L.; Silbey, R.; Boudreaux, D. S.; Chance, R. R. Chain-Length Dependence of Electronic and Electrochemical Properties of Conjugated Systems: Polyacetylene, Polyphenylene, Polythiophene, and Polypyrrole. *J. Am. Chem. Soc.* **1983**, *105* (22), 6555–6559. <https://doi.org/10.1021/ja00360a004>.
- (23) Klaerner, G.; Miller, R. D. Polyfluorene Derivatives: Effective Conjugation Lengths from Well-Defined Oligomers. *Macromolecules* **1998**, *31* (6), 2007–2009. <https://doi.org/10.1021/ma971073e>.
- (24) Schaffer, H. E.; Chance, R. R.; Knoll, K.; Schrock, R. R.; Silbey, R. Linear Optical Properties of a Series of Polyacetylene Oligomers BT - Conjugated Polymeric Materials: Opportunities in Electronics, Optoelectronics, and Molecular Electronics; Brédas, J. L., Chance, R. R., Eds.; Springer Netherlands: Dordrecht, 1990; pp 365–376. [https://doi.org/10.1007/978-94-009-2041-5\\_27](https://doi.org/10.1007/978-94-009-2041-5_27).
- (25) Meier, H.; Stalmach, U.; Kolshorn, H. Effective Conjugation Length and UV/Vis Spectra of Oligomers. *Acta Polym.* **1997**, *48* (9), 379–384. <https://doi.org/10.1002/actp.1997.010480905>.
- (26) Ashraf, R. S.; Meager, I.; Nikolka, M.; Kirkus, M.; Planells, M.; Schroeder, B. C.; Holliday, S.; Hurhangee, M.; Nielsen, C. B.; Siringhaus, H.; McCulloch, I. Chalcogenophene Comonomer Comparison in Small Bandgap Diketopyrrolopyrrole-Based Conjugated Polymers for High-Performing Field-Effect Transistors and Organic Solar Cells. *J. Am. Chem. Soc.* **2015**, *137* (3), 1314–1321. <https://doi.org/10.1021/ja511984q>.
- (27) Hoogmartens, I.; Adriaensens, P.; Vanderzande, D.; Gelan, J.; Quattrocchi, C.; Lazzaroni, R.; Bredas, J. L. Low-Bandgap Conjugated Polymers. A Joint Experimental and Theoretical Study of the Structure of Polyisothianaphthene. *Macromolecules* **1992**, *25* (26), 7347–7356. <https://doi.org/10.1021/ma00052a043>.
- (28) Bouzzine, S. M.; Bouzakraoui, S.; Hamidi, M.; Bouachrine, M. Impact of the Torsion on the Optoelectronic Properties of Poly(3-Alkylthiophene): A Spectroscopic and Theoretical Approaches. *Asian J. Chem.* **2007**, *19* (3), 1651–1657.
- (29) Spencer, H. J.; Skabara, P. J.; Giles, M.; McCulloch, I.; Coles, S. J.; Hursthouse, M. B. The First Direct Experimental Comparison between the Hugely Contrasting Properties of PEDOT and the All-Sulfur Analogue PEDTT by Analogy with Well-Defined EDTT–EDOT Copolymers. *J. Mater. Chem.* **2005**, *15* (45), 4783–4792. <https://doi.org/10.1039/B511075K>.
- (30) Havinga, E. E.; ten Hoeve, W.; Wynberg, H. Alternate Donor-Acceptor Small-Band-Gap Semiconducting Polymers; Polysquaraines and Polycroconaines. *Synth. Met.* **1993**, *55* (1), 299–306. [https://doi.org/https://doi.org/10.1016/0379-6779\(93\)90949-W](https://doi.org/https://doi.org/10.1016/0379-6779(93)90949-W).
- (31) Elbing, M.; Garcia, A.; Urban, S.; Nguyen, T.-Q.; Bazan, G. C. In Situ Conjugated Polyelectrolyte Formation. *Macromolecules* **2008**, *41* (23), 9146–9155. <https://doi.org/10.1021/ma802139j>.
- (32) Meyer, D. L.; Schmidt-Meinzer, N.; Matt, C.; Rein, S.; Lombeck, F.; Sommer, M.; Biskup, T. Side-Chain Engineering of Conjugated Polymers: Distinguishing Its Impact on Film Morphology and Electronic Structure. *J. Phys. Chem. C* **2019**, *123* (33), 20071–20083. <https://doi.org/10.1021/acs.jpcc.9b02835>.
- (33) Grand, C.; Zajaczkowski, W.; Deb, N.; Lo, C. K.; Hernandez, J. L.; Bucknall, D. G.; Müllen, K.; Pisula, W.; Reynolds, J. R. Morphology Control in Films of Isoindigo Polymers by Side-Chain and Molecular Weight Effects. *ACS Appl. Mater. Interfaces* **2017**, *9* (15), 13357–13368. <https://doi.org/10.1021/acsami.6b16502>.
- (34) Lei, T.; Dou, J.-H.; Pei, J. Influence of Alkyl Chain Branching Positions on the Hole Mobilities of Polymer Thin-Film Transistors. *Adv. Mater.* **2012**, *24* (48), 6457–6461.

- <https://doi.org/10.1002/adma.201202689>.
- (35) Graham, K. R.; Cabanetos, C.; Jahnke, J. P.; Idso, M. N.; El Labban, A.; Ngongang Ndjawa, G. O.; Heumueller, T.; Vandewal, K.; Salleo, A.; Chmelka, B. F.; Amassian, A.; Beaujuge, P. M.; McGehee, M. D. Importance of the Donor:Fullerene Intermolecular Arrangement for High-Efficiency Organic Photovoltaics. *J. Am. Chem. Soc.* **2014**, *136* (27), 9608–9618. <https://doi.org/10.1021/ja502985g>.
- (36) Guo, X.; Watson, M. D. Conjugated Polymers from Naphthalene Bisimide. *Org. Lett.* **2008**, *10* (23), 5333–5336. <https://doi.org/10.1021/ol801918y>.
- (37) Smith, Z. C.; Meyer, D. M.; Simon, M. G.; Staii, C.; Shukla, D.; Thomas, S. W. Thiophene-Based Conjugated Polymers with Photolabile Solubilizing Side Chains. *Macromolecules* **2015**, *48* (4), 959–966. <https://doi.org/10.1021/ma502289n>.
- (38) Jakob, S.; Moreno, A.; Zhang, X.; Bertschi, L.; Smith, P.; Schlüter, A. D.; Sakamoto, J. Synthesis of Polyphenylenes from a Soluble Precursor: The “Shaving” Approach. *Macromolecules* **2010**, *43* (19), 7916–7918. <https://doi.org/10.1021/ma101771t>.
- (39) Ito, T.; Shirakawa, H.; Ikeda, S. Simultaneous Polymerization and Formation of Polyacetylene Film on the Surface of Concentrated Soluble Ziegler-Type Catalyst Solution. *J. Polym. Sci. Polym. Chem. Ed.* **1974**, *12* (1), 11–20. <https://doi.org/10.1002/pol.1974.170120102>.
- (40) Sadki, S.; Schottland, P.; Brodie, N.; Sabouraud, G. The Mechanisms of Pyrrole Electropolymerization. *Chem. Soc. Rev.* **2000**, *29* (5), 283–293. <https://doi.org/10.1039/A807124A>.
- (41) Toshima, N.; Hara, S. Direct Synthesis of Conducting Polymers from Simple Monomers. *Prog. Polym. Sci.* **1995**, *20* (1), 155–183. [https://doi.org/https://doi.org/10.1016/0079-6700\(94\)00029-2](https://doi.org/https://doi.org/10.1016/0079-6700(94)00029-2).
- (42) Roncali, J. Conjugated Poly(Thiophenes): Synthesis, Functionalization, and Applications. *Chem. Rev.* **1992**, *92* (4), 711–738. <https://doi.org/10.1021/cr00012a009>.
- (43) Waltman, R. J.; Bargon, J. Electrically Conducting Polymers: A Review of the Electropolymerization Reaction, of the Effects of Chemical Structure on Polymer Film Properties, and of Applications towards Technology. *Can. J. Chem.* **1986**, *64* (1), 76–95. <https://doi.org/10.1139/v86-015>.
- (44) Xu, S.; Kim, E. H.; Wei, A.; Negishi, E. I. Pd- and Ni-Catalyzed Cross-Coupling Reactions in the Synthesis of Organic Electronic Materials. *Sci. Technol. Adv. Mater.* **2014**, *15* (4). <https://doi.org/10.1088/1468-6996/15/4/044201>.
- (45) Carsten, B.; He, F.; Son, H. J.; Xu, T.; Yu, L. Stille Polycondensation for Synthesis of Functional Materials. *Chem. Rev.* **2011**, *111* (3), 1493–1528. <https://doi.org/10.1021/cr100320w>.
- (46) Bao, Z.; Chan, W.; Yu, L. Synthesis of Conjugated Polymer by the Stille Coupling Reaction. *Chem. Mater.* **1993**, *5* (1), 2–3. <https://doi.org/10.1021/cm00025a001>.
- (47) Suzuki, A. Cross-Coupling Reactions Of Organoboranes: An Easy Way To Construct C–C Bonds (Nobel Lecture). *Angew. Chemie Int. Ed.* **2011**, *50* (30), 6722–6737. <https://doi.org/10.1002/anie.201101379>.
- (48) Matos, K.; Soderquist, J. A. Alkylboranes in the Suzuki–Miyaura Coupling: Stereochemical and Mechanistic Studies. *J. Org. Chem.* **1998**, *63* (3), 461–470. <https://doi.org/10.1021/jo971681s>.
- (49) Smith, G. B.; Dezeny, G. C.; Hughes, D. L.; King, A. O.; Verhoeven, T. R. Mechanistic Studies of the Suzuki Cross-Coupling Reaction. *J. Org. Chem.* **1994**, *59* (26), 8151–8156. <https://doi.org/10.1021/jo00105a036>.
- (50) Spivey, A. C.; Fekner, T.; Spey, S. E. Axially Chiral Analogues of 4-(Dimethylamino)Pyridine: Novel Catalysts for Nonenzymatic Enantioselective Acylations. *J. Org. Chem.* **2000**, *65* (10), 3154–3159. <https://doi.org/10.1021/jo0000574>.
- (51) Miyaura, N.; Yamada, K.; Suginome, H.; Suzuki, A. Novel and Convenient Method for the Stereo- and Regiospecific Synthesis of Conjugated Alkadienes and Alkynes via the Palladium-Catalyzed Cross-Coupling Reaction of 1-Alkenylboranes with Bromoalkenes and Bromoalkynes. *J. Am. Chem. Soc.* **1985**, *107* (4), 972–980. <https://doi.org/10.1021/ja00290a037>.
- (52) Doubina, N.; Ho, A.; Jen, A. K.-Y.; Luscombe, C. K. Effect of Initiators on the Kumada

- Catalyst-Transfer Polycondensation Reaction. *Macromolecules* **2009**, *42* (20), 7670–7677. <https://doi.org/10.1021/ma901410k>.
- (53) Leclerc, M.; Diaz, F. M.; Wegner, G. Structural Analysis of Poly(3-Alkylthiophene)s. *Die Makromol. Chemie* **1989**, *190* (12), 3105–3116. <https://doi.org/10.1002/macp.1989.021901208>.
- (54) McCullough, R. D.; Lowe, R. D. Enhanced Electrical Conductivity in Regioselectively Synthesized Poly(3-Alkylthiophenes). *J. Chem. Soc. Chem. Commun.* **1992**, No. 1, 70–72. <https://doi.org/10.1039/C39920000070>.
- (55) Chen, T. A.; Rieke, R. D. The First Regioregular Head-to-Tail Poly(3-Hexylthiophene-2,5-Diyl) and a Regiorandom Isopolymer: Nickel versus Palladium Catalysis of 2(5)-Bromo-5(2)-(Bromozincio)-3-Hexylthiophene Polymerization. *J. Am. Chem. Soc.* **1992**, *114* (25), 10087–10088. <https://doi.org/10.1021/ja00051a066>.
- (56) Iovu, M. C.; Sheina, E. E.; Gil, R. R.; McCullough, R. D. Experimental Evidence for the Quasi-“Living” Nature of the Grignard Metathesis Method for the Synthesis of Regioregular Poly(3-Alkylthiophenes). *Macromolecules* **2005**, *38* (21), 8649–8656. <https://doi.org/10.1021/ma051122k>.
- (57) Kuwabara, J.; Yasuda, T.; Choi, S. J.; Lu, W.; Yamazaki, K.; Kagaya, S.; Han, L.; Kanbara, T. Direct Arylation Polycondensation: A Promising Method for the Synthesis of Highly Pure, High-Molecular-Weight Conjugated Polymers Needed for Improving the Performance of Organic Photovoltaics. *Adv. Funct. Mater.* **2014**, *24* (21), 3226–3233. <https://doi.org/10.1002/adfm.201302851>.
- (58) Wang, Q.; Takita, R.; Kikuzaki, Y.; Ozawa, F. Palladium-Catalyzed Dehydrohalogenative Polycondensation of 2-Bromo-3-Hexylthiophene: An Efficient Approach to Head-to-Tail Poly(3-Hexylthiophene). *J. Am. Chem. Soc.* **2010**, *132* (33), 11420–11421. <https://doi.org/10.1021/ja105767z>.
- (59) Patra, A.; Agrawal, V.; Bhargav, R.; Shahjad; Bhardwaj, D.; Chand, S.; Sheynin, Y.; Bendikov, M. Metal Free Conducting PEDOS, PEDOT, and Their Analogues via an Unusual Bromine-Catalyzed Polymerization. *Macromolecules* **2015**, *48* (24), 8760–8764. <https://doi.org/10.1021/acs.macromol.5b01777>.
- (60) Maji, M. S.; Pfeifer, T.; Studer, A. Transition-Metal-Free Synthesis of Conjugated Polymers from Bis-Grignard Reagents by Using TEMPO as Oxidant. *Chem. – A Eur. J.* **2010**, *16* (20), 5872–5875. <https://doi.org/10.1002/chem.201000236>.
- (61) Kuwabara, J.; Yasuda, T.; Takase, N.; Kanbara, T. Effects of the Terminal Structure, Purity, and Molecular Weight of an Amorphous Conjugated Polymer on Its Photovoltaic Characteristics. *ACS Appl. Mater. Interfaces* **2016**, *8* (3), 1752–1758. <https://doi.org/10.1021/acsami.5b09482>.
- (62) Barik, S.; Skene, W. G. A Fluorescent All-Fluorene Polyazomethine—towards Soluble Conjugated Polymers Exhibiting High Fluorescence and Electrochromic Properties. *Polym. Chem.* **2011**, *2* (5), 1091–1097. <https://doi.org/10.1039/C0PY00394H>.
- (63) Greenham, N. C.; Moratti, S. C.; Bradley, D. D. C.; Friend, R. H.; Holmes, A. B. Efficient Light-Emitting Diodes Based on Polymers with High Electron Affinities. *Nature* **1993**, *365* (6447), 628–630. <https://doi.org/10.1038/365628a0>.
- (64) Zhou, J.; Xiao, X.; Cheng, X.-F.; Gao, B.-J.; He, J.-H.; Xu, Q.-F.; Li, H.; Li, N.-J.; Chen, D.-Y.; Lu, J.-M. Surface Modification of Polysquaraines to Sense Humidity within a Second for Breath Monitoring. *Sensors Actuators B Chem.* **2018**, *271*, 137–146. <https://doi.org/https://doi.org/10.1016/j.snb.2018.05.085>.
- (65) Goto, E.; Ochiai, Y.; Ueda, M.; Higashihara, T. Transition-Metal-Free and Halogen-Free Controlled Synthesis of Poly(3-Alkylthienylene Vinylene) via the Horner–Wadsworth–Emmons Condensation Reaction. *Polym. Chem.* **2018**, *9* (15), 1996–2001. <https://doi.org/10.1039/C8PY00225H>.
- (66) Zhang, G.; Dai, Y.; Liu, Y.; Liu, J.; Lu, H.; Qiu, L.; Cho, K. Facile Green Synthesis of Isoindigo-Based Conjugated Polymers Using Aldol Polycondensation. *Polym. Chem.* **2017**, *8* (22), 3448–3456. <https://doi.org/10.1039/C7PY00484B>.
- (67) Tsumura, A.; Koezuka, H.; Ando, T. Macromolecular Electronic Device: Field-Effect Transistor with a Polythiophene Thin Film. *Appl. Phys. Lett.* **1986**, *49* (18), 1210–1212. <https://doi.org/10.1063/1.97417>.

- (68) Yagi, I.; Hirai, N.; Miyamoto, Y.; Noda, M.; Imaoka, A.; Yoneya, N.; Nomoto, K.; Kasahara, J.; Yumoto, A.; Urabe, T. A Flexible Full-Color AMOLED Display Driven by OTFTs. *J. Soc. Inf. Disp.* **2008**, *16* (1), 15. <https://doi.org/10.1889/1.2835023>.
- (69) Stadlober, B.; Zirkel, M.; Leising, G.; Gaar, N.; Graz, I.; Bauer-Gogonea, S.; Bauer, S. Transparent Pyroelectric Sensors and Organic Field-Effect Transistors with Fluorinated Polymers: Steps towards Organic Infrared Detectors. *IEEE Trans. Dielectr. Electr. Insul.* **2006**, *13* (5), 1087–1092. <https://doi.org/10.1109/TDEI.2006.247836>.
- (70) Baude, P. F.; Ender, D. A.; Haase, M. A.; Kelley, T. W.; Muyres, D. V.; Theiss, S. D. Pentacene-Based Radio-Frequency Identification Circuitry. *Appl. Phys. Lett.* **2003**, *82* (22), 3964–3966. <https://doi.org/10.1063/1.1579554>.
- (71) Wilke, G.; Ortmeier, J. Organic Field Effect Transistors. In *Coatings for Plastics*; 2019; pp 13–18. <https://doi.org/10.1515/9783748602224-002>.
- (72) Sirringhaus, H. Device Physics of Solution-Processed Organic Field-Effect Transistors. *Adv. Mater.* **2005**, *17* (20), 2411–2425. <https://doi.org/10.1002/adma.200501152>.
- (73) Koezuka, H.; Tsumura, A.; Ando, T. Field-Effect Transistor with Polythiophene Thin Film. *Synth. Met.* **1987**, *18* (1), 699–704. [https://doi.org/https://doi.org/10.1016/0379-6779\(87\)90964-7](https://doi.org/https://doi.org/10.1016/0379-6779(87)90964-7).
- (74) Wang, J. Z.; Gu, J.; Zenhausern, F.; Sirringhaus, H. Low-Cost Fabrication of Submicron All Polymer Field Effect Transistors. *Appl. Phys. Lett.* **2006**, *88* (13), 133502. <https://doi.org/10.1063/1.2191088>.
- (75) Sharma, A.; Madhu, C.; Singh, J. Performance Evaluation of Thin Film Transistors: History, Technology Development and Comparison: A Review. *Int. J. Comput. Appl.* **2014**, *89* (15), 36–40. <https://doi.org/10.5120/15710-4603>.
- (76) Zhang, C.; Zhao, G.; Zeng, W.; Tian, K.; Dong, H.; Hu, W.; Qin, J.; Yang, C. Ambipolar Copolymer of Dithienocoronenedi-Imide and Benzo(Bis)Thiadiazole with Balanced Hole and Electron Mobility. *Org. Electron.* **2015**, *16* (November), 101–108. <https://doi.org/10.1016/j.orgel.2014.11.001>.
- (77) Wang, Z.; Al-Jawhari, H. A.; Nayak, P. K.; Caraveo-Frescas, J. A.; Wei, N.; Hedhili, M. N.; Alshareef, H. N. Low Temperature Processed Complementary Metal Oxide Semiconductor (CMOS) Device by Oxidation Effect from Capping Layer. *Sci. Rep.* **2015**, *5*, 1–6. <https://doi.org/10.1038/srep09617>.
- (78) Tiwari, S.; Greenham, N. C. Charge Mobility Measurement Techniques in Organic Semiconductors. *Opt. Quantum Electron.* **2009**, *41* (2), 69–89. <https://doi.org/10.1007/s11082-009-9323-0>.
- (79) Sirringhaus, H. 25th Anniversary Article: Organic Field-Effect Transistors: The Path beyond Amorphous Silicon. *Adv. Mater.* **2014**, *26* (9), 1319–1335. <https://doi.org/10.1002/adma.201304346>.
- (80) Venkateshvaran, D.; Nikolka, M.; Sadhanala, A.; Lemaur, V.; Zelazny, M.; Kepa, M.; Hurhangee, M.; Kronemeijer, A. J.; Pecunia, V.; Nasrallah, I.; Romanov, I.; Broch, K.; McCulloch, I.; Emin, D.; Olivier, Y.; Cornil, J.; Beljonne, D.; Sirringhaus, H. Approaching Disorder-Free Transport in High-Mobility Conjugated Polymers. *Nature* **2014**, *515* (7527), 384–388. <https://doi.org/10.1038/nature13854>.
- (81) Shi, L.; Guo, Y.; Hu, W.; Liu, Y. Design and Effective Synthesis Methods for High-Performance Polymer Semiconductors in Organic Field-Effect Transistors. *Mater. Chem. Front.* **2017**, *1* (12), 2423–2456. <https://doi.org/10.1039/C7QM00169J>.
- (82) Quinn, J. T. E.; Zhu, J.; Li, X.; Wang, J.; Li, Y. Recent Progress in the Development of N-Type Organic Semiconductors for Organic Field Effect Transistors. *J. Mater. Chem. C* **2017**, *5* (34), 8654–8681. <https://doi.org/10.1039/C7TC01680H>.
- (83) Guo, X.; Ortiz, R. P.; Zheng, Y.; Hu, Y.; Noh, Y.-Y.; Baeg, K.-J.; Facchetti, A.; Marks, T. J. Bithiophene-Imide-Based Polymeric Semiconductors for Field-Effect Transistors: Synthesis, Structure–Property Correlations, Charge Carrier Polarity, and Device Stability. *J. Am. Chem. Soc.* **2011**, *133* (5), 1405–1418. <https://doi.org/10.1021/ja107678m>.
- (84) Guo, X.; Facchetti, A.; Marks, T. J. Imide- and Amide-Functionalized Polymer Semiconductors. *Chem. Rev.* **2014**, *114* (18), 8943–9021. <https://doi.org/10.1021/cr500225d>.
- (85) Mei, J.; Bao, Z. Side Chain Engineering in Solution-Processable Conjugated Polymers. *Chem.*

- Mater.* **2014**, *26* (1), 604–615. <https://doi.org/10.1021/cm4020805>.
- (86) Tseng, H. R.; Phan, H.; Luo, C.; Wang, M.; Perez, L. A.; Patel, S. N.; Ying, L.; Kramer, E. J.; Nguyen, T. Q.; Bazan, G. C.; Heeger, A. J. High-Mobility Field-Effect Transistors Fabricated with Macroscopic Aligned Semiconducting Polymers. *Adv. Mater.* **2014**, *26* (19), 2993–2998. <https://doi.org/10.1002/adma.201305084>.
- (87) Lei, T.; Wang, J.-Y.; Pei, J. Design, Synthesis, and Structure–Property Relationships of Isoindigo-Based Conjugated Polymers. *Acc. Chem. Res.* **2014**, *47* (4), 1117–1126. <https://doi.org/10.1021/ar400254j>.
- (88) Zhao, X.; Zhan, X. Electron Transporting Semiconducting Polymers in Organic Electronics. *Chem. Soc. Rev.* **2011**, *40* (7), 3728–3743. <https://doi.org/10.1039/c0cs00194e>.
- (89) Zheng, Y.-Q.; Lei, T.; Dou, J.-H.; Xia, X.; Wang, J.-Y.; Liu, C.-J.; Pei, J. Strong Electron-Deficient Polymers Lead to High Electron Mobility in Air and Their Morphology-Dependent Transport Behaviors. *Adv. Mater.* **2016**, *28* (33), 7213–7219. <https://doi.org/10.1002/adma.201600541>.
- (90) Bura, T.; Beaupré, S.; Ibraikulov, O. A.; Légaré, M.-A.; Quinn, J.; Lévêque, P.; Heiser, T.; Li, Y.; Leclerc, N.; Leclerc, M. New Fluorinated Dithienyldiketopyrrolopyrrole Monomers and Polymers for Organic Electronics. *Macromolecules* **2017**, *50* (18), 7080–7090. <https://doi.org/10.1021/acs.macromol.7b01198>.
- (91) Xiao, C.; Zhao, G.; Zhang, A.; Jiang, W.; Janssen, R. A. J.; Li, W.; Hu, W.; Wang, Z. High Performance Polymer Nanowire Field-Effect Transistors with Distinct Molecular Orientations. *Adv. Mater.* **2015**, *27* (34), 4963–4968. <https://doi.org/10.1002/adma.201502617>.
- (92) Fu, B.; Wang, C.-Y.; Rose, B. D.; Jiang, Y.; Chang, M.; Chu, P.-H.; Yuan, Z.; Fuentes-Hernandez, C.; Kippelen, B.; Brédas, J.-L.; Collard, D. M.; Reichmanis, E. Molecular Engineering of Nonhalogenated Solution-Processable Bithiazole-Based Electron-Transport Polymeric Semiconductors. *Chem. Mater.* **2015**, *27* (8), 2928–2937. <https://doi.org/10.1021/acs.chemmater.5b00173>.
- (93) Ryu, G.-S.; Chen, Z.; Usta, H.; Noh, Y.-Y.; Facchetti, A. Naphthalene Diimide-Based Polymeric Semiconductors. Effect of Chlorine Incorporation and n-Channel Transistors Operating in Water. *MRS Commun.* **2016**, *6* (1), 47–60. <https://doi.org/DOI:10.1557/mrc.2016.4>.
- (94) Lei, T.; Dou, J.-H.; Ma, Z.-J.; Liu, C.-J.; Wang, J.-Y.; Pei, J. Chlorination as a Useful Method to Modulate Conjugated Polymers: Balanced and Ambient-Stable Ambipolar High-Performance Field-Effect Transistors and Inverters Based on Chlorinated Isoindigo Polymers. *Chem. Sci.* **2013**, *4* (6), 2447–2452. <https://doi.org/10.1039/C3SC50245G>.
- (95) Kim, H. S.; Huseynova, G.; Noh, Y.-Y.; Hwang, D.-H. Modulation of Majority Charge Carrier from Hole to Electron by Incorporation of Cyano Groups in Diketopyrrolopyrrole-Based Polymers. *Macromolecules* **2017**, *50* (19), 7550–7558. <https://doi.org/10.1021/acs.macromol.7b01524>.
- (96) Yun, H.-J.; Kang, S.-J.; Xu, Y.; Kim, S. O.; Kim, Y.-H.; Noh, Y.-Y.; Kwon, S.-K. Dramatic Inversion of Charge Polarity in Diketopyrrolopyrrole-Based Organic Field-Effect Transistors via a Simple Nitrile Group Substitution. *Adv. Mater.* **2014**, *26* (43), 7300–7307. <https://doi.org/10.1002/adma.201403262>.
- (97) Long, X.; Gao, Y.; Tian, H.; Dou, C.; Yan, D.; Geng, Y.; Liu, J.; Wang, L. Electron-Transporting Polymers Based on a Double B←N Bridged Bipyridine (BNBP) Unit. *Chem. Commun.* **2017**, *53* (10), 1649–1652. <https://doi.org/10.1039/C6CC09684K>.
- (98) Yang, J.; Wang, H.; Chen, J.; Huang, J.; Jiang, Y.; Zhang, J.; Shi, L.; Sun, Y.; Wei, Z.; Yu, G.; Guo, Y.; Wang, S.; Liu, Y. Bis-Diketopyrrolopyrrole Moiety as a Promising Building Block to Enable Balanced Ambipolar Polymers for Flexible Transistors. *Adv. Mater.* **2017**, *29* (22), 1–7. <https://doi.org/10.1002/adma.201606162>.
- (99) Zhu, C.; Zhao, Z.; Chen, H.; Zheng, L.; Li, X.; Chen, J.; Sun, Y.; Liu, F.; Guo, Y.; Liu, Y. Regioregular Bis-Pyridal[2,1,3]Thiadiazole-Based Semiconducting Polymer for High-Performance Ambipolar Transistors. *J. Am. Chem. Soc.* **2017**, *139* (49), 17735–17738. <https://doi.org/10.1021/jacs.7b10256>.
- (100) Wang, Y.; Yan, Z.; Guo, H.; Uddin, M. A.; Ling, S.; Zhou, X.; Su, H.; Dai, J.; Woo, H. Y.; Guo, X. Effects of Bithiophene Imide Fusion on the Device Performance of Organic Thin-Film

- Transistors and All-Polymer Solar Cells. *Angew. Chemie Int. Ed.* **2017**, *56* (48), 15304–15308. <https://doi.org/10.1002/anie.201708421>.
- (101) Lee, J.; Han, A.-R.; Kim, J.; Kim, Y.; Oh, J. H.; Yang, C. Solution-Processable Ambipolar Diketopyrrolopyrrole–Selenophene Polymer with Unprecedentedly High Hole and Electron Mobilities. *J. Am. Chem. Soc.* **2012**, *134* (51), 20713–20721. <https://doi.org/10.1021/ja308927g>.
- (102) Kang, B.; Kim, R.; Lee, S. B.; Kwon, S.-K.; Kim, Y.-H.; Cho, K. Side-Chain-Induced Rigid Backbone Organization of Polymer Semiconductors through Semifluoroalkyl Side Chains. *J. Am. Chem. Soc.* **2016**, *138* (11), 3679–3686. <https://doi.org/10.1021/jacs.5b10445>.
- (103) Lee, J.; Han, A.-R.; Yu, H.; Shin, T. J.; Yang, C.; Oh, J. H. Boosting the Ambipolar Performance of Solution-Processable Polymer Semiconductors via Hybrid Side-Chain Engineering. *J. Am. Chem. Soc.* **2013**, *135* (25), 9540–9547. <https://doi.org/10.1021/ja403949g>.
- (104) Kelker, H. History of Liquid Crystals. *Mol. Cryst. Liq. Cryst.* **1973**, *21* (1–2), 1–48. <https://doi.org/10.1080/15421407308083312>.
- (105) Swanson, B. D.; Sorensen, L. B. What Forces Bind Liquid Crystals? *Phys. Rev. Lett.* **1995**, *75* (18), 3293–3296. <https://doi.org/10.1103/PhysRevLett.75.3293>.
- (106) Pershan, P. S. (1988) Structure of Liquid Crystal Phases. *World Scientific*. <https://doi.org/doi:10.1142/0661>.
- (107) VISVANATHAN, R. Nanostructures of Liquid Crystals and Semiconductor Device Fabrication, University of Colorado, 2018.
- (108) Yoshizawa, H.; Mihara, T.; Koide\*, N. Thermal Properties and Ionic Conductivity of Imidazolium Salt Derivatives Having a Calamitic Mesogen. *Mol. Cryst. Liq. Cryst.* **2004**, *423* (1), 61–72. <https://doi.org/10.1080/15421400490502481>.
- (109) Vallerien, S. U.; Werth, M.; Kremer, F.; Spiess, H. W. Molecular Dynamics and the Glass Transition in a Columnar Liquid Crystal Formed by a Chiral Discotic Mesogen. *Liq. Cryst.* **1990**, *8* (6), 889–893. <https://doi.org/10.1080/02678299008047400>.
- (110) Repasky, P. J.; Agra-Kooijman, D. M.; Kumar, S.; Hartley, C. S. Smectic-A and Hexatic-B Liquid Crystal Phases of Sanidic Alkyl-Substituted Dibenzo[Fg,Op]Naphthalenes. *J. Phys. Chem. B* **2016**, *120* (10), 2829–2837. <https://doi.org/10.1021/acs.jpcc.5b10990>.
- (111) Haddawi, S.; Tamba, M. G.; Pelzl, G.; Weissflog, W.; Baumeister, U. Induction of “banana Phases” in Binary Systems Composed of Bent-Core and Calamitic Mesogen. *Soft Matter* **2010**, *6* (6), 1170–1181. <https://doi.org/10.1039/b916685h>.
- (112) Wu, X.; Jia, R.; Pan, J.; Zhang, X.; Jie, J. Roles of Interfaces in the Ideality of Organic Field-Effect Transistors. *Nanoscale Horizons* **2020**, *5* (3), 454–472. <https://doi.org/10.1039/C9NH00694J>.
- (113) Ballauff, M. Liquid Crystalline Polymers. *Adv. Mater.* **1992**, *4* (10), 695–696. <https://doi.org/10.1002/adma.19920041028>.
- (114) Siva Kumar, I.; Kumar, S. Tri-: S -Triazine (s -Heptazine), a Novel Electron-Deficient Core for Soft Self-Assembled Supramolecular Structures. *Chem. Commun.* **2017**, *53* (83), 11445–11448. <https://doi.org/10.1039/c7cc05899c>.
- (115) Xiao, Y.; Su, X.; Sosa-Vargas, L.; Lacaze, E.; Heinrich, B.; Donnio, B.; Kreher, D.; Mathevet, F.; Attias, A.-J. Chemical Engineering of Donor–Acceptor Liquid Crystalline Dyads and Triads for the Controlled Nanostructuring of Organic Semiconductors. *CrystEngComm* **2016**, *18* (25), 4787–4798. <https://doi.org/10.1039/C6CE00365F>.
- (116) Iino, H.; Usui, T.; Hanna, J. I. Liquid Crystals for Organic Thin-Film Transistors. *Nat. Commun.* **2015**, *6*, 1–8. <https://doi.org/10.1038/ncomms7828>.
- (117) Wang, H.; Chen, L.; Xing, R.; Liu, J.; Han, Y. Simultaneous Control over Both Molecular Order and Long-Range Alignment in Films of the Donor–Acceptor Copolymer. *Langmuir* **2015**, *31* (1), 469–479. <https://doi.org/10.1021/la5037772>.
- (118) Chen, L.; Zhao, K.; Cao, X.; Liu, J.; Yu, X.; Han, Y. Diketopyrrolopyrrole-Based Polymer Fibrils Formation by Changing Molecular Conformation during Film Formation. *J. Polym. Sci. Part B Polym. Phys.* **2018**, *56* (15), 1079–1086. <https://doi.org/10.1002/polb.24609>.
- (119) Su, Y.; Li, Y.; Liu, J.; Xing, R.; Han, Y. Donor–Acceptor Cocrystal Based on Hexakis(Alkoxy)Triphenylene and Perylenediimide Derivatives with an Ambipolar Transporting Property. *Nanoscale* **2015**, *7* (5), 1944–1955. <https://doi.org/10.1039/C4NR05915H>.

- (120) Noriega, R.; Rivnay, J.; Vandewal, K.; Koch, F. P. V.; Stingelin, N.; Smith, P.; Toney, M. F.; Salleo, A. A General Relationship between Disorder, Aggregation and Charge Transport in Conjugated Polymers. *Nat. Mater.* **2013**, *12* (11), 1038–1044. <https://doi.org/10.1038/nmat3722>.
- (121) Brinkmann, M. Structure and Morphology Control in Thin Films of Regioregular Poly(3-Hexylthiophene). *J. Polym. Sci. Part B Polym. Phys.* **2011**, *49* (17), 1218–1233. <https://doi.org/10.1002/polb.22310>.
- (122) Crossland, E. J. W.; Tremel, K.; Fischer, F.; Rahimi, K.; Reiter, G.; Steiner, U.; Ludwigs, S. Anisotropic Charge Transport in Spherulitic Poly(3-Hexylthiophene) Films. *Adv. Mater.* **2012**, *24* (6), 839–844. <https://doi.org/10.1002/adma.201104284>.
- (123) Braun, D.; Gustafsson, G.; McBranch, D.; Heeger, A. J. Electroluminescence and Electrical Transport in Poly(3-octylthiophene) Diodes. *J. Appl. Phys.* **1992**, *72* (2), 564–568. <https://doi.org/10.1063/1.351834>.
- (124) Friend, R. H.; Bradley, D. D. C.; Pichler, K.; Halliday, D. A.; Pichler, K.; Friend, R. H. Related Content Photoexcited States in Poly ( 3-Alkyl Thienylenes ). *J. Phys. Condens. Matter* **1990**.
- (125) Sirringhaus, H.; Wilson, R. J.; Friend, R. H.; Inbasekaran, M.; Wu, W.; Woo, E. P.; Grell, M.; Bradley, D. D. C. Mobility Enhancement in Conjugated Polymer Field-Effect Transistors through Chain Alignment in a Liquid-Crystalline Phase. *Appl. Phys. Lett.* **2000**, *77* (3), 406–408. <https://doi.org/10.1063/1.126991>.
- (126) Bridges, C. R.; Ford, M. J.; Popere, B. C.; Bazan, G. C.; Segalman, R. A. Formation and Structure of Lyotropic Liquid Crystalline Mesophases in Donor–Acceptor Semiconducting Polymers. *Macromolecules* **2016**, *49* (19), 7220–7229. <https://doi.org/10.1021/acs.macromol.6b01650>.
- (127) Kleinhenz, N.; Rosu, C.; Chatterjee, S.; Chang, M.; Nayani, K.; Xue, Z.; Kim, E.; Middlebrooks, J.; Russo, P. S.; Park, J. O.; Srinivasarao, M.; Reichmanis, E. Liquid Crystalline Poly(3-Hexylthiophene) Solutions Revisited: Role of Time-Dependent Self-Assembly. *Chem. Mater.* **2015**, *27* (7), 2687–2694. <https://doi.org/10.1021/acs.chemmater.5b00635>.
- (128) Ong, B. S.; Wu, Y.; Liu, P.; Gardner, S. High-Performance Semiconducting Polythiophenes for Organic Thin-Film Transistors. *J. Am. Chem. Soc.* **2004**, *126* (11), 3378–3379. <https://doi.org/10.1021/ja039772w>.
- (129) McCulloch, I.; Heeney, M.; Bailey, C.; Genevicius, K.; MacDonald, I.; Shkunov, M.; Sparrowe, D.; Tierney, S.; Wagner, R.; Zhang, W.; Chabinyc, M. L.; Kline, R. J.; McGehee, M. D.; Toney, M. F. Liquid-Crystalline Semiconducting Polymers with High Charge-Carrier Mobility. *Nat. Mater.* **2006**, *5* (4), 328–333. <https://doi.org/10.1038/nmat1612>.
- (130) Oh, S. Y.; Akagi, K.; Shirakawa, H.; Araya, K. Synthesis and Properties of Liquid-Crystalline Polyacetylenes with a Phenylcyclohexyl Mesogenic Moiety in the Side Group. *Macromolecules* **1993**, *26* (23), 6203–6206. <https://doi.org/10.1021/ma00075a011>.
- (131) Chen, L.; Chen, Y.; Yao, K.; Zhou, W.; Li, F.; Chen, L.; Hu, R.; Tang, B. Z. Synthesis and Helical Conformation of Novel Optically Active Liquid Crystalline Poly(p-Phenylene)s Containing Cyanoterphenyl Mesogen as Pendant. *Macromolecules* **2009**, *42* (14), 5053–5061. <https://doi.org/10.1021/ma900751y>.
- (132) Aasmundtveit, K. E.; Samuelsen, E. J.; Inganäs, O.; Pettersson, L. A. A.; Johansson, T.; Ferrer, S. Structural Aspects of Electrochemical Doping and Dedoping of Poly(3,4-Ethylenedioxythiophene). *Synth. Met.* **2000**, *113* (1), 93–97. [https://doi.org/https://doi.org/10.1016/S0379-6779\(00\)00181-8](https://doi.org/https://doi.org/10.1016/S0379-6779(00)00181-8).
- (133) Tashiro, K.; Kobayashi, M.; Kawai, T.; Yoshino, K. Crystal Structural Change in Poly(3-Alkyl Thiophene)s Induced by Iodine Doping as Studied by an Organized Combination of X-Ray Diffraction, Infrared/Raman Spectroscopy and Computer Simulation Techniques. *Polymer (Guildf)*. **1997**, *38* (12), 2867–2879. [https://doi.org/https://doi.org/10.1016/S0032-3861\(96\)00876-2](https://doi.org/https://doi.org/10.1016/S0032-3861(96)00876-2).
- (134) Prosa, T. J.; Winokur, M. J.; McCullough, R. D. Evidence of a Novel Side Chain Structure in Regioregular Poly(3-Alkylthiophenes). *Macromolecules* **1996**, *29* (10), 3654–3656. <https://doi.org/10.1021/ma951510u>.
- (135) Takashima, W.; Pandey, S. S.; Endo, T.; Rikukawa, M.; Tanigaki, N.; Yoshida, Y.; Yase, K.; Kaneto, K. Photocarrier Transports Related to the Morphology of Regioregular Poly(3-

- Hexylthiophene) Films. *Thin Solid Films* **2001**, *393* (1), 334–342. [https://doi.org/https://doi.org/10.1016/S0040-6090\(01\)01109-9](https://doi.org/https://doi.org/10.1016/S0040-6090(01)01109-9).
- (136) Kim, D. H.; Park, Y. D.; Jang, Y.; Kim, S.; Cho, K. Solvent Vapor-Induced Nanowire Formation in Poly(3-Hexylthiophene) Thin Films. *Macromol. Rapid Commun.* **2005**, *26* (10), 834–839. <https://doi.org/10.1002/marc.200400647>.
- (137) Brinkmann, M.; Wittmann, J.-C. Orientation of Regioregular Poly(3-Hexylthiophene) by Directional Solidification: A Simple Method to Reveal the Semicrystalline Structure of a Conjugated Polymer. *Adv. Mater.* **2006**, *18* (7), 860–863. <https://doi.org/10.1002/adma.200501838>.
- (138) Bolognesi, A.; Porzio, W.; Provasoli, A.; Botta, C.; Comotti, A.; Sozzani, P.; Simonutti, R. Structural and Thermal Behavior of Poly(3-Octylthiophene): A DSC, <sup>13</sup>C MAS NMR, XRD, Photoluminescence, and Raman Scattering Study. *Macromol. Chem. Phys.* **2001**, *202* (12), 2586–2591. [https://doi.org/10.1002/1521-3935\(20010801\)202:12<2586::AID-MACP2586>3.0.CO;2-V](https://doi.org/10.1002/1521-3935(20010801)202:12<2586::AID-MACP2586>3.0.CO;2-V).
- (139) Causin, V.; Marega, C.; Marigo, A.; Valentini, L.; Kenny, J. M. Crystallization and Melting Behavior of Poly(3-Butylthiophene), Poly(3-Octylthiophene), and Poly(3-Dodecylthiophene). *Macromolecules* **2005**, *38* (2), 409–415. <https://doi.org/10.1021/ma048159+>.
- (140) Yazawa, K.; Inoue, Y.; Yamamoto, T.; Asakawa, N. Twist Glass Transition in Regioregulated Poly(3-Alkylthiophene). *Phys. Rev. B* **2006**, *74* (9), 94204. <https://doi.org/10.1103/PhysRevB.74.094204>.
- (141) Wang, C.; Dong, H.; Hu, W.; Liu, Y.; Zhu, D. Semiconducting  $\pi$ -Conjugated Systems in Field-Effect Transistors: A Material Odyssey of Organic Electronics. *Chem. Rev.* **2012**, *112* (4), 2208–2267. <https://doi.org/10.1021/cr100380z>.
- (142) Segalman, R. A.; McCulloch, B.; Kirmayer, S.; Urban, J. J. Block Copolymers for Organic Optoelectronics. *Macromolecules* **2009**, *42* (23), 9205–9216. <https://doi.org/10.1021/ma901350w>.
- (143) Yu, Z. Q.; Lam, J. W. Y.; Zhu, C. Z.; Chen, E. Q.; Tang, B. Z. Side-Chain Liquid Crystalline Polyacetylenes with Increasing Length of Alkyl Tails: From Highly Ordered Smectic to Smectic C Phase. *Macromolecules* **2013**, *46* (3), 588–596. <https://doi.org/10.1021/ma302540k>.
- (144) Ku, S.-Y.; Brady, M. A.; Treat, N. D.; Cochran, J. E.; Robb, M. J.; Kramer, E. J.; Chabinyc, M. L.; Hawker, C. J. A Modular Strategy for Fully Conjugated Donor–Acceptor Block Copolymers. *J. Am. Chem. Soc.* **2012**, *134* (38), 16040–16046. <https://doi.org/10.1021/ja307431k>.
- (145) Yasuda, T.; Shimizu, T.; Liu, F.; Ungar, G.; Kato, T. Electro-Functional Octupolar  $\pi$ -Conjugated Columnar Liquid Crystals. *J. Am. Chem. Soc.* **2011**, *133* (34), 13437–13444. <https://doi.org/10.1021/ja2035255>.
- (146) Watanabe, M.; Kijima, M. Smectic-Phase-Induced Interdigitated Orientation of Polythiophenes Bearing Phenylanthralene Mesogen. *Liq. Cryst.* **2014**, *41* (7), 897–907. <https://doi.org/10.1080/02678292.2014.891766>.
- (147) Zeng, D.; Tahar-Djebbar, I.; Xiao, Y.; Kameche, F.; Kayunkid, N.; Brinkmann, M.; Guillon, D.; Heinrich, B.; Donnio, B.; Ivanov, D. A.; Lacaze, E.; Kreher, D.; Mathevet, F.; Attias, A. J. Intertwined Lamello-Columnar Coassemblies in Liquid-Crystalline Side-Chain  $\pi$ -Conjugated Polymers: Toward a New Class of Nanostructured Supramolecular Organic Semiconductors. *Macromolecules* **2014**, *47* (5), 1715–1731. <https://doi.org/10.1021/ma4020356>.
- (148) Tahar-Djebbar, I.; Nekelson, F.; Heinrich, B.; Donnio, B.; Guillon, D.; Kreher, D.; Mathevet, F.; Attias, A. E.-J. Lamello-Columnar Mesophase Formation in a Side-Chain Liquid Crystal  $\pi$ -Conjugated Polymer Architecture Scheme 1. Synthesis of Discotic Side-Chain Polymer PTT N. *Chem. Mater* **2011**, *23*, 4653–4656. <https://doi.org/10.1021/cm2014187>.
- (149) Xiao, Y.; Zeng, D.; Mazur, L. M.; Castiglione, A.; Lacaze, E.; Heinrich, B.; Donnio, B.; Kreher, D.; Attias, A. J.; Ribierre, J. C.; Mathevet, F. A New Class of Nanostructured Supramolecular Organic Semiconductors Based on Intertwined Multi-Lamellar Co-Assemblies in  $\pi$ -Conjugated Liquid-Crystalline Side-Chain Polymers. *Polym. J.* **2017**, *49* (1), 31–39. <https://doi.org/10.1038/pj.2016.107>.
- (150) Xiao, Y. Engineering, Synthesis and Characterization of New -  $\pi$  Conjugated (Macro)Molecular Architectures for Organic Optoelectronics : Application toward Ambipolar

- Materials, 2014.
- (151) Castiglione, A. Liquid Crystalline Macromolecular Architectures Based on Regioregular Poly(3-Alkylthiophene) as Backbone and Calamitic Mesogens as Side-Groups: Towards Ambipolar Materials, 2014.
  - (152) Tahar-Djebbar, I.; Nekelson, F.; Heinrich, B.; Donnio, B.; Guillon, D.; Kreher, D.; Mathevet, F.; Attias, A. J. Lamello-Columnar Mesophase Formation in a Side-Chain Liquid Crystal  $\pi$ -Conjugated Polymer Architecture. *Chem. Mater.* **2011**, *23* (21), 4653–4656. <https://doi.org/10.1021/cm2014187>.
  - (153) Liu, J.; Loewe, R. S.; McCullough, R. D. Employing MALDI-MS on Poly(Alkylthiophenes): Analysis of Molecular Weights, Molecular Weight Distributions, End-Group Structures, and End-Group Modifications. *Macromolecules* **1999**, *32* (18), 5777–5785. <https://doi.org/10.1021/ma9905324>.
  - (154) Tang, C. W.; Vanslyke, S. A. Organic Electroluminescent Diodes. *Appl. Phys. Lett.* **1987**, *51* (12), 913–915. <https://doi.org/10.1063/1.98799>.
  - (155) Tomova, R.; Petrova, P.; Buroff, A.; Stoycheva-Topalova, R. Organic Light-Emitting Diodes (OLEDs) - the Basis of next Generation Light-Emitting Devices. *Bulg. Chem. Commun.* **2007**, *39* (4), 247–259.
  - (156) Duck, I.; Sudarshan, E. C. G. Toward an Understanding of the Spin-Statistics Theorem. *Am. J. Phys.* **1998**, *66* (4), 284–303. <https://doi.org/10.1119/1.18860>.
  - (157) Auffray, M. Cyclophanes, a Bridge between Photophysics and Supramolecular Chemistry, Université Pierre et Marie Curie - Paris VI, 2017.
  - (158) Shibata, M.; Sakai, Y.; Yokoyama, D. Advantages and Disadvantages of Vacuum-Deposited and Spin-Coated Amorphous Organic Semiconductor Films for Organic Light-Emitting Diodes. *J. Mater. Chem. C* **2015**, *3* (42), 11178–11191. <https://doi.org/10.1039/c5tc01911g>.
  - (159) Ingram, G. L.; Lu, Z.-H. Design Principles for Highly Efficient Organic Light-Emitting Diodes. *J. Photonics Energy* **2014**, *4* (1), 040993. <https://doi.org/10.1117/1.jpe.4.040993>.
  - (160) Yue, Q.; Li, W.; Kong, F.; Li, K. Enhancing the Out-Coupling Efficiency of Organic Light-Emitting Diodes Using Two-Dimensional Periodic Nanostructures. *Adv. Mater. Sci. Eng.* **2012**, *2012*, 1–9. <https://doi.org/10.1155/2012/985762>.
  - (161) Song, J.; Lee, H.; Jeong, E. G.; Choi, K. C.; Yoo, S. Organic Light-Emitting Diodes: Pushing toward the Limits and Beyond. *Adv. Mater.* *n/a* (n/a), 1907539. <https://doi.org/10.1002/adma.201907539>.
  - (162) Murawski, C.; Leo, K.; Gather, M. C. Efficiency Roll-off in Organic Light-Emitting Diodes. *Adv. Mater.* **2013**, *25* (47), 6801–6827. <https://doi.org/10.1002/adma.201301603>.
  - (163) Van Slyke, S. A.; Chen, C. H.; Tang, C. W. Organic Electroluminescent Devices with Improved Stability. *Appl. Phys. Lett.* **1996**, *69* (15), 2160–2162. <https://doi.org/10.1063/1.117151>.
  - (164) Gardonio, S.; Gregoratti, L.; Melpignano, P.; Aballe, L.; Biondo, V.; Zamboni, R.; Murgia, M.; Caria, S.; Kiskinova, M. Degradation of Organic Light-Emitting Diodes under Different Environment at High Drive Conditions. *Org. Electron.* **2007**, *8* (1), 37–43. <https://doi.org/10.1016/j.orgel.2006.10.005>.
  - (165) Wang, Y.; Xiao, Y. P.; Zhou, Y. Y.; Hu, C. G.; Tong, B. H.; Ye, S. H.; Mei, Q. B. Novel Phosphorescent Triptycene-Based Ir(III) Complexes for Organic Light-Emitting Diodes. *Dalt. Trans.* **2019**, *48* (43), 16289–16297. <https://doi.org/10.1039/c9dt03182k>.
  - (166) Ting, H. C.; Chen, Y. M.; You, H. W.; Hung, W. Y.; Lin, S. H.; Chaskar, A.; Chou, S. H.; Chi, Y.; Liu, R. H.; Wong, K. T. Indolo[3,2-b]Carbazole/Benzimidazole Hybrid Bipolar Host Materials for Highly Efficient Red, Yellow, and Green Phosphorescent Organic Light Emitting Diodes. *J. Mater. Chem.* **2012**, *22* (17), 8399–8407. <https://doi.org/10.1039/c2jm30207a>.
  - (167) Xu, L. J.; Wang, J. Y.; Zhu, X. F.; Zeng, X. C.; Chen, Z. N. Phosphorescent Cationic Au<sub>4</sub>Ag<sub>2</sub> Alkynyl Cluster Complexes for Efficient Solution-Processed Organic Light-Emitting Diodes. *Adv. Funct. Mater.* **2015**, *25* (20), 3033–3042. <https://doi.org/10.1002/adfm.201500060>.
  - (168) Wang, Z. B.; Helander, M. G.; Hudson, Z. M.; Qiu, J.; Wang, S.; Lu, Z. H. Pt(II) Complex Based Phosphorescent Organic Light Emitting Diodes with External Quantum Efficiencies above 20%. *Appl. Phys. Lett.* **2011**, *98* (21), 213301. <https://doi.org/10.1063/1.3593495>.
  - (169) Hoshino, S.; Suzuki, H. Electroluminescence from Triplet Excited States of Benzophenone.

- Appl. Phys. Lett.* **1996**, *69* (2), 224–226. <https://doi.org/10.1063/1.117379>.
- (170) Tang, Z.; Zhu, J.; Pan, S.; Wang, Z.; Zheng, Y.; Chen, G.; Zhu, W.; Wei, B. Synthesis of Carboline-Based Host Materials for Forming Copper(I) Complexes as Emitters: A Promising Strategy for Achieving High-Efficiency and Low-Cost Phosphorescent Organic Light-Emitting Diodes. *Dye. Pigment.* **2018**, *149* (June 2017), 387–392. <https://doi.org/10.1016/j.dyepig.2017.10.028>.
- (171) Scholz, S.; Kondakov, D.; Lüssem, B.; Leo, K. Degradation Mechanisms and Reactions in Organic Light-Emitting Devices. *Chem. Rev.* **2015**, *115* (16), 8449–8503. <https://doi.org/10.1021/cr400704v>.
- (172) Jayabharathi, J.; Panimozhi, S.; Thanikachalam, V. Hot Exciton Transition for Organic Light-Emitting Diodes: Tailoring Excited-State Properties and Electroluminescence Performances of Donor-Spacer-Acceptor Molecules. *RSC Adv.* **2018**, *8* (65), 37324–37338. <https://doi.org/10.1039/C8RA07891B>.
- (173) Mayr, C.; Schmidt, T. D.; Brütting, W. High-Efficiency Fluorescent Organic Light-Emitting Diodes Enabled by Triplet-Triplet Annihilation and Horizontal Emitter Orientation. *Appl. Phys. Lett.* **2014**, *105* (18), 183304. <https://doi.org/10.1063/1.4901341>.
- (174) Im, Y.; Lee, J. Y. Recent Progress of Green Thermally Activated Delayed Fluorescent Emitters. *J. Inf. Disp.* **2017**, *18* (3), 101–117. <https://doi.org/10.1080/15980316.2017.1333046>.
- (175) Parker, C. A.; Hatchard, C. G. Triplet-Singlet Emission in Fluid Solutions. Phosphorescence of Eosin. *Trans. Faraday Soc.* **1961**, *57* (0), 1894–1904. <https://doi.org/10.1039/TF9615701894>.
- (176) Endo, A.; Ogasawara, M.; Takahashi, A.; Yokoyama, D.; Kato, Y.; Adachi, C. Thermally Activated Delayed Fluorescence from Sn<sup>4+</sup>-Porphyrin Complexes and Their Application to Organic Light Emitting Diodes — A Novel Mechanism for Electroluminescence. *Adv. Mater.* **2009**, *21* (47), 4802–4806. <https://doi.org/10.1002/adma.200900983>.
- (177) Liu, Y.; Li, C.; Ren, Z.; Yan, S.; Bryce, M. R. All-Organic Thermally Activated Delayed Fluorescence Materials for Organic Light-Emitting Diodes. *Nat. Rev. Mater.* **2018**, *3* (4), 18020. <https://doi.org/10.1038/natrevmats.2018.20>.
- (178) Dias, F. B.; Penfold, T. J.; Monkman, A. P. Photophysics of Thermally Activated Delayed Fluorescence Molecules. *Methods Appl. Fluoresc.* **2017**, *5* (1), 012001. <https://doi.org/10.1088/2050-6120/aa537e>.
- (179) Niwa, A.; Kobayashi, T.; Nagase, T.; Goushi, K.; Adachi, C.; Naito, H. Temperature Dependence of Photoluminescence Properties in a Thermally Activated Delayed Fluorescence Emitter. *Appl. Phys. Lett.* **2014**, *104* (21). <https://doi.org/10.1063/1.4878397>.
- (180) Im, Y.; Kim, M.; Cho, Y. J.; Seo, J. A.; Yook, K. S.; Lee, J. Y. Molecular Design Strategy of Organic Thermally Activated Delayed Fluorescence Emitters. *Chem. Mater.* **2017**, *29* (5), 1946–1963. <https://doi.org/10.1021/acs.chemmater.6b05324>.
- (181) Colella, M.; Pander, P.; Pereira, D. de S.; Monkman, A. P. Interfacial TADF Exciplex as a Tool to Localize Excitons, Improve Efficiency, and Increase OLED Lifetime. *ACS Appl. Mater. Interfaces* **2018**, *10* (46), 40001–40007. <https://doi.org/10.1021/acsami.8b15942>.
- (182) Li, J.; Nakagawa, T.; MacDonald, J.; Zhang, Q.; Nomura, H.; Miyazaki, H.; Adachi, C. Highly Efficient Organic Light-Emitting Diode Based on a Hidden Thermally Activated Delayed Fluorescence Channel in a Heptazine Derivative. *Adv. Mater.* **2013**, *25* (24), 3319–3323. <https://doi.org/10.1002/adma.201300575>.
- (183) Li, W.; Zhao, J.; Li, L.; Du, X.; Fan, C.; Zheng, C.; Tao, S. Efficient Solution-Processed Blue and White OLEDs Based on a High-Triplet Bipolar Host and a Blue TADF Emitter. *Org. Electron.* **2018**, *58*, 276–282. <https://doi.org/https://doi.org/10.1016/j.orgel.2018.04.027>.
- (184) Zhang, Q.; Tsang, D.; Kuwabara, H.; Hatae, Y.; Li, B.; Takahashi, T.; Lee, S. Y.; Yasuda, T.; Adachi, C. Nearly 100% Internal Quantum Efficiency in Undoped Electroluminescent Devices Employing Pure Organic Emitters. *Adv. Mater.* **2015**, *27* (12), 2096–2100. <https://doi.org/10.1002/adma.201405474>.
- (185) Cao, X.; Zhang, D.; Zhang, S.; Tao, Y.; Huang, W. CN-Containing Donor-Acceptor-Type Small-Molecule Materials for Thermally Activated Delayed Fluorescence OLEDs. *J. Mater. Chem. C* **2017**, *5* (31), 7699–7714. <https://doi.org/10.1039/c7tc02481a>.
- (186) Cho, Y. J.; Jeon, S. K.; Chin, B. D.; Yu, E.; Lee, J. Y. The Design of Dual Emitting Cores for Green Thermally Activated Delayed Fluorescent Materials. *Angew. Chemie* **2015**, *127* (17),

- 5290–5293. <https://doi.org/10.1002/ange.201412107>.
- (187) Kim, M.; Jeon, S. K.; Hwang, S.-H.; Lee, S.; Yu, E.; Lee, J. Y. Highly Efficient and Color Tunable Thermally Activated Delayed Fluorescent Emitters Using a “Twin Emitter” Molecular Design. *Chem. Commun.* **2016**, 52 (2), 339–342. <https://doi.org/10.1039/C5CC07999C>.
- (188) Lee, H. J.; Han, S. H.; Hong, W. P.; Song, O.-K.; Lee, J. Y. Lifetime Extension in Green Thermally Activated Delayed Fluorescent Organic Light-Emitting Diodes by Increasing Excited State Bond Dissociation Energy. *J. Ind. Eng. Chem.* **2019**, 69, 364–369. <https://doi.org/https://doi.org/10.1016/j.jiec.2018.09.040>.
- (189) Cho, Y. J.; Jeon, S. K.; Lee, S.-S.; Yu, E.; Lee, J. Y. Donor Interlocked Molecular Design for Fluorescence-like Narrow Emission in Deep Blue Thermally Activated Delayed Fluorescent Emitters. *Chem. Mater.* **2016**, 28 (15), 5400–5405. <https://doi.org/10.1021/acs.chemmater.6b01484>.
- (190) Hatakeyama, T.; Shiren, K.; Nakajima, K.; Nomura, S.; Nakatsuka, S.; Kinoshita, K.; Ni, J.; Ono, Y.; Ikuta, T. Ultrapure Blue Thermally Activated Delayed Fluorescence Molecules: Efficient HOMO–LUMO Separation by the Multiple Resonance Effect. *Adv. Mater.* **2016**, 28 (14), 2777–2781. <https://doi.org/10.1002/adma.201505491>.
- (191) Zhang, Q.; Kuwabara, H.; Potscavage, W. J.; Huang, S.; Hatae, Y.; Shibata, T.; Adachi, C. Anthraquinone-Based Intramolecular Charge-Transfer Compounds: Computational Molecular Design, Thermally Activated Delayed Fluorescence, and Highly Efficient Red Electroluminescence. *J. Am. Chem. Soc.* **2014**, 136 (52), 18070–18081. <https://doi.org/10.1021/ja510144h>.
- (192) Han, C.; Duan, C.; Yang, W.; Xie, M.; Xu, H. Allochroic Thermally Activated Delayed Fluorescence Diodes through Field-Induced Solvatochromic Effect. *Sci. Adv.* **2017**, 3 (9), 1–9. <https://doi.org/10.1126/sciadv.1700904>.
- (193) Penfold, T. J.; Dias, F. B.; Monkman, A. P. The Theory of Thermally Activated Delayed Fluorescence for Organic Light Emitting Diodes. *Chem. Commun.* **2018**, 54 (32), 3926–3935. <https://doi.org/10.1039/C7CC09612G>.
- (194) Pander, P.; Dias, F. B. Photophysical Characterisation of Thermally Activated Delayed Fluorescence (TADF) Materials †. *Disp. Imaging* **2017**, 2 (May), 249–263.
- (195) Sarkar, S. K.; Pegu, M.; Behera, S. K.; Narra, S. K.; Thilagar, P. Aggregation-Induced and Polymorphism-Dependent Thermally Activated Delayed Fluorescence (TADF) Characteristics of an Oligothiophene: Applications in Time-Dependent Live Cell Multicolour Imaging. *Chem. – An Asian J.* **2019**, 14 (24), 4588–4593. <https://doi.org/10.1002/asia.201901138>.
- (196) Zhan, L.; Chen, Z.; Gong, S.; Xiang, Y.; Ni, F.; Zeng, X.; Xie, G.; Yang, C. A Simple Organic Molecule Realizing Simultaneous TADF, RTP, AIE, and Mechanoluminescence: Understanding the Mechanism Behind the Multifunctional Emitter. *Angew. Chemie Int. Ed.* **2019**, 58 (49), 17651–17655. <https://doi.org/10.1002/anie.201910719>.
- (197) Braveenth, R.; Chai, K. Y. Triazine-Acceptor-Based Green Thermally Activated Delayed Fluorescence Materials for Organic Light-Emitting Diodes. *Materials (Basel)*. **2019**, 12 (16). <https://doi.org/10.3390/ma12162646>.
- (198) Tsai, W. L.; Huang, M. H.; Lee, W. K.; Hsu, Y. J.; Pan, K. C.; Huang, Y. H.; Ting, H. C.; Sarma, M.; Ho, Y. Y.; Hu, H. C.; Chen, C. C.; Lee, M. T.; Wong, K. T.; Wu, C. C. A Versatile Thermally Activated Delayed Fluorescence Emitter for Both Highly Efficient Doped and Non-Doped Organic Light Emitting Devices. *Chem. Commun.* **2015**, 51 (71), 13662–13665. <https://doi.org/10.1039/c5cc05022g>.
- (199) Wang, Y. Y.; Zhang, Y. L.; Tong, K.; Ding, L.; Fan, J.; Liao, L. S. Highly Efficient Red Thermally Activated Delayed Fluorescence Materials Based on a Cyano-Containing Planar Acceptor. *J. Mater. Chem. C* **2019**, 7 (48), 15301–15307. <https://doi.org/10.1039/c9tc05349b>.
- (200) Zhang, Q.; Li, B.; Huang, S.; Nomura, H.; Tanaka, H.; Adachi, C. Efficient Blue Organic Light-Emitting Diodes Employing Thermally Activated Delayed Fluorescence. *Nat. Photonics* **2014**, 8 (4), 326–332. <https://doi.org/10.1038/nphoton.2014.12>.
- (201) Xiang, S.; Guo, R.; Huang, Z.; Lv, X.; Sun, S.; Chen, H.; Zhang, Q.; Wang, L. Highly Efficient Yellow Nondoped Thermally Activated Delayed Fluorescence OLEDs by Utilizing Energy Transfer between Dual Conformations Based on Phenothiazine Derivatives. *Dye. Pigment.* **2019**, 170 (June), 107636. <https://doi.org/10.1016/j.dyepig.2019.107636>.

- (202) Wei, Q.; Ge, Z.; Voit, B. Thermally Activated Delayed Fluorescent Polymers: Structures, Properties, and Applications in OLED Devices. *Macromol. Rapid Commun.* **2019**, *40* (1), 1800570. <https://doi.org/10.1002/marc.201800570>.
- (203) Jiang, T.; Liu, Y.; Ren, Z.; Yan, S. The Design, Synthesis and Performance of Thermally Activated Delayed Fluorescence Macromolecules. *Polym. Chem.* **2020**, *11* (9), 1555–1571. <https://doi.org/10.1039/d0py00096e>.
- (204) Zou, Y.; Gong, S.; Xie, G.; Yang, C. Design Strategy for Solution-Processable Thermally Activated Delayed Fluorescence Emitters and Their Applications in Organic Light-Emitting Diodes. *Adv. Opt. Mater.* **2018**, *6* (23), 1–25. <https://doi.org/10.1002/adom.201800568>.
- (205) Huang, T.; Jiang, W.; Duan, L. Recent Progress in Solution Processable TADF Materials for Organic Light-Emitting Diodes. *J. Mater. Chem. C* **2018**, *6* (21), 5577–5596. <https://doi.org/10.1039/c8tc01139g>.
- (206) Xie, Y.; Li, Z. Thermally Activated Delayed Fluorescent Polymers. *J. Polym. Sci. Part A Polym. Chem.* **2017**, *55* (4), 575–584. <https://doi.org/10.1002/pola.28448>.
- (207) Luo, J.; Gong, S.; Gu, Y.; Chen, T.; Li, Y.; Zhong, C.; Xie, G.; Yang, C. Multi-Carbazole Encapsulation as a Simple Strategy for the Construction of Solution-Processed, Non-Doped Thermally Activated Delayed Fluorescence Emitters. *J. Mater. Chem. C* **2016**, *4* (13), 2442–2446. <https://doi.org/10.1039/C6TC00418K>.
- (208) Ban, X.; Jiang, W.; Sun, K.; Lin, B.; Sun, Y. Self-Host Blue Dendrimer Comprised of Thermally Activated Delayed Fluorescence Core and Bipolar Dendrons for Efficient Solution-Processable Nondoped Electroluminescence. *ACS Appl. Mater. Interfaces* **2017**, *9* (8), 7339–7346. <https://doi.org/10.1021/acsami.6b14922>.
- (209) Chatterjee, T.; Wong, K.-T. Perspective on Host Materials for Thermally Activated Delayed Fluorescence Organic Light Emitting Diodes. *Adv. Opt. Mater.* **2019**, *7* (1). <https://doi.org/10.1002/adom.201800565>.
- (210) Nikolaenko, A. E.; Cass, M.; Bourcet, F.; Mohamad, D.; Roberts, M. Thermally Activated Delayed Fluorescence in Polymers: A New Route toward Highly Efficient Solution Processable OLEDs. *Adv. Mater.* **2015**, *27* (44), 7236–7240. <https://doi.org/10.1002/adma.201501090>.
- (211) Aso, F.; Kawashima, H.; Fujiki, M.; Kijima, M. Synthesis of Delayed-Emissive Poly(2,7-Carbazole)s Having an Anchored Triazine Pendant at the: N-Position. *Polym. Chem.* **2019**, *10* (24), 3318–3324. <https://doi.org/10.1039/c9py00152b>.
- (212) Lee, S. Y.; Yasuda, T.; Komiyama, H.; Lee, J.; Adachi, C. Thermally Activated Delayed Fluorescence Polymers for Efficient Solution-Processed Organic Light-Emitting Diodes. *Adv. Mater.* **2016**, *28* (21), 4019–4024. <https://doi.org/10.1002/adma.201505026>.
- (213) Wang, Y.; Zhu, Y.; Xie, G.; Xue, Q.; Tao, C.; Le, Y.; Zhan, H.; Cheng, Y. Red Thermally Activated Delayed Fluorescence Polymers Containing 9H-Thioxanthen-9-One-10,10-Dioxide Acceptor Group as Pendant or Incorporated in Backbone. *Org. Electron.* **2018**, *59*, 406–413. <https://doi.org/10.1016/j.orgel.2018.05.058>.
- (214) Luo, J.; Xie, G.; Gong, S.; Chen, T.; Yang, C. Creating a Thermally Activated Delayed Fluorescence Channel in a Single Polymer System to Enhance Exciton Utilization Efficiency for Bluish-Green Electroluminescence. *Chem. Commun.* **2016**, *52* (11), 2292–2295. <https://doi.org/10.1039/c5cc09797e>.
- (215) Lee, J.; Shizu, K.; Tanaka, H.; Nomura, H.; Yasuda, T.; Adachi, C. Oxadiazole- and Triazole-Based Highly-Efficient Thermally Activated Delayed Fluorescence Emitters for Organic Light-Emitting Diodes. *J. Mater. Chem. C* **2013**, *1* (30), 4599–4604. <https://doi.org/10.1039/c3tc30699b>.
- (216) Zhu, Y.; Zhang, Y.; Yao, B.; Wang, Y.; Zhang, Z.; Zhan, H.; Zhang, B.; Xie, Z.; Wang, Y.; Cheng, Y. Synthesis and Electroluminescence of a Conjugated Polymer with Thermally Activated Delayed Fluorescence. *Macromolecules* **2016**, *49* (11), 4373–4377. <https://doi.org/10.1021/acs.macromol.6b00430>.
- (217) Lin, X.; Zhu, Y.; Zhang, B.; Zhao, X.; Yao, B.; Cheng, Y.; Li, Z.; Qu, Y.; Xie, Z. Highly Efficient TADF Polymer Electroluminescence with Reduced Efficiency Roll-off via Interfacial Exciplex Host Strategy. *ACS Appl. Mater. Interfaces* **2018**, *10* (1), 47–52. <https://doi.org/10.1021/acsami.7b16887>.

- (218) Zhu, Y.; Yang, Y.; Wang, Y.; Yao, B.; Lin, X.; Zhang, B.; Zhan, H.; Xie, Z.; Cheng, Y. Improving Luminescent Performances of Thermally Activated Delayed Fluorescence Conjugated Polymer by Inhibiting the Intra- and Interchain Quenching. *Adv. Opt. Mater.* **2018**, *6* (10), 1701320. <https://doi.org/10.1002/adom.201701320>.
- (219) Wang, Y.; Zhu, Y.; Lin, X.; Yang, Y.; Zhang, B.; Zhan, H.; Xie, Z.; Cheng, Y. Efficient Non-Doped Yellow OLEDs Based on Thermally Activated Delayed Fluorescence Conjugated Polymers with an Acridine/Carbazole Donor Backbone and Triphenyltriazine Acceptor Pendant. *J. Mater. Chem. C* **2018**, *6* (3), 568–574. <https://doi.org/10.1039/C7TC04994C>.
- (220) Yang, Y.; Zhu, Y.; Wang, Y.; Wang, S.; Zhan, H.; Cheng, Y. Synthesis and Electroluminescent Performance of Thermally Activated Delayed Fluorescence-Conjugated Polymers with Simple Formylphenyl as Pendant Acceptor. *J. Polym. Sci. Part A Polym. Chem.* **2018**, *56* (17), 1989–1996. <https://doi.org/10.1002/pola.29085>.
- (221) Yang, Y.; Wang, S.; Zhu, Y.; Wang, Y.; Zhan, H.; Cheng, Y. Thermally Activated Delayed Fluorescence Conjugated Polymers with Backbone-Donor/Pendant-Acceptor Architecture for Nondoped OLEDs with High External Quantum Efficiency and Low Roll-Off. *Adv. Funct. Mater.* **2018**, *28* (10), 1706916. <https://doi.org/10.1002/adfm.201706916>.
- (222) Yang, Y.; Li, K.; Wang, C.; Zhan, H.; Cheng, Y. Effect of a Pendant Acceptor on Thermally Activated Delayed Fluorescence Properties of Conjugated Polymers with Backbone-Donor/Pendant-Acceptor Architecture. *Chem. - An Asian J.* **2019**, *14* (4), 574–581. <https://doi.org/10.1002/asia.201801813>.
- (223) Nobuyasu, R. S.; Ren, Z.; Griffiths, G. C.; Batsanov, A. S.; Data, P.; Yan, S.; Monkman, A. P.; Bryce, M. R.; Dias, F. B. Rational Design of TADF Polymers Using a Donor-Acceptor Monomer with Enhanced TADF Efficiency Induced by the Energy Alignment of Charge Transfer and Local Triplet Excited States. *Adv. Opt. Mater.* **2016**, *4* (4), 597–607. <https://doi.org/10.1002/adom.201500689>.
- (224) Liu, Y.; Wang, Y.; Li, C.; Ren, Z.; Ma, D.; Yan, S. Efficient Thermally Activated Delayed Fluorescence Conjugated Polymeric Emitters with Tunable Nature of Excited States Regulated via Carbazole Derivatives for Solution-Processed OLEDs. *Macromolecules* **2018**, *51* (12), 4615–4623. <https://doi.org/10.1021/acs.macromol.8b00565>.
- (225) Liu, Y.; Xie, G.; Ren, Z.; Yan, S. Thermally Activated Delayed Fluorescence Polymer Emitters with Tunable Emission from Yellow to Warm White Regulated by Triphenylamine Derivatives. *ACS Appl. Polym. Mater.* **2019**, *acsapm.9b00461*. <https://doi.org/10.1021/acsapm.9b00461>.
- (226) Wang, Y.; Zhu, Y.; Xie, G.; Zhan, H.; Yang, C.; Cheng, Y. Bright White Electroluminescence from a Single Polymer Containing a Thermally Activated Delayed Fluorescence Unit and a Solution-Processed Orange OLED Approaching 20% External Quantum Efficiency. *J. Mater. Chem. C* **2017**, *5* (41), 10715–10720. <https://doi.org/10.1039/C7TC03769D>.
- (227) Wang, H.; Xie, L.; Peng, Q.; Meng, L.; Wang, Y.; Yi, Y.; Wang, P. Novel Thermally Activated Delayed Fluorescence Materials—Thioxanthone Derivatives and Their Applications for Highly Efficient OLEDs. *Adv. Mater.* **2014**, *26* (30), 5198–5204. <https://doi.org/10.1002/adma.201401393>.
- (228) Hu, Y.; Cai, W.; Ying, L.; Chen, D.; Yang, X.; Jiang, X.-F.; Su, S.; Huang, F.; Cao, Y. Novel Efficient Blue and Bluish-Green Light-Emitting Polymers with Delayed Fluorescence. *J. Mater. Chem. C* **2018**, *6* (11), 2690–2695. <https://doi.org/10.1039/C7TC04064D>.
- (229) Xie, G.; Luo, J.; Huang, M.; Chen, T.; Wu, K.; Gong, S.; Yang, C. Inheriting the Characteristics of TADF Small Molecule by Side-Chain Engineering Strategy to Enable Bluish-Green Polymers with High PLQYs up to 74% and External Quantum Efficiency over 16% in Light-Emitting Diodes. *Adv. Mater.* **2017**, *29* (11), 1604223. <https://doi.org/10.1002/adma.201604223>.
- (230) Li, Y.; Wei, Q.; Cao, L.; Fries, F.; Cucchi, M.; Wu, Z.; Scholz, R.; Lenk, S.; Voit, B.; Ge, Z.; Reineke, S. Organic Light-Emitting Diodes Based on Conjugation-Induced Thermally Activated Delayed Fluorescence Polymers: Interplay Between Intra- and Intermolecular Charge Transfer States. *Front. Chem.* **2019**, *7*, 688. <https://doi.org/10.3389/fchem.2019.00688>.
- (231) Wei, Q.; Kleine, P.; Karpov, Y.; Qiu, X.; Komber, H.; Sahre, K.; Kiriya, A.; Lygaitis, R.; Lenk, S.; Reineke, S.; Voit, B. Conjugation-Induced Thermally Activated Delayed Fluorescence (TADF): From Conventional Non-TADF Units to TADF-Active Polymers. *Adv. Funct. Mater.*

- 2017, 27 (7), 1–11. <https://doi.org/10.1002/adfm.201605051>.
- (232) Rao, J.; Liu, X.; Li, X.; Yang, L.; Zhao, L.; Wang, S.; Ding, J.; Wang, L. Bridging Small Molecules to Conjugated Polymers: Efficient Thermally Activated Delayed Fluorescence with a Methyl-Substituted Phenylene Linker. *Angew. CHEMIE-INTERNATIONAL Ed.* **2020**, *59* (3), 1320–1326. <https://doi.org/10.1002/anie.201912556>.
- (233) Kim, H. J.; Lee, C.; Godumala, M.; Choi, S.; Park, S. Y.; Cho, M. J.; Park, S.; Choi, D. H. Solution-Processed Thermally Activated Delayed Fluorescence Organic Light-Emitting Diodes Using a New Polymeric Emitter Containing Non-Conjugated Cyclohexane Units. *Polymer Chemistry*. 2018, pp 1318–1326. <https://doi.org/10.1039/c7py02113e>.
- (234) Ren, Z.; Nobuyasu, R. S.; Dias, F. B.; Monkman, A. P.; Yan, S.; Bryce, M. R. Pendant Homopolymer and Copolymers as Solution-Processable Thermally Activated Delayed Fluorescence Materials for Organic Light-Emitting Diodes. *Macromolecules* **2016**, *49* (15), 5452–5460. <https://doi.org/10.1021/acs.macromol.6b01216>.
- (235) Li, C.; Wang, Y.; Sun, D.; Li, H.; Sun, X.; Ma, D.; Ren, Z.; Yan, S. Thermally Activated Delayed Fluorescence Pendant Copolymers with Electron- and Hole-Transporting Spacers. *ACS Appl. Mater. Interfaces* **2018**, *10* (6), 5731–5739. <https://doi.org/10.1021/acsami.8b00136>.
- (236) Li, C.; Nobuyasu, R. S.; Wang, Y.; Dias, F. B.; Ren, Z.; Bryce, M. R.; Yan, S. Solution-Processable Thermally Activated Delayed Fluorescence White OLEDs Based on Dual-Emission Polymers with Tunable Emission Colors and Aggregation-Enhanced Emission Properties. *Adv. Opt. Mater.* **2017**, *5* (20), 1700435. <https://doi.org/10.1002/adom.201700435>.
- (237) Zhou, X.; Huang, M.; Zeng, X.; Chen, T.; Xie, G.; Yin, X.; Yang, C. Combining the Qualities of Carbazole and Tetraphenyl Silane in a Desirable Main Chain for Thermally Activated Delayed Fluorescence Polymers. *Polym. Chem.* **2019**, *10* (30), 4201–4208. <https://doi.org/10.1039/c9py00742c>.
- (238) Park, Y. H.; Jang, H. J.; Lee, J. Y. High Efficiency above 20% in Polymeric Thermally Activated Delayed Fluorescent Organic Light-Emitting Diodes by a Host Embedded Backbone Structure. *Polym. Chem.* **2019**, *10* (35), 4872–4878. <https://doi.org/10.1039/c9py00701f>.
- (239) Zeng, X.; Luo, J.; Zhou, T.; Chen, T.; Zhou, X.; Wu, K.; Zou, Y.; Xie, G.; Gong, S.; Yang, C. Using Ring-Opening Metathesis Polymerization of Norbornene to Construct Thermally Activated Delayed Fluorescence Polymers: High-Efficiency Blue Polymer Light-Emitting Diodes. *Macromolecules* **2018**, *51* (5), 1598–1604. <https://doi.org/10.1021/acs.macromol.7b02629>.
- (240) Li, C.; Ren, Z.; Sun, X.; Li, H.; Yan, S. Deep-Blue Thermally Activated Delayed Fluorescence Polymers for Nondoped Solution-Processed Organic Light-Emitting Diodes. *Macromolecules* **2019**, *52* (6), 2296–2303. <https://doi.org/10.1021/acs.macromol.9b00083>.
- (241) Yang, Y.; Zhao, L.; Wang, S.; Ding, J.; Wang, L. Synthesis and Characterization of Red-Emitting Thermally Activated Delayed Fluorescent Polymers Based on Poly(2,7-Carbazole-Co-3,3'-Dimethyldiphenyl Ether) as the Main Chain. *Acta Polymerica Sinica*. 2019, pp 685–694.
- (242) Yang, Y.; Zhao, L.; Wang, S.; Ding, J.; Wang, L. Red-Emitting Thermally Activated Delayed Fluorescence Polymers with Poly(Fluorene-Co-3,3'-Dimethyl Diphenyl Ether) as the Backbone. *Macromolecules* **2018**, *51* (23), 9933–9942. <https://doi.org/10.1021/acs.macromol.8b02050>.
- (243) Shao, S.; Hu, J.; Wang, X.; Wang, L.; Jing, X.; Wang, F. Blue Thermally Activated Delayed Fluorescence Polymers with Nonconjugated Backbone and Through-Space Charge Transfer Effect. *J. Am. Chem. Soc.* **2017**, *139* (49), 17739–17742. <https://doi.org/10.1021/jacs.7b10257>.
- (244) Hu, J.; Li, Q.; Wang, X.; Shao, S.; Wang, L.; Jing, X.; Wang, F. Developing Through-Space Charge Transfer Polymers as a General Approach to Realize Full-Color and White Emission with Thermally Activated Delayed Fluorescence. *Angew. Chemie - Int. Ed.* **2019**, *58* (25), 8405–8409. <https://doi.org/10.1002/anie.201902264>.
- (245) Chen, F.; Hu, J.; Wang, X.; Shao, S.; Wang, L.; Jing, X.; Wang, F. Synthesis and Electroluminescent Properties of Through-Space Charge Transfer Polymers Containing Acridan Donor and Triarylboron Acceptors. *Front. Chem.* **2019**, *7* (December), 1–10. <https://doi.org/10.3389/fchem.2019.00854>.
- (246) Tonge, C. M.; Hudson, Z. M. Interface-Dependent Aggregation-Induced Delayed Fluorescence

- in Bottlebrush Polymer Nanofibers. *J. Am. Chem. Soc.* **2019**, *141* (35), 13970–13976. <https://doi.org/10.1021/jacs.9b07156>.
- (247) Li, C.; Xu, Y.; Liu, Y.; Ren, Z.; Ma, Y.; Yan, S. Highly Efficient White-Emitting Thermally Activated Delayed Fluorescence Polymers: Synthesis, Non-Doped White OLEDs and Electroluminescent Mechanism. *Nano Energy* **2019**, *65* (August). <https://doi.org/10.1016/j.nanoen.2019.104057>.
- (248) Polgar, A. M.; Poisson, J.; Paisley, N. R.; Christopherson, C. J.; Reyes, A. C.; Hudson, Z. M. Blue to Yellow Thermally Activated Delayed Fluorescence with Quantum Yields near Unity in Acrylic Polymers Based on D- $\pi$ -A Pyrimidines. *Macromolecules* **2020**. <https://doi.org/10.1021/acs.macromol.0c00287>.
- (249) BROWN, C. J.; FARTHING, A. C. Preparation and Structure of Di-p-Xylylene. *Nature* **1949**, *164* (4178), 915–916. <https://doi.org/10.1038/164915b0>.
- (250) Shen, P.; Zhuang, Z.; Jiang, X. F.; Li, J.; Yao, S.; Zhao, Z.; Tang, B. Z. Through-Space Conjugation: An Effective Strategy for Stabilizing Intramolecular Charge-Transfer States. *J. Phys. Chem. Lett.* **2019**, *10* (11), 2648–2656. <https://doi.org/10.1021/acs.jpcclett.9b01040>.
- (251) Zafra, J. L.; Molina Ontoria, A.; Mayorga Burrezo, P.; Pena-Alvarez, M.; Samoc, M.; Szeremeta, J.; Ramirez, F. J.; Lovander, M. D.; Droske, C. J.; Pappenfus, T. M.; Echegoyen, L.; Lopez Navarrete, J. T.; Martin, N.; Casado, J. Fingerprints of Through -Bond and Through -Space Exciton and Charge Pi -Electron Delocalization in Linearly Extended {[2.2]Paracyclophanes}. *J. Am. Chem. Soc.* **2017**, *139* (8), 3095–3105. <https://doi.org/10.1021/jacs.6b12520>.
- (252) Tanaka, Y.; Akita, M. Synthesis and Intramolecular Electronic Interactions of Hexaarylbenzene Bearing Redox-Active Cp\*(Dppe)Fe-C $\equiv$ C- Termini. *J. Organomet. Chem.* **2018**, *878*, 30–37. <https://doi.org/https://doi.org/10.1016/j.jorganchem.2018.10.002>.
- (253) Schmidt, H. C.; Spulber, M.; Neuburger, M.; Palivan, C. G.; Meuwly, M.; Wenger, O. S. Charge Transfer Pathways in Three Isomers of Naphthalene-Bridged Organic Mixed Valence Compounds. *J. Org. Chem.* **2016**, *81* (2), 595–602. <https://doi.org/10.1021/acs.joc.5b02427>.
- (254) Tsujimoto, H.; Ha, D.-G.; Markopoulos, G.; Chae, H. S.; Baldo, M. A.; Swager, T. M. Thermally Activated Delayed Fluorescence and Aggregation Induced Emission with Through-Space Charge Transfer. *J. Am. Chem. Soc.* **2017**, *139* (13), 4894–4900. <https://doi.org/10.1021/jacs.7b00873>.
- (255) Kawasumi, K.; Wu, T.; Zhu, T.; Chae, H. S.; Van Voorhis, T.; Baldo, M. A.; Swager, T. M. Thermally Activated Delayed Fluorescence Materials Based on Homoconjugation Effect of Donor–Acceptor Triptycenes. *J. Am. Chem. Soc.* **2015**, *137* (37), 11908–11911. <https://doi.org/10.1021/jacs.5b07932>.
- (256) Ye, J. T.; Wang, L.; Wang, H. Q.; Pan, X. M.; Xie, H. M.; Qiu, Y. Q. Effective Impact of Dielectric Constant on Thermally Activated Delayed Fluorescence and Nonlinear Optical Properties: Through-Bond/-Space Charge Transfer Architectures. *J. Phys. Chem. C* **2018**, *122* (33), 18850–18859. <https://doi.org/10.1021/acs.jpcc.8b05411>.
- (257) Woon, K. L.; Yi, C. L.; Pan, K. C.; Etherington, M. K.; Wu, C. C.; Wong, K. T.; Monkman, A. P. Intramolecular Dimerization Quenching of Delayed Emission in Asymmetric D-D'-A TADF Emitters. *J. Phys. Chem. C* **2019**, *123* (19), 12400–12410. <https://doi.org/10.1021/acs.jpcc.9b01900>.
- (258) Spuling, E.; Sharma, N.; Samuel, I. D. W.; Zysman-Colman, E.; Bräse, S. (Deep) Blue through-Space Conjugated TADF Emitters Based on [2.2]Paracyclophanes. *Chem. Commun.* **2018**, *54* (67), 9278–9281. <https://doi.org/10.1039/c8cc04594a>.
- (259) Auffray, M.; Kim, D. H.; Kim, J. U.; Bencheikh, F.; Kreher, D.; Zhang, Q.; D'Aleo, A.; Ribierre, J.-C.; Mathevet, F.; Adachi, C. Dithia[3.3]Paracyclophane Core: A Versatile Platform for Triplet State Fine-Tuning and Through-Space TADF Emission. *Chem. ASIAN J.* **2019**, *14* (11), 1921–1925. <https://doi.org/10.1002/asia.201900401>.
- (260) Sharma, N.; Spuling, E.; Mattern, C. M.; Li, W.; Fuhr, O.; Tsuchiya, Y.; Adachi, C.; Bräse, S.; Samuel, I. D. W.; Zysman-Colman, E. Turn on of Sky-Blue Thermally Activated Delayed Fluorescence and Circularly Polarized Luminescence (CPL): Via Increased Torsion by a Bulky Carbazolophane Donor. *Chem. Sci.* **2019**, *10* (27), 6689–6696. <https://doi.org/10.1039/c9sc01821b>.

- (261) Gao, F.; Du, R.; Han, C.; Zhang, J.; Wei, Y.; Lu, G.; Xu, H. High-Efficiency Blue Thermally Activated Delayed Fluorescence from Donor-Acceptor-Donor Systems: Via the through-Space Conjugation Effect. *Chem. Sci.* **2019**, *10* (21), 5556–5567. <https://doi.org/10.1039/c9sc01240k>.
- (262) Wang, Y.-K.; Huang, C.-C.; Ye, H.; Zhong, C.; Khan, A.; Yang, S.-Y.; Fung, M.-K.; Jiang, Z.-Q.; Adachi, C.; Liao, L.-S. Through Space Charge Transfer for Efficient Sky-Blue Thermally Activated Delayed Fluorescence (TADF) Emitter with Unconjugated Connection. *Adv. Opt. Mater.* **2020**, *8* (2). <https://doi.org/10.1002/adom.201901150>.
- (263) Vij, V.; Bhalla, V.; Kumar, M. Hexaarylbenzene: Evolution of Properties and Applications of Multitalented Scaffold. *Chem. Rev.* **2016**, *116* (16), 9565–9627. <https://doi.org/10.1021/acs.chemrev.6b00144>.
- (264) Wang, X.; Wang, S.; Lv, J.; Shao, S.; Wang, L.; Jing, X.; Wang, F. Through-Space Charge Transfer Hexaarylbenzene Dendrimers with Thermally Activated Delayed Fluorescence and Aggregation-Induced Emission for Efficient Solution-Processed OLEDs. *Chem. Sci.* **2019**, *10* (10), 2915–2923. <https://doi.org/10.1039/c8sc04991b>.
- (265) Li, B.; Nomura, H.; Miyazaki, H.; Zhang, Q.; Yoshida, K.; Suzuma, Y.; Orita, A.; Otera, J.; Adachi, C. Dicarbazolyldicyanobenzenes as Thermally Activated Delayed Fluorescence Emitters: Effect of Substitution Position on Photoluminescent and Electroluminescent Properties. *Chem. Lett.* **2014**, *43* (3), 319–321. <https://doi.org/10.1246/cl.130907>.
- (266) Pan, K. C.; Li, S. W.; Ho, Y. Y.; Shiu, Y. J.; Tsai, W. L.; Jiao, M.; Lee, W. K.; Wu, C. C.; Chung, C. L.; Chatterjee, T.; Li, Y. S.; Wong, K. T.; Hu, H. C.; Chen, C. C.; Lee, M. T. Efficient and Tunable Thermally Activated Delayed Fluorescence Emitters Having Orientation-Adjustable CN-Substituted Pyridine and Pyrimidine Acceptor Units. *Adv. Funct. Mater.* **2016**, *26* (42), 7560–7571. <https://doi.org/10.1002/adfm.201602501>.
- (267) Cvejn, D.; Michail, E.; Polyzos, I.; Almonasy, N.; Pytela, O.; Klikar, M.; Mikysek, T.; Giannetas, V.; Fakis, M.; Bureš, F. Modulation of (Non)Linear Optical Properties in Tripodal Molecules by Variation of the Peripheral Cyano Acceptor Moieties and the  $\pi$ -Spacer. *J. Mater. Chem. C* **2015**, *3* (28), 7345–7355. <https://doi.org/10.1039/c5tc01293g>.
- (268) Hyvl, J.; Yoshida, W. Y.; Rheingold, A. L.; Hughes, R. P.; Cain, M. F. A Masked Phosphinidene Trapped in a Fluxional NCN Pincer. *Chem. – A Eur. J.* **2016**, *22* (49), 17562–17565. <https://doi.org/10.1002/chem.201604415>.
- (269) Zhang, Z.; Zheng, Y.; Sun, Z.; Dai, Z.; Tang, Z.; Ma, J.; Ma, C. Direct Olefination of Fluorinated Quinoxalines via Cross- Dehydrogenative Coupling Reactions: A New Near-Infrared Probe for Mitochondria. *Adv. Synth. Catal.* **2017**, *359* (13), 2259–2268. <https://doi.org/10.1002/adsc.201700237>.
- (270) Chen, F.; Hu, J.; Wang, X.; Shao, S.; Wang, L.; Jing, X.; Wang, F. Synthesis and Electroluminescent Properties of Through-Space Charge Transfer Polymers Containing Acridan Donor and Triarylboron Acceptors. *Front. Chem.* **2019**, *7*. <https://doi.org/10.3389/fchem.2019.00854>.
- (271) Fulmer, G. R.; Miller, A. J. M.; Sherden, N. H.; Gottlieb, H. E.; Nudelman, A.; Stoltz, B. M.; Bercaw, J. E.; Goldberg, K. I. NMR Chemical Shifts of Trace Impurities: Common Laboratory Solvents, Organics, and Gases in Deuterated Solvents Relevant to the Organometallic Chemist. *Organometallics* **2010**, *29* (9), 2176–2179. <https://doi.org/10.1021/om100106e>.
- (272) Betson, M. S.; Clayden, J.; Worrall, C. P.; Peace, S. Three Groups Good, Four Groups Bad? Atropisomerism in Ortho-Substituted Diaryl Ethers. *Angew. Chemie Int. Ed.* **2006**, *45* (35), 5803–5807. <https://doi.org/10.1002/anie.200601866>.



## Abstract

In this work, new  $\pi$ -conjugated polymers were designed for the OFET and/or OLED applications.

First, two side-chain liquid-crystalline  $\pi$ -conjugated polymers, i.e. **Polythiophene-oxa** and **PBTTT-Tri**, consisting of  $\pi$ -conjugated backbones bearing side-on semiconducting mesogenic groups, were successfully prepared and their structures were determined by NMR, SEC, and elemental analysis. The thermal behavior and self-organization study indicated that **Polythiophene-oxa** and **PBTTT-Tri** can self-organize to lamello-lamellar and columnar-lamellar nanostructures, respectively. Moreover, both polymers exhibit p-type conduction.

Second, four families of new donor-acceptor (D-A) polymers were designed as potential TADF materials. Among them, two families are linear conjugated polymers, and the other two families are vinyl polymers with through-space conjugation (TSC). Their structures were also determined by NMR, SEC, and elemental analysis, and their photophysical properties were investigated. The results revealed that only **S1**, **S2**, and **S4** series exhibit TADF character, among them, **S4** polymers achieve the best performance, which is really encouraging. Anyway, their photophysical properties in blend films and electroluminescent properties will be investigated soon.

Keywords:  $\pi$ -conjugated polymers, organic field-effect transistors (OFETs), thermally activated delayed fluorescence (TADF)



## Résumé en français

Après la découverte de la propriété de conductivité du polyacétylène par A. J. Heeger, A. G. MacDiarmid et H. Shirakawa en 1977, les systèmes organiques  $\pi$ -conjugués et en particulier les polymères, ont été intensivement étudiés. Depuis lors, de nombreux groupes de recherche de premier plan ont conçu, synthétisé et étudié les propriétés de transport de charge de nombreux **semi-conducteurs organiques (OSC)** afin de les incorporer à terme dans des dispositifs électroniques spécifiques, afin de remplacer les semi-conducteurs inorganiques bien connus tels que le silicium.

En effet, ces OSC sont attrayants essentiellement parce qu'ils peuvent tirer parti des propriétés des matériaux organiques, tels que la légèreté, le faible coût potentiel et la fabrication efficace de dispositifs en couches minces et flexibles. Par conséquent, de nos jours, les molécules OSC et les macromolécules sont déjà introduites comme couche active dans les composants électroniques tels que les diodes électroluminescentes organiques (OLED), les cellules photovoltaïques organiques (OPV) et les transistors à effet de champ organique (OFET).

**Pour concevoir ces matériaux OSC pour des applications spécifiques**, il est important de comprendre comment la modification chimique modifie les propriétés électroniques et photophysiques : c'est pourquoi **plusieurs stratégies sont apparues comme des moyens très efficaces pour atteindre cet objectif.**

- L'incorporation de substituants attracteurs d'électrons sur la périphérie des systèmes  $\pi$  peut améliorer la stabilité à l'oxydation de ces structures organiques tout en augmentant l'affinité électronique.
- Le remplacement d'éléments (en particulier les éléments de pontage au sein du système  $\pi$ ) s'avère également efficace pour modifier la structure électronique et influencer l'empilement dans le matériau.
- Enfin, l'utilisation de noyaux aromatique fusionnés donc plus rigides pour générer des systèmes aromatiques polycycliques, peut modifier les énergies des orbitales frontières et moduler/réduire la bande interdite.

**Au cours de ce travail de thèse, ces stratégies ont toutes été utilisées, en conjonction avec un couplage croisé pour créer une large gamme de polymères conjugués.**

Plus précisément, nous nous sommes intéressés au **design, à la synthèse et à la caractérisation de nouveaux polymères  $\pi$ -conjugués spécialement imaginés pour des applications en OFET et en OLED.**

- **Un premier objectif a été de préparer deux polymères  $\pi$ -conjugués liquide-cristallins à groupes pendants**, nommés Polythiophene-oxa et PBT-TT-Tri, qui peuvent s'autoorganiser en nanostructures ordonnées et qui présentent une conduction de type p (transporteur de trous).
- **Un second objectif a été d'explorer 2 familles de nouveaux polymères D-A pouvant présenter un activité TADF (fluorescence retardée activée thermiquement)**: une première famille est composée de polymères (S1, S2) présentant un squelette donneur de carbazole ou acridan et des groupements accepteurs (tels que dicyano-benzene ou cyano-pyrimidine) en groupes pendants. La deuxième famille se compose de deux nouvelles séries de polymères vinylique (S3, S4) à base des mêmes groupement donneurs et accepteurs utilisés dans la première famille, interagissant à travers l'espace. Les propriétés photophysiques en solution et en film de ces composés ont été étudiées et leurs activités TADF ont été caractérisées.

Aussi, c'est la raison pour laquelle dans cette thèse, **le chapitre 1 fournit une introduction générale décrivant les principes de conception et les méthodes de synthèse contrôlée pour le réglage des propriétés électroniques des polymères semi-conducteurs organiques conjugués** en général, avant de décrire également certaines méthodes spécifiques de synthèse contrôlée. Par la suite, nous présentons dans le chapitre 2 (respectivement chapitre 3) la conception, la synthèse et la caractérisation de nouveaux polymères testés comme alternatives aux OFET (respectivement OLED).

**Le chapitre 2 traite de la conception, de la synthèse et de la caractérisation de nouveaux polymères structurés  $\pi$ -conjugués pour les applications OFET.** En effet, dans ce contexte, les propriétés de transport des porteurs de charges dépendent non seulement des propriétés électroniques intrinsèques des matériaux, mais également de la manière dont les molécules sont emballées ensemble en vrac. Par conséquent, l'un des paramètres clés pour améliorer les performances de tels composants à base organique est le développement de systèmes  $\pi$ -conjugués structurés et / ou plus ordonnés. Des exemples technologiques représentatifs sont le domaine de la microélectronique organique où la structuration des semi-conducteurs à canal p et n est l'un des principaux obstacles à l'implantation de l'OSC dans un circuit logique complémentaire organique.

**La première partie de ce chapitre 2 est consacrée à la bibliographie** dans ce domaine spécifique (section 2.1): nous détaillons brièvement les mécanismes fondamentaux régissant les OFET, avant de décrire différentes familles de matériaux cristaux liquides. Ensuite, nous présentons une classe de matériaux organiques capables de donner spontanément des auto-assemblages, c'est-à-dire des cristaux liquides organiques, en se concentrant sur les systèmes  $\pi$ -conjugués et notamment les polymères.

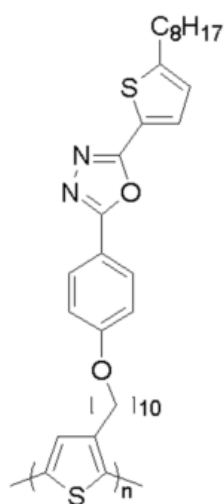
**Les deux sections de résultats suivantes (sections 2.2 et 2.3) traitent de la conception, de la synthèse et de la caractérisation de nouveaux matériaux  $\pi$ -conjugués structurés cristaux liquides pour les futures applications OFET, à la recherche de propriétés ambipolaires potentielles.** En

effet, seules quelques nanostructures présentant les deux propriétés électroniques différentes, telles que les comportements des donneurs d'électrons et des accepteurs d'électrons, ont été étudiées jusqu'à présent pour les applications OFET.

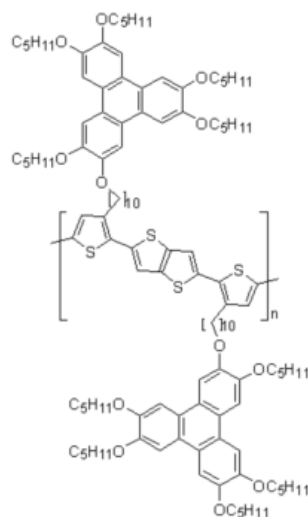
Plus précisément, **dans la section 2.2, nous décrivons la synthèse et la caractérisation d'une architecture supramoléculaire résultant de la séparation de phase, à l'échelle nanométrique, de deux systèmes  $\pi$ -conjugués liés de manière covalente.** Nous rapportons l'étude d'un polymère dit (Polythiophène-oxa), composé d'un poly (3-alkylthiophène) donneur d'électrons régiorégulier comme squelette et d'entités calamitiques types oxadiazole accepteurs d'électrons comme groupes latéraux.

**Dans la section 2.3, de même sont explorées les propriétés d'un polymère nommé (PBTTT-Tri)** qui consiste cette fois en un squelette de type donneur étendu, à savoir le poly (2,5-bis (3-alkylthiophén-2-yl) thiéno [3,2-b] thiophène) (PBTTT), ainsi que des groupes latéraux discotiques de type triphénylène comme contrepartie accepteur.

**Pour les deux types d'architectures macromoléculaires,** nous décrivons d'abord l'optimisation de la stratégie de synthèse mise au point, avant de présenter la structure chimique mise en évidence par RMN et SEC essentiellement. Deuxièmement, le comportement thermique et d'auto-organisation des polymères est étudié plus en détail par POM, DSC et XRD. Troisièmement, les propriétés préliminaires de transport de charge des matériaux, évaluées en configuration OFET, sont discutées. Enfin, nous concluons cette partie par quelques perspectives basées sur les nouvelles lignes directrices de conception que nous avons pu tirer de cette étude.



**Polythiophene-oxa**



**PBTTT-TRI**

**Concernant nos apports dans le cas du (Polythiophène-oxa),** nous avons tout d'abord développé une voie chimique innovante, même si le nombre d'étapes est plus long, pour atteindre un monomère de thiophène à substitution bromo-alkyle plus pur, conduisant à une méthode améliorée de préparation

du squelette polythiophène à substitution bromo-alkyle précurseur régiorégulier. Ensuite, le polymère final, obtenu par post-fonctionnalisation du polymère précurseur, présente une faible polydispersité et un greffage complet des groupements latéraux. Il a été démontré également que ce matériau s'auto-organise avec une alternance de bicouches de groupes latéraux mésogènes calamitiques et de monocouches de squelette polythiophène. Une première tentative de dispositif a été testée afin d'évaluer sa propriété de transport de charge, en configuration OFET : une conduction de trou avec une mobilité d'environ  $1,2 \times 10^{-3} \text{ cm}^2 \cdot \text{V}^{-1} \cdot \text{s}^{-1}$  a été mesurée.

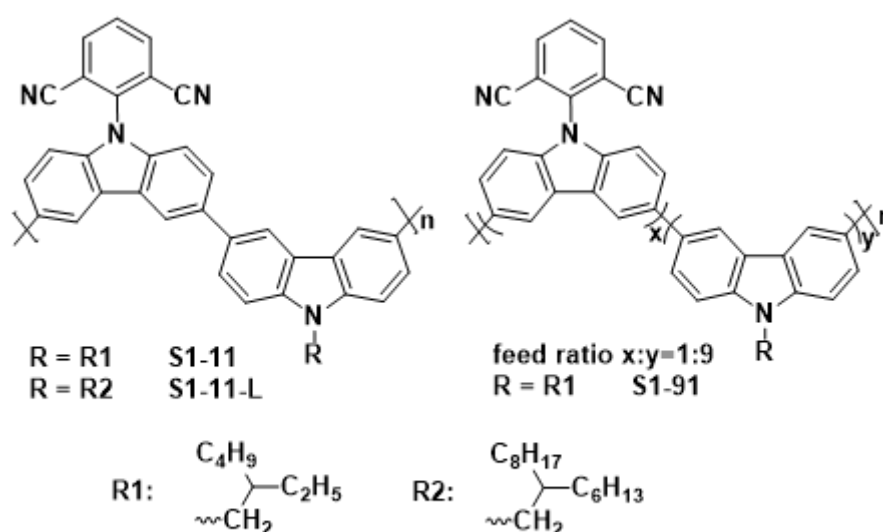
**Pour résumer l'essentiel à propos des autres matériaux du chapitre 2**, nous avons conçu deux nouveaux polymères à chaîne latérale cristaux liquides (PBTTT-Tri et PBTTT-oxa), présentant le poly(2,5-bis(3-alkylthiophène-2-yl) thiéno [3,2- b] thiophène) comme squelette. Cependant, en raison d'une trop faible solubilité, seul le PBTTT-Tri a été synthétisé avec succès, sa structure chimique étant confirmée par des mesures RMN et SEC. Pour cela, premièrement, nous avons reproduit le dérivé monohydroxy triphénylène (Tri) et 2- (4-décyloxy-phényl) -5- (5-octyl-thiophène-2-yl) - [1,3,4] oxadiazole (OF) comme groupes latéraux, selon des procédures optimisées. Deuxièmement, nous avons réussi à synthétiser le monomère BTTT souhaité en cinq étapes, suivi d'un couplage de Stille assisté par micro-ondes pour préparer le précurseur PBTTT-Br, avec un rendement assez élevé de 90%. Enfin, deux polymères (PBTTT-Tri et PBTTT-oxa) ont été préparés par réaction de Williamson, mais seul du PBTTT-Tri pur a été obtenu, avec un rendement de 80%. PBTTT-Tri présente des propriétés cristal liquide et s'auto-organise dans un agencement supramoléculaire avec l'alternance de triples rangées de colonnes de triphénylène et de la monocouche de squelette parallèle au plan du substrat. Une première tentative d'évaluation de ses propriétés de transport de charge a été effectuée en configuration OFET. PBTTT-Tri présente une conduction de type p et sa mobilité des trous en régime saturé est d'environ  $1,2 \times 10^{-5} \text{ cm}^2 \cdot \text{V}^{-1} \cdot \text{s}^{-1}$ .

**Le chapitre 3 du manuscrit débute par une introduction dédiée à la bibliographie** (section 3.1): nous présentons brièvement les mécanismes fondamentaux relatifs aux OLED, avant de détailler les mécanismes fondamentaux du TADF, les relations structure-propriété dans les molécules TADF, ainsi que la photophysique des molécules TADF. Ensuite, nous décrivons quelques exemples des matériaux TADF rapportés dans la littérature, y compris les petites molécules et les dendrimères, mais en insistant en particulier sur les polymères linéaires. Enfin, nous discutons certains aspects liés à la conjugaison « à travers l'espace ».

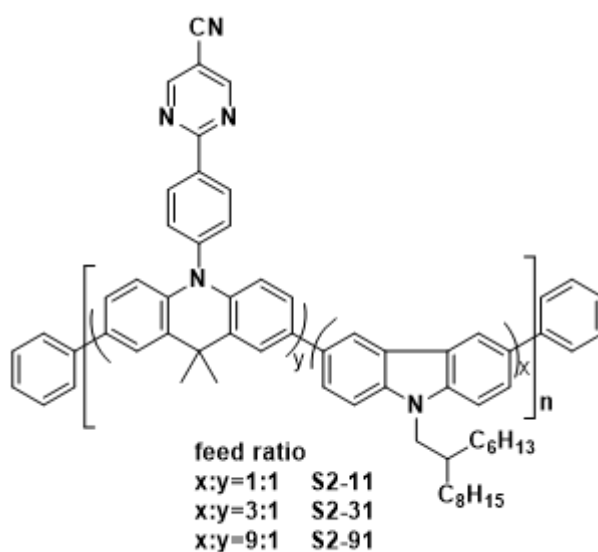
**Les quatre sections de résultats suivantes** (section 3.2-3.5) traitent de la conception, de la synthèse et de la caractérisation de différentes familles de polymères Donneur-Accepteur qui sont rapportées sur la figure ci-après, censés présenter des comportements TADF. Plus précisément, **deux grandes familles de polymères seront étudiées**: dans la section 3.2 et la section 3.3, nous étudierons la première famille constituée de deux nouvelles séries de polymères TADF linéaires potentiels (séries S1 et S2) basées sur un squelette donneur et accepteur à base de carbazole des fragments tels que le

dicyano-benzène ou la cyano-pyrimidine, greffés en tant que groupes latéraux. Dans la section 3.4 et la section 3.5, nous étudierons la deuxième famille composée de deux nouvelles séries de polymères TADF potentiels basés sur la conjugaison à travers l'espace (TSC) entre les mêmes unités donneur et accepteur que celles utilisées dans la première famille (séries S3 et S4).

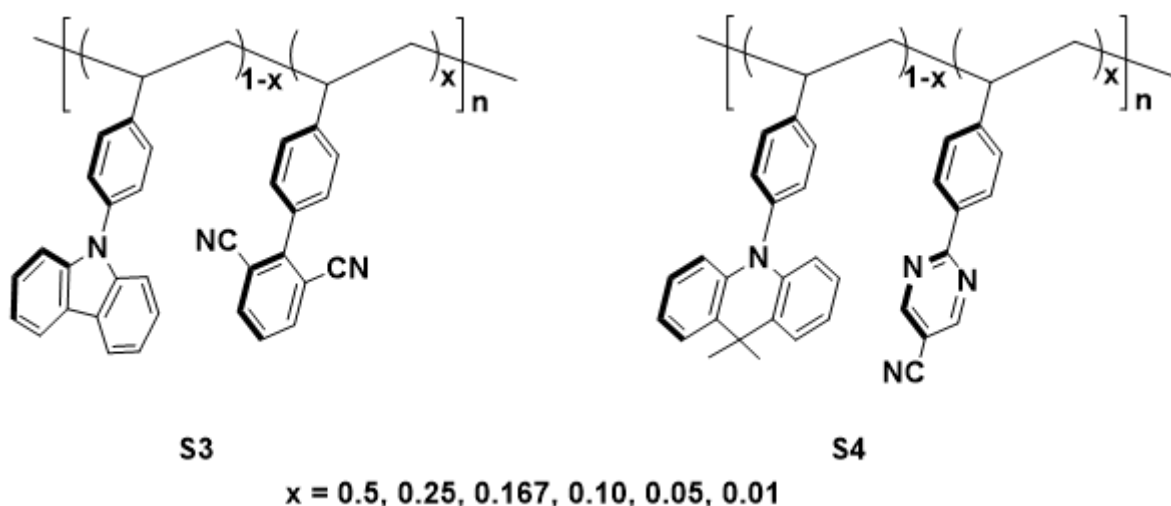
Concernant ces quatre séries de polymères envisagés pour tenter d'obtenir des matériaux TADF potentiels, dans tous les cas, nous décrivons d'abord leur synthèse, avant de les caractériser complètement. En particulier, leurs propriétés photophysiques seront vérifiées en solution, à l'état solide mais aussi dans des configurations de dispositifs, pour tenter de trouver des règles et des relations structure / propriétés qui pourraient être généralisées ultérieurement. Les premiers dispositifs OLED sont finalement réalisés et testés, en collaboration avec le laboratoire OPERA (Japon).



**S1**



**S2**



**Concernant la première famille S1**, pour résumer, ces polymères à émission verte avec du poly (3,6-carbazole) comme squelette et de l'isophthalonitrile comme groupes latéraux, ont été préparés avec succès par polycondensation de Suzuki. Les structures chimiques des monomères et de tous les polymères S1 ont été confirmées par RMN, SEC et par analyse élémentaire. De plus, les spectres d'absorption, d'émission et de phosphorescence (17K) ont été enregistrés en solution et à l'état solide. À partir de ces spectres, nous avons déterminé les niveaux d'énergie des états singulets et des triplets, pour calculer des valeurs de différence entre les états singulet et triplet  $\Delta E_{ST}$  de 0,01-0,02 eV, ce qui suggère d'éventuelles propriétés TADF. De plus, la spectroscopie photoélectronique en films combinée à des mesures optiques résolues en temps, ont mis en évidence que S1-11, S1-11-L et S1-91 présentent une activité TADF à la fois en solution et à l'état solide. Le mCP a enfin été choisi comme matériau hôte pour la réalisation des films en mélange, afin d'améliorer nettement les rendements quantiques d'émission (PLQY) à l'état solide. Parmi les polymères, S1-11-L détient le PLQY le plus élevé (29%) dans le toluène sans oxygène. Par contre en film pur, un PLQY faible de 1,7% dans l'argon est observé, cette valeur pouvant être améliorée (24%) en préparant un film dopé mCP à 5% en poids. Cependant, par rapport aux polymères TADF rapportés dans la littérature, les PLQY de cette série S1 sont assez modestes.

**Concernant la deuxième famille S2**, nous avons conçu et synthétisé une nouvelle série de polymères TADF émettant dans le jaune avec acridine / carbazole dans le squelette et des unités cyano-pyrimidine comme groupes latéraux. Les polymères S2 ont été préparés avec succès par polycondensation de Suzuki, comme prouvé par RMN, SEC et analyse élémentaire. Leurs propriétés photophysiques ont été étudiées en solution (toluène et  $\text{CHCl}_3$ ) et à l'état solide également, en particulier par des mesures résolues dans le temps. Les spectres d'absorption UV-Vis, PL et phosphorescence (17K) ont été enregistrés, pour de nouveau estimer les positions HOMO et LUMO puis évaluer les  $\Delta E_{ST}$  (0,06-0,1 eV) ont de nouveau été estimées suggérant des propriétés TADF potentielles. Ces niveaux d'énergie HOMO / LUMO ont été corrélés avec ceux obtenus déterminés

dans des films purs par spectroscopie photoélectronique. Plus intéressant, à partir des mesures résolues en temps, nous pouvons confirmer que tous les polymères S2 présentent une activité TADF. S2-31 détient le PLQY le plus élevé, 44% dans le toluène sans oxygène. Dans un film pur, des PLQY sont plus faibles, de 6% à 23%, même sous argon, mais une valeur aussi élevée de 44% peut être observée en préparant un film dopé CBP à 5% en poids (S2-11). Enfin, un dispositif OLED à base d'un film de mélange S2-11 CBP comme couche émettrice EML a été préparé et a atteint une luminance maximale ( $L_{max}$ ) de around 5600 cd / m<sup>2</sup>, avec un rendement quantique externe EQE de 1,9%. Ce résultat est encourageant et pourrait être encore optimisé.

**Concernant la troisième famille S3**, des polymères vinyliques avec des interactions TSB entre les unités donneur (carbazole) et accepteur (isophtalonitrile), nous avons d'abord synthétisé avec succès les monomères donneur et accepteur en 6 étapes. Les polymères S3 ont alors été préparés par polymérisation radicalaire à 60 ° C pendant 48 h avec 5% d'AIBN comme initiateur et du toluène sec comme solvant. Les structures chimiques des monomères et des polymères ont été confirmées par RMN du proton et du carbone. Les mesures SEC ont démontré que les polymères S3 maintiennent les poids moléculaires moyens en nombre relatifs ( $M_n$ , SEC) de 18-27 kDa, avec un indice de polydispersité ( $M_w/M_n$ ) de 1,40-1,76 et un degré de polymérisation ( $X_n$ ) entre 67 et 103. De plus, la composition réelle de ces polymères a pu être calculée à partir de l'analyse élémentaire. La photophysique complète a été effectuée. Le niveau d'énergie optique ( $E_g$ ), les niveaux d'énergie singulet et triplet des polymères ont aussi été déterminés à partir des spectres d'absorption UV-Vis, de photoluminescence et de phosphorescence à l'état solide. Les courbes de décroissance de photoluminescence en temps (PL transitoire) sous atmosphère d'air et d'azote montrent de plus des changements fonction de la teneur en oxygène, ce qui suggère que les états triplets sont impliqués. Cette observation est également en accord avec les changements de valeur des PLQY : de 46 à 65%, ils diminuent beaucoup en présence d'oxygène. Et dans les films purs, les PLQY ne sont que de 13 à 15%, révélant la présence d'un quenching provoqué par l'agrégation à l'état solide. Tout ceci a été confirmé par des analyses en température de 50 à 300K et sous vide. Cette série ne présente donc pas de propriétés TADF à l'état solide : cela pourrait s'expliquer par un  $\Delta E_{ST}$  relativement importante ( $> 0,27$  eV) pour cette série.

**Concernant la quatrième et dernière famille S4**, nous avons suivi une stratégie de synthèse équivalente. De plus, les mesures SEC ont démontré que les poids moléculaires moyens en nombre relatifs ( $M_n$ , SEC) de ces polymères vont de 19 à 39 kDa, avec un indice de polydispersité relativement faible (1,44-1,98). De plus, un petit  $\Delta E_{ST}$  de 0,03-0,05 eV a été calculé cette fois-ci, indiquant une possible conversion ascendante facile des états triplet en singulet (RISC). L'étude des propriétés photophysiques de ces polymères en solution et en film pur a été également réalisée. Dans le toluène, les PLQY sont d'environ 57 à 63% sans oxygène et les mesures de photoluminescence résolues en temps ont montré des propriétés TADF appropriées, avec des durées de vie de fluorescence de plusieurs  $\mu s$ . À l'état solide (film pur), les PLQY des polymères ont atteint des valeurs

relativement élevées telles que 52% pour le S4-91, confirmant les propriétés TADF de ces systèmes macromoléculaires conjugués à travers l'espace. Le potentiel de ces matériaux dans les OLED sera étudié très prochainement et nous nous attendons à des rendements relativement bons.

**En conclusion,** ce travail de thèse permet de confirmer l'importance de l'optimisation du design moléculaire en vue d'améliorer les propriétés des matériaux, à l'état solide, en configuration dispositifs, que ce soit pour optimiser les propriétés de transport (dans le cas des applications OFETs) ou pour des applications types éclairage (dans le cas des OLEDs).